A Numerical Study of Stretch Forming over a Sparsely Populated Reconfigurable Die

John Kelly

MEng (Distinction) Mechanical Engineering

AMFOR

Faculty of Computing and Engineering

Ulster University

Thesis submitted for the degree of Doctor of Philosophy

October 2017

I confirm that the word count of this thesis is less than 100,000 words

Contents

Contents i
List of Figures v
List of Tables xxi
Acknowledgements xxii
Abstract xxiii
Nomenclature xxiv
Note on Access to Contents xxxi
Chapter 1. Introduction 1
1.1 Background 1
1.2 Sheet Metal Stretch Forming Processes 2
1.2.1 Drape Forming 3
1.2.2 Advantages and Disadvantages of Stretch Forming 4
1.3 Stretch Forming over Reconfigurable Tooling 5
1.3.1 Advantages and Disadvantages of Stretch Forming over Reconfigurable Tooling 6
1.3.2 Recent Research into Stretch Forming over Reconfigurable Tooling 7
1.4 Aims and Objectives 8
1.5 Methodology 9
Chapter 2. Literature Review 12
2.1 Introduction 12
2.2 Early Research into Reconfigurable Tooling 12
2.3 MIT and the RTFF Project 15
2.3.1 Modelling of the RTFF Process 21
2.4 The DATAFORM Project 23
2.4.1 Modelling of the DATAFORM Process 25
2.4.2 The DATAFORM Gripping/Stretching System 28
2.4.3 DATAFORM Case Studies 31
2.5 Recent Research from Other Sources 32
2.6 2007 Review of Reconfigurable Tooling 36
2.7 Conclusions 42

Chapter 3. Material Characterisation 46
3.1 Introduction 46
3.2 The 2024-T3 Material Model 48
3.3 The 316L Material Model 52
3.3.1 Strain Rate Sensitivity 60
3.3.2 Validation of the 316L Material Models 64
3.4 Loads Transmitted to the Interpolator from the 316L Material during a Stretch Forming Process 66
3.5 The Interpolator Material Models 69
3.5.1 Validation of the Interpolator Material Models 74
3.5.2 Cyclic Loading of Interpolator Materials 78
3.6 Conclusions 85
Chapter 4. Pin Geometry and Arrangement 88
4.1 Introduction 88
4.2 Simulation Parameters 89
4.3 Phase 1 Pin Shape and Die Layouts 93
4.4 Phase 1 Results 98
4.5 Phase 2 Pivoted Pin Tips 113
4.6 Phase 2 Results 115
4.7 Simulation Mesh Size Comparison 121
4.8 A Disadvantage of the HCP Pin Arrangement 122
4.9 Conclusions 124
Chapter 5. Process Modelling and Interpolator Selection 126
5.1 Introduction 126
5.2 The Preferred AMFOR Machine Layout 127
5.3 Simulation Parameters 131
5.4 Analytical Techniques 142
5.5 Results using a Single Layer of Interpolation 144
5.6 Pin Height Corrections 155
5.7 Results using Multiple Layers of Interpolation 160
5.7.1 Three Layers of Interpolation 161
5.7.2 Four Layers of Interpolation 168

5.8 Simulation Validation 172
5.9 Projection to an Industrial Scale 181
5.9.1 Modifications to the Simulation Setup 181
5.9.2 Results from the Industrial Scale Simulations 184
5.10 Conclusions 189
Chapter 6. Conclusions & Further Work 197
6.1 Introduction 197
6.2 Conclusions 198
6.2.1 Uses for the New Reconfigurable Die 205
6.3 Proposed Further Work 206
Appendix A. Additional Stretch Forming Processes 209
A.1 The Wrap Forming Process 209
A.2 The Cyril Bath Process 210
Appendix B. Hill 48 Calibration Methods 211
Appendix C. Uniaxial Tensile Stress/Strain Curves 216
Appendix D. The Mooney Rivlin Equation 220
Appendix E. Mooney Rivlin Plots 223
Appendix F. Polyurethane Compression Plots 226
Appendix G. Polyurethane Cyclic Loading Plots 228
Appendix H. Additional Phase 1 Results 234
Appendix I. Additional Phase 2 Results 244
Appendix J. Chapter 4 Analyses Comparisons 260
Appendix K. The 3 Axes Pin Actuation Drive Unit 262
Appendix L. Additional Contour Maps Relating to Simulations over a Single Layer of Interpolation 265
Appendix M. Contour Maps Relating to Simulations with Corrected Pin Heights 274
Appendix N. Additional Contour Maps Relating to Simulations over Multiple Layers of Interpolation 287
Appendix O. Contour Maps Relating to Simulation Validation 305
Appendix P. Additional Contour Maps Relating to Simulations of an Industrial Scale Process 306

Appendix Q. Possible Solutions to Issues Identified with AMFOR's Preferred Machine Layout 310
References 313

List of Figures

Figure 1-1: Drape Forming shown at the beginning (a) and end (b) of the process .. 4

Figure 1-2: Reconfigurable tooling comprised of a bed of pins..... 6

Figure 2-1: Information flow from the CAD system to the adjustment device..... 14

Figure 2-2: Set-up procedure for the RPI stretch forming tool 17

Figure 2-3: The sequential set-up (SSU) concept and the preferred direct coupling system 18

Figure 2-4: The shaft-driven leadscrew (SDL) concept and prototype..... 19

Figure 2-5: Full scale prototype stretch forming machine with reconfigurable tooling built by Cyril Bath..... 21

Figure 2-6: Four modes of MPF developed at the Jilin University..... 23

Figure 2-7: A flow chart of the MPDF system from Jilin University..... 24

Figure 2-8: Wang's pin density (a) and pin tip radii (b) comparisons..... 27

Figure 2-9: DATAFORM's flexible stretch forming machine..... 29

Figure 2-10: The industry standard (a) and DATAFORM's (b) grip positioning..... 30

Figure 2-11: The machines developed at Yonsei University in Seoul (a) and Jilin University in China (b)..... 31

Figure 2-12: Schematic representation of Munro & Walczyk's characteristics..... 37

Figure 2-13: Patents relating to reconfigurable tool design..... 41

Figure 3-1: The BBC 2005 normalised yield strengths (a) and r-values (b) plotted with experimental results..... 49

Figure 3-2: The BBC 2005 normalised yield locus for the 2024-T3 alloy 50

Figure 3-3: 2024-T3 hardening curve comparison..... 51

Figure 3-4: The tensile test set-up and the geometry of the dog bone specimen..... 53

Figure 3-5: The Hill 48 (calibrated with r-values) normalised yield strengths (a) and r-values (b) plotted with experimental results 55

Figure 3-6: The Hill 48 (calibrated from 0° to 45° and 90° to 45°) normalised yield strengths (a) and r-values (b) plotted with experimental results..... 57

Figure 3-7: The 0°-45° and 90°-45° calibrated Hill 48 normalised yield loci for the 316L stainless steel 59

Figure 3-8: 316L hardening curve comparison 60

Figure 3-9: The strain rate sensitivity of the hardening behaviour in 316L stainless steel 62

Figure 3-10: The uniaxial tensile test simulated in PAM-STAMP 64

Figure 3-11: Stress/strain curves from the uniaxial tensile test in the 0° direction with a crosshead speed of 1000 mm/min 65

Figure 3-12: Stress/strain curves from the uniaxial tensile test in the 90° direction with a crosshead speed of 1000 mm/min 65

Figure 3-13: Forces acting on a die section due to tension in the sheet 67

Figure 3-14: Tangential relationship between the gripped end of the blank and the edge of the die 69

Figure 3-15: Compression test set-up and specimen geometry 70

Figure 3-16: Tensile test specimen geometry for the 10 mm thick polyurethane ... 71

Figure 3-17: Comparison of the experimental and fitted Mooney Rivlin stress/stretch ratio curves for Kaylan D40 Orange 72

Figure 3-18: Compression test simulation set-up 75

Figure 3-19: True stress/stretch ratio compression curves for the Kaylan D40 Orange polyurethane material 76

Figure 3-20: True stress/stretch ratio compression curves for the Kaylan D20 Red polyurethane material 76

Figure 3-21: True stress/stretch ratio compression curves for the Kaylan D70X Grey polyurethane material 77

Figure 3-22: Engineering stress versus strain plot showing all 20 cycles (a) together with a plot of residual strain versus cycle count (b) for the Green-0.5mm cyclic compression test 80

Figure 3-23: A plot of crosshead displacement versus time for the Brown-5MPa cyclic compression test 81

Figure 3-24: Engineering stress versus strain plot showing all 20 cycles (a) together with a plot of residual strain versus cycle count (b) for the Brown-0.35mm cyclic compression test..... 83

Figure 4-1: The AutoForm simulation setup where the stretch former grips are defined as the die and binder while the reconfigurable die is defined as the punch..... 89

Figure 4-2: Positioning of pivoted pin tips with flat surfaces (c) together with fixed (a) and pivoted (b) semi-hemispherical pin tips in relation to the nominal die radius 90

Figure 4-3: The tooling positions at the end of the bending (a) and drawing (b) process steps 92

Figure 4-4: (a) Hexagonal, (b) square, (c) equilateral triangular and (d) right angled triangular pin cross sections 93

Figure 4-5: The variables used in pin height calculations for pins with semi-hemispherical pin tips 94

Figure 4-6: The two die layouts using pins of a hexagonal cross section arranged in a hexagonal close packed matrix..... 95

Figure 4-7: The three die layouts using pins of a square cross section arranged in a rectangular close packed matrix 96

Figure 4-8: The six die layouts using pins of an equilateral triangular cross section arranged in triangular close packed matrices 96

Figure 4-9: The three die layouts using pins of a right angled triangular cross section arranged in triangular close packed matrices 97

Figure 4-10: HCP1r50 section line (a) & surface defect (b) analyses results 103

Figure 4-11: HCP2r50 section line (a) & surface defect (b) analyses results 104

Figure 4-12: RCP1r50 section line (a) & surface defect (b) analyses results..... 105

Figure 4-13: RCP3r50 surface defect analysis results 105

Figure 4-14: Semi-hemispherical pin tip 50 &75 mm radii comparison..... 106

Figure 4-15: TCP1 surface defect analysis results..... 108

Figure 4-16: TCP3 surface defect analysis results..... 108

Figure 4-17: RTCP3 surface defect analysis results..... 109

Figure 4-18: Complete phase 1 section line analysis results showing the influence of matrix density, equi-spacing between pins, gap size between rows of pins & gap size between pins in the stretching direction..... 112

Figure 4-19: The RCP3 die with shaped flat pivoted pin tips (a), the four pivoted pin tip geometries shaped to suit a square pin (b) (c) (d) & (e), the round pivoted pin tips (f) with a flat mating face (I), and domed mating faces with radii of 800 mm (II) 600 mm (III) 400 mm (IV) & 200 mm (V)..... 113

Figure 4-20: The HCP2 die with shaped flat pivoted pin tips (a) and the four pivoted pin tip geometries shaped to the hexagonal pin (b) (c) (d) & (e)..... 114

Figure 4-21: Variables used in pin height calculations for pins with flat pin tips 114

Figure 4-22: Phase 2 section line analysis results for pivoted pin tips..... 116

Figure 4-23: RCP3 with pivoted round flat pin tips section line (a) & surface defect (b) analyses results..... 118

Figure 4-24: HCP1 with pivoted round flat pin tips section line (a) & surface defect (b) analyses results..... 119

Figure 4-25: HCP2 with pivoted round flat pin tips section line (a) & surface defect (b) analyses results..... 120

Figure 4-26: HCP2 round flat fine mesh simulation section line (a) & surface defect (b) analyses results..... 121

Figure 4-27: The statically indeterminate force system present in the HCP2 pin arrangement..... 123

Figure 5-1: AMFOR's preferred gripping and stretching mechanism..... 127

Figure 5-2: The rotation of an eccentric cam grip..... 128

Figure 5-3: The lab scale pin box and pin design..... 129

Figure 5-4: AMFOR's lab scale stretch forming machine with a reconfigurable die using cylindrical pins in the HCP2 layout and round flat pivoted pin tips..... 130

Figure 5-5: Pin tip identification within the lab scale die..... 133

Figure 5-6: The initial position of models in the single layer of interpolation simulations (a) together with illustrations of the three (b) and four (c) layers of interpolation systems 134

Figure 5-7: The rotation and translation mesh transformations applied to pin tips at the beginning of the position stage 135

Figure 5-8: The kinematic behaviour of the pin tips and the tension applied to the blank during the position stage..... 136

Figure 5-9: Rotation of the drum and clamping line during the stretch stage..... 138

Figure 5-10: A kinematic analysis highlighting excessive rotation of the pin tips during the stretch stage..... 138

Figure 5-11: The trimmed blank mesh used in further analyses of surface quality obtained from different interpolation systems..... 139

Figure 5-12: Surface Tools used at the interfaces between interpolators to prevent penetration..... 140

Figure 5-13: The model representing a four layer system of interpolation where the bottom interpolator is replaced by cylindrical volume tools attached to the top surfaces of the pin tips..... 141

Figure 5-14: PAM-STAMP's stoning analysis to measure defects caused by bumps (a) and hollows (b) on a flat or convex blank..... 144

Figure 5-15: A limitation of the stoning analysis..... 145

Figure 5-16: The Cosmetic defect (a) C2C absolute distance (b) Thickness of solids (c) and Major strain (d) contour maps for the 20 Red simulation 146

Figure 5-17: (a) The deformed blank sinking into the gap between pin tips A1 & C1 (b) The final position of the pin tips 147

Figure 5-18: Simulations showing the comparative behaviour of (a) a single column of elements and (b) sheet comprised of multiple columns of elements, when subjected to a uniformly distributed load 148

Figure 5-19: (a) Results from the analyses of all the simulations using a single layer of interpolation (b) Results excluding the two softest materials..... 150

Figure 5-20: The Cosmetic defect (a) C2C absolute distance (b) Thickness of solids (c) and Major strain (d) contour maps for the 30 Green simulation..... 152

Figure 5-21: The Cosmetic defect (a) C2C absolute distance (b) Thickness of solids (c) and Major strain (d) contour maps for the 30 Grey simulation..... 154

Figure 5-22: (a) Results from the analyses of corrected pin heights using a single layer of interpolation 30 mm thick (b) Results excluding the two softest materials 157

Figure 5-23: Results from the analyses of the simulations using three layers of interpolation 162

Figure 5-24: The Cosmetic defect (a) C2C absolute distance (b) and Thickness of solids (c) contour maps for the 30 Brown-Green-Brown simulation..... 163

Figure 5-25: The Cosmetic defect (a) C2C absolute distance (b) Thickness of solids-5 mm (c) and Thickness of solids-20 mm (d) contour maps for the 30 Grey(5)-Green(20)-Grey(5)* simulation..... 165

Figure 5-26: The Cosmetic defect (a) C2C absolute distance (b) Thickness of solids-6 mm (c) and Thickness of solids-10 mm (d) contour maps for the 22 Grey(6)-Green(10)-Grey(6)* simulation..... 167

Figure 5-27: Results from the analyses of the simulations using four layers of interpolation 168

Figure 5-28: Stoning comparison between the three and four layers of interpolation systems..... 170

Figure 5-29: Penetration at the outer edge of the interpolator disc attached to the B2 pin tip in both the 30 Green(5)-Brown(5)-Green(15)-Brown(5) Discs* and the 30 Green(5)-Grey(5)-Green(15)-Grey(5) Discs* simulations 171

Figure 5-30: Method used to set the heights of pins for the practical tests..... 172

Figure 5-31: Scanning of the deformed surfaces from the practical tests 174

Figure 5-32: A contour map showing deviation of the trimmed surface from a scan of the 20 Red practical test to that from the corresponding simulation..... 176

Figure 5-33: A contour map showing deviation of the trimmed surface from a scan of the 30 Green practical test to that from the corresponding simulation..... 177

Figure 5-34: A contour map showing deviation of the trimmed surface from a scan of the 30 BGB practical test to that from the corresponding simulation 178

Figure 5-35: Contour maps showing a comparison of the stoning defects detected in the 20 Red practical test (b) and the corresponding simulation (a) 179

Figure 5-36: Contour maps showing a comparison of the stoning defects detected in the 30 Green practical test (b) and the corresponding simulation (a)..... 179

Figure 5-37: Contour maps showing a comparison of the stoning defects detected in the 30 BGB practical test (b) and the corresponding simulation (a)..... 180

Figure 5-38: Starting position of the industrial scale simulations 183

Figure 5-39: Results from the analyses of the industrial scale simulations..... 184

Figure 5-40: The Cosmetic defect (a) and C2C absolute distance (b) contour maps for the 1.2m 30 Brown-Green-Brown simulation..... 185

Figure 5-41: The Cosmetic defect (a) and C2C absolute distance (b) contour maps for the 1.2m 30 Grey(5)-Green(20)-Grey(5)* simulation..... 187

Figure 5-42: Irregular strain present when a double curvature part is formed with the blank gripped in a straight clamping line over a cylindrical drum..... 189

Figure 5-43: Single layer of interpolation 20 mm (a) & 30 mm (b) thick stoning defects plotted against material properties 191

Appendices

Figure A-1: Wrap Forming shown at early (a) mid (b) and late (c) stages of the process..... 209

Figure A-2: The stretch forming (a) and press forming (b) stages of the Cyril Bath process..... 210

Figure B-1: The Hill 48 (Calibration 1) normalised yield strengths (a) and r-values (b) plotted with experimental results..... 211

Figure B-2: The Hill 48 (Calibration 2) normalised yield strengths (a) and r-values (b) plotted with experimental results..... 212

Figure B-3: The Hill 48 (Calibration 3) normalised yield strengths (a) and r-values (b) plotted with experimental results..... 212

Figure B-4: The Hill 48 (Calibration 4) normalised yield strengths (a) and r-values (b) plotted with experimental results..... 213

Figure B-5: The Hill 48 (Calibration 5) normalised yield strengths (a) and r-values (b) plotted with experimental results 214

Figure B-6: The Hill 48 (Calibration 6) normalised yield strengths (a) and r-values (b) plotted with experimental results 214

Figure B-7: The Hill 48 (Calibration 7) normalised yield strengths (a) and r-values (b) plotted with experimental results 215

Figure C-1: Stress/strain curves from the uniaxial tensile test in the 0° direction with a crosshead speed of 0.1 mm/min 216

Figure C-2: Stress/strain curves from the uniaxial tensile test in the 90° direction with a crosshead speed of 0.1 mm/min 216

Figure C-3: Stress/strain curves from the uniaxial tensile test in the 0° direction with a crosshead speed of 1 mm/min 217

Figure C-4: Stress/strain curves from the uniaxial tensile test in the 90° direction with a crosshead speed of 1 mm/min 217

Figure C-5: Stress/strain curves from the uniaxial tensile test in the 0° direction with a crosshead speed of 10 mm/min 218

Figure C-6: Stress/strain curves from the uniaxial tensile test in the 90° direction with a crosshead speed of 10 mm/min 218

Figure C-7: Stress/strain curves from the uniaxial tensile test in the 0° direction with a crosshead speed of 100 mm/min 219

Figure C-8: Stress/strain curves from the uniaxial tensile test in the 90° direction with a crosshead speed of 100 mm/min 219

Figure E-1: Mooney Rivlin plot to determine the M & A parameters 224

Figure E-2: Mooney Rivlin plot to determine the C_1 & C_2 constants 225

Figure F-1: True stress/stretch ratio compression curves for the Kaylan D25 Purple polyurethane material 226

Figure F-2: True stress/stretch ratio compression curves for the Kaylan D30 Green polyurethane material 226

Figure F-3: True stress/stretch ratio compression curves for the Kaylan D50 Blue polyurethane material 227

Figure F-4: True stress/stretch ratio compression curves for the Kaylan D60 Brown polyurethane material 227

Figure F-5: True stress/stretch ratio compression curves for the Kaylan D60X Violet polyurethane material 227

Figure G-1: Engineering stress versus strain plots showing cycles 1, 2, 10 & 20 for the Green-0.5mm (a) and Brown-0.35mm (b) cyclic compression tests..... 228

Figure G-2: Engineering stress versus strain plots showing all 20 cycles (a) and cycles 1, 2, 10 & 20 (b) together with a plot of residual strain versus cycle count (c) for the Red-5mm cyclic compression test 229

Figure G-3: Engineering stress versus strain plots showing all 20 cycles (a) and cycles 1, 2, 10 & 20 (b) together with a plot of residual strain versus cycle count (c) for the Green-2.56mm cyclic compression test..... 230

Figure G-4: Engineering stress versus strain plots showing all 20 cycles (a) and cycles 1, 2, 10 & 20 (b) together with a plot of residual strain versus cycle count (c) for the Orange-1.8mm cyclic compression test..... 231

Figure G-5: Engineering stress versus strain plots showing all 20 cycles (a) and cycles 1, 2, 10 & 20 (b) together with a plot of residual strain versus cycle count (c) for the Blue-0.8mm cyclic compression test 232

Figure G-6: Engineering stress versus strain plots showing all 20 cycles (a) and cycles 1, 2, 10 & 20 (b) together with a plot of residual strain versus cycle count (c) for the Violet-0.7mm cyclic compression test 233

Figure H-1: HCP1r75 section line (a) & surface defect (b) analyses results 234

Figure H-2: HCP2r75 section line (a) & surface defect (b) analyses results 235

Figure H-3: RCP2r50 section line (a) & surface defect (b) analyses results..... 235

Figure H-4: RCP3r50 section line analysis results 236

Figure H-5: RCP1r75 section line (a) & surface defect (b) analyses results..... 236

Figure H-6: RCP2r75 section line (a) & surface defect (b) analyses results..... 237

Figure H-7: RCP3r75 section line (a) & surface defect (b) analyses results..... 238

Figure H-8: TCP1 section line analysis results 238

Figure H-9: TCP2 section line (a) & surface defect (b) analyses results 239

Figure H-10: TCP3 section line analysis results 239

Figure H-11: TCP4 section line (a) & surface defect (b) analyses results..... 240

Figure H-12: TCP5 section line (a) & surface defect (b) analyses results..... 240

Figure H-13: TCP6 section line (a) & surface defect (b) analyses results..... 241

Figure H-14: RTCP1 section line (a) & surface defect (b) analyses results 242

Figure H-15: RTCP1 section line (a) & surface defect (b) analyses results 242

Figure H-16: RTCP3 section line analysis results..... 243

Figure I-1: The HCP1 Round r200 section line (a) & surface defect (b) analyses results 244

Figure I-2: The HCP1 Round r400 section line (a) & surface defect (b) analyses results 245

Figure I-3: The HCP1 Round r600 section line (a) & surface defect (b) analyses results 245

Figure I-4: The HCP1 Round r800 section line (a) & surface defect (b) analyses results 246

Figure I-5: The HCP1 Shaped Flat section line (a) & surface defect (b) analyses results 247

Figure I-6: The HCP1 Shaped Flat MP section line (a) & surface defect (b) analyses results 247

Figure I-7: The HCP1 Shaped r800 section line (a) & surface defect (b) analyses results 248

Figure I-8: The HCP1 Shaped r800 MP section line (a) & surface defect (b) analyses results 249

Figure I-9: The HCP2 Round r200 section line (a) & surface defect (b) analyses results 249

Figure I-10: The HCP2 Round r400 section line (a) & surface defect (b) analyses results 250

Figure I-11: The HCP2 Round r600 section line (a) & surface defect (b) analyses results 251

Figure I-12: The HCP2 Round r800 section line (a) & surface defect (b) analyses results 251

Figure I-13: The HCP2 Shaped Flat section line (a) & surface defect (b) analyses results 252

Figure I-14: The HCP1 Shaped Flat MP section line (a) & surface defect (b) analyses results 253

Figure I-15: The HCP2 Shaped r800 section line (a) & surface defect (b) analyses results 253

Figure I-16: The HCP2 Shaped r800 MP section line (a) & surface defect (b) analyses results 254

Figure I-17: The RCP3 Round r200 section line (a) & surface defect (b) analyses results 255

Figure I-18: The RCP3 Round r400 section line (a) & surface defect (b) analyses results 255

Figure I-19: The RCP3 Round r600 section line (a) & surface defect (b) analyses results 256

Figure I-20: The RCP3 Round r800 section line (a) & surface defect (b) analyses results 257

Figure I-21: The RCP3 Shaped Flat section line (a) & surface defect (b) analyses results 257

Figure I-22: The RCP3 Shaped Flat MP section line (a) & surface defect (b) analyses results 258

Figure I-23: The RCP3 Shaped r800 section line (a) & surface defect (b) analyses results 259

Figure I-24: The RCP3 Shaped r800 MP section line (a) & surface defect (b) analyses results 259

Figure J-1: A comparison of the results from the surface defect & section line analyses presented in Chapter 4 260

Figure J-2: Chapter 4 HCP2 with round flat pivoted pin tips standard mesh & fine mesh simulations section line analyses results comparison 261

Figure K-1: A proposed design for actuation of 32 mm diameter pins from above showing motion along the X axis 262

Figure K-2: Motion of the pin actuation unit along the Y axis (a) and along the Z axis (b) 263

Figure K-3: Spring loading of the telescopic universal joint units (a) and coupling system (b) with an exploded view of the captive collet (c) 264

Figure L-1: Cosmetic defect (a) C2C absolute distance (b) Thickness of solids (c) & Major strain (d) contour maps for the 30 Red simulation 265

Figure L-2: Cosmetic defect (a) C2C absolute distance (b) Thickness of solids (c) & Major strain (d) contour maps for the 20 Purple simulation 266

Figure L-3: Cosmetic defect (a) C2C absolute distance (b) Thickness of solids (c) & Major strain (d) contour maps for the 30 Purple simulation 266

Figure L-4: Cosmetic defect (a) C2C absolute distance (b) Thickness of solids (c) & Major strain (d) contour maps for the 20 Green simulation 267

Figure L-5: Cosmetic defect (a) C2C absolute distance (b) Thickness of solids (c) & Major strain (d) contour maps for the 20 Orange simulation 268

Figure L-6: Cosmetic defect (a) C2C absolute distance (b) Thickness of solids (c) & Major strain (d) contour maps for the 30 Orange simulation 268

Figure L-7: Cosmetic defect (a) C2C absolute distance (b) Thickness of solids (c) & Major strain (d) contour maps for the 20 Blue simulation 269

Figure L-8: Cosmetic defect (a) C2C absolute distance (b) Thickness of solids (c) & Major strain (d) contour maps for the 30 Blue simulation 270

Figure L-9: Cosmetic defect (a) C2C absolute distance (b) Thickness of solids (c) & Major strain (d) contour maps for the 20 Brown simulation 270

Figure L-10: Cosmetic defect (a) C2C absolute distance (b) Thickness of solids (c) & Major strain (d) contour maps for the 30 Brown simulation 271

Figure L-11: Cosmetic defect (a) C2C absolute distance (b) Thickness of solids (c) & Major strain (d) contour maps for the 20 Violet simulation 272

Figure L-12: Cosmetic defect (a) C2C absolute distance (b) Thickness of solids (c) & Major strain (d) contour maps for the 30 Violet simulation 272

Figure L-13: Cosmetic defect (a) C2C absolute distance (b) Thickness of solids (c) & Major strain (d) contour maps for the 20 Grey simulation..... 273

Figure M-1: Cosmetic defect (a) C2C absolute distance (b) Thickness of solids (c) & Major strain (d) contour maps for the Corrected 30 Red simulation..... 274

Figure M-2: Cosmetic defect (a) C2C absolute distance (b) Thickness of solids (c) & Major strain (d) contour maps for the Corrected 2 30 Red simulation..... 275

Figure M-3: Cosmetic defect (a) C2C absolute distance (b) Thickness of solids (c) & Major strain (d) contour maps for the Corrected 3 30 Red simulation..... 275

Figure M-4: Cosmetic defect (a) C2C absolute distance (b) Thickness of solids (c) & Major strain (d) contour maps for the Estimated 30 Red simulation..... 276

Figure M-5: Cosmetic defect (a) C2C absolute distance (b) Thickness of solids (c) & Major strain (d) contour maps for the Corrected 30 Purple simulation..... 277

Figure M-6: Cosmetic defect (a) C2C absolute distance (b) Thickness of solids (c) & Major strain (d) contour maps for the Corrected 2 30 Purple simulation..... 277

Figure M-7: Cosmetic defect (a) C2C absolute distance (b) Thickness of solids (c) & Major strain (d) contour maps for the Corrected 3 30 Purple simulation..... 278

Figure M-8: Cosmetic defect (a) C2C absolute distance (b) Thickness of solids (c) & Major strain (d) contour maps for the Estimated 30 Purple simulation..... 279

Figure M-9: Cosmetic defect (a) C2C absolute distance (b) Thickness of solids (c) & Major strain (d) contour maps for the Corrected 30 Green simulation..... 279

Figure M-10: Cosmetic defect (a) C2C absolute distance (b) Thickness of solids (c) & Major strain (d) contour maps for the Corrected 2 30 Green simulation..... 280

Figure M-11: Cosmetic defect (a) C2C absolute distance (b) Thickness of solids (c) & Major strain (d) contour maps for the Corrected 3 30 Green simulation..... 281

Figure M-12: Cosmetic defect (a) C2C absolute distance (b) Thickness of solids (c) & Major strain (d) contour maps for the Estimated 30 Green simulation..... 281

Figure M-13: Cosmetic defect (a) C2C absolute distance (b) Thickness of solids (c) & Major strain (d) contour maps for the Corrected 30 Orange simulation..... 282

Figure M-14: Cosmetic defect (a) C2C absolute distance (b) Thickness of solids (c) & Major strain (d) contour maps for the Corrected 2 30 Orange simulation..... 283

Figure M-15: Cosmetic defect (a) C2C absolute distance (b) Thickness of solids (c) & Major strain (d) contour maps for the Corrected 30 Blue simulation 283

Figure M-16: Cosmetic defect (a) C2C absolute distance (b) Thickness of solids (c) & Major strain (d) contour maps for the Corrected 2 30 Blue simulation 284

Figure M-17: Cosmetic defect (a) C2C absolute distance (b) Thickness of solids (c) & Major strain (d) contour maps for the Corrected 30 Brown simulation 285

Figure M-18: Cosmetic defect (a) C2C absolute distance (b) Thickness of solids (c) & Major strain (d) contour maps for the Corrected 30 Violet simulation 285

Figure M-19: Cosmetic defect (a) C2C absolute distance (b) Thickness of solids (c) & Major strain (d) contour maps for the Corrected 30 Grey simulation..... 286

Figure N-1: Cosmetic defect (a) C2C absolute distance (b) & Thickness of solids (c) contour maps for the 30 Brown-Green-Brown* simulation with C2C comparisons with the trimmed part from the 30 Brown-Green-Brown simulation at the reference (d) & simulation (e) positions 287

Figure N-2: Cosmetic defect (a) C2C absolute distance (b) Thickness of solids (c) and Major strain (d) contour maps for the 30 Brown-Green-Brown Glued simulation 288

Figure N-3: Cosmetic defect (a) C2C absolute distance (b) and Thickness of solids (c) contour maps for the 30 Blue-Green-Blue simulation 289

Figure N-4: Cosmetic defect (a) C2C absolute distance (b) and Thickness of solids (c) contour maps for the 30 Violet-Orange-Violet simulation..... 289

Figure N-5: Cosmetic defect (a) C2C absolute distance (b) and Thickness of solids (c) contour maps for the 30 Brown-Orange-Brown simulation..... 290

Figure N-6: Cosmetic defect (a) C2C absolute distance (b) and Thickness of solids (c) contour maps for the 30 Violet-Green-Violet simulation..... 291

Figure N-7: Cosmetic defect (a) C2C absolute distance (b) Thickness of solids-5 mm (c) and Thickness of solids-20 mm (d) contour maps for the 30 Brown(5)-Green(20)-Brown(5)* simulation..... 291

Figure N-8: Cosmetic defect (a) C2C absolute distance (b) and Thickness of solids (c) contour maps for the 24 Brown-Green-Brown simulation..... 292

Figure N-9: Cosmetic defect (a) C2C absolute distance (b) Thickness of solids-6 mm (c) and Thickness of solids-10 mm (d) contour maps for the 22 Brown(6)-Green(10)-Brown(6)* simulation 293

Figure N-10: Cosmetic defect (a) C2C absolute distance (b) and Thickness of solids (c) contour maps for the 18 Brown-Green-Brown simulation 293

Figure N-11: Cosmetic defect (a) C2C absolute distance (b) and Thickness of solids (c) contour maps for the 18 Grey-Green-Grey* simulation 294

Figure N-12: Cosmetic defect (a) C2C absolute distance (b) Thickness of solids-5 mm (c) and Thickness of solids-10 mm (d) contour maps for the 30 Orange-Brown-Orange-Brown simulation 295

Figure N-13: Cosmetic defect (a) C2C absolute distance (b) Thickness of solids (c) and Major strain (d) contour maps for the 30 Green-Brown-Green-Brown Glued simulation 296

Figure N-14: Cosmetic defect (a) C2C absolute distance (b) Thickness of solids (c) and Major strain (d) contour maps for the 30 Green-Brown-Green-Brown Glued Discs* simulation 296

Figure N-15: Cosmetic defect (a) C2C absolute distance (b) Thickness of solids-5 mm (c) Thickness of solids-15 mm (d) and Major strain (e) contour maps for the 30 Green(5)-Brown(5)-Green(15)-Brown(5)* simulation 297

Figure N-16: Cosmetic defect (a) C2C absolute distance (b) Thickness of solids-5 mm (c) Thickness of solids-15 mm (d) and Major strain (e) contour maps for the 30 Green(5)-Brown(5)-Green(15)-Brown(5) Discs* simulation 298

Figure N-17: Cosmetic defect (a) C2C absolute distance (b) Thickness of solids-5 mm (c) Thickness of solids-15 mm (d) and Major strain (e) contour maps for the 30 Green(5)-Grey(5)-Green(15)-Grey(5)* simulation 299

Figure N-18: Cosmetic defect (a) C2C absolute distance (b) Thickness of solids-5 mm (c) Thickness of solids-15 mm (d) and Major strain (e) contour maps for the 30 Green(5)-Grey(5)-Green(15)-Grey(5) Discs* simulation 300

Figure N-19: Cosmetic defect (a) C2C absolute distance (b) Thickness of solids-4 mm (c) and Thickness of solids-8 mm (d) contour maps for the 24 Green-Brown-Green-Brown simulation 301

Figure N-20: Cosmetic defect (a) C2C absolute distance (b) Thickness of solids-3 mm (c) and Thickness of solids-6 mm (d) contour maps for the 18 Green-Brown-Green-Brown simulation 302

Figure N-21: Cosmetic defect (a) C2C absolute distance (b) Thickness of solids-5 mm (c) and Thickness of solids-10 mm (d) contour maps for the 30 Green-Brown-Green-Brown simulation 303

Figure N-22: Cosmetic defect (a) C2C absolute distance (b) Thickness of solids-3 mm (c) and Thickness of solids-6 mm (d) contour maps for the 18 Green-Grey-Green-Grey simulation 304

Figure O-1: A contour map showing deviation of the trimmed surface from a scan of the 30 GBGB practical test to that from the corresponding simulation 305

Figure O-2: Contour maps showing a comparison of the stoning defects detected in the 30 GBGB practical test (b) and the corresponding simulation (a) 305

Figure P-1: The Thickness of solids (a) and Major strain (b) contour maps for the 1.2m 30 Brown-Green-Brown simulation 307

Figure P-2: The Thickness of solids-5 mm (a) Thickness of solids-20 mm (b) and Major strain (c) contour maps for the 1.2m 30 Grey(5)-Green(20)-Grey(5)* simulation 309

Figure Q-1: Guide fitted to the industrial scale machine to minimise non-tangential contact between the blank and die 310

Figure Q-2: A possible design of a sectional drum and grip mechanism 311

Figure Q-3: A pin design incorporating a hexagonal sleeve 312

Figure Q-4: A cross-sectional view of a possible partial drum design 312

List of Tables

Table 2-1: Nakajima's comparison between wire type moulds and conventional moulds 13

Table 2-2: Munro & Walczyk's characteristics of an ideal reconfigurable tool 36

Table 2-3: Munro & Walczyk's top ten designs 37

Table 2-4: Munro & Walczyk's top patents 39

Table 3-1: Stretchability ratings of aluminium alloys 47

Table 3-2: The uniaxial tension test data retrieved from the AMFOR database 48

Table 3-3: BBC 2005 material parameter values for 2024-T3 generated by the BBC.exe solver 49

Table 3-4: The material properties required to implement the 2024-T3 material model in the AutoForm software 52

Table 3-5: The yield strengths and r-values from initial tensile tests on the 316L stainless steel 53

Table 3-6: Colour coded quality of fit results for Hill 48 calibration methods 58

Table 3-7: Yield strengths at 0° and 90° observed in tensile tests on the 316L stainless steel at crosshead speeds between 0.1 and 1000 mm/min 61

Table 3-8: Material properties and material dependent constants required to implement the 316L material models in PAM-STAMP 63

Table 3-9: Kaylan D series material properties 74

Table 3-10: The displacement controlled cyclic compression tests 84

Table 5-1: Distribution of the calculated average true stress over each pin tip 159

Acknowledgements

I would sincerely like to thank my supervisors, Dr. Alan Leacock, Dr. Desmond Brown and Dr. David McCraken for giving me the opportunity to complete such a challenging piece of research within the AMFOR group. Their support and knowledge have been invaluable to me during the darker days of this research project. The dedication, and unrelenting enthusiasm, shown by Dr. Alan Leacock for this project and the subject matter in general have been inspirational. I would also like to thank Dr. Alan Leacock and Dr. Desmond Brown for their excellent teaching during my MEng (Distinction) Mechanical Engineering programme and for supervising my final year dissertation.

I would also like to express my appreciation to Mr Jon Ward, the Managing Director of Kay-Dee Engineering Plastics Ltd for supplying me with gratis samples of all eight materials from the Kaylan D series. This project could not have been completed without his generosity and support.

Thanks also go to Dr. Gregor Volk for his assistance in the AMFOR laboratory and for putting up with me in a shared research office.

I would also like to offer my sincere thanks to the technicians at Ulster University's laboratories/workshops for their patience, and the skills they showed in manufacturing fixtures used during this project, especially John Kidd and Gary Finlay.

Special thanks are also offered to Dr. Ken Gilmore and Dr. Alan Brown for their enthusiastic and skilful teaching of the mechanical sciences during my degree programme. Dr. Ken Gilmore showed me great support and understanding when I questioned my very presence at the University.

Finally I would like to thank the staff at the Northwest Regional College for their excellent teaching during my HND (Distinction) Mechanical Engineering programme, in particular: Paul Young, Gary Mallett and Liam Tully. Their encouragement gave me the incentive to continue in higher education.

Abstract

In this thesis a newly proposed design of pin tips for the stretch forming of sheet metal over a reconfigurable die is examined. The new pin tips are mounted on ball studs at the tops of the reconfigurable pins and allowed to pivot freely. Since the tops surfaces of the pin tips can slide against the bottom surface of the interpolator, during the stretching process, their final position is dependent on the overall curvature of the die.

In phase one, of a two-phase numerical study (designed to identify a suitable pin arrangement and pin tip geometry for the employment of the new pin tips in a coarser bed of pins), where semi-hemispherical pin tips are used, several features are identified that are detrimental to the production of smooth parts. Hexagonal close packed matrices aligned in either of two directions, and a rectangular close packed matrix aligned diagonally to the stretching direction are shown to offer superior performance. In phase two of this study the geometry of the new pivoted pin tips is examined. Although it is possible to produce parts with superior smoothness using part-specific pin tip geometry, it was found here that using circular pivoted pin tips with flat mating surfaces (in a HCP pin matrix) offers a better global solution, with a clear advantage over their commonly used semi-hemispherical counterparts.

A second numerical study is presented here to identify a suitable interpolator for use with this new system, where smoothness targets of 0.1 mm, for stoning, and ± 0.2 mm, for overall dimensional accuracy, are used. It was found that, with the new pivoted pin tips, the required interpolator thickness is no longer equivalent to the diameter of the pins, as it is with semi-hemispherical pin tips. An interpolator thickness of 30 mm is shown here to produce parts with acceptable smoothness, with 70 mm diameter pins. It was also found that using a three layer of interpolation system, where a softer polyurethane material is sandwiched between two layers comprised of a harder polyurethane material, further reduces dimpling, and hence produces parts with superior smoothness.

Nomenclature

Abbreviations

ABS	Acrylonitrile Butadiene Styrene
ACIS	Andy, Charles, Ian's System
AMFOR	Advanced Metal Forming Research Group
API	American Precision Industries
ASCII	American Standard for Information Interchange
ASM	American Society for Metals
ASTM	American Section of the International Association for Testing Materials
BBC	Banabic, Barlat & Cazacu (yield criterion)
BSc	Bachelor of Science
CAD	Computer Aided Design
CADS	CAD integrated software sub-System
CCS	Computer Control sub-System
CAM	Computer Aided Manufacture
CMM	Coordinate Measuring Machine
CNC	Computer Numerical Control
CPU	Central Processing Unit
CSV	Comma-Separated Values
C2C	Cloud To Cloud
DARPA	Defence Advanced Research Projects Agency
DATAFORM	Digitally Adjustable Tooling for manufacturing of Aircraft panels using multi-point FORMing methodology
DOM	Drawn Over Mandrel
DP	Dual Phase (steel)
EDF	Électricité de France

ESI	Engineering Systems International
FBX	Filmbox
FEA	Finite Element Analysis
GmbH	German limited company
HCP	Hexagonal Close Packed
ICP	Iterative Closest Point
IGES	Initial Graphics Exchange Specification
Ltd.	Limited company
MG	Morris Garage
MIT	Massachusetts Institute of Technology
MPD	Multi-Point Die
MPDF	Multi Point Die Forming
MPF	Multi Point Forming
MSc	Master of Science
NC	Numerical Control
NURBS	Non-Uniform Rational Basis Spline
PC	Personal Computer
PhD	Doctor of Philosophy
PIC	Precision Mechanical Components
RCP	Rectangular Close Packed
RMF	Reconfigurable Multipoint Forming
RMS	Root Mean Square
RPI	Rensselaer Polytechnic Institute
RSF	Reconfigurable Stretch Forming
(R)TCP	(Right angled) Triangular Close Packed
RTFF	Reconfigurable Tooling for Flexible Fabrication
SAT	Standard ACIS Text

SD	Stretching Direction
SDL	Shaft driven leadscrew
SSU	Sequential set-up
STL	Stereolithography
TD	Transverse Direction

Symbols

A	Area
A	MIT's proportional constant
A	Woods' Mooney-Rivlin coefficient
A & B	PAM-STAMP's Mooney-Rivlin constants
A, B & C	Modified Krupkowsky material constants
a, b, k, L, M, N, P, Q & R	Material parameters of the BBC 2005 yield criterion
a & P	Hockett-Sherby material constants
Al	Aluminium
C	Swift & Gosh hardening coefficient
C_1 & C_2	Mooney-Rivlin constants
C_r & R_{sat}	Kinematic material dependent hardening variables
d	Diameter of a pin tip
D	Gosh hardening constant
e	Engineering strain (subscripts 1, 2 & 3 denote direction)
e_i	Engineering strain at s = 1 MPa (PAM-STAMP)
E	Elastic modulus
F_b	Critical buckling load
F_p	Critical bending load
F, G, H & N	Hill 48 coefficients

h	Pin height relating to a pivoted pin tip in contact with a blank (AutoForm)
h_1	Pin height when the curved surface of a semi-hemispherical pin tip is in contact with a blank (AutoForm)
h_2	Pin height when the edge of a semi-hemispherical pin tip is in contact with a blank (AutoForm)
h_{pp}	Distance from the top of a pin tip to its pivot point
I	Second moment of area
I_1, I_2 & I_3	1st, 2nd and 3rd right Cauchy-Green strain invariants
J_1, J_2 & J_3	1st, 2nd and 3rd Green-Lagrange strain invariants
K	Strength coefficient
L	Length
m	Swift & Gosh hardening exponent
M	Woods' assumed elastic modulus for rubberlike materials
n or N	Number of data points or specimens
n	Strain hardening exponent
P_i	MIT's vector describing the position of the pins after the i^{th} iteration
P_{i+1}	MIT's vector describing the new position of pins
P_0	MIT's vector describing the position of pins in a desired part
r	Lankford or anisotropy coefficient (subscripts 0, 45, 90 etc. denote angle from a sheet's rolling direction)
r	Radius of curvature
r_D	Die radius (AutoForm)
r_i	Radius of curvature at a given sample point (PAM-STAMP to Excel)
r_{PT}	Pin tip radius (AutoForm)
R	Reaction force

R_d	Radius of the drum (PAM-STAMP)
®	Registered Trademark
ref	Denotes reference values (subscript)
s	Engineering stress (subscripts 1, 2, & 3 denote direction)
S	Kutt's chord length after springback
t	Thickness
t_i	Initial interpolator thickness (PAM-STAMP)
t_f	Final interpolator thickness (PAM-STAMP)
T	Tension in a sheet
T	Kutt's chord length before springback
Ti	Titanium
T_i	Tension in the sheet at a given point
T_0	Tension in the sheet at a reference point
w	Width
W	Mooney-Rivlin strain energy density function
x_E	horizontal distance from the centre of a pin to an edge in contact with a blank (AutoForm)
x_i	Data value for a given specimen
X_d	Horizontal distance from the YZ symmetry plane to the centre of the drum (PAM-STAMP)
X_i	distance a given pin tip (or sampled point) is positioned from the YZ symmetry plane [PAM-STAMP (to Excel)]
X_{if}	Horizontal distances from the YZ symmetry plane to the edge of the deformed interpolator (PAM-STAMP)
x_P	Horizontal distance from the centreline of a die to the centre of a pin (AutoForm)
Y_c	Height of the sampled point intersected by the two symmetry planes (PAM-STAMP to Excel)

Y_D	Translation of the die in the Y direction (PAM-STAMP)
Y_i	Translation applied to pin tips in the Y direction (PAM-STAMP)
Y_{ic}	Corrected height of a given sampled point (PAM-STAMP to Excel)
Y_{ir}	Recorded height of a sampled point (PAM-STAMP to Excel)
Y_0	Vertical distance from the centre of the drum to the top surface of a pin tip in its initial positions (PAM-STAMP)
z_i	Wang's height of a sampled point
z_{ti}	Wang's target height of a sampled point
α	Combined Swift/Hockett-Sherby proportional coefficient
$_\alpha$	Denotes angle to sheet's rolling direction (subscript)
$\dot{\alpha}$	Ratio of a given to reference strain rate
Γ, Λ & Ψ	Combined constants of the BBC 2005 yield criterion
$\Delta\sigma$ & Δr	Measure of yield strength and r-value accuracy
ε	True strain
ε_p	True plastic strain
ε_0	Initial strain
$\dot{\varepsilon}$	Strain rate
ε_1	Major strain
ε_2	Transverse strain
ε_3	Thickness strain
θ	Angle at which tension acts
θ_f	angle between a vertical plane and a line bisecting the centre of curvature and the edge of the deformed interpolator (PAM-STAMP)
θ_i	Angle between the reference tension point and a given point
λ	Stretch ratio (subscripts 1, 2, & 3 denote direction)
μ	Mean data value for all specimens

μ	Coefficient of friction
σ	True stress (subscripts 1, 2, & 3 denote direction)
σ_y	Yield strength
σ_0, σ_{45}, σ_{90} etc.	Yield strength at a given angle from a sheet's rolling direction
$\bar{\sigma}$	Equivalent stress
σ_{12} & σ_{21}	Shear stresses
σ_{sat}	Saturated stress
σ_i	Hockett-Sherby yield stress
σ(e) & r(e)	Experimental yield strength and r-value
$\sigma(\alpha)$ & r(α)	Predicted yield strength and r-value

Note on Access to Contents

I hereby declare that for 2 years following the date on which the thesis is deposited in Research Student Administration of Ulster University, the thesis shall remain confidential with access or copying prohibited. Following expiry of this period I permit

1. the Librarian of the University to allow the thesis to be copied in whole or in part without reference to me on the understanding that such authority applies to the provision of single copies made for study purposes or for inclusion within the stock of another library.

2. the thesis to be made available through the Ulster Institutional Repository and/or EThOS under the terms of the Ulster eTheses Deposit Agreement which I have signed.

IT IS A CONDITION OF USE OF THIS THESIS THAT ANYONE WHO CONSULTS IT MUST RECOGNISE THAT THE COPYRIGHT RESTS WITH THE UNIVERSITY AND THEN SUBSEQUENTLY TO THE AUTHOR ON THE EXPIRY OF THIS PERIOD AND THAT NO QUOTATION FROM THE THESIS AND NO INFORMATION DERIVED FROM IT MAY BE PUBLISHED UNLESS THE SOURCE IS PROPERLY ACKNOWLEDGED.

Chapter 1. Introduction

1.1 Background

The production of sheet metal parts can be split into two main categories, the fabrication of sheet metal parts, and the forming of sheet metal parts. In the fabrication of sheet metal parts, the component being manufactured is broken down into manageable sections, which can be shaped on readily available machinery using common processes such as roll bending or folding, before being joined through bolting, riveting or welding. While the forces required to fabricate sheet metal parts are small, the size of parts manufactured with this method is limited, as joints can often weaken the structural integrity of the fabricated component. The forming of larger sheet metal parts (or the mass production of smaller parts through a reduced number of processes) normally requires greater force, to operate purpose-built machinery. The capital outlay required to set up a sheet metal forming plant is much greater than that required to set up a fabrication workshop because of the requirement of heavy purpose-built machinery. While a diverse array of parts can be manufactured within a fabrication workshop, the scope of a sheet metal forming plant is limited by the bespoke nature of forming machinery and tooling. Reconfigurable tooling can greatly increase the scope of a sheet metal forming plant without the need for major capital investment.

Sheet metal forming is a term that can be applied to a number processes including drawing and stamping (press forming), where sheet metal blanks are formed between a matching set of (normally) solid metal tools (punch and die), and stretch forming, where a sheet metal blank is pulled over a

single tool (die). In this thesis reconfigurable tooling is examined for the stretch forming process only. Normally, a solid metal die is used for the stretch forming of sheet metal, but it should be noted that, since the forces on the die are caused by the tension in the sheet being stretched (see Section 3.4), forces encountered in stretch forming are lower than those encountered in stamping and drawing and hence, fabricated tooling can be used where thin sheets, and/or material of a relatively low strength, are being stretched.

Solid metal tools and the machining required to produce them, result in a high capital outlay before a single part is produced. The cost and time needed to produce sold tools mean that the stretch forming process is not always a viable option in small volume production runs. Reliance on solid tooling can also have a detrimental effect on lead times, and the speed of the research and development of new product lines. The stretch forming of sheet metal parts is not a high volume production process. While the stamping of parts can be costed with production time measured in 'hits per minute' (where a single hit can produce a number of formed and trimmed parts), it is not unusual for one or more skilled technicians to spend an hour or more forming and trimming a single stretch formed part. These problems have long been evident; hence, stretch forming of sheet metal has become a process that is almost exclusively used in the aerospace industry where the extra expense can be justified.

1.2 Sheet Metal Stretch Forming Processes

Stretch forming can be used in the forming of sheet, bars and sections but in this thesis only the forming of sheet metal is considered. The stretch forming of sheet metal is normally considered as a uniaxial forming process where the blank is gripped at opposite ends and stretched over a solid die through displacement of the grip carriages, the die, or a combination of both. Neglecting the effects of bending (which due to the relative gentle curvature of the die, are normally small in comparison to stretching effects) and friction between the die and blank, and assuming that the material being stretched is isotropic, the strain distribution in the blank during stretching

is similar to that found in a uniaxial tensile test, where the major strain (ε_1) is dependent on the applied force, and the transverse (ε_2) and through thickness (ε_3) strains can be given as minus $\varepsilon_1/2$. Plane strain conditions exist at the grips where the transverse strain is restricted by the clamping forces between the jaws of the grips. Friction between the blank and die results in a reduction of the effective tension in the blank, and so it's strain, approaching the top central point of the die. Some stretch forming machines are fitted with a second set of grips, creating a second axis perpendicular to the first and, using a cruciform blank, the forming process is effectively changed from uniaxial to biaxial. In this thesis, only uniaxial stretch forming is considered, where there are three commonly used sheet stretch forming processes, drape forming, wrap forming and the Cyril Bath process. Since drape forming is the process of most relevance in this study it is illustrated and described briefly in Section 1.2.1. The wrap forming, and Cyril Bath processes are illustrated with brief descriptions in Appendix A. of this document.

1.2.1 Drape Forming

Drape forming, illustrated in Figure 1-1, is the simplest of the stretch forming processes. Since the thickness of a sheet metal blank is very small compared to its length it is natural for a blank placed onto a curved die to bend with the effects of gravity acting upon it. This effect can be used to the advantage of the operator. With the grips located so that they can accommodate the ends of the blank, near contact positioning between the blank and die can be achieved before the stretching process begins [Figure 1-1 (a)]. With thicker or stronger material, it may be necessary to apply pressure to attain this near contact positioning. Sometimes a degree of preforming (normally in rollers) may also be necessary. The part is then stretched through displacement of the grip carriages and/or extension of the table rams. Achieving contact between the blank and die at an early stage reduces the mechanical and energy requirements of the stretch forming equipment.

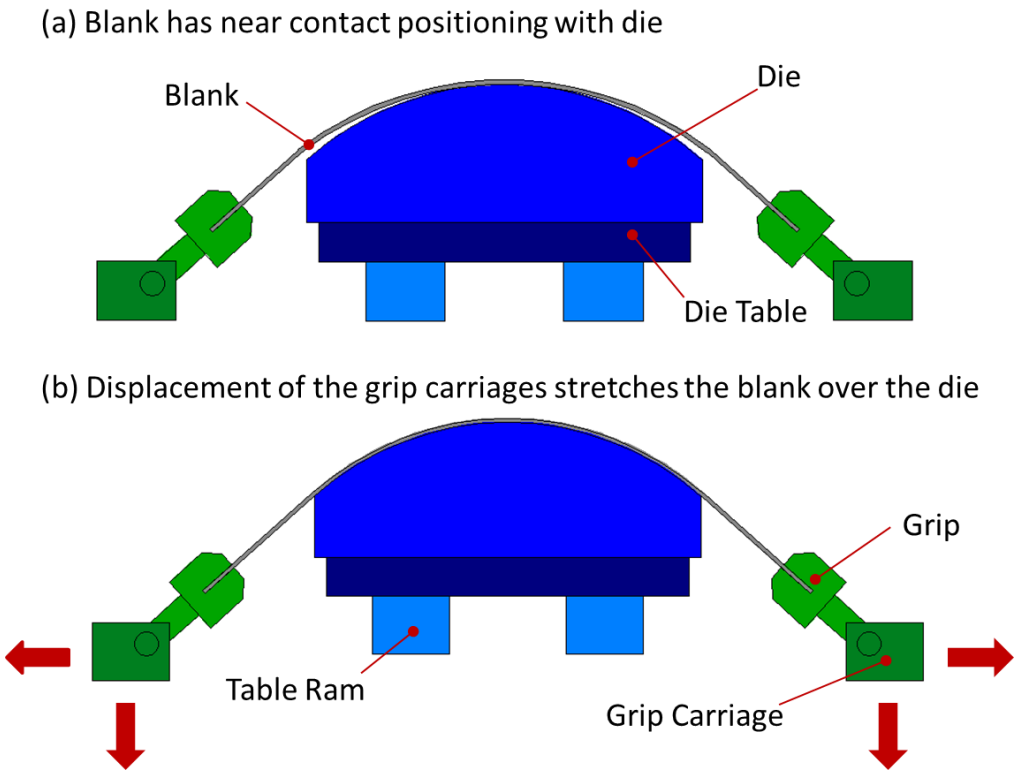

Figure 1-1: Drape Forming shown at the beginning (a) and end (b) of the process

1.2.2 Advantages and Disadvantages of Stretch Forming

Normally the cost of tooling in a stretch forming process is much lower than in a press forming process, since in traditional stretch forming only one tool is required while press forming requires a matching set of tools. Saving on the tooling costs can be greater where a fabricated die (or a die made from a less expensive material) is used. In a stretch forming operation all of the part is worked in the plastic region of the material's stress/strain curve, leading to an increase in hardness and tensile strength over the entire surface area, and a reduced likelihood of wrinkles and buckles appearing on the trimmed part. Springback is small in stretch formed parts compared to that evident in press formed parts. Since approximately 70% less force is required in stretch forming (ASM International, 1988) than that required in press forming, hence machinery is generally more lightweight and energy costs are lower. Material costs can also be lower in traditional stretch forming where the blank is gripped at two ends as opposed to being held in all directions in a press forming operation.

Stretch forming is more suited to parts with gentle curvature and shallow contours where press forming can produce a greater range of parts with more depth and sharper contours. Once the tooling and machine set-up has been finalised, press forming can also be a more rapid process better suited to the high volume production of components. Where a single die is used in the stretch forming process surface irregularities cannot be overcome through coining.

1.3 Stretch Forming over Reconfigurable Tooling

Reconfigurable tooling allows the contours of a die to be altered so that a range of parts can be formed using a single tool. There has been a sustained interest in reconfigurable tooling (for moulding, stamping, and stretch forming) for more than 150 years. Yet, despite most of the research into reconfigurable tooling being sponsored by industry, a machine which industry deems to be both affordable and fit for purpose has yet to be produced. To date no stretch forming equipment fitted with reconfigurable tooling is being mass produced and used to form components on a regular basis. Flexible bars and laminated contoured panels have been experimented with to create the reconfigurable die surface, but a bed of pins is currently the most widely accepted method of fashioning the die. Figure 1-2 shows the most commonly used arrangement for the bed of pins reconfigurable die. The cross-section of each pin is normally square in shape and pins are normally arranged in a rectangular close packed matrix. Pins are adjustable in height and have a semi-hemispherical tip at one end. Since this matrix of curved pin tips does not present a smooth surface at the top of the die, a layer of interpolation is required between the bed of pins and the blank being stretched. A flexible rubberlike material is normally used in the layer of interpolation. The metallic pin tips provide hard contact points which are adjusted to meet a control plane offset from the required contour [Figure 1-2 (b)]. As the blank is stretched reaction forces normal to the die (caused by the tension in the blank) push down on the soft interpolator causing it to deform and fill the gaps between these contact points [Figure

1-2 (c)]. With the correct choice of interpolator material and thickness the top surface of the interpolator should remain smooth so that parts can be formed with the required curvature and surface flatness.

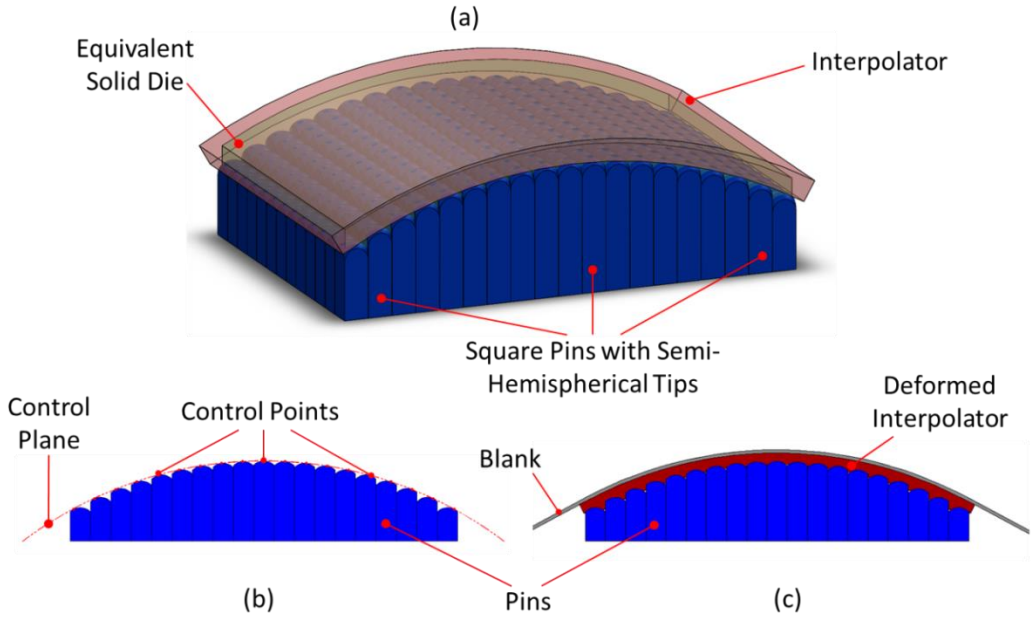

Figure 1-2: Reconfigurable tooling comprised of a bed of pins

1.3.1 Advantages and Disadvantages of Stretch Forming over Reconfigurable Tooling

Stretch forming over reconfigurable tooling offers a great saving in tooling costs since bespoke dies no longer need to be machined or fabricated for each job. Since heavy dies no longer need to be positioned on the forming bed for each job there is no need for heavy lifting equipment at the stretch forming machine and, with a computer controlled pin height setting system, set-up time between jobs can also be reduced. When using solid dies, it is not cost effective to machine a die unless the job batch size is of sufficient quantity to cover the cost of tooling, with the use of reconfigurable dies it is possible to use the stretch forming process to make one-off parts. When designing a new product that includes stretch formed parts, prototype parts can be produced much more rapidly and cost effectively since a new die does not need to be made for each iteration of the component during the design process. There is no need to rework dies when unexpected springback effects

are encountered after forming a part, as the part's contours can be corrected by simply adjusting the height of pins.

Edge effects (where the blank curls along its free edges in the stretching direction, due to transverse strain) can be more severe as the blank is acting on the flexible interpolator rather than a solid surface. Hence there can be more trimming requirements across the width of a part formed over a reconfigurable die. It may not be possible to obtain a smooth part over the outer rows of pins along the length and width of a reconfigurable die since there are no hard control points beyond these pins. Again, this can increase trimming requirements and material costs. The interpolator can be seen as a consumable material since its properties will change as it is compressed and relaxed during forming operations. Hence the cost of interpolators can be seen as a tooling cost which simply replaces the cost of solid tooling.

Witness marks (referred to as dimples), are often visible on parts formed over a reconfigurable die. There are two causes of dimpling, the blank can sink into the gaps between the control points of pins where the interpolator offers insufficient support, and the blank can show additional strain where it is stretched over exposed control points. Dimples decrease in severity as the thickness and properties of the interpolator approach their optimum for any given pin arrangement. Hence a system of interpolation, which sufficiently reduces dimples to the point that parts can be produced with the required surface flatness, needs to be identified. The strain in, and so the final thickness of, the selected system of interpolation needs to be predicted so that pins can be set to appropriate heights so that parts can be produced with the required shape and surface accuracy.

1.3.2 Recent Research into Stretch Forming over Reconfigurable Tooling

Recently, two multi-million dollar projects, concerning reconfigurable tooling for the stretch forming process, have been completed; where, both an American group (including MIT) involved in the "Reconfigurable Tooling for

Flexible Fabrication" (RTFF) project, and a Chinese built, European funded project named "Digitally Adjustable Tooling for manufacturing of Aircraft panels using multi-point FORMing methodology" (DATAFORM), produced multi-point forming tools, where the cost and complexity of their systems are greatly increased by the desire to minimise the cross-sectional area of pins. Both projects used the widely accepted arrangement of square pins with semi-hemispherical tips in a rectangular close packed matrix.

Meanwhile, the AMFOR group, at Ulster University have been investigating the viability of developing a reconfigurable tooling system, based on a relatively coarse bed of pins in a hexagonal closely packed arrangement. A faceted die surface (180 mm by 120 mm), representing a number of 70 mm diameter pin tips rotated to a 1700 mm radius, was made from ABSplus, at a rapid prototyping machine, before a 3000-series aluminium blank 1 mm thick was stretched over it, at an Instron test rig. Initial results indicated that this pin arrangement could be used to form surfaces of gentle curvature with the aid of a relatively thin layer of interpolation.

1.4 Aims and Objectives

This thesis will further test AMFOR's argument that, because parts manufactured through the stretch forming process normally have a relatively gentle curvature, a fine bed of pins is not necessary, and that parts of similar quality can be produced using pins, fitted with flat pin tips rotated about ball joints, and arranged in a coarser hexagonal close packed matrix. Rather than attempting to identify a solution that would allow reconfigurable tooling to be used in all processes, as the MIT team did (Munro & Walczyk, 2007) (see Section 2.6), this thesis concentrates on tooling for the stretch forming process alone. The main aim of this thesis is to illustrate that AMFOR's new design can produce parts, with the necessary smoothness, appropriate for a wide range of commercial applications. The DATAFORM project, where aluminium boat hulls (Bae, et al., 2012) and façade panels on a curved building (Lee & Kim, 2012) (see

Section 2.4) have been manufactured using a reconfigurable stretch forming system, has already demonstrated, to a degree, that this process to be considered in a wider range of commercial applications. Yet the complexity of their machine (and so its cost) would rule out the purchase of such equipment for the use in many additional projects. The lower cost of the new AMFOR design would allow the purchase of a reconfigurable system for larger projects, and may even enable this process to become commonplace in general sheet metal workshops. To achieve this aim, three major objectives must be met.

1) Ascertain what features of a pin arrangement and pin tip design detract from the production of dimple free parts in stretch forming over reconfigurable tooling, and select a pin arrangement that is suitable for use with a coarse bed of pins.
2) Select a suitable geometry for the new pivoted pin tips that would facilitate their cost effective manufacture, and will allow for the production of relatively dimple free parts in a stretch forming process over a coarse bed of pins.
3) Investigate the suitability of a range of polyurethane materials for use as an interpolator, in the production of relatively dimple free parts formed over the new tooling system.

1.5 Methodology

The current state of knowledge pertaining to the stretch forming of sheet metal is examined through a literature review, presented in Chapter 2 of this thesis. A series of mechanical tests (presented in Chapter 3) are carried out on the materials considered in this project. Data from these tests is analysed in Microsoft Excel and material models are then constructed for use in simulations of the stretch forming process. Material models pertaining to the blank and interpolator materials used in the more detailed PAM-STAMP models are validated by simulating the mechanical tests, using these material models, in the same software, and comparing the results gathered to corresponding measurements from the physical tests.

Results from phase one of the FEA simulations, carried out using the AutoForm^{plus} R3 explicit finite element code are presented in Chapter 4 (Section 4.4) of this thesis, to address objective 1. The dies used in this comparative study are to the same scale as the final RTFF die (approximately 1200 mm by 1830 mm). The AutoForm^{plus} R3 software has been selected for this task since it employs a rapid solver resulting in reduced computational times when working on models of this scale. Results from phase two of the AutoForm simulations are presented in Chapter 4 (Section 4.6) of this thesis, to aid in the selection of a suitable geometry for the new pivoted pin tips, and address objective 2.

The design of a lab scale machine, with a die approximately 490 mm by 310 mm, is presented in Section 5.2 of this thesis. The lab scale simple gripping and stretching mechanism, which is suitable scaling up to the proportions required for industrial use, is also illustrated with a brief description in Section 5.2. While the pin heights of the lab scale reconfigurable die are initially adjusted by hand, a cost-effective mechanism to facilitate automated sequential height adjustment of AMFOR's circular pins is proposed, and presented in Appendix K.

Results from a series of FEA simulations representing the lab scale process, carried out using the PAM-STAMP 2G v2015.0 explicit finite element code, are presented in Chapter 5 of this thesis, to address objective 3. The Kaylan D series of polyurethane materials are tested here for use with AMFOR's proposed pin tips and pin arrangement. Key models from this series are validated, in Section 5.8, through comparisons of scans of the surfaces of parts obtained from physical testing, on the lab scale machine, to the deformed meshes from corresponding simulations. Results from this lab scale study are then projected to an industrial scale, in Section 5.9, through two simulations of the stretch forming process over a reconfigurable die with dimensions of approximately 1.2 m by 1.2 m.

Finally, conclusions, which have been drawn from the study presented in this thesis, are laid out in Chapter 6, together with suggestions for further work that can be carried out to improve the understanding of the subject matter covered here.

Chapter 2. Literature Review

2.1 Introduction

This chapter is presented in a further six sections. Section 2.2 describes some of the early research into reconfigurable tooling. Sections 2.3 & 2.4 are used to review papers pertaining to the two recent multi-million dollar projects (RTFF & DATAFORM respectively). Section 2.5 highlights some of the research presented since the beginning of the new millennium from other sources, and Section 2.6 outlines the findings from a review into the advances in reconfigurable tooling carried out in 2007. Finally, Section 2.7 relates the previous research to the work carried out for this project.

2.2 Early Research into Reconfigurable Tooling

The first piece of research to be examined in this report is the work carried out at the University of Tokyo more than fifty years ago (Nakajima, 1969), where reconfigurable tooling was proposed for press working of sheet metal, forming of plastics, die casting, and electrolytic machining. The dies/moulds were constructed of a number of thin wires bound together by a retainer so that the ends of the wires make up the required surface of the die/mould. The curved surface of the die/mould was generated by a numerically controlled machine with either a point to point technique where each wire is pushed into place individually, or a sweep technique where each row or column is positioned through the sweeping motion of an angled tool. Nakajima reported a repositioning accuracy in the order of 0.05 mm. He found that when using this tooling for sheet metal stamping, a thin rubber sheet was required to overcome scratches and dimples produced in the sheet metal by the ends of the wires.

Combinations of Punches & Dies Punch – Die (or Die – Punch)	Relative Cost of the Manufacture of the Mould	Relative Time of Manufacture of the Mould	Maximum Number of Production (x 10^8)	Relative Cost (when Production Number is 100)	Surface & Accuracy of Products
1 – 1	4 – 8	4 – 8	5 – 10	4 – 8	bad
2 – 2	4	5	5 – 10	4	bad – good
2 – 3	6	6	1 – 5	6	good
2 – 4	?	?	10 – 100	?	good – very good
2 – 8	57	58	1 – 5	58	very good
3 – 3	11	10	10 – 100	11	good
4 – 4	?	?	1 – 5	?	good – very good
5 – 5	8	9	1 – 5	8	good – very good
6 – 6*	29	24	1 – 5	30	good – very good
7 – 7*	43	43	1 – 5	43	very good
7 – 9*	24	23	10 – 100	24	good
8 – 8*	100	100	10 – 100	100	very good
9 – 8*	60	62	10 – 100	60	good

*Conventional Combinations

Types of Punches and Dies

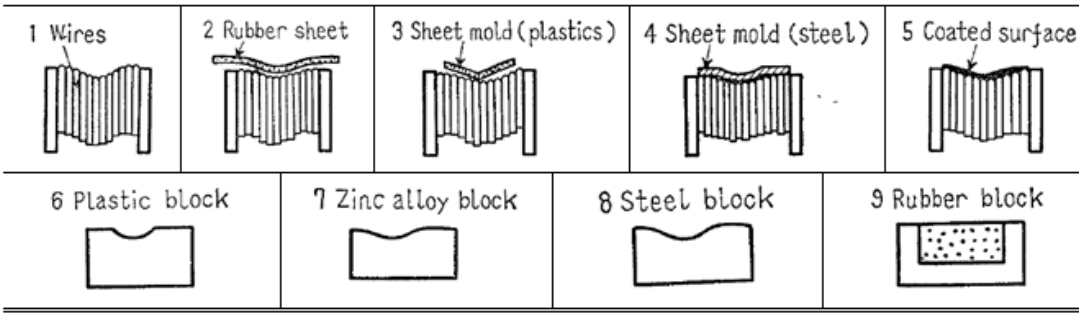

Table 2-1: Nakajima's comparison between wire type moulds and conventional moulds

Nakajima's comparison between combinations of punches and dies, both conventional and reconfigurable with different interpolator layers, in terms of cost and manufacture time, has been reproduced here in Table 2-1. It is evident from the table that, when 100 components are to be manufactured, parts stamped on a matching set of reconfigurable tools with thin rubber interpolators resulted in a product cost that is only 4% of that for parts

stamped on solid steel tools. Although he did not try to optimise the interpolator, he concluded that, where a high surface quality is required, moulded surfaces supported by wires can be used.

In the late sixties, early seventies a study at the University of Washington, sponsored by Boeing (Wolak, et al., 1973) developed an infinitely variable surface generator. A tool was produced consisting of a matrix of uniformly spaced threaded rods with hemispherical tips. This tool was located in a Plexiglas box and covered with a rubber sheet before a vacuum bag was used to cast a solid Rigidax tool for the stretch forming of aluminium alloys. There is no evidence that any stretch forming was carried out using this tooling.

Collaboration by a number of German universities (Finckenstein & Kleiner, 1991) led to a tool being developed using a matrix of uniformly spaced threaded rods, similar to that described by Wolak. In this design the threaded rods were used to adjust the height of a matrix of closely packed square pins with hemispherical tips. CAD models were used to determine the height of each pin and a computer controlled servo system was used to actuate the threaded rods (see Figure 2-1). The tooling was used in the hydro-mechanical deep drawing of sheet metal.

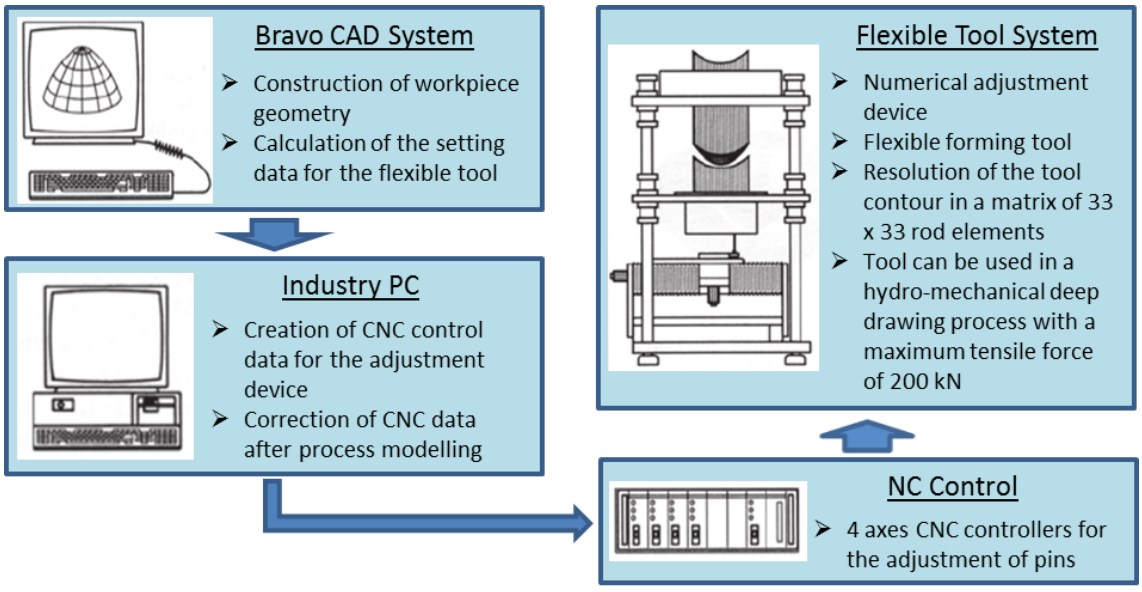

Figure 2-1: Information flow from the CAD system to the adjustment device

2.3 MIT and the RTFF Project

By far the largest body of work, pertaining to reconfigurable tool in sheet metal forming, belongs to the Massachusetts Institute of Technology, and has been led by David E. Hardt. The rational for designing a reconfigurable tooling system is given in a paper detailing their early work (Hardt, et al., 1982). They stated that the largest economic factor involved in producing smaller batches of sheet metal parts is the cost of manufacturing forming dies. This is due to them being designed in a number of iterations involving trial setups at the machine, due to the complexity of the three-dimensional plasticity problem, springback (the elastic recovery of sheet after it is unloaded), and variations in material properties/thickness. They proposed using a reconfigurable die together with a measuring system producing a closed loop system, where part geometry is inspected for accuracy and consistency at the machine, before corrections are carried out as part of the process. Corrections in pin length were determined using the simple proportional control equation;

$$P_{i+1} = P_i + (P_0 - P_i)A, \tag{1}$$

where P_0 is a vector describing the position of pins in a desired part, P_i is a vector describing the position of the pins after the i^{th} iteration. The difference between P_0 and P_i is the error in the part, P_{i+1} is a vector describing the new position of pins, and A is a proportional constant. Results from their first experiment were somewhat corrupted by insufficient force in the apparatus and slippage of pins, yet convergence towards the desired shape was evident. Results from their second experiment show good convergence, with the desired shape of the part being formed in only two iterations.

Research into reconfigurable tooling continued at MIT, with Dr Hardt supervising numerous projects (BSc, MSc and PhD) concerning discrete dies, until the mid-nineties when MIT joined the Rensselaer Polytechnic Institute, Northrop Grumman Commercial Aircraft Division, and Cyril Bath in a fourteen million dollar project, sponsored by the U.S. government

Defence Advanced Research Projects Agency (DARPA), that led to the development and demonstration of a commercial machine by October 1999. The first commercial reconfigurable tool produced by the RTFF project consisted of a closely packed matrix of 2688 pins, 28.6 mm square and 533.4 mm in length. The rationale used to arrive at this pin arrangement and cross section can be found in a paper printed in the Journal of Manufacturing Systems (Walczyk & Hardt, 1998), where a generalised procedure for designing discrete dies is laid out and then applied to the design and fabrication of a pair of high resolution sheet metal stamping dies. The reasoning behind the spherical tips is given as "*one of the easiest ways to avoid having sharp edges on pins which could pierce through the interpolator and into the sheet during forming*". Minimising the diameter of the spherical tip was prioritised because "*smaller pin tip diameters mean that pin spacing is decreased and the die surface has a finer resolution*". A number of different pin arrangements and cross sections are examined with preference given to layouts which could be easily clamped in a rigid frame, rather than properties such as bending stiffness, buckling strength or bending stress. While these are valid reasons for taking their tool design in the chosen direction, the door is left open for further research into pin arrangement, and pin tip geometry. Fundamental equations for calculating a pin's critical bending load (F_p) and critical buckling load (F_b) were identified as;

$$F_p = \frac{\sigma_y I}{LC_{max}} \tag{2}$$

$$F_b = \frac{\pi^2 EI}{4L^2} \tag{3}$$

where, σ_y is the material's yield strength, I is the second moment of area pertaining to the pin's cross section, L is the length of unsupported pin, C_{max} is the maximum distance from the neutral layer to the outside of the pin, and E is the material's elastic modulus.

A study was carried out by the Rensselaer Polytechnic Institute (Walczyk, et al., 1998) to apply these design principles to the stretch forming process.

A 4 x 4 prototype tool was constructed with 25 mm square pins arranged in a closely packed matrix clamped rigidly in a frame. The pins were actuated by hydraulics, where the pin body made up the outer casing of a hydraulic cylinder and the cylinder rod was fixed to a base plate. Row dividers were used to prevent buckling of rows due to clamping force. CAD data was used to determine the height of pins. Each pin was set as its tip came into contact with a setting platen, before an off signal was sent to its servo valve to cut off fluid flow which raises each pin (see Figure 2-2).

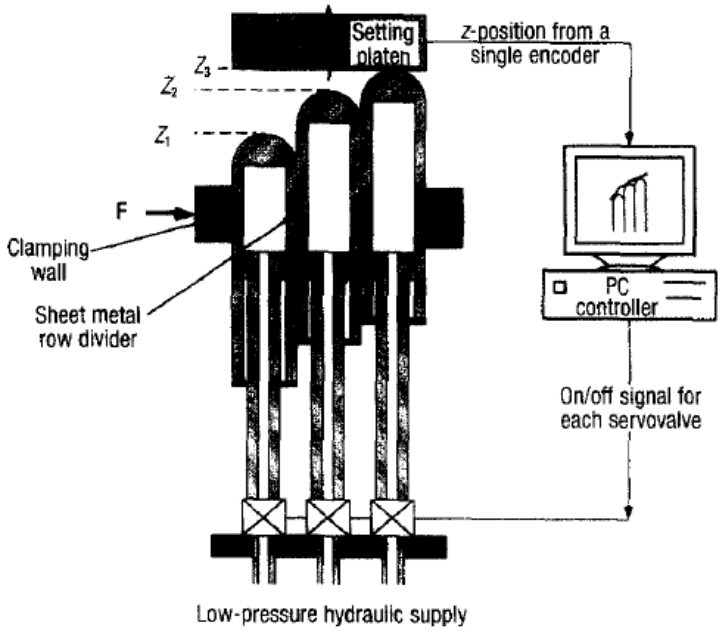

Figure 2-2: Set-up procedure for the RPI stretch forming tool

This actuation method, together with two further actuation methods were compared in a joint paper (Im, et al., 2000). The second concept was first proposed in an MSc project (Boas, 1997) undertaken at MIT and supervised by Dr Hardt. It employs a sequential set-up system (see Figure 2-3) to manipulate a matrix of closely packed 28.6 mm square hollow pins with hemispherical tips. A nut was inserted at the open end of the pin. Each nut was mated with a leadscrew mounted vertically on a horizontal base plate. A 4 x 4 matrix of motors is used to adjust the height of 16 pins at a time. The motor matrix is positioned via an x-y servo table until all pins are set at the correct height. Pin matrix clamping is not required for this concept since the pins remain at their set heights when subjected to a vertical load equal

to that expected during the forming process. Coupling between the vertical leadscrews and motors was also examined. A taper coupling system was firstly explored, with this system's biggest advantage being that no forced rotation of the leadscrew will occur during engagement. The authors anticipated problems with using more than one coupling unit on a full sized industrial machine. As friction supplies the drive in a taper coupling system, alignment between the leadscrew and drive, and positioning of the drive would require great accuracy. There was a doubt whether these accuracy requirements could be met with repeated use in a shop floor environment. Hence a direct coupling system was chosen for further development. This system uses a hexagon head at the end of the leadscrew with a 12 point female connection on the drive mechanism as shown in Figure 2-3.

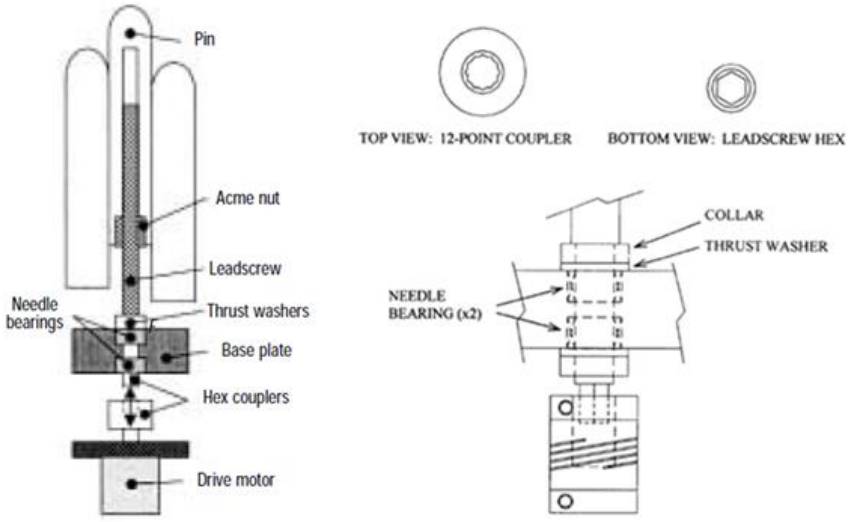

Figure 2-3: The sequential set-up (SSU) concept and the preferred direct coupling system

The final concept, a shaft driven leadscrew system (see Figure 2-4), was similar to the sequential set-up system with a matrix of closely packed 28.6 mm square hollow pins with hemispherical tips again being used. Again a nut was inserted at the open end of the pins, with each nut mated with a leadscrew mounted vertically on a horizontal base plate. The vertical leadscrews were connected to a worm gear via a clutch.

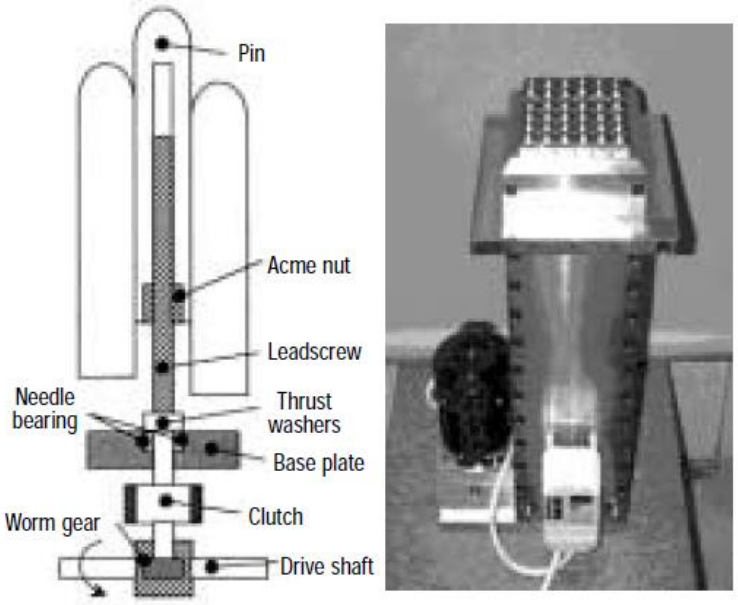

Figure 2-4: The shaft-driven leadscrew (SDL) concept and prototype

The set-up procedure starts with all pins at their lowest position. A single motor drives each horizontal shaft. The worm gears transfer rotational motion through 90° so that the vertical leadscrews are driven and the pin height is adjusted. When pins reach their desired height, their individual clutches are disengaged so that the vertical leadscrew is no longer driven. The entire system is computer controlled. Again, no pin matrix clamping is required for this concept.

The sequential set-up system showed the best pin adjustment accuracy at 0.005 mm, although all three systems were within the target accuracy of ±0.05 mm. The repeatability of pin positioning proved more than adequate for all three actuation systems. Set-up times from each prototype apparatus were adjusted so that comparisons could be made for a full sized industrial machine, with dimensions of 1.8 m in length by 1.2 m in width and pin motion of 0.3 m. The sequential set-up system was shown to have the slowest overall set-up time at approximately twice that of the shaft driven leadscrew system. Although the hydraulic system had the best set-up time (approximately 12 minutes compared to 30 minutes for the sequential set-up system and 16 minutes for the shaft driven leadscrew system), problems concerning the size of the pin clamping frame are anticipated in the full

sized machine. An over complicated wiring system, when compared to that of the sequential set-up concept, is also anticipated in full sized machines using both the hydraulic and shaft driven leadscrew concepts. The overall cost of a full sized machine was also calculated, using all three systems. It was found that the overall cost of the shaft driven leadscrew system, at $876,000, would be twice that of either of the other two systems.

The shaft driven leadscrew system was further developed in a paper originating from the Northrop Grumman Technology Development (Haas, et al., 2002). This paper justified using a maximum vertical load of 22.5 kN and a maximum horizontal load of 5 kN when calculating the stiffness of pins. It was also determined that the change in relative height between any pin and its neighbours should not exceed 50 mm. The torque required to lift pins was calculated at 0.39 Nm. Tests showed that, using the relationship between clutch engagement time and pin motion, pins could be positioned with an accuracy of 0.1 mm and repeatability of 0.02 mm. Tests also showed that both clutch types tested (API Deltran & PIC Design) would be suitable, in terms of torque and reliability, to engage the vertical leadscrews without slippage. The 36 pin prototype forming bed, shown in Figure 2-4, was found to meet all design requirements. Due to having a clutch on each leadscrew, a problem was encountered with the wiring of this prototype which would be magnified when attempting to manufacture a full sized industrial machine, due to the sheer number of pins.

An MIT MSc project (Eigen, 1992) was used to determine the ideal interpolator for smoothing dimples in sheet metal formed on discrete dies. A number of thermoplastics were investigated and ethylene vinyl acetate (Elvax) was found to produce the best results when heated and preformed to the shape of the tool. The ideal thickness of the interpolating elastic cushion was found to be equal to or slightly thicker than the pin width. According to the excellent summary of the RTFF project entitled “Tools of Change” (Papazian, 2002), experience has shown that preforming of the interpolator is not necessary. To date the RTFF project has resulted in two machines being built by the Cyril Bath Company for commercial use. Figure 2-5 shows

a full-scale prototype stretch forming machine with reconfigurable tooling built at Cyril Bath.

Figure 2-5: Full scale prototype stretch forming machine with reconfigurable tooling built by Cyril Bath

2.3.1 Modelling of the RTFF Process

Responsibility for simulation and finite element analysis of the new stretch forming process over discrete dies was shared between MIT and Northrop Grunnam. A contribution from the MIT team (Socrate & Boyce, 2001) explained the degree of complexity associated with modelling the new process, with a rigid tool comprised of pins, a deformable metal sheet, and a polymer interpolator going through large local deformations. The simulation was developed in three stages. Stage 1 was to set up detailed FEA models to investigate the discrete nature of the die and the presence of the interpolator. Stage 2 was to simplify the model so that an equivalent model of the complete process could be assembled where the die and interpolator were treated as one with the model using softened contact properties between the sheet and die at the positions of the initial contact between individual pins and the interpolator. The final stage was to apply a springback algorithm to reflect conditions following unloading of the sheet.

A more detailed model was used in the Northrop Grumman study used to predict springback (Kutt, et al., 1999). The Abaqus Explicit FEA software was used to simulate the forming process while the non-linear, static option in the implicit Abaqus Standard was used to simulate the springback. The sheet was meshed with quadrilateral shell elements containing four nodes and the die surfaces were meshed as rigid surfaces again with four noded quadrilateral elements. The polyurethane interpolator was meshed with eight noded solid hexahedral elements formulated for large strains and deformations. The simulations were validated through lab scale tests where Ti-15-3 titanium sheets of 0.8 mm thickness were stretched over discrete dies to form spherical and saddle shaped (anticlastic) parts. There was good agreement evident, in terms of both springback and final shape profile, between experimental results and simulations. The simulation even managed to capture the negative springback, or spring-in, anomalous behaviour found in anticlastic parts. Simulations were also carried out with two additional sheet thicknesses (1 mm and 1.5 mm) and the material properties of Ti-B21S titanium sheet, so that springback could be studied for different parameters. A new way of quantifying springback, called Average Normal Distance, was proposed as;

$$Average\ Normal\ Distance = \frac{2A}{S+T} \tag{4}$$

where, A is the area between the two chord lines before and after springback, T is the chord length before springback, and S is the chord length after springback (these two can be reversed for spring-in). Using the Average Normal Distance, Kutt was able to discern that in a generalised springback situation, for the range of parts considered, springback remains a monotonically increasing function of;

$$^{1}/_{t}\ \&\ ^{\sigma_y}/_{E} \tag{5-6}$$

where, t is the material thickness, σ_y is the material's yield strength and E is its elastic modulus. He also commented that other factors influence the magnitude of springback independently of these two ratios, such as the

tensile stress in the direction of stretching and the geometry of the required part, which relate directly to the stretching and bending strains present during the forming process.

2.4 The DATAFORM Project

A second major study into the viability of the use of discrete dies in sheet metal forming began in October 2006. The main objective of this 3 year €3,725,230 project, entitled DATAFORM, was the development and application of digitally adjustable multi-point forming tooling and multi-point positioning tooling for fabrication of aircraft panels. In particular, DATAFORM set out to enable flexible and digital manufacturing of skin panels in aircraft bodies. Cardiff University were given the lead in this project with the development of a multipoint forming machine led by Jilin University in China.

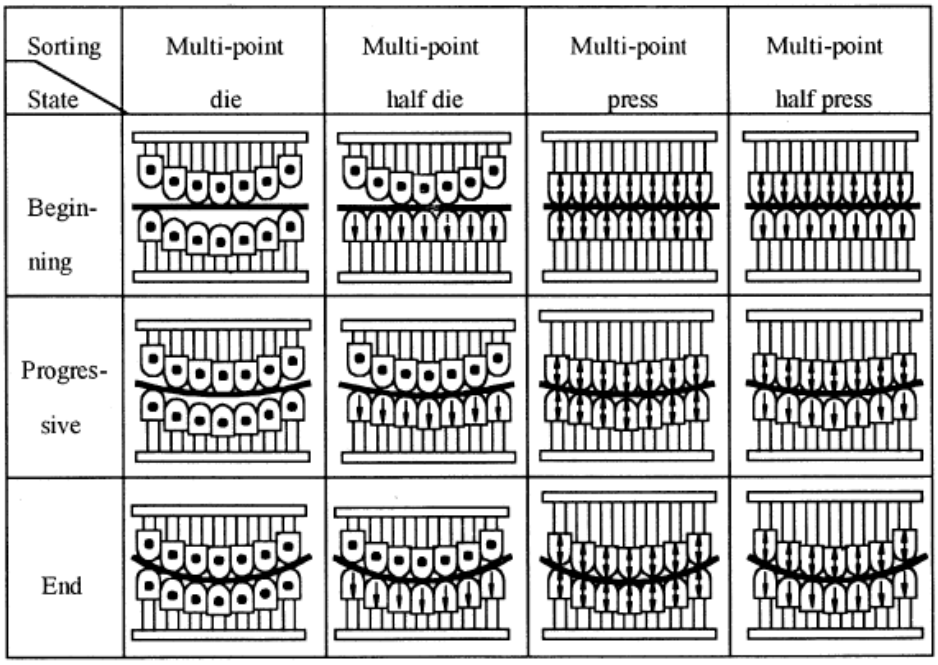

Figure 2-6: Four modes of MPF developed at the Jilin University

The first paper to be considered in this section (Li, et al., 1997), is an example of the research carried out at Jilin University prior to the commencement of the DATAFORM project. The authors illustrate four modes of multipoint forming (MPF) which can be carried out on a matching set of discrete dies (see Figure 2-6). The paper goes on to demonstrate the

different loading paths and hence, the distribution of residual stress, in the finished parts when pins are actuated during the process in an active manner.

In a study originating from the Jilin University, during the DATAFORM project (Liu, et al., 2008), the authors describe a closed loop control system which they have called Multi Point Die Forming (MPDF).

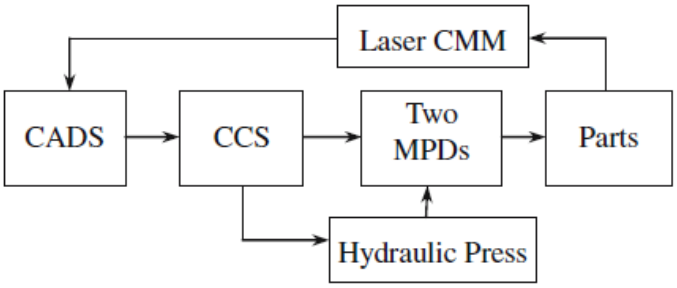

Figure 2-7: A flow chart of the MPDF system from Jilin University

The system, illustrated in a flow chart (Figure 2-7) employs CAD/CAM software, developed at the university and referred to as CADS, which uses CAD models to determine the height of individual pins, within the die matrix. Data from the CAD software is passed to a multi-axial numerical control system referred to as CCS, which manipulates each pin to its desired height. The forming is carried out between two multi-point dies in a hydraulic press. A laser Coordinate Measuring Machine is employed to detect shape errors which are passed back to CADS where new pin heights are determined. There is no reference in this study to the time taken to reconfigure a die, or whether the pins are repositioned in a sequential manner or simultaneously. The study indicates that Jilin's MPF system is best suited to forming metallic sheets of medium thickness, without stating an actual range of material thickness. Two special MPDF techniques are described. The first is a sectional MPDF technique used to form thicker plates (10 to 70 mm) of a large surface area, section by section. In the example given, a matching set of dies was used with a 9 by 9 matrix of pins having a cross section 150 mm by 150 mm in dimension. The second is a MPDF technique that was developed for forming thin sheet metal parts. For this process a fine bed of pins was clamped firmly together to mimic a solid

die. In the example given a 40 by 32 matrix of pins, with a cross section 10 mm by 10 mm in dimension, was used to form a face in 08AL sheet of 0.5 mm thickness. While Polyurethane hemispherical tips are used in the forming of thick plate, steel hemispherical tips together with two deformable elastic pads (interpolators) are used for thin sheet. It was reported that dimpling was successfully avoided in the parts produced with both of these techniques.

In a paper presented at the 2010 International Conference on Digital Manufacturing and Automation (Liu, et al., 2010) the design of the DATAFORM prototype tool for stretching aircraft panels was discussed. The pin matrix was designed to minimise pin cross sectional area while maximising the stroke. Following simulations and physical testing, it was found that 25 mm square pins could support the pin loading conditions. A 48 by 32 matrix of pins was assembled with a 1200 mm by 800 mm forming area. Each pin had a circular end piece with a 10 mm radius hemispherical tip. Although this was a lab scale tool, its forming area was sufficient for the forming of some full sized aircraft panels. The heights of individual pins were determined from CAD models before sequential positioning using a robotic arm. No information was given concerning the time taken to set up the tool. The tool can be used on the bed of a conventional stretch forming machine. With the addition of a CMM and a shape error algorithm a closed loop system can be set up, although the part needs to be removed from the tool before the die is reconfigured.

2.4.1 Modelling of the DATAFORM Process

As part of the DATAFORM project, a numerical investigation was carried out to determine the optimum pin geometry for the new multi-point stretch forming machine (Wang, et al., 2010). While being very relevant to this project, it should be noted that the authors only considered tool geometry for their existing system i.e. square pins with round tips arranged in a rectangular close packed matrix. Abaqus/Explicit is used for simulations, with a set up very similar to that of the Northrop Grumman team except

that springback is neglected. Shell elements S4R are used to represent the sheet, solid elements C3D8R are used to represent the interpolator, and the discrete die is represented as a rigid surface with the R3D4 elements. Properties of the aluminium alloy 2024-0 are used for the sheet with the von Mises yield criteria, the Prandtl-Ruess flow rule, and isotropic hardening. A polyurethane material was selected for the interpolator with the Mooney-Rivlin model being applied in simulations. A friction coefficient of 0.1 is used between the sheet and interpolator, while 0.2 is used between the interpolator and die. Simulations were carried out with material being stretched over discrete dies, of a 400 mm by 400 mm forming surface, comprised of matrices ranging from 10 by 10 to 80 by 80.

Results [see Figure 2-8 (a)] show that the change in thickness strain, which can be taken as evidence of dimpling, is stronger as pin density decreases. It was also shown that, when the pin matrix was finer than 32 by 32, dimples virtually disappeared. A matrix of 20 by 20 pins was used in simulations to compare the effect of pin tip radii, where the radius of hemispherical tips ranged from 10 mm to 32 mm. Results [see Figure 2-8 (b)] show that dimpling is reduced as the pin tip radius is increased. Increasing the radius of hemispherical tips increases the surface contact area between the tips and sheet, and hence reduces the uneven distribution of thickness strain and formation of dimples. To quantify their surface quality, the authors used the simple error equation,

$$Error = \sqrt{\frac{1}{n}\sum_{i=1}^{n}(z_i - z_{ti})^2} \tag{7}$$

where n is the number of points, z_i is the height of the sampled point, and z_{ti} is the target height at that point. An error of less than 0.2 was illustrated for matrices finer than 32 by 32. It should be noted that a 10 mm thick interpolator was used in all simulations. The RTFF team have found, in previous work, that there is a direct relationship between pin dimensions and the thickness of the interpolator required to suppress dimples. Therefore using an interpolator 10 mm in thickness on this 400 mm by

400 mm forming surface would result in the requirement of a matrix consisting of 40 by 40 pins.

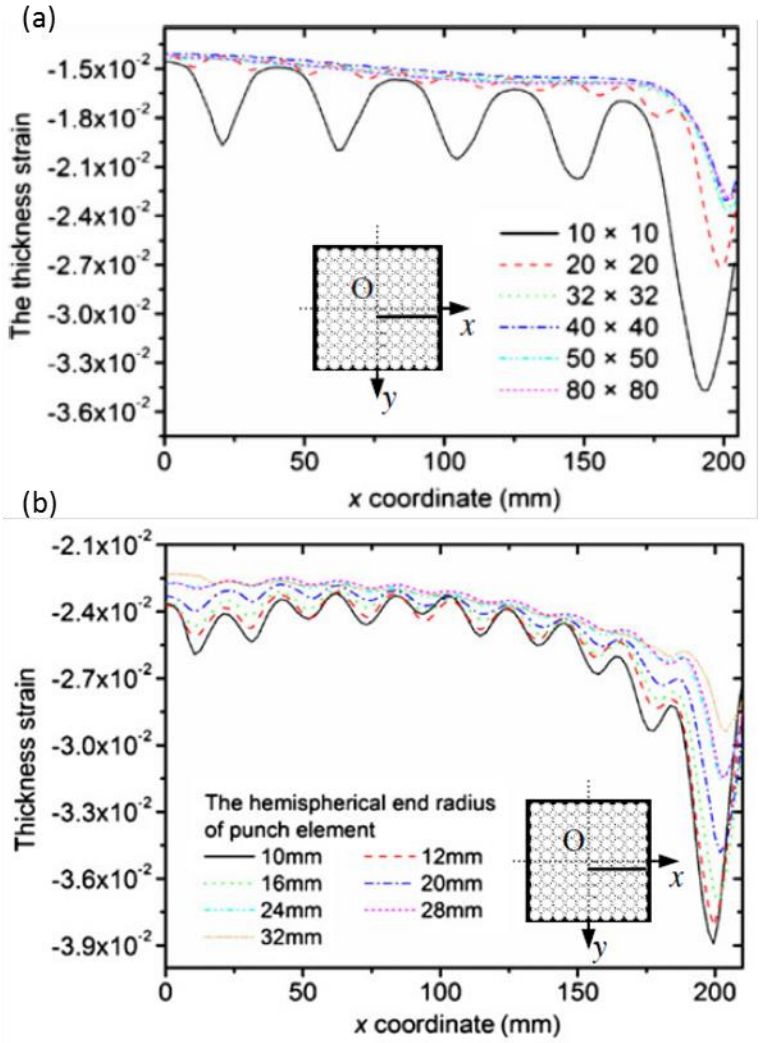

Figure 2-8: Wang's pin density (a) and pin tip radii (b) comparisons

In a very similar study (Cai, et al., 2009), a 40 by 20 matrix of 10 mm square pins was used to determine the effect of interpolator thickness on shape error through a number of simulations where the interpolator thickness varied between 2 mm and 10 mm. Again best results were obtained when the 10 mm thick interpolator was used with the 10 mm square pins. A smaller forming area of 240 mm by 240 mm was used in a set of simulations to determine the optimum pin size with this interpolator. Results were again predictable i.e. it was found that better shape accuracy was achieved with pins of a cross sectional dimension less than 10 mm.

In a study carried out at the Pusan National University in Korea (Seo, et al., 2012), regression analysis and a neural network where used to determine the influence of part geometry, together with pin and interpolator design parameters on the surface quality of parts produced. The study was applied to the pin arrangement used in the Asian tooling (square pins with round ends and hemispheric tips in a rectangular close packed arrangement), while the design parameters looked at were, the punch size (diameter), the objective curvature of the part, and the thickness of the interpolator (Shore hardness of 90). The data set used in the study came from FEA simulations with the forming process being analysed by the explicit ANSYS LS-DYNA solver and springback being handled by the implicit ANSYS solver. A forming area of 300 mm by 200 mm was used, with the sheet material properties of Al 5052-H34, and the interpolator behaviour being described with a Monney-Rivlin model. Simulations were validated through laboratory tests where, the sheet was gripped on both sides in a press before the tool, comprising of 150 of 20 mm square pins, was lowered down to stretch the material. Simulations were carried out with interpolator thicknesses of zero, 5 and 10 mm, punches ranging from 10 to 100 mm in diameter, and objective radii of curvature of 300, 350, and 400 mm. The authors found that the main parameters that effect surface error across the width (transverse to the direction of stretch) are punch size and interpolator thickness, while the main parameters that effect surface error in the direction of stretch are punch size and objective curvature. While this type of study is useful, there are many more parameters which affect the quality of the surface produced; such as, material properties/thickness, interpolator properties, surface area being formed, pin tip geometry, and pin arrangement.

2.4.2 The DATAFORM Gripping/Stretching System

A paper presented at the 10th International Conference on Technology of Plasticity (Li, et al., 2011) details the development of DATAFORM's flexible stretch forming machine illustrated in Figure 2-9. The machine was

designed to overcome three problems associated with conventional stretch forming machines; the inability to curve the blank so that it is tight fitting to the die during stretching, the inability to apply different stretch rates to sections of the blank, and material wastage due to gripping and the overhang between die and grips. The final design utilises 20 gripping jaw sections (10 per grip) mounted via universal joints. Twenty vertical hydraulic rams primarily control the height of each grip section, while 20 diagonal rams primarily control the angle of tilt in each section, and 20 horizontal rams primary control/supply the pulling force at each section. The grip sections are set, close to the edge of the die, at different heights to create a curve which approximates the curvature of the die, and allows the blank to be close fitting to the total forming surface during all of the stretching process. The horizontal rams provide 1200 kN of tensile force per grip (10 sections), while contributions from the vertical and diagonal rams increase the total pulling force per grip to 2000 kN.

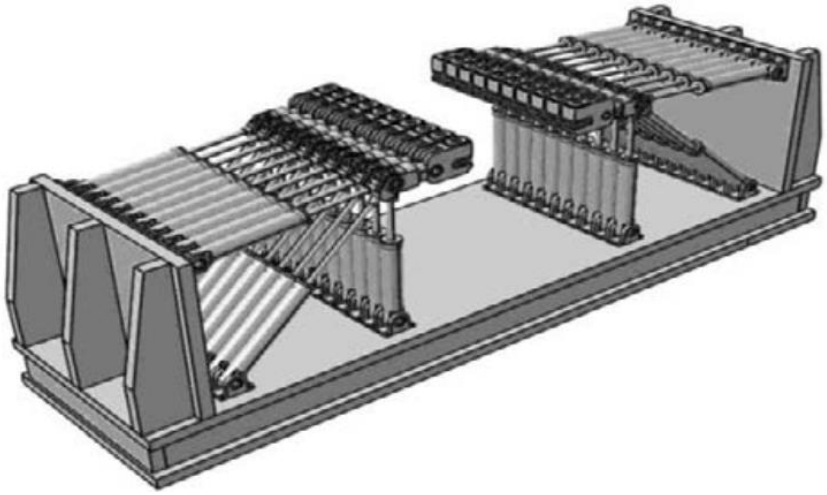

Figure 2-9: DATAFORM's flexible stretch forming machine

While tests have shown the machine to function within its set parameters, the gripping system appears to be over-engineered. It should be remembered that plane strain conditions exist at the grips where deformation is restricted across the width of the blank, hence ε_2 is zero and ε_3 is equal to ε_1. Figure 2-10 (a) shows the industry standard grip position where the gap, between the die edge and grip is approximately equal to half the width of the blank. This ensures that the effects of plane strain

conditions at the grips have dissipated so that the material over the die is stretched under uniaxial conditions. While moving the grips closer to the die shortens the required length of the blank and hence reduces waste material, Figure 2-10 (b), there is a danger that the effects of plane strain at the grips have not diminished sufficiently in the blank area towards the ends of the die. Since the blank is being subjected to excessive thinning, as it is stretched over the ends of the die, this would lead to reduced formability and premature fracture. By maintaining tangential positioning of the grips in relation to the curvature of the die, material will remain in contact with the die during the forming process. Allowing the grip sections to move at different velocities would imply that varying strain rates are present across the width of the blank. This would introduce a shear strain on the blank at the areas between the grip sections, again leading to reduced formability in the stretching direction and premature fracture.

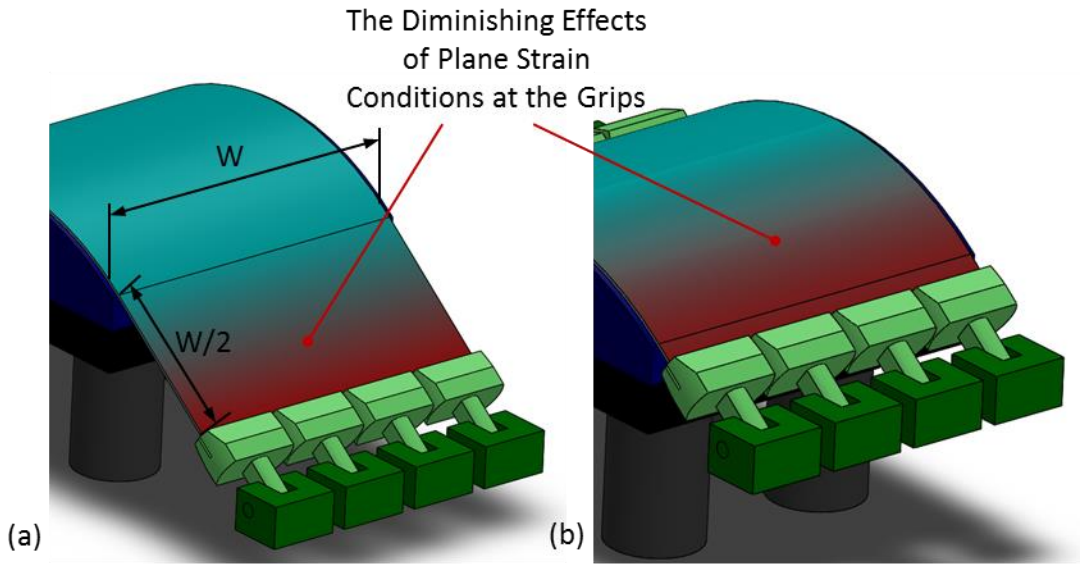

Figure 2-10: The industry standard (a) and DATAFORM's (b) grip positioning

The authors propose a closed loop system where shape errors can be detected, and pin heights altered to produce a part within tolerance at the end of an incremental process. As the heights of pins are adjusted through robotics the workpiece will need to be removed between increments, leading to repositioning problems where material is deformed around the grip sections. While the RTFF team can boast of a tooling system that is

reconfigurable in less than 15 minutes, sequential manipulation of the 1536 pins in the DATAFORM system would surely require a number of hours.

2.4.3 DATAFORM Case Studies

A case study (Lee & Kim, 2012) reports on the development of a new hybrid process developed to produce curved façade panels for the Dongdaemun Design Park building in Seoul. A total of approximately 45000 panels were required with more than 32000 being curved and almost 22000 having double curvature. The 1.2 m by 1.6 m panels were formed from an unspecified aluminium alloy of 4 mm thickness. The new hybrid process is actually a combination of multi-point stretch forming and multi-point forming, which is very similar to the Cyril Bath Process (see Section A.1 of Appendix A.) where a second forming tool is used to press concave shapes into convex stretched parts. In this case the second tool is used to increase the curvature of the blank. The machinery used (see Figure 2-11) looked remarkably similar to that developed at the Jilin University.

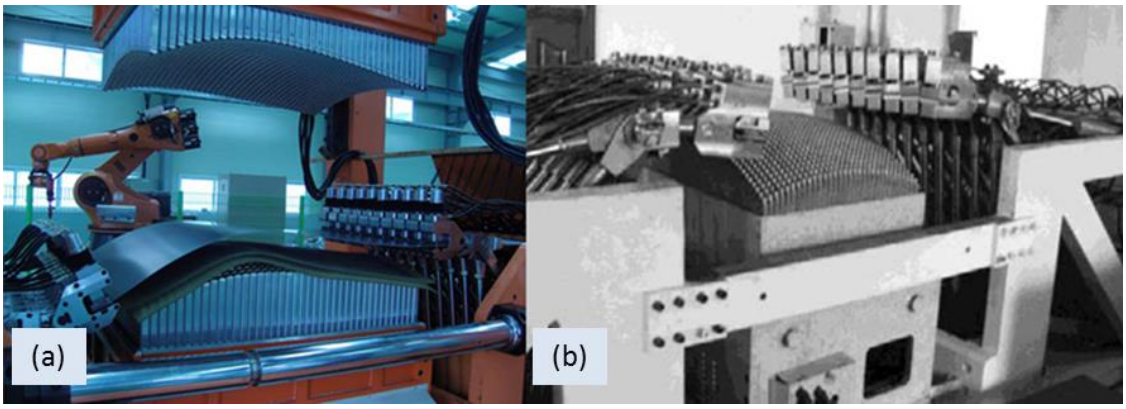

Figure 2-11: The machines developed at Yonsei University in Seoul (a) and Jilin University in China (b)

The 40 by 30 pin matrix employs 40 mm square pins with hemispherical tips. No means of actuation is discussed. Although the authors claim that the pin matrix was reconfigured in between 3 and 5 minutes between panels, pictures show a single robotic arm; if this was the means of actuation then pin height adjustment between panels must have been very slight. In their review of existing processes, the authors are of the mistaken opinion that multi-point stretch forming made it possible to stretch

components with double curvature; in fact double curvature is achievable when stretching sheet over solid dies on a conventional machine. They also reported that multi-point forming, between a matching set of dies, leaves golf ball like dimples. There is no mention of dimpling on the panels which have been finished off with this process. It should be noted that placing the grips close to the die makes more sense when carrying out this hybrid process, as the grips will act as a constraint during the stamping operation. The main conclusion of this report was a comparison of the cost of producing these panels through die casting \$7000/m^2, hydroforming \$3000/m^2 and the new process \$260/m^2. While these figures are very impressive, no breakdown of costs was included. It is suspected that no tooling costs were included for this new process despite the high cost involved in the development of a new machine.

A study was carried out by the Inha University of Korea (Bae, et al., 2012) to determine whether it was feasible to use the same hybrid process (and machinery) to form the hull of a boat, from A3003 H14 aluminium sheet of 4 mm thickness. A combination of FEA and physical testing was used to show that this process could form the material in question into twist, saddle and convex parts. The depth and curvature achieved were sufficient to manufacture sections for a 30 foot Kordy yacht and a 50 ton patrol boat. The surface finish, of parts produced, was acceptable and shape accuracy was well within the reported industry tolerance of 10 mm per metre.

2.5 Recent Research from Other Sources

An earlier paper (Rao & Dhande, 2002) details initial findings from a study into a new tooling system, referred to as 'flexible surface tooling', at the Indian Institute of Technology. The new tooling system is basically a reconfigurable forming tool. This system is proposed for sheet forming processes where the loads on the tooling are minimal, and is recommended for wet or prepreg composite layup. Emphasis in this study is put on the quality of surface presented by the interpolator, and calculations are based on the potential energy of a deformed membrane. A deformation analysis

was carried out as the non-linear elastic membrane made contact with the discrete die at multiple points. The plane stress state associated with sheet made it possible to model the interpolator as a thin incompressible isotropic hyper-elastic membrane. The object of the analysis was to minimise the potential energy in the presence of contact restraints. The main findings of this study show that surface shape error was reduced when the interpolator material's ratio of first and second Moony constants (C_1/C_2) increased. Best results were observed when this ratio was approximately 5. It was also found that an increased uniformly distributed load on the interpolator will increase error, but that the error can be minimised by increasing interpolator thickness. A maximum load of 0.5 kPa was used which is well below that present in a typical stretch forming process (see Section 3.4). It must be noted that this paper is purely theoretical, as a lack of resources meant that FEA models were not validated through physical tests. The authors recommend the building of a prototype tool as a priority in further work. No materials were tested during this study but the author states that a higher C_1/C_2 ratio indicates a more elastic material, while a paper presented at a LS-DYNA users conference (Feng & Hallquist, 2012) shows that an increase in the C_1/C_2 ratio indicates a reduction in material strength (especially in a biaxial deformation mode).

Over the past decade a body of work, concerning reconfigurable tooling, has been amassed at the University of Galati in Romania under the leadership of Dr V. Paunoiu. Their first paper on the subject (Paunoiu, et al., 2004), which was presented at an international conference, details the simulation of the MPF process using DYNAFORM FEA software. Four node shell elements were used to represent a 10 mm thick steel plate 560 by 1000 mm in dimension. The pins were modelled as rigid bodies while no interpolator layer was included. A mathematical model for determining pin heights using surface generation theory was also presented. Results showed material thickness variation at dimples where the material made contact with pin tips, yet stress maps showed that the part deformed plastically, without local stress levels (around contact points) exceeding the material's

ultimate tensile strength. The work that followed is almost exclusively pertaining to the MPF process (or Reconfigurable Multipoint Forming as they renamed it). Their logical linear progression through the subject material and the methodology used, as indicated by the subject matter of the papers published by this group in chronological order, is most relevant to this study.

The next paper published by this group (Paunoiu, et al., 2006) was a review of sheet metal forming process employing reconfigurable dies. Here, the authors introduced MPF in the context of a wider group of reconfigurable manufacturing systems including, dieless incremental forming, spinning over a telescopic mandrel, hydroforming with a reconfigurable punch, and multipoint stretch forming.

This was closely followed by a short paper (Paunoiu, et al., 2006) outlining the design and development of lab scale test equipment. The first set of design parameters examined in this paper was pin cross sectional shape, pin tip geometry, pin numbers and pin arrangement. While square, triangular, round and hexagonal pins were mentioned, no real study into the merits of each shape and applicable packing arrangements was undertaken. Budget restrictions seemed to be the main driver in the design of the tooling. The final tooling consisted of a matching set of dies constructed from a 10 by 10 matrix of 10 mm steel square bars with hemispherical tips. The height of pins was adjustable through set screws, which made contact with the base of each pin. Square pins were selected, in a rectangular close packed arrangement, so that the pin matrix could be easily clamped together, using wedges, to mimic a solid tool. As the forming area, of the tool, was only 100 mm by 100 mm, it was located in a jig for operation in a standard press.

As the design of the tool would also facilitate the use of round pins in a rectangular close packed arrangement, the next paper in the series (Paunoiu, et al., 2008) compared the effects of round and square pins (both in a rectangular close packed arrangement). Here the authors found that deformation with the round pins was almost identical to that obtained when

square pins were used, with stress, forming forces, and springback levels all being approximately the same in both setups despite the different contact conditions. It was found that, the bigger radius on the rectangular pins increased the contact area between pins and blank, and hence, reduced the severity of dimples.

The next three papers published by this team all related to determining the height at which individual pins would need to be set to produce parts with dimensional accuracy. The first of these dealt with springback compensation (Paunoiu, et al., 2009), where a simple method based on displacement adjustment was proposed. This method consists of measuring FEA simulations of the deformed part, before, release at contact points, and comparing to similar points on the desired shape, before adjusting the pins by the difference. Next an algorithm for geometric configuration of the pins was published (Paunoiu, et al., 2009), where a method of offsetting the desired surface and selecting points on a matrix using MatLab software was proposed. Geometric configuration of the pins through reverse engineering was considered in their next paper (Puanoiu & Teodor, 2009), where 3D scan where taken, to construct a CAD model of the part, from which pin heights were determined. These three short studies gave the group the opportunity to build a number of FEA models over a short period of time. The FEA models were then used in a study of tool geometry pertaining to MPF (Paunoiu, et al., 2011).

In the most recent paper featured in this review (Rivai, et al., 2014), numerical simulation was used to compare the effects of forming with round pins in hexagonal and rectangular close packed arrangements. The authors found that round pins in a hexagonal close packed arrangement produced a more even stress distribution with a smaller value of maximum stress present in the blank. They also found that the through thickness strain distribution was again more even with the HCP arrangement. This will result in less severe dimpling when using the hexagonal close packed arrangement. In contrast to this, HCP is a denser arrangement; hence more

dimples will be created. Although this paper pertains to MPF rather than MPSF, its findings are encouraging for this study.

2.6 2007 Review of Reconfigurable Tooling

The last paper (Munro & Walczyk, 2007) to be included in this chapter is a comprehensive review of patents and research pertaining to the use of reconfigurable tooling, in forming sheet metal and composite materials. This paper originated from the Rensselaer Polytechnic Institute, after completion of the RTFF project. The authors began by describing the ideal reconfigurable tool as having a number of characteristics (Table 2-2 and Figure 2-12).

No.	Characteristic	Rationale	Relative weighting factor (w_i)[a]
1	High surface resolution	Allows for fine part details and minimizes surface smoothing required	1.0
2	Smooth forming surface	Needed for producing high quality parts	0.9
3	Rapid reconfiguration of the forming surface	Minimizes tool set up time	1.0
4	Individual position and velocity control of points on the forming surface	Allows the tool shape to be changed in real time for enhanced process control	0.5
5	Easily configured for a variety of manufacturing process	Supports the concept of a universal tool	0.5
6	Capable of withstanding high forming loads with minimal surface deformation while forming surface is either stationary or moving	Allows for accurate part fabrication in situations where high tooling loads are encountered such as stretch forming of sheet metal	0.4
7	Abe to accommodate a wide range of manufacturing process temperatures	Allows for tooling flexibility	0.5
8	Allows a vacuum to be drawn within the tool cavity (i.e., air-right chamber)	Necessary for certain manufacturing processes such as thermoforming and composites forming	0.7
9	Portable and lightweight	Conducive to lean manufacturing principles	1.0

[a] i=1 to 9 corresponding to the characteristic number 1–9.

Table 2-2: Munro & Walczyk's characteristics of an ideal reconfigurable tool

These characteristics pertain to a family of tools, suitable for stamping and stretch forming sheet metal and composite materials, together with the moulding of plastics. 35 patents and 15 designs (or improvements to existing designs) were rated; Table 2-3 shows Munro & Walczyk's top ten rated designs, while Table 2-4 shows their top ten patents. It should be noted that early designs, before CNC machinery became commonplace, have been rated zero for the characteristic “individual positioning and velocity control”. This has resulted in lower overall scores for tooling invented prior to 1980.

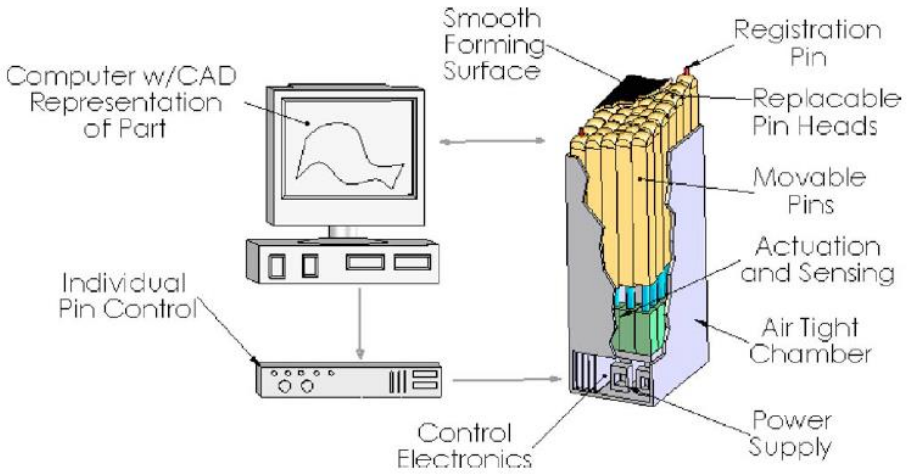

Figure 2-12: Schematic representation of Munro & Walczyk's characteristics

Name	Year	Rating	% of max
Walczyk	2003	23.7	73%
Prabhakara	2002	23.7	73%
Munro	2004	23.7	73%
Papazain	2002	22.3	69%
Nakajima	1969	21.7	67%
Eigen	1992	21.4	66%
Boas	1997	21.0	65%
Walczyk	1998	20.8	64%
Haas	2002	20.8	64%
Finckenstein	1991	19.5	60%

Table 2-3: Munro & Walczyk's top ten designs

From the top ten designs, which have been rated in terms of reduction to practice, only the Nakajima and Finckenstein designs have no connection to the RTFF project. The top three rated designs all pertain to forming composite material with heat or simply using the reconfigurable surface for composite layups. Fourth in the table is the RTFF tooling system which has been attributed to Papazian. The work carried out by Eigen on interpolators is rated sixth, while the designs credited to Boas, Walczyk (1998), and Haas, rated seventh, eighth, and ninth, refer to the sequential setup mechanism, the hydraulic pin concept, and the shaft driven leadscrew concept, respectively.

As the DATAFORM project was in its infancy when this review was carried out, the final DATAFORM machine was not rated. The MPF technology which already existed at Jilin University at this time was also omitted from this review. While any rating system is subjective in nature, it is suspected that the characteristics used in this system are very close to the design criteria set out at the beginning of the RTFF project and subsequent projects undertaken by associated teams. Creating an objective rating system or rating further projects, in this study, on Munro & Walczyk's characteristics would require an equal volume of data on each project being rated. Since insufficient (or unequal volumes of) data is accessible, no attempt has been made to compile a new rating table in this project.

Nevertheless, using the data available, it would be reasonable to assume that should the DATAFORM/MTF tooling have been included in Munro & Walczyk's review, using pins with a bigger cross sectional area would enable it receive a relatively high score in characteristic 6 (load bearing capability) while these pins would be of a disadvantage in characteristic 1 (resolution). Its mass, per unit square of the forming area, would be comparable to that of the RTFF tooling hence a similar rating would be expected in characteristic 9. Since square pins are used in similar arrangements in both systems, a rating comparable to the RTFF designs would also be expected in characteristics 7 and 8 (range and ability for a vacuum to be formed). It is difficult to compare the final smoothness of parts achieved from each design without definitive data, while it could be assumed that DATAFORM's reliance on robotics would result in lower ratings in both characteristics 3 and 4 (rapidity and position control).

From Munro & Walczyk's review it can be discerned that, despite the long term interest from industry, reconfigurable tooling for sheet metal forming is not making its way to the shopfloor. The authors attribute this to a limited marketplace due to high retail cost (over $1 million per machine), limited resolution (25 mm square pins), and high weight (it is not unusual for a machine to weigh as much as 20 tons). Surely if designers continue to work towards improving the resolution of the tool, by reducing the pin size,

the inevitable outcome will be tooling systems which are overly complex and therefore, of a high capital cost and weight. It is argued here, that for producing stretch formed parts the first characteristic of "high surface resolution" is not necessary if the second characteristic of a "smooth forming surface" is realised. There is also concern about the interpolator, which is regarded as consumable. Without long term data on the change to interpolator properties after forming, there will be additional, unknown costs associated with altering setups as interpolator properties change, and with replacing worn interpolators.

Name	Year	Rating	% of max
Berteau	1994	23.0	71%
Sullivan	2000	22.3	69%
Humphrey	1971	21.9	67%
Hoffman	1992	21.1	65%
Whitacre	1971	21.2	65%
Schroeder	1998	20.6	63%
Hicks	1961	20.4	63%
Haas	1996	19.3	59%
Papazian	2001	19.3	59%
Haas	2000	19.3	59%

Table 2-4: Munro & Walczyk's top patents

Munro & Walczyk's top ten patents relating to reconfigurable tool design are illustrated in Figure 2-13 (a) – (l), together with two other patents which are relevant to this project. The highest rated patent (a) is for a variable shaped mould (Berteau, 1994). This patent, which has expired, describes a closely packed matrix of threaded rods used to configure a moulding surface. A second patent employing a closely packed matrix of threaded rods (j) is currently held by General Motors. This device for generating a fixture (Schroeder & Stevenson, 1998) seems to have been designed for assembly purposes. Four more expired patents have made it into Munro's top ten. The highest rated of these (c) shows a mould forming device (Humphrey, 1971) which is comprised of a number of longitudinally adjustable rods located in a relatively small housing. A similar system is shown in the patent for a conformable tool (Hoffman, 1992). This device (e), which was

primarily used in the repair or replacement of small aircraft parts, copies an existing contour from a part so that it can be reproduced in a second part. Another patent (f) shows a fine bed of pins on a relatively small scale to create a three dimensional die (Hicks, 1961), which was originally intended for pressing designs into soft plastic, and evolved into a popular toy in the seventies. The final lapsed patent from Munro's table (d) shows an incremental die construction having a hole piercing capability (Whitacre, 1971), where hexagonal rods cut to size and shaped, are packed together to form a punch or die. By removing rods from the die and using longer rods in corresponding places on the punch, holes can be punched in sheet as it is being formed.

The first patent from the RTFF project (g) shows an adjustable form die (Haas & Kesselman, 1996). This patent (which was granted in Europe) is quite wide ranging, in its language, as it attempts to cover both pressing and stretch forming of sheet metal. As die construction and pin positioning, are only loosely described, this as an attempt to patent the very notion of multipoint stretch forming. The most significant patent to come from the RTFF project (b) shows an individual motor pin module (Sullivan, et al., 2000). This is a device which acts as a sub controller, and controls the height of 4 pins within a module. This design was used in conjunction with the 4x4 matrix of motors in the sequential setup system of control, discussed earlier. By configuring the pins in modules the setup time was effectively divided by 4, giving the average setup time of 12 minutes claimed for the final version of the RTFF stretch forming machine. The next patent shown (h) comes from work that followed the RTFF project. Here the technology used to develop the sheet metal stretch forming machine has been adapted to create a modularised reconfigurable heated forming tool (Haas, et al., 2000) used to form composite materials. This is basically a matching set of RTFF dies enclosed in a housing where the temperature can be controlled. Figure 2-13 (i) shows the patented pin tip assembly in tooling apparatus for forming honeycomb cores (Papazian, et al., 2001). This collection of pin tips is meant for use with the previous patent for the reconfigurable heated forming tool.

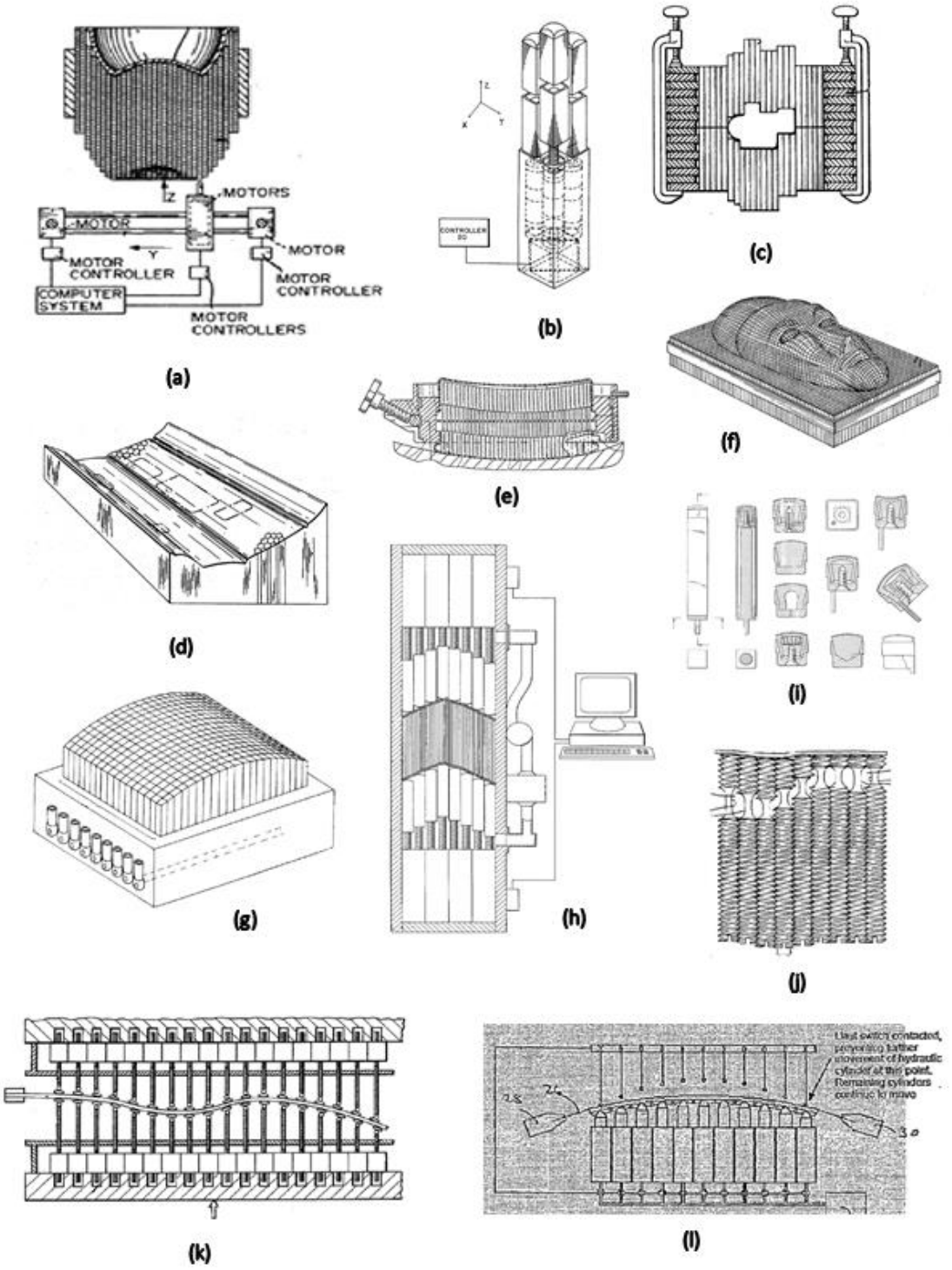

Figure 2-13: Patents relating to reconfigurable tool design

A lapsed patent (k) which did not make Munro's top ten shows an apparatus for forming sheet metal (Pinson, 1980). This sheet metal forming machine uses a matching set of dies constructed as an equally spaced matrix of threaded rods with pivoted tips. The tips used here are similar in design to possible tips discussed for use in this project. They are hexagonal in

shape, and are spring loaded, so that they remain horizontal until contact is made with the sheet being formed.

The final patent featured here (l) shows a machine for active reconfigurable stretch forming (Forsyth, 2007). This current patent describes an interesting machine where the pins are made up of sparse array of hydraulic cylinders, each of which extend until the material being stretched makes contact with a limit switch situated directly above each cylinder. This design goes against the grain somewhat as hydraulic cylinders are used for pins, and the span between pins is much greater than that of the DATAFORM and RTFF projects.

2.7 Conclusions

The cost savings identified by Nakajima (Nakajima, 1969) (Section 2.2) are still of great interest to researchers and the metal forming industrial sector. Research continues to this day to apply reconfigurable tooling to a wide range of processes. An example of this is the current project (running from 2014 to 2017), involving a British consortium including, The Manufacturing Technology Centre, The University of Strathclyde, Ultra Precision Motion Ltd. and MG Motor UK Ltd., which investigates the feasibility of using a matching set of reconfigurable tools in the press forming of sheet metal parts (The Manufacturing Technology Centre, 1999). The case studies presented in Section 2.4.3 illustrate that the range of industrial applications, where the stretch forming process can be used, are greatly increased with the use of more cost effective reconfigurable tooling.

The pin layout utilising a matrix of interlocking threaded rods, originally used in the Boeing sponsored tooling (Wolak, et al., 1973) (Section 2.2), and described again in two of the patents highlighted in Munro & Walczyk's review (Section 2.6), was considered in AMFOR's pin design, due to its suitability in a hexagonal close packed pin matrix, but was rejected due to concern over intellectual property rights. In the second step of pin height setting routine shown in Figure 2-1 (Section 2.2) a correction is made to the

pin heights after process modelling. A similar method is employed here in the numerical pin height correction routine presented in Section 5.6.

The RTFF project proposes a closed loop pin height correction routine, where the part is inspected while in position on the machine and a proportional control equation (Eq. 1) is used to calculate corrections. On AMFOR's preferred machine layout a sequential setting device is proposed where the pin heights are adjusted from above (see Appendix K.). This does not allow for adjustment while a part is on the machine. Eq. 1 will be used when part geometry is inspected through scanning on an inspection jig or on a Coordinate Measuring Machine. The RTFF project examined a number of pin height actuation methods where the heights of pins are adjusted from below (Section 2.3). One of the major factors used to rate their actuation methods was rapidity of reconfiguration. AMFOR's proposed pin actuation method sacrifices a degree of rapidity in favour of the cost saving gained through the adjustment of the proposed round pins from above. Eq. 2 and Eq. 3 are used in the design of these round pins to ensure that they can support the loads present in a typical stretch forming process.

The RTFF designed reconfigurable bed of pins is designed to be employed on a conventional stretch forming machine fitted with a segmented gripping system (see Figure 2-5). The DATAFORM group designed a new stretching machine employing a bespoke segmented gripping system (see Figure 2-9). The position and pulling force of each grip segment is controlled through the manipulation of three hydraulic rams (one horizontal, one vertical and one inclined). While AMFOR's proposed reconfigurable bed of pins can also be employed on a conventional stretch forming machine, our preferred machine layout (presented in Section 5.2) offers a considerable cost saving by using a single drum and eccentric cam grip on each side of the die.

The MIT team carried out a study concerning the cross sectional shapes of pins in a reconfigurable die (Walczyk & Hardt, 1998) (see Section 2.3). One of the main factors used to rate the geometries considered was the ability to clamp a matrix of pins (of the given geometries) into a rigid tool. They relied

on increasing the resolution of the pin matrix to improve the surface quality of parts obtained using a die of any given pin geometry. The DATAFORM team carried out numerical studies to determine the relationship between the cross sectional dimensions of their square pins, and their pin tip radius, to the interpolator thickness required to supress dimples on the final parts obtained after their forming process (see Section 2.4.1). The Indonesian numerical study (Rivai, et al., 2014) outlined in Section 2.5 compares the surface quality of parts obtained from a press forming process, where reconfigurable tools employing round pins arranged in hexagonal and square close packed matrices. No comprehensive study was discovered where the influence of pin cross sectional geometry, and pin arrangement, on the surface quality of parts, was examined. Hence a comparative numerical study is carried out in this thesis and presented in Chapter 4.

While the review of reconfigurable tooling outlined in Section 2.6 (Munro & Walczyk, 2007) rates design and patents on a number of characteristics that make reconfigurable tooling applicable to a range of processes, only a reconfigurable die suitable for the stretch forming process is considered in this thesis. Nevertheless the information contained in this review was invaluable during the design stage of the AMFOR machine and pins. Pivoted pin tips, similar to those employed in AMFOR's proposed pin design, were previously used in a lapsed patent (Pinson, 1980) which did not make the top ten rated patents (shown in Table 2-4). Munro and Walczyk found it noteworthy to report on the degree of overlapping found in the claims outlined in patents relating to reconfigurable tooling. This can lead to difficulty in a small design/research enterprise being granted defendable intellectual properties rights for any newly proposed modifications to the conventional bed of pins form of reconfigurable tooling.

A similar methodology to that evident from the published work from the University of Galati (see Section 2.5) is used in this thesis, where a lab scale tool using the proposed pin design, and a lab scale machine in the preferred AMFOR machine layout (see Section 5.2), has been built, following a review of prior practice. Whereas the Galati group uses the finite element method

to examine pin height settings and the springback effect, in the MPF process, before validating their findings through laboratory experiments, this thesis uses the finite element method to examine the influences of pin geometry and arrangement on surface quality (Chapter 4). A second study, again employing the finite element method, is used in this thesis, to examine the interpolator requirements for stretch forming over the proposed discrete die, before the results are finally validated through laboratory experiments (Chapter 5).

The MIT team (Socrate & Boyce, 2001) used an interesting approach to simulating the stretch forming process, where the model is simplified so that the die and interpolator are treated as a single smooth surface, and contact properties are modified in different regions of the interface between the blank and die. Although a variety of FEA software packages are employed [Abaqus (Kutt, et al., 1999), (Wang, et al., 2010) & (Cai, et al., 2009), ANSYS LS-DYNA (Seo, et al., 2012) & DYNAFORM (Paunoiu, et al., 2009)] all other simulations examined during this literature review use relatively detailed models, where rigid bodies are used to represent tools, shell elements are used to represent the sheet metal blanks and volume elements are used to represent the interpolators. This approach is also used in the numerical studies presented within this thesis, with rigid bodies used for the tooling and shell elements used to represent blanks in both the AutoForm (Chapter 4) and PAM-STAMP (Chapter 5) models. In the more detailed PAM-STAMP models volume elements are used to represent the interpolators.

Chapter 3. Material Characterisation

3.1 Introduction

Materials are being characterised here to construct material models for use in the finite element analyses of the stretch forming process presented in Chapter 4 and Chapter 5. There are two different types of material models used in this thesis, a hyperelastic model used for the polyurethane interpolator materials and a plane stress metallic model used for the blanks. The hyperelastic model used here, to describe a range of polyurethane materials, is the Mooney Rivlin model which was also used to describe the behaviour of the interpolator during simulations carried out by the DATAFORM group (see Section 2.4.1). The Mooney Rivlin model uses a strain energy density equation to describe the stress/strain behaviour of a rubber-like material. Polyurethane has previously been used as an interpolator material in both the RTFF and DATAFORM projects (see Section 2.3.1 and Section 2.4.1 respectively).

Plane stress metallic material models use a strain hardening curve equation to describe stress/strain behaviour as the material deforms plastically, and a yield criterion to predict flow stress in different modes of deformation. Since the rolling process used to manufacture sheet metal elongates its grain structure in the direction of rolling, sheet metal can be described as anisotropic i.e. having different properties depending on the direction in which they are measured. The Lankford or anisotropy coefficient (normally referred to as the r-value) measures the variation of plastic behaviour with direction. The r-values can be defined as;

$$\mathrm{r-value} = \frac{\varepsilon_2}{\varepsilon_3} \tag{8}$$

where, ε_2 is the true strain across the width of a tensile testing specimen and ε_3 is the true strain through the thickness of a tensile testing specimen. Both r-values and yield strengths, determined during uniaxial tensile testing of material at 0°, 15°, 30°, 45°, 60°, 75° and 90° to the rolling direction, are used to calibrate a selected yield criterion. The procedure used to construct and validate material models for materials used in simulations are described in this chapter.

Since stretchability can be difficult to evaluate, a rating system is often used where the suitability of materials for use in the stretch forming process is assessed by direct comparison to an ideal material, given as the aluminium alloy 7075-W, which has a stretchability rating of 100%. Table 3-1, reproduced from the ASM Handbook (ASM International, 1988), shows the influence of yield strength, the forming range, and percent elongation on the stretchability rating of aluminium alloys. While a 2024-0 aluminium sheet is used in simulations of the DATAFORM process, a similar material with the T3 temper description (solution heat treated, cold worked and naturally aged) is used in the comparative study presented in Chapter 4. These tempering conditions increase the stretchability rating of the material from 80 to 95.

Alloy	Tensile Strength (MPa)	Yield Strength (MPa)	Forming Range (MPa)	% Elongation in 50 mm	Stretchability Rating
7075-W*	331	138	193	19	100
2024-W*	317	124	193	20	98
2024-T3	441	303	138	18	95
6061-W*	241	145	97	22	90
7075-O	221	97	124	17	80
2024-O	186	76	110	19	80
6061-O	124	55	69	22	75
3003-O	110	41	69	30	75
1100-O	90	35	55	35	70
7075-T6	524	462	62	11	10

* Freshly quenched after solution heat treatment

Table 3-1: Stretchability ratings of aluminium alloys

3.2 The 2024-T3 Material Model

Uniaxial tensile tests to determine yield strength have previously been performed as per ASTM E8M on 2024-T3 sheet of 2 mm in thickness by the AMFOR group. The r-values were calculated during the same tests as per ASTM E517. The material model illustrated here is based on the tensile test data retrieved from the AMFOR database (Table 3-2). Since no data was available for the yield stress in equibiaxial deformation conditions, equibiaxial yield stress is assumed to be equal to that given as the mean uniaxial value in the rolling direction of the sheet. The BBC 2005 yield criterion has previously been proven to give an accurate description of the anisotropy of aluminium alloys (Banabic & Sester, 2012), is available in the AutoForm software, and hence is selected here to describe the 2024-T3 aluminium alloy.

Angle from Rolling Direction (°)	Mean r-value (-)	Mean Yield Stress (MPa)
0	0.72	347.9
15	0.87	340.5
30	0.99	330.2
45	1.13	317.9
60	0.99	318.0
75	0.70	322.3
90	0.67	328.2

Table 3-2: The uniaxial tension test data retrieved from the AMFOR database

The BBC 2005 yield criterion defines equivalent stress ($\bar{\sigma}$) as,

$$\bar{\sigma} = [a(\Lambda + \Gamma)^{2k} + a(\Lambda - \Gamma)^{2k} + b(\Lambda + \Psi)^{2k} + b(\Lambda - \Psi)^{2k}]^{\frac{1}{2k}} \quad (9)$$

where,

$$\Gamma = L\sigma_1 + M\sigma_2, \quad (10)$$

$$\Lambda = \sqrt{(N\sigma_1 - P\sigma_2)^2 + \sigma_{12}\sigma_{21}}, \quad (11)$$

$$\& \ \Psi = \sqrt{(Q\sigma_1 - R\sigma_2)^2 + \sigma_{12}\sigma_{21}}, \quad (12)$$

hence the nine material parameters required in the BBC 2005 yield criterion's expression of equivalent stress are *a, b, k, L, M, N, P, Q* and *R*.

The procedure and equations used to determine values for these material parameters are laid out in a paper presented at Numisheet 2008 (Banabic, et al., 2008). In this project the BBC.exe solver, shared with the AMFOR group by the CERTETA group during previous collaboration, is used to determine values for the material parameters (Table 3-3), and provide r-value data together with major and minor stress data enabling the plotting of a yield locus.

a	b	L	M	N	P	Q	R	k
2.1001	0.9944	0.3908	0.4449	0.4675	0.4675	0.4196	0.4684	4

Table 3-3: BBC 2005 material parameter values for 2024-T3 generated by the BBC.exe solver

Figure 3-1 (a) shows both the experimental and BBC 2005 predicted uniaxial yield strengths at 0, 15, 30, 45, 60, 75, and 90° to the rolling direction of the sheet normalised to the experimental yield strength along the rolling direction. Good agreement is evident between experimental and predicted yield strengths as it is between the experimental and BBC 2005 predicted r-values shown in Figure 3-1 (b). The BBC 2005 yield locus for the 2024-T3 alloy is plotted in Figure 3-2.

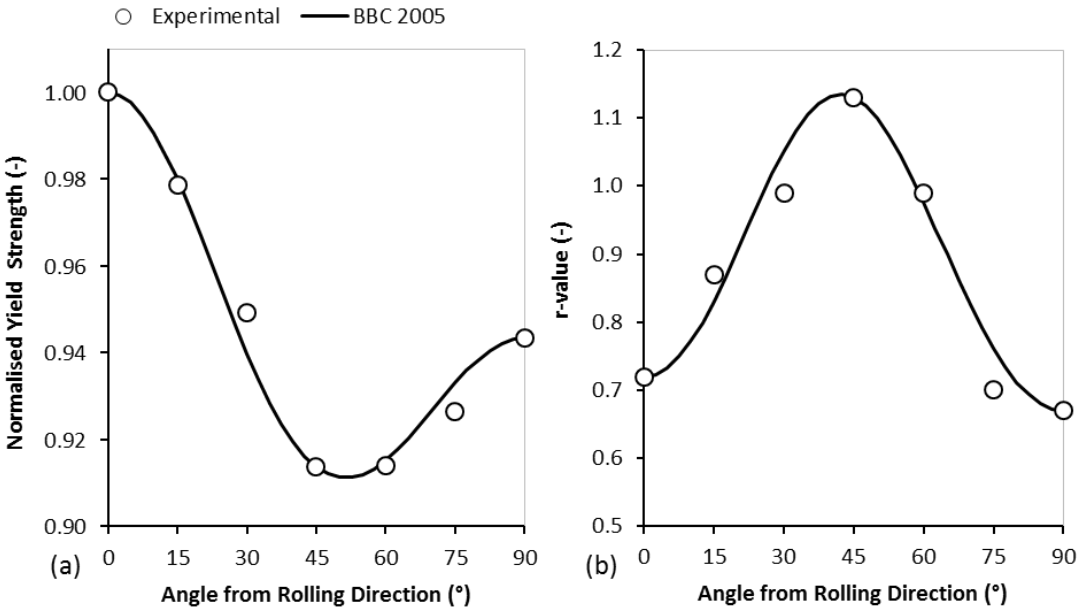

Figure 3-1: The BBC 2005 normalised yield strengths (a) and r-values (b) plotted with experimental results

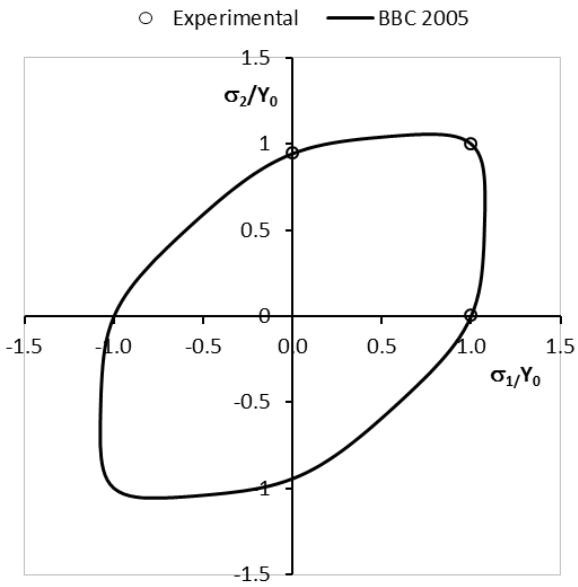

Figure 3-2: The BBC 2005 normalised yield locus for the 2024-T3 alloy

Note that both the experimental uniaxial, at 0 & 90°, and the assumed biaxial yield strengths fall on the yield locus since these values are used in the calibration of the BBC 2005 yield criterion.

A number of empirical laws are available in AutoForm to describe the strain hardening behaviour of a material. A least squared fitting routine is used where the square root of the sum of squared error between calculated and experimental stress is minimised with the Excel solver. Curves from four of these laws are compared, in Figure 3-3, to plastic stress and strain data for this material also retrieved from the AMFOR database. The stress expressions from the laws illustrated are defined as the Swift (Eq. 13), Gosh (Eq. 14), Hockett-Sherby (Eq. 15), and the combined Swift/Hockett-Sherby (Eq. 16) laws;

$$\sigma = C\left(\varepsilon_p + \varepsilon_0\right)^m, \tag{13}$$

$$\sigma = C\left(\varepsilon_p + \varepsilon_0\right)^m - \mathrm{D}, \tag{14}$$

$$\sigma = \sigma_{sat} - (\sigma_{sat} - \sigma_i)e^{-a{\varepsilon_p}^P}, \tag{15}$$

$$(1-\alpha)\left[C\left(\varepsilon_p + \varepsilon_0\right)^m\right] + \alpha\left[\sigma_{sat} - (\sigma_{sat} - \sigma_i)e^{-a{\varepsilon_p}^P}\right], \tag{16}$$

where σ & ε are stress & strain with the subscripts $_p$, $_0$, $_{sat}$, & $_i$ denoting plastic, initial, saturated and yield respectively, and C, D, m, a, P, & α all represent material dependent fitting parameters.

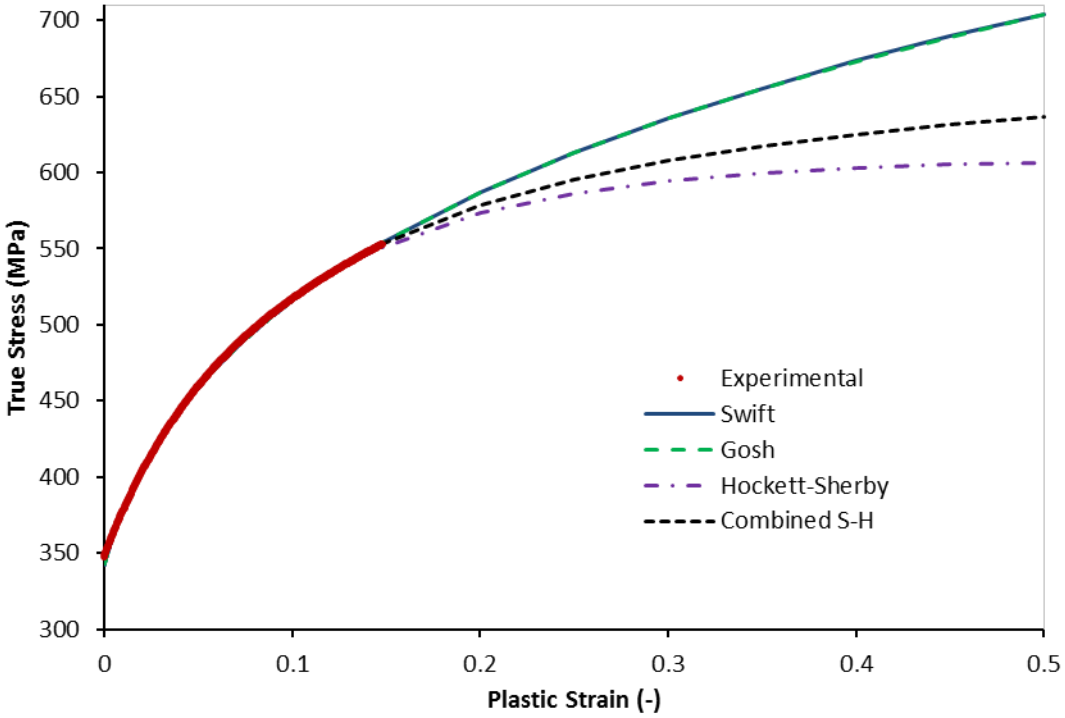

Figure 3-3: 2024-T3 hardening curve comparison

While it is unlikely that the material will be stretched beyond the fracture strain observed in the uniaxial tensile tests (magnitude of plastic strain equals 0.16) it is good practice to extrapolate the stress strain beyond this and select a hardening curve that neither overestimates nor underestimates work hardening at higher magnitudes of strain. The fitted Swift and Gosh curves both underestimate the yield point, before showing good accordance with the experimental data up to a strain of 0.16. On extrapolation up to a strain of 0.5 both curves can be judged to overestimate the material's strain hardening at higher strain levels. While both the Hockett-Sherby and combined Swift/Hockett-Sherby give a good prediction of yield and show good accordance with the experimental data up to a strain of 0.16, the saturation parameter in the first leads to a lower prediction of strain hardening levels at higher strains. The combined Swift/Hockett-Sherby law

gives a more continuous curve at higher strains and is selected to describe strain hardening in this material model.

Since the aforementioned BBC 2005 parameter identification procedure is already implemented in the AutoForm software only the yield strengths and r-values need to be entered in its material generator. The complete list of material properties and parameters required to implement this material model in AutoForm are given in Table 3-4.

BBC 2005 Material Properties							
σ_0 (MPa)	σ_{45} (MPa)	σ_{90} (MPa)	σ_b (MPa)	r_0 (-)	r_{45} (-)	r_{90} (-)	M* (-)
347.9	317.9	328.2	347.9	0.72	1.13	0.67	8
* where M = 2k and is always 8 for aluminium alloys							

Combined Swift/Hockett-Sherby Parameters							
ε_0 (-)	m (-)	C (MPa)	σ_i (MPa)	σ_{sat} (MPa)	a (-)	p (-)	α (-)
0.016	0.209	808.4	347.9	608.9	8.82	0.925	0.705

General Material Properties		
Young's Modulus (MPa)	Poisson's Ratio (-)	Specific Weight (MPa)
70000	0.3	2.7×10^{-5}

Table 3-4: The material properties required to implement the 2024-T3 material model in the AutoForm software

3.3 The 316L Material Model

Uniaxial tensile tests to determine yield strength have been performed as per ASTM E8M on the 316L stainless steel sheet of 0.88 mm in thickness. The r-values were calculated during the same tests as per ASTM E517. An initial crosshead velocity of 1.27 mm/min was used in tests on three dog bone specimens cut at 0, 15, 30, 45, 60, 75, and 90° to the rolling direction of the sheet. Figure 3-4 shows the tensile test set-up and the geometry of the dog bone specimen used, while Table 3-5 shows the yield strengths and r-values obtained from the initial tests.

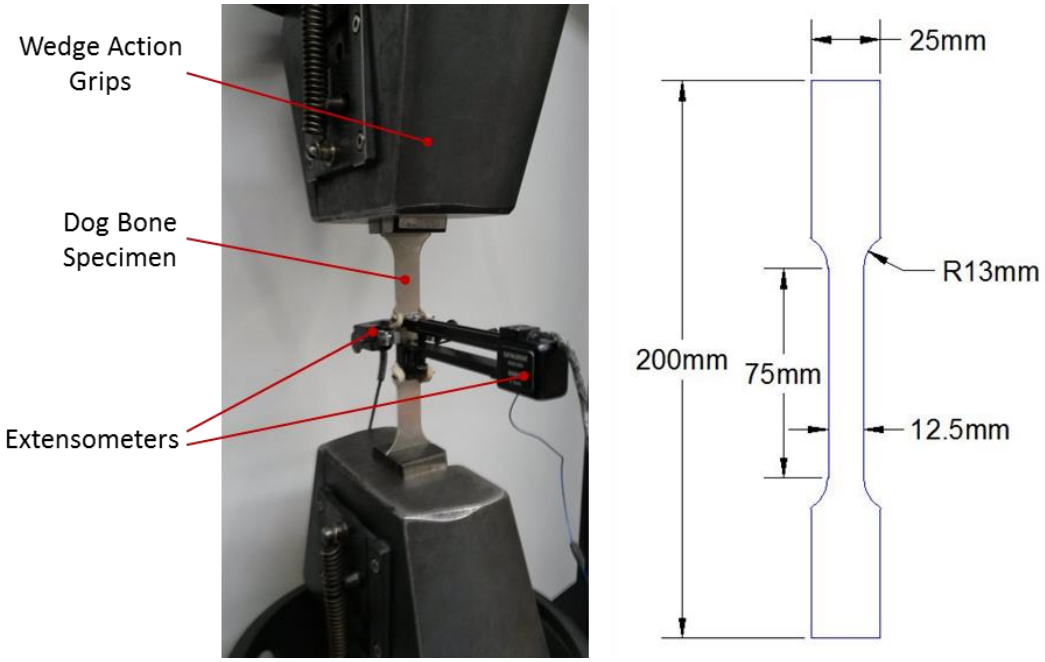

Figure 3-4: The tensile test set-up and the geometry of the dog bone specimen

Angle from Rolling Direction (°)	r-value (-)			Yield Stress (MPa)		
	Mean	Standard Deviation	Standard Error	Mean	Standard Deviation	Standard Error
0	0.388	0.0216	0.0125	350.1	2.949	1.702
15	0.479	0.0402	0.0232	351.9	1.859	1.074
30	0.540	0.0033	0.0019	348.8	2.668	1.540
45	0.731	0.0504	0.0291	349.3	7.991	4.614
60	0.687	0.1238	0.0715	353.1	7.811	4.510
75	0.578	0.0301	0.0174	363.1	9.099	5.253
90	0.681	0.0210	0.0121	374.5	3.029	1.749

Table 3-5: The yield strengths and r-values from initial tensile tests on the 316L stainless steel

The standard deviation and standard error is calculated for each data set using Eq. 17 and Eq. 18.

$$Standard\ Deviation = \sqrt{\frac{1}{N}\sum_{i=1}^{N}(x_i - \mu)^2} \tag{17}$$

$$\&\ Standard\ Error = Standard\ Deviation/\sqrt{N} \tag{18}$$

where, N is the number of specimens, x_i is the data value for each specimen, and μ is the mean of these values.

Despite the passing of almost seventy years of research, the Hill 48 yield criterion is still the most commonly used criterion in describing the behaviour of steels in numerical computations, since it is available for selection in most FEA software packages and only requires data from three tensile tests in its calibration. Hence the Hill 48 yield criterion is selected to model the 316L material. PAM-STAMP uses the following variation of the Hill 48 plane stress yield function,

$$f(\sigma) = \left[\frac{(G+H)\sigma_1{}^2+(H+F)\sigma_2{}^2-2H\sigma_1\sigma_2+2N\sigma_{12}{}^2}{2}\right]^{\frac{1}{2}} \tag{19}$$

where, G, F, H, and N are the four Hill coefficients, σ_{11} and σ_{22} are the stresses in the principle directions and σ_{12} is the shear stress in plane stress deformation. The yield stress and r-value corresponding to tensile tests on specimens cut at different angles to the sheet's rolling direction, given by Hill (Hill, 1950) and amended for the variation used by PAM-STAMP, are;

$$\sigma_\alpha = \left[\frac{F\sin^2\alpha+G\cos^2\alpha+H+(2N-F-G-4H)\sin^2\alpha\cos^2\alpha}{2}\right]^{-\frac{1}{2}} \tag{20}$$

$$r_\alpha = \frac{H+(2N-F-G-4H)\sin^2\alpha\cos^2\alpha}{F\sin^2\alpha+G\cos^2\alpha} \tag{21}$$

where, σ_α and r_α are the yield stress and r-value at a given angle to the sheet's rolling direction and α is the angle. PAM-STAMP offers the user the facility to automatically calibrate the yield criterion when the r-values at 0, 45 and 90° to the rolling direction are entered. The r-values are transformed into coefficients using Eq. 22, Eq. 23, Eq. 24 and Eq. 25.

$$G = \frac{2}{1+r_0}, \tag{22}$$

$$H = 2 - G, \tag{23}$$

$$F = \frac{2r_0}{r_{90}(1+r_0)}, \tag{24}$$

$$\&\ N = \frac{(2r_{45}+1)(r_{90}+r_0)}{r_{90}(1+r_0)} \tag{25}$$

where, r_0, r_{45} and r_{90} are the r-values obtained from tensile tests at 0, 45 and 90° to the sheet's rolling direction.

Figure 3-5 shows a comparison of the experimental and predicted yield strengths (normalised to yield along the sheet's rolling direction) and r-values. Using this automatic calibration method, Hill's coefficients are calculated using Eq. 22, Eq. 23, Eq. 24 and Eq. 25, while the yield strength and r-values are calculated using Eq. 20 and Eq. 21 respectively. The error bars shown on the experimental results represent standard error calculated using Eq. 18.

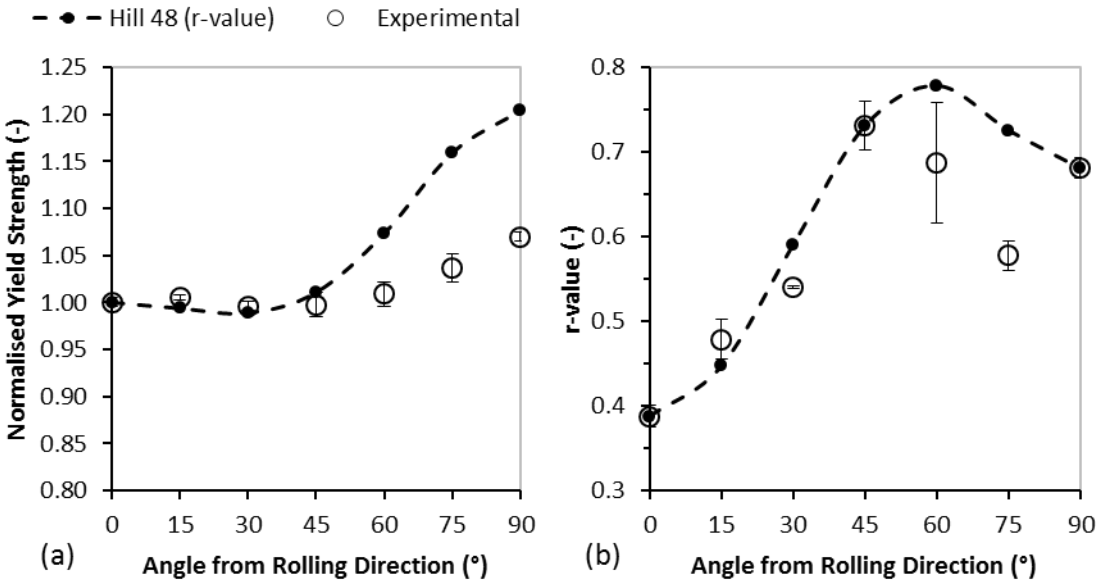

Figure 3-5: The Hill 48 (calibrated with r-values) normalised yield strengths (a) and r-values (b) plotted with experimental results

It can be seen from Figure 3-5 that this method of calibration predicts the r-values in the 0, 45 and 90° directions accurately since they are used in the calibration but r-values in the 60 and 75° directions are not well predicted. While Eq. 23 ensures an accurate prediction of yield along the rolling direction, the error between predicted and experimental values increases as the angle from the rolling direction increases and at 90° to the rolling direction the accuracy of the predicted yield is quite poor.

PAM-STAMP also offers the user the facility to calibrate the yield criterion with calculated values of the G, F and N coefficients although Eq. 23 is always used to determine the value of the H coefficient. Three additional calibrations methods beginning from 0° and four additional

calibrations methods beginning from 90° are used in an attempt to predict the behaviour of this material using the Hill 48 yield criterion with more accuracy. Plots of their predicted normalised yield strengths and r-values together with the equations used to determine values of Hill's coefficients are included in this document as Appendix B. The final calibration method used here is similar to one previously used with the Hill 90 yield criterion (Leacock, 2006) where two different values are determined for Hill's coefficients through calibration from 0° to 45° and from 90° to 45°.

Figure 3-6 shows a comparison of the experimental and theoretical yield strengths (normalised to yield along the sheet's rolling direction) and r-values, using this combined calibration method. When calibrating between 0° and 45° this method uses Eq. 22 and Eq. 23 to determine values for the G and H coefficients. Both the yield strength (normalised to yield at 0°) and r-value at 45° are used to determine a value for the F coefficient with Eq. 26,

$$F = \frac{4}{(r_{45}+1)}\left(\frac{1}{\sigma_{45}}\right)^2 - G. \tag{26}$$

Both the yield strength (normalised to yield at 0°) and r-value at 30° are used to determine a value for the N coefficient with Eq. 27,

$$N = \frac{8}{3}\left(\frac{1}{\sigma_{30}}\right)^2 + \frac{F(2r_{30}+1)}{6} + \frac{G(2r_{30}-1)}{2} - \frac{2H}{3}. \tag{27}$$

When calibrating between 90° and 45° this method uses both the yield strength (normalised to yield at 90°) and r-value at 90° to determine values for the G and H coefficients with Eq. 23 and Eq. 28,

$$G = \frac{2}{(1+r_{90})}. \tag{28}$$

Both the yield strength (normalised to yield at 90°) and r-value at 45° are used to determine a value for the F coefficient with Eq. 26. Both the yield strength (normalised to yield at 90°) and r-value at 60° are used to determine a value for the N coefficient with Eq. 29,

$$N = \frac{8}{3}\left(\frac{1}{\sigma_{60}}\right)^2 + \frac{F(2r_{60}+1)}{6} + \frac{G(2r_{60}-1)}{2} - \frac{2H}{3}. \tag{29}$$

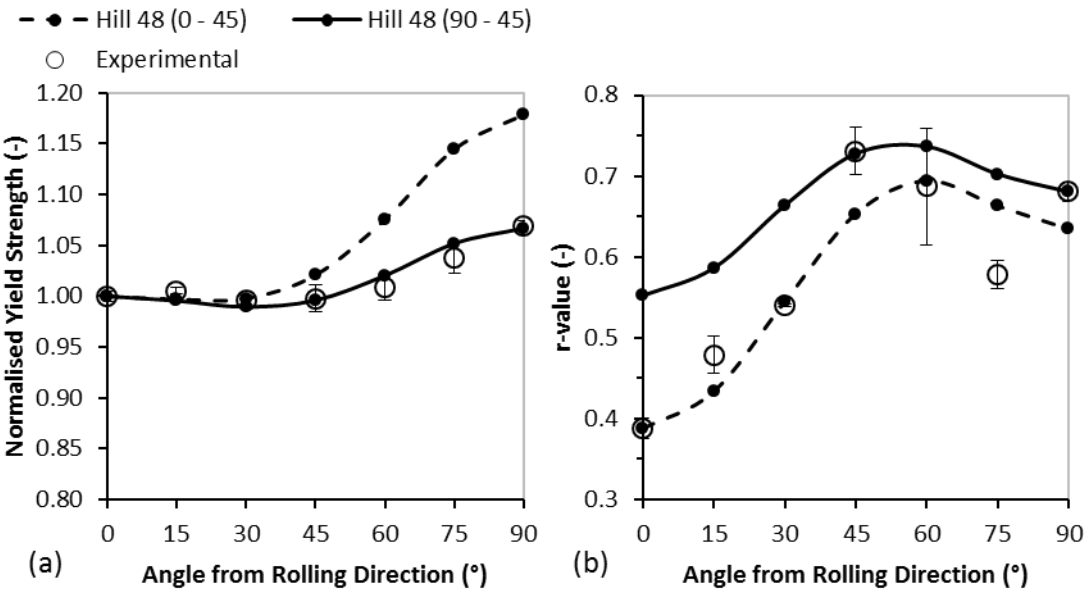

Figure 3-6: The Hill 48 (calibrated from 0° to 45° and 90° to 45°) normalised yield strengths (a) and r-values (b) plotted with experimental results

It is evident from Figure 3-6 that should coefficient values from the 0° to 45° calibration be used when describing material stretched at less than 45° with the Hill 48 yield criterion a prediction of both yield strength and r-value with good accuracy would be obtained. Should coefficient values from the 90° to 45° calibration be used when describing material stretched at 45° or more to the rolling direction, a prediction of yield strength with good accuracy would be obtained. While this method also gives good accuracy in terms of predicted r-values at 45° and 90°, the anomalous thinning behaviour observed in uniaxial tensile tests at 60° and 75° to the rolling direction is not predicted with good accuracy.

A 'quality of fit' test, used in previous studies (Leacock, 2006), is used here to evaluate the accuracy of each calibration method. This test provides a statistical measure of the accuracy of predicted yield strength given as;

$$\Delta\sigma = \frac{\sqrt{\sum_{i=0}^{n}(\sigma(e)_i - \sigma(\alpha)_i)^2/n}}{(\sigma_0 + 2\sigma_{45} + \sigma_{90})/4} \tag{30}$$

where, $\Delta\sigma$ is the measure of accuracy of the predicted yield strengths, n is the number of data values, i is the data value identifier, $\sigma(e)$ is the yield strength from the tensile tests, $\sigma(\alpha)$ is the predicted yield strength and σ_0,

σ_{45} & σ_{90} are the experimental yield strengths at the given angles. The equivalent equation for the r-values is given as;

$$\Delta r = \frac{\sqrt{\sum_{i=0}^{n}(r(e)_i - r(\alpha)_i)^2/n}}{(r_0+2r_{45}+r_{90})/4} \tag{31}$$

where, Δr is the measure of accuracy of the predicted r-values, $r(e)$ is the r-value from the tensile tests, $r(\alpha)$ is the predicted r-value and r_0, r_{45} & r_{90} are the experimental r-values at the given angles. Table 3-6 shows the yield strength and r-value errors for the nine calibration methods considered here. The results have been colour coded on a gradient from yellow to red. The cells highlighted in bright yellow indicate the most accurate calibration method in each category. The combined 0°-45° and 0°-45° calibration method yields the smallest overall error.

Method	Δσ	Δr	Overall
r-values Calibrated	0.0720	0.1097	0.1817
Calibration Method 1	0.0336	0.1371	0.1707
Calibration Method 2	0.0092	0.2122	0.2214
Calibration Method 3	0.0289	0.0966	0.1255
Calibration Method 4	0.0090	0.1587	0.1677
Calibration Method 5	0.0092	0.1555	0.1648
Calibration Method 6	0.0866	0.1097	0.1963
Calibration Method 7	0.0249	0.1090	0.1338
Combined 0-45 & 90-45 Calibration	0.0185	0.0793	0.0978

Table 3-6: Colour coded quality of fit results for Hill 48 calibration methods

Figure 3-7, plotted using data generated by the CERTETA group's BBC.exe solver, shows the 0°-45° and 0°-45° calibrated Hill 48 yield loci for the 316L stainless steel. Data on equibiaxial yield has been retrieved from the AMFOR database and is shown on the plot together with the uniaxial yield in the 0° and 90° directions. It can be seen that while the experimental yield point at 0° falls on both loci, the experimental yield point at 90° is represented only by the 90° to 45° calibrated locus. Both Hill 48 yield loci underestimate the equibiaxial yield strength of 316L material. While this yield criterion would not accurately describe the behaviour of the 316L material in a typical drawing process, given that material over the die in the

stretch forming process is deformed in a uniaxial manner, the Hill 48 yield criterion can be used to give an accurate description of the material in this study. Since blanks are cut along the length and, across the width of the sheet, and the Hill 48 yield criterion cannot accurately predict yield strength 0° and 90° with a single model, two material models are constructed for use in detailed simulations of the stretch forming process (Chapter 5).

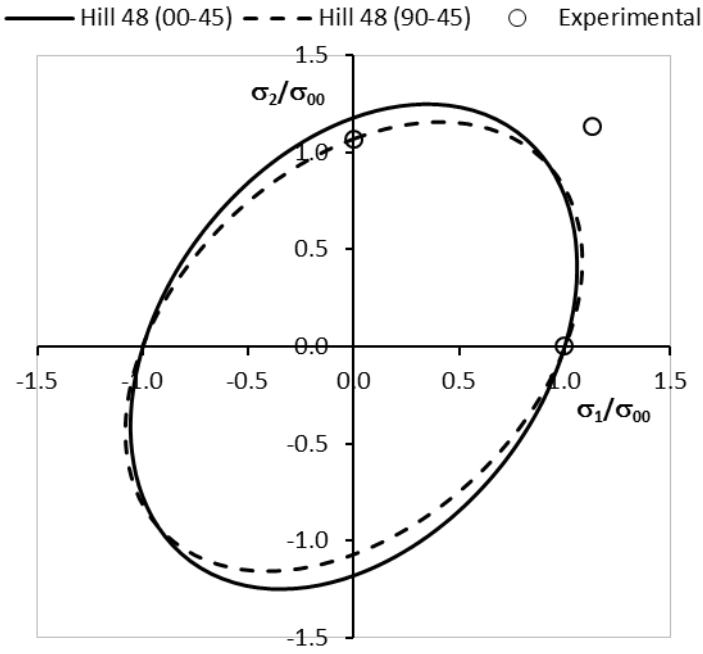

Figure 3-7: The 0°-45° and 90°-45° calibrated Hill 48 normalised yield loci for the 316L stainless steel

PAM-STAMP offers the user a number of laws to describe the strain hardening of a metallic material. Figure 3-8 shows a comparison of four of these hardening laws when fitted to the experimental stress/strain curves from the three uniaxial tensile tests, along the rolling direction of the sheet, using a least squared fitting routine. The stress expressions from the laws illustrated are defined as the Kinematic (Eq. 33), Hollomon (Eq. 32), Krupkowsky (Eq. 34), and Power (Eq. 35) laws;

$$\sigma(\varepsilon_p) = K\varepsilon^n, \tag{32}$$

$$\sigma(\varepsilon_p) = \sigma_y + R_{sat}(1 - e^{-C_r\varepsilon_p}), \tag{33}$$

$$\sigma(\varepsilon_p) = K(\varepsilon_p + \varepsilon_0)^n, \tag{34}$$

$$\sigma(\varepsilon_p) = \sigma_y + K\varepsilon_p{}^n, \tag{35}$$

where $\sigma(\varepsilon_p)$ is the true stress at a given plastic strain, σ_y is yield stress, R_{sat} and C_r are material dependent hardening variables, ε_p is plastic strain, ε_0 is initial strain, K is the strength coefficient, and n is the strain hardening exponent. The Hollomon law, which uses total strain rather than plastic strain, underestimates the material's yield strength and its ultimate tensile strength. While the three remaining laws all describe the material's strain hardening behaviour with good accuracy between yield and ultimate tensile strength, on extrapolation up to a true plastic strain of 0.8, the Krupkowsky law gives a more continuous curve. Hence, the Krupkowsky law is selected to describe the strain hardening behaviour of the 316L material.

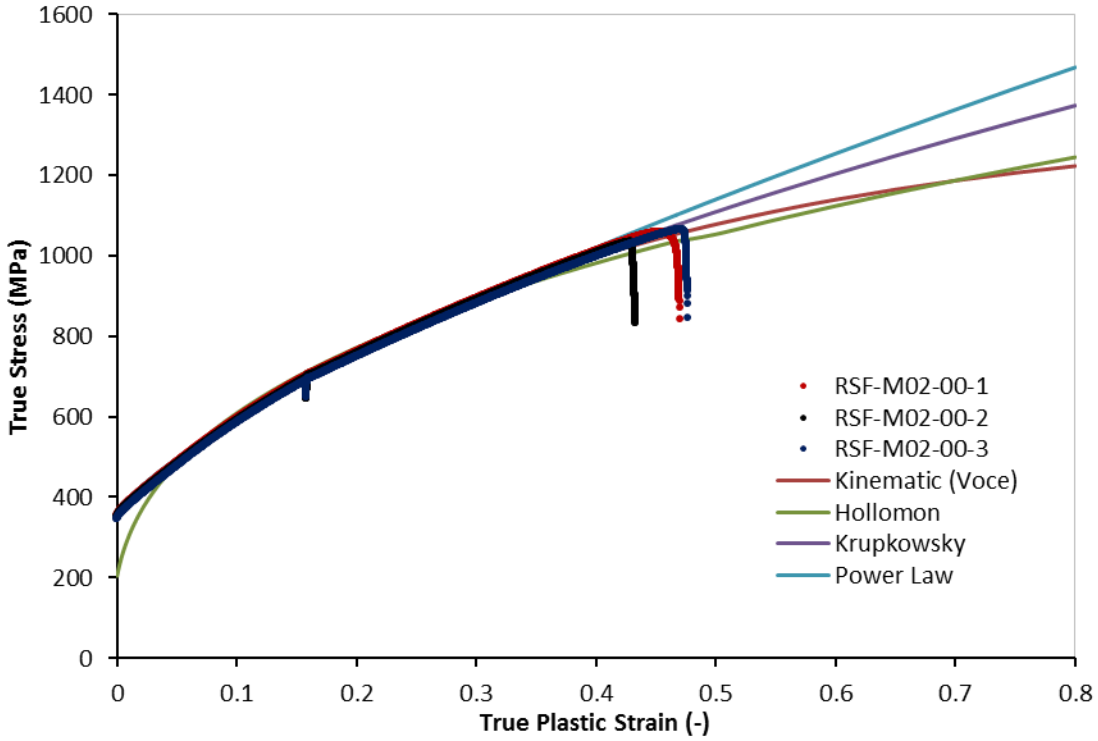

Figure 3-8: 316L hardening curve comparison

3.3.1 Strain Rate Sensitivity

Early trials on the AMFOR lab scale machine (see Section 5.2) showed that, where a pressure of 100 bar was applied in the two hydraulic cylinders, the 316L material stretched at an approximate rate of 1 mm per

second. This is equivalent to a strain rate of approximately 0.0025 ε/s, or a crosshead displacement rate of approximately 11.25 mm/minute in a uniaxial tensile test using the standard dog bone specimens (see Figure 3-4). This process strain rate can be adjusted by increasing or decreasing the hydraulic pressure at the cylinders.

While behaviour of aluminium alloys under loading is not normally considered to be strain rate sensitive the behaviour of steels is. Hence, additional uniaxial tensile tests were carried out, at varying crosshead speeds, to investigate the strain rate sensitivity of the 316L material. The test set-up and dog bone specimen geometry illustrated in Figure 3-4 is again used in uniaxial tensile tests on three specimens cut along and perpendicular to the sheet's rolling direction at crosshead speeds of 0.1, 1.0, 10, 100 and 1000 mm/min. Table 3-7, where standard deviation and standard error is again calculated using Eq. 17 and Eq. 18, shows the variable yield strengths observed during these tests. As a general rule it can be said that yield strength increases with increasing strain rate, but this is not always evident at very low strain rates. Note that the mean yield strength observed in the 0° direction at a crosshead speed of 1 mm/min is actually slightly lower that that observed at a crosshead speed of 0.1 mm/min in the same direction.

Test Rate (mm/min)	Angle from Rolling Direction (°)	Yield Strength (MPa)		
		Mean	Standard Deviation	Standard Error
0.1	0	336.7	8.062	4.655
1	0	336.4	0.561	0.324
10	0	354.4	12.165	7.023
100	0	378.1	4.858	2.805
1000	0	388.9	2.261	1.305
0.1	90	343.0	7.182	4.147
1	90	353.9	4.743	2.738
10	90	378.9	6.623	3.824
100	90	405.3	0.910	0.525
1000	90	414.8	8.550	4.937

Table 3-7: Yield strengths at 0° and 90° observed in tensile tests on the 316L stainless steel at crosshead speeds between 0.1 and 1000 mm/min

Figure 3-9 shows the strain rate sensitivity of the hardening behaviour in 316L stainless steel. The curves illustrated here are of the Krupkowsky hardening law, fitted to data from the three tests in the 0° direction, and extrapolated up to a plastic strain of 1.0, at each crosshead speed. It can be seen that, while the yield strengths are generally lower at lower crosshead speeds, the hardening behaviour of the material is more extreme. This relationship is also evident in the hardening behaviour of the material when tested at 90° to the rolling direction of the sheet.

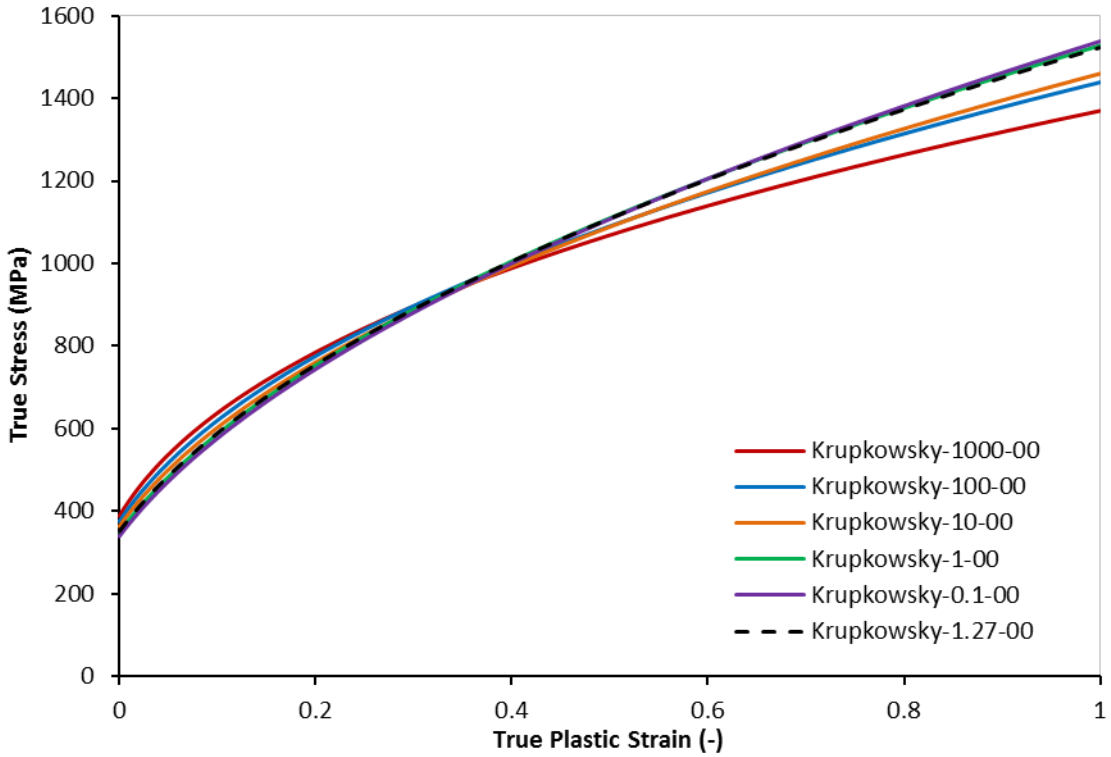

Figure 3-9: The strain rate sensitivity of the hardening behaviour in 316L stainless steel

Again PAM-STAMP offers a number of options to describe strain rate sensitivity in a material model. Since the Krupkowsky law has been shown to successfully describe the 316L material's hardening behaviour the modified Krupkowsky law is selected to describe its strain rate sensitivity. The modified Krupkowsky law is given as;

$$\sigma(\varepsilon_p, \dot{\varepsilon}) = K_{ref}\dot{\alpha}^A \left(\varepsilon_p + \varepsilon_{0_{ref}}\dot{\alpha}^B\right)^{n_{ref}\dot{\alpha}^C} \tag{36}$$

where, $\sigma(\varepsilon_p, \dot{\varepsilon})$ is stress at a given plastic strain and strain rate, $\dot{\alpha}$ is the actual strain rate divided by the reference strain rate, *A*, *B* & *C* are material constants and the subscript *ref* denotes a reference value.

The results from the initial uniaxial tensile tests at the crosshead speed of 1.27 mm/min are used as reference values and the least squared fitting routine is again used to determine the values of the *A*, *B* and *C* material constants. Since material models at 0° and 90° are constructed for the 316L material corresponding values of Krupkowsky law constants are used to determine the *A*, *B* and *C* material constants in each direction. Table 3-8 shows the complete list of material properties and material dependent constants required to implement these material models in PAM-STAMP.

	RSF-M02-SR-00	RSF-M02-SR-90
Young's Modulus (GPa)	122.9	182.9
Poisson's Ratio (-)	0.3	0.3
Density (kg/mm^3)	7.8 x 10^{-6}	7.8 x 10^{-6}
Plasticity Law	Hill 48	
Anisotropic Type	Orthotropic	
Hill 48 Coefficient *F* (-)	0.88039	1.46674
Hill 48 Coefficient *G* (-)	1.44120	1.19003
Hill 48 Coefficient *N* (-)	2.67753	3.26209
Hardening Curve Definition	Krupkowsky Law	
Initial Strain ε_0 & ε_{0ref} (-)	0.05390	0.08302
Strength Coefficient *K* & K_{ref} (GPa)	1.48430	1.51054
Strain Hardening Exponent *n* & n_{ref} (-)	0.49364	0.55236
Strain Rate Model	Modified Krupkowsky Law	
Reference Strain Rate $\dot{\varepsilon}_{ref}$ (ms^{-1})	2.82 x 10^{-7}	2.82 x 10^{-7}
Material Constant *A* (-)	-0.01268	-0.01115
Material Constant *B* (-)	-0.02076	-0.00246
Material Constant *C* (-)	-0.03215	-0.02637

Table 3-8: Material properties and material dependent constants required to implement the 316L material models in PAM-STAMP

3.3.2 Validation of the 316L Material Models

The material models for the 316L stainless steel are validated through simulation of the uniaxial tensile tests. Figure 3-10 shows the set-up used in these simulations. A quarter of the tensile test dog bone specimen geometry is modelled with vertical and horizontal symmetry planes used to project the remainder of the specimen. A mesh constructed from quadrangular shell elements, with sides having a maximum size of 1.25 mm, is used to represent the test specimen. The RSF-M02-SR-00 material model, with the rolling direction indicated as being along the specimen length, is assigned to the mesh to represent tensile tests on specimens cut along the rolling direction of the sheet. The RSF-M02-SR-90 material model, with the rolling direction again indicated as being along the specimen length, is assigned to the mesh to represent tensile tests on specimens cut perpendicular to the rolling direction of the sheet. Simulations, where a material model using the Hill 48 yield criterion calibrated with r-values, are also run in order to compare results to those from the preferred material models. Elements in the area of increased width are shared with a rigid body used to represent the grips. An imposed velocity attribute is used to move the rigid body and hence stretch the specimen mesh during the explicit simulations. Variable velocity scale factors are set in CPU control attributes, to characterise the corresponding crosshead speeds of the tensile tests listed in Table 3-7.

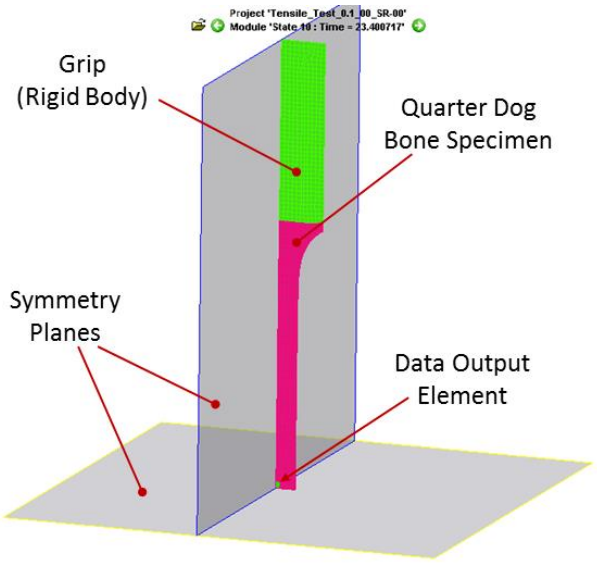

Figure 3-10: The uniaxial tensile test simulated in PAM-STAMP

History curves are used to extract data from the simulations pertaining to the central element indicated in Figure 3-10. Figure 3-11 and Figure 3-12 show the results from the uniaxial tensile test in the 0° direction with a crosshead speed of 1000 mm/min. Stress/strain curves from the remainder of the tests are included with this document as Appendix C.

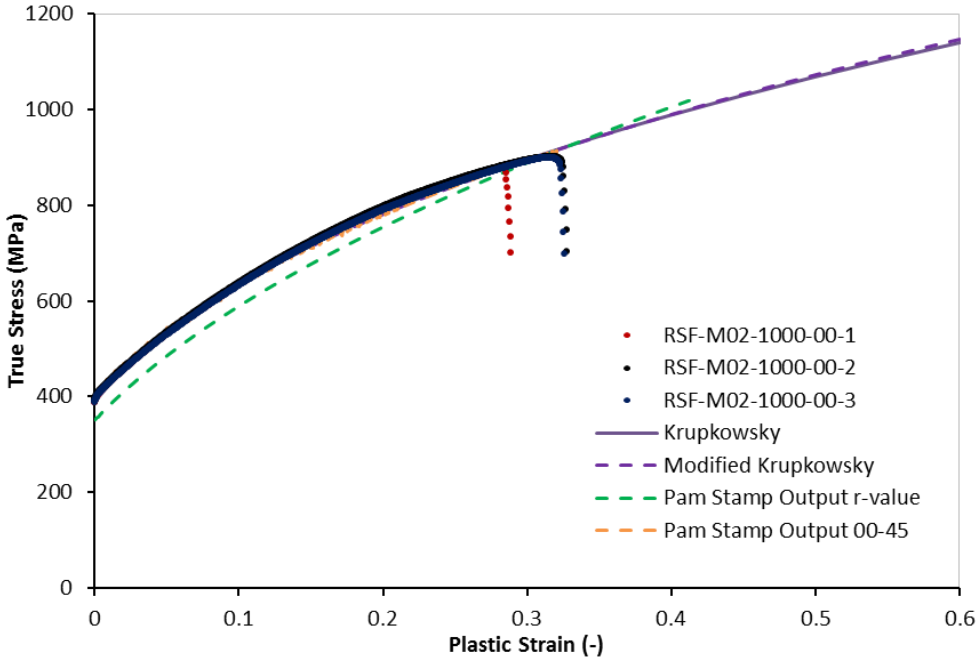

Figure 3-11: Stress/strain curves from the uniaxial tensile test in the 0° direction with a crosshead speed of 1000 mm/min

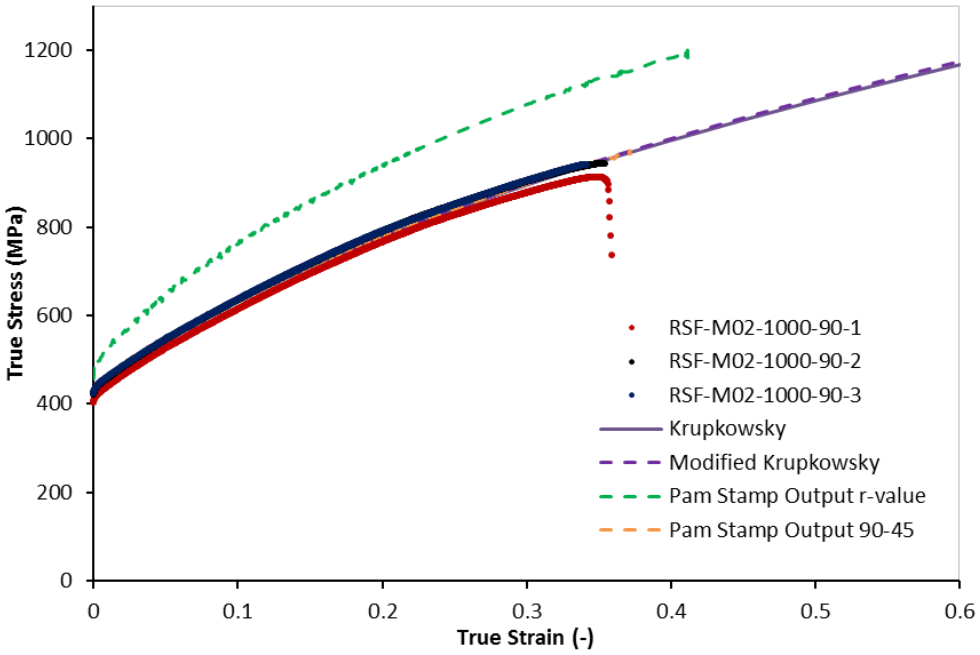

Figure 3-12: Stress/strain curves from the uniaxial tensile test in the 90° direction with a crosshead speed of 1000 mm/min

The first three curves illustrated pertain to the experimental results where the labels indicate, project name, material identification, crosshead speed, angle from the rolling direction and specimen number. The curve labelled Krupkowsky represents the hardening law fitted directly to these experimental results. The Modified Krupkowsky curve uses the values listed in Table 3-8 to modify a baseline curve (1.27 mm/min) in the corresponding direction. The two PAM-STAMP output curves have the Hill 48 calibration method indicated. The values used in the PAM-STAMP output curves are true stress and true plastic strain on the membrane of the central shell element.

It is evident from these plots that Modified Krupkowsky strain rate model is giving good results, with curves being in good agreement to those from the directly fitted Krupkowsky law. While the material model using the Hill 48 yield criterion calibrated with r-values is giving reasonable results in the 0° direction, poor results are evident in the 90° direction. In every plot, curves representing results from simulations using the preferred material are almost completely obscured by the curves from experimental results. This indicates that the two 316L material models provide a very accurate description of this material's behaviour when subjected to uniaxial deformation.

3.4 Loads Transmitted to the Interpolator from the 316L Material during a Stretch Forming Process

During a traditional stretch forming process reaction forces onto the die are caused by the tension in the sheet being stretched. Neglecting frictional effects, the tension in the sheet (T) can be given as;

$$T = \sigma w t, \tag{37}$$

where, σ is the stress in the sheet, w is the width of the sheet and t is the sheet's thickness. To determine the maximum tension that the sheet can be subjected to, stress can be substituted by the material's ultimate tensile

strength. Referring to Figure 3-13, the reaction force onto any section of tooling of a given length (d) can be given as;

$$R = 2T \sin\theta, \tag{38}$$

where, R is the total reaction force acting on the die over the distance d, T is the tension in the sheet and θ is the angle between the direction at which the tension acts and a plane bisecting the given length of tooling. Assuming constant curvature, and again neglecting frictional effects, the tension in the sheet will remain constant along the length of the die.

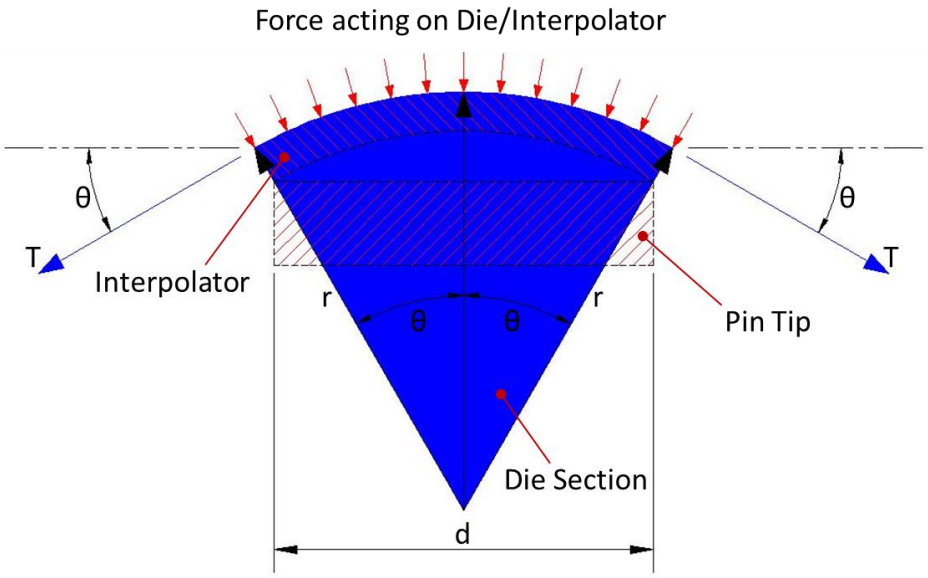

Figure 3-13: Forces acting on a die section due to tension in the sheet

When considering the forces acting on the interpolator in a reconfigurable tooling system, where flat round pivoted pin tips are used, the interpolator is compressed over each pin tip and the angle θ can be given as;

$$\theta = \sin^{-1}\left(\frac{0.5d}{r}\right) \tag{39}$$

where, d is the diameter of the pin tip and r is the radius of curvature. In the reconfigurable system being simulated in Chapter 5 the pin tips are 68 mm in diameter and the radius of curvature is 750 mm hence the angle θ is 2.598°. Assuming that the 316L stainless steel is stretched to approximately 15%, the true plastic strain in the sheet will be approximately 0.14. Since the Krupkowsky law is used to describe the work

hardening behaviour of this material, Eq.34 is used to determine the stress in the sheet, as being 660.5 MPa. Since the width of sheet being considered is also the diameter of a pin tip, and the material is 0.88 mm in thickness, the tension in the sheet can be determined, using Eq.37, as being 39.5 kN. Hence the normal force transmitted onto the interpolator over each pin tip can be determined, using Eq.38, as being 3.58 kN. The area of interpolator being subjected to this normal force is equal to the area of a single pin tip. Hence the engineering stress in the interpolator, as it is compressed over each pin tip, can be determined as being 0.99 MPa, by simply dividing force by area.

3.4.1 Tangential Contact between the Blank and Die

As long as the blank is in contact with the die, the direction at which the tension acts remains tangential to the tool's surface. A special case arises at the edge of the die where the gripped end of the blank is no longer in contact with the die. In order to keep the force on the die constant, it is important that the grip location is controlled so that tangential contact between the die and the gripped end of the blank is maintained [Figure 3-14 (b)]. When the angle between a radial line from the die's centre of curvature to the edge and the blank is greater than 90° [Figure 3-14 (a)] the blank will not be in contact with the edge of the die, and the outer section of die will not be not utilised in the forming process. When the angle between this radial line and the blank is less than 90° [Figure 3-14 (c)] the angle θ from Eq. 38 is increased at this side and the reaction force on the die edge is also increased.

If the force on the edge of a traditional die is excessive the die can sustain damage and/or be subjected to excessive wear reducing its lifespan. Tangency between the gripped end of the blank and the edge of the die is of greater importance in a reconfigurable tooling system given that individual pins in these locations will need to bear any additional forces without buckling, and, since the force on the interpolator will also be greater, it will be subjected to more compressive strain, reducing its final thickness. This

will increase the difficulty in achieving the correct pin height at these locations. If the force on the interpolator is excessive at the die edges its lifespan will be drastically reduced.

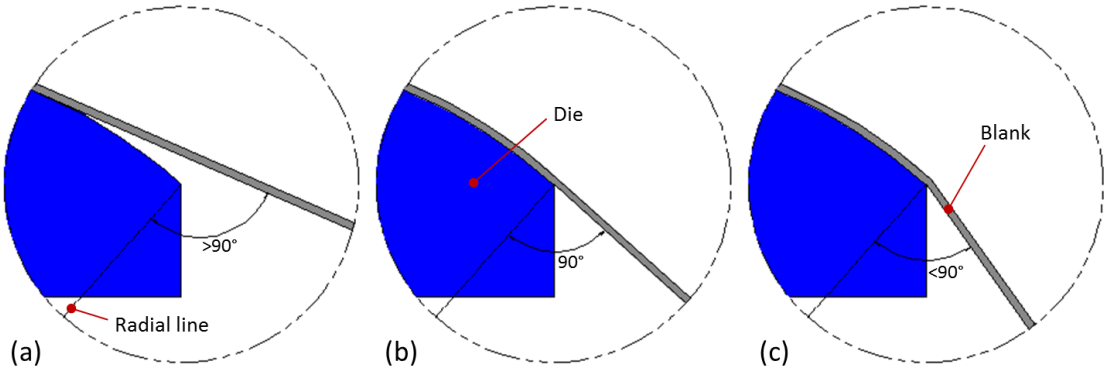

Figure 3-14: Tangential relationship between the gripped end of the blank and the edge of the die

3.5 The Interpolator Material Models

The interpolator materials tested here are polyurethane sheets supplied by KD Plastics Ltd., from their Kaylan® D series. Polyurethane is a thermoplastic with a two-phase microstructure, consisting of both hard (a diisocyanate and curing agent) and soft (a polymer glycol) regions. The hard regions act as a cross-linking mechanism between the soft regions. The soft regions remain above their glass transition temperature, at room temperature, giving the polyurethane material it's rubberlike qualities. The hard regions enhance the material's strength and hardness. Hence, polyurethane can be produced with a range of hardness (and strength) depending on the ratio of the material's molecular weight contributed by the hard regions to that contributed by the soft regions (Hepburn, 1992). The Kaylan® D series materials, used here, range in hardness from 20 to 73 on the Shore D scale. These materials have been selected due to polyurethane's excellent load bearing capacity, high flexibility, and environmental resistance properties.

PAM-STAMP uses a two term Mooney Rivlin equation to describe the behaviour of hyperelastic materials when subjected to loads. A description of

the strain energy density function, used in the Mooney Rivlin equation, and derivation of the true stress expressions used in uniaxial tension and compression are included with this document as Appendix D.

Compression tests were carried out on samples of all the materials in Kaylan® D series. Samples with a thickness of 10 or 15 mm were provided by KD Plastics Ltd. free of charge. Where a 10 mm thick sample was available specimens of 22 mm in diameter were used, and where a 15 mm thick sample was supplied specimens of 33 mm in diameter were used (as shown in Figure 3-15). The specimens were compressed between two hardened steel platens, on an Instron 5500R universal testing machine, as illustrated in Figure 3-15. The interfaces between the specimen ends and platens were lubricated with Cimflo 20 stamping and drawing oil, from Cimcool Fluid Technology. Although some barrelling was evident during testing it was assumed that friction free conditions were achieved. Hence, engineering stress was calculated as the applied force divided by the original area of the specimen's circular face, while strain was measured through crosshead displacement.

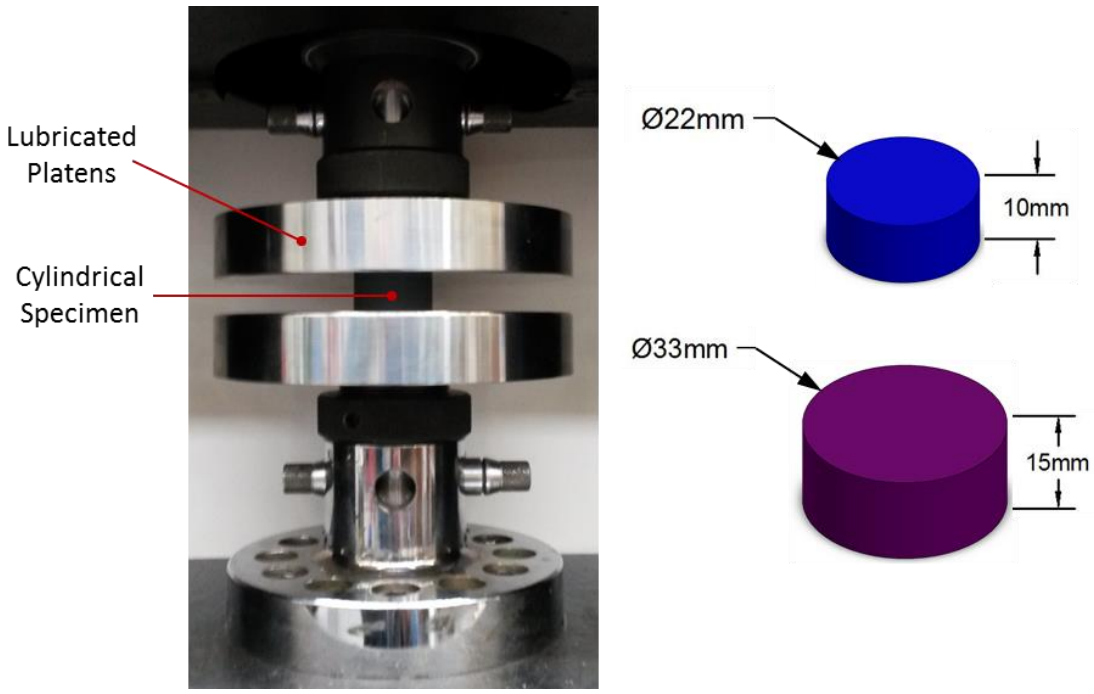

Figure 3-15: Compression test set-up and specimen geometry

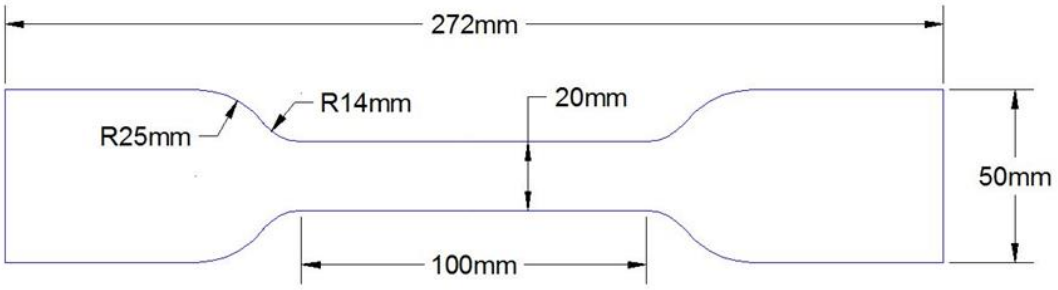

Figure 3-16: Tensile test specimen geometry for the 10 mm thick polyurethane

Tensile tests were also carried out on a mid-range material (D40 Orange) 10 mm in thickness and cut to the specimen geometry shown in Figure 3-16. The tensile specimens were gripped between two wedge action grips, similar to those illustrated in Figure 3-4, and stretched at a rate of ten millimetres per minute. Strain was calculated as crosshead displacement applied to the 100 mm length of reduced width.

Figure 3-17 shows the results from the uniaxial tests in compression and tension, on the D40 Orange material, plotted with Mooney Rivlin curves fitted to the data from the full range of strain observed during testing. Eq.40 and Eq.41 are used to calculate engineering stress in tension and compression respectively;

$$s_1 = 2\left(C_1 + C_2{\lambda_1}^{-1}\right)\left(\lambda_1 - {\lambda_1}^{-2}\right), \tag{40}$$

$$s_3 = 2\left(C_1 + C_2{\lambda_3}^{-1}\right)\left(\lambda_3 - {\lambda_3}^{-2}\right), \tag{41}$$

where, s is engineering stress, C_1 and C_2 are the Mooney Rivlin constants, λ is the stretch ratio and the subscripts $_1$ & $_3$ denote directions. A separate least squared fitting routine is used for each deformation mode, and it should be noted that very different Mooney Rivlin constant values are obtained from tensile and compressive data.

Given that the stretch ratio is equal to one plus the magnitude of engineering strain, it is evident from Figure 3-17 that while the two term Mooney Rivlin model describes the behaviour of this polyurethane materials quite well at larger strains, in both tension and compression, it fails to describe behaviour at small strains.

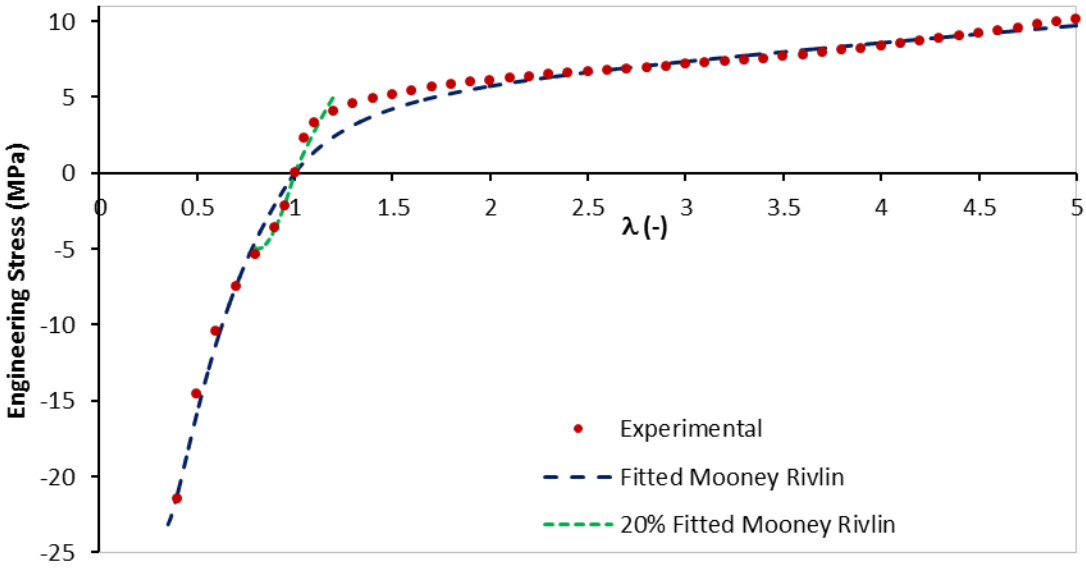

Figure 3-17: Comparison of the experimental and fitted Mooney Rivlin stress/stretch ratio curves for Kaylan D40 Orange

Normally a single set of values can be obtained for the Mooney Rivlin constants by fitting results from uniaxial and equibiaxial tensile tests to their corresponding Mooney Rivlin stress expressions. While a compromised set of values are obtained, for the C_1 and C_2 constants, they are normally of sufficient accuracy to allow for description of the material in any given deformation mode (at larger strains).

In this project, the interpolator is known to be subjected to compression between the blank and pin tips. In addition to this there will be some stress and strain associated to the bending of the interpolator around the curvature of the die, but since the overall die curvature is relatively gentle, bending stress and strain will be very small. In Section 3.4, when 0.88 mm thick 316L stainless steel is stretched over a die with a 750 mm radius of curvature, the compressive stress in the interpolator was found to be approximately 1 MPa. With the harder materials from the Kaylan D series this level of stress will result in relatively small strains being present in the interpolator at the end of the stretch forming process.

It should be noted that Polyurethane is also a strain rate sensitive material (Qi & Boyce, 2005), but PAM STAMP does not allow for strain rate sensitivity to be included for material models used with volume tools. While

PAM STAMP does allow for the implementation of custom user material models, compiled with the FORTRAN programming language, this is a complex procedure which was not deemed necessary for this project. Instead, the Polyurethane materials were tested at a relatively low rate of crosshead displacement (1 mm/minute), resulting in a similar average strain rate to that present in the lab scale stretch forming process, where the force of 1 MPa is applied over a period of approximately 1 minute. The PAM-STAMP software can accept either tensile or compressive data when implementing the Mooney Rivlin material model. Compression data is used here to determine the Mooney Rivlin constants for all the polyurethane materials in the Kaylan D series. Rather than fitting the Mooney Rivlin model to the complete range of data from compression tests, it is fitted to a reduced volume of data so that small strains are more accurately described. The increased accuracy obtained, at small strains, from fitting the Mooney Rivlin curve to a range of engineering strain ±20% in magnitude, for the Kaylan D40 Orange material, is shown in Figure 3-17. Table 3-9 shows the Mooney Rivlin constants, the range of strain used to fit the Mooney Rivlin equation, the strain in each material at a compressive engineering stress of 1 MPa and the common properties required to implement material models in the PAM-STAMP software.

It has been demonstrated in Appendix E. and is evident in the Mooney Rivlin Plot illustrated in Figure E-2, that the C_2 constant is always negative when compression data is used to determine the Mooney Rivlin constants. When one of the Mooney Rivlin constants is negative the resulting material model is unstable i.e. at some stage stress will decrease rather than increase with growing strain. Since the material models used with simulations in Chapter 5 remain stable beyond the strain levels present in the interpolator at the end at the end of the stretch forming process, the use of negative C_2 constants in material models will not have a detrimental effect on the results obtained from these simulations.

Material	Mooney Rivlin Constants		Fitting Strain Range (%)	Strain when s* = 1 MPa (%)
	C_1 (GPa)	C_2 (GPa)		
D20 Red	6.901×10^{-4}	-1.578×10^{-4}	0 to -40	-25.68
D25 Purple	1.247×10^{-3}	-1.912×10^{-5}	0 to -40	-12.05
D30 Green	1.153×10^{-2}	-7.210×10^{-3}	0 to -20	-4.03
D40 Orange	2.320×10^{-2}	-1.596×10^{-2}	0 to -20	-2.16
D50 Blue	5.487×10^{-2}	-4.121×10^{-2}	0 to -15	-1.19
D60 Brown	1.607×10^{-1}	-1.326×10^{-1}	0 to -10	-0.53
D60X Violet	9.913×10^{-2}	-8.107×10^{-2}	0 to -10	-0.79
D70X Grey	2.857×10^{-1}	-2.350×10^{-1}	0 to -10	-0.43
Common Properties				
Density (kg/mm^3)	1.2×10^{-6}			
Poisson's Ratio (-)	0.499			
* s = Compressive Engineering Stress				

Table 3-9: Kaylan D series material properties

3.5.1 Validation of the Interpolator Material Models

The interpolator material models represented by the data in Table 3-9 are validated through simulation of the compression tests in the PAM-STAMP software. The simulations are set up as illustrated in Figure 3-18 where, the top and bottom compression platens are represented as rigid bodies. In each simulation the cylindrical test specimens are represented as volume tools with the same dimensions as in the corresponding compression test. Each volume tool / test specimen is defined as a mesh comprising of hexahedral elements with edges of a maximum size of 2.5 mm. This corresponds with the element size used to define the interpolator in simulations of the stretch forming process (see Chapter 5). A blank is included as part of the top compression platen, since PAM-STAMP requires a metallic blank in all simulations. The blank is represented as a mesh comprised of quadrangular shell elements with sides of a maximum dimension of 2 mm. Blanks have been given a thickness of 5 mm and are assigned with the material model corresponding to a high strength steel (DP800) from the PAM-STAMP material database. A friction coefficient of 0.05 (ESI Group, 2013) is used at the interfaces between the blank and specimen and between the bottom platen and specimen, to represent the lubrication conditions present in the

experimental compression tests. Mesh transformations are used to close the gaps between objects in the model, before an imposed constant velocity of 0.25 mm/ms is applied to rigid body representing the top compression platen.

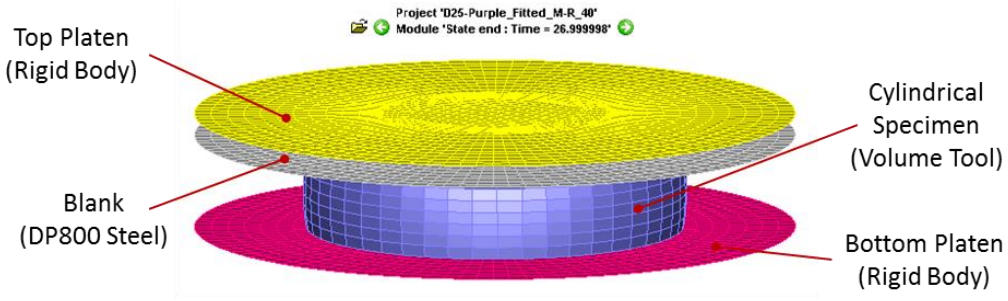

Figure 3-18: Compression test simulation set-up

PAM-STAMP is not the ideal software when extracting data from simulations representing the compression of a polyurethane material, since there are no stress and strain contour maps available on the specimen when it is represented as a volume tool. It is assumed that no thinning of the blank occurs during simulation of the compression tests since a maximum of only 3.0×10^{-6} mm is observed at its centre when simulating the compression of the stiffest material (D70X Grey). Hence stress and strain in the cylindrical specimen is calculated from the simulations in the same manner as it was from experimental compression tests. The output from history curves pertaining to the displacement of the top platen and the contact force on the specimen corresponds to the crosshead displacement and load cell data from experimental compression tests. Hence, engineering strain is calculated as the ratio of displacement to the original thickness of the cylindrical specimen and engineering stress is calculated as the ratio of contact force on the cylindrical specimen to its original cross sectional area. Both are assumed to be negative since they refer to compression. The stretch ratio is then taken as one plus the recorded engineering strain and true stress in the specimen is taken as the product of the stretch ratio and engineering stress.

Figure 3-19, Figure 3-20 and Figure 3-21 show plots of the compression data pertaining to a mid-range Kaylan D material (D40 Orange), the softest

material in the Kaylan D series (D20 Red) and the hardest material in the Kaylan D series (D70X Grey), respectively. The curves illustrated represent data from experimental compression tests, data from the Mooney Rivlin equation fitted over the range of strain indicated in Table 3-9 and output from simulations of the compression tests where the specimen is assigned with the corresponding Mooney Rivlin material model. The horizontal and vertical dashed lines indicate the true stress in the material at an engineering stress of -1 MPa and the corresponding stretch ratio, respectively. Equivalent plots pertaining to the remaining five materials are included with this document as Appendix F.

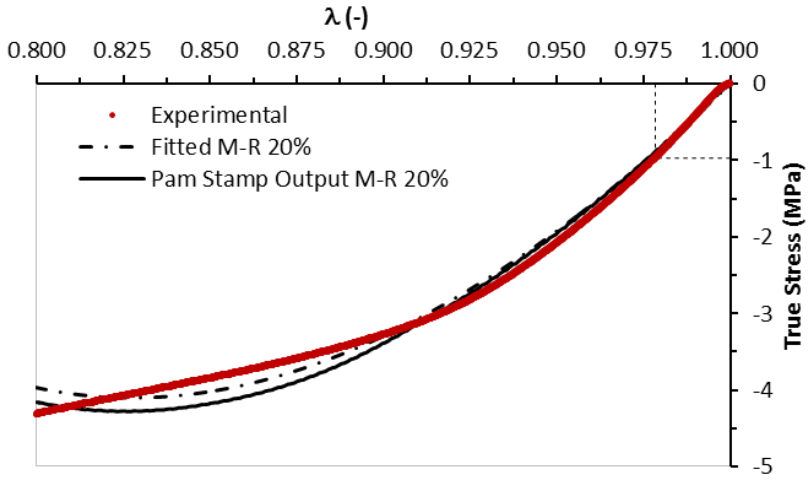

Figure 3-19: True stress/stretch ratio compression curves for the Kaylan D40 Orange polyurethane material

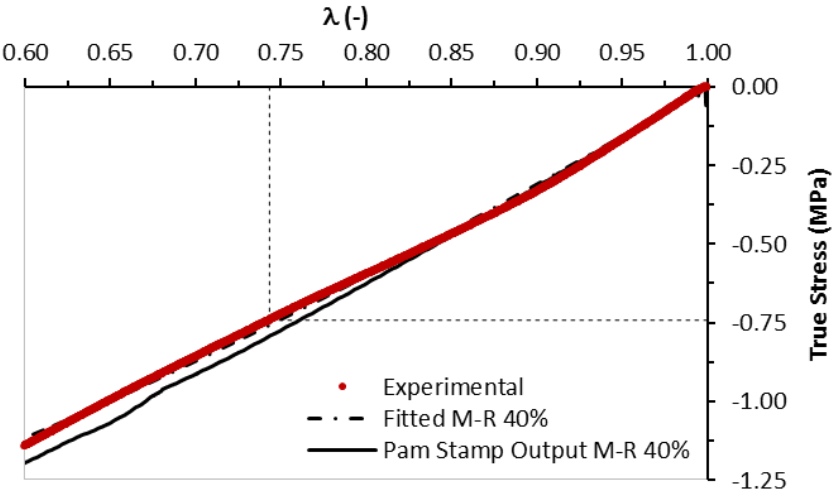

Figure 3-20: True stress/stretch ratio compression curves for the Kaylan D20 Red polyurethane material

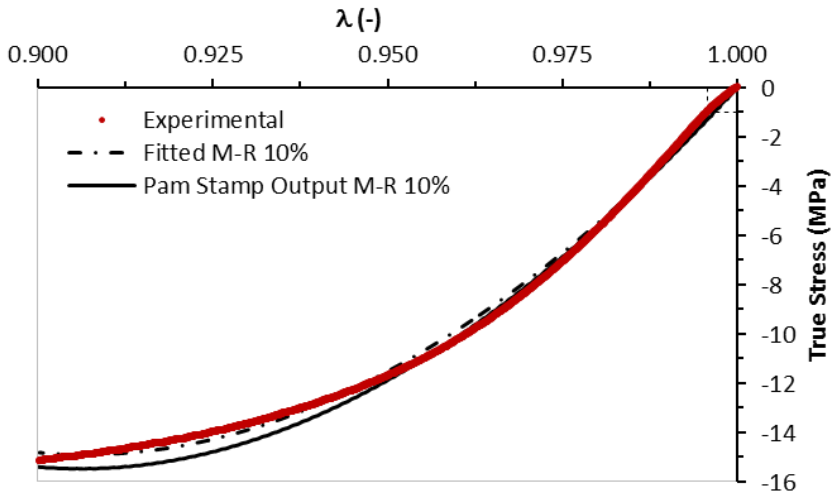

Figure 3-21: True stress/stretch ratio compression curves for the Kaylan D70X Grey polyurethane material

In each plot the compressive stress, at higher levels of strain, observed in data from the PAM-STAMP simulations is slightly higher that that observed in data from the fitted Mooney Rivlin equation utilising the same constants.

It should be noted that the PAM-STAMP software does not use the conventional form of the Mooney Rivlin equation used here. PAM-STAMP uses a Lagrangian approach, common in the study of the mechanics of solids, where the strain invariants are not defined in terms of the stretch ratios as shown in Appendix D. Instead PAM-STAMP (ESI Group, 2013) defines the first, second and third strain invariants as;

$$I_1 = 3 + 2J_1, \tag{42}$$

$$I_2 = 3 + 4J_1 - 4J_2, \tag{43}$$

$$\& \; I_3 = 1 + 2J_1 - 4J_2 + 8J_3, \tag{44}$$

where I_1, I_2 and I_3 are the first, second and third Right Cauchy-Green strain invariants and J_1, J_2 and J_3 are the first, second and third Green-Lagrange strain invariants, which can be further defined through the use of linear algebra. PAM-STAMP then defines the strain energy density function as;

$$W = A(I_1 - 3) + B(I_2 - 3) + W(I_3) \tag{45}$$

where, W is the strain energy density function, A and B are the Mooney Rivlin constants and $W(I_3)$ is said to be a penalty function for incompressibility.

Overall the models developed here for the Kaylan D series of materials are shown to provide a reasonable description of each material's behaviour up to and beyond the compressive engineering stress of 1 MPa present in the interpolator, in the stretch forming process presented in Chapter 5. It can be observed in Figure 3-20, Figure F-1 Figure F-2 that no instability is evident over the fitted strain range in the softer materials, but models of the harder materials in the Kaylan D series are showing instability towards the end of their fitted strain range (Figure 3-19, Figure 3-21, Figure F-3, Figure F-4 and Figure F-5). Since instability is not present close to the line indicating the compressive engineering stress of 1 MPa, in any of the plots, these material models can be used with a good degree of confidence in simulations of the stretch forming process presented in Chapter 5.

3.5.2 Cyclic Loading of Interpolator Materials

In this section the results from a number of cyclic compression tests are examined to determine the repeatability of obtaining dimensional accurate parts from a stretch forming process over a reconfigurable die where Kaylan D series materials are used as interpolators. Specimens, similar to those shown in Figure 3-15 (22 mm in diameter), are cut from six materials from the Kaylan D series (D20 Red, D30 Green, D40 Orange, D50 Blue, D60 Brown and D60X Violet). Tests are again carried out on the Instron 5500R universal testing machine, with a setup similar to that used in previous compression tests and shown in Figure 3-15.

The parameters used in the cyclic compression tests are designed to mimic the conditions that the interpolators experience when stretching parts on the AMFOR lab scale machine (see Section 5.2). Seven tests are carried out using crosshead displacement as the control variable, while one additional test is carried out using engineering stress as the control variable. During a single cycle of each test, loading of the specimen is carried out over a period

of five minutes, before holding at the target maximum control variable for a further five minutes. The load is removed over a period of one minute, before another holding stage at the target minimum control variable (zero), for a final period of five minutes. Each test consists of a total of twenty cycles. All tests are carried out under dry conditions i.e. with no lubricant applied the interfaces between the specimen and platens. Tests are named using the material Shore hardness, the colour associated with the specimen material and the target maximum control variable.

The first set of results discussed here relate to the Green-0.5 mm test. The maximum engineering stress recorded during this test is 1.43 MPa. Using the calculations laid out in Section 3.4 that is equivalent to the stress present in an interpolator when the 316L material (described in Section 3.3) of 1.26 mm in thickness is stretched to an approximate strain of 14% at a 750 mm radius of curvature. Figure 3-22 (a) shows the engineering stress/strain curves obtained from all twenty cycles of the Green-0.5 mm test. It is notable that the material behaves differently in loading and unloading. While the relationship between engineering stress and strain is relatively linear in loading, it is not in unloading. There is a vertical drop in stress during the first holding stage, at the end of the loading stage, as the magnitude of force recorded by the load cell (measuring the load in a vertical axis through the test apparatus) drops. There are two reasons why the strain in the specimen appears to be time dependant. The first is a creep response in the polyurethane materials, where the strain in the direction of loading continues to increase when subjected to a constant load. The second is a response to the barrelling effect, which is very noticeable when carrying out compression tests on rubberlike materials, where the diameter of the specimen increases more rapidly at the centre of the specimen than at its top and bottom surfaces in contact with the tooling. Over a period of time the specimen continues to expand, as the friction between the specimen and platens is overcome, when the crosshead stops moving.

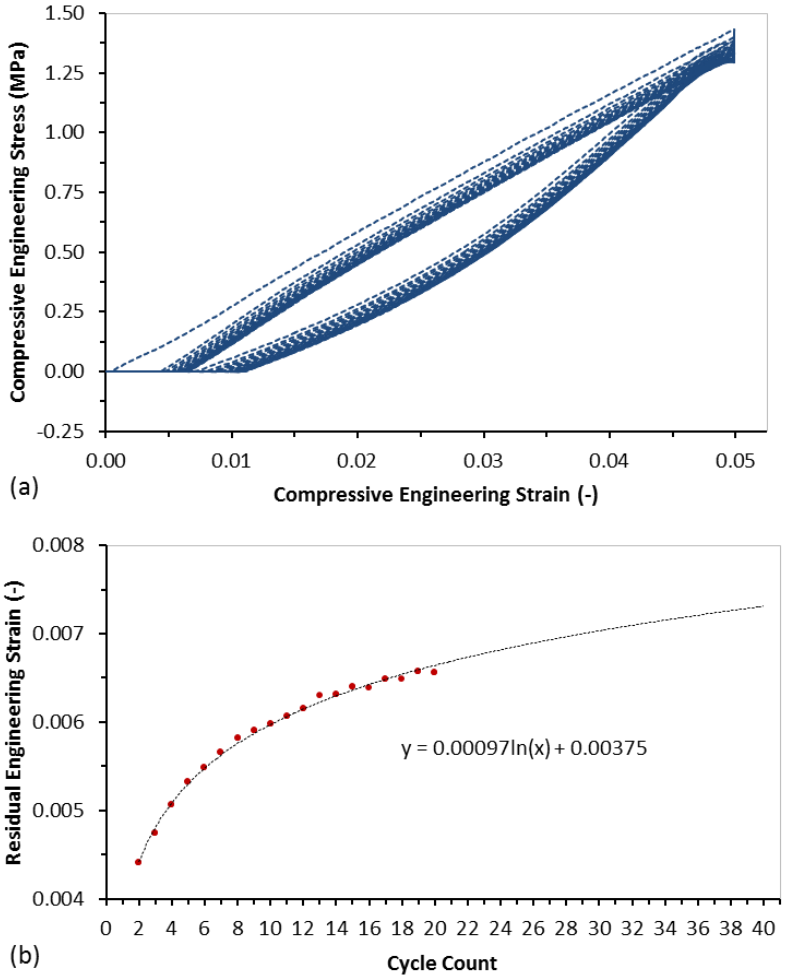

Figure 3-22: Engineering stress versus strain plot showing all 20 cycles (a) together with a plot of residual strain versus cycle count (b) for the Green-0.5mm cyclic compression test

There is a reduction in strain (indicated by the horizontal line at the bottom of the curves) during the second hold stage, when the load is removed. This shows that the specimen continues to relax and hence increase in thickness when the load has been removed. Note that the test data displayed here has been cleaned up in this area, where negative stress values are taken as zero, to emphasise the strain reduction.

This phenomenon is illustrated in a clearer manner in the plot of crosshead displacement versus time, taken from the data recorded during the stress controlled test (Brown-5 MPa) and shown in Figure 3-23. It can be seen that during the first holding stage, in each cycle, the crosshead continues to move downwards to maintain the specified stress level in the

specimen. During the second holding stage, in each cycle, the crosshead continues to move upwards maintaining zero force recorded at the load cell, and hence a zero stress level in the specimen as it thickens. It can be discerned from this phenomenon that, for dimensional accuracy, when a number of similar parts are being formed in the stretch forming process, the load/hold time period should be kept constant. If the blank is held in loading for a longer time period the interpolator will continue to compress, reducing the part's final radius of curvature.

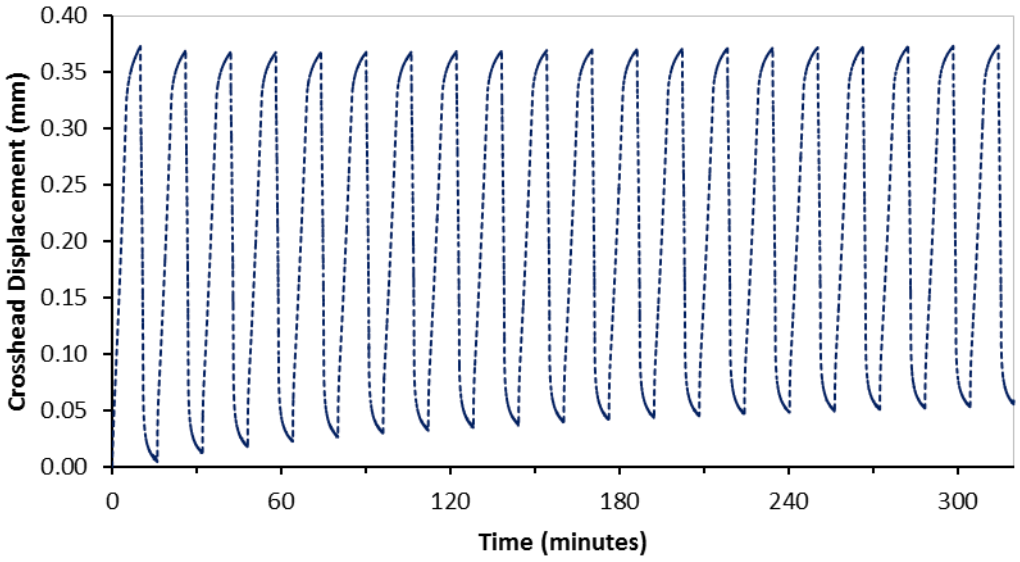

Figure 3-23: A plot of crosshead displacement versus time for the Brown-5MPa cyclic compression test

Referring again to Figure 3-22 (a), it is noticeable that the stress/strain curve relating to each cycle shifts to the right as the cycle count increases. This is an indication that a residual strain in left in the specimen at the end of each cycle, where the specimen fails to return to its previous thickness. Figure G-1 (a) (included in Appendix G. of this document) shows the engineering stress/strain curves pertaining only to cycles 1, 2, 10 and 20 of the Green-0.5 mm test. It is more noticeable on this plot that the rightward shift reduces as the cycle count increases. The shift between cycles 1 and 2 is greater than the shift between cycles 2 and 10, while the shift between cycles 10 and 20 is very small in comparison. This is an indication that the

additional residual strain held in the specimen at the end of the 16 minute cycles reduces as the cycle count increases.

Figure 3-22 (b) shows the total residual strain detected at the beginning of each cycle during the Green-0.5 mm cyclic compression test. The strain values used here are those recorded when the load cell detects a force of sufficient magnitude to induce an engineering stress greater than 0.1 kPa in the specimen. The accuracy of this method of deducing residual strain depends on the data capture rate used and the rapidity of the increase in the magnitude of the force detected in the early stage of the tests. Despite capturing data from approximately 2000 data points per cycle, the residual strain values for the Green-0.5 mm test were taken from the strain corresponding to stress values ranging between 0.1 and 3.7 kPa.

An initial trendline curve, with a natural logarithmic regression, has been fitted to the available data and extrapolated up to a cycle count of 40. While the trendline curve shown in Figure 3-22 (b) is a relatively good fit to the available data the steepness of the curve between cycles 20 and 40 is questionable. At the end of the test (20 cycles) this residual strain results in the specimen retaining only 0.066 mm of its compression. Hence for the process examined in Chapter 5, where a 316L material of 0.88 mm in thickness is stretched to a 750 mm radius of curvature, any residual strain in the D30 Green material would have a negligible influence on the surface accuracy of parts formed. It should be noted that when measured again 24 hours after the end of the test the thickness of the Green-0.5 mm test specimen had returned to that originally recorded and no residual strain remained.

Figure 3-24 (a) shows the engineering stress/strain curves obtained from all twenty cycles of the Brown-0.35 mm test. While residual strain values are of a similar magnitude to those seen in the Green-0.5 mm test, the maximum engineering stress recorded is much higher. The magnitude of stress recorded in the test specimen (4.92 MPa) is equivalent to the stress

present in an interpolator when the 316L material 4.33 mm thick is stretched to an approximate strain of 14% at a 750 mm radius of curvature.

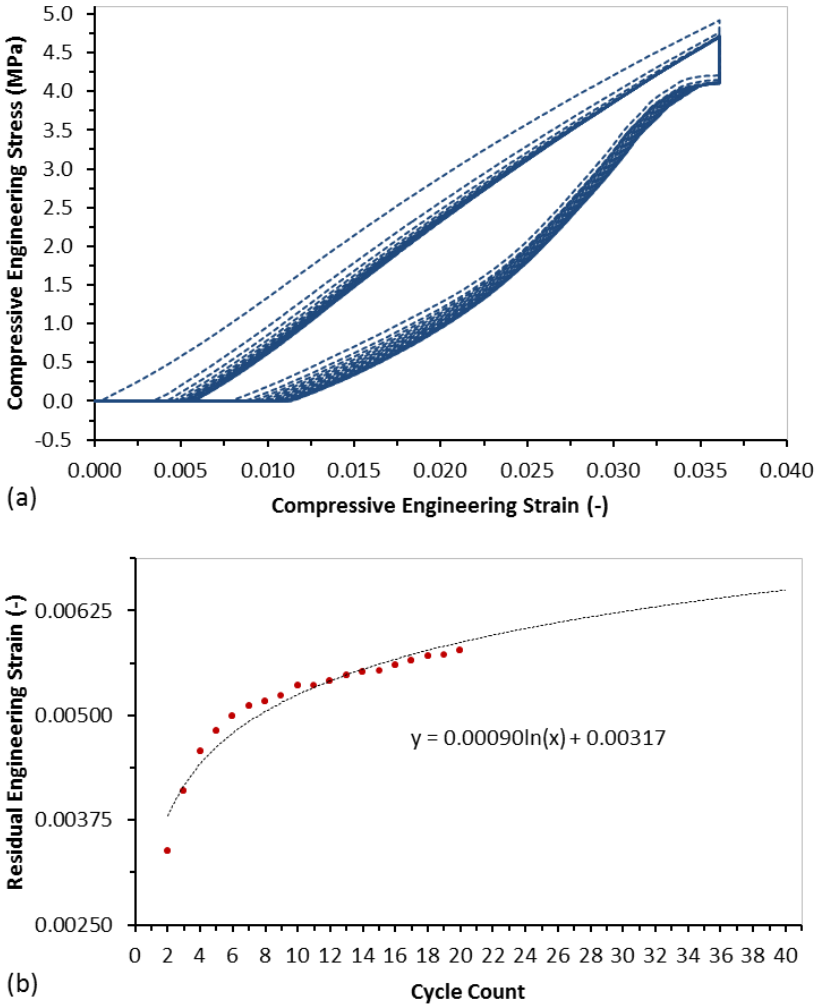

Figure 3-24: Engineering stress versus strain plot showing all 20 cycles (a) together with a plot of residual strain versus cycle count (b) for the Brown-0.35mm cyclic compression test

While the stress/strain curves relating to the loading stage of each cycle can be observed to be relatively parallel in results from the Green-0.5 mm test, these curves converge at the end of the loading stage in results from the Brown-0.35 mm test. This is an indication that the stiffness of the material increases slightly with each cycle. Overall the shape of the stress/strain curves recorded in both tests is similar but the drop in stress (due to barrelling) recorded during the Brown-0.35 mm test more pronounced where a stiffer material is subjected to a greater force. Again it

is noticeable in Figure G-1 (b) (included in Appendix G. of this document) that the rightward shift in the stress/strain curves relating to individual cycles is slightly greater between cycles 1 and 2 than between cycles 2 and 10, while the shift between cycles 10 and 20 is very small in comparison.

Figure 3-24 (b) shows the total residual strain detected at the beginning of each cycle during the Brown-0.35 mm cyclic compression test. The residual strain values for this test were taken from the strain corresponding to stress values ranging between 0.4 and 7.9 kPa. The natural logarithmic trendline curve is not such a good fit to the data recorded due to the sharper downturn observed between cycles 6 and 8. Again the steepness of the curve between cycles 20 and 40 is questionable. At the end of the test (20 cycles) the residual strain results in the test specimen retaining only 0.058 mm of its compression. Again 24 hours after the end of the test the thickness of the Brown-0.35 mm test specimen returned to that originally recorded.

Sample Name (Shore Hardness-Colour Code-Displacement)	Maximum Stress* (MPa)	316L Material Thickness** (mm)	Original Sample Thickness (mm)	Sample Thickness After Test (mm)	Sample Thickness 24hrs After Test (mm)
D20-Red-5mm	3.98	3.50	9.96	9.19	9.88
D30-Green-0.5mm	1.43	1.26	10.03	9.96	10.03
D30-Green-2.56mm	4.63	4.07	9.96	9.80	9.94
D40-Orange-1.8mm	4.34	3.82	10.65	10.37	10.55
D50-Blue-0.8mm	4.45	3.91	10.60	10.50	10.55
D60-Violet-0.7mm	4.29	3.77	10.26	10.15	10.24
D60-Brown-0.35mm	4.92	4.33	9.70	9.64	9.70

*Compressive Engineering Stress
**Stretching a Part with a 750 mm Radius of Curvature to an approximate strain of 14%

Table 3-10: The displacement controlled cyclic compression tests

Table 3-10 shows the maximum stress recorded, the thickness of a 316L blank (stretched with a 750 mm Radius of Curvature to an approximate strain of 14%) that would impart an equivalent stress in the interpolator, the original specimen thickness, the final specimen thickness and the specimen thickness recorded 24 hours after the test, for all seven displacement controlled cyclic compression tests. Plots showing the stress/strain curves and residual strain for each of these tests have been included in Appendix G. of this document.

3.6 Conclusions

The BBC 2005 yield criterion has been used in the construction of the 2024-T3 material model presented in Section 3.2. Since this yield criterion has previously been shown to give an accurate description of the anisotropy of aluminium alloys (Banabic & Sester, 2012), and since this material model is applied in all of the simulations in the comparative study presented in Chapter 4, no further validation of the material model is required here.

Since the Hill 48 yield criterion is the most commonly used criterion in describing the behaviour of steels, it has been used here (Section 3.3) in the construction of the 316L material model. Only the data obtained from uniaxial tensile tests is used in the calibration of this yield criterion. Figure 3-7 shows that the yield loci of two material models constructed using this yield criterion fail to predict the equibiaxial yield strength, retrieved from the AMFOR database, for the 316L material. Hence it can be stated that this yield criterion does not accurately describe the behaviour of the 316L material in all strain paths that can be encountered during a forming operation. A total of nine calibration methods were tested here, but it has been shown that the Hill 48 yield criterion cannot be used to accurately predict both the yield strengths, and r-values, observed in uniaxial tests of the 316L material at 0, 15, 30, 45, 60, 75, and 90° to the rolling direction of the sheet. Despite this, it has been shown that, when separate models are constructed using data from uniaxial tensile tests at 0° to 45° and 45° to 90° to the rolling direction of the sheet, the Hill 48 yield criterion can be used to accurately describe the 316 stainless steel's behaviour in uniaxial tension at 0° and 90° to the rolling direction of the sheet.

These two material models were validated by simulating the uniaxial tensile tests at 0 and 90°, to the rolling direction of the sheet, with a number of crosshead displacement velocities. Stress/strain curves, constructed using output from these simulations, show that the Modified Krupkowsky rule can be used to accurately describe the strain rate sensitivity of this material (see Figure 3-11, Figure 3-12 and Figure C-1 to Figure C-8). Since the blank in

detailed simulations of the stretch forming process, presented in Chapter 5, is subjected to uniaxial tensile (in the area of interest) the Hill 48 material models can be used here with a good deal of confidence.

PAM-STAMP uses a two term Mooney Rivlin equation to describe the behaviour of hyperelastic materials (such as the Kaylan D series of polyurethanes used here) when subjected to loads. Although the PAM-STAMP software can accept tensile or compressive data to determine the C_1 and C_2 Mooney Rivlin constants, it has been shown, in Appendix E. that when compressive data is used the C_2 constant is always negative. This results in an unstable material model where, at some stage, stress decreases rather than increases with growing strain. Nevertheless, since the interpolator is subjected to compression during the stretch forming process, and the size of the material samples available is restrictive on the number of tests and type of tests carried out, uniaxial compressive tests are used here to determine values for the C_1 and C_2 Mooney Rivlin constants. Therefore, since the maximum engineering stress, in the interpolator, has been shown to be approximately 1 MPa (see Section 3.4), a reduced data sample (incorporating this value) is used to determine the constants, hence, ensuring that the material model is stable over the range where it is to be used in simulations of the stretch forming process. Output from simulations of the compression tests (see Figure 3-19, Figure 3-20, Figure 3-21 and Figure F-1 to Figure F-5), used to validate the polyurethane material models, show that the material models are relatively accurate, over this reduced range.

It can be deduced from the cyclic test results that, where the stiffer materials in the Kaylan D series are used, residual strain in the interpolators will have very little influence on the surface accuracy of parts produced within a batch. Where the softer materials are used, residual strain, in the interpolator, will have an increased negative influence in surface accuracy, as the cycle count in a batch increases. Pin heights will need to be adjusted to compensate for the reduced interpolator thickness. One method that can be used to reduce the influence of residual strain on

the surface accuracy of parts produced, during a batch, is to allow the softer interpolators more time to relax to their original thickness between. This can be achieved, without increasing the overall process time, by using a number of interpolators and rotating through them during cycles of the forming process. Hence, when rotating through four interpolators, interpolator 1 would be used to form parts 1, 5, 9 etc., interpolator 2 would be used to form parts 2, 6, 10 etc., interpolator 3 would be used to form parts 3, 7, 11 etc. and interpolator 4 would be used to form parts 4, 8, 12 etc.. Another method that can be used is to attempt to set pin heights to initially produce a part at the higher end of the surface accuracy tolerance i.e. if the tolerance used is ±0.2 mm and the first part is measured at the target shape +0.2 mm then a greater number of parts can be formed before residual strain in the interpolator results in a part being formed at the target shape -0.2 mm. Interpolators can also be stored under loaded conditions so that the initial greater levels of residual strain observed here can be avoided. The barrelling effect, in interpolators, which results in surface accuracy being dependent on the consistency of the loading/holding time period, can be reduced by using lubricant at the effected interfaces around interpolators.

Chapter 4. Pin Geometry and Arrangement

4.1 Introduction

A critical stage to simplifying the design and reducing the cost of reconfigurable stretch forming equipment is reducing the number of pins used in the tooling. In this chapter AutoForm simulations are used in a comparative study to judge the suitability of a number of pin arrangements for use in stretch forming over a die constructed from pins of a greater cross-sectional area than those used in the RTFF and DATAFORM tooling. Surface defects on quartered blanks from these simulations are examined through both a section line analysis and a surface analysis to identify features of pin arrangements and pin tip geometry that increase the difficulty of obtaining a dimple free surface on parts formed over reconfigurable dies. The dies being considered are of single curvature with a radius of 1200 mm, and have a similar working envelope to the RTFF die (approximately 1200 mm by 1830 mm) but employing less than a quarter the number of pins. No layer of interpolation is used between the die surface and the blank during simulations. The theory being that if the dimpling effects can be minimised, when no interpolator is used, since the interpolator is designed to smooth out the peaks and hollows on a reconfigurable die, less contribution will be required from the interpolator (to produce smooth parts) in the complete system, and hence its thickness can also be minimised. The study is carried out in two phases. In the first phase dies comprised of pins with semi-hemispherical pin tips are compared. In the second phase the die surfaces are representative of the

new pivoted pin tips, proposed by the AMFOR group, where a solid pin tip is allowed to pivot about a ball stud located at the top of each pin. Since the top surface of each pin tip is allowed to slide along the bottom surface of the interpolator their final angular positions are dependent on the overall curvature of the die.

4.2 Simulation Parameters

All the AutoForm simulation models presented in this chapter are set up as stamping operations. The surfaces used to represent the tooling and blanks are constructed in AutoCAD and imported as .IGES (Initial Graphics Exchange Specification) files. Figure 4-1 shows the components of a typical model in their initial positions. The reconfigurable stretch forming die is defined as the punch in these models while the jaws of the stretch former's grips are defined as two separate tools. The lower jaw is defined as the binder while the upper jaw is defined as the die. The die, which remains stationary during the simulation, is constructed with a curved surface at the edge closest to the punch in order to limit stress concentration where the blank bends during the forming operation, while the binder is represented as a flat surface.

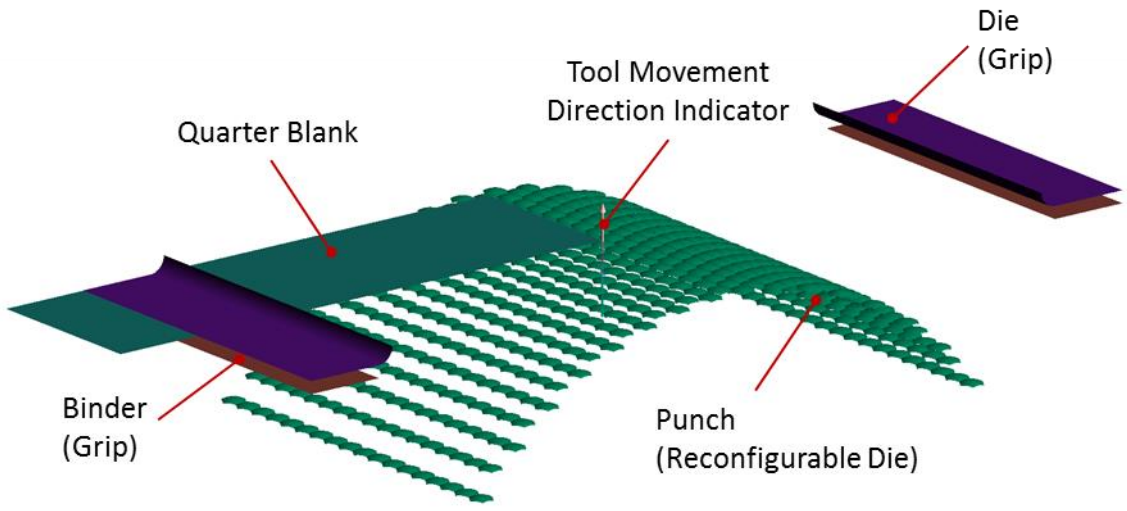

Figure 4-1: The AutoForm simulation setup where the stretch former grips are defined as the die and binder while the reconfigurable die is defined as the punch.

The punches used in these models are constructed from a number of curved surfaces representing the pin tips of a stretch forming reconfigurable die. Note that a quartered blank is shown in the figures relating to the simulations in order to make the surfaces representing the pin tips visible. The heights of the pin tips are adjusted so that they make contact with a curve of 1200 mm radius as shown in Figure 4-2. Since the RTFF tooling was designed primarily to manufacture aircraft fuselage panels a die radius of 1200 mm is utilised to approximate the curvature of a typical aircraft body. Note from Figure 4-2 that while the fixed (a) and pivoted (b) semi-hemispherical pin tips are positioned entirely below the arc representing the die radius, the pivoted pin tips with a flat surface (c) protrude above the arc since the centre point of each pin tip is taken as its control point. At first glance this setup may seem to unfairly bias the comparative results (relating deviation of the formed part from the nominal die radius) in favour of the flat pin tips shown in Figure 4-2 (c), since the nominal radius actually passes through the thickness. Since the deviation data presented here is measured from peak to trough (i.e. deviation above the nominal radius to deviation below the nominal radius) this is not the case. In fact, if anything, the flat pin tips have an initial disadvantage since both deviations above (where the part passes over the edge of the pin tips) and below (between the pin tips) would be expected in formed parts. The equations used to determine the height of each row of pins are given in Sections 4.3 & 4.5.

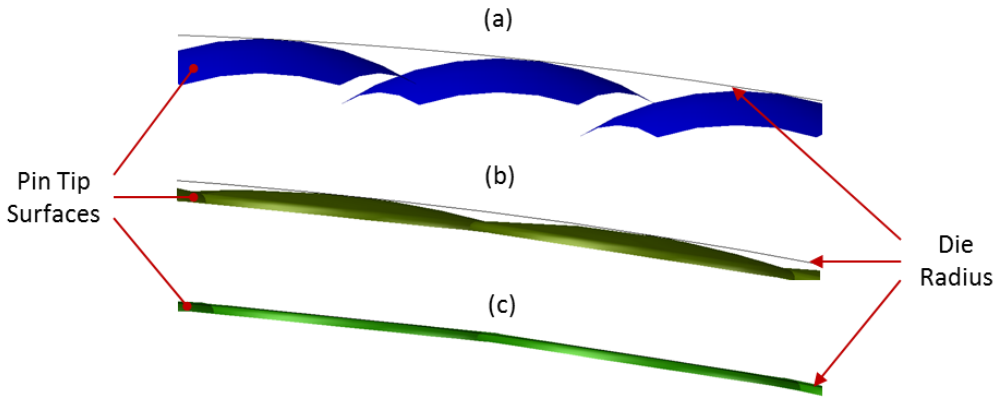

Figure 4-2: Positioning of pivoted pin tips with flat surfaces (c) together with fixed (a) and pivoted (b) semi-hemispherical pin tips in relation to the nominal die radius

To reduce the likelihood of slippage during the forming operation a friction coefficient of 0.95 is used at the interfaces between the gripping surfaces and blank (die/blank & binder/blank). A typical coefficient of 0.15 indicating dry friction conditions (Schuler GmbH, 1998) is applied at the interface between the punch and blank.

Three process steps are used to represent the forming operation, bending, closing and drawing. Elastic plastic shells are used to describe the blank surface during the closing step while bending enhanced membrane elements are used during the bending and drawing steps. Each of these shell elements have five layers through the blank thickness of 2 mm. Standard accuracy is used with an automatic element size setting and automatic refinement controlled through the radius penetration setting of 0.22 mm and a maximum element angle of 30°. Note that shell elements are 2D plane stress elements which are normally used to represent sheet metal, where the through thickness dimension is small relative to the 1 & 2 dimensions in the plane of the sheet. Strain (and hence stress) is computed directly on the plane of the sheet and assumed to be constant through its thickness. Thinning (or thickening) of the sheet will occur during loading, and this can be computed with the assumption that, during plastic deformation, the volume of the sheet will remain constant. A number of integration points are included through the thickness of shell elements to aid in the computation of strain in the thickness direction. Bending enhanced membrane elements have been developed by AutoForm to better describe the deep drawing process, and are used here to detect and highlight wrinkling effects.

During the initial bending process step the die and binder surfaces remain stationary while the punch moves to the position illustrated in Figure 4-3 (a). This is representative of a wrap or drape stage in a stretch forming process. During the closing process step the die and punch surface remain stationary while the binder surfaces move up until closure is detected with the die. This is representative of a clamping stage in a stretch forming process. During the final drawing process step a clamping force of 1000 kN

is applied at the binder and the punch moves up to its final position, illustrated in Figure 4-3 (b), while stretching the blank over the surfaces representing the reconfigurable die. This is representative of the actual stretching stage in a stretch forming process.

Where symmetry allows a quartered blank is used during the simulation to save on time and CPU usage. In dies where only one a single plane is present a half blank is used and in dies where no symmetry plane is present a full sized blank is used but, for consistency, a quartered blank is analysed in all cases. In all simulations the aluminium alloy 2024-T3 is utilised as the blank material due to its high stretchability rating of 95 (see Table 3-1).

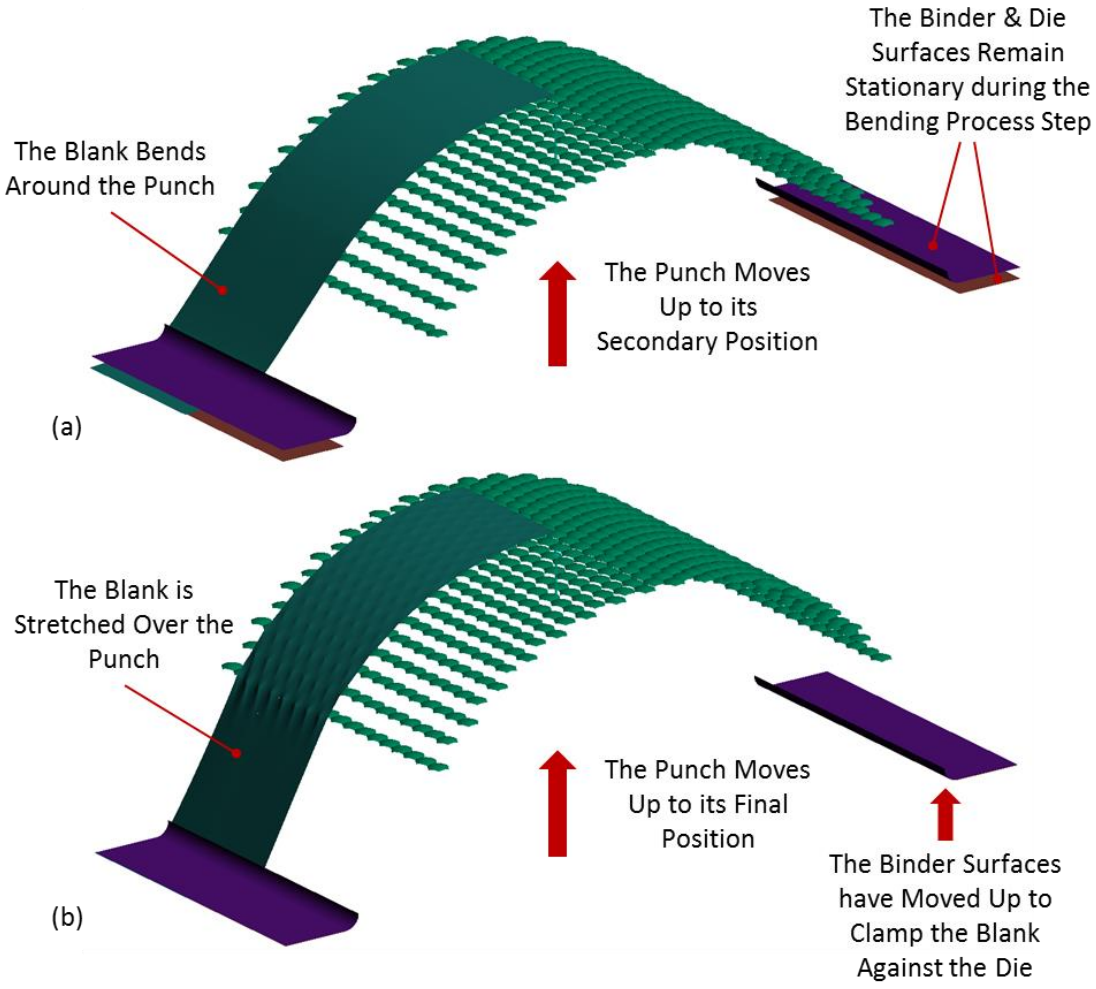

Figure 4-3: The tooling positions at the end of the bending (a) and drawing (b) process steps

While the values from section line analyses are used for comparison purposes in this chapter a surface defect analysis is also carried out for each simulation. A comparison of the results from these two methods of analysis is plotted in Figure J-1 of Appendix J. In each case the surface defect analysis shows greater deviation since data is compared over a greater area.

Since the cost and practical implications of carrying out experiments to the scale of the RTFF tooling are beyond the scope of this project no attempt has been made to validate the material model used together with the simulation parameters laid out in this section. Instead the results from these simulations are used solely for comparison purposes, with an identical material model and boundary conditions being implemented in all phase 1 & 2 simulations.

4.3 Phase 1 Pin Shape and Die Layouts

Pins of four different cross-sectional profiles, square, hexagonal, equilateral triangular and right-angled triangular, are represented in the construction of the die surfaces. Since a threaded screw is fitted through the length of each pin to make its height variable, and for consistency, each cross-section is constructed about an identical inscribed circle. To achieve the reduction in the number of pins required for this project the circle is of 70 mm in diameter (Figure 4-4).

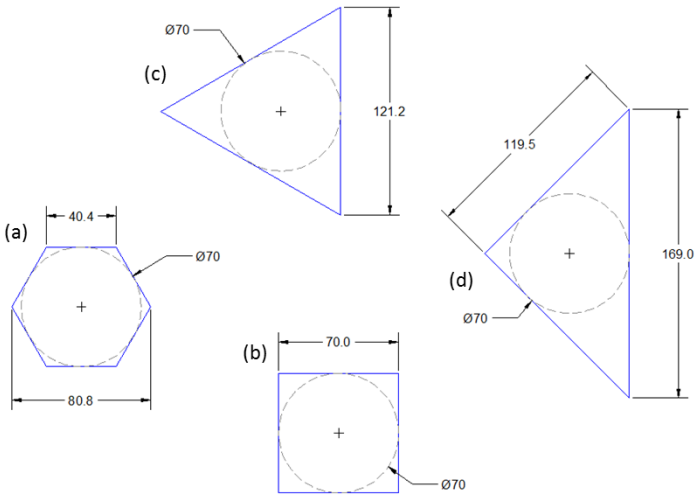

Figure 4-4: (a) Hexagonal, (b) square, (c) equilateral triangular and (d) right angled triangular pin cross sections

All the surfaces used to represent dies in phase 1 are based on the semi-hemispherical pin tips where the pin is of a constant cross section along its length. Referring to Figure 4-5, the expressions used to calculate the heights of pins, and so the vertical positioning of pin tip surfaces, when the curved surface of a semi-hemispherical pin tip is in contact with the blank (h_1), and when an edge of the pin tip is in contact with the blank (h_2) are;

$$h_1 = r_{PT} + \sqrt{(r_D - r_{PT})^2 - x_P{}^2} \tag{46}$$

$$\& \; h_2 = r_{PT} + \sqrt{r_D{}^2 - (x_P + x_E)^2} - \sqrt{r_{PT}{}^2 - x_E{}^2} \tag{47}$$

where, r_{PT} is the radius of the pin tip, r_D is the radius of the die, x_P is the horizontal distance between the centreline of the die and centre point of the semi-hemispherical surface, and x_E is the horizontal distance between the edge in contact with the blank and centre point of the semi-hemispherical surface.

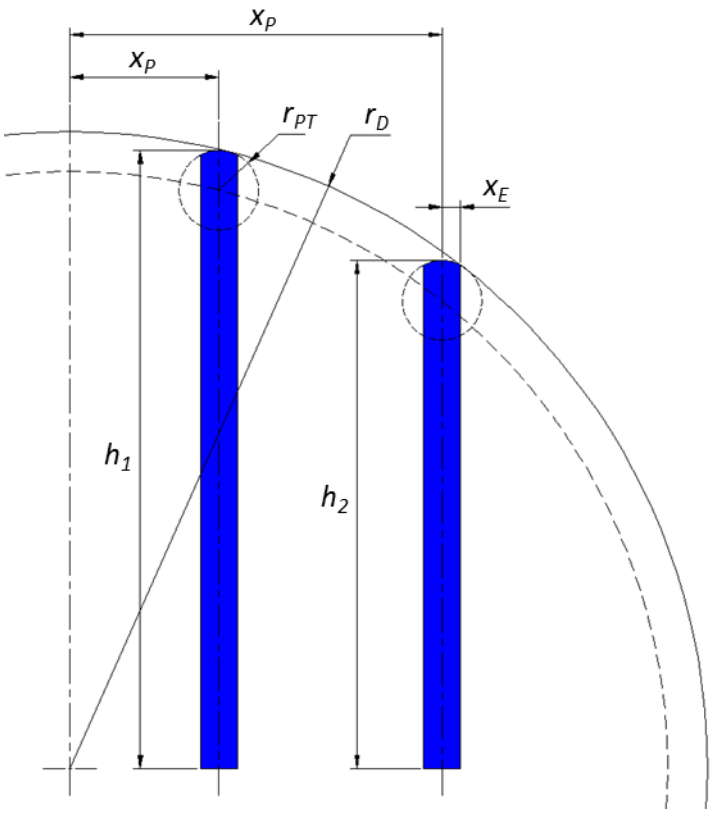

Figure 4-5: The variables used in pin height calculations for pins with semi-hemispherical pin tips

Pins of a hexagonal cross section are arranged in a hexagonal close packed matrix. This matrix of pins lends itself naturally to two die layouts. The first is where angular edges of the pins are orientated in the stretching direction (Figure 4-6 HCP1) and the second is where flat surfaces of the pins are orientated in the stretching direction (Figure 4-6 HCP2).

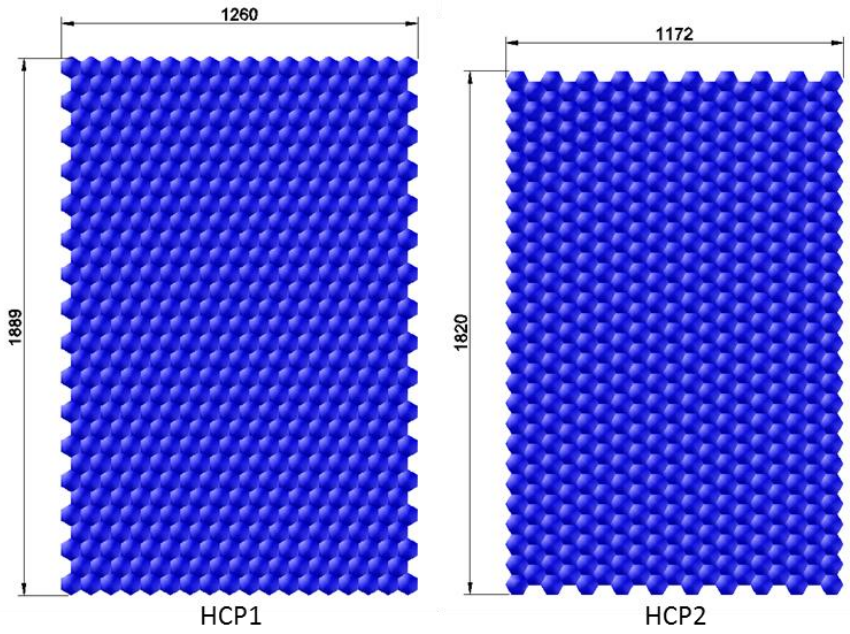

Figure 4-6: The two die layouts using pins of a hexagonal cross section arranged in a hexagonal close packed matrix

Pins of a square cross section are arranged in a rectangular close packed matrix. This matrix of pins is normally used in its most natural die layout (Figure 4-7 RCP1), where the pins are in line in both the stretching and transverse directions. In this project two additional rectangular close packed die layouts are tested. Figure 4-7 RCP2 shows a die layout where alternate rows of pins in the stretching direction are offset by half the pin width in the transverse direction. This creates a die layout where a series of gaps between the apexes of hemispherical pin tips is no longer present in the stretching direction. Figure 4-7 RCP3 shows a die layout in which RCP1 is rotated through 45° and a series of gaps is no longer present in either the transverse or stretching direction.

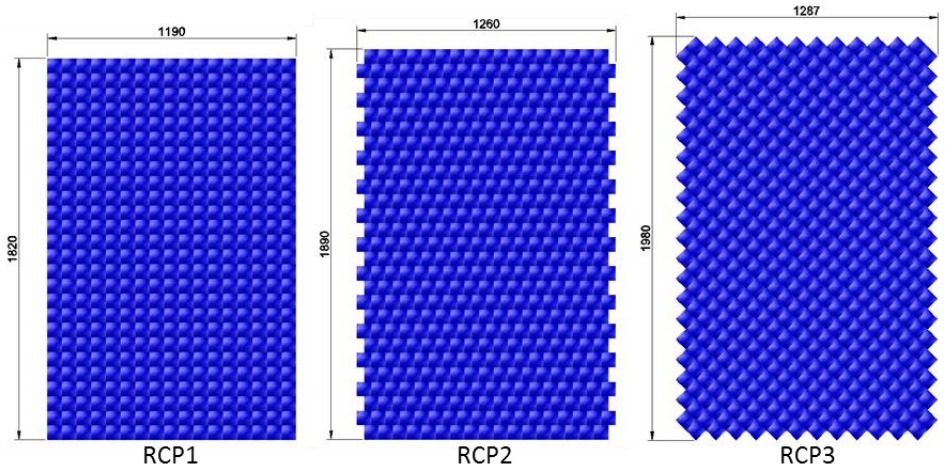

Figure 4-7: The three die layouts using pins of a square cross section arranged in a rectangular close packed matrix

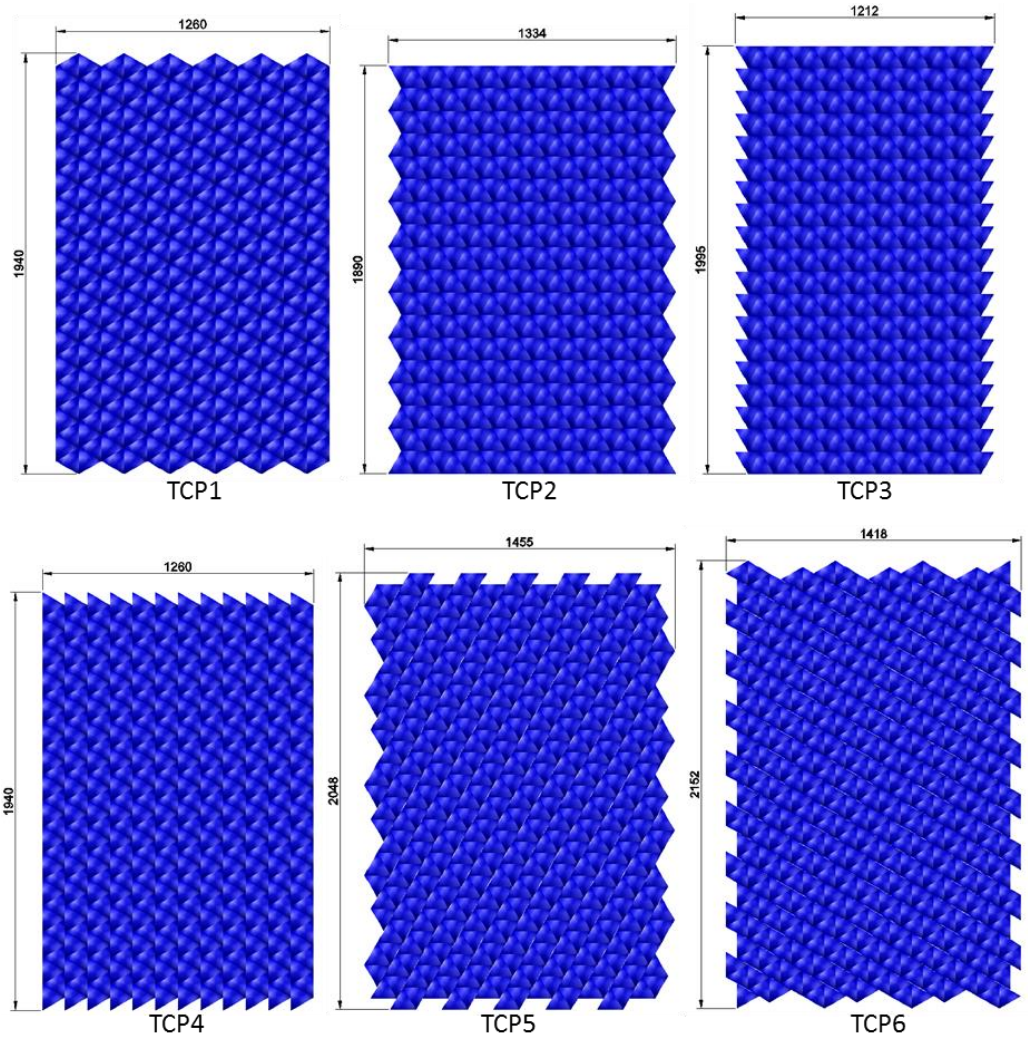

Figure 4-8: The six die layouts using pins of an equilateral triangular cross section arranged in triangular close packed matrices

Pins of an equilateral triangular cross section can be arranged in two different triangular close packed matrices. Figure 4-8 TCP1 shows a die layout where six pins are arranged to form a hexagon and the matrix can be described as both triangular and hexagonal. This layout is rotated through 90° to create the die layout named TCP2. A different triangular close packed matrix in used in the die layout shown in Figure 4-8 TCP3 where any two triangles in a traverse row create a rhombus. This layout is rotated through 90, 60, and 150° to create the die layouts named TCP4, TCP5, and TCP6 respectively.

Where the die layouts using pins of an equilateral triangular cross section all contain jagged edges, pins of a right angled triangular cross section can be arranged to form squares and matrices which can be described as both triangular and rectangular close packed. Figure 4-9 RTCP1 shows a die layout where four pins of a right angled triangular cross section have arranged to form a square and these squares are arranged in their natural rectangular matrix.

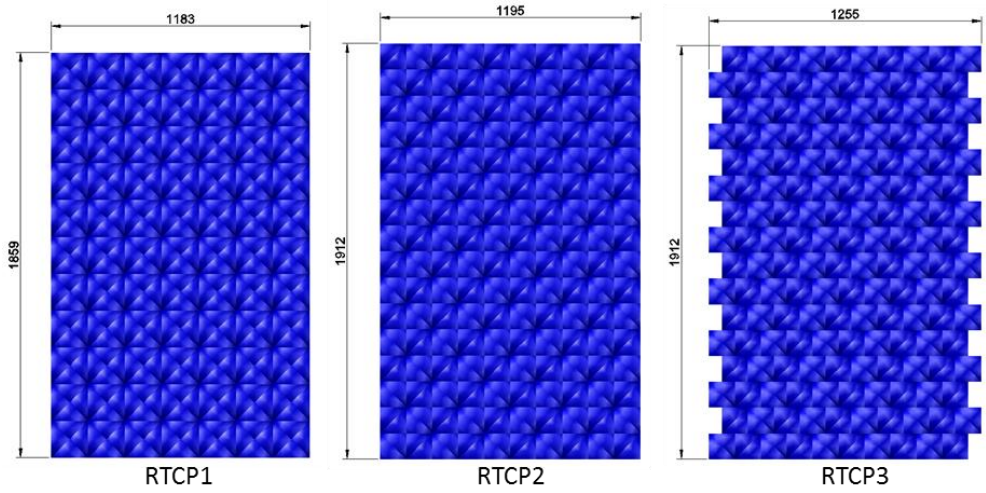

Figure 4-9: The three die layouts using pins of a right angled triangular cross section arranged in triangular close packed matrices

In the die layout named RTCP2 a similar matrix is used where the square is constructed from two pins of a right angled triangular cross section. Finally, in the die layout named RTCP3, alternate rows of these squares are offset by half the pin width in the transverse direction to create a layout where a series of gaps is no longer present in the stretching direction.

4.4 Phase 1 Results

Section lines have been used to obtain profiles of the deformed blank over and between rows of pins nearest to the centreline in both the stretching and transverse directions. These profiles are imported into Microsoft Excel and Pythagoras theorem is used to compare the height of the blank at coordinates along curves to those calculated for a die radius of 1200 mm. The deviation of profile curves from the required radius is plotted over distances of 850 mm along the stretching direction of the die and 500 mm across its width. These results are referred to as the section line analysis and presented here, for a small sample of simulations, in Figure 4-10, Figure 4-11 and Figure 4-12.

CloudCompare has been used to generate all the surface deviation contour plots presented in this chapter. CloudCompare is a popular open source point cloud processing software, which can be used to compute the distances between points on pairs of 3D point clouds or meshes. The software was developed, by the research and development department of EDF (Électricité de France), and provides a workable compromise between data storage and computational speed. The software can load as many as 4 billion points, when used with a 64-bit operating system, although even with an exceptional graphics card, working with this number of pints can lead to problems related to display and user interactivity. The software's user manual (Girardeau-Montaut, 2015) states that, normally, up to 150 million points can be used without any major detrimental influence on the system's graphical and analytical capabilities. A scanned image normally consists of a point cloud with an unspecified number of randomly dispersed points. A surface (deformed blank) imported to CloudCompare from a FEA program is normally in the form of a mesh. CloudCompare can sample, resample or subsample points on either of these object types to increase (or decrease) their density. The software offers a number of options for sampling points, including, density (where the user specifies the number of points per square unit), the approximate number of points required and the distance between points. In addition to these options an octree can be used to increase or

decrease the depth of the point cloud. An octree uses cubed bounding boxes of a set dimension or around each point. The number of points can be reduced by keeping only the point nearest the centre of the cube, or increased by placing addition (child) points at the 8 corners of each cube. The octree level controls the size of each cube. In this project objects have been sampled using the total number of points. It should be noted that when a mesh of low density (i.e. a mesh with a relatively small number of nodes and relatively large elements) is imported, the elements are flat objects and points will be created on these flat surfaces with no relationship to the overall curvature of the mesh. This can lead to errors in computing the distances to a reference object.

CloudCompare uses an Iterative Closest Point (ICP) algorithm in both rough alignment and fine registration of point cloud pairs. The software displays the 4x4 translation matrix after both alignment and registration, so that the user can reuse it (or its inverse) at a later stage. It also displays the RMS (Root Mean Square) error, the number of points the RMS is computed on, scaling used and the theoretical overlap (given as a percentage) of the two clouds. Clouds' rectangular cuboid bounding boxes can be used for rough alignment, where the centres of the bounding boxes are aligned first before their corners. The user can also use the Apply Transformation tool to manually align point clouds through a combination of translation and/or rotation. The Apply Transformation tool offers users 3 options, transformation via the 4x4 matrix, rotation about a user defined axis together with translation in the X, Y & Z directions, or transformation using a combination of Euler angles and translation in the X, Y & Z directions. After cloud pairs have been roughly aligned, the software offers two methods for fine registration. The first is alignment through selecting at least 4 corresponding points (or registration spheres) on both the reference cloud and the cloud to be aligned. The second is alignment via the Fine Registration tool using the full ICP algorithm. The Fine Registration tool can be used with a number of options. The user can define the number of iterations or the target RMS error. The user can allow rotation about all

axes or a single axis. Translation in 1, 2 or 3 directions can also be constrained. The user can also determine the number of random sampled points to be used in the registration process. Remove furthest point can also be enabled to help in the registration of point clouds where there is significant noise present. A mathematical description (and accuracy evaluation) of the algorithms used in CloudCompare's registration processes can be found in an article published in the RevCAD journal (Oniga, et al., 2016). In this article the authors concluded that CloudCompare was a cheap and fast solution which gave results consistent with those calculated using individual point's coordinates.

When the software first computes cloud to cloud distances, it uses a nearest neighbour routine with no local modelling. This method is not very accurate since the point measured to, on the reference cloud, may not be in a position normal to the original point on the comparison cloud. CloudCompare uses the data from this initial computation to set default values, such as octree level, the number of computation points on the comparison cloud (for constructing planes or taking average distances), and the radius of a comparison sphere. The user manual recommends that these default values are used in further computations using local modelling. There are 3 options for computing cloud to cloud distances using local modelling which are the all based on least squared plane fitted to the reference cloud. The first option is the Least Square Plane, which measures the distance of each point normal to the plane. The second is the 2D1/2 Triangulation, which uses the fitted plane and the original points in a form of Delaunay triangulation. The third is the Height Function, which again uses the fitted plane together with a 6 parameter quadratic function to determine the normal direction. The software's user manual states that the Height Function is the most precise of these 3 methods, especially when comparing relatively noise free clouds represent curved surfaces. Initial trials using CloudCompare, to determine the distance between the clouds representing deformed blanks from the AutoForm simulations and their reference cloud, showed that the maximum distance between points on the clouds was a

magnitude of approximately 0.1 mm greater using the Height Function against the other 2 methods (which show no discernible difference. It was also found that increasing the default octree level by 30% resulted in there being to few points to create a plane and hence the distance computation cloud not take place. Increasing the default octree level by approximately 15% resulted in there being at least 2 points in each comparison sphere, which yielded slightly higher distances, as the least squared fitting plane was less accurate. Decreasing the radius of the comparison sphere had a similar effect. Using the comparison sphere (rather than a fixed number of points) is more accurate when random points are sampled on the initial clouds/meshes. High noise resulting in a thicker cloud can be one of the greatest sources of error when comparing point clouds. This is not a factor when comparing sampled meshes from the simulations to their corresponding reference clouds. Noise may become a factor that has a negative effect on accuracy when carrying out the comparisons during validation (Section 5.8), since clouds from scans are known to contain relatively high levels of noise.

The deformed blanks from the AutoForm simulations are compared against a reference surface which is constructed in AutoCAD from an extruded spline with control points at the end points of a polar array of radial lines. The reference surface is imported into CloudCompare as a FBX (Filmbox) mesh while the deformed blank is imported as a STL mesh. Both meshes are then sampled to create two point clouds with one million points in each. Aligning the two point clouds is a relatively subjective exercise. The high spots on the deformed blank, where it is stretched over the control points on pins, are the areas on the part that should correspond with the reference surface. CloudCompare's fine registration tool is not suitable for the task since it aligns the surfaces to a best fit of points over the majority of the surfaces. The point pair picking tool aligns some pairs of clouds well but, is not consistently successful when the points are randomly dispersed throughout the cloud. When the selected points on one cloud do not have a corresponding point on the other it tends to twist the blank to find the

closest fit. Since the reference surface was created with the same orientation and approximate position as the imported blank, it was found that a better method was to manually translate the blank vertically so that its high spots make contact with the reference surface. Local modelling is used with the height function and default sphere radius to obtain more accurate distances between the surfaces being compared. The accuracy of the results obtained from the section line analysis technique is dependent on the accuracy of the simulation and the final mesh size of the blank. Since the surface defect analysis uses the blank from the simulation, its accuracy cannot be better than that of the section line analysis, and since user judgement is utilised to align the two clouds, accuracy will be detrimentally affected. Hence the results from the section line analysis are taken as being the more accurate and are used in plots comparing the performance of die layouts. The results from CloudCompare are used here to give an overall pictorial representation of the dimpling effects on the deformed blank after it is stretched over the different die layouts being considered.

Examining the simulation results of the hexagonal and rectangular close packed die layouts with a pin tip radius of 50 mm, illustrated in Figure 4-6 and Figure 4-7 respectively, a number of die features detrimental to the production of dimple free parts can immediately be identified. Firstly from the surface defect analysis of the HCP1, HCP2 & RCP1 die layouts, illustrated in Figure 4-10 (b), Figure 4-11 (b) and Figure 4-12 (b) respectively, it can be seen that when a gap between rows of pins in the stretching direction is present (in the HCP1 and RCP1 layouts), material is drawn down into the gap and a groove is evident on the deformed blank. While the values of deviation from the required die radius in the section lines between pins in the stretching direction [illustrated with the dotted blue line in Figure 4-10 (a), and Figure 4-11 (a)] show little change due to support from the closely packed offset pins in the latter (note the shape of the solid red curves denoting deviation on top of pins across the blank), Figure 4-12 (a) shows that in the RCP1 layout a much flatter curve is

produced with increased deviation (since the pins are aligned in the stretching direction).

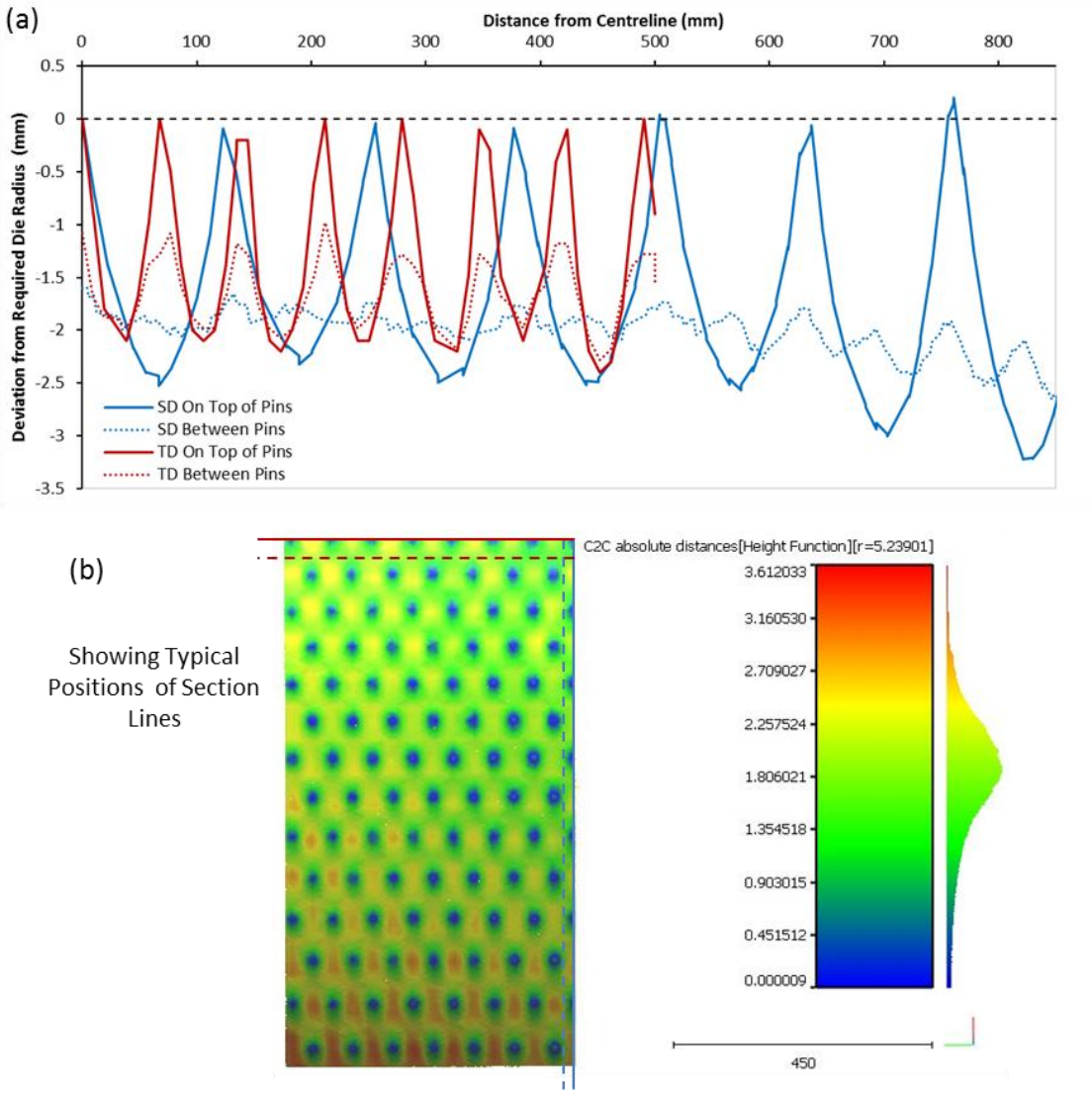

Figure 4-10: HCP1r50 section line (a) & surface defect (b) analyses results

A second die feature which is detrimental to the production of dimple free parts can be identified from the simulation results of the hexagonal closely packed die layouts. Note the depth of the solid blue curves indicating deviation from the required die radius on section lines along the stretching direction [Figure 4-10 (a), and Figure 4-11 (a)]. The HCP1 die layout shows much greater deviation here due to the increased distance between pins in the stretching direction.

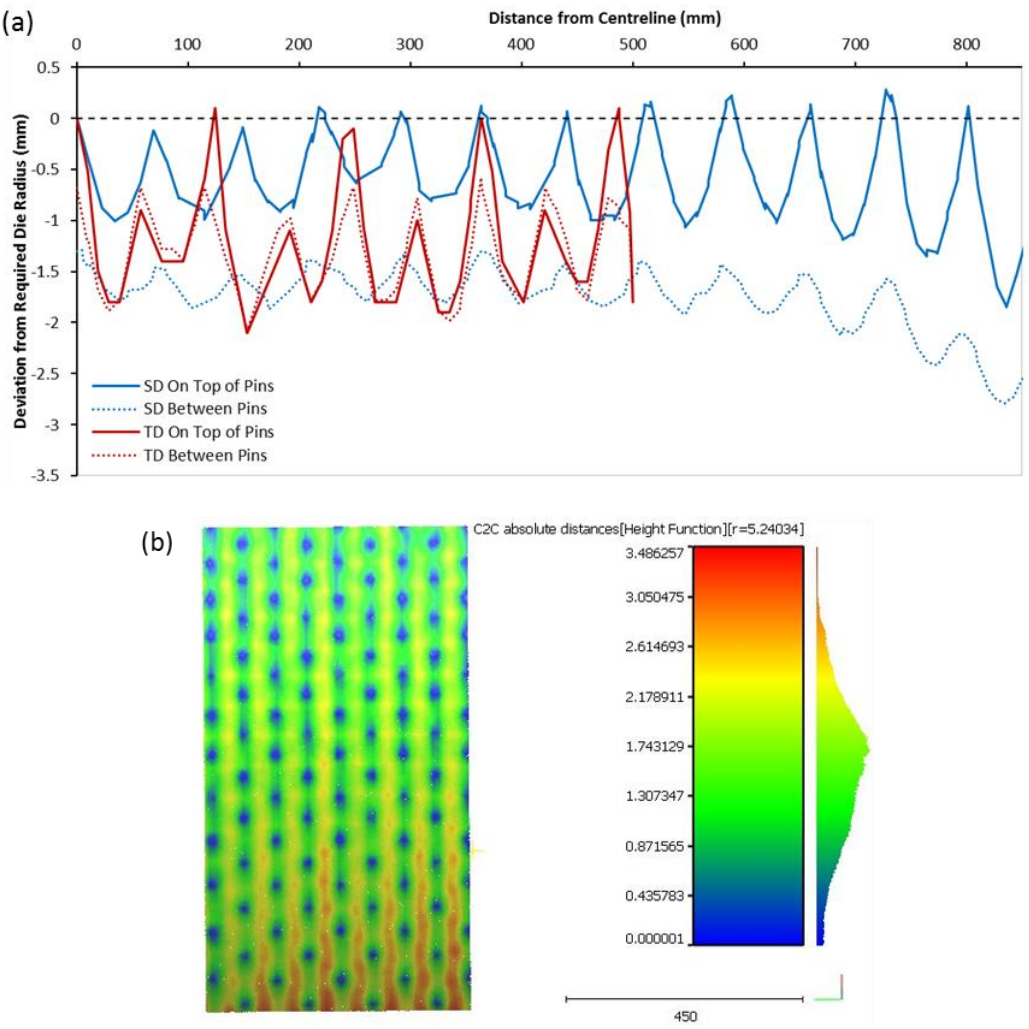

Figure 4-11: HCP2r50 section line (a) & surface defect (b) analyses results

While the offset used in the RCP2 die layout reduced deviation due to the groove effect (see Figure H-3), deviation due to increased distance between pins in the stretching direction was greater. The overall profile accuracy of the deformed blank over that of the RCP1 layout, with a pin tip radius of 50 mm, is minimal. Figure 4-13 shows the surface defect analysis results from the RCP3 die layout which produces the best profile accuracy of the three rectangular close packed arrangements.

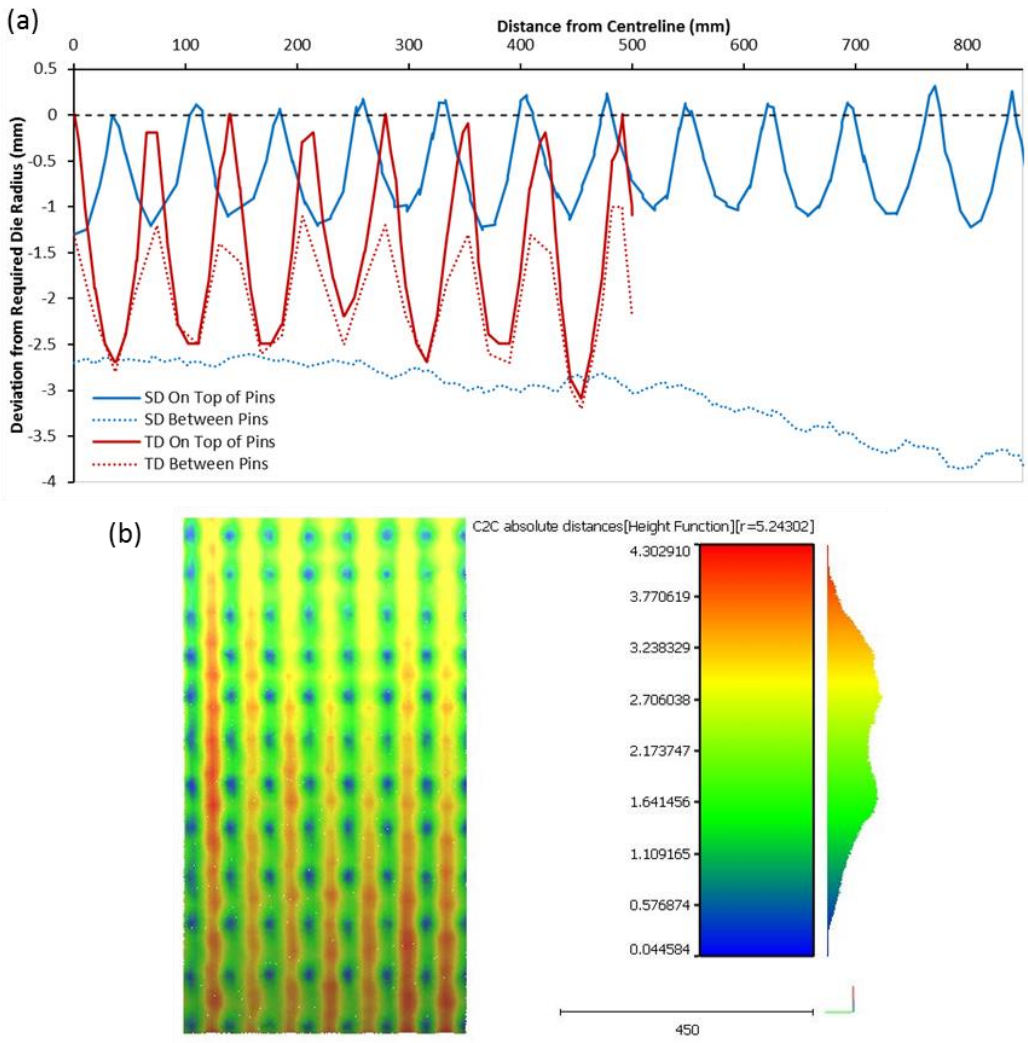

Figure 4-12: RCP1r50 section line (a) & surface defect (b) analyses results

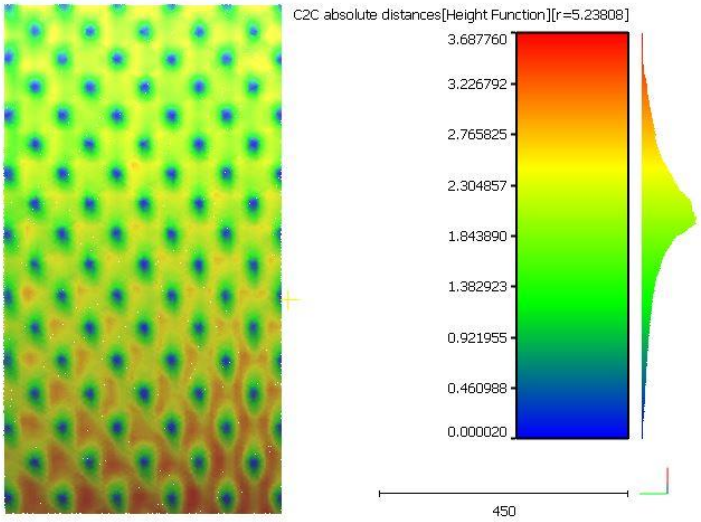

Figure 4-13: RCP3r50 surface defect analysis results

While it has previously been reported that increasing the radius of pin tips result in a reduction in dimpling (Wang, et al., 2010) (see Section 2.4.1), this is not always the case when using a matrix of pins with pin tips all orientated in the same direction. When forming a relatively deep part such as that used is these simulations the number of semi-hemispherical pin tips making edge contact with the blank, as shown in Figure 4-5, will increase as the pin tip radius is increased. Edge contact and especially corner edge contact is a further detrimental die feature since it results in stress concentration points and increases dimpling. Figure 4-14 shows a comparison of results from simulations of the hexagonal and rectangular close packed die layouts where pin tips have radii of 50 & 75 mm.

Whereas an increased radius on the pin tip gives more support to the blank, only the HCP2 and RCP1 layouts, with pin faces orientated to and close pin packing in, the stretching direction, result in reduced dimpling with pin tips of 75 mm in radius. The RCP3 layout, with pin corners orientated to and relatively close pin packing in, the stretching direction, shows slightly more dimpling. Both the HCP1 and RCP2 layouts, with the greatest distance between pins in the stretching direction, show significantly increased dimpling with pin tips of 75 mm in radius.

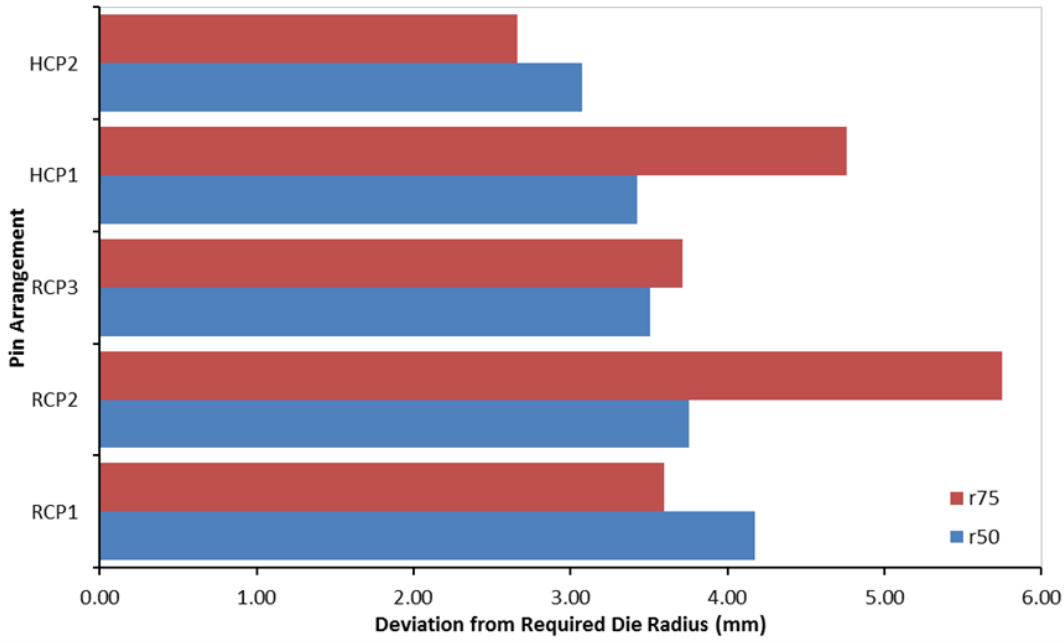

Figure 4-14: Semi-hemispherical pin tip 50 &75 mm radii comparison

Since triangulation is commonly used within CAD and FEA software to represent curved surfaces a concerted effort has been made here to identify a triangular close packed pin matrix which would be suitable for use in a reconfigurable die. However the triangular close packed die layouts illustrated in Figure 4-7 and Figure 4-8, and simulated in this study did not show any advantage over the commonly used rectangular close packed die layout. With a minimum pin tip radius for coverage of the equilateral and right angled triangular pins of 75 mm and 91.5 mm respectively, a comparatively high number of edge contacts are present in all the triangular close packed die layouts. Two additional die features detrimental to the production of dimple free parts can also be identified using the results from simulations of the triangular close packed die layouts. The first is that of reduced pin density has been widely reported (Wang, et al., 2010) and is the first ideal die characteristic reported in the review of reconfigurable dies (Munro & Walczyk, 2007) (see Section 2.6) i.e. when using semi-hemispherical pin tips a high density of pins leads to a high density of contact points and a reduction in dimpling. The final detrimental die feature which is evident in these results is unequal spacing between pins.

Figure 4-15 shows the results from surface defects analysis of the TCP1 die layout. A hexagonal deformation effect is evident and without a pin located at the centre of the hexagon the groove effect between rows of pins in the stretching direction is prominent. When this layout is rotated through 90° as in TCP2 the surface defect map shows offset pairs of closely packed pins in the stretching direction with gaps and increased deviation appearing between pin pairs in both the stretching and transverse directions (see Figure H-9).

The TCP3 die layout simulation results return the lowest deviation values of all the triangular close packed layouts. Its surface defect map, Figure 4-16, shows that the pin control points are more evenly dispersed, in a pattern similar to that present in the RCP3 layout. When the TCP3 layout is rotated through 90° to become the TCP4 layout alignment of the pins again causes a prominent groove effect in the stretching direction of the

deformed blank (see Figure H-11). The surface defect map of the TCP5 layout (TCP3 rotated through 60°) results again shows the presence of closely packed pin pairs in the stretching direction with increased deviation in the gaps between them (see Figure H-12). The alignment of pins in the TCP6 die layout (TCP3 rotated through 150°) results in a groove effect appearing on the deformed blank at approximately 20° to the stretching direction (see Figure H-13).

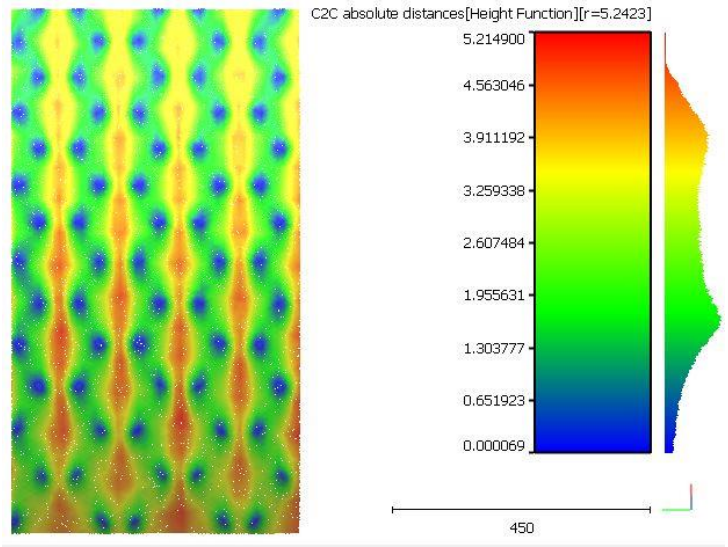

Figure 4-15: TCP1 surface defect analysis results

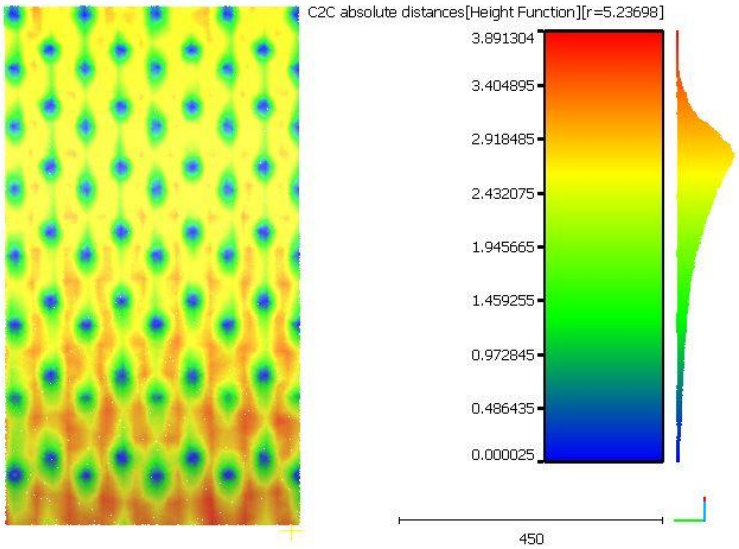

Figure 4-16: TCP3 surface defect analysis results

The right angled triangular cross section pins have the greatest cross sectional area of all the pins considered here, resulting in die layouts with

the lowest pin density and highest degree of unequal spacing between neighbouring pin control points. The surface defect maps of simulation results from the RTCP1, RTCP2 and RTCP3 die layouts all show the presence of unsupported areas on the deformed blank due to the unequal dispersion of pin control points.

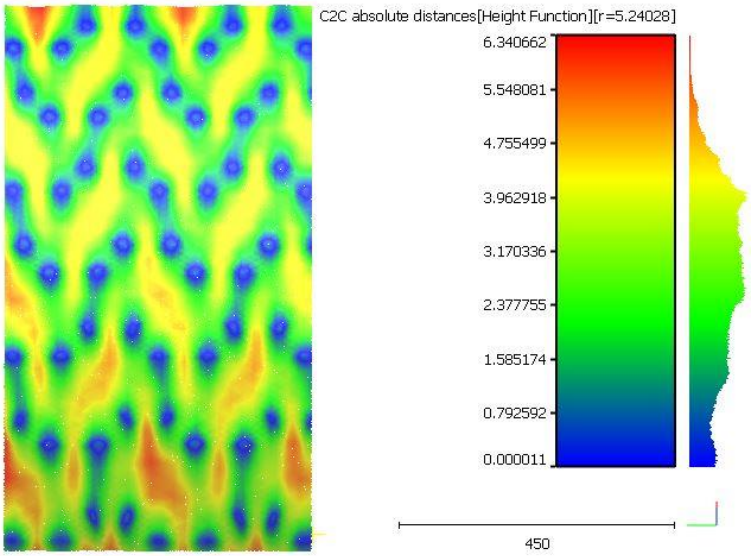

Figure 4-17: RTCP3 surface defect analysis results

Results show that deviation of the deformed blank surface from the required profile is greatest in the RTCP1 die layout, where four pins are arranged to form a base square. The surface defect map of the deformed blank from the simulation using the RTCP2 die layout, where two pins are arranged to form the base square, shows the presence of the groove effect in unsupported lines along the stretching direction, but lower overall deviation. Figure 4-17 shows the surface defect map from the simulation using the RTCP3 die layout, which yielded the best results of the three right angled triangular close packed layouts. With a deviation value of 5.41 mm, taken from the section line analysis, this is well above the lowest overall deviation value of 3.07 mm present in results from the simulation of the HCP2 layout (with a pin tip radius of 50 mm).

The section line analysis plots and surface defect maps not shown in this section are included as Appendix H. of this document. Figure 4-18 shows the deviation from the section line analysis results for all the die layouts

simulated in phase 1of this study, together with a measure representing the influence of four of the five detrimental die features identified here. The influence of edge contact between the pin tip and blank is not represented in this graph. Profile accuracy is plotted, on the secondary axis, as the maximum distance between the peaks and troughs of all four deviation curves used in each section line analysis. A measure of pin density, in each die layout, is given as the cross sectional area of its pin profile normalised using the area of the 70 mm diameter inscribed circle, and plotted on the graph's primary axis. A measure of equi-spacing between pins is plotted on the primary axis and given as the distance to the furthest neighbour from a base pin normalised using the distance to its closest neighbour (always equal to the distance diameter of the inscribed circle), where neighbours are taken as all the surrounding pins in contact with the base pin. The maximum gap between neighbouring rows of pins aligned in the stretching direction is normalised using the diameter of the inscribed circle and again plotted on the primary axis. The maximum gap between individual pins, in these rows, is again normalised using the diameter of the inscribed circle and also plotted on the primary axis.

Although the profile accuracy results have also been influenced by edge contact, it can be seen that there is a definite correlation between profile accuracy and the four detrimental die features identified here. Note that the maximum gap between pins in the stretching direction parameter is misleading for the RTCP3, TCP5 and TCP6 layouts since the gap is measured between the apexes of pin tips that are perfectly in line and the gap to pins that are offset by a small distance is ignored. In the RTCP3 layout the gap is taken as 239 mm yet a pin exists with an offset of only 17.7 mm at half this distance. In the TCP6 layout the gap is taken as 242.5 mm yet a pin exists with an offset of only 17.5 mm at a distance of 151.5 mm from the base pin. In the TCP5 layout the gap is taken as 350 mm yet four pins are located within this gap with an offset of only 30 mm.

It can be concluded, from phase 1 of this study, that the most suitable pin arrangements for use in a more course reconfigurable die matrix are the

hexagonal close packed matrices of HCP1 & HCP2 together with the diagonally orientated rectangular close packed matrix of RCP3. In phase 2 of this study simulations using dies, comprised of surfaces representing pivoted pin tips of varying geometry, and arranged in these three matrices, are used to determine whether pivoted pin tips offer an advantage over solid semi-hemispherical pin tips and to discover a suitable combination of pin tip geometry and pin arrangement for use in this coarser reconfigurable die matrix.

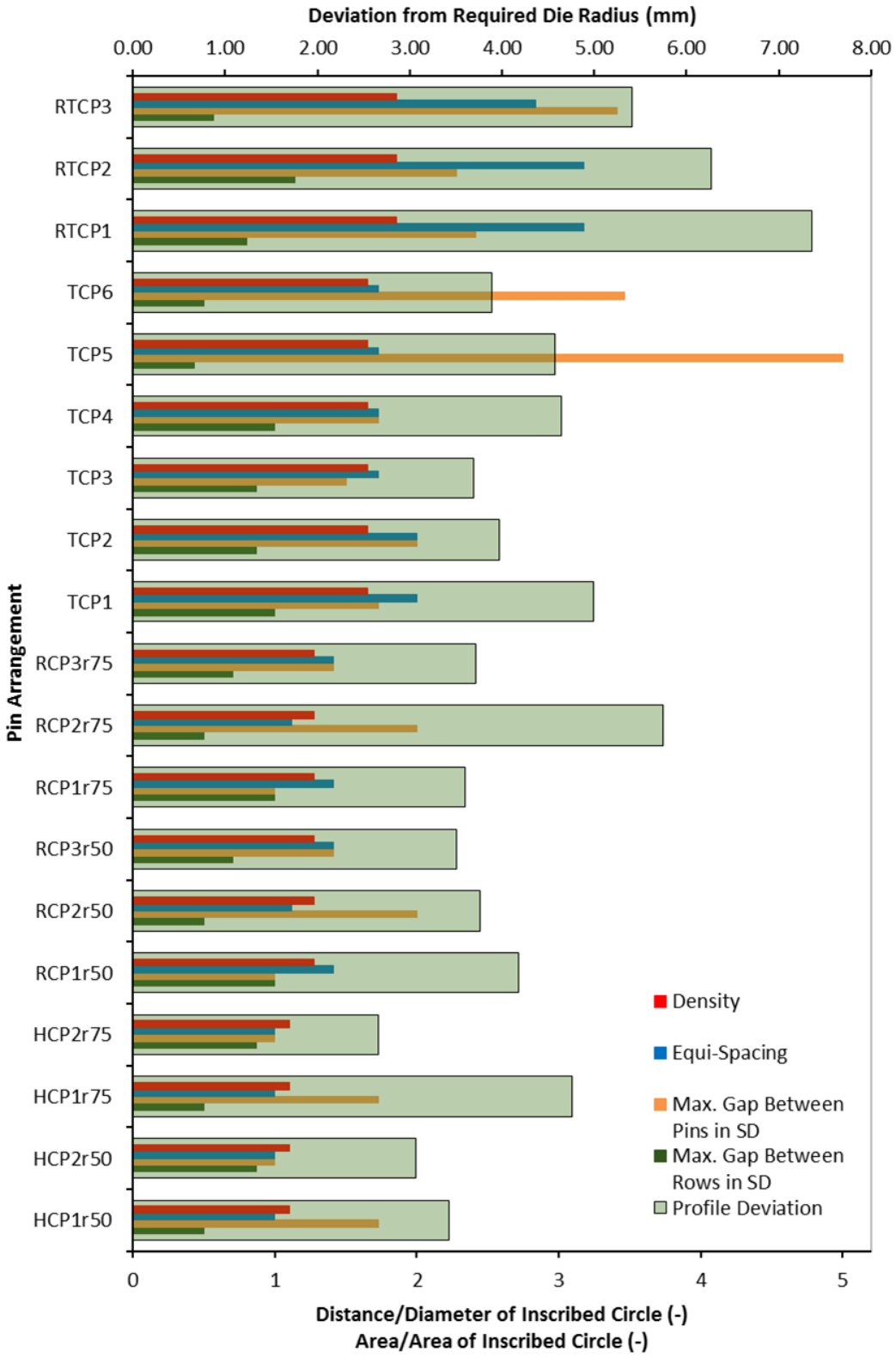

Figure 4-18: Complete phase 1 section line analysis results showing the influence of matrix density, equi-spacing between pins, gap size between rows of pins & gap size between pins in the stretching direction

4.5 Phase 2 Pivoted Pin Tips

A total of nine different pivoted pin tip geometries are considered in each arrangement. This includes four shaped pin tips, one with a smooth flat mating face [Figure 4-19 (b) and Figure 4-20 (b)], and another with a smooth semi-hemispherical mating surface of 800 mm in radius [Figure 4-19 (c) and Figure 4-20 (c)]. Since pin density was shown to have an influence of the deformed blank surface smoothness, in phase 1 of this study, two additional shaped pin tips are tested with multi-pointed mating surfaces mimicking the surfaces of pin tips in a much finer pin matrix. The apexes of these multi-point surfaces are on a flat plane [Figure 4-19 (d) and Figure 4-20 (d)], and on a domed plane of 800 mm in radius [Figure 4-19 (e) & Figure 4-20 (e)]. A simpler round pivoted pin tip is also tested [Figure 4-19 (f)] with a flat mating surface [Figure 4-19 (I)] and domed mating surfaces with radii of 800 mm 600 mm 400 mm & 200 mm (Figure 4-19 II, III, IV & V respectively).

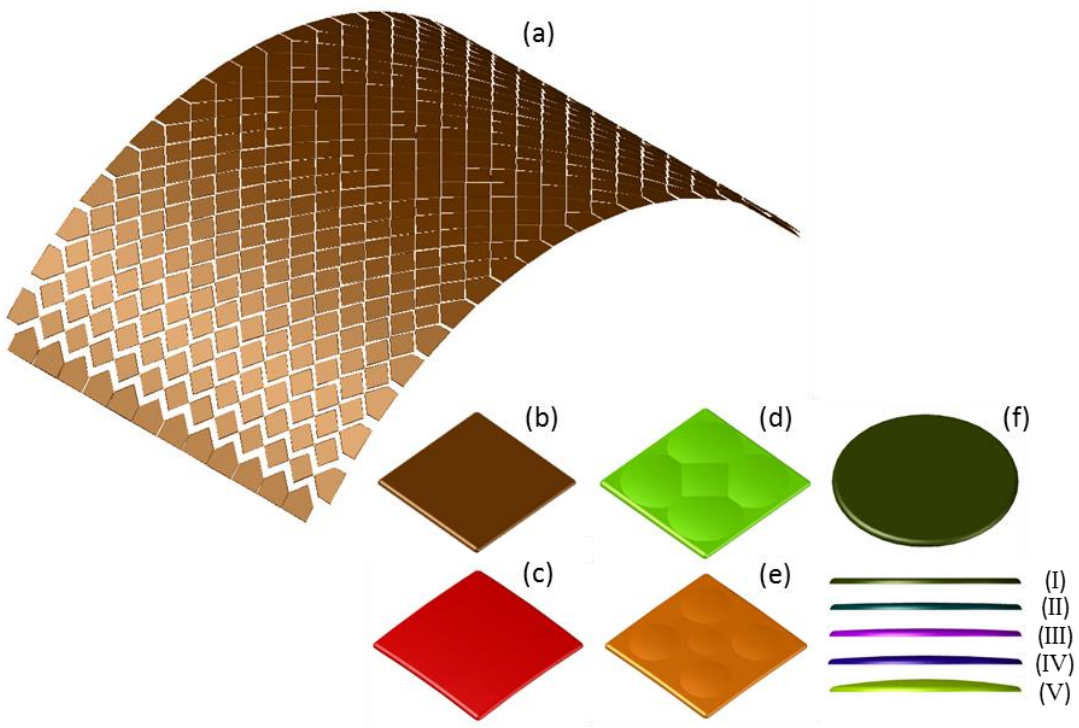

Figure 4-19: The RCP3 die with shaped flat pivoted pin tips (a), the four pivoted pin tip geometries shaped to suit a square pin (b) (c) (d) & (e), the round pivoted pin tips (f) with a flat mating face (I), and domed mating faces with radii of 800 mm (II) 600 mm (III) 400 mm (IV) & 200 mm (V)

Each pivoted pin tip 2 mm radius edge fillets. It should be noted that the shaped pivoted pin tips on the outer edges of the RCP3 die have been modified so that the outer edges of the die as a whole are straight rather than jagged as would be the case if these outer edges consisted of rows of corners from square pin tips.

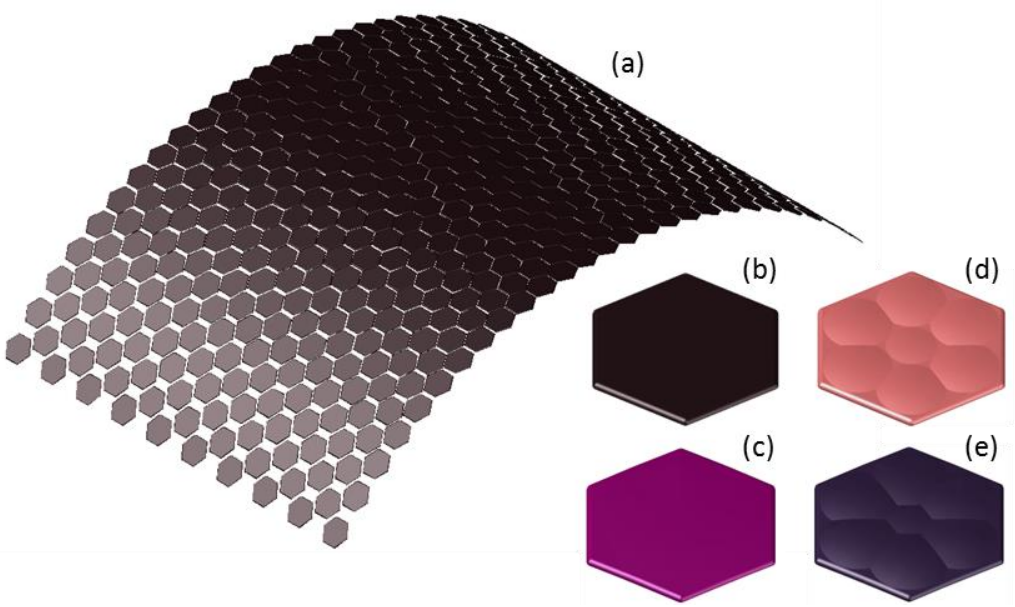

Figure 4-20: The HCP2 die with shaped flat pivoted pin tips (a) and the four pivoted pin tip geometries shaped to the hexagonal pin (b) (c) (d) & (e)

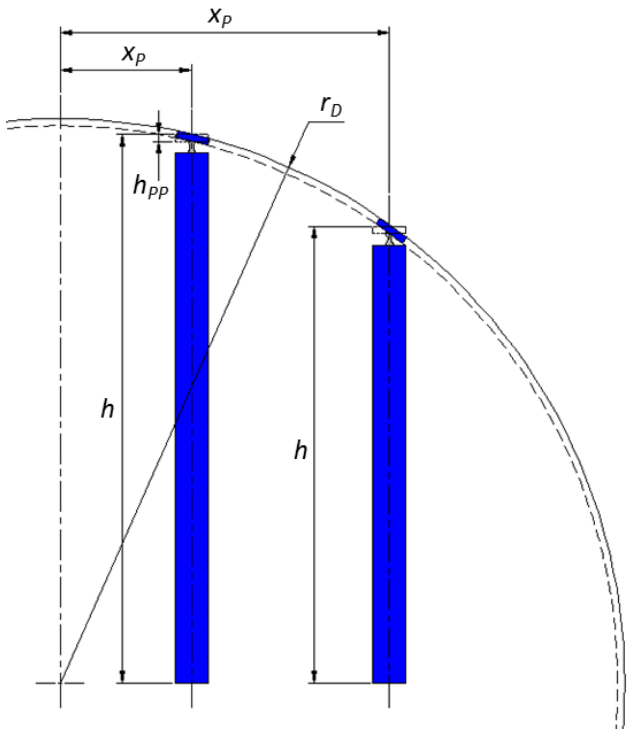

Figure 4-21: Variables used in pin height calculations for pins with flat pin tips

Referring to Figure 4-21, the expression used to calculate the height (h) of pins with pivoted pin tips, and so the vertical positioning of pin tip surfaces used to represent dies is;

$$h = y_{PT} + \sqrt{(r_D - y_{PT})^2 - {x_P}^2} \tag{48}$$

where, y_{PT} is the vertical distance from the top of a pin tip to its pivot point, r_D is the radius of the die and x_P is the horizontal distance between the centreline of the die and the pin tip's pivot point. This expression remains constant regardless of a pin's position on the die radius as its control point is always at the centre point of the pin tip.

Phase 2 simulations use the same parameters as those in phase 1 and results are analysed in the same way. It should be noted that the surfaces representing pivoted pin tips are rotated to their final position and each die is imported as a single tool, hence the surfaces are not allowed to pivot during the actual simulation. It is not possible or practical (since the computational time for each simulation would be huge) to use a large number of individual partly restrained surfaces to represent the reconfigurable die in the AutoForm software.

4.6 Phase 2 Results

Coordinates on the deformed blanks are taken from section lines along the centrelines in both the stretching and transverse directions (SD & TD respectively). As there is a pin located at the centre point in each of the three pin arrangements used, these section lines are denoted as being 'on top of pins'. An offset is used to create a second set of section lines, denoted as being 'between pins' and passing through the areas with the greatest gaps between pins. In the RCP3 pin arrangement the offsets in the stretching and transverse directions are equal. In the HCP1 pin arrangement a greater offset is used in the stretching direction, while in the HCP2 pin arrangement a greater offset is used in the transverse direction, to ensure that the section lines are always located where the greatest magnitude of dimpling would be expected. Figure 4-22 shows the deviation

from the required die radius, measured as the distance between the highest peak and lowest trough of the four section lines, for all the dies simulated in phase 2.

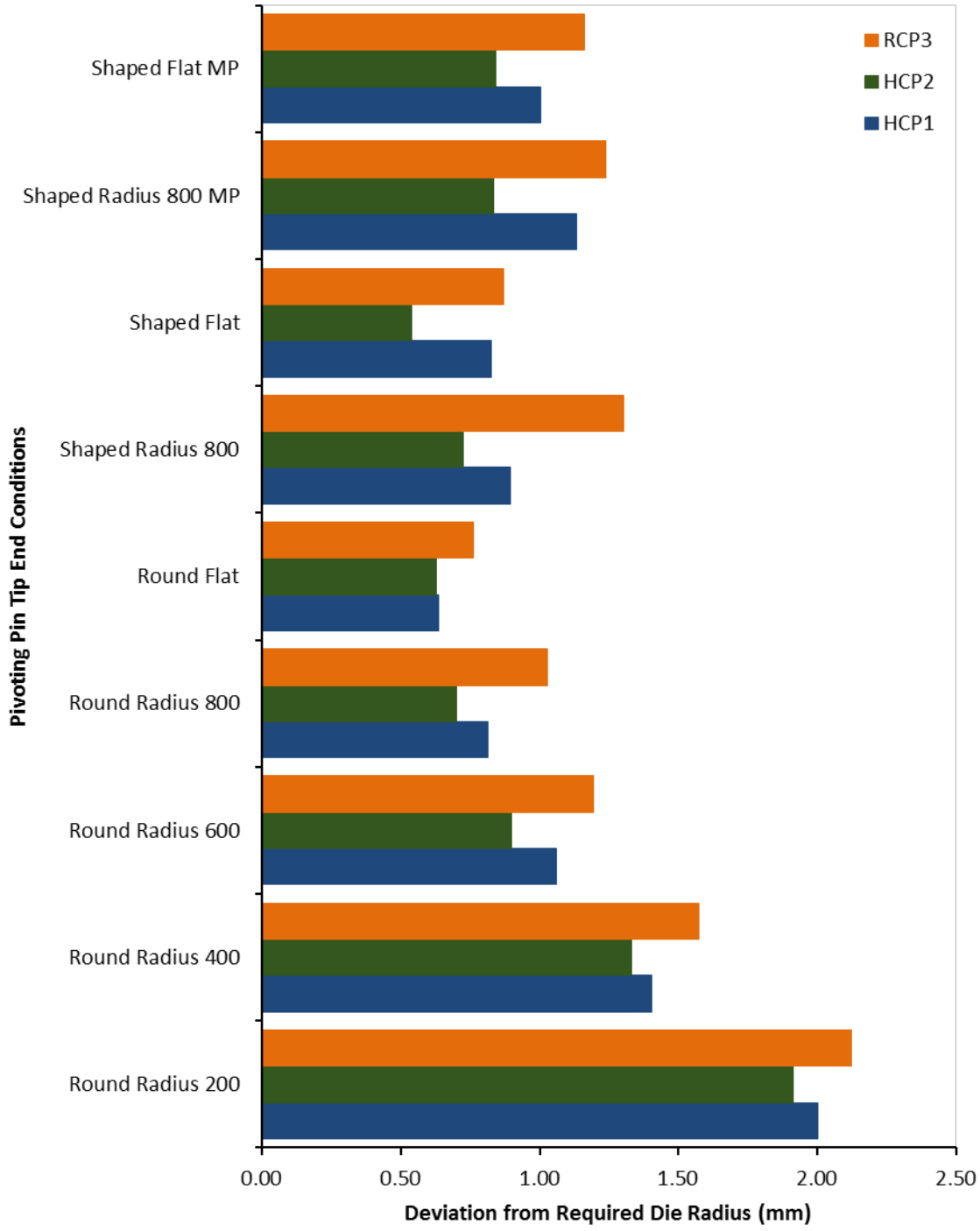

Figure 4-22: Phase 2 section line analysis results for pivoted pin tips

It is readily noticeable from this plot that, in contrast to results for the semi-hemispherical pin tips (Figure 4-14), there is a direct correlation

between the sizes of the radius on the mating faces of the pivoted pin tips and the smoothness of the parts produced. Since pivoted pin tips are orientated to the curve of the blank more support is offered as this radius approaches that of the die as a whole. To allow for springback, the ideal radius used on pivoted pin tips would be one that is just below the die radius. Hence it can be surmised that smoother parts could be obtained if the radius on the pin tips was chosen to match the radius of the die, but it would be a part-specific solution which would negate part of the cost reduction benefit of using reconfigurable dies. While it is impractical to change the pin tips when the die radius changes, results from the simulations using round flat pin tips show that, when the die curvature is relatively gentle (as it is with a die radius of 1200 mm) parts with good smoothness can be obtained using pin tips with a flat mating face.

Shaping the pin tips to that of the pin cross section or pin matrix offers more support to the blank with the size of gaps between pin tips being reduced. However, results show that, with this single curvature die, an improvement in deformed blank smoothness is only obtained in the HCP2 pin arrangement where the parallel edges of the hexagonal pin tips are orientated normal to the stretching direction. Conversely where the corners of the square and hexagonal pin tips are orientated in the direction of blank curvature (stretching direction) the length of the flat surface is increased and so too is the normal distance between a centre point on the flat surface and an apex on the required curvature along this length. It can be surmised that when a part of clastic curvature, with equal curvature in both the stretching and transverse directions, is being formed the smoothness of parts stretched over a die with the HCP2 pin arrangement using hexagonal pin tips would be similar to that shown here for the HCP1 pin arrangement.

Despite their increase in complexity, results from simulations using pin tips with a multipoint mating surface, mimicking that found in a finer pin matrix, also show no improvement in the smoothness of deformed blanks when compared to results from simulations using the round flat pin tips.

Since the hexagonal pin tips only show a reduction in the magnitude of defects (compared to those found when a round pin tip is used) when their parallel edges can be aligned normal to curvature (and only in a part of single curvature), results show that using round flat pin tips offers a better global solution. Figure 4-23, Figure 4-24 & Figure 4-25 show plots of the section line analyses results (a) and maps of the surface defect analysis results (b) for the RCP3, HCP1 and HCP2 pin arrangements respectively, all using the round flat pin tip geometry. Results from the section line and surface defect analyses pertaining to the remaining 24 simulations are included as Appendix I. of this document.

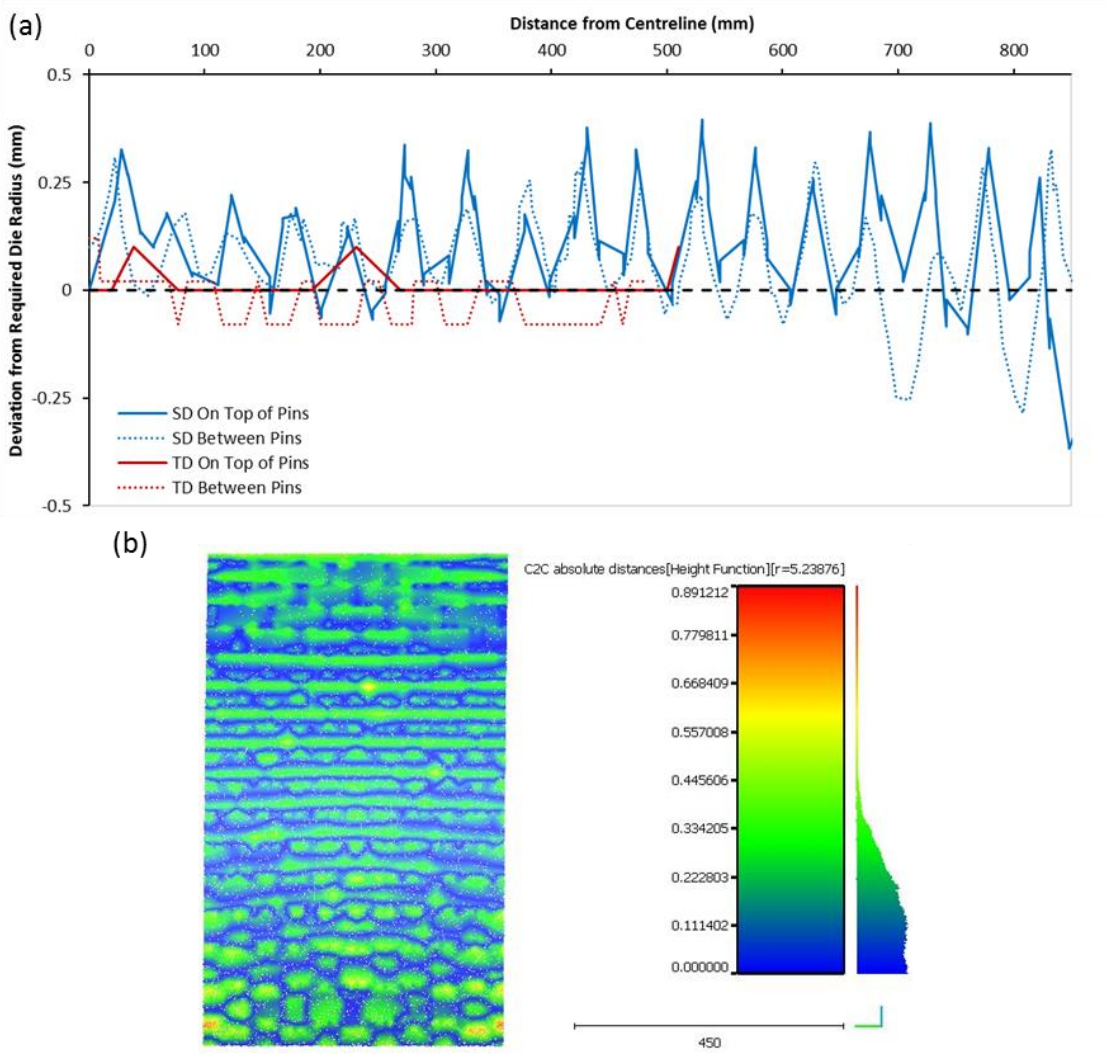

Figure 4-23: RCP3 with pivoted round flat pin tips section line (a) & surface defect (b) analyses results

The surface line analysis of the RCP3 pin arrangement with pivoted round flat pin tips shows a total deviation, measured from the highest peak to the lowest trough of all four section line curves, of 0.76 mm. This is slightly higher than the total deviation of 0.64 mm and 0.63 mm shown in the HCP1 and HCP2 results respectively, due to the lower density of the rectangular close packed matrix and hence the bigger gaps between the round pin tips.

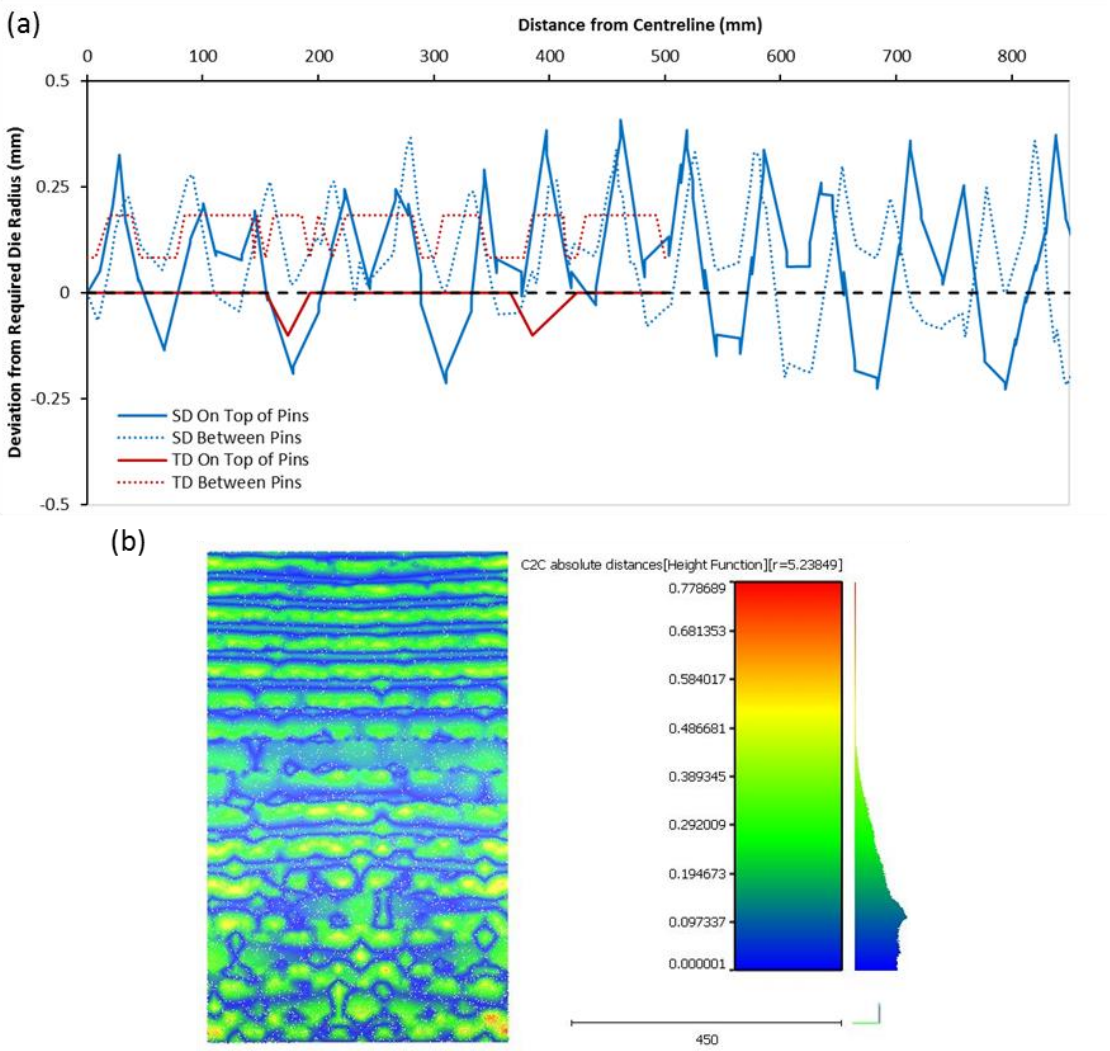

Figure 4-24: HCP1 with pivoted round flat pin tips section line (a) & surface defect (b) analyses results

Note that the peaks of curves in all three pin arrangements are now yielding positive deviation values denoting high spots since the control points of the round flat pin tips are taken as their centre points on the mating surfaces and hence the outer filleted edges of the pin tips sit proud of the required radius in the direction of curvature. Also note that the

distance between neighbouring peaks and troughs increases at the higher end of the measured area (approaching 850 mm from the centreline) due to the increased true distance, along the curvature of the die, between control points of pin tips and hence an increase in gap size. It is also noticeable that the section lines along the transverse direction produce smoother deviation curves in the HCP1 results than they do in the HCP2 results due to the closeness of pin tips in that direction. The opposite effect can be seen in the deviation curves of section lines along the stretching direction where pin tips are more closely packed in that direction with the HCP2 pin arrangement.

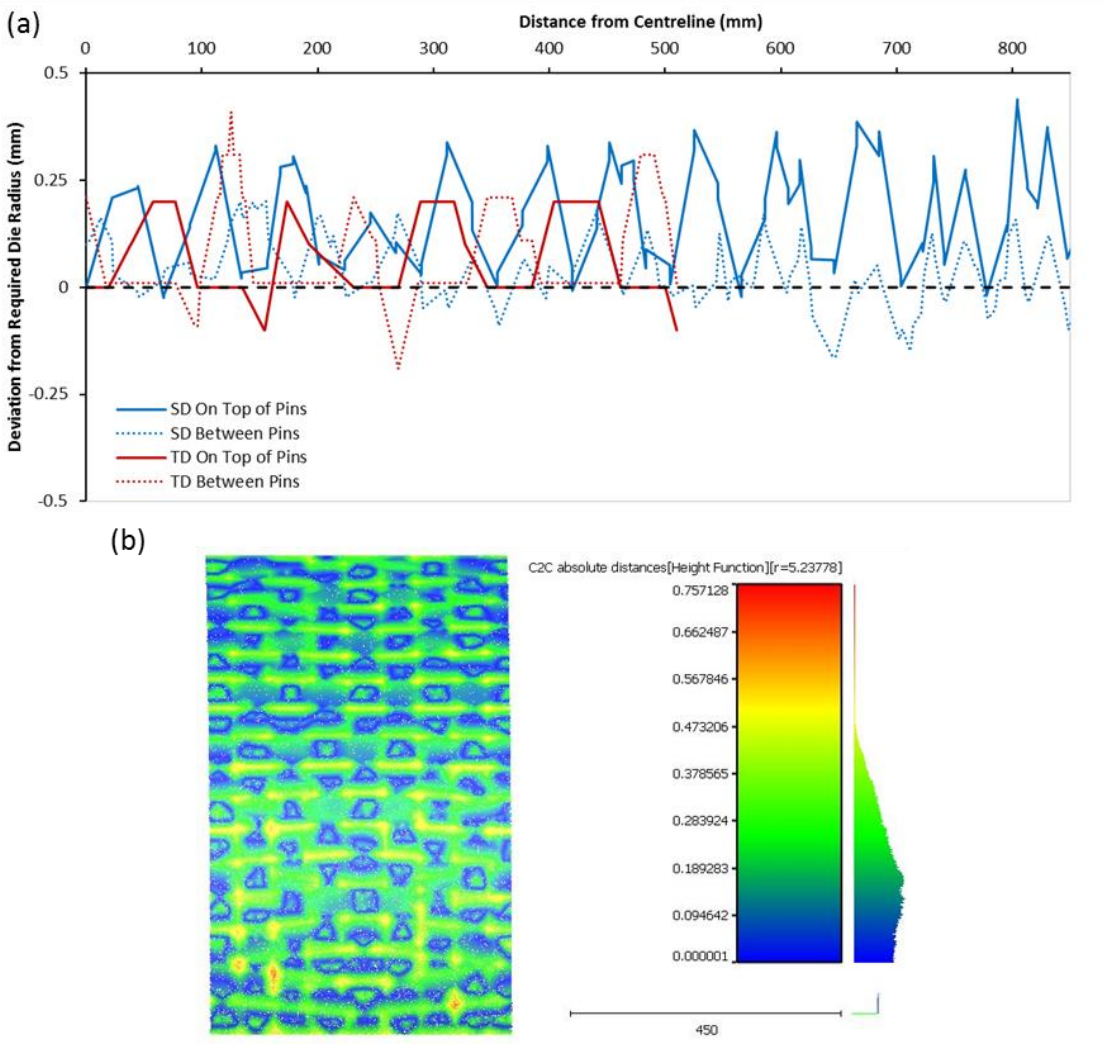

Figure 4-25: HCP2 with pivoted round flat pin tips section line (a) & surface defect (b) analyses results

4.7 Simulation Mesh Size Comparison

In this section the analysis results from two HCP2 Round Flat simulations are compared. The first simulation is that presented in Section 4.6 where a standard mesh size with default setting is employed (these settings are used in all the phase 1 & 2 simulations). Figure 4-25 shows the analyses results for this simulation. In the second simulation fine accuracy is used with an initial element size of 5.7 mm, together with a maximum refinement level of 3, controlled through the radius penetration setting of 0.16 mm and a maximum element angle of 22.5°. The same CDA models and process setup is used in both simulations. Figure 4-26 shows the results of the section line (a) and surface defect (b) analyses from the fine mesh simulation.

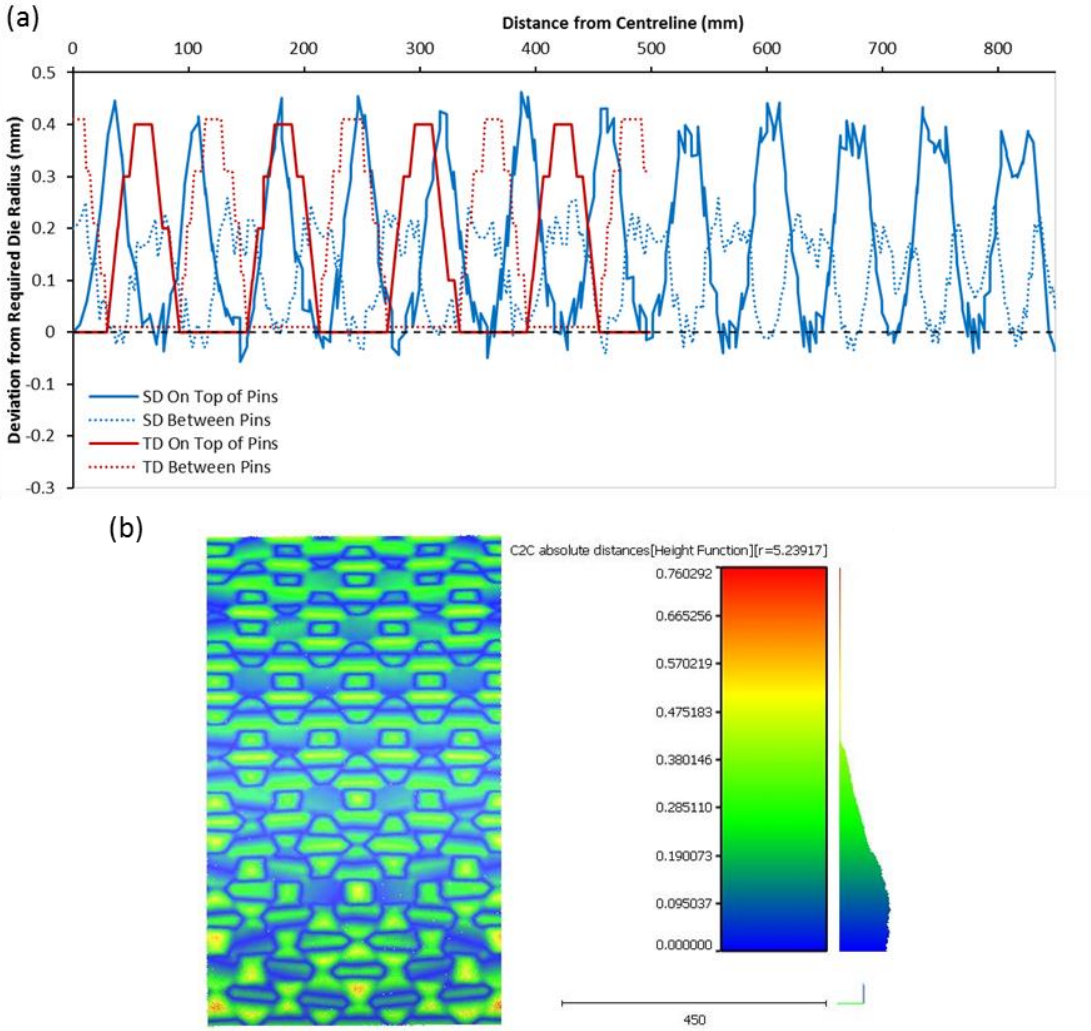

Figure 4-26: HCP2 round flat fine mesh simulation section line (a) & surface defect (b) analyses results

In the section line analysis, the total deviation from the HCP2 Round Flat standard mesh simulation is shown to be 0.63 mm. The total deviation from the HCP2 Round Flat fine mesh simulation, again measured from the highest peak to the lowest trough of all four deviation curves, is shown to be 0.52 mm, in the section line analysis. Considering that the fine mesh simulation has a run time in excess of 7 hours but the standard mesh simulation takes less than 30 minutes to complete, these total deviation values are relatively close. Note that all the AutoForm simulations were run on a HP Pavilion G6-1241SA laptop containing an Intel Core i5-2430M processor with 2 cores and a processor base frequency of 2.4 GHz. This laptop uses the Windows 7 64-bit operating system with 8 Gigabits of RAM. Simulations were run sequentially using both cores.

A breakdown of the maximum and minimum deviation over each section line is plotted in Figure J-2 of Appendix J. It can be seen that while total deviation is measured between a peak & trough on the deviation curves denoted as 'SD On Top of Pins' & 'TD Between Pins' respectively, in the standard mesh simulation, it is measured between a peak & trough both on the deviation curve denoted as 'SD On Top of Pins' in the fine mesh simulation. The frequency, and consistency, of peaks and troughs on the section line analysis results from the fine mesh simulation shows an improvement over those from the standard mesh simulation with values very close to zero at contact points at the centre of the pin. While the surface defect maps from both simulations show a comparative blue area, indicating very close proximity between the reference and compared point clouds (approximate deviation magnitudes of less than 0.1 mm), the pattern of these areas is again more consistent in the contour map from the fine mesh simulation. Both contour maps show a maximum deviation of approximately 0.76 mm.

4.8 A Disadvantage of the HCP Pin Arrangement

It should be noted that where a rectangular close packed pin arrangement is used, and single curvature parts are being formed very little force is being

transferred onto the longitudinal walls of a machine. Horizontal components of forces normal to the curvature of the part compress the pins in the reconfigurable die towards its transverse centreline. The only forces acting on the machine's longitudinal walls are caused by the buckling of longitudinal rows of pins. This is not the case when a hexagonal close packed pin arrangement is used, where it was found that a statically indeterminate force system exists, as horizontal components of forces normal to the curvature of the part are distributed along contacting pins (see Figure 4-27). A short study was carried out where it was found that the bending moment on the longitudinal walls of a machine, fitted with a reconfigurable die employing the HCP2 pin arrangement, could be reduced by fixing ribs to the walls, in the gaps between pins.

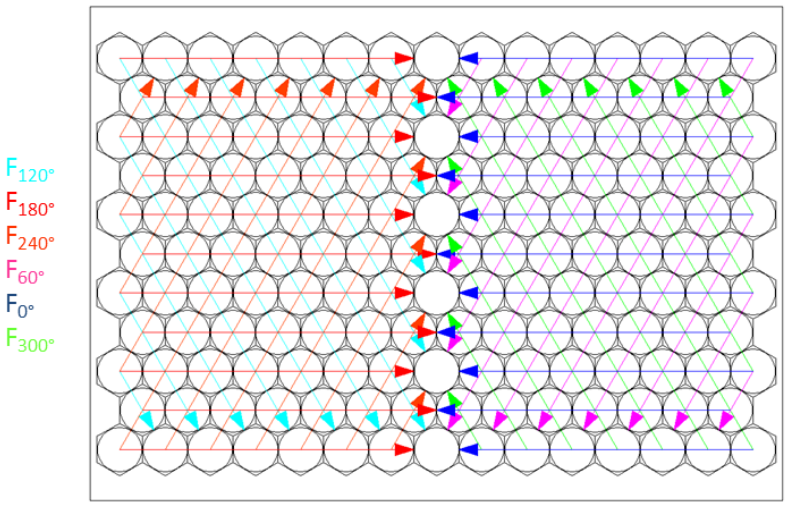

Figure 4-27: The statically indeterminate force system present in the HCP2 pin arrangement

Regardless of the pin arrangement employed, forces on the longitudinal walls of a machine increase when an anticlastic part is being formed, since additional horizontal components of forces normal to the curvature of the part push pins away from a longitudinal centreline on the die. Likewise, when a part with clastic curvature is being formed forces on the longitudinal walls of a machine decrease, since additional horizontal force components push pins towards a longitudinal centreline on the die.

4.9 Conclusions

Results from the phase 1 AutoForm simulations, discussed in this chapter, where semi-hemispherical pin tips are used in a total of 14 different die layouts, show that only the hexagonal close packed layouts HCP1, HCP2 and the diagonally orientated rectangular close packed layout RCP3 are suitable for use with a reconfigurable die constructed from a relatively coarse bed of pins. These results also reveal that;

- edge contact between pin tips and the blank (or interpolator),
- low pin density in the die matrix,
- unequal spacing between pin tips,
- increased magnitude of gaps between rows of pins aligned in the direction of stretching, and,
- increased magnitude of gaps between neighbouring pins in the direction of stretching,

are all features on a reconfigurable die which increase the difficulty in obtaining smooth parts, from a stretch forming process over the given die.

On closer examination of these three pin arrangements, in the phase 2 simulations, it has been found that single curvature parts with superior smoothness can be obtained using the HCP2 pin arrangement. This is in general agreement with previous research where less severe dimpling was reported when using the hexagonal close packed arrangement (Rivai, et al., 2014) (see Section 2.5).

A comparison of the smallest total deviation (from the nominal curvature) found using the HCP2 in both the phase 1 and 2 simulations [2.66 mm and 0.63 mm respectively (see Figure 4-18 and Figure 4-22)] demonstrate that pivoted pin tips give a considerable advantage over their commonly used semi-hemispherical counterparts. While it is possible to produce parts with superior surface smoothness with part-specific pin tip geometry (which would negate part of the cost reduction benefit of using reconfigurable dies), it has been demonstrated here that using round pin tips with a flat mating surface offers a better global solution.

While standard meshes with default setting are used in the phase 1 & 2 simulations, a comparison of the total deviation from the section line analysis results for the HCP2 Round Flat simulations using both a standard mesh and a fine mesh is used in Section 4.7 to demonstrate that reasonable results are obtained from these simulations.

Chapter 5. Process Modelling and Interpolator Selection

5.1 Introduction

In this chapter the preferred AMFOR machine layout is introduced and the lab scale stretch forming machine, designed by the AMFOR group, is described (Section 5.2). Note that the calculations used to design this machine are contained in internal AMFOR reports. The stretch forming process over a reconfigurable die comprised from a dense matrix of pins, corresponding to the parameters of the lab scale machine, is modelled, using the PAM-STAMP 2G software. The HCP2 pin layout and the round flat pivoted pin tips, tested in Chapter 4, are used in these simulations. The parameters and boundary conditions used are described in Section 5.3. Blanks with a thickness of 0.88 mm are defined with the stainless steel 316L material model, developed in Section 3.3. Material models pertaining to the polyurethane materials from the Kaylan® D series, developed in Section 3.5, are used to define the layers of interpolation between the pin tips and blanks. The quality of the surface on the deformed blanks, from these simulations, is used to identify the interpolators suitable for use with this type of reconfigurable die, in terms of materials, thickness and number of layers. The three methods used to analysis surface quality, in this chapter, are outlined in Section 5.4. In Sections 5.5 and 5.7 results are presented pertaining to systems utilising, a single layer of interpolation, and three layers of interpolation, respectively. The surface quality of a

number of parts stretched on the lab scale machine is compared to that of deformed blanks from corresponding simulations, and presented in Section 5.8, as validation of the boundary conditions used in the PAM-STAMP simulations of the lab scale machine. The expected surface quality of parts stretched on an industrial scale machine is investigated in Section 5.9, though simulations of the stretch forming process over a similar reconfigurable die with a working envelope of 1.2 m by 1.2 m, utilising identical boundary conditions to those validated for the lab scale machine. Conclusions as to the usefulness of the proposed reconfigurable die, and the make-up of suitable interpolators, derived from the PAM-STAMP simulations, are then presented in Section 5.10.

5.2 The Preferred AMFOR Machine Layout

The preferred AMFOR machine layout has been developed with a desire to reduce the cost of the stretch forming process. It employs a simple combined gripping and stretching mechanism which only requires two double action hydraulic cylinders in its operation. Figure 5-1 shows this mechanism where, the drums rotate about their fixed axes as the rams are extruded from the cylinders. The two balance linkages illustrated here ensure that both drums rotate at similar rates.

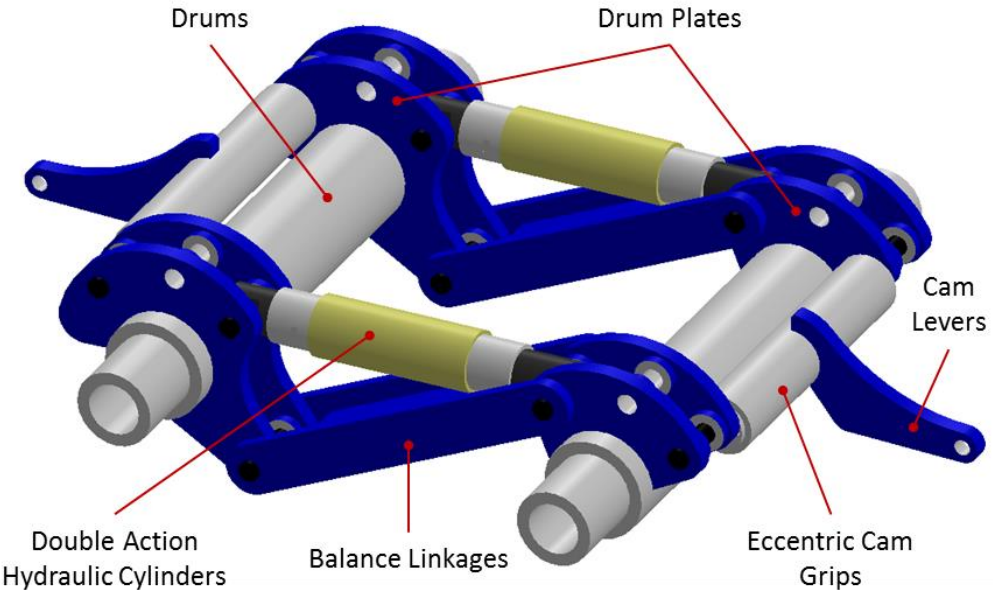

Figure 5-1: AMFOR's preferred gripping and stretching mechanism

The blank being formed is gripped at opposite ends between the drums and eccentric cam grips as shown in Figure 5-2. An initial gripping force is achieved through manipulation of the cam levers. Thereafter, as the drums rotate and the blank is stretched of the die, a friction force between the tensioned blank and the cam surface drags the cams around their eccentric axes with rotation of each cam being in the same direction as their corresponding drum. The eccentric cam gripping system has an attribute very desirable in stretch forming where the clamping force is increased during the process as the tension in the blank increases (Lange, 1985).

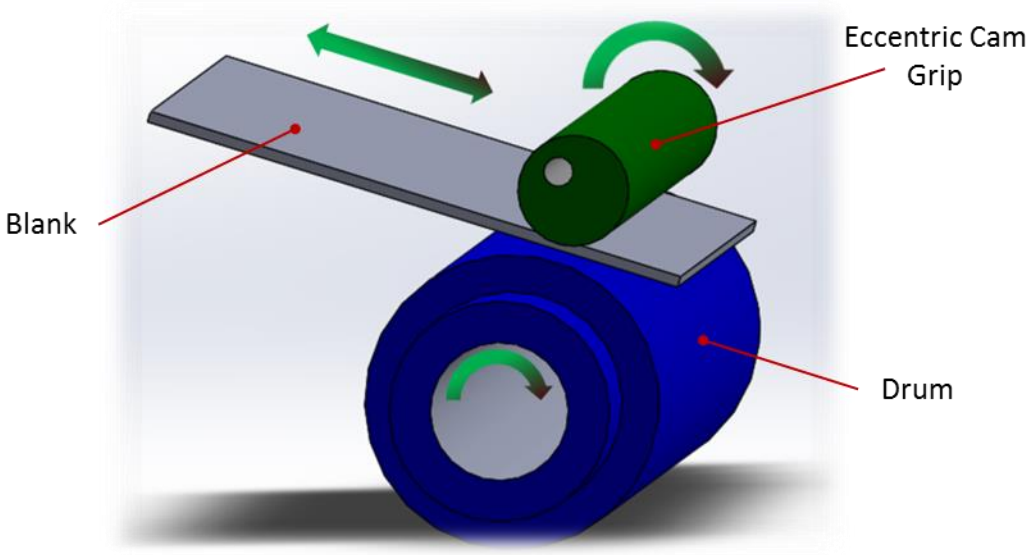

Figure 5-2: The rotation of an eccentric cam grip

In the lab scale version of the AMFOR machine the reconfigurable die consists of a matrix of 33 pins arranged in the HCP2 pin layout and contained within a steel pin box (see Figure 5-3). The pins in the lab scale reconfigurable die are a shortened version of industrial scale pins. The pin bodies are manufactured from DOM (Drawn Over Mandrel) mechanical steel tubing, 70 mm in diameter with an 18 mm wall thickness. Each pin body is capped at the top end with round bar and at the bottom end with a M30 hexagonal nut. The top of each pin body is drafted to allow for additional rotation of the pin tip. The pin tips used are the round flat type investigated in Section 4.5. Pin tips are allowed to pivot over a ball stud located at the centre of the top pin body cap. For ease of manufacture each

pin tip is fitted with a plastic insert incorporating a spherical pocket which mates with the spherical surface of the ball stud. The bottom section of each pin is simply a length of M30 threaded rod with a M30 hexagonal nut tack welded flush to its bottom surface. Pins are located in the pin box through fitting these nuts into corresponding hexagonal cut outs in a pin seating plate.

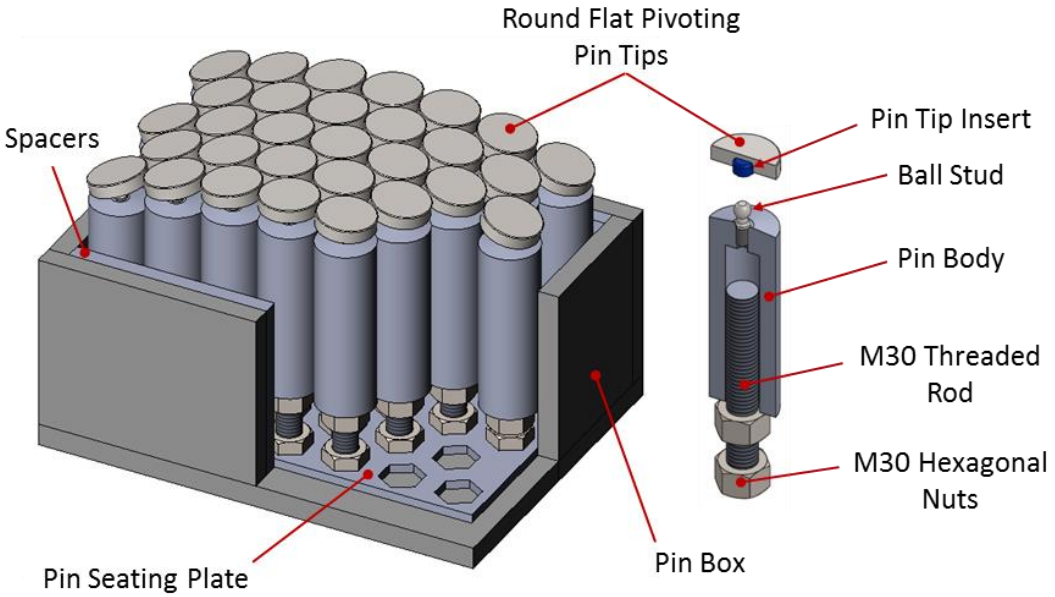

Figure 5-3: The lab scale pin box and pin design

While a second pin seating plate was manufactured with cut outs in the HCP1 arrangement, the HCP2 pin layout has been used here since this layout performed slightly better in the simulations carried out in Chapter 4. The same pin box is used for both layouts with spacers fitted to fill the gaps between pins and the sides of the box, and hence minimise the danger of the pin matrix spreading across its width during the stretch forming process.

The minimum height of each lab scale pin is 275 mm. With an approximate travel of 150 mm along the threaded rod, pins can be extended to a maximum height of 425 mm. With the materials used in their manufacture there is no danger of buckling in the lab scale pins during this project. The equivalent industrial scale pins are approximately 700 mm in length with 500 mm travel. Eq.2 and Eq.3 have been used to ensure that these pins can be used to stretch the 2024-T3 aluminium alloy 5 mm in

thickness over a one metre radius without exceeding their maximum bending and buckling loads. The pins are cylindrical in shape so that their height can be adjusted from above the machine. While the heights of the 70 mm lab scale pins are adjusted at a bench before they are located in the pin box, a possible design of a drive system is shown in Appendix K.

A lab scale machine was built using the mechanism shown in Figure 5-1. A base was manufactured from 50 mm thick steel plate reinforced with four 50 mm by 180 mm steel sections and two thick walled steel tubes (120 mm in diameter with 19.5 mm thick walls) running along its width. Two 50 mm thick steel plate walls were used with the machine held together with five tie bars manufactured from M30 threaded rods and lengths of steel tubing 50 mm in diameter with 9 mm thick walls. The final cost of the lab scale machine, illustrated in Figure 5-4, was less than £6000, excluding the cost of the hydraulic cylinders and pump set which already existed in the AMFOR laboratory.

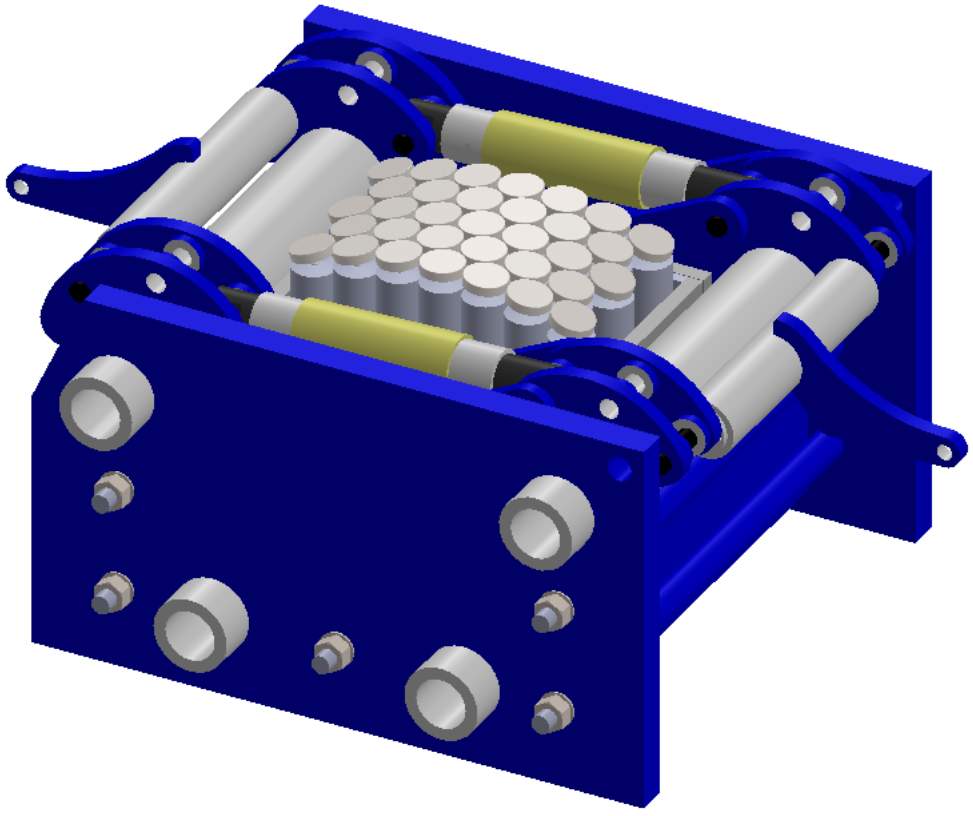

Figure 5-4: AMFOR's lab scale stretch forming machine with a reconfigurable die using cylindrical pins in the HCP2 layout and round flat pivoted pin tips

5.3 Simulation Parameters

The primary purpose of the interpolator is to bridge the gaps between pin tips to produce a dimple free part. The top surfaces of the tip pins used here are flat and the forming surface obtained from a die using these pins is therefore constructed from an array of smaller flat surfaces. Hence a secondary requirement from the interpolators is to smooth out this faceted surface to produce a continuous curved surface on the formed part. Three different methods of interpolation are examined using the PAM-STAMP simulations presented in this chapter.

Firstly, a single layer of interpolation is considered using the eight materials in the Kaylan D series. A very thick interpolator is undesirable as it appears to be an obstacle to the adaptation of reconfigurable tooling in industry. Hence only parts formed over a single layer of interpolation 20 mm and 30 mm thick are examined here.

The second system considered here utilises three layers of interpolation where a softer material is sandwiched between two interpolators manufactured from a harder material. The theory being that, when the forming forces are applied, the bottom interpolator dips down into the gaps between pin tips leaving a series of hollows. The softer material is used to fill these hollows while compressing sufficiently to allow the top interpolator to deform in a state close to equilibrium (with a continuous curve), and hence produce a smooth surface at its interface with the blank.

The third system is an extension of the second where a fourth layer fashioned from the softer material is also used in contact with the die surface. Assuming that the layer of relatively stiff material at the bottom of the sandwich is also deforming in a state close to equilibrium, it will curve over the flat surface of a pin tip, making contact at its outer edges and leaving a gap at its centre. The purpose of the softer fourth layer of interpolation is to compress at the outer edges of pin tips (hence relieving some of the stress at contact points in the harder material above) and to add support where gaps have formed at the centre of pin tips.

The versatility of the PAM-STAMP 2G software allows the user to construct simulations to represent virtually any forming process. In this section the parameters and boundary conditions used to set up simulations representing the stretch forming process, on the lab scale machine, utilising all three systems of interpolation, are outlined. A simple part with single curvature, to a target radius of 750 mm, is used to examine the extent of dimpling when variable combinations of interpolator system, materials, and thickness are employed. To save on computational time and memory, and since the parts, the reconfigurable die, and the machine, are all symmetrical about centrelines running along their lengths and across their widths, only a quarter of the tooling and blanks are represented in models. Two symmetry planes are used to project the remainder of the model. The Unit system used in these simulations is millimetres, kilograms, milliseconds and degrees centigrade.

The 316L material model constructed in Section 3.3 is used to represent blanks being formed in these simulations. Since the length of a typical blank used on the lab scale machine is equal to the width of the available sheets, it is easier to cut blanks at 90° to the rolling direction of the sheet. Hence, for consistency in comparing results, the RSF-M02-SR-90 model is used in all simulations. Blanks are meshed using quadrangular Belytschko-Tsay shell elements (2D plane stress elements) with sides of 5 mm in length. The Gauss thickness integration rule is used with five integration points across a material thickness of 0.88 mm.

The material models constructed in Section 3.5 for the Kaylan® D series of polyurethanes are used here to represent layers of interpolation between the blanks and tools. Each interpolator is defined as a volume tool and meshed with hexahedral solid elements 2.5 mm in length along the length and across the width of sheets. Solid elements use a uniform integration rule and the Flanagan-Belytschko stiffness routine with default coefficients used to control hourglassing. At least four elements, with a maximum height of 2.5 mm, are used though the thickness of all interpolators.

The tools used in simulations are representations of a single drum and eleven round flat pin tips. Models of the tooling are constructed in the SOLIDWORKS software and saved as IGES files. The validation DeltaMESH strategy is used to automatically mesh tool surfaces while importing them into the PAM-STAMP software. The round flat pin tips shown in Figure 5-3 are of 68 mm in diameter with their top edges filleted and their pivot points 15 mm from their top surfaces. The models used here are of cylinders 68 mm in diameter with a height of 30 mm and fillets applied at both the top and bottom surfaces. This allows their centre of gravity to be used as pivot points while maintaining the critical distance to the top surface. The meshed surfaces representing the drum and eleven pin tips are all assigned to separate objects and each object is defined as a surface tool with material. As advised in the PAM-STAMP user guide (ESI Group, 2013), a thickness of 0.1 mm is added to each tool to aid in accurate contact during simulations. The pin tip objects are assigned with names relating to their positions in the die, beginning with the purple object furthermost from the YZ symmetry plane and located on the XY symmetry plane, as illustrated in Figure 5-5, which is named A1. The pink object in the second row of pin tips is named B2. Continuing in this fashion, the final green pin tip object in the row furthermost from the YX symmetry plane and located on the XZ symmetry is assigned the name C7.

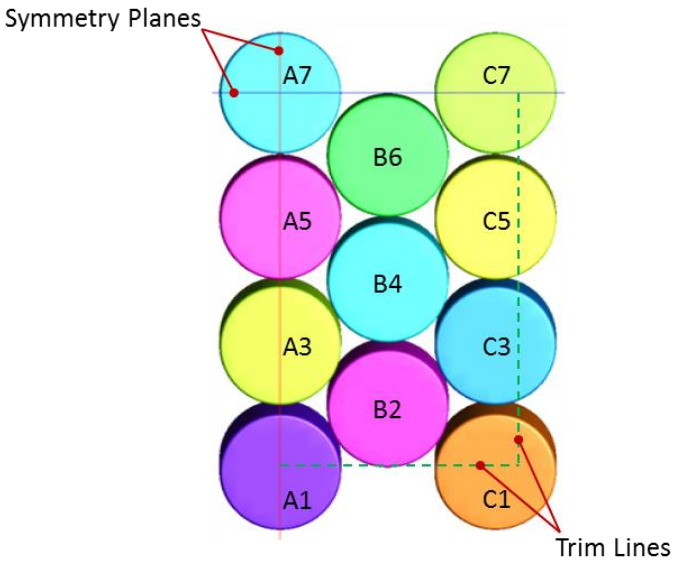

Figure 5-5: Pin tip identification within the lab scale die

Each simulation contains two explicit stages denoted as 'Position' and 'Stretch' and an advanced implicit springback stage. At the beginning of the position stage the pin tip objects are defined as regular rigid bodies and are all positioned on a horizontal plane as shown in Figure 5-6. The interpolators are located above the pin tips with a small gap between each object. The blank is located above the interpolators and the drum, again maintaining gaps between their surfaces. A mesh transformation attribute is used in the global parameters to reposition the objects before the simulation begins. Firstly auto-positioning is used to move the blank onto the drum (which is also defined as a regular rigid body). Next objects A1, B2, C1, A3, B4, C3, A5, B6 and C5 are all moved in the –Y direction to the heights required in the reconfigurable die, before they are rotated to their required angle as shown in Figure 5-7. Finally auto-positioning is again used to move the interpolator onto the highest pin tip. It should be noted that, in its rotated position, the filleted edge of the B6 pin tip protrudes above the central pin tips (A7 and C7) and is therefore used to reposition the interpolators and ensure that no initial penetration is present at the beginning of the position stage.

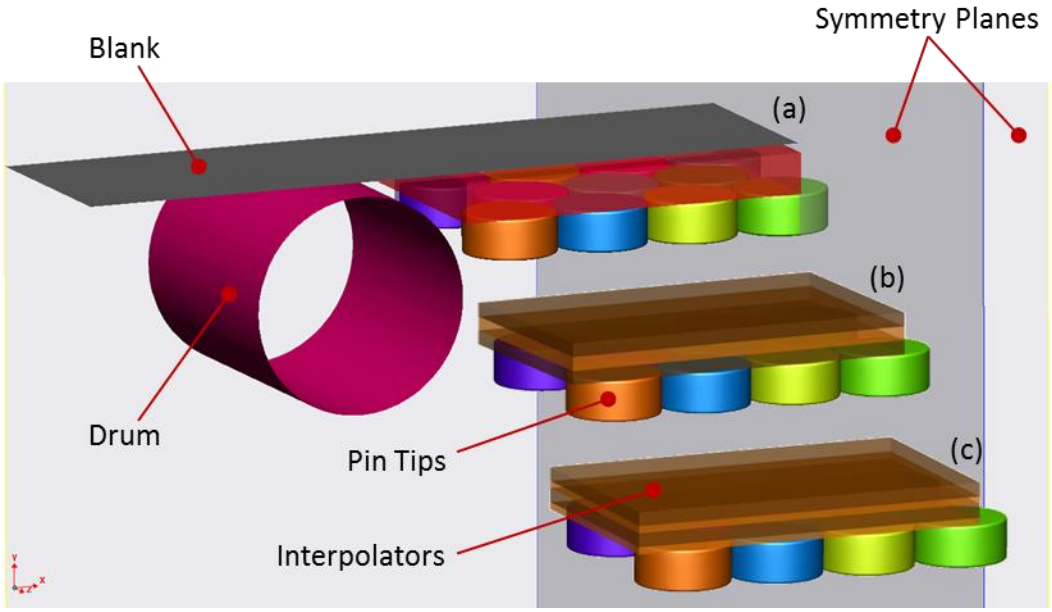

Figure 5-6: The initial position of models in the single layer of interpolation simulations (a) together with illustrations of the three (b) and four (c) layers of interpolation systems

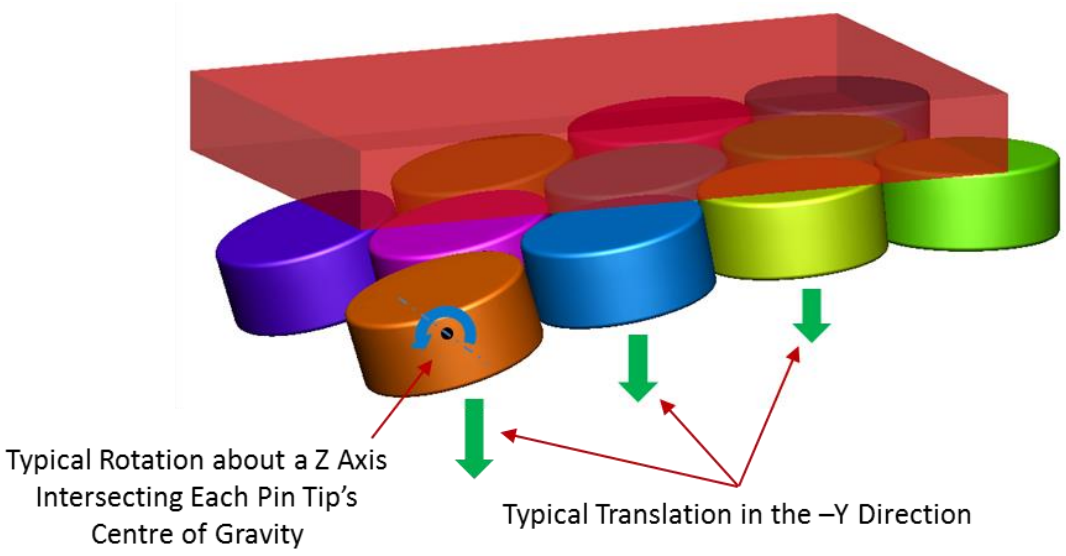

Figure 5-7: The rotation and translation mesh transformations applied to pin tips at the beginning of the position stage

The engineering strain at an engineering stress of 1 MPa in each polyurethane material present (given in Table 3-9) is used to determine the final interpolator thickness, which is used in turn to determine the translation and rotation required to reposition each pin tip. The final interpolator thickness is determined as;

$$t_f = \sum(t_i - t_i e_i) \tag{49}$$

where, t_f is the final interpolator thickness, t_i is the initial thickness of each interpolator present and e_i is the engineering strain at an engineering stress of 1 MPa in each interpolator material. The translation applied to each pin tip in the Y direction is then determined as;

$$Y_i = \sqrt{\left(r - t_f - h_{pp}\right)^2 - {X_i}^2} - \left(r - t_f - h_{pp}\right) \tag{50}$$

where, Y_i is the translation applied to a given pin tip in the Y direction, R is the target radius of the part, h_{pp} is the vertical distance from the top surface of a pin tip to its pivot point and X_i is the distance that the given pin tip is positioned from the YZ symmetry plane. The rotation angle of each pin tip (θ_i) is then givens as;

$$\theta_i = \sin^{-1}\frac{X_i}{r - t_f - h_{pp}}. \tag{51}$$

The free edge of the blank is defined as two separate objects sharing their nodes with the blank itself. During the position stage forces are applied to these objects in the –X and –Y directions to put the blank in tension, and pull the interpolator down onto the pin tips, while the reconfigurable die moves to its final position, as shown in Figure 5-8. The drum has all its degrees of freedom locked, while the pin tips have all rotation and translation in the X and Z directions locked during the position stage. Trigonometry is used to determine the die translation required in the Y direction to ensure that tangential contact is obtained on the blank between the drum and die. Translation of the die in the Y direction is determined as;

$$Y_D = R_d \cos\theta_f + \tan\theta_f \left(R_d \sin\theta_f + X_d - X_{If}\right) + r\left(1 - \cos\theta_f\right) - t_f - Y_0 \qquad (52)$$

where, Y_D is the translation of the die in the Y direction, R_d is the radius of the drum and R is the target radius of curvature. X_d and X_{If} are the horizontal distances from the YZ symmetry plane to the centre of the drum and the edge of the deformed interpolator respectively, while Y_0 is the vertical distance between the centre of the drum and the top surfaces of the pin tips in their initial positions. θ_f is the angle from a vertical plane to a line bisecting the centre of curvature and the edge of the deformed interpolator, which can be given as;

$$\theta_f = \sin^{-1}\frac{X_{If}}{r}. \qquad (53)$$

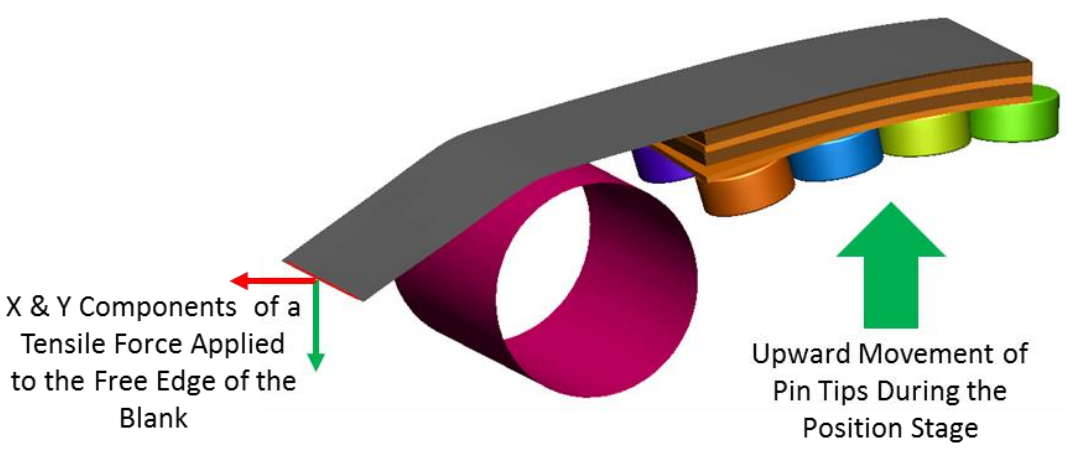

Figure 5-8: The kinematic behaviour of the pin tips and the tension applied to the blank during the position stage

Accurate contact is used in both explicit stages. Taking guidance from the PAM-STAMP users guide (ESI Group, 2013), friction coefficients of 0.12 are used to represent accurate contact between the pin tips and interpolator, and 0.1 at the interfaces between individual interpolation layers. During the position stage a friction coefficient of 0.05 is used to aid sliding of the blank over the drum and interpolator. Imposed force, velocity and angular velocity is controlled through curves where ramps of approximately 10% of the total time are used to help regulate kinematic behaviour in both explicit stages. Since the 316L material is strain rate sensitive, a velocity scale factor attribute of 0.001 is used to convert the velocity and angular velocity values used to more realistic rates in both explicit stages.

During the stretch stage the two objects containing the nodes at the free end of the die are deactivated and an object containing a line of nodes on the blank in contact with the drum is activated. The friction coefficient between the interpolator and the blank is changed to 0.12 while a coefficient of 0.2 is used between the blank and drum to reduce sliding. A ramped imposed angular velocity, equivalent to a stretching rate of 1 mm/ms, is used to rotate the clamping line object and drum 45 degrees about a Z axis running through the centre of the drum, as shown in Figure 5-9. All the drum's remaining degrees of freedom are locked. The translations of all the pin tip objects are locked in all three directions while they are free to rotate in any direction.

In trial setups of this simulation a second tubular object was used to represent the gripping cam. A clamping stage was used, where an imposed force gripped the blank between the cam and drum, but it was found that when the blank was put in tension the contact attribute between the cam and blank was no longer recognised and the cam continued to pass straight through the blank and drum. Hence the cam was replaced with the clamping line object and the clamping stage was deleted.

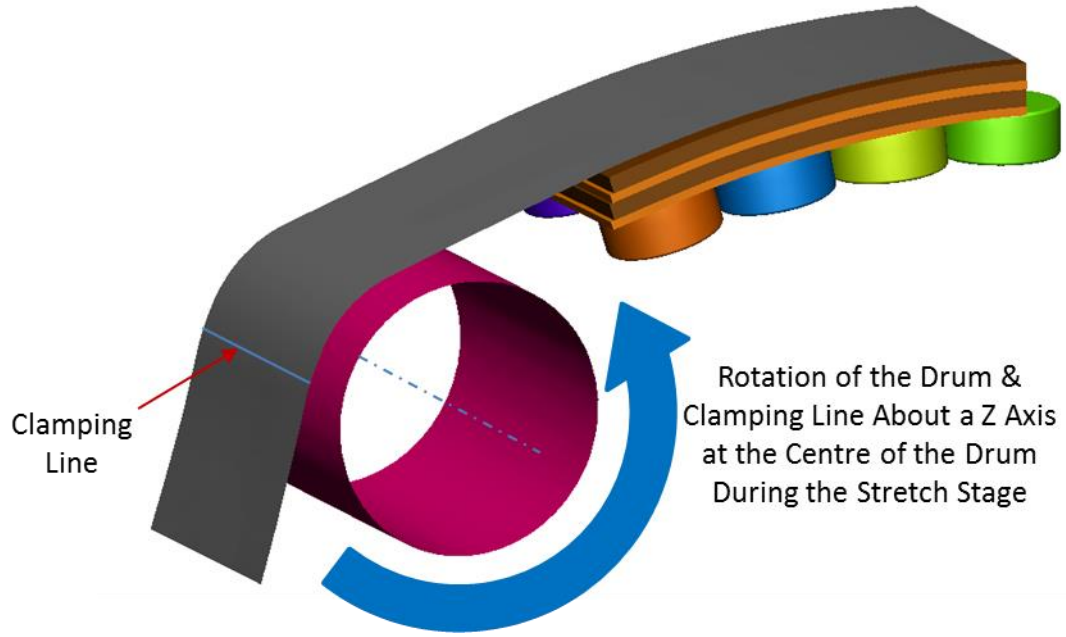

Figure 5-9: Rotation of the drum and clamping line during the stretch stage

In a trial run where the target radius of curvature was 500 mm and a relatively soft interpolator of 10 mm in thickness was used, excessive rotation of the pin tips was observed. Figure 5-10 shows the velocity of nodes contour at the end of the stretch stage in this simulation. It is apparent that the pin tips are no longer in their optimal positions, and they are still rotating despite the cessation of drum rotation. This behaviour was not evident in process trials carried out on the lab scale machine under similar conditions.

Figure 5-10: A kinematic analysis highlighting excessive rotation of the pin tips during the stretch stage

Further trial runs of this simulation were carried out where it was found that excessive rotation was reduced by increasing the inertia of the pin tip objects. Excessive rotation was eliminated when inertia was increased by a factor of 10. Hence an inertia factor of 10 is added to the rigid body attributes of the pin tip objects during the stretch stage of the final simulation setup used here.

While springback is not considered here, in this interpolator selection study, an advanced implicit springback stage is used, in the simulations, to trim the deformed mesh for further analysis. Trimming is set up with a mesh transformation attribute and occurs before the springback is calculated. The two trim lines shown in Figure 5-11 are imported and moved to a position above the deformed part so that the final dimensions (when measured horizontally) of the mesh are 210 mm by 135 mm. The part is been trimmed along its length to a position up the filleted edge of the B2 pin tip. Since this is a quarter blank the corresponding dimensions of the final part are 420 mm by 270 mm.

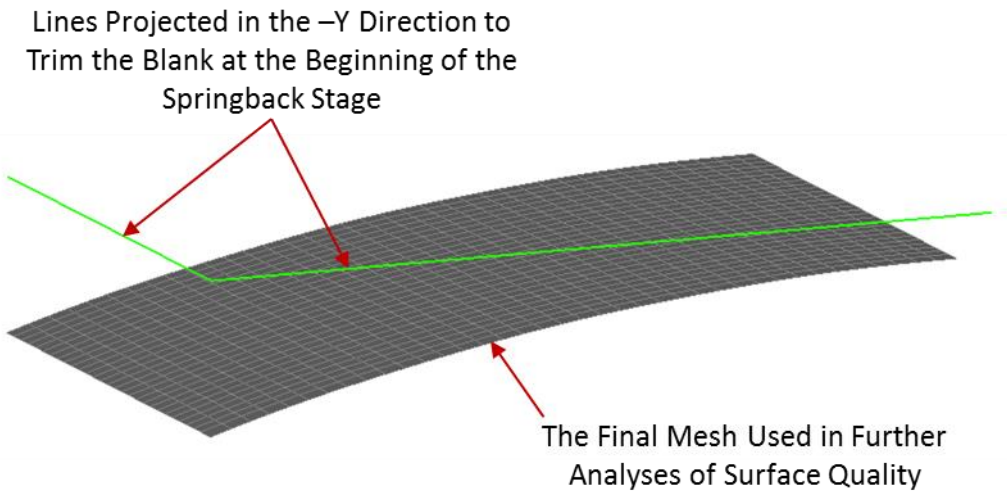

Figure 5-11: The trimmed blank mesh used in further analyses of surface quality obtained from different interpolation systems

It should be noted that not all the final meshes obtained from these simulations contain only the uniform elements observed in Figure 5-11. In order to improve the accuracy of the surface obtained from these simulations a refinement attribute is added to the blank in both the explicit

stages with a maximum level of three, and the respect curvature criteria is activated in the global parameters. Mesh refinement is not evident in the mesh shown in Figure 5-11, but in a number of the simulations using the softer interpolator materials refinement is evident along both the free edges furthest from the symmetry planes.

Simulations representing a variation of the interpolation systems employing multiple layers, where each interpolator is glued to its neighbour are included here. Since a glue contact cannot be used in a stage where accurate contact is also used, interpolators are joined together through the sharing of nodes on their outer planar surfaces.

Penetration at the interface between the volume tools, used to represent interpolators, was encountered in a number of simulations representing interpolation systems employing multiple layers. This problem has been overcome by attaching surface tools comprised of shell elements (with material) to the outer planar surfaces of the volume tools at the interfaces, as illustrated in Figure 5-12. Surface tools are given a thickness of 0.1 mm to aid in accurate contact and same coefficient of friction are used between the surface tools as are used between the volume tools. The surface tools are again attached to the interpolators through the sharing of nodes.

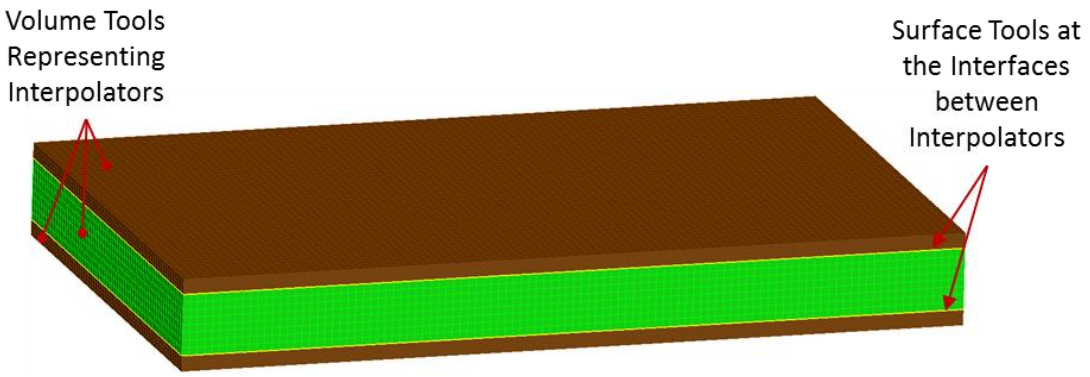

Figure 5-12: Surface Tools used at the interfaces between interpolators to prevent penetration

Simulations representing a variation of the four layer system of interpolation, where the bottom interpolator is replaced by a number of cylindrical volume tools attached to the top surfaces of the pin tips, are also

included here. In these models (Figure 5-13) the pin tip objects have been modified with the radii at the top and bottom edges of the cylinders removed. A radius is instead added the top edge of the cylindrical volume tools attached to the top surfaces of the pin tip objects. The cylindrical volume tools are assigned with the same polyurethane material as the interpolator that they replace. Surface tools are again used at the interfaces between layers of interpolation to aid in accurate contact. Again the surface tools are attached to the interpolators and the cylindrical volume tools are attached to the pin tip objects through the sharing of nodes. It is not possible to move and rotate the pin tip objects, together with their corresponding cylindrical volume tools and surface tools with a mesh transformation attribute, hence these objects were positioned before running the simulation.

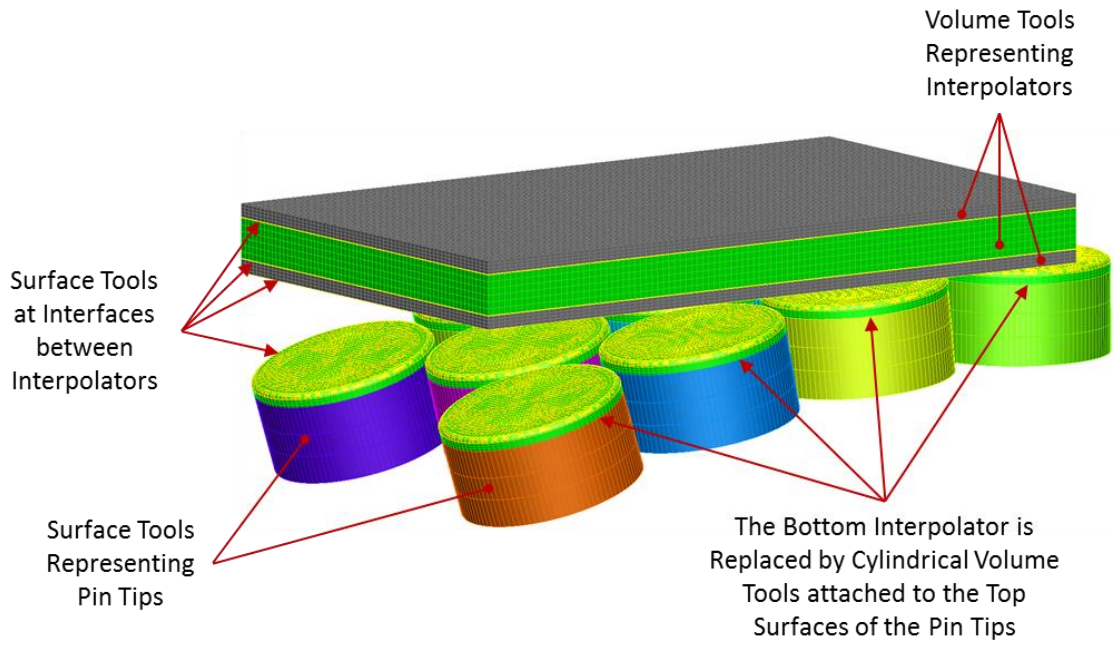

Figure 5-13: The model representing a four layer system of interpolation where the bottom interpolator is replaced by cylindrical volume tools attached to the top surfaces of the pin tips

The approximate run times of these lab scale simulations range between eight hours for the simulations using a single layer of interpolation of 20 mm in thickness with a relatively soft material, to four days for simulations representing a four layer system of interpolation where the

bottom interpolator is replaced by cylindrical volume tools and surface tools are used at the interfaces between interpolators. Note that all the PAM-STAMP simulations were run on AMFOR's DELL T7400 desktop, which contains 2 Intel Xeon X5482 processors with 4 cores per processor and a processor base frequency of 3.2 GHz. This computer uses the Windows 7 64-bit operating system with 32 Gigabits of RAM. Two simulations were run simultaneously using 4 cores per simulation.

5.4 Analytical Techniques

Three techniques are used here to analyse the quality of the surface on the deformed blanks from the PAM-STAMP simulations. The first is a methodology used to analyse the position of nodes in the mesh representing the trimmed blank, which is carried out in Microsoft Excel, and referred to as the radial error analysis in this document. This analytical procedure provides a quantitative measure of the accuracy in the achieved radius of curvature, over the surface of the trimmed blank, in the form of a single value representing the average deviation between the achieved surface and a target surface. It is similar to the method previously used during the DATAFORM project (Wang, et al., 2010) and given as Eq.7 in Section 2.4.1 of this document. Assuming that the point intersected by the two symmetry planes is on the target radius, the recorded height of the sampled points (nodes) are corrected in Microsoft Excel as;

$$Y_{ic} = Y_{ir} + r - Y_c \tag{54}$$

where, Y_{ic} is the corrected height of each sampled point, Y_{ir} is the recorded height of a sampled point, Y_c is the height of the sampled point intersected by the two symmetry planes, and R is the radius of curvature of the target surface. The radius of curvature at each sampled point is calculated using Pythagoras' theorem as;

$$r_i = \sqrt{{Y_{ic}}^2 + {X_i}^2} \tag{55}$$

where, r_i is the radius of curvature at each sampled point and X_i is the horizontal distance from each sampled point to the *YZ* symmetry plane. The radial error between the actual position of nodes and their corresponding position on a target radius of curvature is determined as;

$$Error = \sqrt{\frac{1}{n}\sum_{i=1}^{n}(r_i - r)^2} \tag{56}$$

where, n is the number of points. Whereas Eq.7 measures the error in height Eq.56 measures a radial error.

The second is a methodology comparing the surface of the trimmed blank to that of a target radius of curvature which is carried out in CloudCompare and referred to as the surface accuracy analysis in this document. This analytical procedure provides a visual representation of the accuracy in the achieved radius of curvature, over the surface of the trimmed blank, in the form of a contour map of deviation between the achieved surface and a target surface. The target surface is created in AutoCAD by firstly creating a spline with control vertices at 0.125° intervals along a radius of 750.44 mm with its centre at the 0,0,0 coordinates. The spline is then extruded over a length of 135 mm before being converted to a NURBS object and rebuilt with a total of one million vertices. The surface is generated in the same orientation as the blank from the simulations, and exported to Microsoft Excel in the standard ACIS text format (.sat file). Data is then trimmed so that only the three columns relating to the X, Y and Z coordinates of the one million points remained, before a fourth column representing a scalar field is added. A value of 255 is used in the scalar field column, which gives each point a blue colour and makes the point cloud visible in the CloudCompare software. Data representing the point cloud of the target surface is exported from Microsoft Excel to the CloudCompare software in the comma separated values format (.csv file) while the mesh representing each trimmed blank is exported from PAM-STAMP to the CloudCompare software as an STL file. Again, assuming that the central point (0,Y,0) of the quarter blank is on the target radius, aligning the surfaces is simply a matter of checking the Y coordinates of this point on

each of the surfaces and moving the mesh in the Y direction so that these points coincide. The mesh is then sampled with one million points to create a point cloud before point to point distances are computed using local modelling and the height function.

Finally an analysis measuring defects i.e. bumps and hollows, on the outer surface of the trimmed blank is carried out in PAM-STAMP and referred to as the stoning analysis in this document. This analytical process is equivalent to the stoning process carried out on the shopfloor where a block and set of feeler gauges are used to measure surface defects. Figure 5-14, which has been reproduced from the PAM-STAMP user's guide (ESI Group, 2013), shows how their stoning method measures defects caused by bumps and hollows on a flat or convex part.

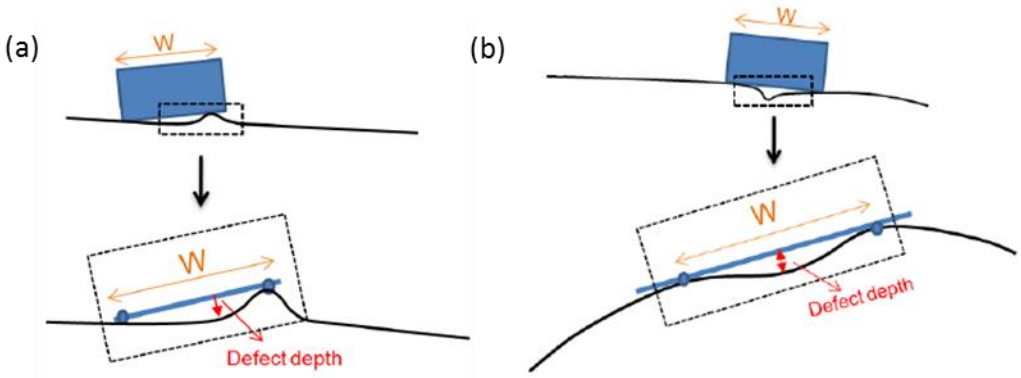

Figure 5-14: PAM-STAMP's stoning analysis to measure defects caused by bumps (a) and hollows (b) on a flat or convex blank

The length of the stone used here is 70 mm (the inline distance between pins). Measurements are taken at lines running across the width of the blank (in the Z direction) and spaced at 1 mm intervals along its curvature.

5.5 Results using a Single Layer of Interpolation

Results from the simulations, where a single layer of interpolation is used, are presented here using a number of colour coded contour maps. The 'Cosmetic defects' contour maps depict the results from the stoning analysis, where the defect depth measured by the PAM-STAMP software (in mm), as shown in Figure 5-14, is mapped on the surface of the trimmed part. The

'C2C absolute distances' contour maps depict the results from the surface accuracy analysis, where the distances between points on the target surface and corresponding points in a cloud generated from the trimmed mesh are measured by the CloudCompare software (in mm) and again mapped on the surface of the trimmed part. The 'Thickness of solids' contour maps shown the final thickness of the interpolator at the end of the stretch stage, measured by the PAM-STAMP software (in mm) and mapped on the volume tool mesh. The 'Major strain' contour maps presented here give a visual representation of the true strain, along the stretching direction, on the mesh representing the central membrane of the trimmed part, before springback. The approximate position of the circular pin tips is superimposed on each contour map to give a better understanding of the material behaviour in each case. Contour maps are all displayed with their top left corners corresponding with the centre point of the part i.e. where the two symmetry planes intersect in the PAM-STAMP simulations.

While both the radial error and surface accuracy analyses call attention to inclines across the width of blank and deviation from a target radius of curvature along its length, together with the effects of dimpling, the stoning analysis is more refined in highlighting the effects of dimpling where the blank has sunk down into the gaps between pin tips. The stoning analysis does not register deviation due to inclines across the width, as shown in Figure 5-15 since the stone will also be set at an incline.

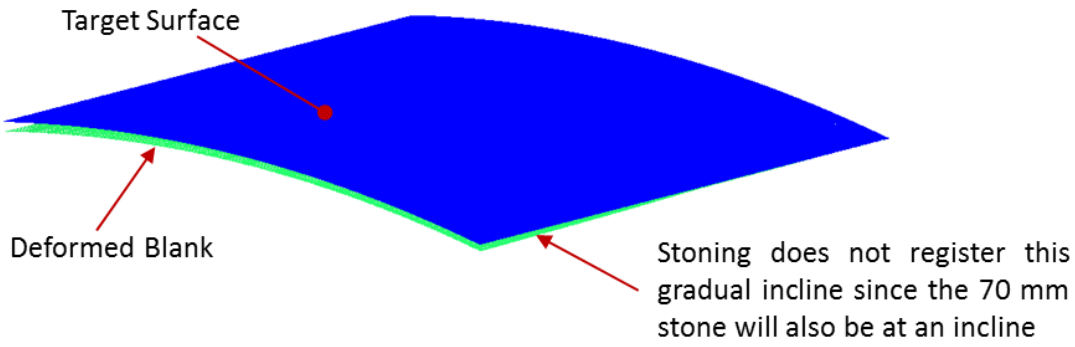

Figure 5-15: A limitation of the stoning analysis

Results from a total of sixteen simulations are examined in this section. Simulations are named using the interpolator thickness (given in mm) and the colour associated with each of the Kaylan materials. Contour maps illustrating the results from the simulation representing a blank of the 316L material, 0.88 mm in thickness, stretched to a 750 mm target radius of curvature, utilising an interpolator 20 mm in thickness made from the D20 Red material (the softest material in the Kaylan D series), are shown in Figure 5-16.

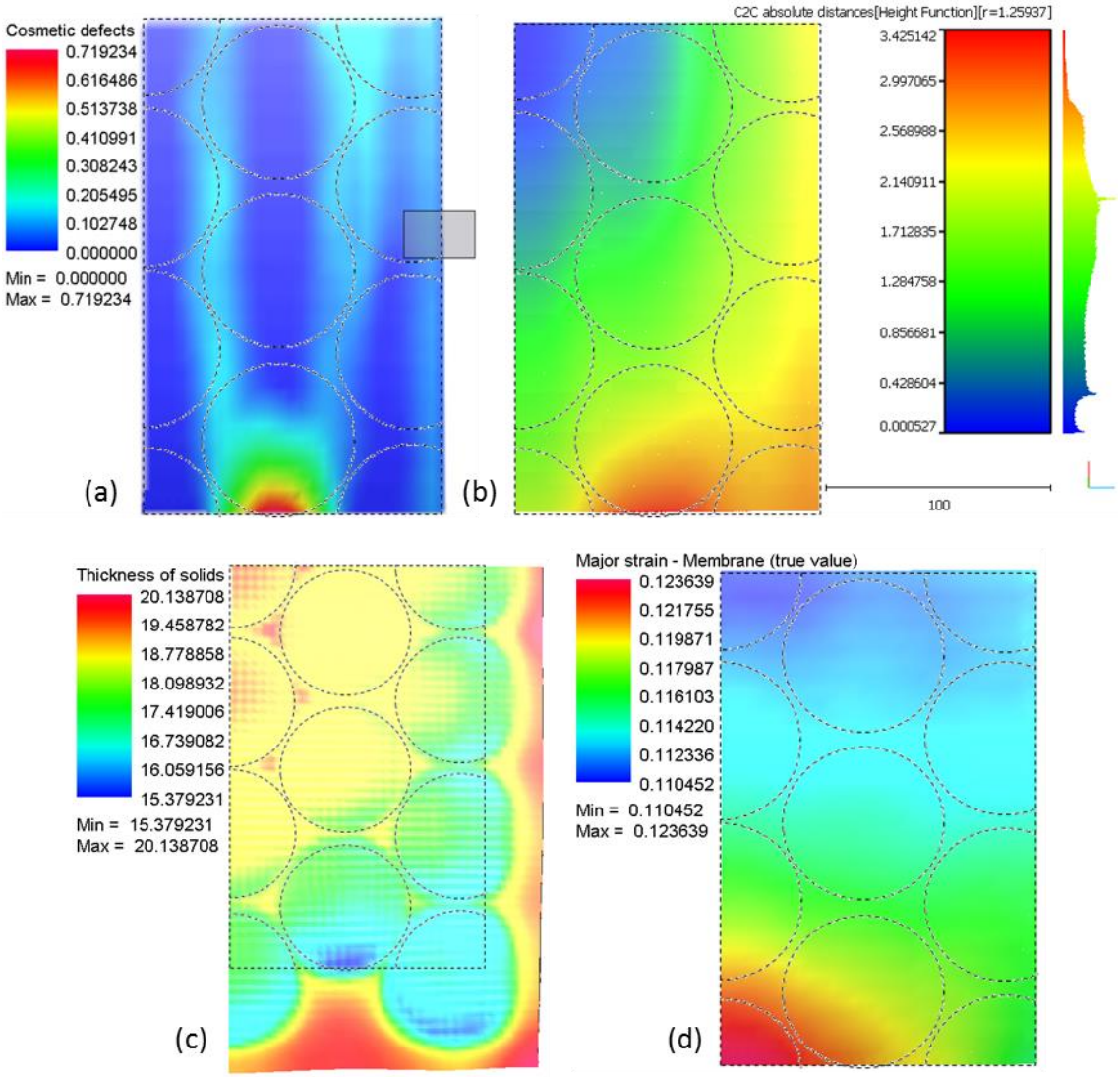

Figure 5-16: The Cosmetic defect (a) C2C absolute distance (b) Thickness of solids (c) and Major strain (d) contour maps for the 20 Red simulation

The contour maps relating to the stoning and the surface accuracy analyses, Figure 5-16 (a) and Figure 5-16 (b) respectively, both show that

the maximum deviation from the target part is present on the trimmed blank in the area over the end of the B2 pin tip. The interpolator thickness contour map Figure 5-16 (c) also shows that the interpolator is at its thinnest in this region at the end of the stretch stage. This is due to a combination of factors. Firstly, the blank is sinking down into the gap between the A1 and C1 pin tips during the stretching process, as shown in Figure 5-17 (a). Secondly, since the centre of the pin tip is taken as its control point, the outer edges of pin tips protrude above their neighbours (in the transverse direction) along the curvature of the part as shown in Figure 5-17 (b). These two factors result in non-tangential contact between the blank and die, in the region over the outer edge of the B2 pin tip (in the stretching direction), similar to that illustrated in Figure 3-14 (c). Hence a greater force is transmitted through the interpolator in this region.

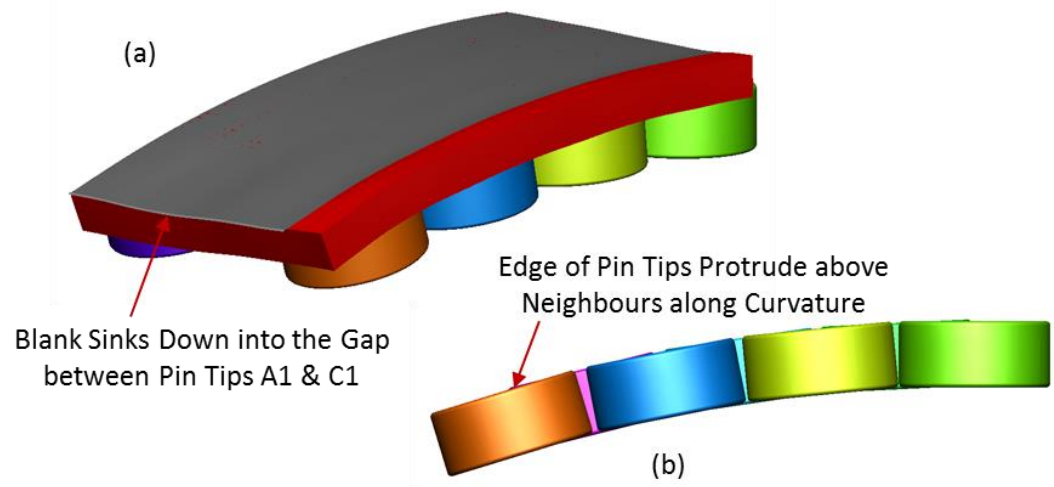

Figure 5-17: (a) The deformed blank sinking into the gap between pin tips A1 & C1 (b) The final position of the pin tips

The contour map relating to the surface accuracy analysis, Figure 5-16 (b) shows that the trimmed blank is deviating from its target shape to a greater degree towards the bottom right-hand corner i.e. its outer corner furthest from the symmetry planes. The contour map relating to the final interpolator thickness, Figure 5-16 (c), shows that compression of the interpolator increases from its centre (the top left-hand corner in this quarter model) to its outer corners (the bottom right-hand corner in this quarter model) over its loaded area. This is due to the effects of hydrostatic

pressure on different regions of the polyurethane interpolator, where expansion of the material in the plane of the sheet is obstructed, by the surrounding material as it is compressed through its thickness. While the effects of hydrostatic pressure on through thickness strain are negligible in an incompressible rubberlike material when it is compressed between a relatively solid punch and die set, in a stretch forming process the load on the interpolator is supplied by the deformable blank and the effect on the interpolator material is similar to that when it is compressed by a uniformly distributed load. The resulting deformed meshes from two PAM-STAMP simulations are shown in Figure 5-18 to demonstrate the effects of hydrostatic pressure on the compression of an interpolator. In both simulations the elements of the meshes used are assigned with the Kaylan D20 Red material model, the nodes at the top surface are locked in translation in the X and Y directions, while the nodes at the bottom surface are locked in translation in the X, Y and Z directions.

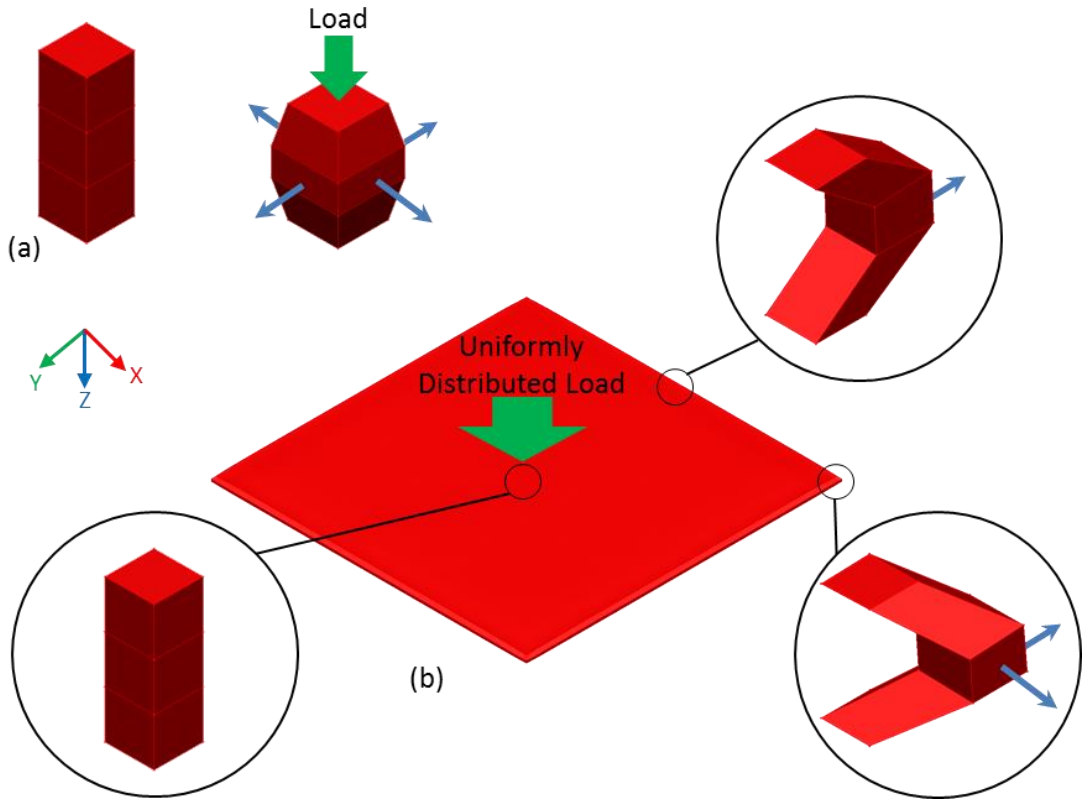

Figure 5-18: Simulations showing the comparative behaviour of (a) a single column of elements and (b) sheet comprised of multiple columns of elements, when subjected to a uniformly distributed load

Figure 5-18 (a) shows how a single column of elements deforms when subjected to a uniformly distributed load. Typical deformation of the central element can be observed where it expands in the positive and negative X and Y directions as the load is applied in the Z direction. Figure 5-18 (b) shows how a sheet comprised from a number of element columns deforms when subjected to a similar uniformly distributed load. In this case it can be observed that the column of elements located at the centre of the sheet shows negligible deformation since expansion in the X and Y directions is obstructed by the surrounding material also under the compressive load. Element columns at the centre of each edge show expansion (or translation) in one direction only, since expansion is obstructed by neighbouring material in the remaining three directions. Element columns at the corners of the sheet, where the through thickness strain is at a maximum, show expansion (or translation) in the two free directions.

Research by the U.S. army (Hoppel, et al., 1995) has shown that the effective elastic modulus of unreinforced polymers increases with an increase in hydrostatic pressure, and that the pressure dependence of the elastic modulus is greater for materials with lower moduli at atmospheric pressure. The surrounding material on an interpolator subjected to compressive load effectively produces hydrostatic pressure on elements within the interpolator as a whole. The influence of the effective hydrostatic pressure on the compression of the interpolator, and so the net shape of the deformed blank over different regions of the reconfigurable die, can be overcome by correcting the pin heights to allow for this phenomenon. Calculating the magnitude of hydrostatic pressure in different regions of the interpolator is complicated by the pattern of loaded sections over the pin tips and unloaded sections over the gaps between pin tips, together with the transition between the flat surfaces on the pin tips and the curved surface on the deformed blank.

Figure 5-19 (a) shows the results of the three analytical techniques described in Section 5.4 for all the simulations employing a single layer of interpolation. Figure 5-19 (b) shows the same data with results for the two

softest materials omitted for clarity. A stoning limit of 0.1 mm is used as this small defect (over a stone length of 70 mm) would be very difficult to detect with the naked eye, while a general sheet metal working tolerance of ±0.2 mm is used for the surface accuracy limit.

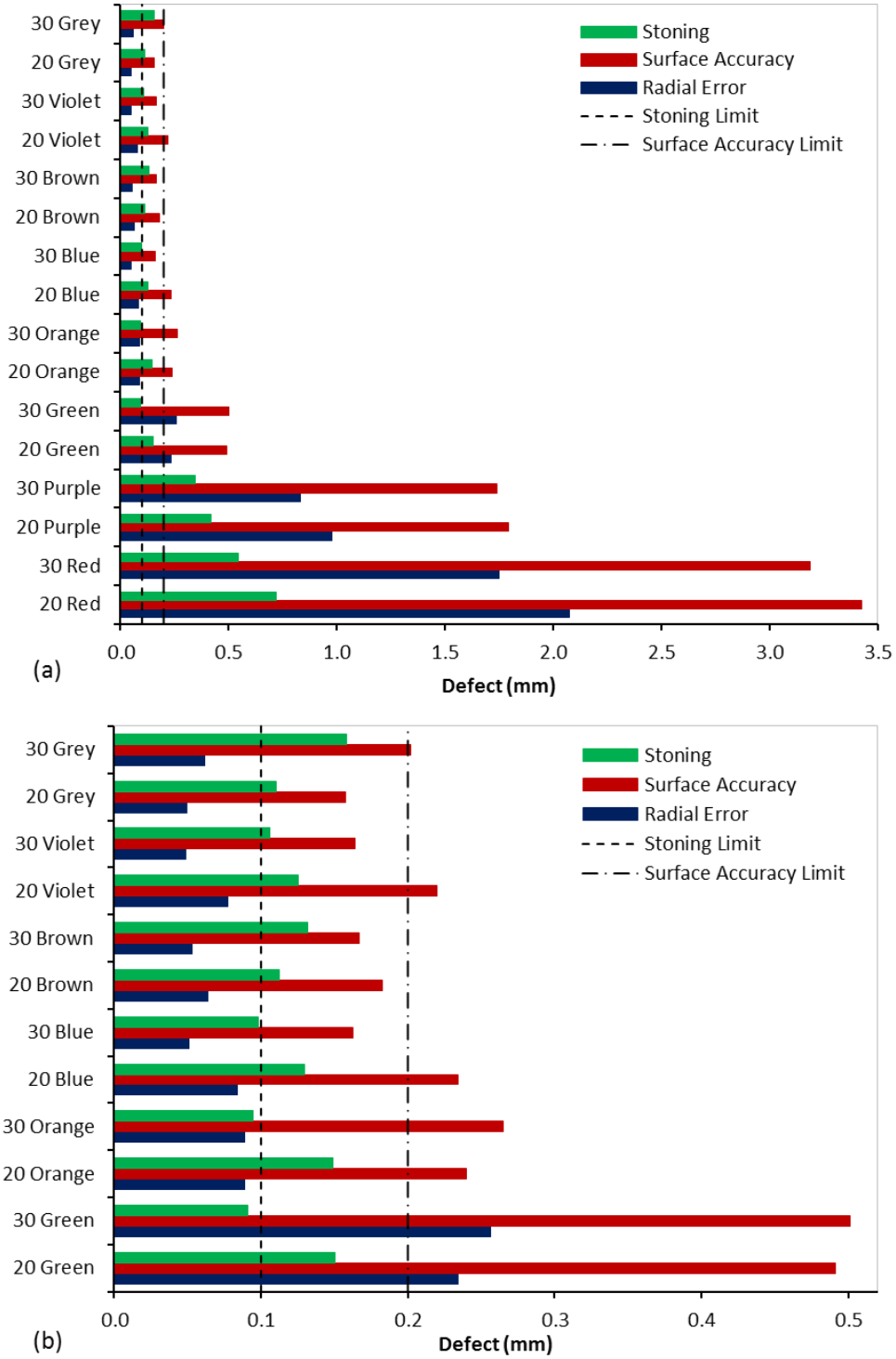

Figure 5-19: (a) Results from the analyses of all the simulations using a single layer of interpolation (b) Results excluding the two softest materials

It can be observed from the simulation results displayed on Figure 5-20 (a) that increasing the thickness of the Kaylan D20 Red interpolator from 20 mm to 30 mm reduces the detected stoning defect from 0.719 mm to 0.547 mm, but this is still well outside the target stoning defect limit. When the D25 Purple material model is used in simulations, stoning defects of 0.419 mm and 0.345 mm are detected for interpolator thicknesses of 30 mm and 20 mm respectively. Again, this is well outside the target stoning defect limit. Neither of these materials offer enough support over the gaps between pin tips to produce parts with sufficiently reduced dimpling. When the D30 Green material model is used in simulations, stoning defects of 0.149 mm and 0.091 mm are detected for interpolator thicknesses of 20 mm and 30 mm respectively. It can be discerned, from the simulation results, that when an interpolator thickness of 30 mm is used, the D30 Green material is the softest material, in the Kaylan D series, that is suitable for producing parts with sufficiently reduced dimpling, when forming the 316L material over a reconfigurable die constructed from circular pivoted pin tips (approximately 70 mm in diameter with a flat surface) in the HCP2 pin arrangement.

It can be observed in the stoning analysis contour map from this simulation, illustrated in Figure 5-20 (a), that the maximum stoning defects are present over the end of the B2 pin tip, and in the overlapping area between each row of pin tips. The stoning defects are reduced slightly towards the centre of the blank where Figure 5-20 (c) shows that the final interpolator thickness is at its greatest and the effective elastic modulus of the interpolator material is greater due to the effects of hydrostatic pressure. The final interpolator thickness (at the centre of pin tips) ranges between 29.79 mm over the A7 pin tip and 29.41 mm over the C1 pin tip. Figure 5-20 (b) shows that the maximum surface accuracy defect is again over the end of the B2 pin tip where loading is increased due to non-tangential contact. Again, greater overall surface accuracy can be observed at the centre of the part with surface accuracy defects increasing towards the outer edges due to the effects of hydrostatic pressure. At the bottom

right-hand corner of the C2C contour map (close to the centre of the C1 pin tip on the trimmed part) a scalar defect of 0.268 mm is detectable between the reference cloud and the cloud generated from the deformed blank, while the radial error analysis shows a defect of -0.265 mm at the outermost node in the same area. Figure 5-20 (d) shows that the major strain distribution pattern is very similar to that observed in the 20 Red simulation.

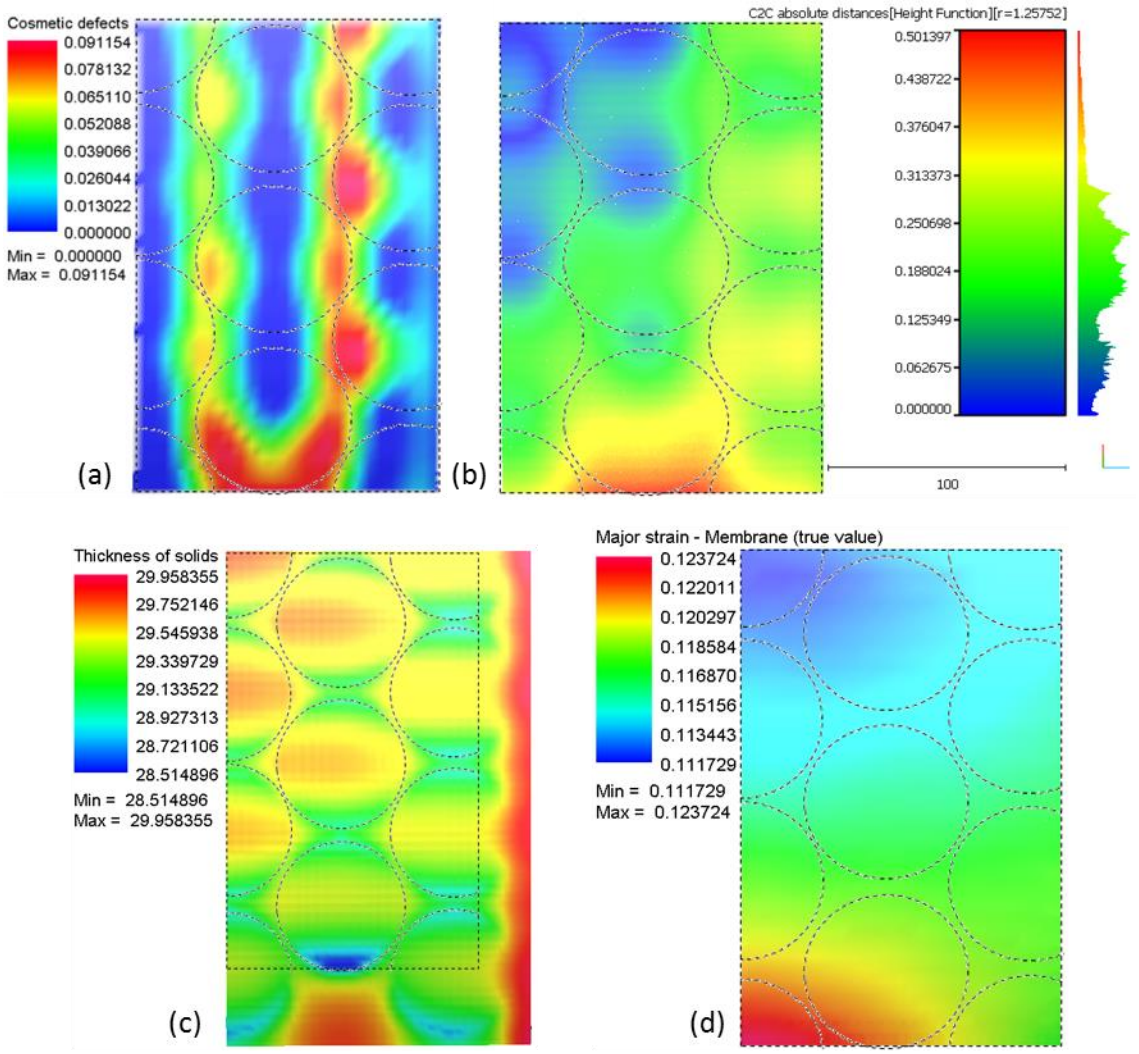

Figure 5-20: The Cosmetic defect (a) C2C absolute distance (b) Thickness of solids (c) and Major strain (d) contour maps for the 30 Green simulation

Referring to the results displayed in Figure 5-19 it can be observed that no simulations using a single layer of interpolation with a thickness of 20 mm produce maximum stoning defects below the stoning defect limit of 0.1 mm. When the interpolator thickness is increased to 30 mm, the simulation using the D30 Green material model shows the smallest maximum stoning defect.

Simulations using the D40 Orange and the D50 Blue material models also show maximum stoning defects below the stoning defect limit, but the maximum recorded defect increases slightly with material hardness (0.095 mm for the Orange material and 0.098 mm for the Blue Material). The simulation using the D60X Violet material model shows a maximum stoning defect just outside the limit (0.106 mm). Only the D50 Blue material show both stoning and surface accuracy (0.163 mm) defects inside their limits without pin height correction for the effects of hydrostatic pressure. Simulations using the D60 Brown and D70X Grey material models show that the maximum recorded stoning defect increases further with increased stiffness.

Simulations using the D60 Brown and D70X Grey material models show an increase in stoning defects when the interpolator thickness is increased rather than the reduction that is observable when using the remaining materials in the Kaylan D series. This is due to the effects of the unloaded strip of interpolator at the outside edge of the blank (along its width) together with the greater hardness and stiffness of these materials. This unloaded strip cannot be avoided since the width of the blank reduces as it is stretched along its length. Figure 5-21 shows the contour maps from the simulation using the D70X Grey material model i.e. the hardest and stiffest of the materials in the Kaylan D series, with an interpolator 30 mm in thickness. It can be observed in the stoning analysis contour map from this simulation, illustrated in Figure 5-21 (a), that the maximum stoning defects are present over the overlapping area between the B and C rows of pin tips. Table 3-9 shows that while the softest interpolator material (D20 Red) is subjected to an average compressive strain to the magnitude of 25.68% at a compressive engineering stress of 1 MPa, the D70X Grey material is only subjected to a compressive strain to the magnitude of 0.43%. Hence the softer interpolator materials deform around the pin tips while the D70X Grey material only deforms at the outer edges of the pin tips (in the stretching direction) as evident from the final interpolator thickness contour map, illustrated in Figure 5-21 (c). The unloaded strip of interpolator

therefore retains its thickness and position relative to the loaded section of interpolator. This results in the deformed blank sitting higher at its outer edge along the width. The surface accuracy (C2C) contour map, illustrated in Figure 5-21 (d), detects a scalar defect of 0.168 mm on outside edge of the trimmed blank closest to the centre of the C3 pin tip, while the radial error analysis shows a defect of 0.170 mm at the outermost node in the same area. Since the magnitude of compression over the loaded section of interpolator (taken as a distance) is greater when thickness increases, the stoning defect caused by the high outer edge is greater for the simulations using an interpolator thickness of 30 mm rather than a thickness of 20 mm for these stiffer materials. Note that the effects of hydrostatic pressure are negligible for the stiffer interpolator materials.

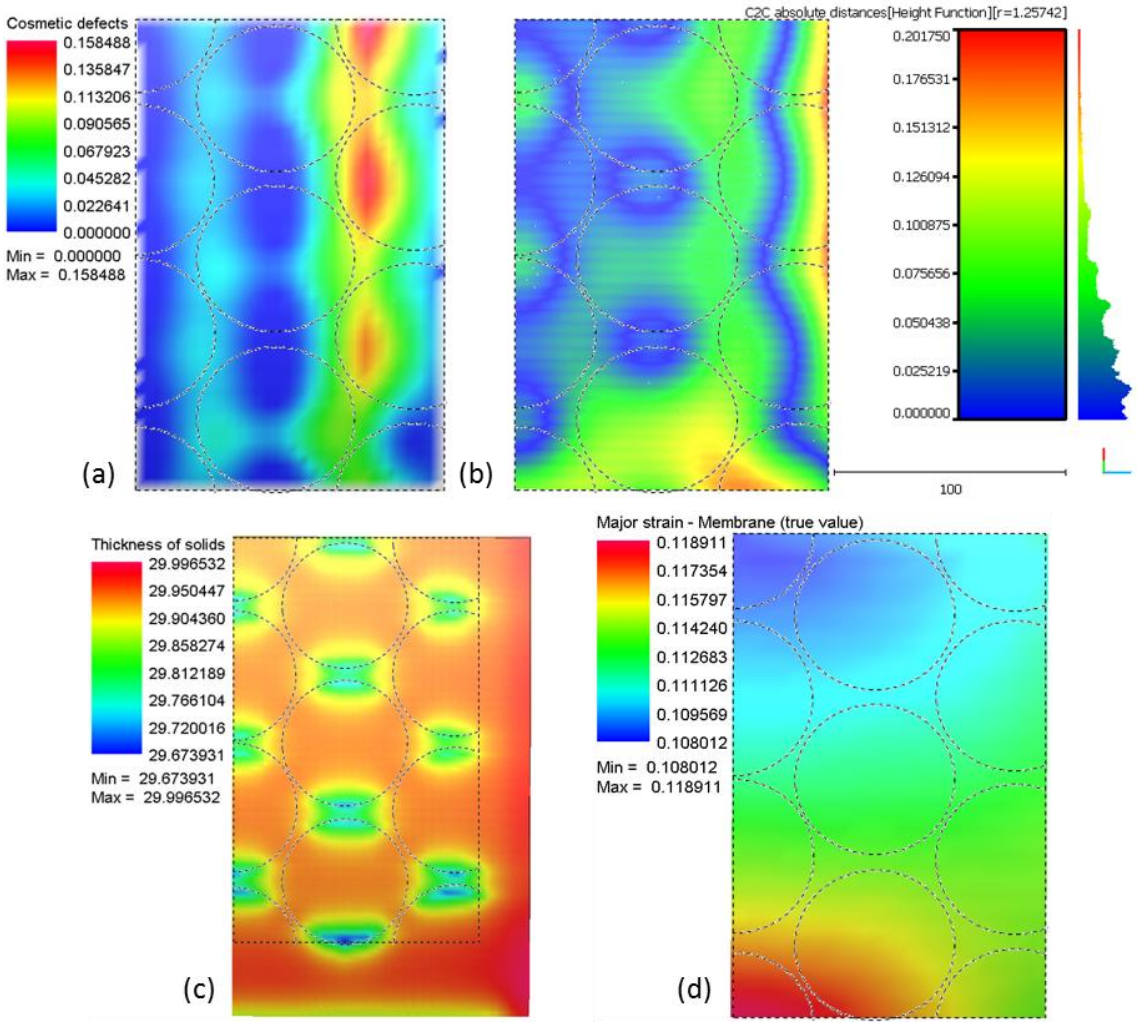

Figure 5-21: The Cosmetic defect (a) C2C absolute distance (b) Thickness of solids (c) and Major strain (d) contour maps for the 30 Grey simulation

The contour maps for the remaining 13 simulations, using a single layer of interpolation, that are not displayed in this section have been included as Appendix L. of this document.

5.6 Pin Height Corrections

In Section 5.5 pin heights are calculated with the assumptions that, the tension in the sheet is constant along the curvature of the part and the interpolator compression is constant over every pin tip in the reconfigurable die. The accuracy of pin height adjustment can be improved by examining these assumptions.

Firstly, the tension in the sheet at different points along its curvature is influenced by friction at the interface between the bottom surface of the part and the top surface of the die (interpolator). The expression used to calculate tension at a given point in a sheet stretched over a curved surface (Marciniak, et al., 2002) is given as;

$$T_i = T_0 e^{\mu\theta_i} \tag{57}$$

where, T_i is the tension in the sheet at a given point, T_0 is initial tension, e is Euler's number, μ is the coefficient of friction and θ_i is the angle between the point of initial tension and the given point expressed in radians. Hence, when the tension calculated with Eq.37 is taken as the initial tension in the sheet, at a point of zero friction at the top quadrant of the die, the angle from a vertical plane to a line intercepting both the centre of curvature and the pivot point of each pin tip can be used to calculate a more accurate magnitude of tension in the sheet over each pin tip.

While using Eq.57 to determine the tension in the sheet over each pin tip results in variable forces acting on the interpolator and hence variable degrees of interpolator compression, where a relatively soft material is used, the effects of hydrostatic pressure will have a greater bearing on the magnitude of interpolator compression over each pin tip. Given the difficulties in calculating the magnitude of hydrostatic pressure over each pin tip outlined in Section 5.5, a numerical pin height correction routine is

used here to overcome the effects of hydrostatic pressure. Corrected pin heights are calculated by replacing the t_f term in Eq.50 with the recorded final interpolator thickness over each pin tip at the end of the stretch stage in simulations of the process.

Figure 5-22 (a) shows the results of the analyses of the trimmed blanks from all the corrected pin height simulations employing a single layer of interpolation 30 mm in thickness. Figure 5-19 (b) shows the same data with results for the two softest materials omitted for clarity. Improvement in the surface accuracy is evident over a number of iterations, where the final interpolator thickness is recorded after each simulation, since the final thickness of the interpolator is dependent (in part) on the pin height used. The two softest materials (D20 Red and D25 Purple) show improvement in surface accuracy over three iterations, but the surface accuracy defect is still greater than the target defect limit. In simulations using the D30 Green material, the target surface accuracy defect limit is achieved after the first iteration, while defect reduction between the second and third iterations is negligible. In simulations using the D40 Orange material, the target surface accuracy defect limit is again achieved after the first iteration, while no defect reduction is evident between the first and second iterations. With the D50 Blue material the original simulation show surface accuracy defects below the specified limit while further defect reduction is evident over the first iteration of the pin height correction routine only. In simulations using the three hardest materials (D70X Grey, D60X Violet and D60 Brown) any surface accuracy defect reduction achieved through the pin height correction routine is negligible.

Since the effects of hydrostatic pressure are greater for materials with lower moduli of elasticity, empirical data form the numerical pin height correction routine, for the three softest materials (D20 Red, D25 Purple and D30 Green), is used to devise a routine for estimating pin height correction to overcome the effects of hydrostatic pressure. Results of the analyses where this empirical routine is used to determine pin heights are also displayed in Figure 5-22.

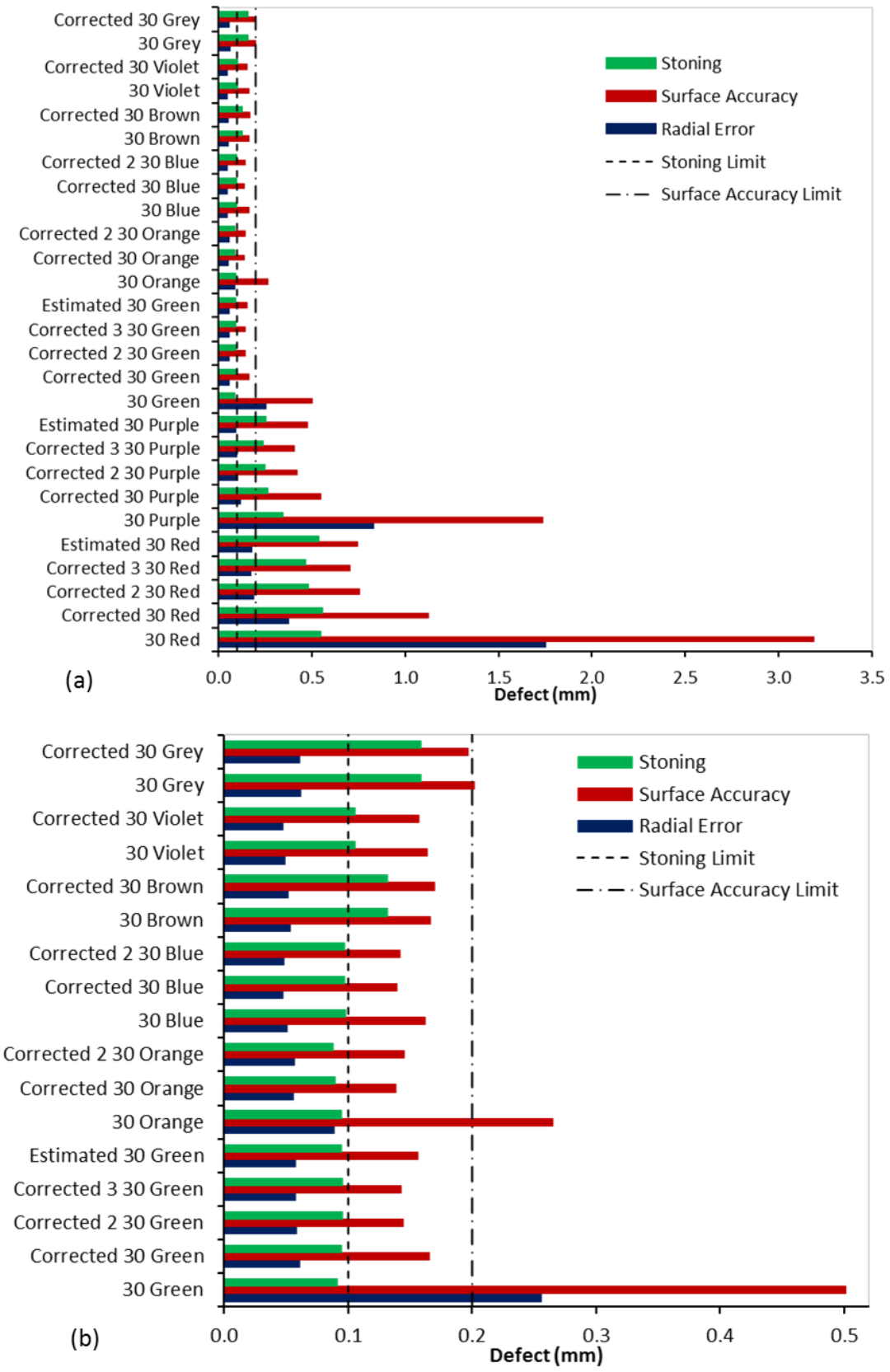

Figure 5-22: (a) Results from the analyses of corrected pin heights using a single layer of interpolation 30 mm thick (b) Results excluding the two softest materials

The empirical routine for correcting pin heights to overcome the effects of hydrostatic pressure begins by correcting the force over each pin tip to account for the effects of friction. Since the force acting on each pin tip is directly proportional to the tension in the sheet (as shown in Eq.38), in a single curvature part the force acting on each pin tip can be corrected using Eq.57 (assuming constant interpolator compression in determining the angle at the pivot point of each pin tip). The average engineering stress in the interpolator can then be calculated as the ratio of force to the area at the top surface of a pin tip. Assuming a linear relationship between the engineering stress and strain in the interpolator material (which holds reasonably true in the Kaylan D series of materials up to the maximum engineering stress of 1 MPa used here), an elastic modulus based on engineering stress and strain can be determined, for each material, and used to determine the average compressive engineering strain in the interpolator over each pin tip. The average true stress in the interpolator over each pin tip can then be determined using the calculated values of engineering stress and strain. The average true stress over the C1 pin tip is corrected to account for the stiffness of the interpolator material by finding the product of the previously calculated true stress and $E^{0.15}$ (where E is the elastic modulus of each material based on true stress and strain at the compressive engineering stress of 1 MPa). Table 5-1 shows the distribution of this calculated average true stress found in the simulations using the interpolator materials D20 Red, D25 Purple and D30 Green with a thickness of 30 mm. Note that in these simulations the interpolator over the pin tips C1, C3, C5 and are not fully loaded since the blank does not completely cover them at the end of the stretch stage of the simulations. Added to this non-tangential contact was detected over pin tip B2, which has a knock-on effect on the loading of pin tips A1 and C1. While there is a definite pattern emerging in the distribution of the calculated true over each pin tip, depending on its position in the reconfigurable die, since only the pin tips A3, A5, A7, B4 and B6 are subjected to typical loading conditions,

there are an insufficient number of pin tips in these simulations to fit an equation to predict the percentage of stress over each pin tip.

A1	A3	A5	A7
99.7%	77.0%	63.9%	50.7%

B2	B4	B6
103.6%	74.9%	64.9%

C1	C3	C5	C7
100%	93.9%	87.5%	82.7%

Table 5-1: Distribution of the calculated average true stress over each pin tip

Since the Mooney Rivlin expression used to describe the relationship between stress and strain in these materials yields a cumbersome equation when solved for true strain, a simple second order polynomial equation (based on the linear relationship between engineering stress and strain) is used to determine the true average strain over each pin tip. To determine the approximate difference between average true strain and true strain at the centre of a pin tip a comparison was made between the heights of two cylindrical figures with diameters equal to that of a pin tip and equal volumes; the first having flat surfaces top and bottom while the second having a flat surface at the bottom but a curved surface with a radius of 750 mm at the top. When the true strain at the centre of each pin tip has been calculated it is simply a matter of converting this to engineering strain to determine the final thickness of the interpolator over each pin tip, before using these values as the t_f term in Eq.50 to estimate pin heights.

When using this empirical routine to predict pin heights for the 30 Red simulation, and comparing compression of the interpolator over the centre of pin tips to that recorded from the most accurate simulation using the numerical pin height correction routine, an average error of 3.0% was found while the greatest error (-5.9% or 0.158 mm) was found over the A1 pin tip. With the 30 Purple simulation an average error of 4.4% was found while the greatest error (+9.2% or +0.088 mm) was found over the A7 pin tip. With the 30 Green simulation an average error of 3.0% was found while the greatest error (+8.0% or +0.039 mm) was found over the A7 pin tip. Note that a negative value indicates that the empirical routine underestimates the

interpolator compression when compared to the best results from the numerical pin height correction routine. Direction is ignored in the calculation of average error values.

For a better understanding of where defects are reduced, using both the numerical and empirical routines, readers are directed to the contour maps relating to the corrected pin height simulations included as Appendix M. of this document.

5.7 Results using Multiple Layers of Interpolation

In this section simulations are named with the total thickness of the combined multiple layers interpolation followed by the colours associated with individual layers (beginning with the interpolator in contact with the pin tips). In the three layer system the thicknesses of individual layers are equal unless otherwise indicated. In the four layer system interpolators 1 and 3 are half the thickness of the remaining interpolators unless otherwise indicated. Where the word 'Glued' is included in the name, this indicates that nodes are shared at the interfaces between interpolators to represent a system where individual layers of interpolation are glued together. Where the word 'Discs' is included in the name models represent a system where the first layer of interpolation comprises of a series of discs attached to the tops of pin tips, as illustrated in Figure 5-13. An asterisk at the end of simulation names indicates that surface tools are used at the interface between interpolators to aid in accurate contact. Since the shell elements used in these surface tools are given a thickness of 0.1 mm, contact surfaces are offset 0.05 mm in both directions normal to surface tools. It should be noted that pin heights are not adjusted to account for this offset.

The simulation representing a system where a 10 mm thick D30 Green interpolator is sandwiched between two layers of the D60 Brown material, also 10 mm in thickness, has been run with and without the aid of surface tools. Figure N-1 (d) shows a comparison of the surfaces representing the trimmed blanks from each of these simulations, where the central nodes at the intersection of the two symmetry planes have been aligned. Results

show a maximum deviation of only 0.016 mm between the two surfaces in this reference position. Figure N-1 (e) shows a comparison of the surfaces, in the positions they finished in at the end of their respective simulations. Results show a maximum deviation of 0.083 mm between the two surfaces in their final simulation positions. This reflects the offsets of the contact surfaces. These values indicate that the use of surface tools has a negligible effect on the stoning analysis results, a small effect on the surface accuracy results where comparisons are carried out in the registered position, and a slightly greater effect on the radial error results where the analysis is carried out in the final simulation position. Results from the analyses of the two simulations show an error of 1.9% in the stoning analysis, 3.7% in surface accuracy analysis and an error of 4.9% between the two radial error analyses.

The remaining contour maps relating to simulations with multiple layers of interpolation that are not displayed in this section are also included in Appendix N. of this document. Note that since the distribution of strain remains relatively constant, in all the trimmed blanks from these simulations, contour maps illustrating major strain are only displayed where space permits their inclusion.

5.7.1 Three Layers of Interpolation

Figure 5-23 shows the results from the analyses of all the simulations using three layers of interpolation. Since the two softest materials in the Kaylan D series (D20 Red and D25 Purple) have been shown to be unsuitable for use over the proposed pin tip system, when using a single layer of interpolation, these materials are excluded for consideration in the multiple layers of interpolation systems. The two softest remaining materials (D30 Green and D40 Orange) are considered here for the inner layer in the three layers of interpolation system. The hardest material in the Kaylan D series (D70X Grey) is a very stiff material which would not be suitable for the drape forming process at greater thicknesses, since the drapeability of a sheet is directly proportional to a material's thickness and

stiffness. Hence this material is only considered, for the multiple layers of interpolation systems, at a thickness of 6 mm or less.

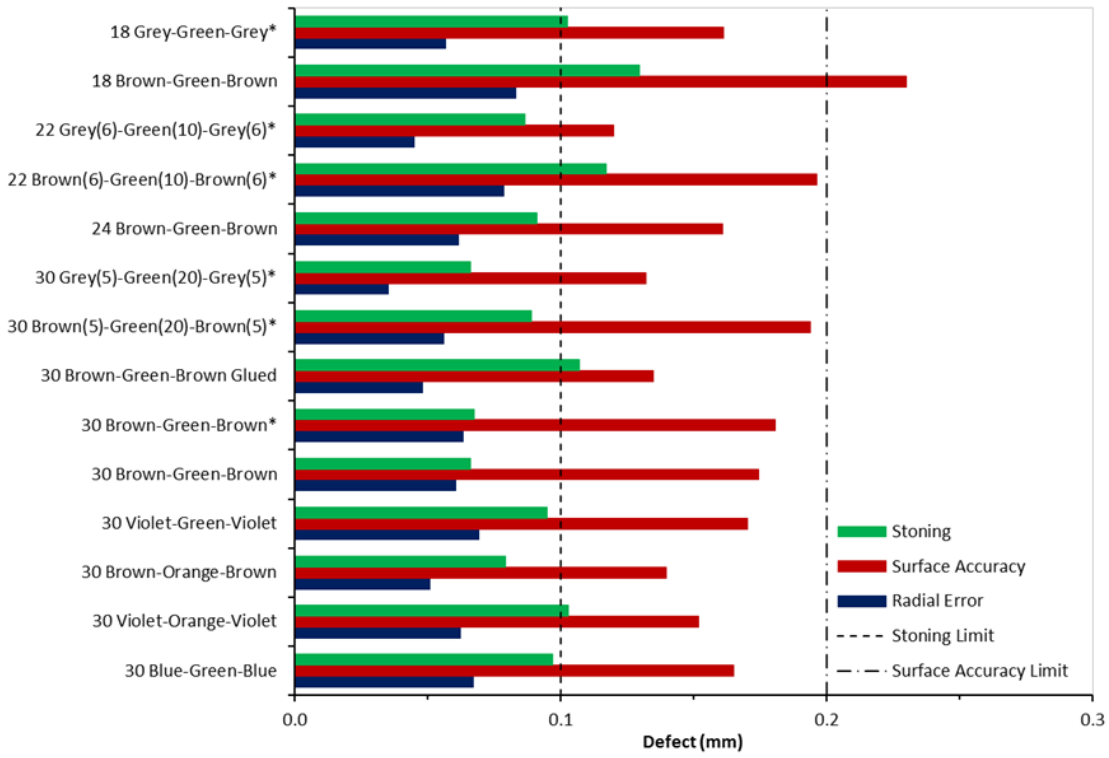

Figure 5-23: Results from the analyses of the simulations using three layers of interpolation

Three relatively hard materials (D50 Blue, D60 Brown and D60X Violet) are considered for the outer layers, in the three layers of interpolation system, with a total interpolator thickness of 30 mm where each layer is of equal thickness. All five combinations simulated (Blue-Green-Blue, Violet-Orange-Violet, Brown-Orange-Brown, Violet-Green-Violet and Brown-Green-Brown) show surface accuracy results less than the target limit, without the need for pin height correction. Where the less stiff materials are used in the outer layers the stoning analyses show very similar results, with defects close to the target limit, (0.097 mm for the 30 Blue-Green-Blue simulation, 0.095 mm for the 30 Violet-Green-Violet simulation and 0.103 mm for the 30 Violet-Orange-Violet simulation). The stoning defect is reduced where the D60 Brown is used in the outer layers and the smallest maximum stoning defect is evident where the softer of the two materials (D30 Green) considered for the inner layer is used (0.066 mm for the 30

Brown-Green-Brown simulation versus 0.079 mm for the 30 Brown-Orange-Brown simulation). Hence the Brown-Green-Brown combination is selected from the initial five combinations for further investigation.

Figure 5-24 shows the contour maps relating to the 30 Brown-Green-Brown simulation. The Cosmetic defects contour map relating to the stoning analysis, illustrated as Figure 5-24 (a), shows that the maximum stoning defect is distributed relatively even in the overlapping areas between the A and B, and the B and C rows of pin tips.

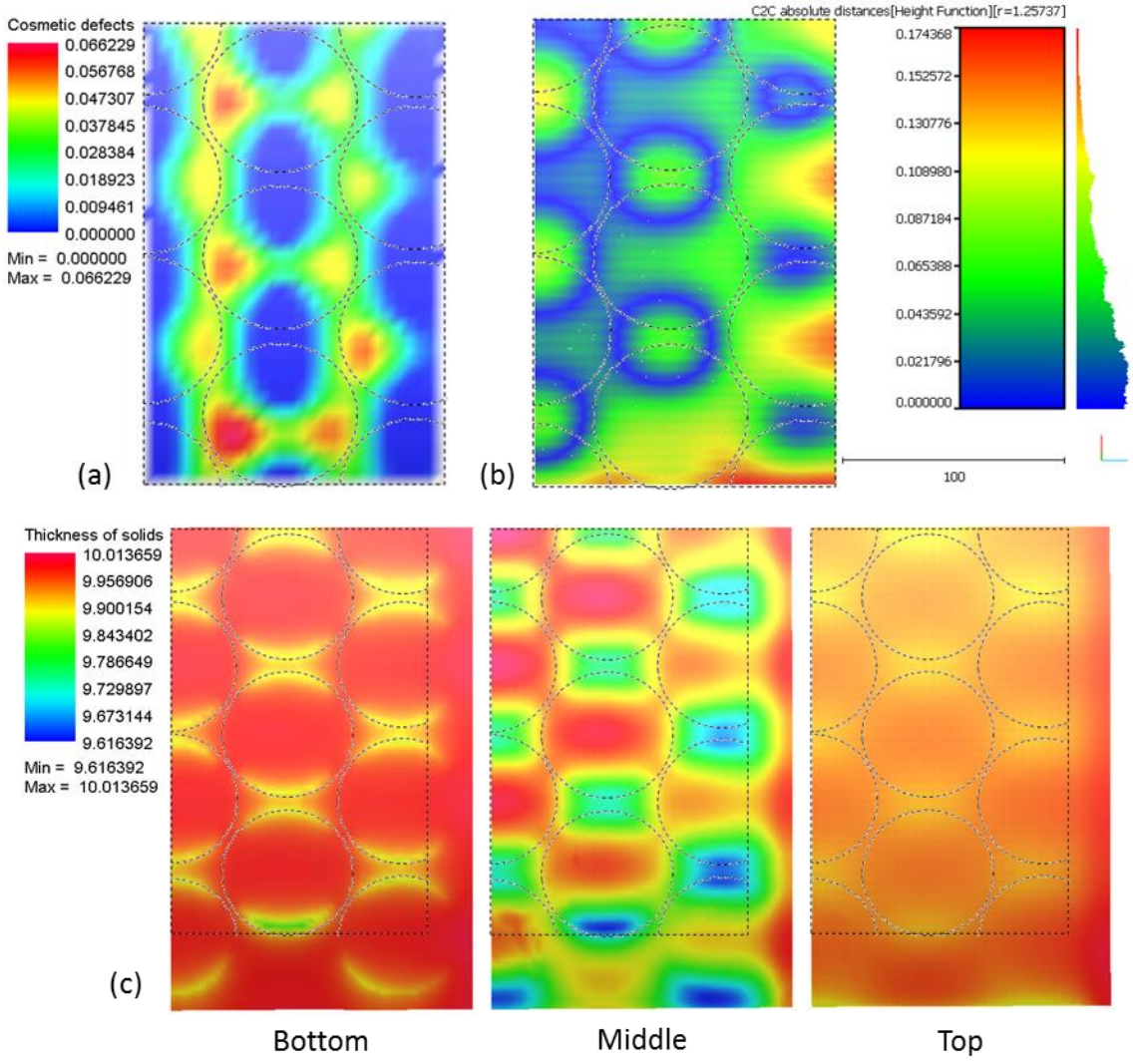

Figure 5-24: The Cosmetic defect (a) C2C absolute distance (b) and Thickness of solids (c) contour maps for the 30 Brown-Green-Brown simulation

The Thickness of solids contour maps, Figure 5-24 (c) show that on the bottom interpolator compression ranges between 0.02 mm and 0.16 mm,

while the top interpolator shows compression ranging between 0.05 mm and 0.09 mm. The middle interpolator made from the softer D30 Green material shows compression ranging between zero and 0.38 mm. This together with the distribution of surface accuracy defects (where the defect increases towards the bottom right-hand corner of the trimmed blank), evident in Figure 5-24 (b), suggest that the overall surface accuracy of a part formed over this system of interpolation could be improved further with compensation for the effects of hydrostatic pressure on the inner interpolator only.

Results of the analyses relating to the 30 Brown-Green-Brown Glued simulation (Figure N-2) are similar to those for a single layer of interpolation where the stiffest materials are used. The maximum stoning defect, which is just greater than the stoning defect limit, is evident in the overlapping areas between the B and C rows of pin tips. Gluing the interpolators together has the effect of increasing the stiffness of the inner softer layer, since the material in this interpolator, close to its interfaces with the outer interpolators, is restricted from expanding (in the plane of the sheet) as it is being compressed.

Results from the simulation where the thickness of the inner layer is increased to 20 mm and the thicknesses of the outer layers are reduced to 5 mm (30 Brown(5)-Green(20)-Brown(5)) show an increase in both the stoning and surface accuracy defects (0.089 mm and 0.194 mm respectively), although they both remain below their target limits. Where the D70X Grey material is used for the outer interpolators (30 Grey(5)-Green(20)-Grey(5)*), the stoning defect detected is similar to that detected in the 30 Brown-Green-Brown simulation (0.066 mm). Figure 5-25 shows the contour maps relating to the 30 Grey(5)-Green(20)-Grey(5)* simulation. It is observable from the Cosmetic defects contour map, illustrated in Figure 5-25 (a), that the stoning defects are slightly higher in the overlapping area between the B and C rows of pin tips than in a similar area between the A and B rows of pin tips. Figure 5-25 (b) shows a relatively small surface accuracy defect of 0.132 mm mostly due to the improved fit around the B2 pin tip. It should be

remembered that since surfaces are used at the interfaces between interpolators in this simulation the surface accuracy defect is susceptible to an error when comparing values to simulations where surfaces are not used.

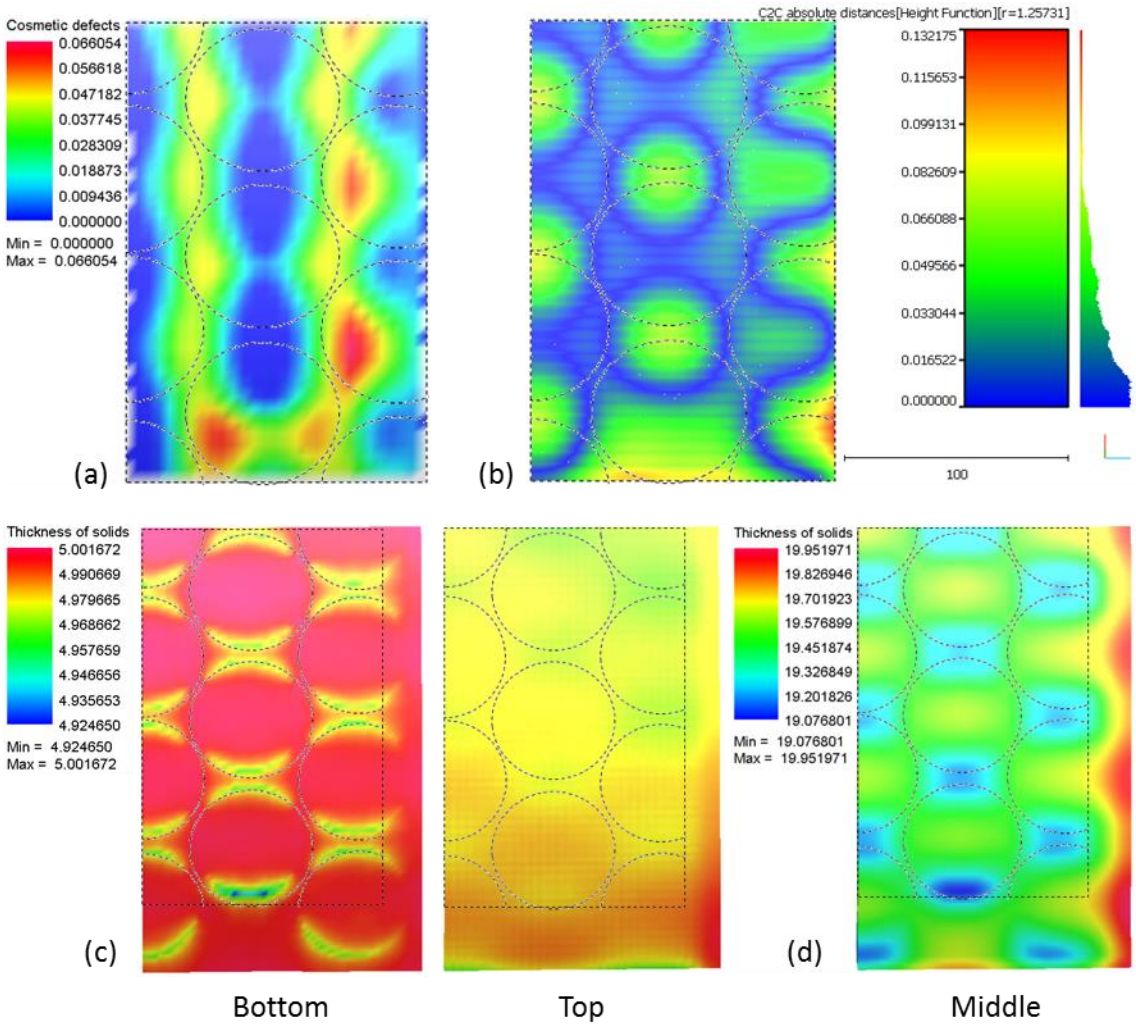

Figure 5-25: The Cosmetic defect (a) C2C absolute distance (b) Thickness of solids-5 mm (c) and Thickness of solids-20 mm (d) contour maps for the 30 Grey(5)-Green(20)-Grey(5)* simulation

The Thickness of solids-5 mm contour maps, illustrated in Figure 5-25 (c), show relatively consistent compression (especially at the centre of pin tips) of the top and bottom interpolators. This is to be expected since the stiffest material is used. The Thickness of solids-20 mm contour map, illustrated in Figure 5-25 (d), also shows consistent compression of the middle interpolator at the centre of pin tips. Final interpolator thickness ranges from 19.56 mm at the centre of the B2 pin tip to 19.62 mm at the centre of

the C3 pin tip. This is an unexpected phenomenon which can be attributed to better bending of the thin bottom interpolator onto the flat surfaces of pin tips. This unexpected phenomenon is also observable in Figure N-7 (d) which relates to the thickness of the middle interpolator from the 30 Brown(5)-Green(20)-Brown(5) simulation.

Results from the 24 Brown-Green-Brown simulation show that stoning and surface accuracy defects (0.092 mm and 0.166 mm respectively) below the defect target limits can also be achieved when three interpolators 8 mm in thickness are used. Results from the 18 Brown-Green-Brown simulation show that stoning and surface accuracy defects below the defect target limits can no longer be achieved when three interpolators 6 mm in thickness are used. Where the D70X Grey material is used for the outer interpolators, at this thickness (18 Grey-Green-Grey*), the stoning defect detected (0.103 mm) is just above the target limit.

Where the D60 Brown material is used for outer interpolators of 6 mm in thickness and the D30 Green material is used for an inner interpolator of 10 mm in thickness, the maximum stoning defect detected is again outside the target limit. Where the D70X Grey material is used for the outer interpolators, at this thickness (22 Grey(6)-Green(10)-Grey(6)*), both the stoning and surface accuracy defects (0.086 mm and 0.12 mm respectively) are below the target defect limits. This overall interpolator thickness of 22 mm is the thinnest found here, where the target defect limits are achieved using the three layers of interpolation system. Figure 5-26 shows the contour maps relating to the 22 Grey(6)-Green(10)-Grey(6)* simulation. Again the Cosmetic defects contour map relating to the stoning analysis, illustrated as Figure 5-26 (a), shows that the maximum stoning defect is distributed relatively even in the overlapping areas between the A and B, and the B and C rows of pin tips. Figure 5-26 (b) shows the small maximum surface accuracy defect distributed in the areas between the pin tips. Note that while the radial error analysis detects a defect of 0.107 mm between the C1 and C3 pin tips, indicating that a high spot exists here, a defect of minus 0.089 mm is detected at the end of the B2 pin tip (next to the A1 pin

tip), indicating a dip. Since surfaces are also used in this simulation, the surface accuracy defect is again susceptible to an error when comparing values to simulations where surfaces are not used. Once again the Thickness of solids-6 mm contour maps, illustrated in Figure 5-26 (c), show relatively consistent compression to a small magnitude, at the centre of pin tips, on the top and bottom interpolators. The Thickness of solids-10 mm contour map, illustrated in Figure 5-26 (d), also shows consistent compression of the middle interpolator at the centre of pin tips. Final interpolator thickness ranges from 9.80 mm close to the centre of the A1 pin tip to 9.84 mm close to the centre of the C1 pin tip.

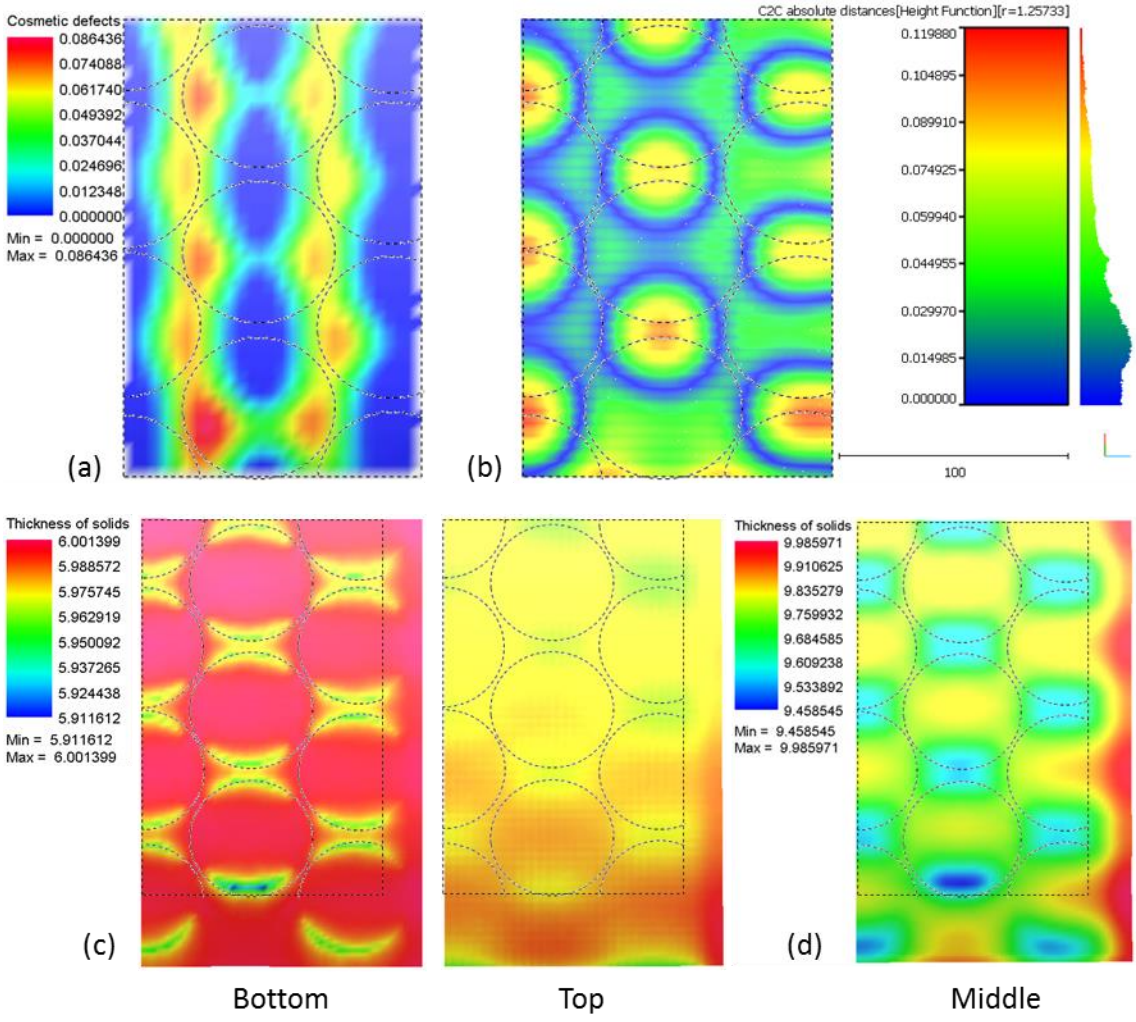

Figure 5-26: The Cosmetic defect (a) C2C absolute distance (b) Thickness of solids-6 mm (c) and Thickness of solids-10 mm (d) contour maps for the 22 Grey(6)-Green(10)-Grey(6)* simulation

5.7.2 Four Layers of Interpolation

Figure 5-27 shows the results of all the analyses relating to simulations of the lab scale process using four layers of interpolation. The smallest maximum stoning defects (0.065 mm) are present in the trimmed blanks from the 30 Green-Brown-Green-Brown and 30 Green(5)-Grey(5)-Green(15)-Grey(5)* simulations. Only the simulations representing models where the individual sheets in the interpolation system are glued together, and the 18 Green-Brown-Green-Brown simulation, show maximum stoning defects above the target limit. The 18 Green-Brown-Green-Brown simulation also shows maximum surface accuracy defects above the target limit. The 18 Green-Grey-Green-Grey simulation shows maximum stoning and surface accuracy defects (0.097 mm and 0.159 mm respectively) below the target limit. This is the system with the smallest overall interpolator thickness (18 mm) where the analyses have uncovered maximum stoning and surface accuracy below the target limits. Yet since the maximum stoning defect detected is only 0.003 mm below the limit, repeatability of achieving acceptable flatness in formed parts would be questionable.

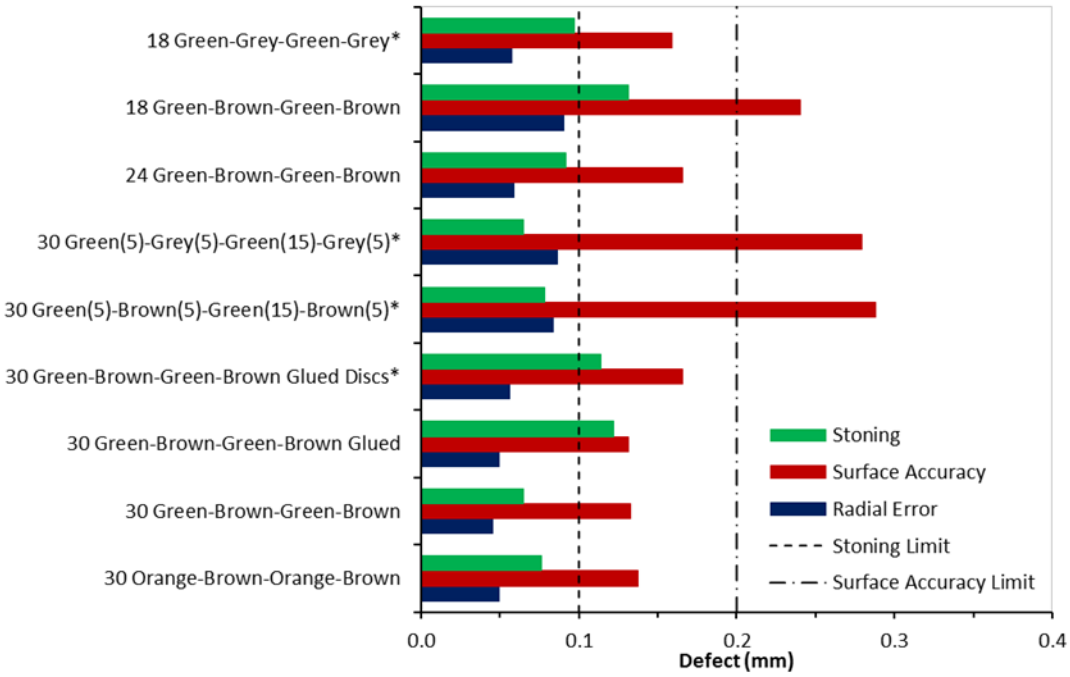

Figure 5-27: Results from the analyses of the simulations using four layers of interpolation

All but one (30 Green-Brown-Green-Brown Discs*) of the systems relating to the analytical results shown in Figure 5-27 have a three layer of interpolation equivalent. In the systems where three layers of interpolation of equal thickness are used, the middle interpolator is simply sliced in two (through its thickness) to give an additional interpolator placed at the bottom in contact with the pin tips. In the systems where a 20 mm thick interpolator is sandwiched between two interpolators 5 mm in thickness, the thickness of the middle interpolator is reduced to 15 mm to give an additional interpolator (5 mm in thickness) placed at the bottom in contact with the pin tips. It should be noted that while results from the 30 Brown(5)-Green(20-Brown(5)* and 30 Grey(5)-Green(20-Grey(5)* simulations show that compression of the thicker interpolator is relatively consistent over all the pin tips (see Section 5.7.1), results from their equivalent four layer of interpolation systems do not show this consistency of compression in the thicker interpolators [see Figure N-15 (d) and Figure N-17 (d)]. Hence the surface accuracy defects detected in the 30 Green(5)-Brown(5)-Green(15)-Brown(5)* and 30 Green(5)-Grey(5)-Green(15)-Grey(5)* simulations are much greater than those for their equivalent three layer of interpolation systems, and are indeed above the surface accuracy target limit, without pin height compensation for the effects of hydrostatic pressure.

Figure 5-28 shows a comparison of the maximum stoning defects detected in equivalent three and four layers of interpolation systems. In five out of eight cases the four layers of interpolation systems showed a small reduction in the maximum stoning defects detected in their three layers of interpolation system equivalents. The greatest reduction (0.011 mm) is observable in the 30 Green(5)-Brown(5)-Green(15)-Brown(5) system over the equivalent 30 Brown(5)-Green(20)-Brown(5) system. Two of the remaining three comparisons show a small increase (0.001 mm) in the maximum stoning defect detected in the four layers of interpolation systems over that evident in their three layers of interpolation system equivalents. The maximum stoning defect detected in the 30 Green-Brown-Green-Brown

Glued system is 0.015 mm greater than the equivalent 30 Brown-Green-Brown Glued system. The 30 Green-Brown-Green-Brown Glued Discs* simulation revealed a maximum stoning defect of 0.114 mm, which is almost exactly half way between those detected in other afore mentioned systems. The small differences in the magnitude of stoning defects, revealed in these comparisons, can be taken as an indication that any advantage or disadvantage that the four layers of interpolation system has over the three layers of interpolation system is negligible. The lack of correlation between the increase or reduction in the magnitude of stoning defects, revealed in these comparisons, can also be viewed as an indication that the SMP (symmetric multiprocessing) double precision solver and/or the simulation setup (where 5 mm square shell elements are used in the blank and volume elements 2.5 mm square in the XY plane are used in the interpolators) are of insufficient precision to give accurately capture small changes in part flatness, where a number of volume tools assigned with Mooney Rivlin materials are in contact.

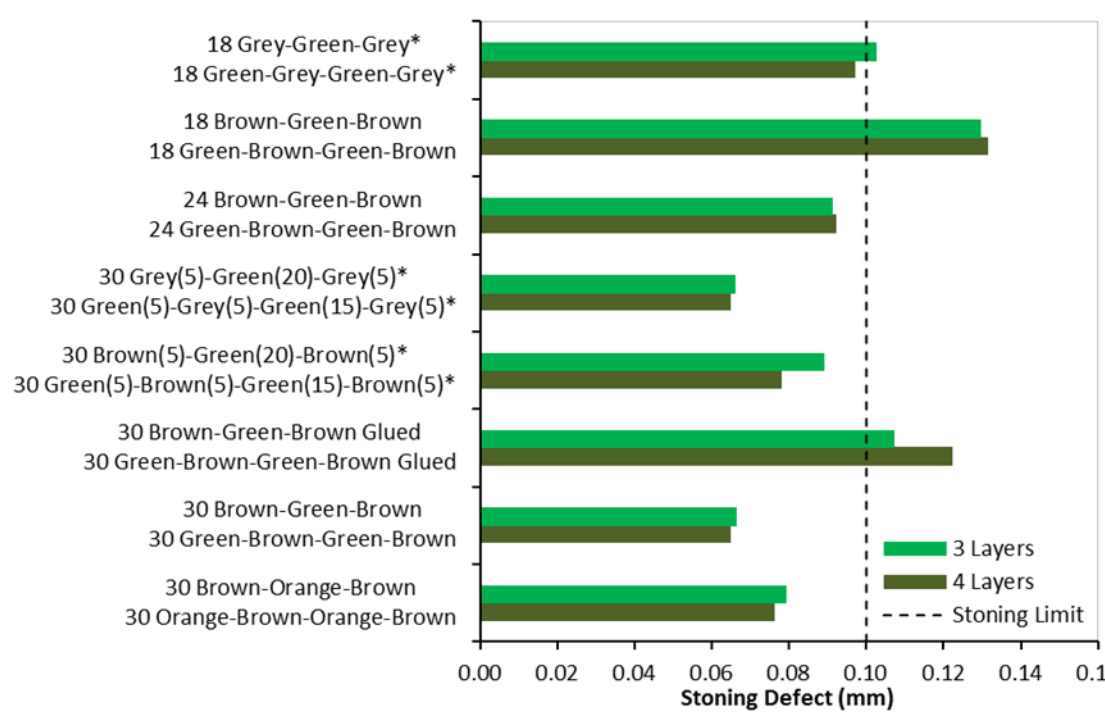

Figure 5-28: Stoning comparison between the three and four layers of interpolation systems

It should be noted that two additional simulations representing systems where discs are attached to the top of pin tips were attempted during this project. While both these simulations appeared to run successfully, closer inspection (with the aid of section views) during analyses of the results, from the 30 Green(5)-Brown(5)-Green(15)-Brown(5) Discs* and the 30 Green(5)-Grey(5)-Green(15)-Grey(5) Discs* simulations, revealed that penetration had taken place between the bottom interpolator sheet and the outer edge of the disc attached to the top of the B2 pin tip (see Figure 5-29). This penetration is much more conspicuous in the simulation shown in Figure 5-29 (b), where the stiffer D70X Grey material is in contact with the D30 Green material assigned to the cylindrical volume tools representing the interpolator discs. The contour maps relating to the analyses of these two simulations (Figure N-16 and Figure N-18) show that penetration only occurred at the area of the highest contact pressure, where non-tangential contact is evident.

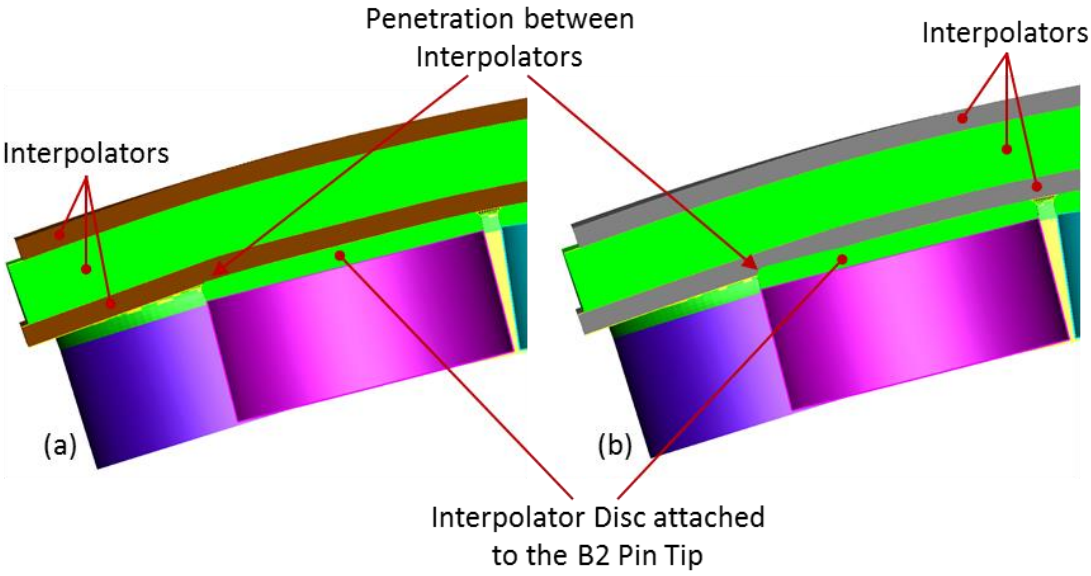

Figure 5-29: Penetration at the outer edge of the interpolator disc attached to the B2 pin tip in both the 30 Green(5)-Brown(5)-Green(15)-Brown(5) Discs* and the 30 Green(5)-Grey(5)-Green(15)-Grey(5) Discs* simulations

5.8 Simulation Validation

Results from this series of simulations are validated through comparison of trimmed blanks obtained from physical tests to the trimmed blanks from the corresponding PAM-STAMP simulations. Pin heights, for the physical tests, are set on a bench with the aid of a Vernier height gauge (as shown in Figure 5-30) before the pins are located in the AMFOR lab scale machine's pin box. Although the Vernier scale allows measurement to the nearest one hundredth of a millimetre, it is difficult to claim pin height accuracy better than ±0.2 mm with this manual setting routine. This is due to inconsistency of compression between the pin tip, insert and ball stud during the setting routine, inconsistency in maintaining a 90° angle between axes of the threaded rods and the base of the locating nuts during the manufacture of the pins, and the possibility that dirt particles can get trapped between the locating nut and base of the pin box when the pins are located in the reconfigurable die. It should also be noted that, due to the excessive minimum height of the pins, it was not possible to maintain tangency of the blank at the edge of the die when the total thickness of the interpolator used was 30 mm.

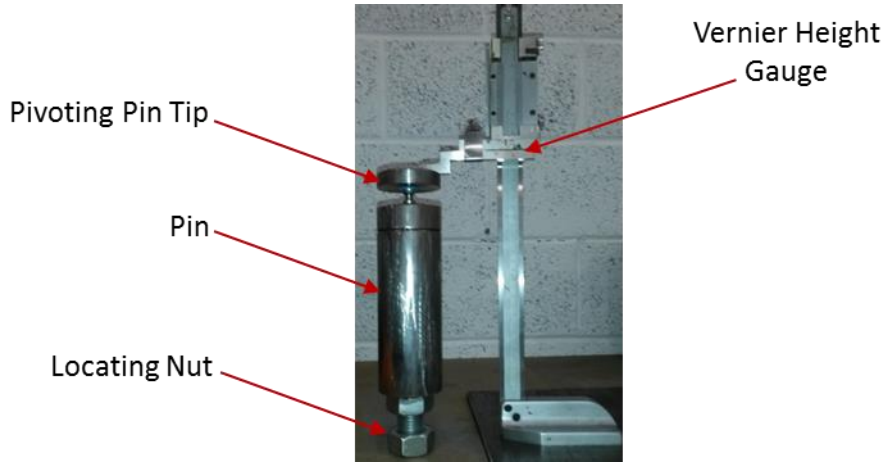

Figure 5-30: Method used to set the heights of pins for the practical tests

Four different systems of interpolation are examined in this validation. Firstly, two single layer of interpolation systems employing the Kaylan D20 Red polyurethane material, 20 mm in thickness, and the Kaylan D30 Green material, 30 mm in thickness. These tests are referred to here as 20 Red and

30 Green, respectively. Then a three layer of interpolation system is employed where a layer of the D30 Green material is sandwiched between two layers of the D60 Brown material, all 10 mm thick. This test is referred to here as 30 BGB. Finally, a four layer of interpolation system is employed where a 5 mm thick layer of the D30 Green material, is in contact with the pin tips, followed by a 10 mm thick layer of the D60 Brown material, followed by a second 5 mm thick layer of the D30 Green material and topped off with a second 10 mm thick layer of the D60 Brown material. This test is referred to here as 30 GBGB. Each system is used in the stretching of a 316L stainless steel blank, 0.88 mm thick, to an approximate strain of 10%, at a 750 mm radius of curvature. Each blank is 310 mm in width, 1250 mm in length and has been cut at 90° to the rolling direction of the sheet.

It should be noted that when the AMFOR lab scale machine was first assembled, the eccentric cam system gripped the thin sheet well. These tests were carried out three years later. In the interim the machine has been used to stretch a variety of materials of much greater thickness than that used here. This has had an impact on the surface quality and straightness of the gripping cams and as a result slippage was encountered between the blank and cams during these tests. To overcome the slippage, it was necessary to place lengths of emery cloth between the blanks and cams. Residual slippage led to the necessity of re-gripping the blanks up to three times in order to attain the magnitude of strain required here. Crosshairs were drawn at the centre of the blanks to aid in locating them central on the die. This re-gripping procedure increased the difficulties encountered in keeping the blanks at a central position during the stretching process.

When the required magnitude of strain was reached deformed blanks were held in tension, for up to 5 minutes, so that their top surfaces could be scanned in situ, using the DAVID SLS-1 structured light scanning system, from DAVID Vision Systems GmbH.. Figure 5-31 shows the scanning process used to capture a 3D image of the deformed blanks for each test. Structured light scanning is a type of 3D scanning where a known pattern is projected onto an unknown surface. Through analysis of the deformation in

the pattern visible on the part being scanned, software can reconstruct the 3D surfaces of the part in a virtual environment. The DAVID SLS-1 system uses a video projector, mounted on a tripod, to project a number of striped patterns onto the object as it is being scanned. A digital camera, also mounted on the tripod, monitors the part from a different viewpoint, capturing images of each deformed pattern before the DAVID software computes a 3D mesh of the surface. A comparison website, pertaining to additive manufacturing, reports the accuracy of images obtained from the DAVID SLS-1 system as being up to 0.05% of the scan size (van West, 2017). Since the area over the die, with an approximate length of 450 mm, is being scanned the finest accuracy that can be claimed here is ±0.225 mm. A series of bands are visible on all the 3D surfaces from the scans presented here. These bands can be attributed to movement of the blanks during the scanning process, which takes approximately 30 seconds to complete. It has been observed during the cyclic compression tests carried out on the Kaylan materials (see Section 3.5.2) that the final magnitude of compressive strain in samples was time dependent. Since the blanks are held in tension, the interpolators continue to compress during the scanning process, and hence the scanned surface is actually still in motion.

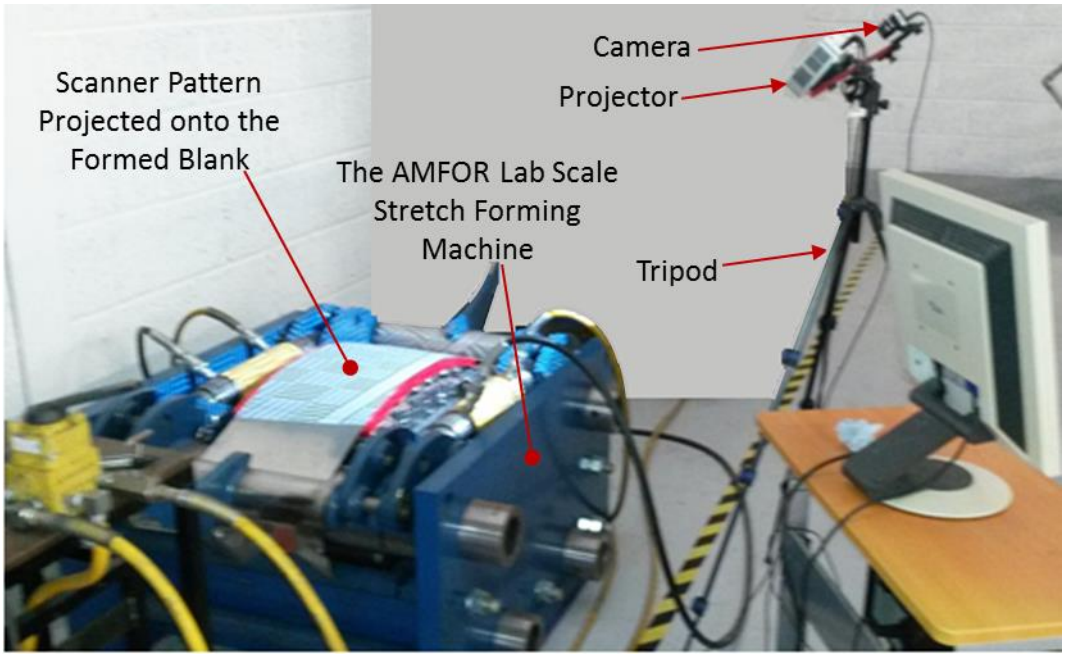

Figure 5-31: Scanning of the deformed surfaces from the practical tests

The scanned surfaces were saved as STL meshes and imported into the CloudCompare for analysis. It was found that the final thickness of the trimmed parts obtained from the corresponding simulations ranged between 0.819 and 0.829 mm, depending on the magnitude of strain observed at different positions on the part. Since the blank meshes represent a surface at the centre of the material thickness, the surfaces representing the trimmed parts were offset by 0.41 mm, before being saved as STL meshes and imported into the CloudCompare for comparison to the scanned surfaces. Each mesh representing a scanned surface was repositioned, through a series of translations and rotations, to approximately align with their corresponding simulation mesh before being trimmed to the approximate dimensions of the simulation mesh. Note that since the single curvature part contains two symmetry planes, only a quarter of the surfaces were used in comparisons. Each mesh was converted into a point cloud with 5,000,000 vertices before the final alignment was carried out with the use of the fine registration tool. Contour maps depicting the results from comparisons of the surfaces obtained from the 20 Red, 30 Green and 30 BGB tests, to those from their corresponding simulations, are shown as Figure 5-32 Figure 5-33 and Figure 5-34, respectively, while the contour map relating to the 30 GBGB test is shown in Figure O-1 of Appendix O.

It is evident from Figure 5-32 that the two surfaces relating to the 20 Red test and simulation align to a maximum deviation of approximately ± 0.4 mm over the majority of the part. A maximum misalignment of approximately ± 0.8 mm is evident at the outer edges of the part (right and bottom areas of the contour map). This is an indication that the simulation underestimated the uneven compression of the interpolator, due to the effects of hydrostatic pressure, when the softest of the Kaylan materials is used. There is a similar maximum misalignment evident over the A3 pin tip (see Figure 5-5 for pin tip designations). This is an indication that the height of the A3 pin was not set accurately. It can also be noted that the magnitude of deviation between the surfaces is not consistent over main body of the part (central area of the contour map). This can be attributed to

the soft interpolator material compressing around the pin tips, to grip them, and actually rotate them about their pivot points, during the stretching process where the interpolator expands in the plane of the sheet. The effects of this phenomenon were removed from the simulations by increasing the inertia of the pin tips by a factor of 10. In hindsight, this inertia factor could be reduced (at least where the softer materials are used for the interpolator).

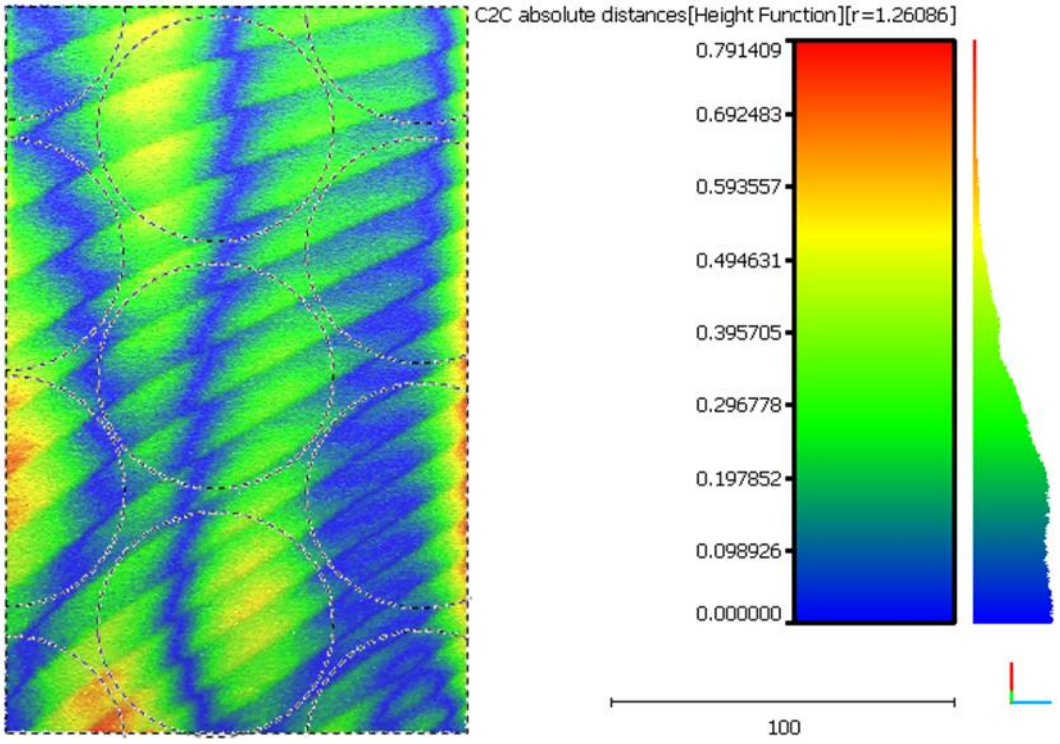

Figure 5-32: A contour map showing deviation of the trimmed surface from a scan of the 20 Red practical test to that from the corresponding simulation

Figure 5-33 shows a comparison of the two surfaces relating to the 30 Green test and simulation. The consistency of the magnitude of misalignment is relatively good over the body of the part. A maximum deviation of approximately ± 0.3 mm is evident over the majority of the part. A notable exception is evident at the outer edge of the part, where the relatively soft interpolator has been pulled down between the A1 and C1 pin tips. This is due to the non-tangential contact, at the edge of the die, discussed earlier in this section.

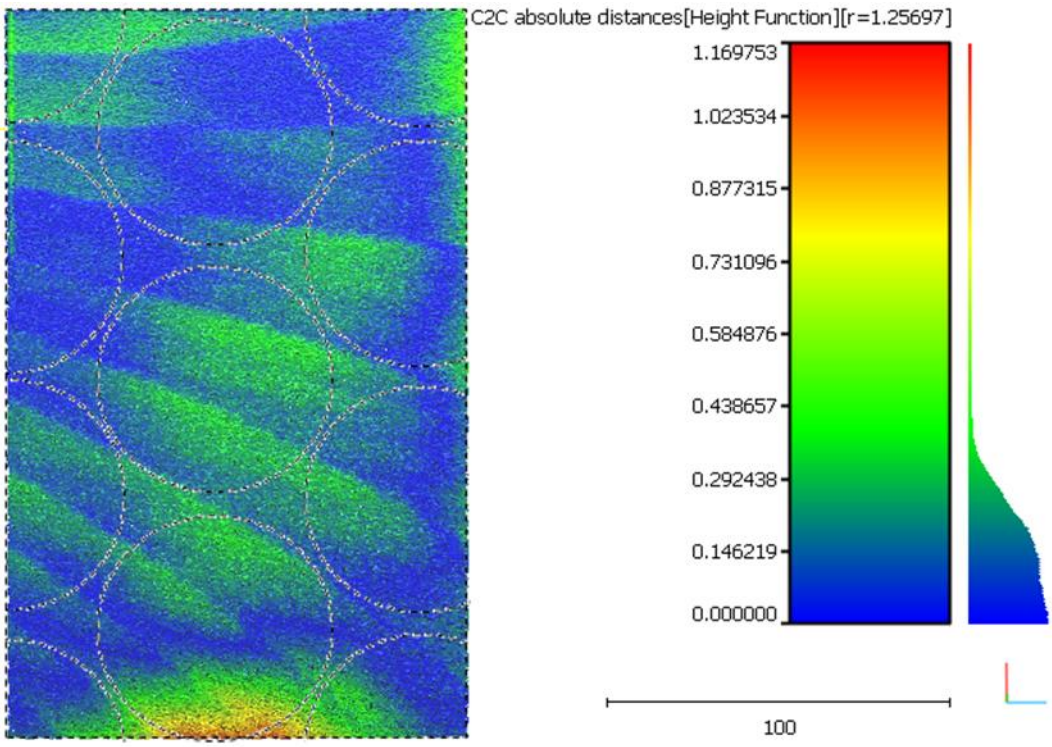

Figure 5-33: A contour map showing deviation of the trimmed surface from a scan of the 30 Green practical test to that from the corresponding simulation

Figure 5-34 shows a comparison of the two surfaces relating to the 30 BGB test and the 30 Brown-Green-Brown simulation. Again the consistency of the magnitude of misalignment is relatively good over the body of the part. A maximum deviation of approximately ± 0.2 mm is evident over the majority of the part. An exception is evident over the A7 pin tip, indicating that this pin has been set slightly high. Again the maximum deviation of alignment is evident at the gripping end of the part, due to the non-tangential contact. In contrast to the results relating to the 30 Green comparison, in this comparison the greater deviation is spread over the last three pin tips (A1, B2 and C1). This can be attributed to the stiffer B60 Brown Kaylan material's greater resistance to bending. It can be noted from a comparison of Figure O-1 (relating to the 30 GBGB test) and Figure 5-34 that both the contour patterns and magnitude of deviation from alignment are very similar. This is in agreement with the analysis of the simulation results, where no improvement of surface quality was found when a fourth softer layer of interpolation was used in contact with the pin tips.

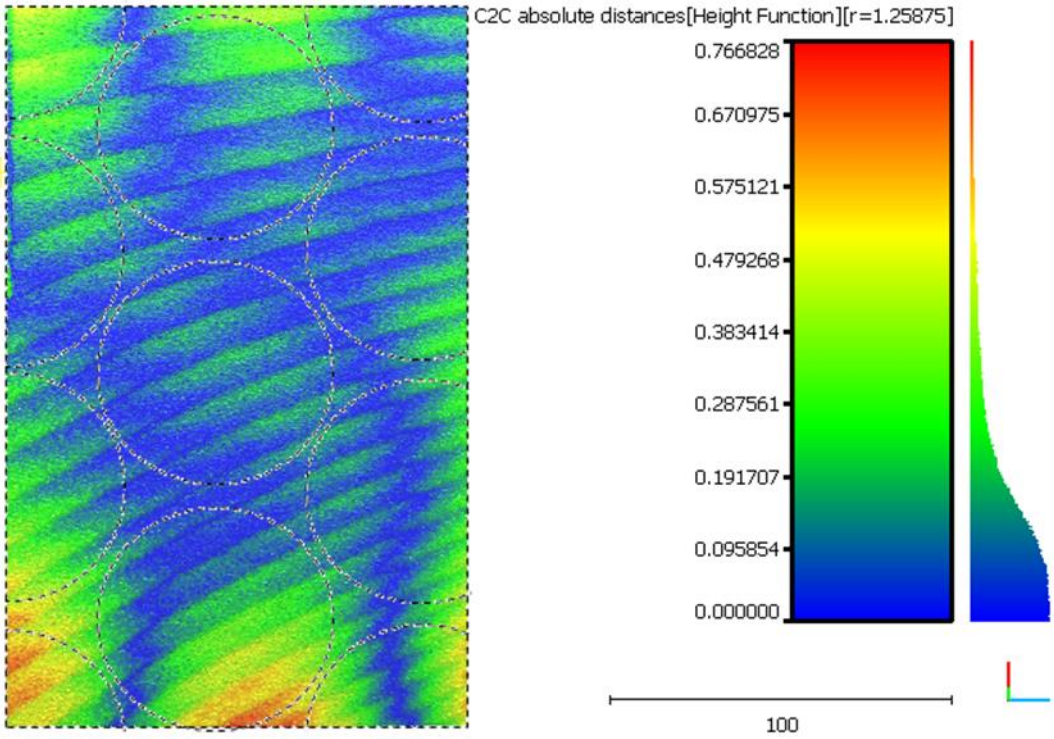

Figure 5-34: A contour map showing deviation of the trimmed surface from a scan of the 30 BGB practical test to that from the corresponding simulation

A second analytical method is included here where the stoning results from the simulations is compared to results from stoning analyses of the scanned surfaces from the practical tests. Since it is possible to import the STL meshes, obtained from the scanning process, directly into the PAM-STAMP software, both sets of stoning analyses have been carried out under exactly the same conditions.

Figure 5-35 shows the results from the stoning analysis of the trimmed surface from the 20 Red simulation (a) adjacent to the results from the stoning analysis of the trimmed scanned surface from the 20 Red practical test. The magnitude of the stoning defects between pin tip rows B and C is approximately 0.2 mm in both the surfaces from the simulations and the practical tests. While the magnitude of the stoning defects between pin tip rows A and B is also approximately 0.2 mm on the surface from the simulation, it ranges approximately between 0.6 and 0.7 mm on the surface from the practical test. This can be attributed to the pin tips rotating in the transverse direction during the practical test.

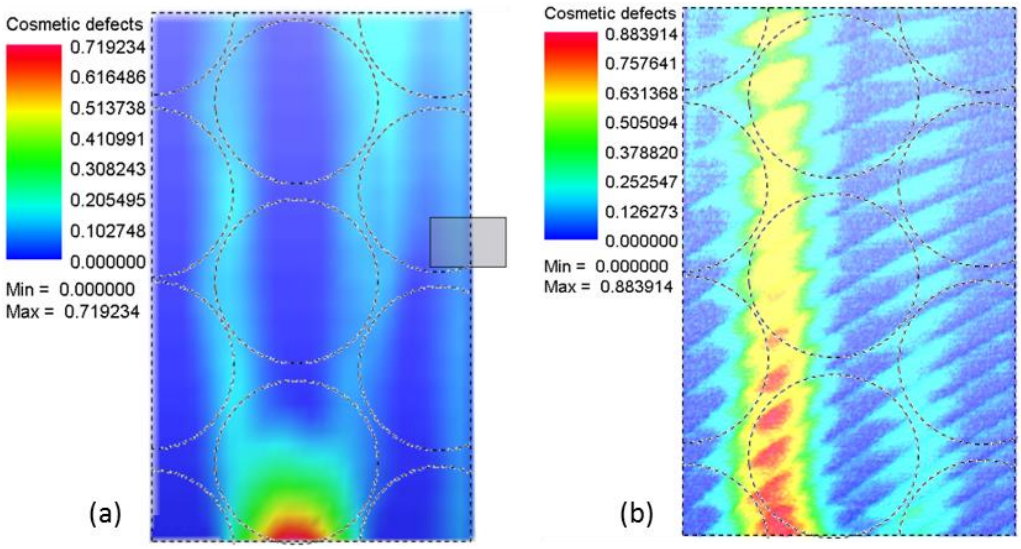

Figure 5-35: Contour maps showing a comparison of the stoning defects detected in the 20 Red practical test (b) and the corresponding simulation (a)

Figure 5-36 shows the results from the stoning analysis of the trimmed surface from the 30 Green simulation (a) adjacent to the results from the stoning analysis of the trimmed scanned surface from the 30 Green practical test. The stoning defect evident between pin rows ranges approximately between 0.06 and 0.09 mm on the surface from the simulation. A consistent stoning defect of approximately 0.2 mm is evident on the surface from the practical test. Given that the accuracy of the scans is ± 0.2 mm, this can be said to be of a similar magnitude to that evident in the simulation.

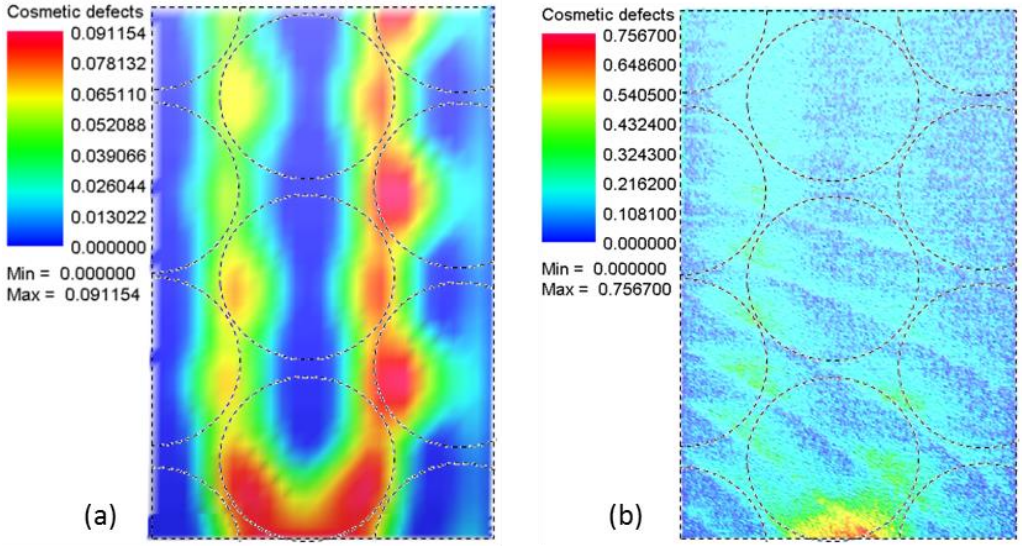

Figure 5-36: Contour maps showing a comparison of the stoning defects detected in the 30 Green practical test (b) and the corresponding simulation (a)

Figure 5-37 shows the results from the stoning analysis of the trimmed surface from the 30 Brown-Green-Brown simulation (a) adjacent to the results from the stoning analysis of the trimmed scanned surface from the 30 BGB practical test. The stoning defect evident between pin rows ranges approximately between 0.05 and 0.07 mm on the surface from the simulation. A consistent stoning defect of approximately 0.16 mm is evident on the surface from the practical test. This is approximately 0.04 mm less that observed in the 30 Green practical test, as opposed to a difference of 0.025 mm observed between stoning defects from the corresponding simulations. Again a comparison of Figure O-2 (b) (the stoning analysis relating to the 30 GBGB test) and Figure 5-37 (b) show that both the contour patterns and magnitude of stoning deviation are very similar. This similarity is also evident when comparing the stoning defects detected in the corresponding simulations [Figure O-2 (a) and Figure 5-37 (a)]. Overall there is a definite correlation between results from the stoning analyses carried out on the surfaces from the practical tests to those carried out on the surfaces from their corresponding simulations.

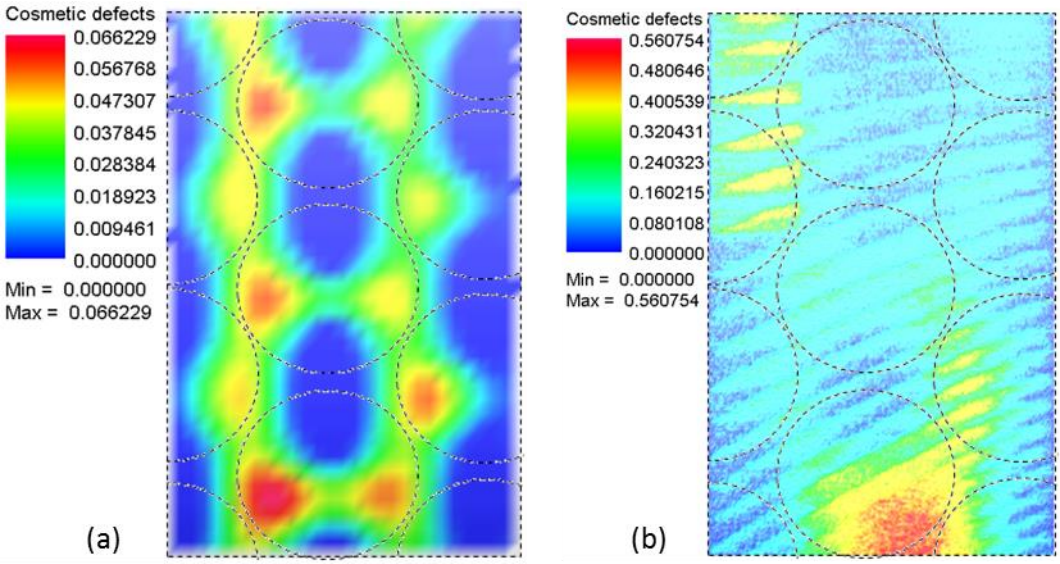

Figure 5-37: Contour maps showing a comparison of the stoning defects detected in the 30 BGB practical test (b) and the corresponding simulation (a)

5.9 Projection to an Industrial Scale

In this section the results from two simulations are used to project the findings of Section 5.7 to an industrial scale. Models used here represent a quarter of a reconfigurable die, approximately 1.2 m squared with a total of 368 pin tips. Two symmetry planes are again used to project the part to its full size. For reference, the pin tips are named in the same manner as in the lab scale simulations, with A1 being the outer pin tip on the XY symmetry plane and the letters B, D, F, H and J assigned to the shorter rows in the HCP2 pin arrangement. The 316L material of 0.88 mm in thickness is again being formed in single curvature, but to a greater radius of one metre. Trim lines 575 mm from the symmetry planes are used to give a part 1.15 m wide and approximately 70° over its radius of curvature.

5.9.1 Modifications to the Simulation Setup

In order to accurately portray the industrial scale process, identical boundary conditions and element sizes/types to those used in the lab scale models, validated in Section 5.8, should be used. Element sizes/types used in the industrial scale models, on the deformable objects (the blank and interpolators), are identical to those used in the lab scale models. Adhering to these element sizes results in typical industrial scale models where a quarter blank contains 41,875 shell elements (5 mm by 5 mm). Both the 5 mm and 10 mm thick interpolators contain 286,720 volume elements, while a 20 mm thick interpolator contains 573,440 volume elements. Since no refinement is available on the volume tools representing interpolators, elements are 2.5 mm by 2.5 mm in the XZ plane to allow the interpolators to deform into the gaps between pin tips. Where four surfaces tools are used at the interfaces between interpolators in the 1.2m 30 Grey(5)-Green(20)-Grey(5)* model, each surface tool typically contains an additional 71,680 shell elements. Boundary conditions are also identical during the stretch stage of both sets of simulations.

Difficulties were encountered when applying the positioning routine outlined in Section 5.3, and illustrated in Figure 5-6,Figure 5-7 and Figure

5-8, to the industrial scale simulations. In order to achieve tangential contact of the blank, between the drum and die, the pin tips, in the industrial scale simulations, were required to translate approximately 660 mm from their initial position just below the highest point of the drum. This created two problems. Firstly, the computational time of the position stage was greatly increased by this large translation distance. Secondly the softer inner interpolators oscillated wildly during the translation of the tooling. This oscillation is also evident in the lab scale simulations but, since the interpolators are held in place at their centre (close to the YZ symmetry plane) by the position of the blank, the distance to the free end is much smaller and hence the oscillation is of a much smaller magnitude. The small oscillation evident in the lab scale simulations does not have an influence on the final results or, the ability of the simulation to run to a successful conclusion, since the interpolators are held in place by the position and curvature of the blank before the onset of the stretch stage. In the industrial scale simulations, where the D30 Green material model was assigned to the inner interpolator, the more prominent oscillation caused the inner interpolator mesh to penetrate through the top surface of the bottom interpolator mesh before the tooling was fully positioned. Initially a tensile force was added to the free end of each interpolator in an attempt to reduce this oscillation to a level where penetration no longer took place. It was found that the tensile force on the inner interpolator, needed to sufficiently reduce its oscillation, had to be increased to such a magnitude that it caused the interpolator to stretch and so reduce in thickness.

The solution used here to overcome these problems, both reducing the computational time of the position stage and allowing the tooling to move to its required position without penetration between interpolator meshes, is to use a curved blank and a number of curved interpolator meshes. The initial position and shape of the blank and tooling, used in the industrial scale simulations, are shown in Figure 5-38. It should be noted that, where a stiffer material was used for the inner interpolator, oscillation was not of a magnitude so great as to cause penetration between interpolators. The

deformed blank and interpolator meshes from such a simulation, one state before the end of the position stage, have been imported to construct the 1.2m 30 Brown-Green-Brown model shown in Figure 5-38. While it is possible to exclude the position stage altogether, when using curved meshes, it was decided that, in order to retain conditions closest to those validated for the lab scale simulation, a small tooling translation should be retained in the position stage while the blank is in tension. The same imported mesh is used in the 1.2m 30 Grey(5)-Green(20)-Grey(5)* model. The nodes, from the imported interpolator meshes, on the XY symmetry plane, have been manipulated before shell elements were created, and extruded in the Z direction, to create the volume tools representing the interpolators in the 1.2m 30 Grey(5)-Green(20)-Grey(5)* model. The surface tools, at the interfaces between interpolators, were created by extruding bar elements created between corresponding nodes, in the same direction.

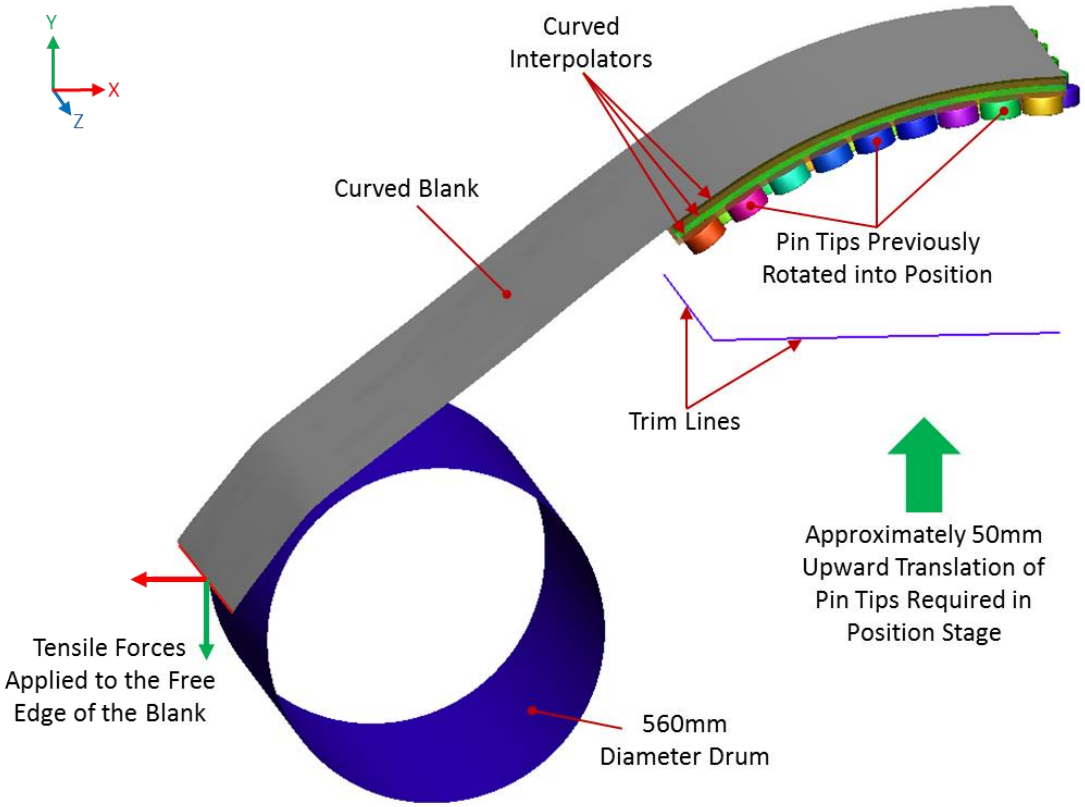

Figure 5-38: Starting position of the industrial scale simulations

Since the imported curved meshes did not include data on stress and strain, the magnitude of the bending stress and strain calculated during the

position stage of the industrial scale simulations, is much smaller than would actually exist. This will have a negligible influence on the final results of interpolator deformation, generated from these simulations, since bending stress and strain is very small in comparison to the compressive stress and strain in the interpolators. The absence of bending stress and strain in the blank would make these simulations unsuitable for the prediction of springback in the final part. That will not be an issue here, since these simulations are designed to examine the surface quality of parts.

5.9.2 Results from the Industrial Scale Simulations

The two systems of interpolation showing the smallest stoning defects in results from the lab scale simulations, discussed in Section 5.7.1, are re-examined here, on an industrial scale, using the same analytical techniques. Results generated using all three analytical techniques of both the trimmed parts from the 1.2m 30 Grey(5)-Green(20)-Grey(5)* and the 1.2m 30 Brown-Green-Brown simulations are shown in Figure 5-39.

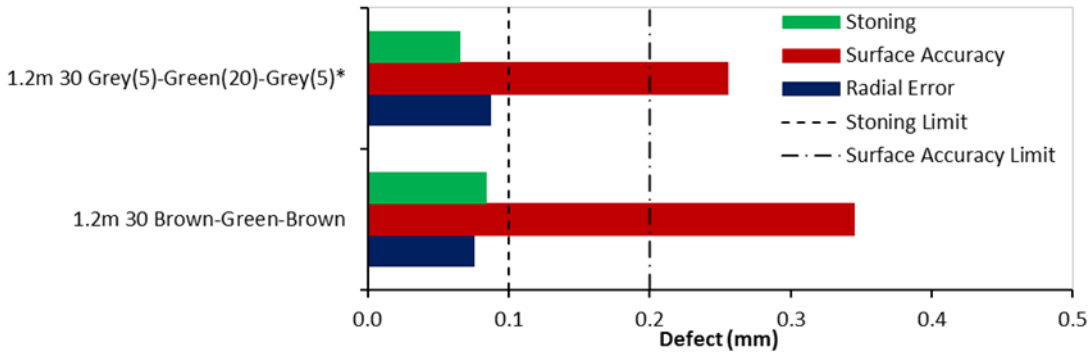

Figure 5-39: Results from the analyses of the industrial scale simulations

Results from the stoning analysis of the 1.2m 30 Brown-Green-Brown simulation show a maximum defect of 0.084 mm compared to the 0.066 mm present in the equivalent lab scale simulation. Figure 5-40 (a) shows that in general the stoning defect is greater in the overlapping area between rows of pin tips and increases along the curvature of the part as the gap between pin tips increases. The radial error analysis shows an increase from 0.06 mm in the equivalent lab scale simulation to 0.075 mm in the industrial scale simulation. That is a very small increase in the average

accuracy at the nodes considering that the area of the trimmed part has increased more than twelvefold.

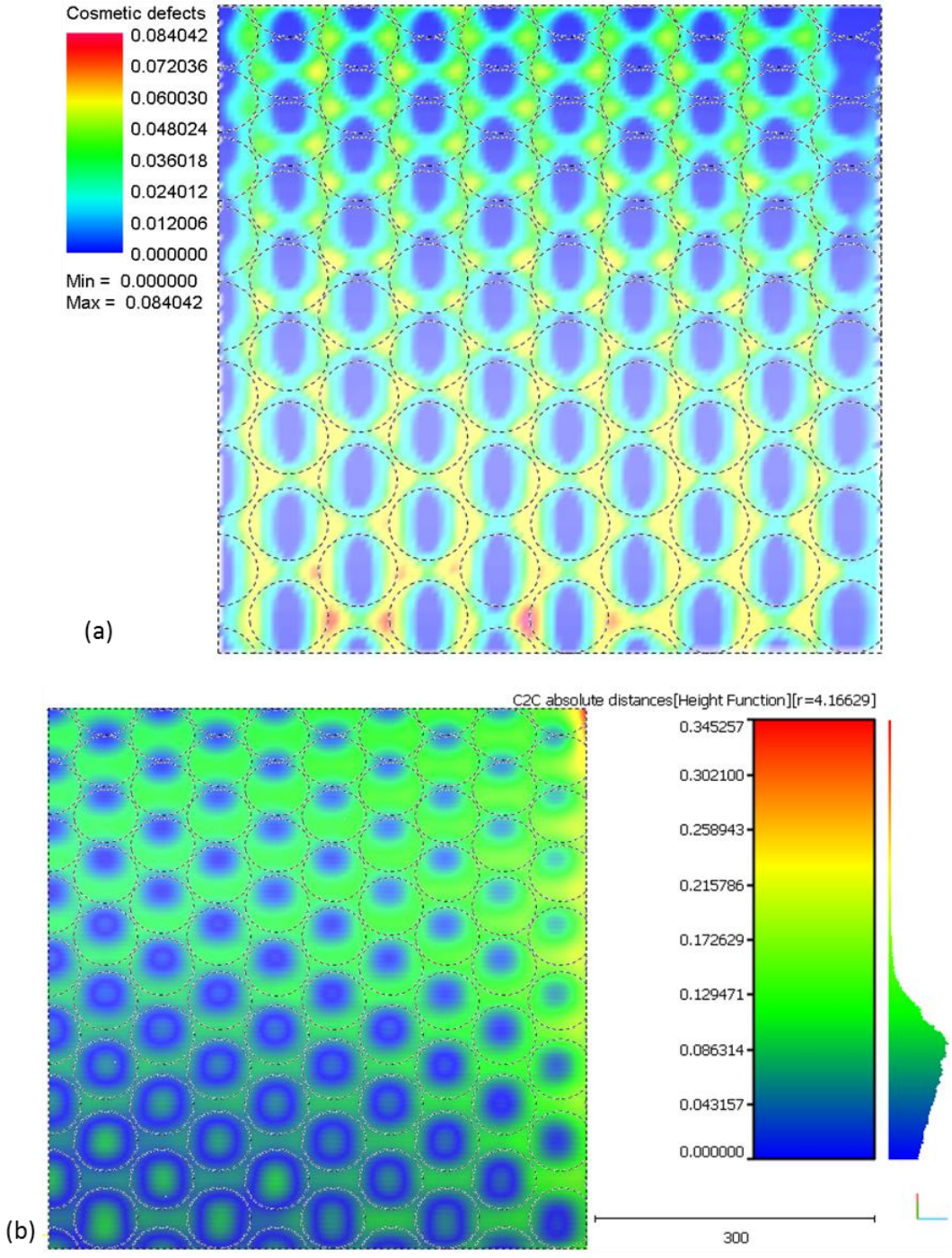

Figure 5-40: The Cosmetic defect (a) and C2C absolute distance (b) contour maps for the 1.2m 30 Brown-Green-Brown simulation

The surface accuracy analysis, illustrated in Figure 5-40 (b), reveals a maximum surface accuracy defect, in the industrial scale simulation, of 0.345 mm compared to the 0.174 mm from the equivalent lab scale

simulation. The maximum defect is present at the outer edge of the part close to the YZ symmetry plane. Only 15 mm in from this edge and over the remainder of the part, a surface accuracy defect of less than 0.2 mm can be measured. This suggests more trimming may be required across the width of the part to meet the target surface accuracy. The radial error analysis reveals that the node at this top corner has a position error of -0.344 mm. The negative sign indicates a low spot. In fact 11,700 of the 13,085 nodes present in the trimmed mesh are sitting low. This suggests that surface accuracy could be improved by adjusting the heights of all the pins.

The contour maps relating to interpolator thickness and major strain for both these simulations have been included as Appendix P. of this document. Figure P-1 (a) shows that compression of top and bottom interpolators is relatively even at the centres of the pin tips with a range of only 0.02 mm on the bottom interpolator and a range of only 0.03 mm on the top interpolator from the 1.2m 30 Brown-Green-Brown simulation. The middle interpolator shows compression at the centres of pin tips ranging between zero (over A17) and 0.08 mm (over J2). This suggests that hydrostatic pressure is not such an issue when the surface area of the part is increased to that encountered on an industrial scale. Note that the maximum thickness displayed in the legend is present in the middle interpolator at the wrinkles on the free edge between rows C, E, G, I and K.

Results from the stoning analysis of the 1.2m 30 Grey(5)-Green(20)-Grey(5)* simulation show a maximum defect of 0.066 mm which is equal to that found in the equivalent lab scale simulation. Figure 5-41 (a) shows that the maximum stoning defect is present in the overlapping area between rows of pin tips furthest from the YZ symmetry plane, where the gaps between pin tips is greatest. The radial error analysis shows an increase (closer to that expected) from 0.035 mm in the equivalent lab scale simulation to 0.088 mm in the industrial scale simulation.

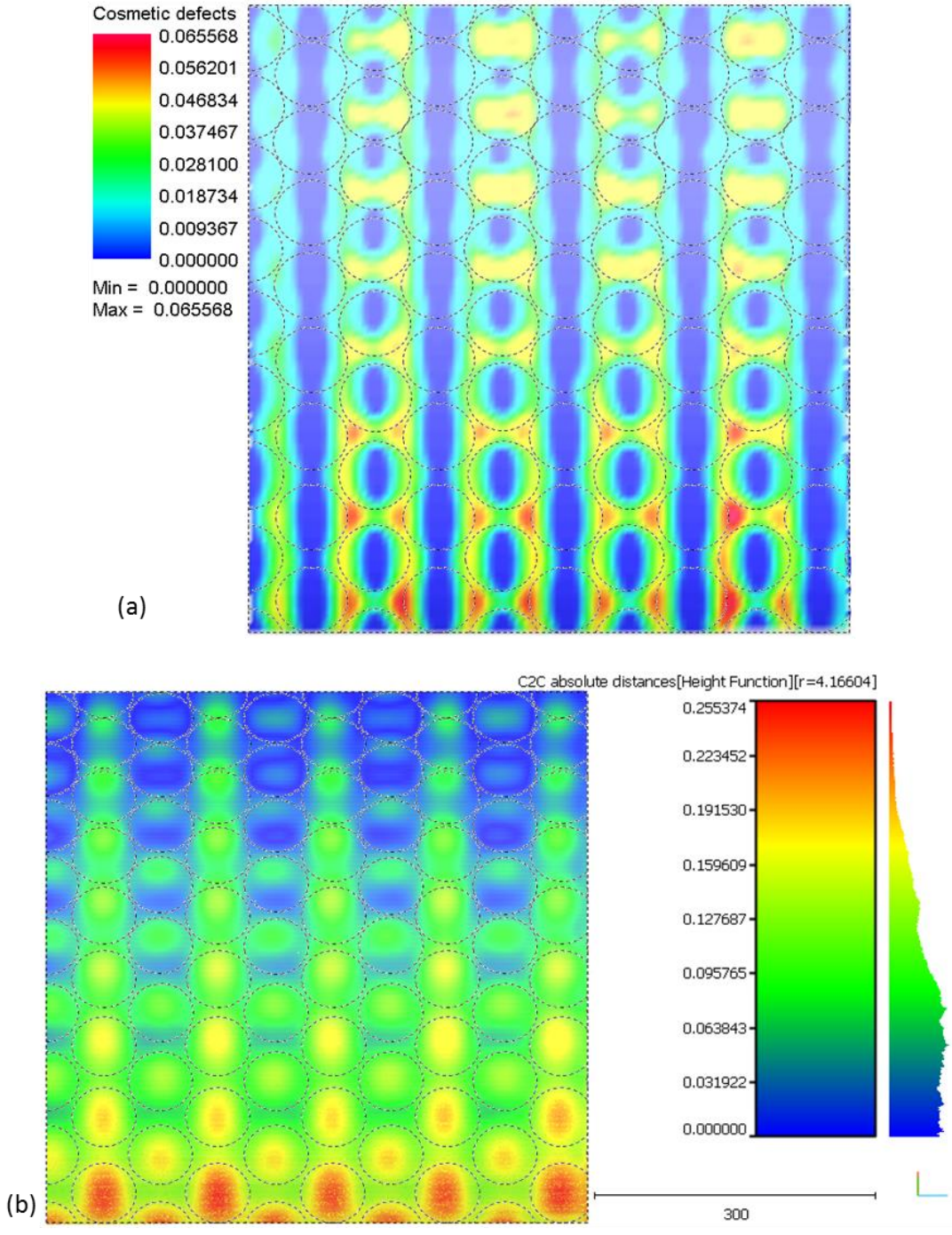

Figure 5-41: The Cosmetic defect (a) and C2C absolute distance (b) contour maps for the 1.2m 30 Grey(5)-Green(20)-Grey(5)* simulation

Figure 5-41 (b) shows a maximum surface accuracy defect, in the industrial scale simulation, of 0.255 mm compared to the 0.132 mm from the equivalent lab scale simulation. The surface accuracy defect is at its maximum over the pin tips furthest from the YZ symmetry plane. The radial error analysis reveals that 12,422 of the 13,095 points examined are

sitting high of their target positions. This is likely due to the inclusion of surface tools with a thickness of 0.1 mm at the interfaces between interpolators. Again, this suggests that surface accuracy could be improved by adjusting the heights of all the pins.

Figure P-2 (a) shows the Thickness of solids contour maps relating to the top and bottom interpolators of the 1.2m 30 Grey(5)-Green(20)-Grey(5)* simulation. These 5 mm thick interpolators, made from the stiffest material in the Kaylan D series, are compressed evenly over the centres of the pin tips, where a difference in final interpolator thickness of only 0.01 mm is evident over each interpolator. Figure P-2 (b) shows that the 20 mm thick interpolator, made from the softer D30 Green material, is also compressed evenly over the centres of the pin tips, where a similar difference in final interpolator thickness is evident. This is smaller than the 0.06 mm difference in final interpolator thickness detected in the equivalent lab scale simulation, and again suggests that the influence of hydrostatic pressure on the magnitude of interpolator compression over individual pin tips is reduced when the surface area of the part/interpolator is increased.

In results from both simulations the minimum interpolator thickness can be found at the outer edge of the B2, D2, F2, H2 and J2. This is an indication that the wider blank is still bending down into the gaps at between the longer rows in the HCP2 pin arrangement, and non-tangential contact is present at the afore mentioned pin tips. Figure P-1 (b) and Figure P-2 (c) show the distribution of major strain in the trimmed parts form each simulation. It is evident that the range of strain in the industrial scale parts is higher (0.04) than in the lab scale parts (0.02) due to the effects of friction at the interface between the blank and die over a greater angle of curvature. The run times for these industrial scale simulations is influenced by the great number of deformable elements present within the models. The 1.2m 30 Brown-Green-Brown simulation has a run time of approximately 6 days, while the 1.2m 30 Grey(5)-Green(20)-Grey(5)*simulation, which includes surface tools at the interfaces between interpolators, has a run time of approximately 14 days.

5.10 Conclusions

AMFOR's preferred machine layout works very well when forming parts of single curvature. One problem that was encountered during tests on the lab scale machine involved a difficulty in the releasing of the eccentric cam grips manually at the end of the stretching process. A mechanical means of releasing the grips needs to be included in the design of an industrial scale machine. It was also discovered that an error in the placement of the balance linkages (see Figure 5-1) resulted in one drum rotating more than the other. Since the lab scale pin box only has five rows of pins across its width, and the outer rows of pins are not fully loaded at the end of the stretching process, when the width of the blank decreases due to transverse strain, it was decided that the lab scale machine was not suitable for accessing the surface quality of parts formed in double curvature over the 70 mm diameter pins. Nevertheless, it can be predicted that where a double curvature part is formed with the blank gripped in a straight clamping line over a cylindrical drum, the resulting strain in the part will be irregular. Figure 5-42 shows a half model of an industrial scale machine employing AMFOR's preferred layout. The die shown is configured to form an outer section of a torus with a 1 m radius of curvature in each direction.

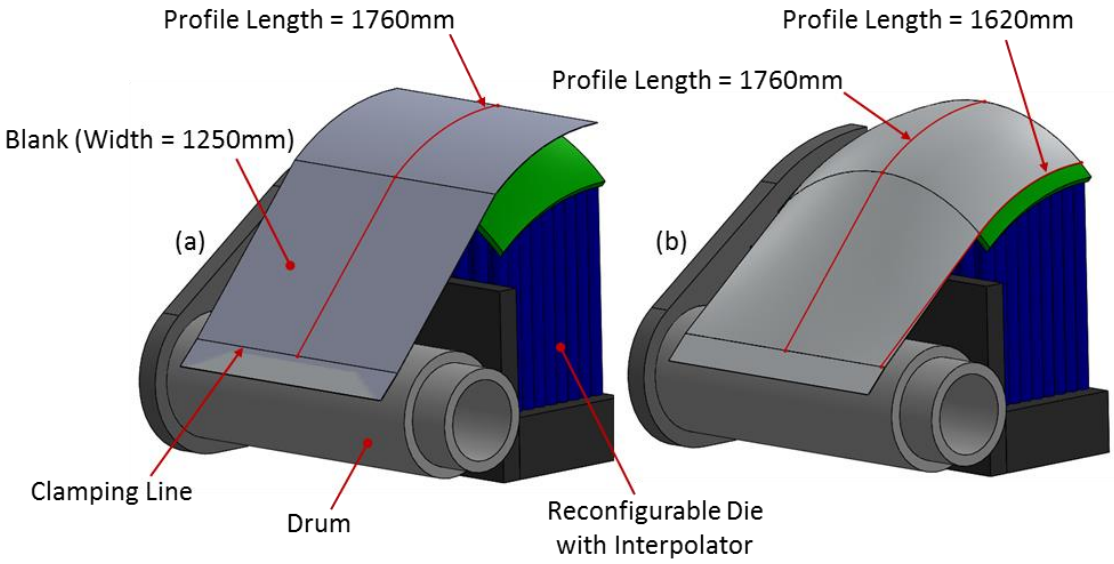

Figure 5-42: Irregular strain present when a double curvature part is formed with the blank gripped in a straight clamping line over a cylindrical drum

In Figure 5-42 (a) where the blank is touching the die at a centreline along its length, the profile length of the half blank (1620 mm between the clamping line and a transverse symmetry line) is consistent across the width of the blank. In Figure 5-42 (b) where the outer edges of blank are now touching the die, the profile length is now 140 mm greater at the centre than it is at the outer edges. Since tension along its length is used, to wrap the blank around the die across the width of the die (rather than bending) the resulting part will have a greater strain (8% in magnitude) present at its centre than that present at its outer edges.

It is also evident from Figure 5-42 that it is not possible for the blank to retain tangential contact, between the drum and die, across its width, when the die is of double curvature. This will add to the problems, encountered in this chapter, of predicting the final thickness of the interpolator, and hence the pin heights required to form dimensionally accurate parts.

While the use of circular pins allows the pin heights to be adjusted from above, where circular pins are stacked in a row, and forces are applied, there is a chaotic element present, since pins can slide to either the right or left of their neighbours. The effect that this has on the final position of individual pins in a matrix, and the difficulty in forming dimensionally accurate parts, will depend on the diametrical tolerance used in the manufacture of the pins, the number of pins, and the magnitude of tolerance stacking over the matrix as a whole.

The stoning analyses of the trimmed parts from the PAM-STAMP simulations yield the most relevant results, as the surface analyses results are subject to errors relating to the effects of hydrostatic pressure where the interpolator compresses to different magnitudes over pins at different positions in the die matrix. The radial error analyses effectively give an average value of the surface accuracy.

Figure 5-43 shows of the Kaylan D series material properties plotted against deviations detected from the stoning analyses of the trimmed blanks from all the PAM-STAMP simulations of the lab scale process. The material

properties shown here are taken directly from the material datasheets supplied by Kay-Dee Engineering Plastics Ltd.. Shore D hardness values are used (rather than the Shore A values normally used to describe rubberlike materials) since the hardness of the D70X Grey material is beyond the Shore A scale. The 100% modulus values shown here are simply the ratios of engineering stress to engineering strain at 100% elongation of specimens in tension.

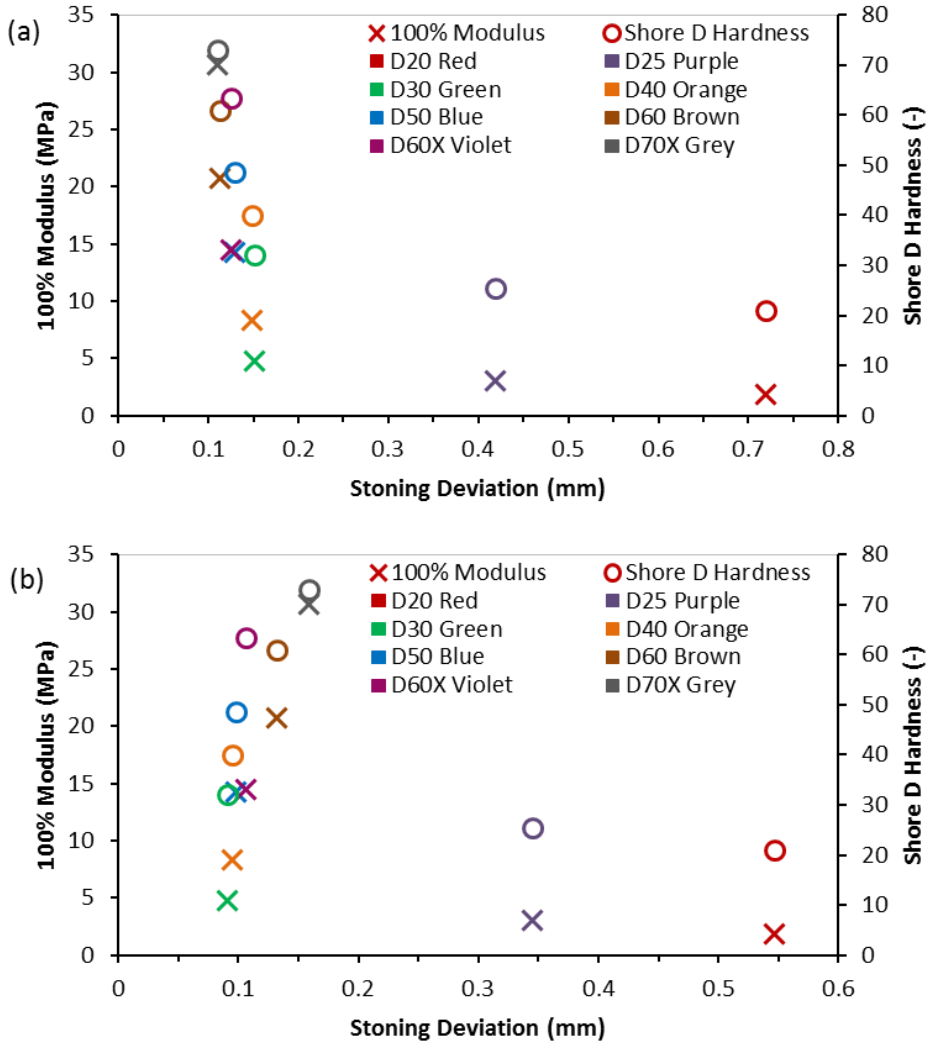

Figure 5-43: Single layer of interpolation 20 mm (a) & 30 mm (b) thick stoning defects plotted against material properties

Results from the lab scale simulations employing a single layer of interpolation show that, where a 20 mm thick interpolator is used, deviations detected through stoning are proportional to both the stiffness

and hardness of the interpolator material [Figure 5-43 (a)]. None of the simulations of the lab scale process produced maximum stoning defects below the target value of 0.1 mm.

The simulations employing a single layer of interpolation 30 mm thick do not show a correlation between the maximum stoning defects detected and the interpolators' mechanical properties [Figure 5-43 (a)]. Simulations where the interpolators are assigned with the D30 Green, D40 Orange and D50 Blue material models all yielded maximum stoning defects below the target value. Of these, the softer material (D30 Green) is the most suitable for the drape forming process, since drapeability increases with a reduction of stiffness. The Shore A hardness of these three materials (as given in the datasheets produced by the material supplier) is 80-85 for the D30 Green material, 90-93 for the D40 Orange material and 94-96 for the D50 Blue material. Hence these materials are similar to the polyurethane materials used in both the RTFF and DATAFORM projects with Shore A hardness values of 90 (Eigen, 1992) & (Seo, et al., 2012) respectively. It is evident, from these results that where pivoted pin tips, with a flat surface, are used the thickness of the required interpolator is not linked to the diameter of the pins employed in the reconfigurable die, in the same manner as it is when semi-hemispherical pin tips are used. Maximum stoning defects increase where the three stiffest material models are used in simulations of the lab scale process. This is due to the reduction of compression and bending, around the pin tips, at the unloaded region of interpolator, at its outer edge (across the width), as the stiffness of the interpolator increases. This results in a trimmed part with a concave profile across its width.

Two methods of pin height correction, to overcome the effects of hydrostatic pressure, are presented here. A numerical routine is used, where a number of iterations are required, with pin heights corrected after each simulation, depending on the final thickness of the interpolator over individual pin tips. The magnitude of the computational times required for detailed simulations limit the practical applications where the numerical routine would be suitable for use. An empirical routine is presented here for

the lab scale die, and the single curvature used in these simulations. More data is required to develop this empirical routine further for an industrial scale die with variable curvature.

Overall the maximum stoning defects detected are reduced in simulations where three layers of interpolation are employed. The best results (in terms of a reduction in the stoning defects) are evident in simulations where the D30 Green material is sandwiched between two layers assigned with the material model representing one of two stiffest materials (D60 Brown and D70X Grey). The simulations 30 Brown-Green-Brown and 30 Grey(5)-Green(20)-Grey(5)* show a maximum stoning defect of only 0.066 mm. The thinnest overall three layer of interpolation system simulation that yields a maximum stoning defect smaller than the stoning defect target is the 22 Grey(6)-Green(10)-Grey(6)* simulation. Despite the overall interpolator thickness of only 22 mm, this simulation shows a maximum stoning defect of 0.086 mm, which is less than that found in any of the simulations where a single layer of interpolation 30 mm thick is employed. It should be noted that the D70X Grey material is relatively stiff (100% modulus of 30.7 MPa), and is only deemed suitable for the drape forming process where the maximum thickness of each sheet is 6 mm. Nevertheless, even with a reduced thickness, interpolators manufactured from this material may need to be preformed into a net shape, to allow the blank to drape over the reconfigurable die. Ideally the interpolator stiffness (and initial shape) should have a minimal effect on the ability of the blank to be draped over the tooling with contact over a high percentage of the die before the drums rotate to instigate stretching. It should also be noted that the negative effects of hydrostatic pressure are reduced, where a three layer of interpolation system is used, and the middle layer compresses with greater consistency across the die as a whole.

In this study, no reduction of stoning defects (when compared to results from equivalent three layer of interpolation systems) are apparent in simulations employing four layers of interpolation. Hence there is no evidence that the addition of a thin softer layer of interpolation, in contact

with pin tips, leads to the production of parts with greater flatness and better surface accuracy.

The lab scale PAM-STAMP simulations have been validated here by carrying out four practical tests on the AMFOR lab scale stretch forming machine, and comparing the surface quality of the trimmed blanks obtained to that from corresponding simulations. Two single layer of interpolation systems have been examined, employing the D20 Red and D30 Green Kaylan materials, 20 and 30 mm thick, respectively. A three and four layer of interpolation system, both employing combinations of the D30 Green and D60 Brown Kaylan materials with a total thickness of 30 mm, have also been examined. Pin heights, for the physical tests, were set prior to each test, on a bench with the aid of a Vernier height gauge. The surfaces of the stretched blanks, from the practical tests, have been captured using the DAVID SLS-1 structured light scanning system, where scanned surfaces were saved as STL meshes. The accuracy of both the pin height setting routine and the scanned images was estimated at ±0.2 mm. The CloudCompare software was used to compare meshes representing the stretched and trimmed blanks from those from their corresponding simulations. The STL meshes relating to the physical tests were also imported into the PAM-STAMP software for stoning analyses.

Surfaces relating to the 20 Red test and simulation aligned with a deviation of less than 0.2 mm over approximately 50% of the surface area examined. The maximum deviation between the two surfaces was found at the outer edges, where the simulation underestimated the effects of hydrostatic pressure, and over the A3 pin which was set slightly high. Alignment between the main bodies of the surfaces was inconsistent. This can be attributed to the pin tips rotating about their pivot points, during the stretching process, where a very soft material is used for interpolation. The stoning analysis, relating to this test found a deviation of approximately 0.25 mm between the B and C pin rows, which is in close agreement to the 0.2 mm present in the corresponding simulation in this area. Where a similar deviation (0.2 mm) was found between the A and B pin rows, in the

analysis of the simulation, the stoning analysis of the physical test found a greater deviation (up to approximately 0.9 mm). This can again be attributed to the pin tips rotating about their pivot points, during the physical test.

Surfaces relating to the 30 Green test and simulation aligned with a deviation of less than 0.3 mm over the vast majority of the surface area examined. A greater deviation was found at the outer edge of the trimmed part (over the B2 pin), due to the inability to attain tangential contact between the blank and outer edge of the die where a 30 mm thick interpolator was used. The stoning analysis, relating to this test, found a deviation of approximately 0.2 mm between both the A and B and the B and C pin rows. Considering the accuracy of the pin height setting routine and the scanned images, this is in relatively good agreement with the 0.09 mm found in the stoning analysis relating to the corresponding simulation. Again, a greater stoning deviation was detected, in the surface from the practical test, over the B2 pin, due to the aforementioned inability to attain tangential contact.

Surfaces relating to the 30 BGB test and the 30 Brown-Green-Brown simulation aligned with a deviation of less than 0.2 mm over the majority of the surface area examined. A greater deviation of alignment was found at the centre of the part where pin A7 was set slightly high. In the previous test a greater alignment deviation, due to the inability to attain tangential contact, was found over pin B2, where the relatively soft material bends down into the gap between pins A1 and C1. In this test, where the relatively stiff D60 Brown material was used, the greater alignment deviation, due to the non-tangential contact, was spread over the three end pins (A1, B2 and C1). The stoning analysis, relating to this test, found a deviation of approximately 0.16 mm between both the A and B and the B and C pin rows. The stoning defect was also increased where pin A7 was set slightly high, and in the area closest to the gripped edge, due to the non-tangential contact.

The same pin height positions were used for 30 GBGB physical test as were used for the 30 BGB test. Surfaces relating to the 30 GBGB test and the 30 Green-Brown-Green-Brown simulation aligned with deviations very similar to those in the previous comparison, both in terms of position and magnitude. Likewise, the stoning defects detected were very similar to those detected on the surface from the 30 BGB test, again both in terms of position and magnitude. This is in good agreement to stoning results from the simulations, where it was difficult to differentiate between results from models where a four layer of interpolation was used and the corresponding three layer of interpolation system. Overall there is a definite correlation between results from the stoning analyses carried out on the surfaces from the practical tests to those carried out on the surfaces from their corresponding simulations.

Two simulations (1.2m 30 Grey(5)-Green(20)-Grey(5)* and 1.2m 30 Brown-Green-Brown) are used here to project the findings from the lab scale study to an industrial scale. Results show that the interpolator systems that performed best in the lab scale simulations can be used on an industrial scale die with only a small increase in surface defects, despite the greater gaps between pin tips. The final interpolator thickness contour maps, from these two simulations, suggest that the effects of hydrostatic pressure on the consistency of interpolator compression (relative to pin position in the die matrix) are reduced when the ratio of interpolator surface to thickness is increased. It should be noted that when AMFOR's preferred machine layout is scaled up, the industrial scale models reveal that the distance between the clamping line and the edge of the die appears excessive, since oversized sheets (approximately 3.5 metres long) are required to produce trimmed parts approximately 1.2 m square.

Chapter 6. Conclusions & Further Work

6.1 Introduction

In this thesis a new pin tip design is introduced for employment in a reconfigurable die, suitable for use in the stretch forming process. The new tooling system is integrated into a simplified lab scale stretch forming machine, the design of which, when scaled up to a size suitable for industrial use, would provide a cost effective means for the rapid production of complex curvature sheet metal components. The stand-alone nature of the new machine would enable it to work alongside existing stretch forming equipment, to increase forming capacity without the need for additional hard tooling, or to effect a smooth transition from a hard tooling system to a reconfigurable faceted surface tooling system.

The AutoForm^{plus} R3 finite element software is used in the implementation of a comparative numerical study used to, firstly, ascertain the features that detract from the production of dimple free parts in any given layout of the matrix, in a bed of pins, where tips are semi-hemispherical in geometry. A second phase of this study is used to determine a suitable geometry for the new pivoted pin tips in the preferred pin layout, before the smoothness of parts produced from a stretch forming process over a die comprised of the new pivoted pin tips are compared to that produced using the RTFF tooling.

Data from a series of mechanical tests are used to determine the properties of the metallic materials used as blanks in finite element studies

before material models are constructed for use in the relevant software. A series of mechanical tests are also carried out on the Kaylan D series of polyurethane materials (supplied by Kay Dee Engineering Plastics Ltd.). Data from these tests are used to construct Mooney Rivlin models of the polyurethane materials, used to test their suitability for use as interpolators in a numerical study utilising the PAM-STAMP finite element software. Material models used in the PAM-STAMP simulations are validated by comparing data from the physical tests to data generated from simulations of the corresponding tests. Results generated from the PAM-STAMP simulations of the lab scale stretch forming process (in terms of the smoothness of parts produced) are validated through a comparison to parts produced from experiments carried out on the lab scale machine.

6.2 Conclusions

Although the Hill 48 yield criterion is the model most commonly used to describe steels when simulating forming processes, it has been found in Section 3.3 that this model does not give an accurate description of the 316 stainless steel's behaviour in all strain paths that can be encountered during a forming operation, or in all directions relative to a sheets rolling direction. Despite this, it has been shown that, when separate models are constructed using data from uniaxial tensile tests at 0° to 45° and 45° to 90° to the rolling direction of the sheet, the Hill 48 yield criterion can be used to accurately describe the 316 stainless steel's behaviour in uniaxial tension at 0° and 90° to the rolling direction of the sheet. Output from simulations of tensile tests, using the material models constructed in Section 3.4, also show that the Modified Krupkowsky rule can be used to accurately describe the strain rate sensitivity of this material (see Figure 3-11, Figure 3-12 and Figure C-1 to Figure C-8). Since the blank in the stretch forming process, simulated in this thesis, is subjected to uniaxial tensile (in the area of interest) the Hill 48 material models are used in the detailed PAM-STAMP simulations.

PAM-STAMP uses a two term Mooney Rivlin equation to describe the behaviour of hyperelastic materials (such as the Kaylan D series of polyurethanes used here) when subjected to loads. Although the PAM-STAMP software can accept tensile or compressive data to determine the C_1 and C_2 Mooney Rivlin constants, it has been shown, in Appendix E. that when compressive data is used the C_2 constant is always negative. This results in an unstable material model where, at some stage, stress decreases rather than increases with growing strain. Nevertheless, since the interpolator is subjected to compression during the stretch forming process, and the size of the material samples available is restrictive on the number of tests and type of tests carried out, uniaxial compressive tests are used here to determine values for the C_1 and C_2 Mooney Rivlin constants. Therefore, since the maximum engineering stress, in the interpolator, has been shown to be approximately 1 MPa (see Section 3.4), a reduced data sample (incorporating this value) is used to determine the constants, hence, ensuring that the material model is stable over the range where it is to be used in simulations of the stretch forming process. Output from simulations of the compression tests (see Figure 3-19, Figure 3-20, Figure 3-21 and Figure F-1 to Figure F-5), used to validate the polyurethane material models, show that the material models are relatively accurate, over this reduced range.

Results from the phase 1 AutoForm simulations (see Section 4.4) of semi-hemispherical pin tips, in a total of 14 different die layouts, show that only the hexagonal close packed layouts HCP1, HCP2 and the diagonally orientated rectangular close packed layout RCP3 are suitable for use with a reconfigurable die constructed from a relatively coarse bed of pins. These results also reveal that;

- edge contact between pin tips and the blank (or interpolator),
- low pin density in the die matrix,
- unequal spacing between pin tips,
- increased magnitude of gaps between rows of pins aligned in the direction of stretching, and,

- increased magnitude of gaps between neighbouring pins in the direction of stretching,

are all features on a reconfigurable die which increase the difficulty in obtaining smooth parts, from a stretch forming process over the given die (see Figure 4-18).

Results from the phase 2 AutoForm simulations show that pivoted pin tips give an advantage over their commonly used semi-hemispherical counterparts, and that pivoted pin tips that are circular in geometry, with a flat mating surface, arranged in a hexagonal close packed matrix can produce parts with superior smoothness (see Section 4.6 and Figure 4-22). Results from simulations, presented in Section 4.7, show that where pins of 70 mm in diameter are used, and arranged in a hexagonal close packed matrix, parts with a comparative smoothness to those produced from the RTFF tooling can be produced (total deviations of 0.52 mm and 0.41 mm respectively), despite a great reduction in the number of pins used (from 2688 to 485).

It should be noted that standard meshes with default setting are used in the phase 1 & 2 AutoForm models, to reduce the computational time required to run these simulations. A comparison of the total deviation from the section line analysis results for the HCP2 Round Flat simulations using both a standard mesh and a fine mesh (0.63 mm and 0.52 mm respectively) shows that reasonable results are obtained from the standard mesh simulations. It should also be noted that the AutoForm studies, presented in Chapter 4, are purely comparative, and no attempt is made here to validate the results, since the cost of constructing a number of dies to the scale used here would be beyond the scope of this project.

The Kaylan D series of polyurethane materials are considered, in Chapter 5, for their suitability for employment as interpolators, on a new reconfigurable die, constructed from pins 70 mm in diameter, fitted with round pivoted pin tips, with a flat mating surface, and arranged in a hexagonal close packed matrix. There are a total of eight materials in the

Kaylan D series, with Shore D hardness values ranging from 20 to 73. Results from PAM-STAMP simulations employing a single layer of interpolation 20 mm and 30 mm thick, show that, where the stiffer materials are used, the unloaded section of the interpolator beyond the width of the blank, does not compress or bend around the pin tips, and hence the profile of the resulting parts are concave across their width. Results from the simulations where a single interpolator 30 mm thick is employed show that the softer materials do not offer sufficient support to prevent dimpling over the gaps between pin tips. The three materials of medium hardness (D30 Green, D40 Orange and D50 Blue) are of most interest where a single layer of interpolation 30 mm thick is employed, since results from simulations show that they all produce parts with maximum stoning defects smaller than the defect target of 0.1 mm. Of these, the softer material (D30 Green) is the most suitable for the drape forming process, since drapeability increases with a reduction of stiffness. The Shore A hardness of this material (given in the datasheet supplied by Kay-Dee Engineering Plastics Ltd.) of 80-85 shows that it is slightly softer than the materials identified in both the RTFF and DATAFORM projects with Shore A hardness values of approximately 90. It is evident, from these results that where pivoted pin tips, with a flat surface, are used the thickness of the required interpolator is not linked to the diameter of the pins employed in the reconfigurable die, in the same manner as it is when semi-hemispherical pin tips are used (Eigen, 1992).

The lab scale simulations, employing a single layer of interpolation, also reveal that the magnitude of interpolator compression reduces towards the centre point of the die, due to the effects of hydrostatic pressure. This increases the difficulty of setting the pin heights in a reconfigurable to produce parts with good dimensional surface accuracy. Two methods of correcting pin heights for the effects of hydrostatic pressure, a numerical routine and an empirical routine, are outlined in Section 5.6. The empirical routine used here is specific to the dimensions, curvature and materials used in the lab scale simulations. The numerical routine used here involves

running a series of simulations where the final thickness of the interpolator over each pin tip, at the end of simulations, is used to correct pin heights between iterations. The magnitude of the computational times required for detailed simulations limit the practical applications where the numerical routine would be suitable for use.

In general, results from the lab scale simulations reveal that the maximum stoning defects detected can be reduced by employing a three layer of interpolation system, where a sheet of interpolation comprised from a softer material is sandwiched between two sheets comprised from a harder (and stiffer) material (see Figure 5-23). Where the overall interpolator thickness of 30 mm is retained, and the thickness of each layer is equal, the 30 Brown-Green-Brown simulation yields the smallest maximum stoning defects (0.066 mm). Maximum stoning defects equal in magnitude, but not position, are evident in a simulation (30 Grey(5)-Green(20)-Grey(5)*) where the stiffest material (D70X Grey) is used at 5 mm thick outer layers, and the D30 Green material is used at the inner layer 20 mm in thickness. With this combination of materials the overall thickness of the interpolators can be reduced to 22 mm (22 Grey(6)-Green(10)-Grey(6)*), with the maximum stoning defect detected in the lab scale simulation (0.086 mm) still remaining below the defect target of 0.1 mm. It should be noted that the D70X Grey material is relatively stiff (100% modulus of 30.7 MPa). Hence this material is only considered here in a three layer of interpolation where the maximum thickness of the outer layers is 6 mm. Nevertheless interpolators manufactured from this material may require preforming to enable their use in a drape forming process. It is also notable, from the lab scale simulation results, that the influence of hydrostatic pressure, on the dimensional surface accuracy of the part, is reduced where a three layer of interpolation system is employed. There is no evidence, from the lab scale simulations, that the addition of a thin softer layer of interpolation, in contact with pin tips (in a four layer of interpolation system), leads to the production of parts with greater flatness and better surface accuracy.

Two simulations, using the best preforming three layer of interpolation systems (with an overall thickness of 30 mm) from the lab scale simulations, are used here to project the findings from the lab scale study to an industrial scale (with a die surface approximately 1.2 m by 1.2 m. Results show that while there is no increase in the stoning defects detected on the Grey (5 mm thick), Green (20 mm thick), Grey (5 mm thick) system, using the industrial scale tooling, only a small increase of less than 0.02 mm is evident on the Brown, Green, Brown system (where all three layers are 10 mm thick). Results also suggest that the influence of hydrostatic pressure, on the consistency of interpolator compression, is reduced when the ratio of interpolator surface to thickness is increased.

Results from the lab scale simulations have been validated through physical tests on the AMFOR stretch forming lab scale machine. Two physical tests were carried out using a single layer of interpolation (20 Red and 30 Green). One test was carried out using a three layer of interpolation system (30 BGB), and one test was carried out using a four layer of interpolation system (30 GBGB). Pin heights were set prior to each test, on a bench with the aid of a Vernier height gauge. The surfaces of the stretched blanks, from the tests, have been captured using the DAVID SLS-1 structured light scanning system. The accuracy of both the pin height setting routine and the scanned images was estimated at ±0.2 mm. Surfaces from the physical tests were compared to those from corresponding simulations using the CloudCompare software. It should be noted that a degree of accuracy, in the validation surface comparisons, was lost (when compared to the simulation surface comparisons), due to higher noise levels in the scanned point clouds. Stoning analyses of the scanned surfaces was carried out using the PAM-STAMP software. Wear on the machine's eccentric cam gripping system increased the difficulty of obtaining accurate results from the physical tests. Difficulty was encountered centring the blanks on the die during re-gripping processes. Despite this the scanned surfaces from the tests aligned to the surfaces from simulations with reasonable accuracy. Overall there is a definite correlation between results

from the stoning analyses carried out on the surfaces from the practical tests to those carried out on the surfaces from their corresponding simulations.

Overall the lab scale machine performs well in trials where parts of single curvature are stretched. There are an insufficient number of rows (across the width) of 70 mm diameter pins in the lab scale die to give a good assessment of the performance of the new reconfigurable die in stretching double curvature parts. Nevertheless, two potential problems associated with the stretching of industrial scale double curvature parts, on a machine employing AMFOR's preferred machine layout and the new reconfigurable die, are outlined in Section 5.10. These are given as; the inability to maintain tangential contact of the blank between the fixed drum and the edge of the die, and the unequal magnitude of strain across the width of a stretched part when using a straight clamping line. Figure Q-1 and Figure Q-2 show possible solutions to these two potential problems.

Another potential problem, identified in Section 5.10, concerns the stacking of round pins in a row. When forces are applied, to such a system, pins can slide to either the right or left of their neighbours, creating an element of chaos pertaining to the final position of each pin in a matrix. This will add to problems of tolerance stacking associated to any reconfigurable die consisting of a bed of pins. Figure Q-3 shows a pin design incorporating a hexagonal sleeve which could be used to overcome this problem.

Industrial scale models of the single curvature part also reveal that the distance between the clamping line and the edge of the die appears excessive, where tangential contact is maintained, using AMFOR's preferred machine layout. The partial drum shown in Figure Q-4 would allow the drum to be moved closer to the die and reduce overall material wastage. A potential problem associated with using a hexagonal close packed bed of pins is also outlined in Section 4.9, where, a potentially excessive force can be transferred through the pin matrix to the machine walls. However, these are only minor problems, which can be ironed out during a design process. It

should always be remembered that the new reconfigurable die can be used in an existing stretch forming machine, and traditional dies can be used with AMFOR's preferred machine layout.

Overall, results from the simulations carried out here show that a fine bed of pins is not necessary in the stretch forming of a high volume of metallic parts, since curvature is normally relatively gentle, and relatively smooth parts can be formed over the new coarser reconfigurable die, fitted with pivoted pin tips. Reconfigurable tooling already offers a cost saving over traditional solid dies and costs can be further reduced by employing a coarser reconfigurable die. When the new die is fitted to a simplified machine, such as that detailed here, the overall cost of stretch formed parts can be reduced so that the process becomes applicable in a wider industrial context. The AMFOR group has recently been quoted a price of approximately £11,000 for a double curvature solid steel die approximately 1.2 m by 1.2 m. When the relatively small cost of their industrial scale machine and die (approximately £230,000 including hydraulics) has been recovered, pin heights on the reconfigurable die can be adjusted to make an equivalent die for only the cost of the interpolators. While the consumable nature of the interpolators is often seen as a hidden cost to reconfigurable tooling, and regarded as a barrier to the implementation of reconfigurable tooling systems in the workplace, results from the rudimentary cyclic testing of the Kaylan D series of materials (see Section 3.5.2) suggest that they can be used over and over again, without significant changes to their mechanical properties. In general, interpolators used over the new flat pivoted pin tips will suffer less deterioration since they are not subjected to the extreme point loading system present in reconfigurable dies comprised of pins with traditional semi-hemispherical pin tips.

6.2.1 Uses for the New Reconfigurable Die

The new reconfigurable die can be used in manufacturing parts for use in a number of industrial applications, including the two demonstrated in the DATAFORM project, i.e. manufacturing aluminium boat hulls and parabolic

façade panels to enhance the appearance of curved buildings (see Section 2.4.3). While the simulations in Chapter 5 concentrate on selecting an interpolator that gives a smooth surface on the thin material (20 gauge stainless steel 316) formed over the reconfigurable, surface smoothness is not always a requirement. Construction companies have shown a great deal of interest in the honeycombed surface obtained where a part is stretched over the flat pivoted pin tips with no interpolation, and a corrugated surface obtained from stretching a part over a ribbed interpolator. Where the surface flatness, of parts formed over the new die, is not of sufficient quality to meet the requirements of any given application the new die can still be used to reduce the tooling costs through the manufacture of skins for a solid die. A blank can be stretched over the new die to the net shape required, before sides are attached to the trimmed part, and the resulting pocket is filled with concrete to create a solid die. Minimal skimming and polishing is all that is required to create smooth surfaces on dies manufactured in this manner.

6.3 Proposed Further Work

It has been shown in this thesis that relatively smooth parts can be produced from a stretch forming process over a lab scale version of the new reconfigurable die but quite a bit of further work will be required before the new system is ready for use in industrial applications. It is recommended that focus is switched to the industrial scale machine where a number of trials should be undertaken in an attempt the replicate the results obtained here on the lab scale machine. The range of parts produced should be widened to include both clastic and anticlastic curvature, from a number of different materials of various thicknesses, with data gathered on the behaviour of the interpolators used in each trial (including the influence of hydrostatic pressure), the flatness obtained on, and the dimensional accuracy of the parts produced. Data from these tests can also be used to ascertain the springback behaviour of materials formed to a range of shapes over the new reconfigurable die. A rapid method of determining initial pin

heights directly from CAD models, of the target parts, for uniform and non-uniform parts, should be developed. Data gathered from the trials should then be used to further develop the empirical routine, introduced in Section 5.6, to settle on a method of correcting pin heights to compensate for the compressive behaviour of the interpolator in different regions of the reconfigurable die, and the effects of springback. Data from the trials together with data from further detailed PAM-STAMP simulations can also be used to develop a simplified model, similar to the model developed by the MIT team (Socrate & Boyce, 2001) (see Section 2.3.1), using FEA software which employs a rapid solver, to develop a new numerical routine for pin height correction, where computational time will not be such an issue.

Since the stretch forming process is mostly used in the aerospace industry, a further series of tests should be carried out to ascertain whether the new industrial scale die can be directly employed in the manufacture of panels, with sufficient flatness, to repair fuselages. New and replacement panels, at the doors and windows of the fuselage, may also be able to be manufactured on the new industrial scale machine, but its working envelope of approximately 1.2 m by 1.2 m is of insufficient size to manufacture new fuselage panels 90° about their curvature.

With the rise in popularity of additive manufacture technologies and the growth in the number and type of materials available, there is a lot of interest in manufacturing tooling with these new technologies. This is an area that merits further study. Reconfigurable tooling can be used to support the interlocking sections of a die surface manufactured through additive technology. The AMFOR group has had some success stretching clastic and anticlastic parts over four die sections supported on the lab scale machine. While the hexagonal close packed layout employed on AMFOR's industrial scale die is not ideal for supporting these die sections, the round pins can be realigned in a rectangular close packed layout for testing new die surfaces.

No machine design is ever really complete, since design is dependent on a number of factors including, the funding and the technology available. It should be noted that the design of AMFOR's preferred machine layout centres around reducing the cost of stretch forming equipment. AMFOR's preferred machine layout should evolve over time as lessons are learnt and more finance becomes available.

Appendix A. Additional Stretch Forming Processes

A.1 The Wrap Forming Process

Wrap forming, illustrated in Figure A-1, is a process where a blank is gripped in a flat plane before an initial tension is applied [Figure A-1 (a)].

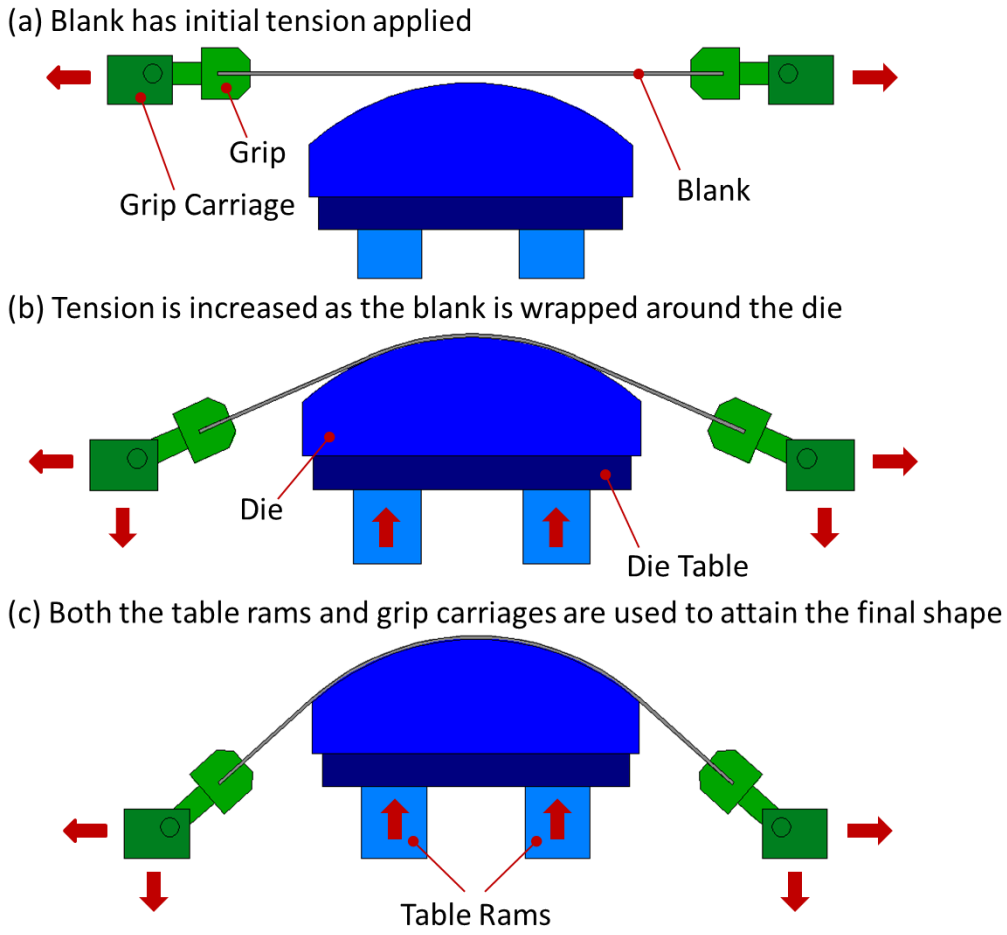

Figure A-1: Wrap Forming shown at early (a) mid (b) and late (c) stages of the process

The now pre-strained blank, is wrapped around the die through displacement of both the die and grip carriages [Figure A-1 (b)]. The tension in the blank is increased during the wrapping process to its final value achieved just after tangential contact between the blank and the ends of dies is met [Figure A-1 (c)]. Since the tension is increased as the blank comes into contact with more of the die, this process can be used to help

combat the effects of friction between the blank and die, and produce a more evenly strained part.

A.2The Cyril Bath Process

The Cyril Bath process, illustrated in Figure A-2, is a hybrid process combining press forming with stretch forming. Either drape or wrap forming can be used in the initial stretch forming stage [Figure A-2 (a)] before a second tool is introduced from above in the press forming stage [Figure A-2 (b)]. The press forming stage can be used to make internal cut-outs and/or press concave contours into the convex part created in the stretch forming stage. A matching set of tools are required for this process which increases its cost. Energy requirements are also increased due to the higher forces present in the press forming stage.

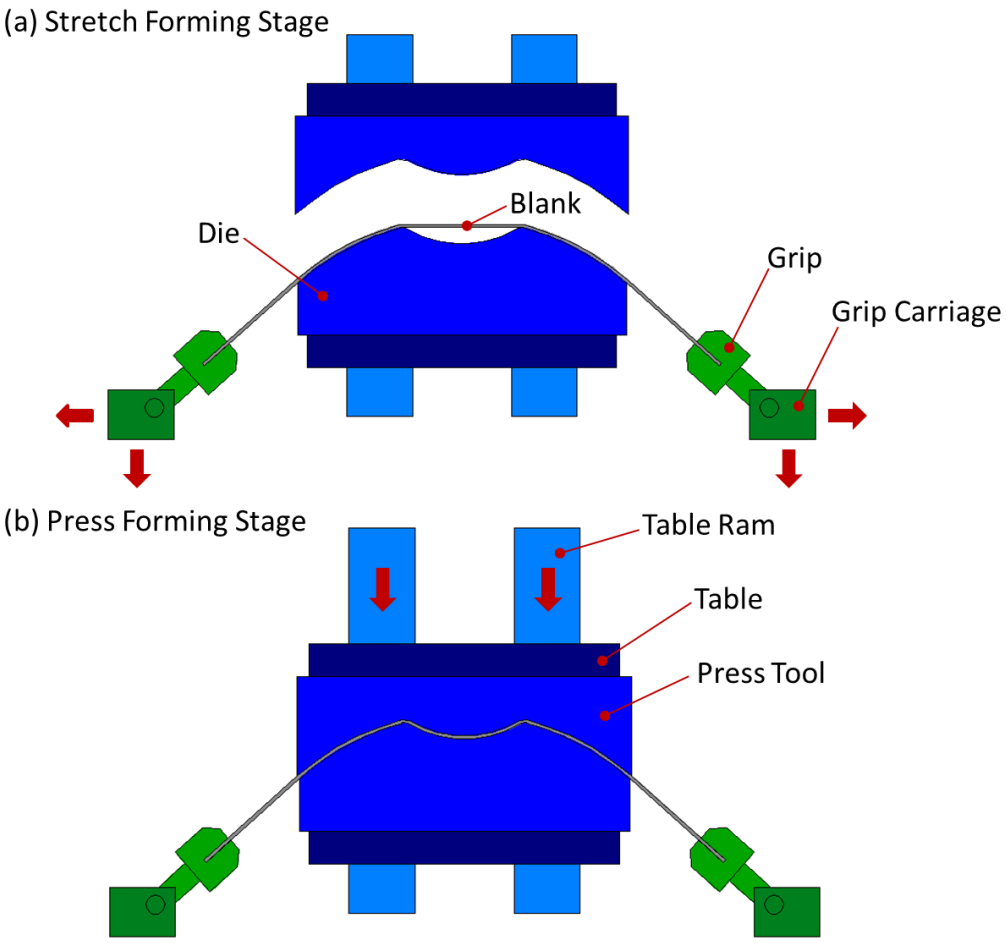

Figure A-2: The stretch forming (a) and press forming (b) stages of the Cyril Bath process

Appendix B. Hill 48 Calibration Methods

Calibration 1

This method uses the normalised (to yield at 0°) yield strength and r-value at 0° to determine values for G and H with Eq. 22 and Eq. 23. It uses the normalised yield strength at 90° to determine a value for F with Eq. B.1,

$$F = 2\left(\frac{1}{\sigma_{90}}\right)^2 - H. \tag{B.1}$$

It uses the r-value at 45° to determine a value for N with Eq. B.2,

$$N = r_{45}(F + G) + \frac{F}{2} + \frac{G}{2}. \tag{B.2}$$

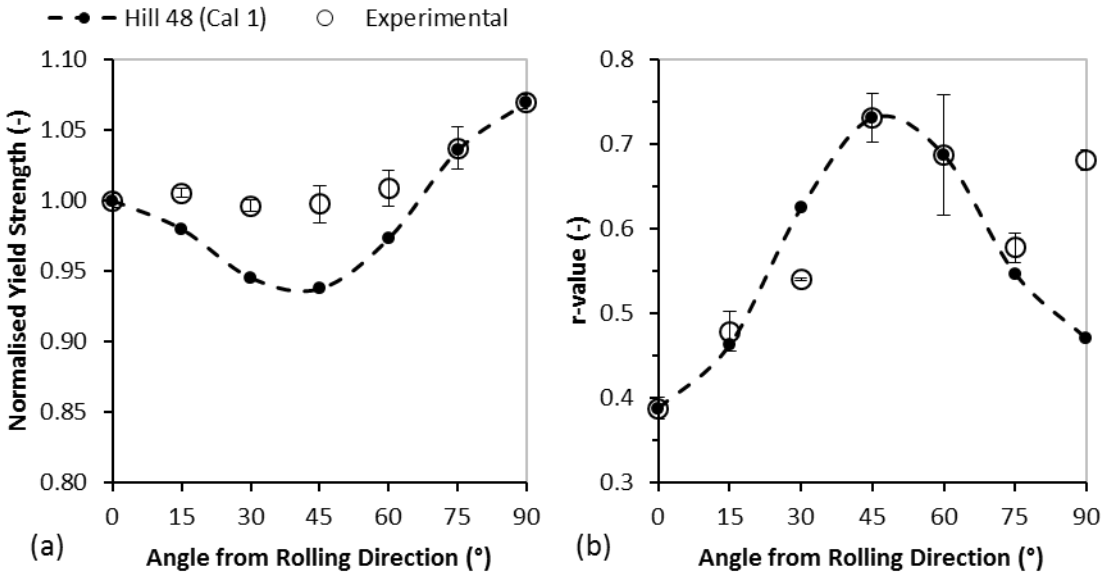

Figure B-1: The Hill 48 (Calibration 1) normalised yield strengths (a) and r-values (b) plotted with experimental results

Calibration 2

This method uses the normalised (to yield at 0°) yield strength and r-value at 0° to determine values for G and H with Eq. 22 and Eq. 23. It uses the normalised yield strength at 90° to determine a value for F with Eq. B.1, and uses the normalised yield strength at 45° to determine a value for N with Eq. B.3,

$$N = 4\left(\frac{1}{\sigma_{45}}\right)^2 - \frac{F}{2} - \frac{G}{2}. \tag{B.3}$$

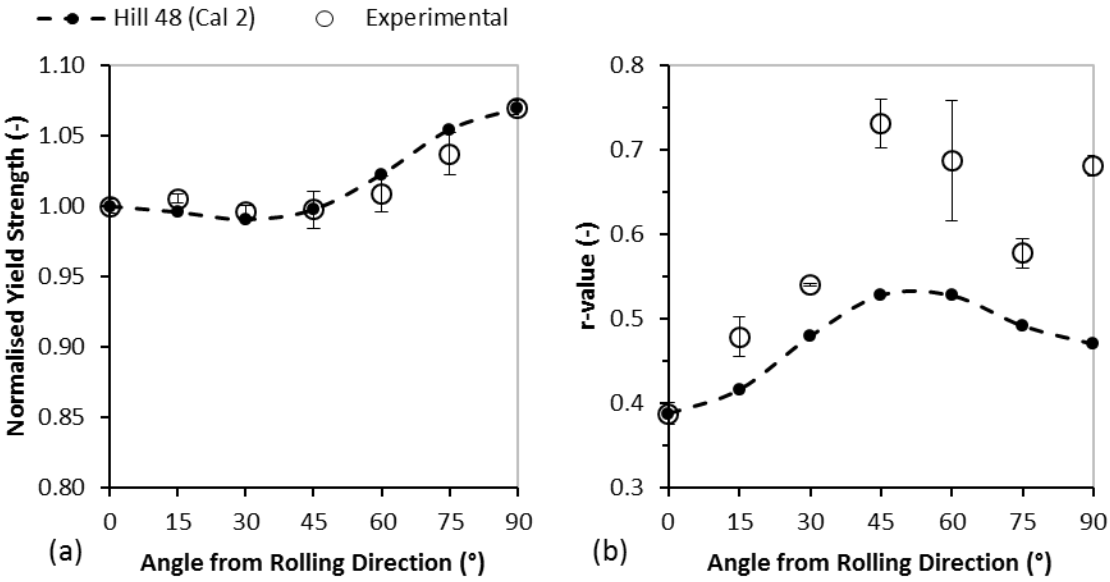

Figure B-2: The Hill 48 (Calibration 2) normalised yield strengths (a) and r-values (b) plotted with experimental results

Calibration 3

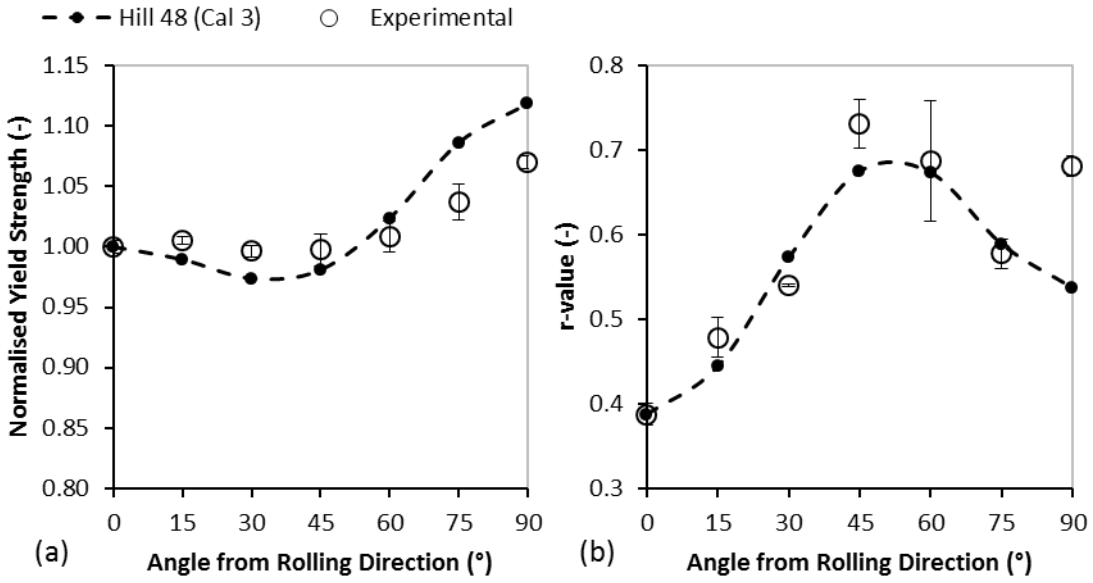

Figure B-3: The Hill 48 (Calibration 3) normalised yield strengths (a) and r-values (b) plotted with experimental results

Again this method uses Eq. 22 and Eq. 23 to determine values for G and H. It uses both the normalised (to yield at 0°) yield strength and the r-value at 90° to determine a value for F with Eq. B.4,

$$F = \frac{2\left(\frac{1}{\sigma_{90}}\right)^2}{(1+r_{90})}. \tag{B.4}$$

It uses both the normalised yield strength and the r-value at 45° to determine a value for N with Eq. B.5,

$$N = 2\left(\frac{1}{\sigma_{45}}\right)^2 + \frac{r_{45}}{2}(F + G). \tag{B.5}$$

Calibration 4

This method uses the normalised (to yield at 90°) yield strength and r-value at 0° to determine values for G and H with Eq. 28 and Eq. 23. It uses the normalised yield strength at 0° to determine a value for F with Eq. B.6,

$$F = 2\left(\frac{1}{\sigma_{00}}\right)^2 - H. \tag{B.6}$$

It uses the r-value at 45° to determine a value for N with Eq. B.2.

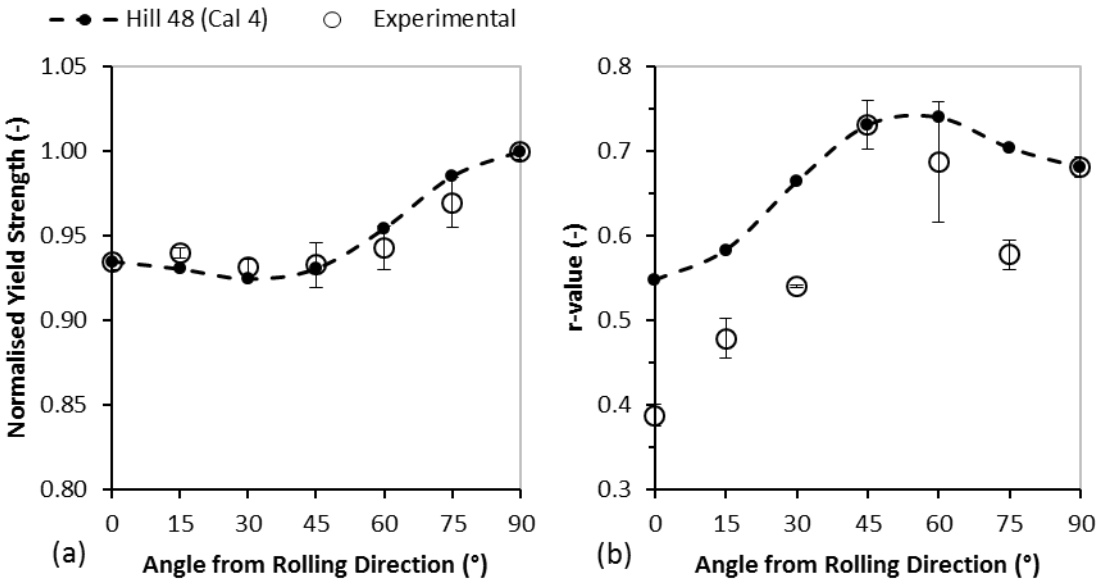

Figure B-4: The Hill 48 (Calibration 4) normalised yield strengths (a) and r-values (b) plotted with experimental results

Calibration 5

This method uses the normalised (to yield at 90°) yield strength and r-value at 0° to determine values for G and H with Eq. 28 and Eq. 23, and again uses Eq. B.6 to determine a value for F, before using the normalised yield strength at 45° to determine a value for N with Eq. B.3.

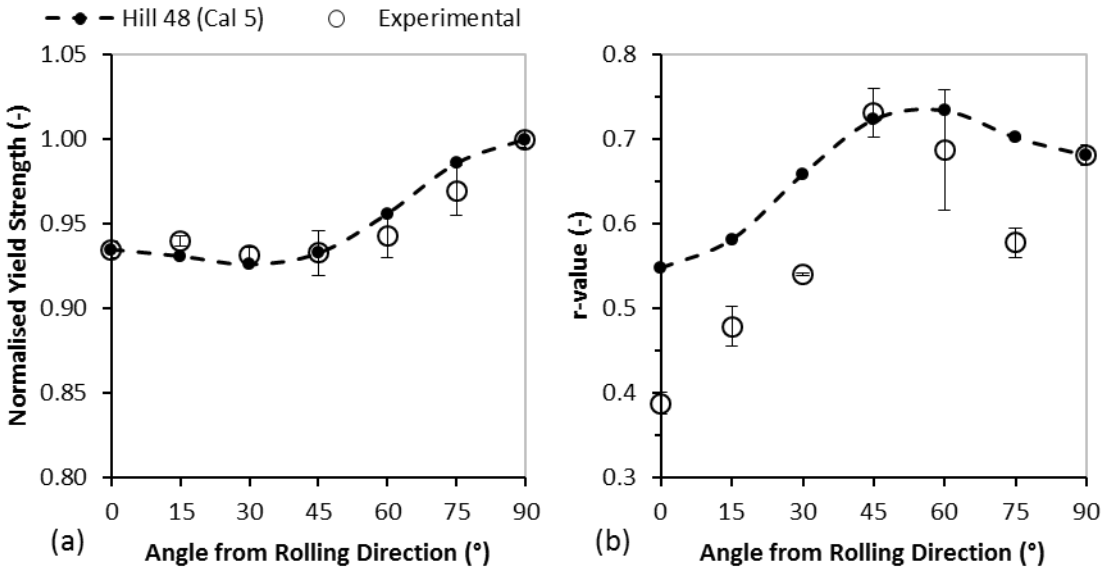

Figure B-5: The Hill 48 (Calibration 5) normalised yield strengths (a) and r-values (b) plotted with experimental results

Calibration 6

Again this method uses Eq. 28 and Eq. 23 to determine values for G and H, with Eq. B.2 used to determine a value for N, after the r-value at 0° is used to determine a value for F with Eq. B.7,

$$F = \frac{H}{r_{00}}. \tag{B.7}$$

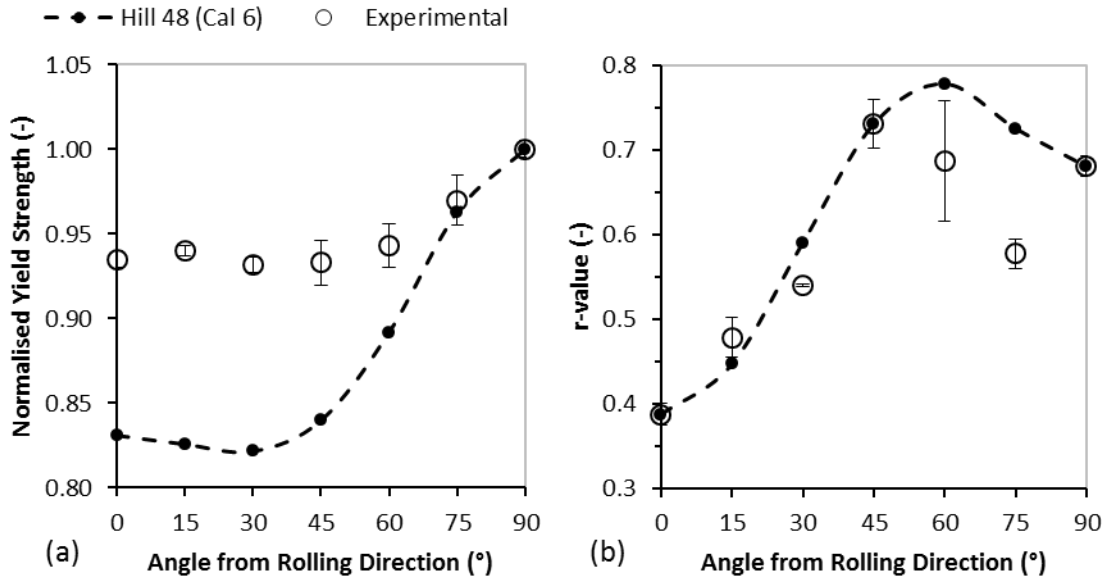

Figure B-6: The Hill 48 (Calibration 6) normalised yield strengths (a) and r-values (b) plotted with experimental results

Calibration 7

Again this method uses Eq. 28 and Eq. 23 to determine values for G and H, with Eq. B.5 used to determine a value for N, after both the normalised (to yield at 90°) yield strength and r-value at 0° is used to determine a value for F with Eq. B.8,

$$F = \frac{2\left(\frac{1}{\sigma_{00}}\right)^2}{(1+r_{00})}. \tag{B.8}$$

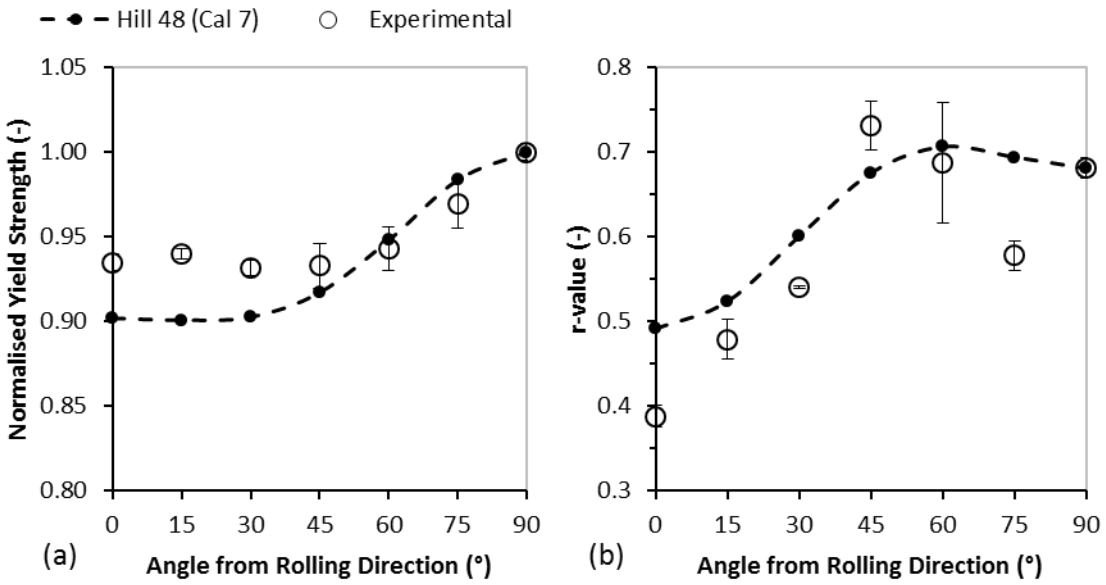

Figure B-7: The Hill 48 (Calibration 7) normalised yield strengths (a) and r-values (b) plotted with experimental results

Appendix C. Uniaxial Tensile Stress/Strain Curves

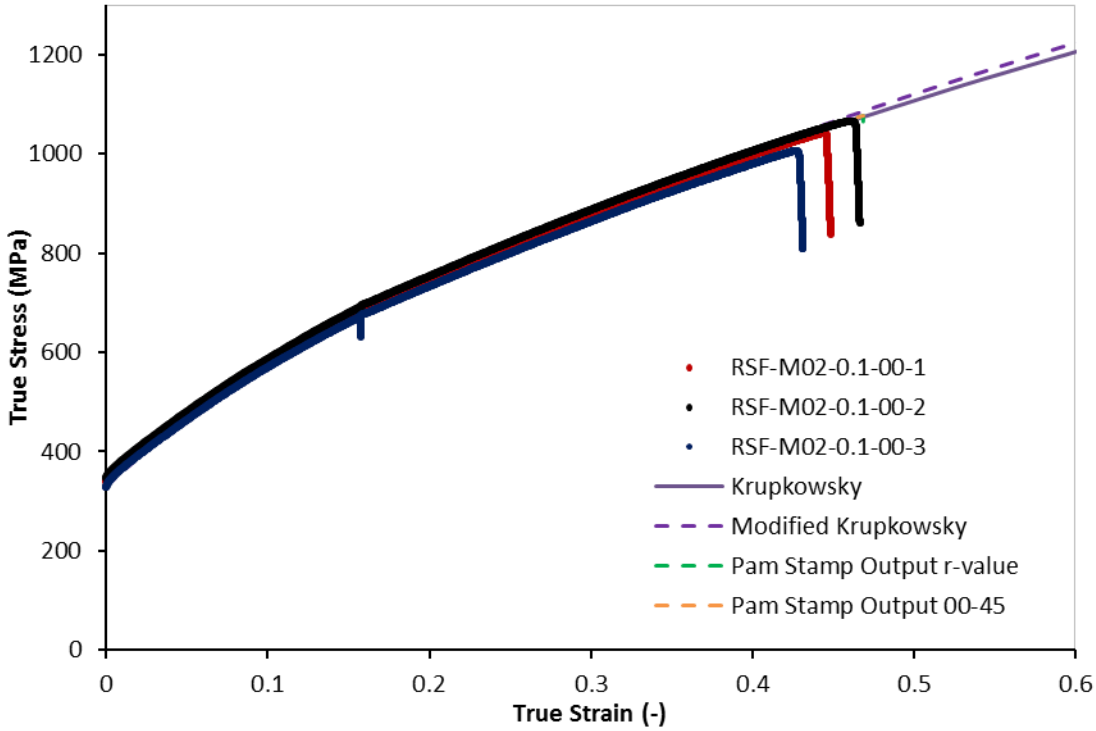

Figure C-1: Stress/strain curves from the uniaxial tensile test in the 0° direction with a crosshead speed of 0.1 mm/min

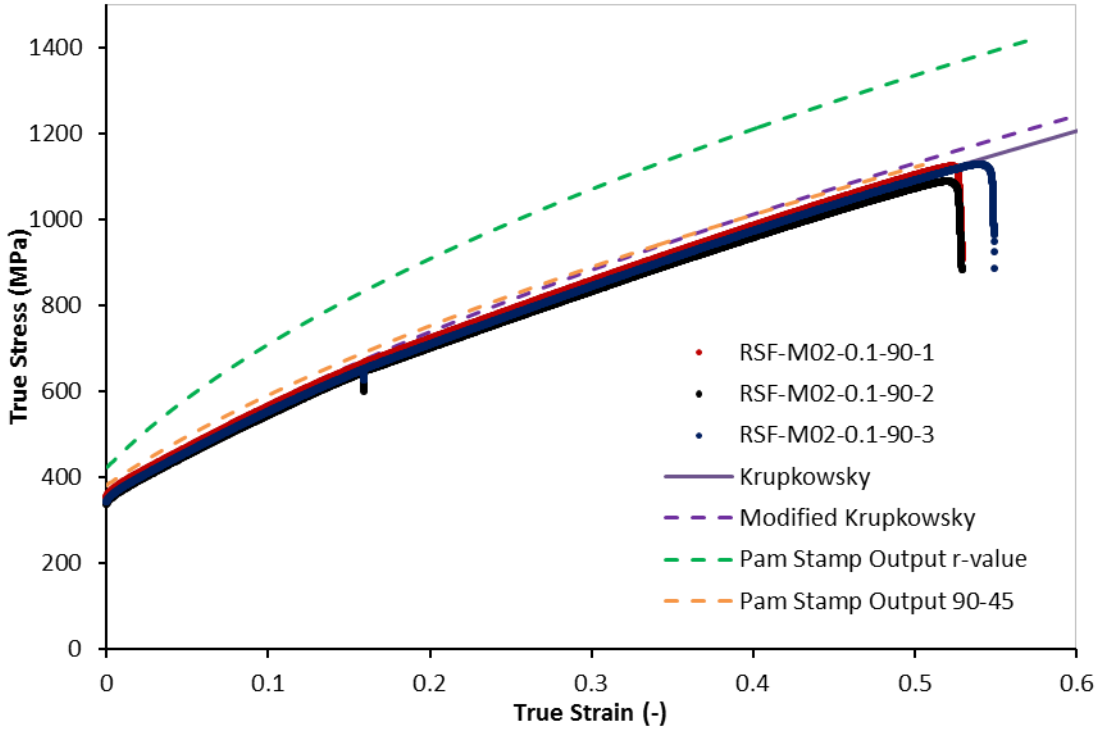

Figure C-2: Stress/strain curves from the uniaxial tensile test in the 90° direction with a crosshead speed of 0.1 mm/min

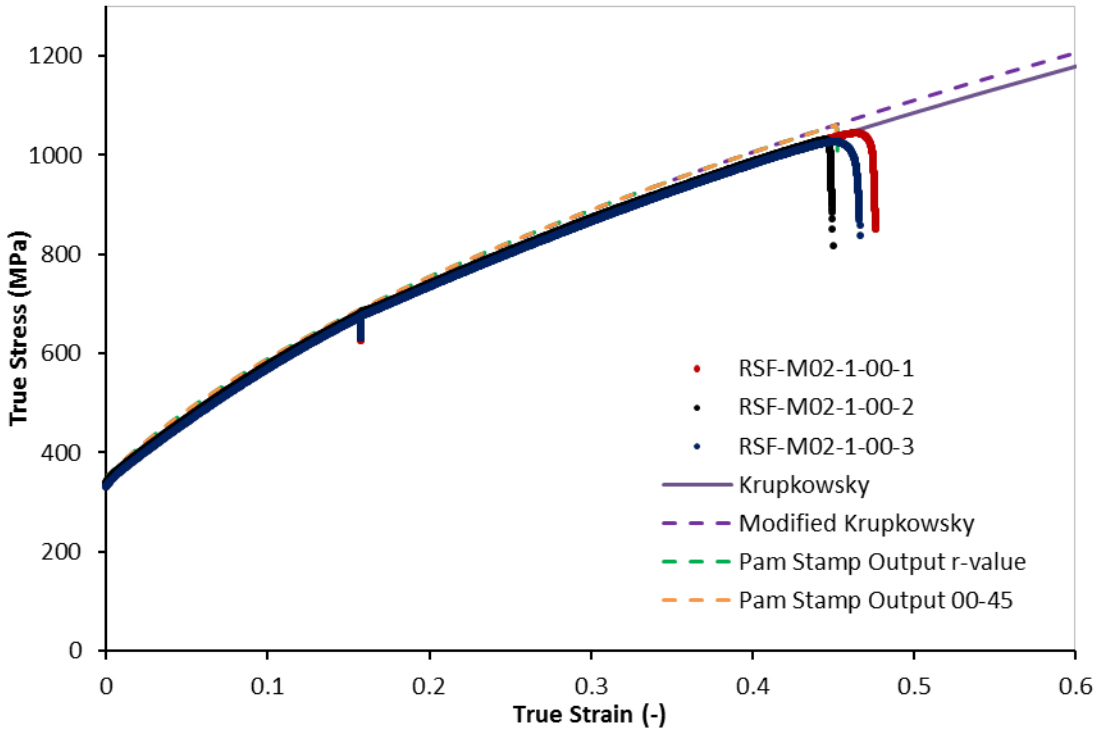

Figure C-3: Stress/strain curves from the uniaxial tensile test in the 0° direction with a crosshead speed of 1 mm/min

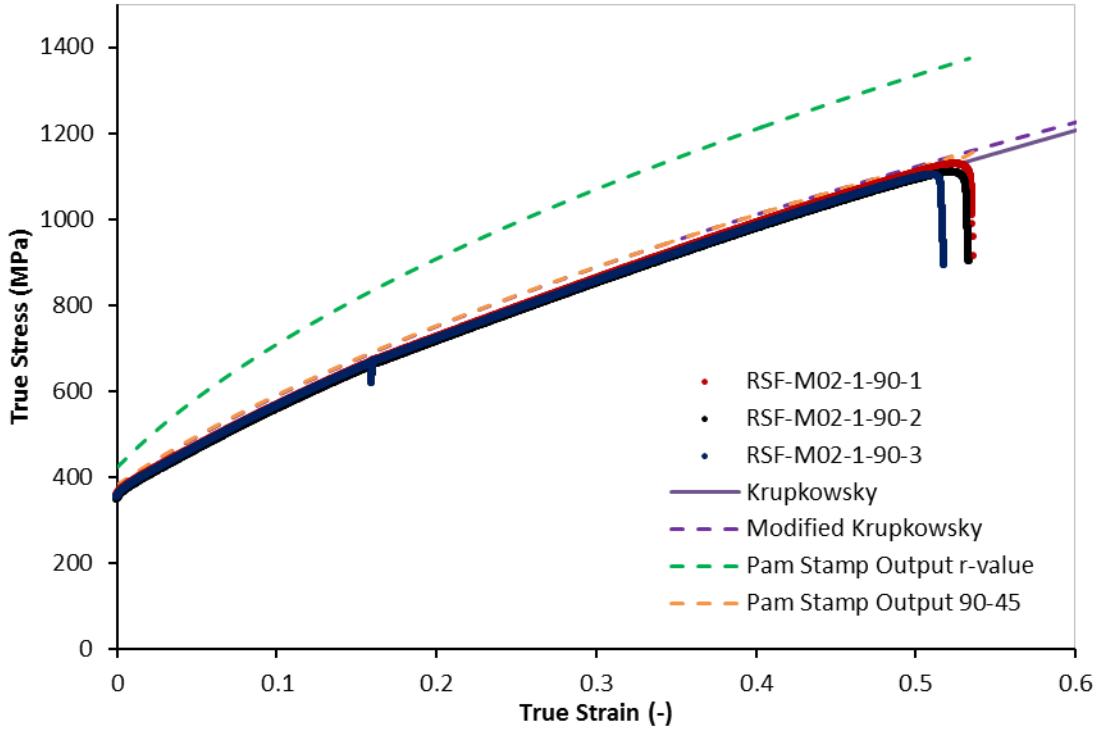

Figure C-4: Stress/strain curves from the uniaxial tensile test in the 90° direction with a crosshead speed of 1 mm/min

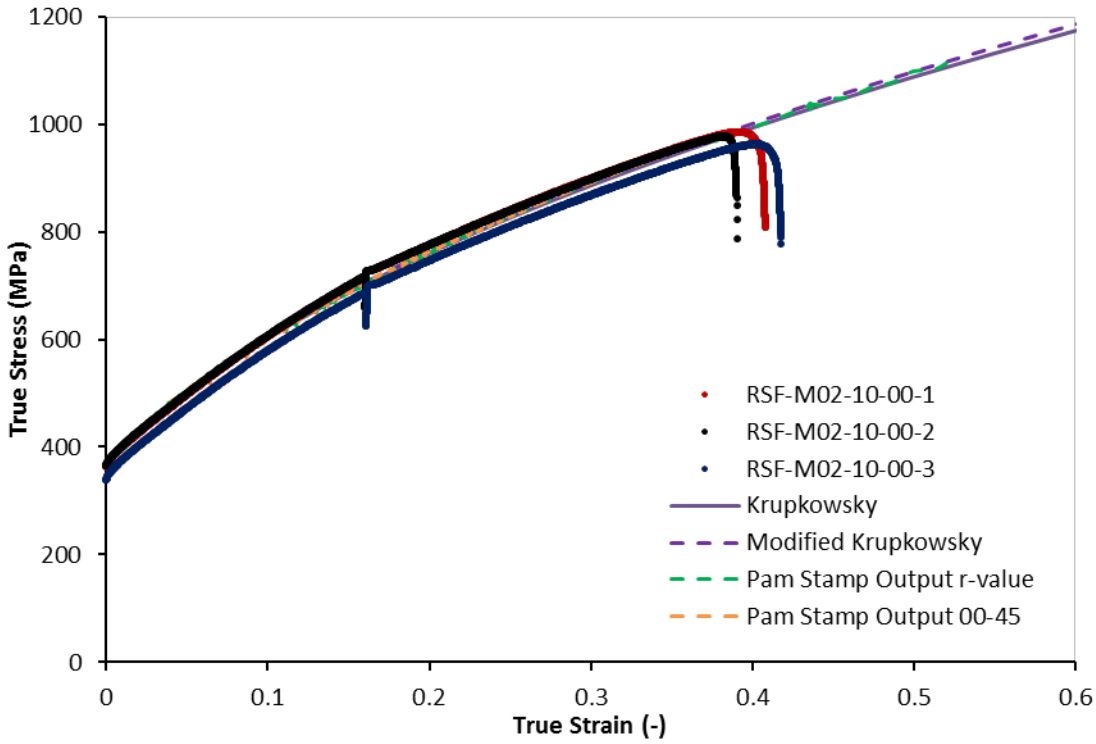

Figure C-5: Stress/strain curves from the uniaxial tensile test in the 0° direction with a crosshead speed of 10 mm/min

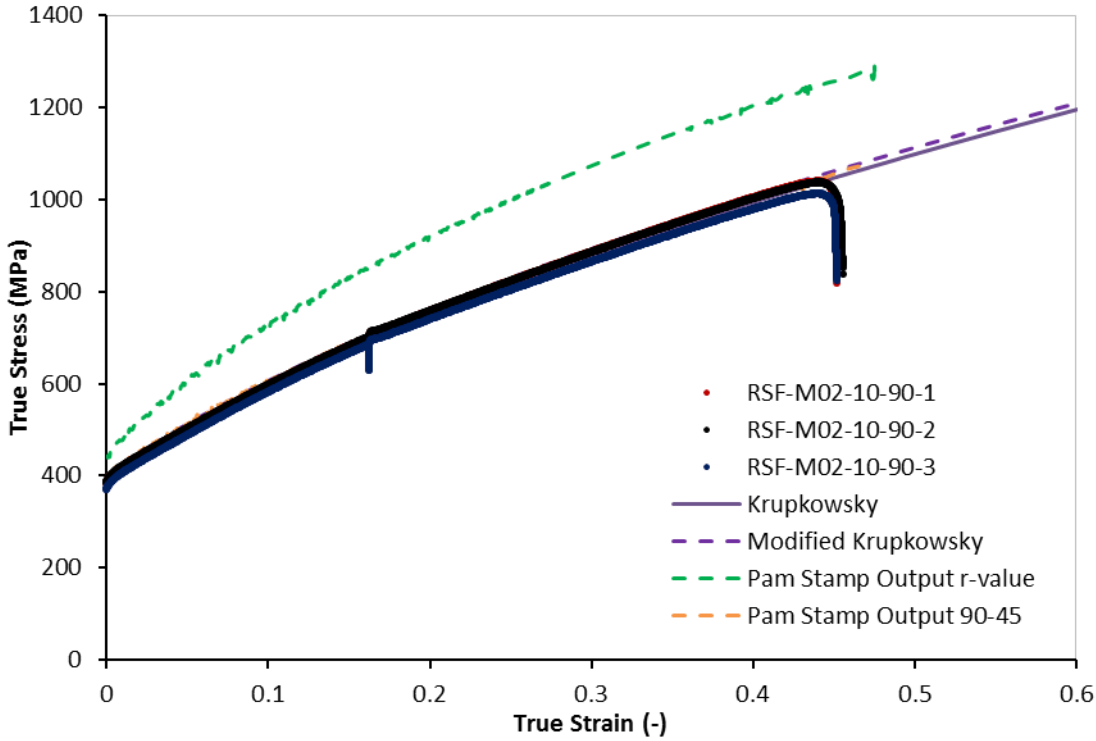

Figure C-6: Stress/strain curves from the uniaxial tensile test in the 90° direction with a crosshead speed of 10 mm/min

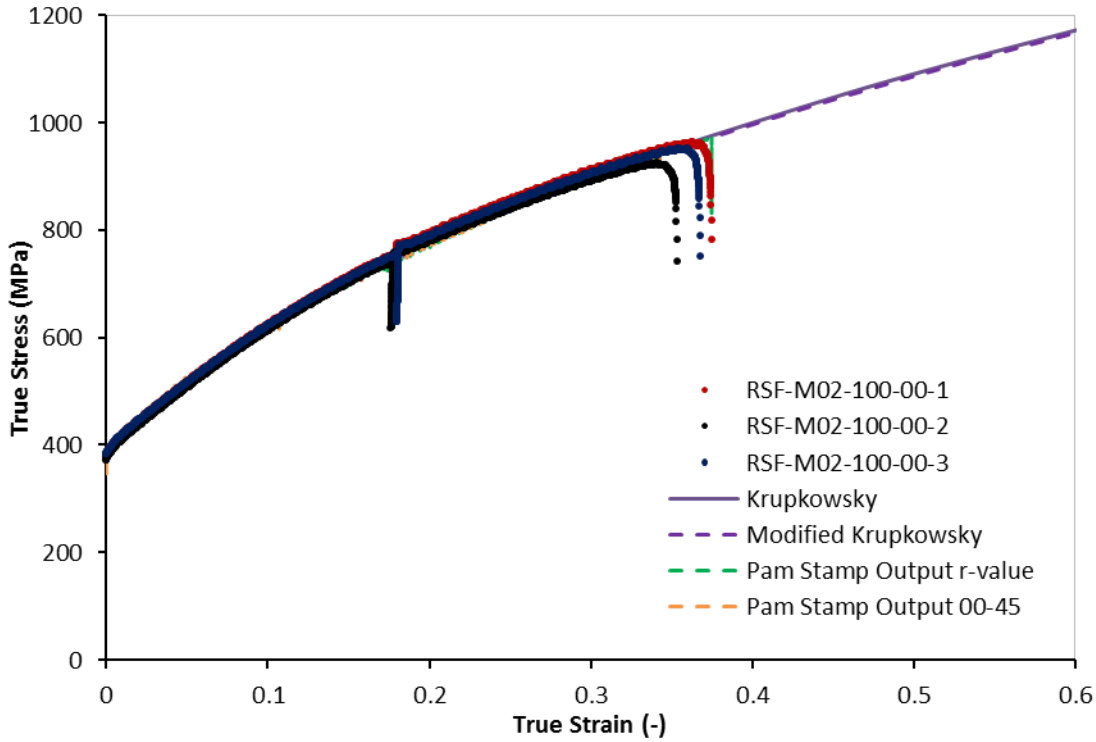

Figure C-7: Stress/strain curves from the uniaxial tensile test in the 0° direction with a crosshead speed of 100 mm/min

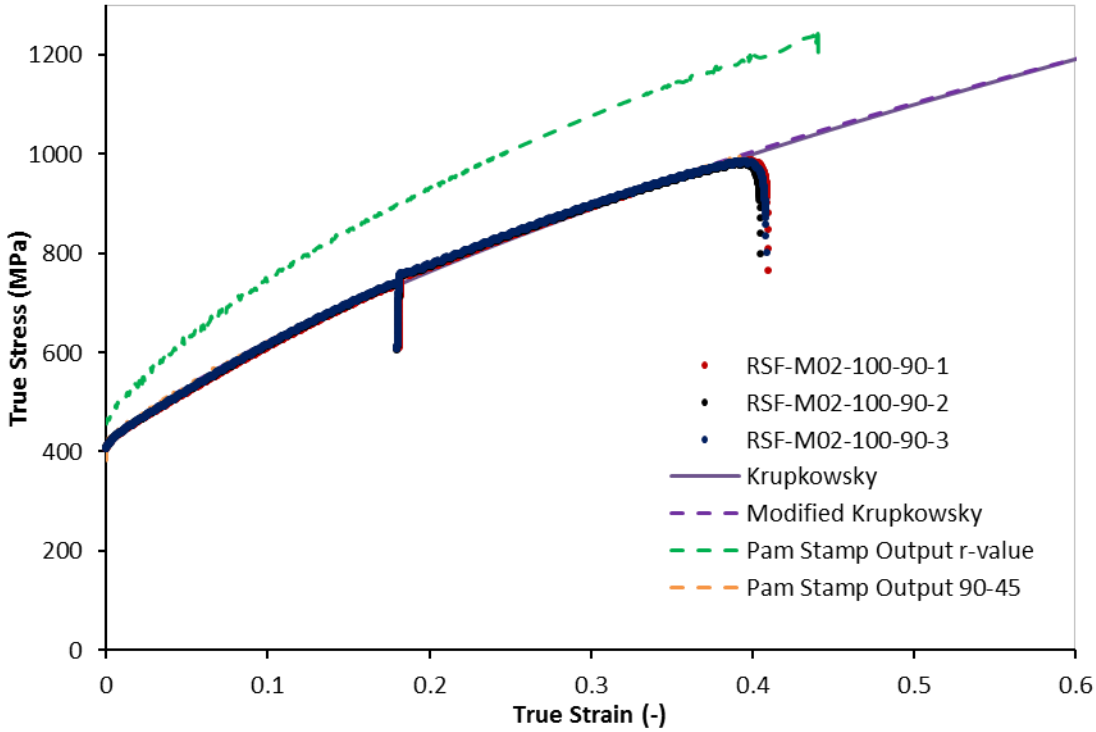

Figure C-8: Stress/strain curves from the uniaxial tensile test in the 90° direction with a crosshead speed of 100 mm/min

Appendix D. The Mooney Rivlin Equation

The two term Mooney Rivlin equation can be given as;

$$W = C_1(I_1 - 3) + C_2(I_2 - 3) \tag{D.1}$$

where, W is the strain energy density function, C_1 & C_2 are the Mooney Rivlin constants and I_1 & I_2 are the first and second strain invariants. The first and second strain invariants can be given in terms of the principle stretch ratios (1 + engineering strain) as;

$$I_1 = {\lambda_1}^2 + {\lambda_2}^2 + {\lambda_3}^2 \tag{D.2}$$

$$\& \; I_2 = {\lambda_1}^2{\lambda_2}^2 + {\lambda_2}^2{\lambda_3}^2 + {\lambda_1}^2{\lambda_3}^2 \tag{D.3}$$

where, λ_1, λ_2 & λ_3 are the stretch ratios in the three principle directions. Hence the strain energy density function can be rewritten in terms of the three principle stretch ratios as;

$$W = C_1\left({\lambda_1}^2 + {\lambda_2}^2 + {\lambda_3}^2 - 3\right) + C_2\left({\lambda_1}^2{\lambda_2}^2 + {\lambda_2}^2{\lambda_3}^2 + {\lambda_1}^2{\lambda_3}^2 - 3\right). \tag{D.4}$$

The strain energy density function represents the stored energy under the curve of an engineering stress / stretch ratio plot (Brown, 2006). Since true stress can be defined as the product of the stretch ratio and engineering stress, true stress in each of the three principle directions can be determined from differentiation of the Mooney Rivlin equation as;

$$\sigma_1 = \lambda_1\frac{dW}{d\lambda_1} = 2C_1{\lambda_1}^2 + 2C_2{\lambda_1}^2\left({\lambda_2}^2 + {\lambda_3}^2\right), \tag{D.5}$$

$$\sigma_2 = \lambda_2\frac{dW}{d\lambda_2} = 2C_1{\lambda_2}^2 + 2C_2{\lambda_2}^2\left({\lambda_1}^2 + {\lambda_3}^2\right) \tag{D.6}$$

$$\& \; \sigma_3 = \lambda_3\frac{dW}{d\lambda_3} = 2C_1{\lambda_3}^2 + 2C_2{\lambda_3}^2\left({\lambda_2}^2 + {\lambda_1}^2\right) \tag{D.7}$$

where σ_1, σ_2, and σ_3 are true stresses in each of the principle directions. When the material is considered to be incompressible the product of the three stretch ratios is equal to one, hence the product of each of stretch ratios squared is also equal to one. Therefore the product of any two of these terms is equal to the inverse of the third, and the principle stress equations can be rewritten as;

$$\sigma_1 = \lambda_1 \frac{dW}{d\lambda_1} = 2C_1{\lambda_1}^2 + 2C_2\left({\lambda_3}^{-2} + {\lambda_2}^{-2}\right), \quad \text{(D.8)}$$

$$\sigma_2 = \lambda_2 \frac{dW}{d\lambda_2} = 2C_1{\lambda_2}^2 + 2C_2\left({\lambda_3}^{-2} + {\lambda_1}^{-2}\right) \quad \text{(D.9)}$$

$$\& \ \sigma_3 = \lambda_3 \frac{dW}{d\lambda_3} = 2C_1{\lambda_3}^2 + 2C_2\left({\lambda_1}^{-2} + {\lambda_2}^{-2}\right). \quad \text{(D.10)}$$

The final Mooney Rivlin equation for any deformation state is determined by considering the true stress difference in two of the principle directions,

$$\sigma_1 - \sigma_3 = 2C_1{\lambda_1}^2 + 2C_2\left({\lambda_3}^{-2} + {\lambda_2}^{-2}\right) - 2C_1{\lambda_3}^2 + 2C_2\left({\lambda_1}^{-2} + {\lambda_2}^{-2}\right)$$

$$\sigma_1 - \sigma_3 = 2C_1\left({\lambda_1}^2 - {\lambda_3}^2\right) + 2C_2\left({\lambda_3}^{-2} - {\lambda_1}^{-2}\right). \quad \text{(D.11)}$$

Therefore, in uniaxial tension where, $\sigma_2 = \sigma_3 = 0 \ \& \ \lambda_2 = \lambda_3 = {\lambda_1}^{-0.5}$, true stress can be determined in the stretch direction as;

$$\sigma_1 - \sigma_3 = \sigma_1 = 2C_1\left({\lambda_1}^2 - {\lambda_3}^2\right) + 2C_2\left({\lambda_3}^{-2} - {\lambda_1}^{-2}\right)$$

$$\sigma_1 = 2C_1\left({\lambda_1}^2 - {\lambda_1}^{-1}\right) + 2C_2\left(\lambda_1 - {\lambda_1}^{-2}\right)$$

$$\sigma_1 = 2C_1\left({\lambda_1}^2 - {\lambda_1}^{-1}\right) + 2C_2{\lambda_1}^{-1}\left({\lambda_1}^2 - {\lambda_1}^{-1}\right)$$

$$\sigma_1 = 2\left(C_1 + C_2{\lambda_1}^{-1}\right)\left({\lambda_1}^2 - {\lambda_1}^{-1}\right). \quad \text{(D.12)}$$

In equibiaxial tension where, $\sigma_1 = \sigma_2, \sigma_3 = 0, \lambda_1 = \lambda_2 \ \& \ \lambda_3 = {\lambda_{1,2}}^{-2}$, true stress can be determined in either of the stretch directions as;

$$\sigma_1 - \sigma_3 = 2C_1\left({\lambda_1}^2 - {\lambda_3}^2\right) + 2C_2\left({\lambda_3}^{-2} - {\lambda_1}^{-2}\right)$$

$$\sigma_1 = \sigma_2 = 2C_1\left({\lambda_1}^2 - {\lambda_1}^{-4}\right) + 2C_2\left({\lambda_1}^4 - {\lambda_1}^{-2}\right)$$

$$\sigma_1 = \sigma_2 = 2C_1\left({\lambda_1}^2 - {\lambda_1}^{-4}\right) + 2C_2{\lambda_1}^2\left({\lambda_1}^2 - {\lambda_1}^{-4}\right)$$

$$\sigma_1 = \sigma_2 = 2\left(C_1 + C_2{\lambda_1}^2\right)\left({\lambda_1}^2 - {\lambda_1}^{-4}\right). \quad \text{(D.13)}$$

In uniaxial compression where, $\sigma_1 = \sigma_2 = 0, \& \ \lambda_1 = \lambda_2 = {\lambda_3}^{-0.5}$ true stress can be determined in the direction of compression as;

$$\sigma_1 - \sigma_3 = -\sigma_3 = 2C_1\left({\lambda_1}^2 - {\lambda_3}^2\right) + 2C_2\left({\lambda_3}^{-2} - {\lambda_1}^{-2}\right)$$

$$-\sigma_3 = 2C_1\left({\lambda_3}^{-1} - {\lambda_3}^2\right) + 2C_2\left({\lambda_3}^{-2} - \lambda_3\right)$$

$$\sigma_3 = 2C_1\left({\lambda_3}^2 - {\lambda_3}^{-1}\right) + 2C_2\left(\lambda_3 - {\lambda_3}^{-2}\right)$$

$$\sigma_3 = 2C_1\left({\lambda_3}^2 - {\lambda_3}^{-1}\right) + 2C_2{\lambda_3}^{-1}\left({\lambda_3}^2 - {\lambda_3}^{-1}\right)$$

$$\sigma_3 = 2\left(C_1 + C_2{\lambda_3}^{-1}\right)\left({\lambda_3}^2 - {\lambda_3}^{-1}\right). \quad \text{(D.14)}$$

Note that while Eq.D.14 takes the same form as Eq.D.12, it is actually equivalent to Eq.D.13 with the stretch ratio converted to correspond to the defined stress direction.

Appendix E. Mooney Rivlin Plots

Before curve fitting routines became readily available on a standard personal computer, for a given hyperelastic material Mooney Rivlin plots were used to determine the Mooney Rivlin constants C_1 and C_2. Since true stress can be defined as a product of engineering stress and the stretch ratio the Mooney Rivlin equation for a hyperelastic material in uniaxial tension or compression can be given as;

$$s = 2(C_1 + C_2\lambda^{-1})(\lambda - \lambda^{-2}) \tag{E.1}$$

where, s is engineering stress, C_1 and C_2 are the Mooney Rivlin constants and λ is the stretch ration in the stress direction. A paper published by employees of the US National Bureau of Standards (Martin, et al., 1957) develops an equation which includes Young's Modulus in its definition of stress as;

$$s = M(\lambda^{-1} - \lambda^{-2}) \exp A(\lambda - \lambda^{-1}) \tag{E.2}$$

where, M is Young's Modulus and A is a material dependent parameter. The following procedure, described in a paper published in the National Bureau of Standards' Journal of Research (Wood, 1977), illustrates how the Mooney Rivlin constants can be determined using plots of this relationship.

Firstly, rearranging Eq.E.2 gives;

$$s/(\lambda^{-1} - \lambda^{-2}) = M \exp A(\lambda - \lambda^{-1}). \tag{E.3}$$

Plotting the log of the left-hand side of Eq.E.3 against $\lambda - \lambda^{-1}$ should reveal a linear relationship at higher strains in tension and compression. Results from uniaxial tension and compression tests on the D40-Orange polyurethane material have been plotted using this method in Figure E-1. If the linear relationship illustrated in Figure E-1 is not evident, the material cannot be described accurately with a Mooney Rivlin equation. The equation of this straight line can be used to determine value for M (Young's modulus) and A. To convert from the log scale, ten to the power of the intercept yields a value for Young's modulus (in the units used for stress) and the slope of

the line divided by 0.4343 (the log of Euler's number) yields a value for the parameter A.

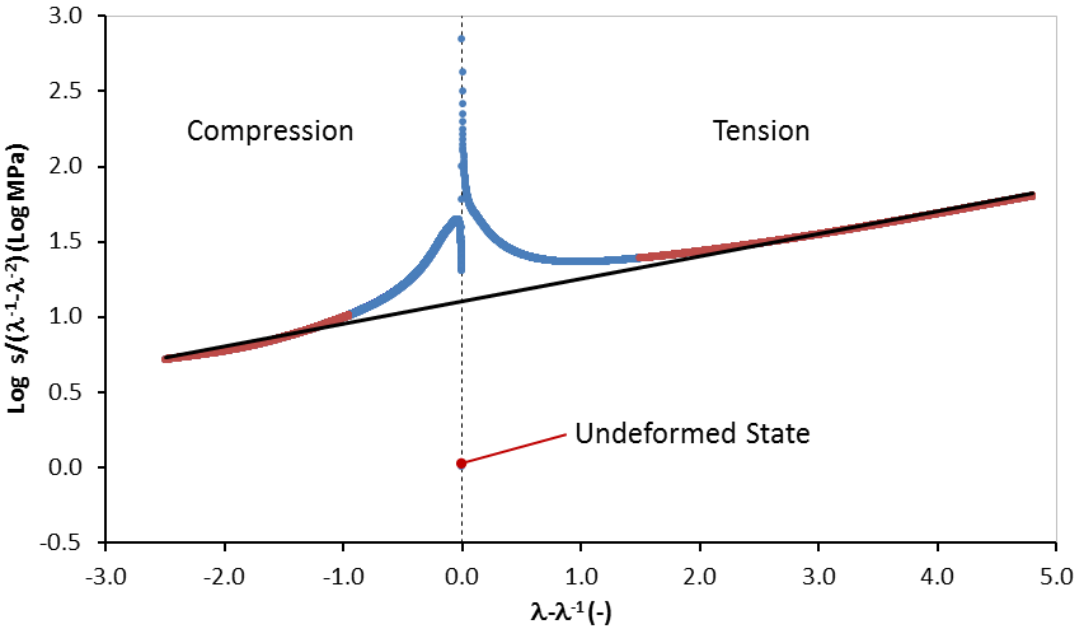

Figure E-1: Mooney Rivlin plot to determine the *M* & *A* parameters

Rearranging Eq.E.1 gives;

$$s/2(\lambda - \lambda^{-2}) = C_1 + C_2\lambda^{-1}, \tag{E.4}$$

where the right-hand side is the equation of a straight line. Using the values of M and A determined from the first Mooney Rivlin plot and describing stress with Eq.E.2 it is evident that in the undeformed state both the numerator and denominator of the left-hand side term are zero. Hence both are differentiated in relation to λ and the L'Hopital rule is applied to obtain;

$$\phi M = \frac{M\lambda^{-1}[\exp A(\lambda-\lambda^{-1})][A(1-\lambda^{-1}+\lambda^{-2}-\lambda^{-3})-\lambda^{-1}+2\lambda^{-2}]}{2+4\lambda^{-3}}, \tag{E.5}$$

before plotting against λ^{-1} to reveal linear regions where C_1 and C_2 are constant in tension and in compression.

Figure E-2 shows a plot using this method to determine the C_1 and C_2 constants for the D40-Orange polyurethane material. The C_1 and C_2 constants in tension and compression are determined as the intercept and slope, respectively, of the lines describing the linear regions of the curve. While the slope of the linear region is positive in tension, it is clear that the

slope of the linear region in compression is always negative. Hence when uniaxial compression data is used to determine values for the Mooney Rivlin constants, C_2 will always be negative.

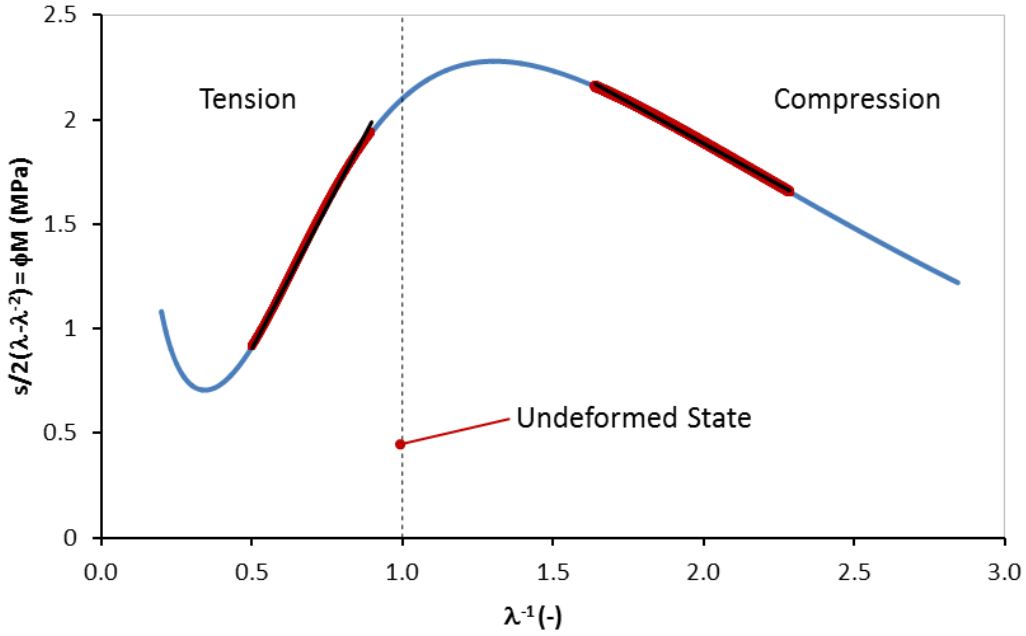

Figure E-2: Mooney Rivlin plot to determine the C_1 & C_2 constants

Appendix F. Polyurethane Compression Plots

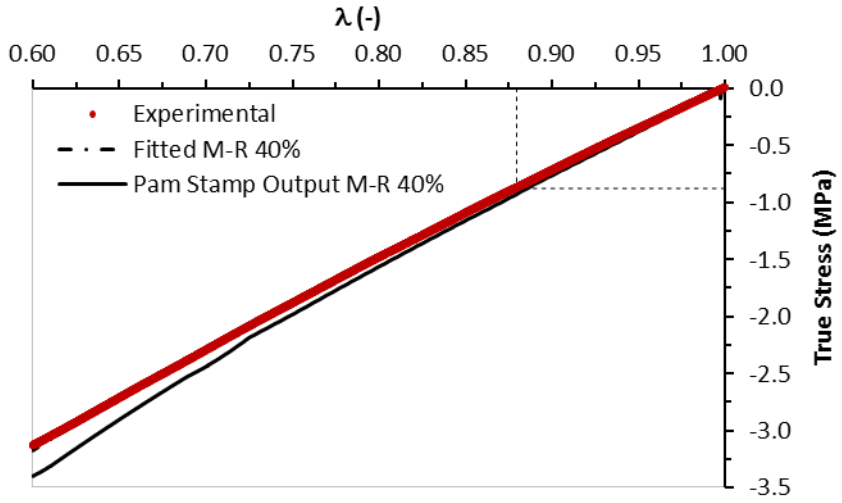

Figure F-1: True stress/stretch ratio compression curves for the Kaylan D25 Purple polyurethane material

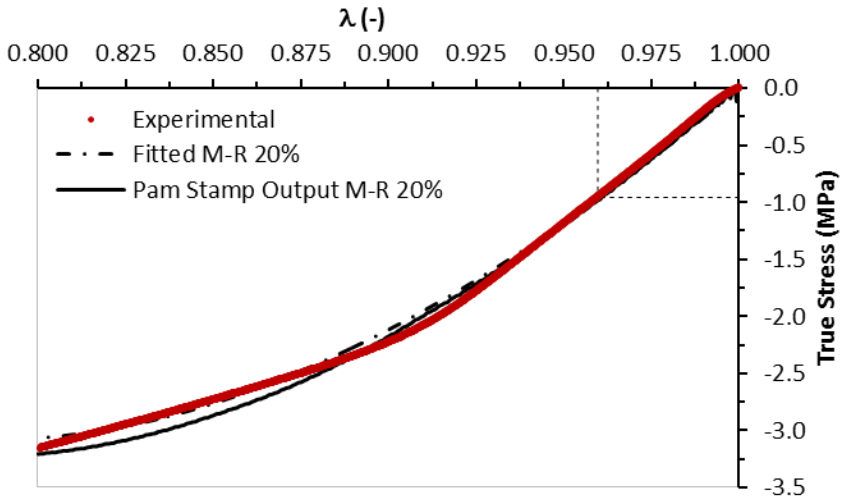

Figure F-2: True stress/stretch ratio compression curves for the Kaylan D30 Green polyurethane material

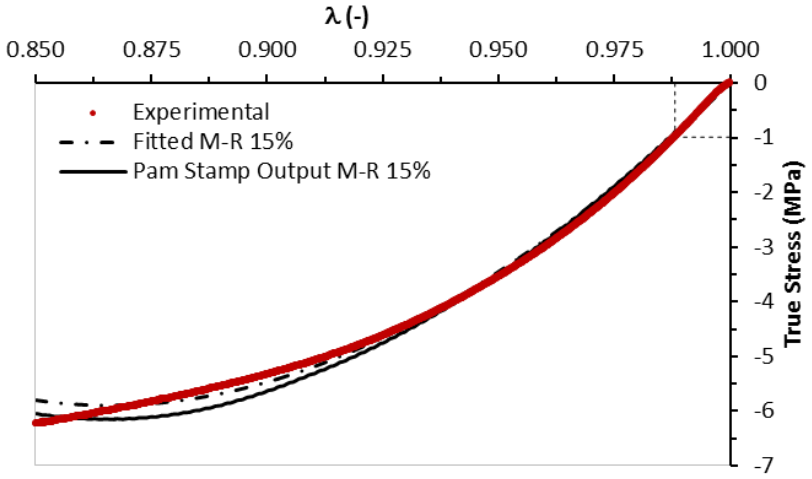

Figure F-3: True stress/stretch ratio compression curves for the Kaylan D50 Blue polyurethane material

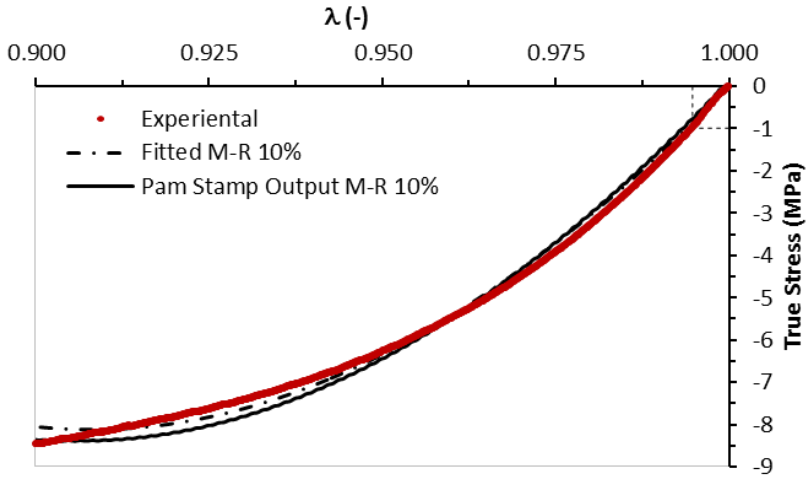

Figure F-4: True stress/stretch ratio compression curves for the Kaylan D60 Brown polyurethane material

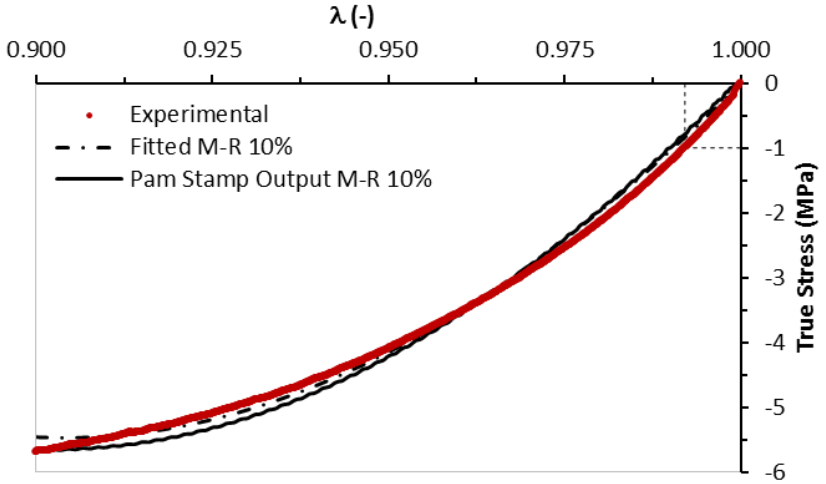

Figure F-5: True stress/stretch ratio compression curves for the Kaylan D60X Violet polyurethane material

Appendix G. Polyurethane Cyclic Loading Plots

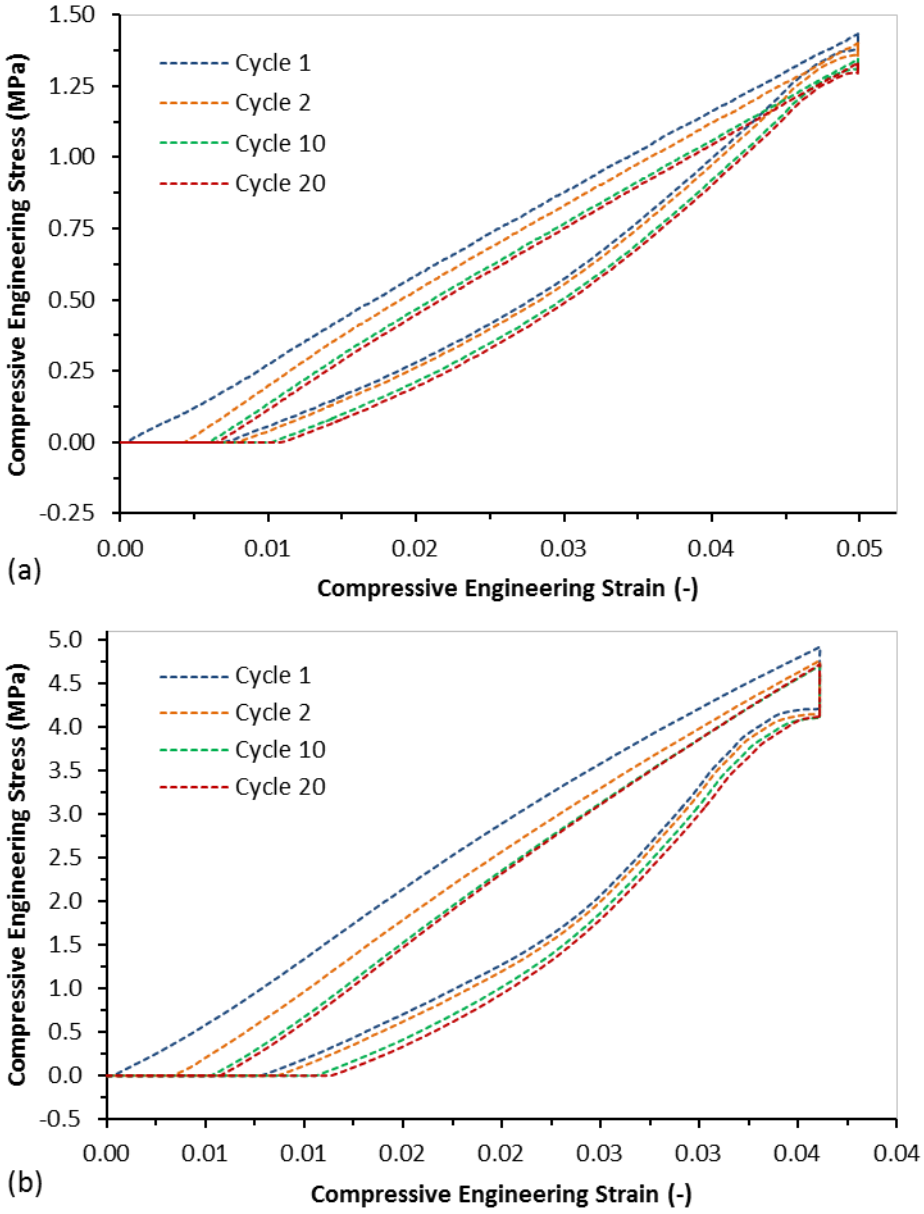

Figure G-1: Engineering stress versus strain plots showing cycles 1, 2, 10 & 20 for the Green-0.5mm (a) and Brown-0.35mm (b) cyclic compression tests

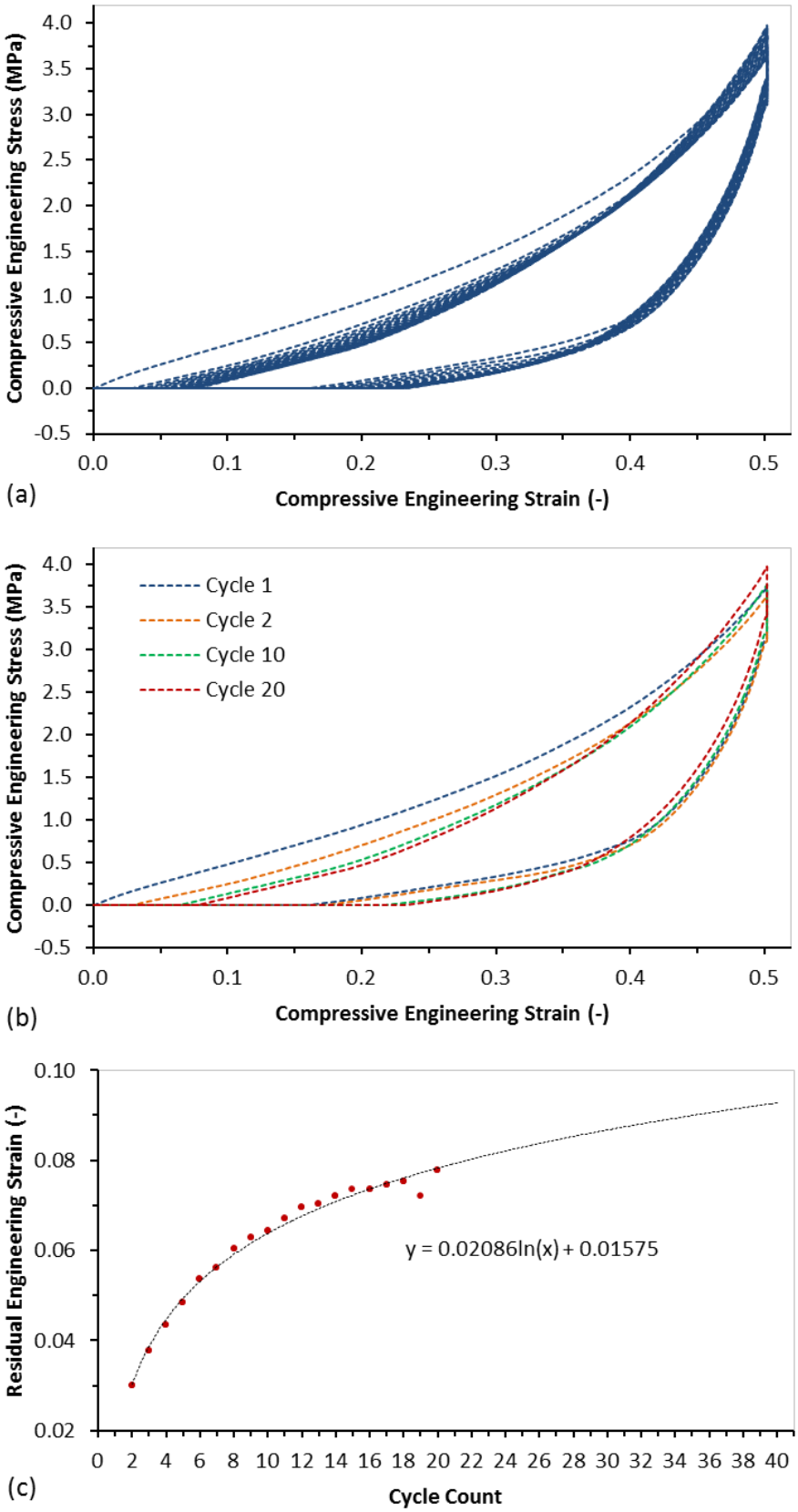

Figure G-2: Engineering stress versus strain plots showing all 20 cycles (a) and cycles 1, 2, 10 & 20 (b) together with a plot of residual strain versus cycle count (c) for the Red-5mm cyclic compression test

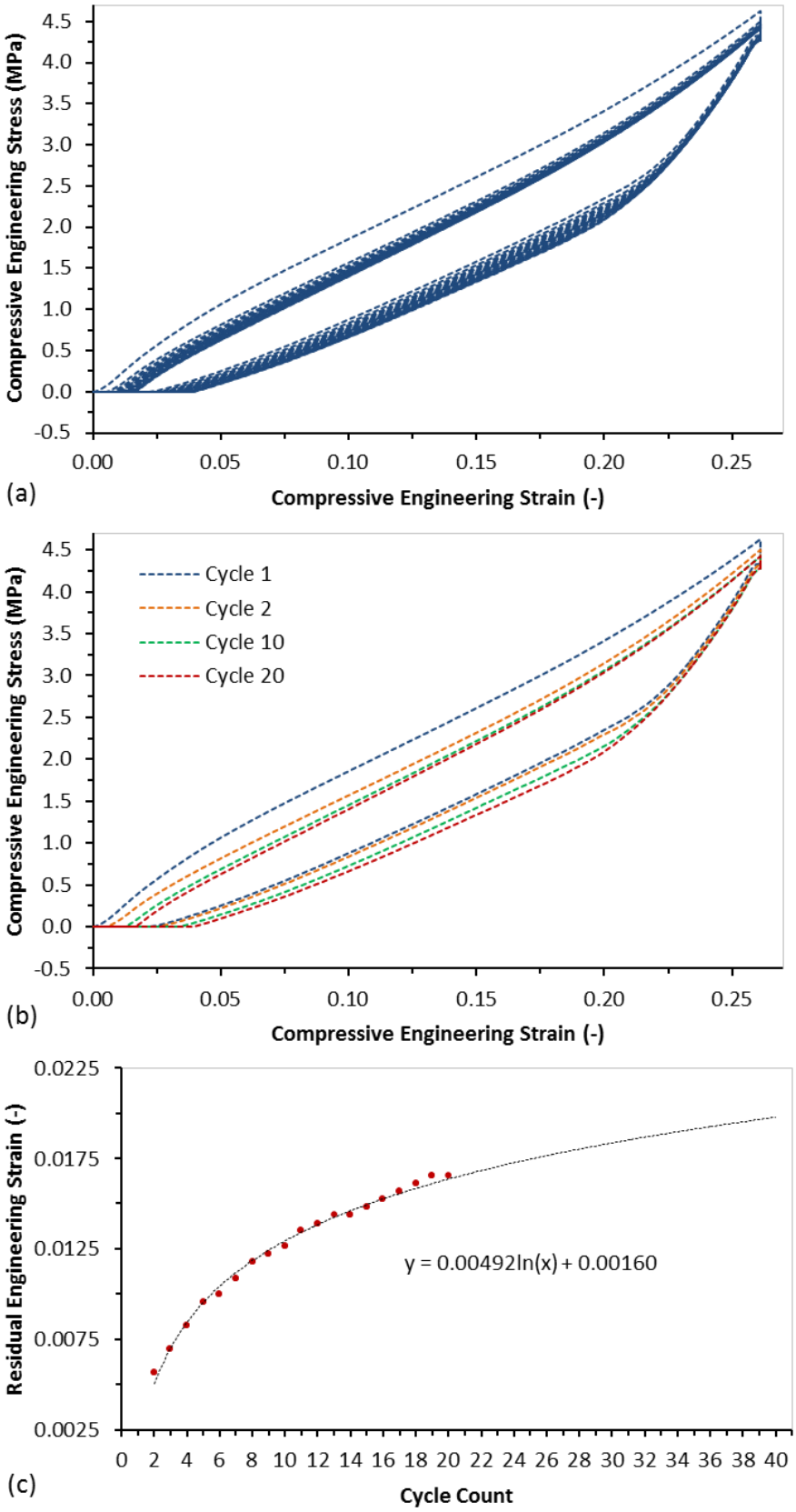

Figure G-3: Engineering stress versus strain plots showing all 20 cycles (a) and cycles 1, 2, 10 & 20 (b) together with a plot of residual strain versus cycle count (c) for the Green-2.56mm cyclic compression test

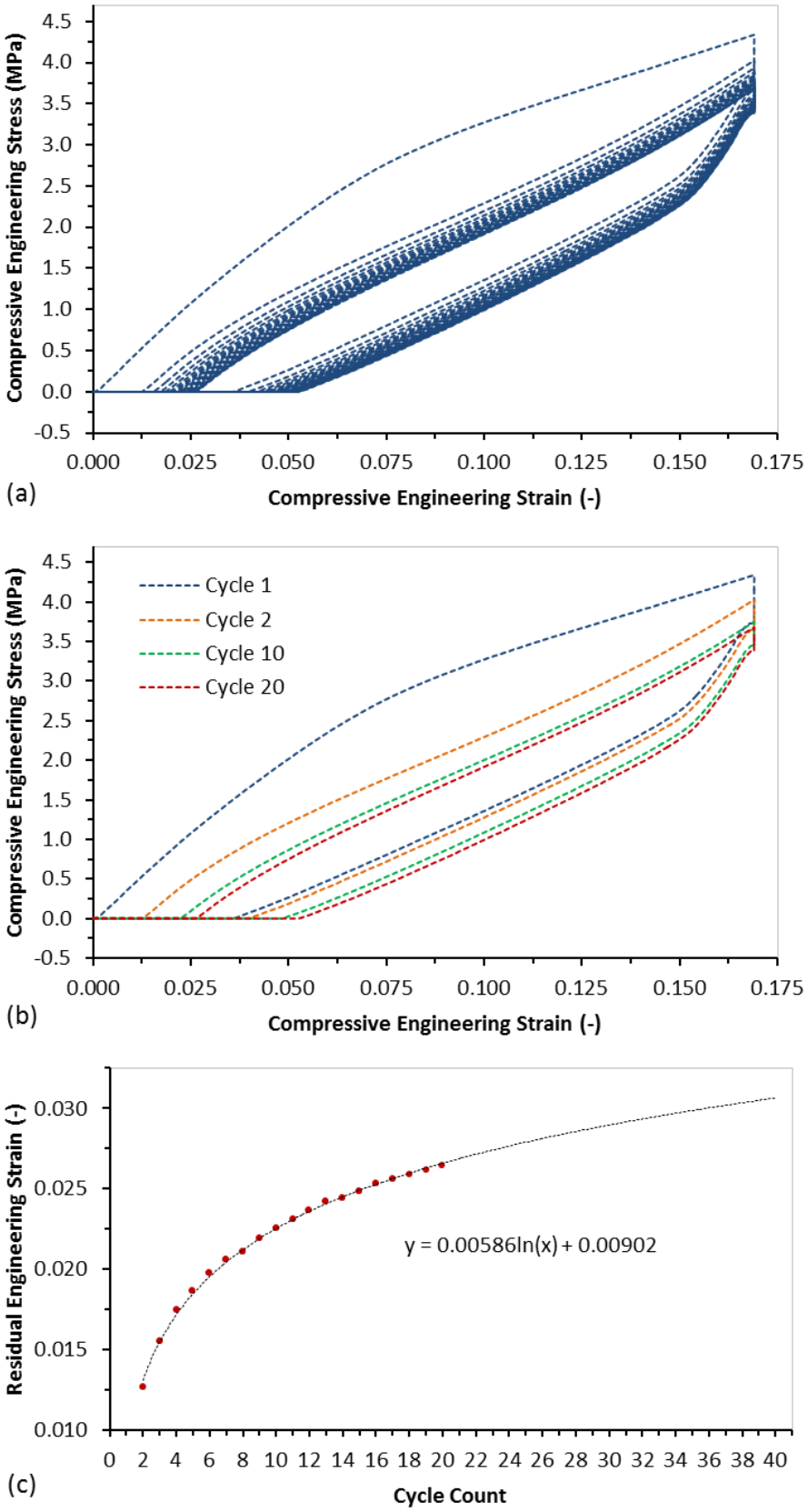

Figure G-4: Engineering stress versus strain plots showing all 20 cycles (a) and cycles 1, 2, 10 & 20 (b) together with a plot of residual strain versus cycle count (c) for the Orange-1.8mm cyclic compression test

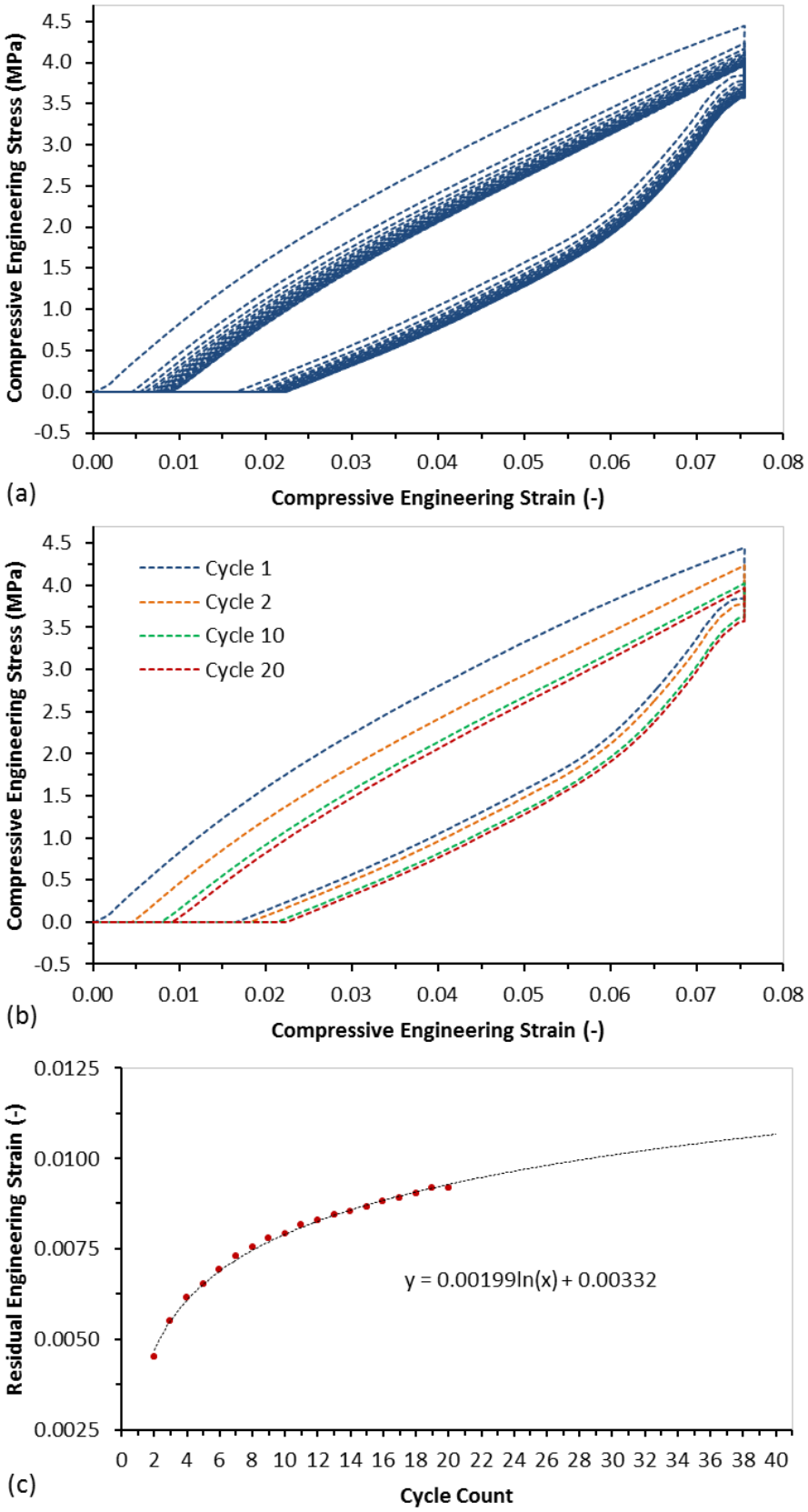

Figure G-5: Engineering stress versus strain plots showing all 20 cycles (a) and cycles 1, 2, 10 & 20 (b) together with a plot of residual strain versus cycle count (c) for the Blue-0.8mm cyclic compression test

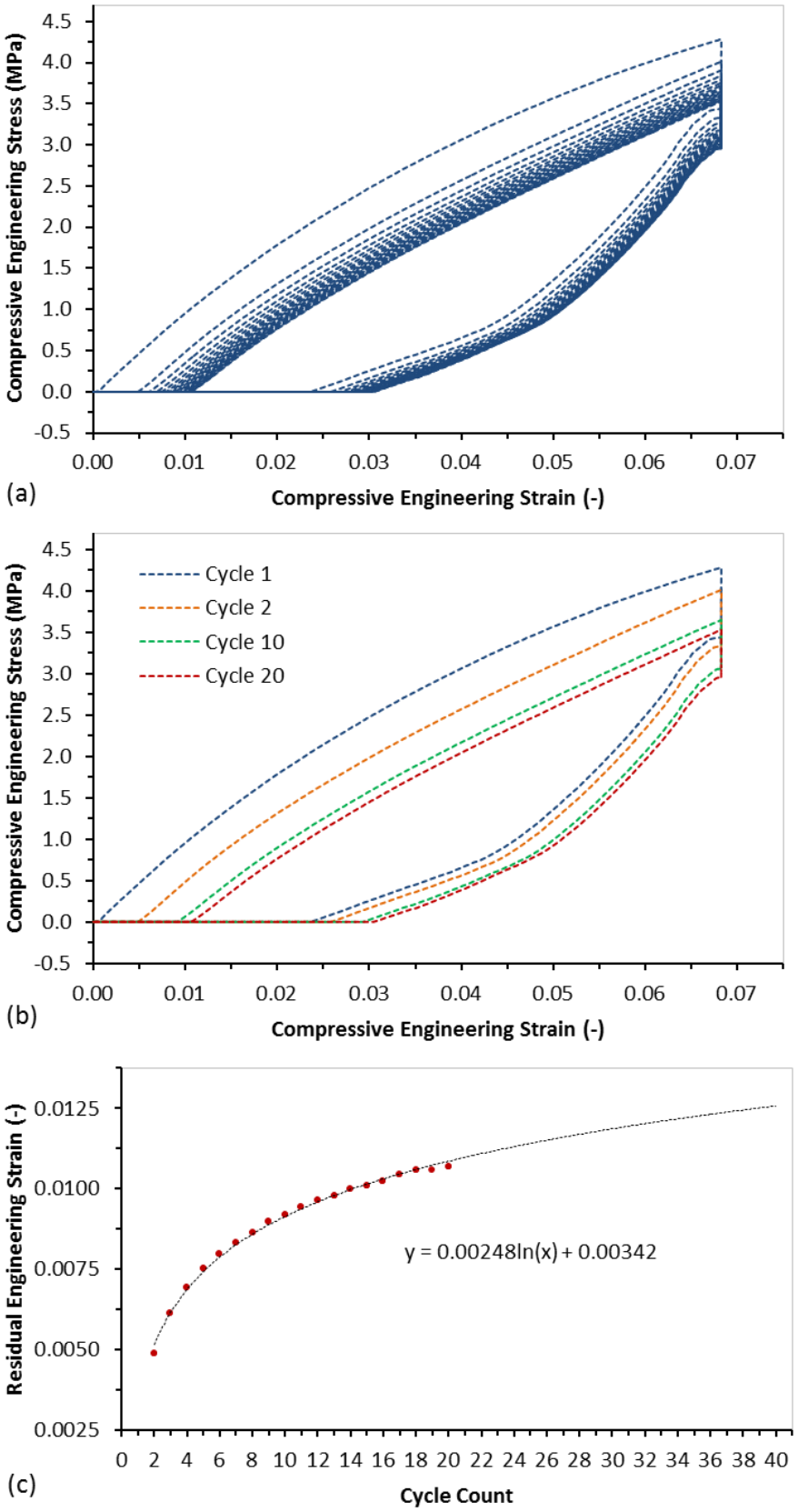

Figure G-6: Engineering stress versus strain plots showing all 20 cycles (a) and cycles 1, 2, 10 & 20 (b) together with a plot of residual strain versus cycle count (c) for the Violet-0.7mm cyclic compression test

Appendix H. Additional Phase 1 Results

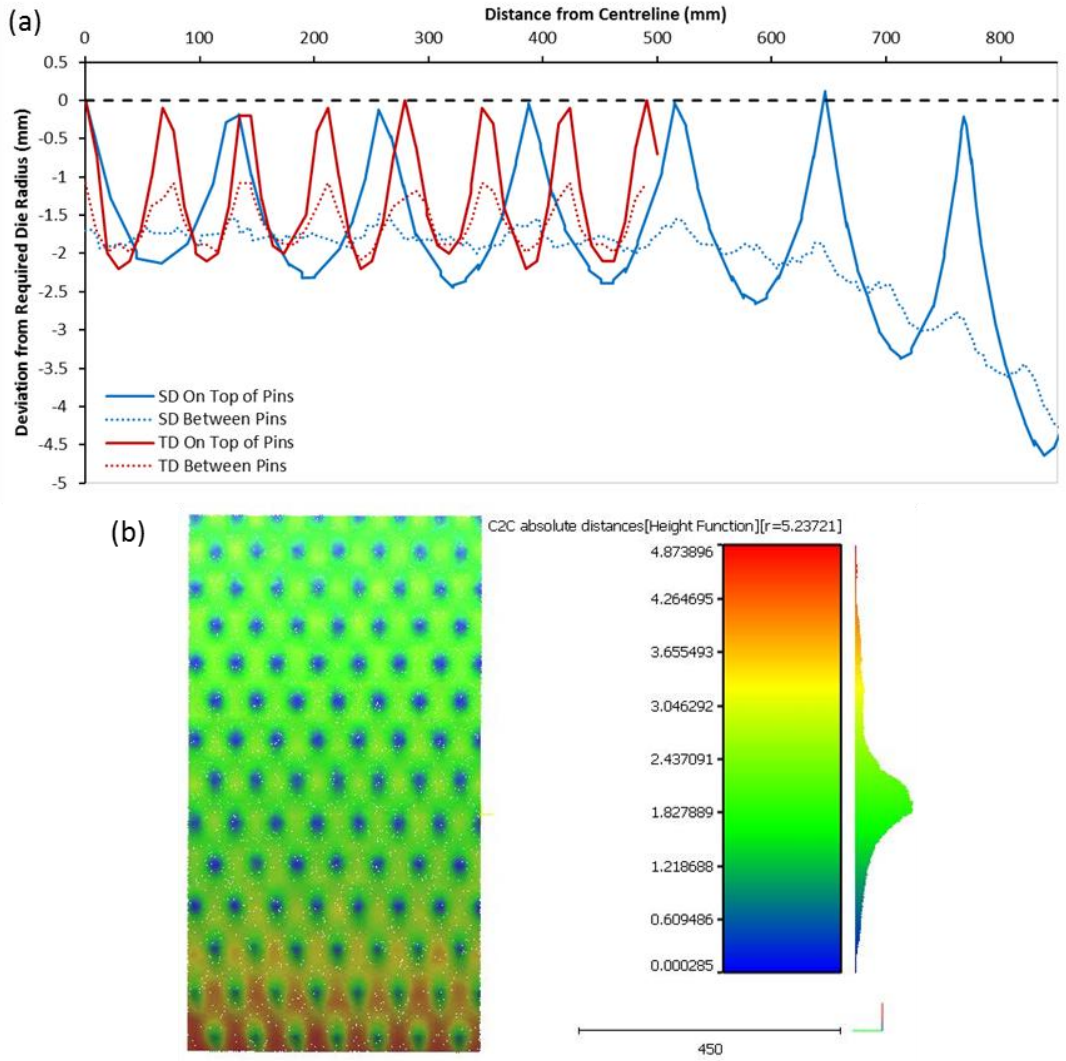

Figure H-1: HCP1r75 section line (a) & surface defect (b) analyses results

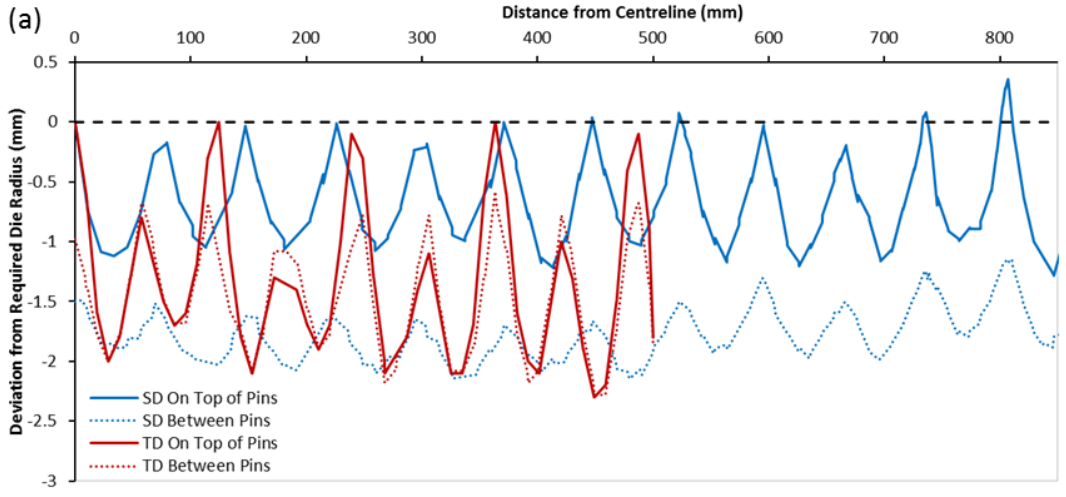

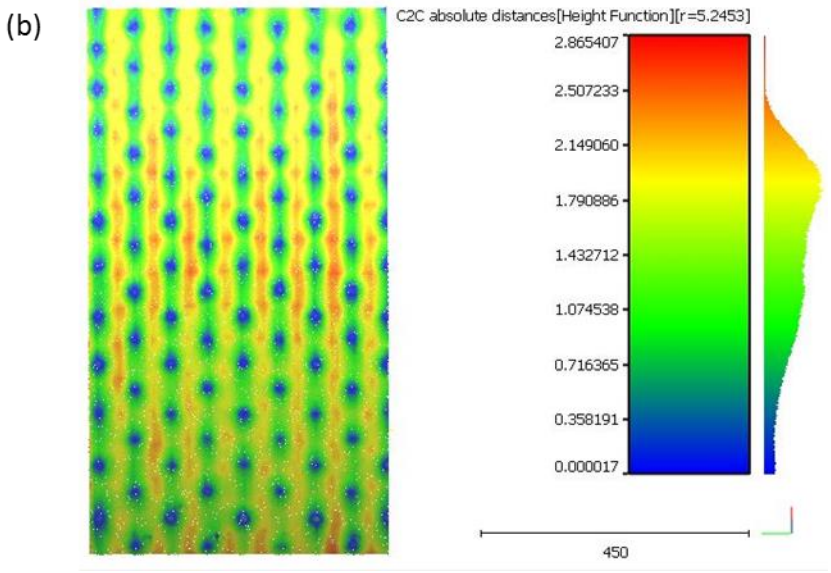

Figure H-2: HCP2r75 section line (a) & surface defect (b) analyses results

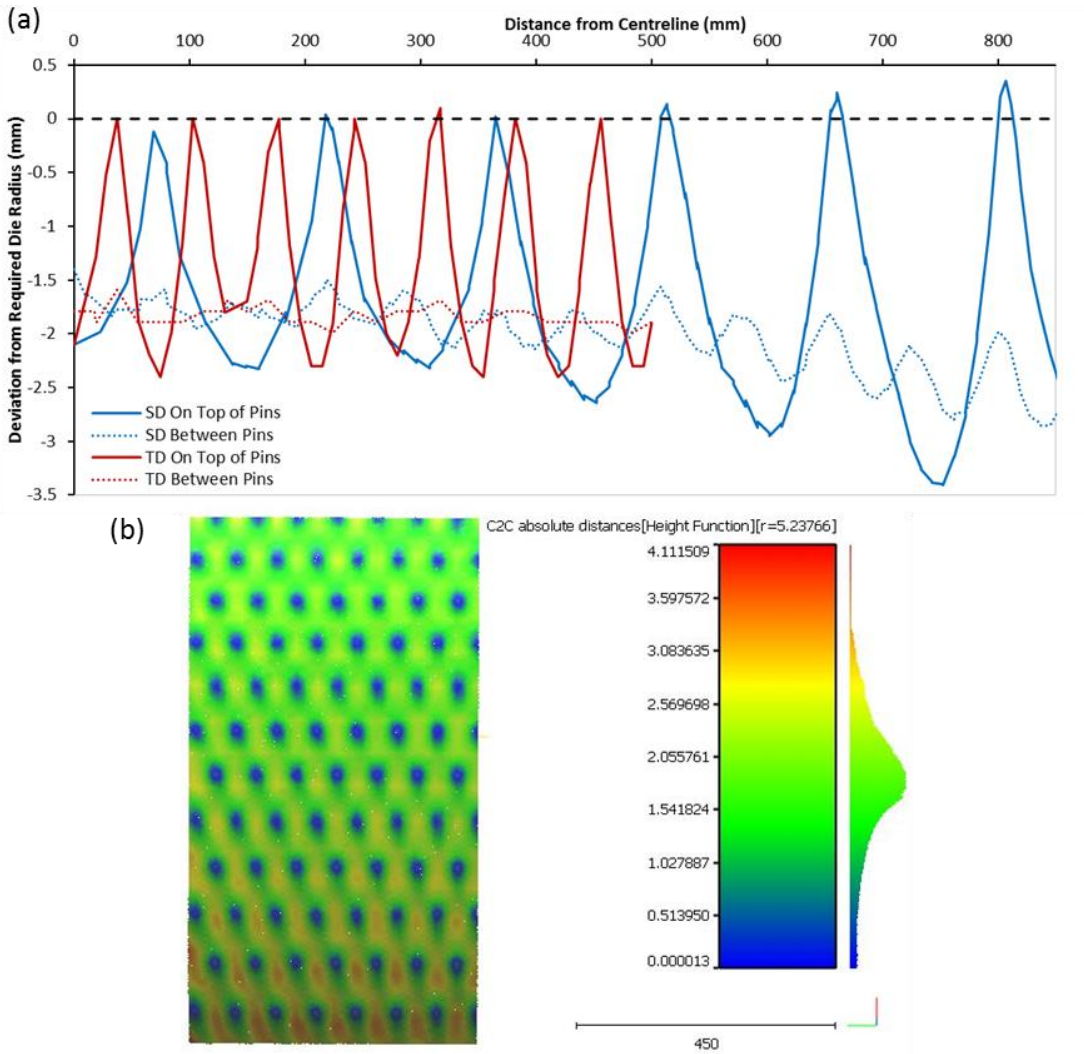

Figure H-3: RCP2r50 section line (a) & surface defect (b) analyses results

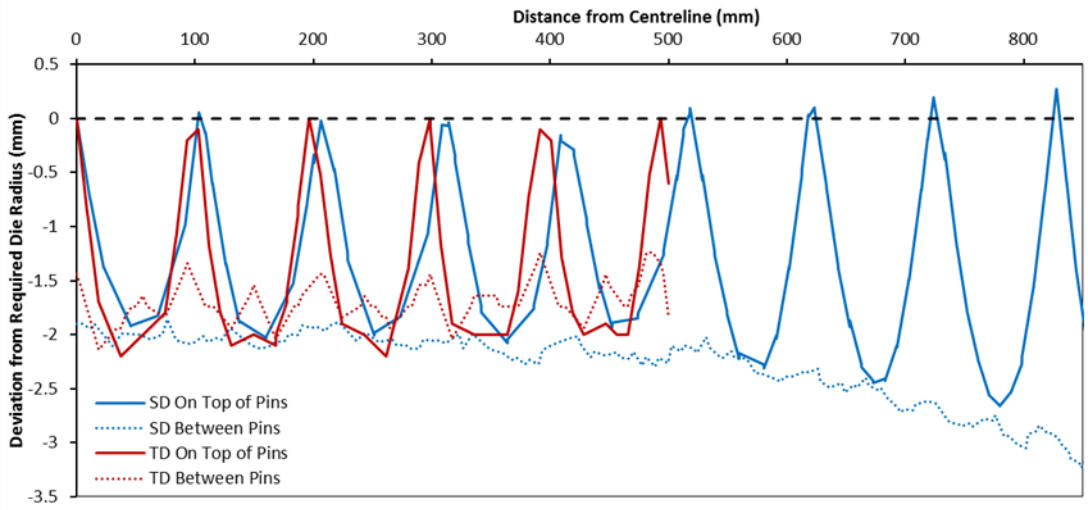

Figure H-4: RCP3r50 section line analysis results

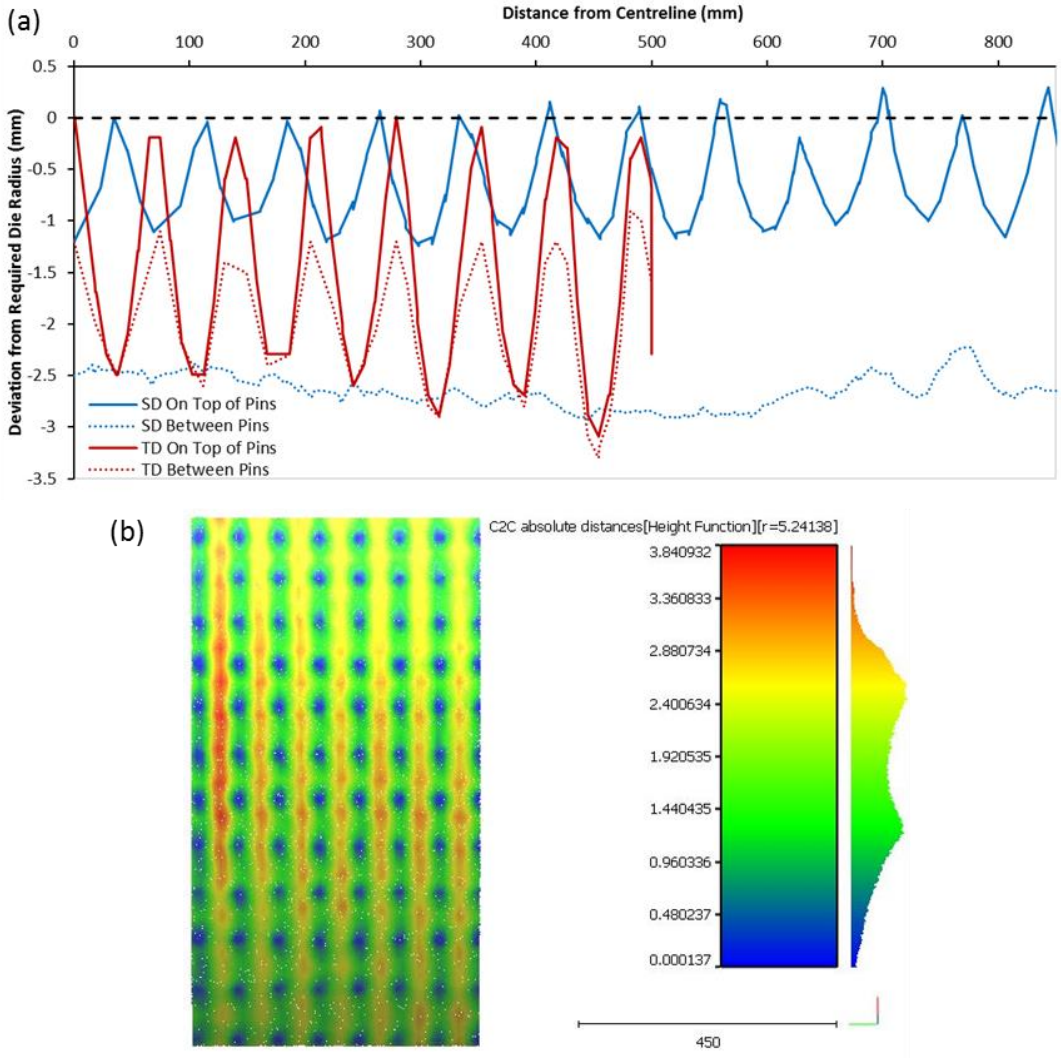

Figure H-5: RCP1r75 section line (a) & surface defect (b) analyses results

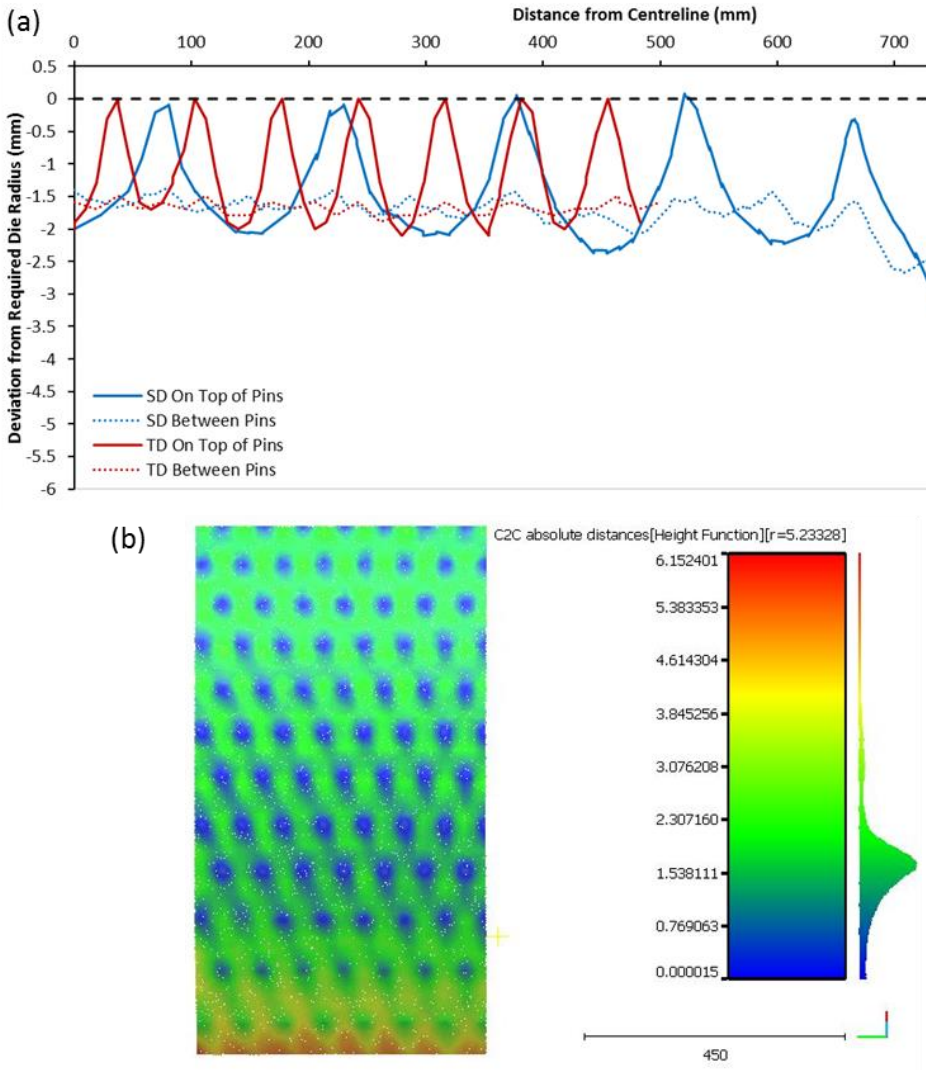

Figure H-6: RCP2r75 section line (a) & surface defect (b) analyses results

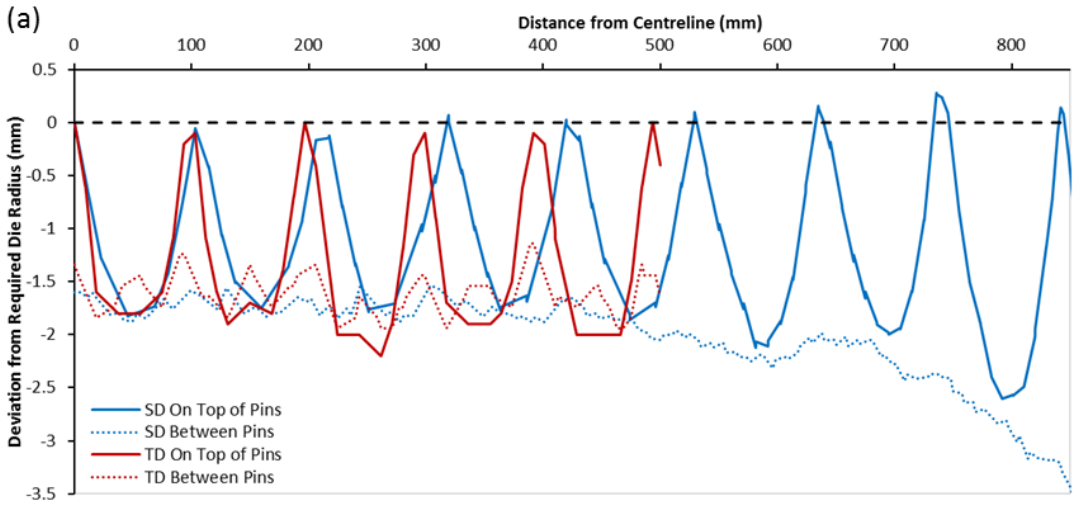

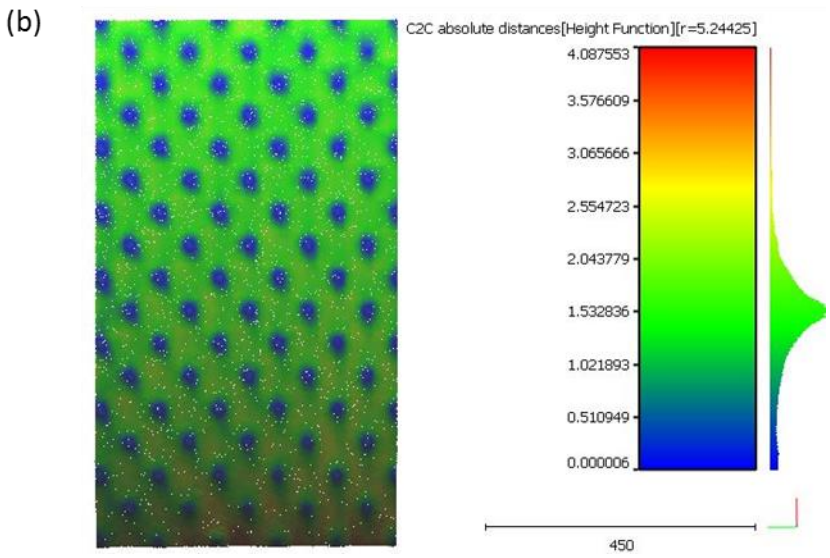

Figure H-7: RCP3r75 section line (a) & surface defect (b) analyses results

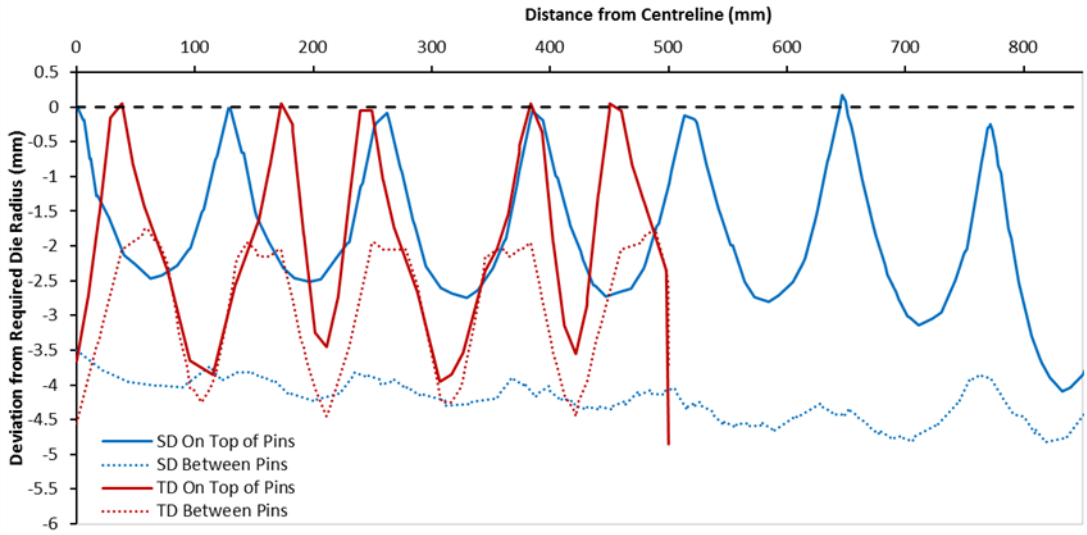

Figure H-8: TCP1 section line analysis results

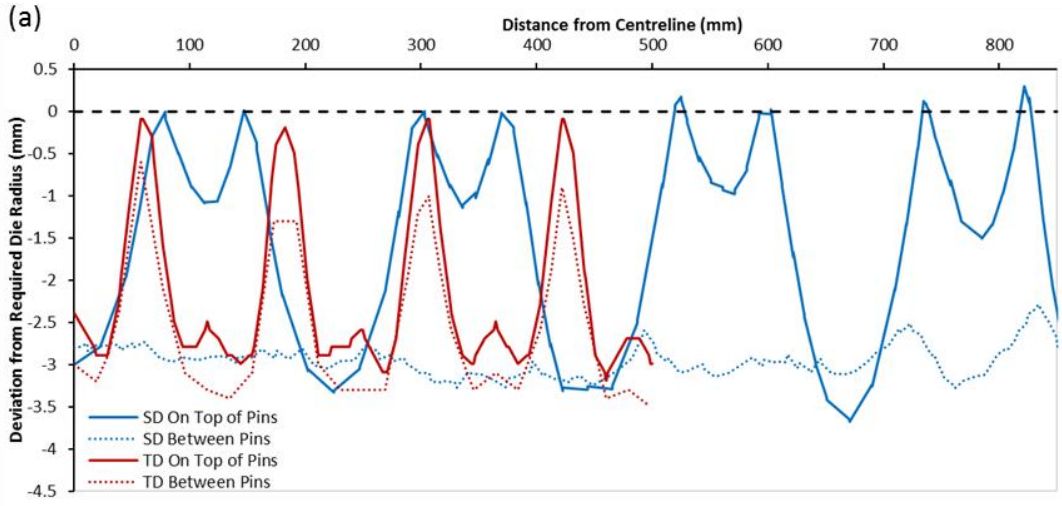

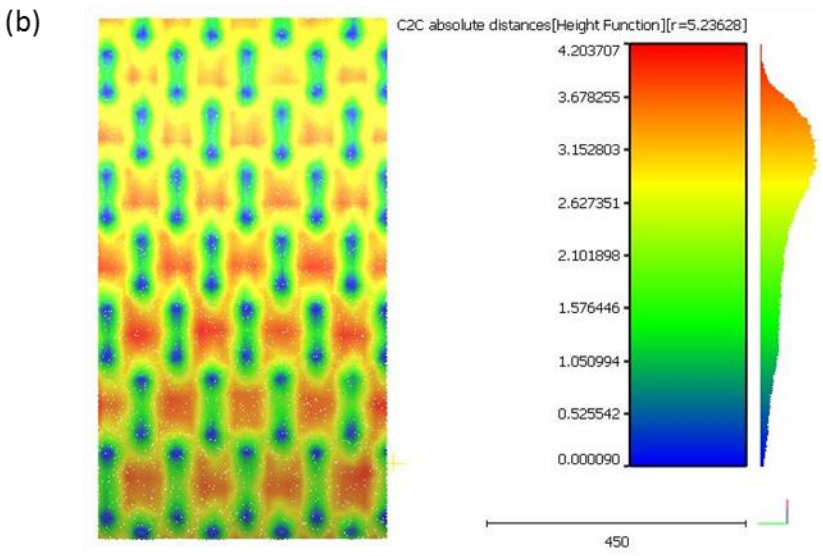

Figure H-9: TCP2 section line (a) & surface defect (b) analyses results

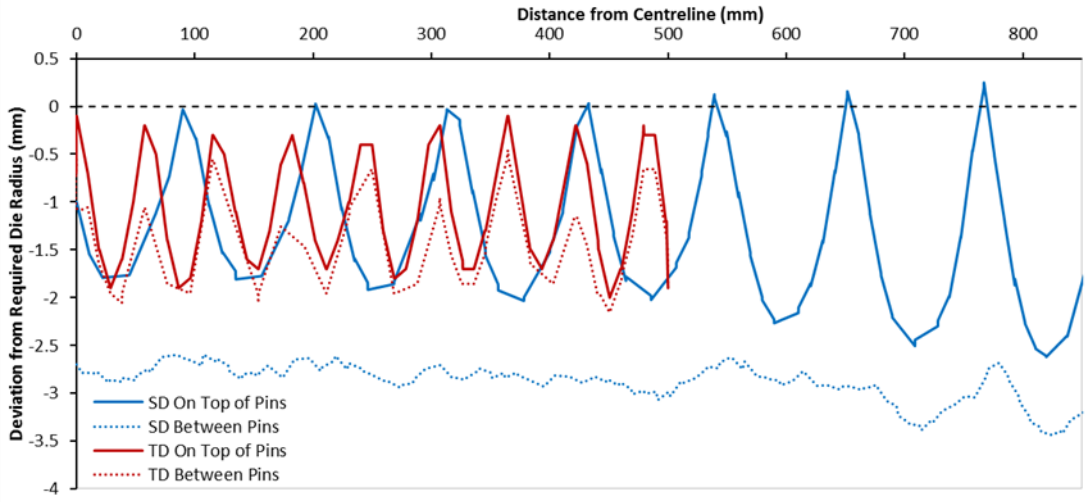

Figure H-10: TCP3 section line analysis results

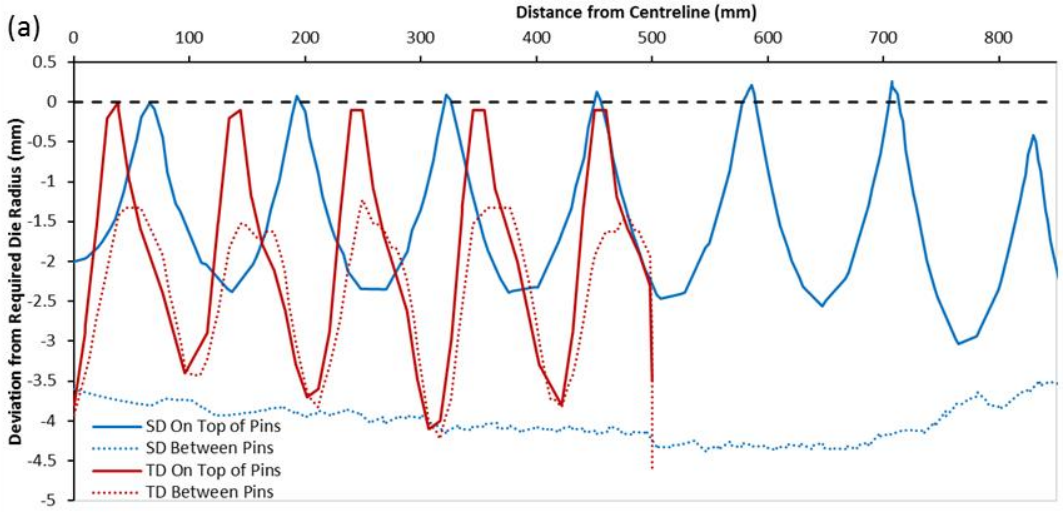

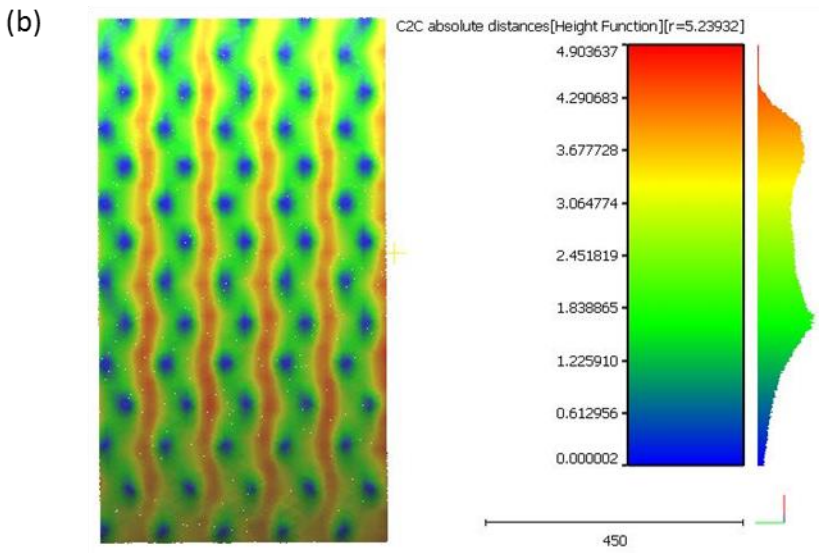

Figure H-11: TCP4 section line (a) & surface defect (b) analyses results

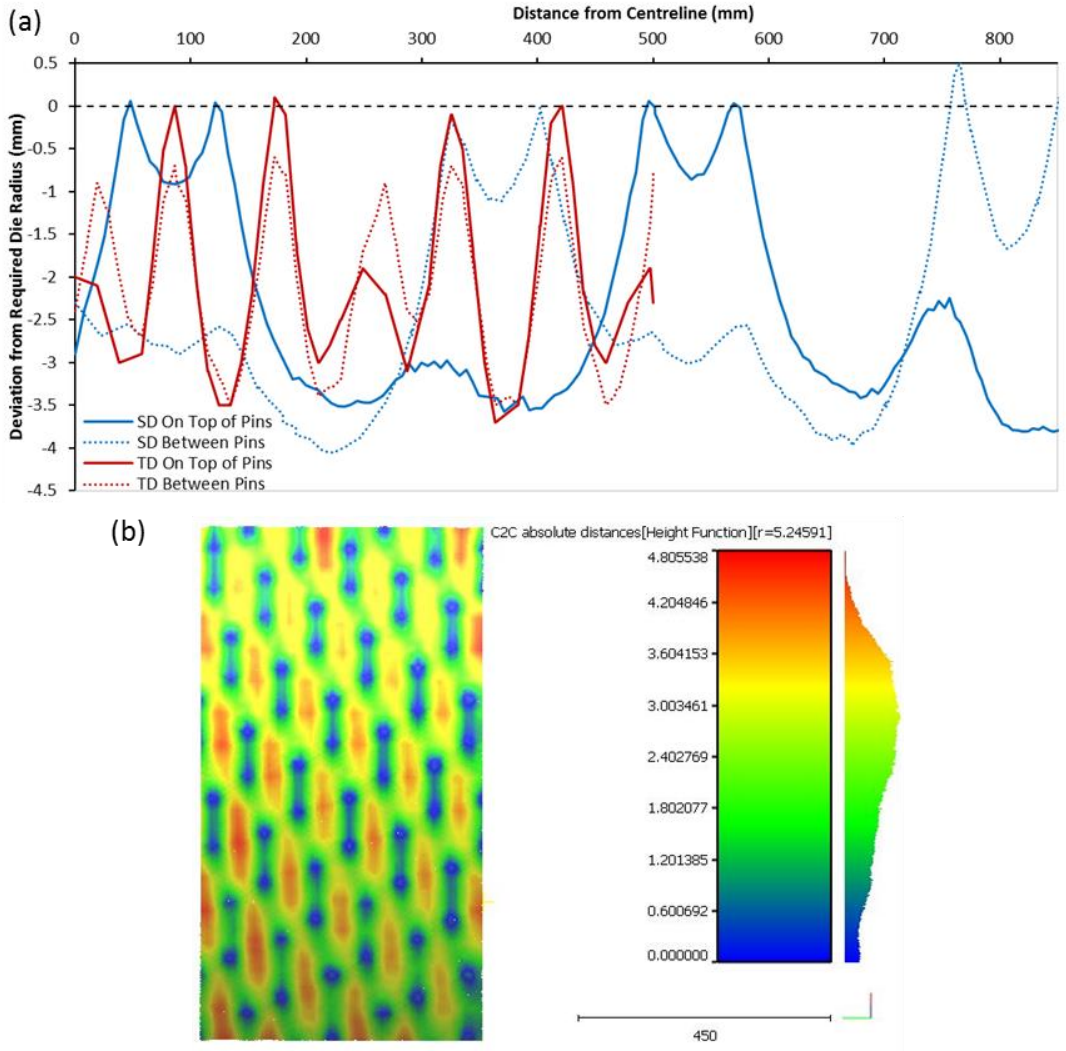

Figure H-12: TCP5 section line (a) & surface defect (b) analyses results

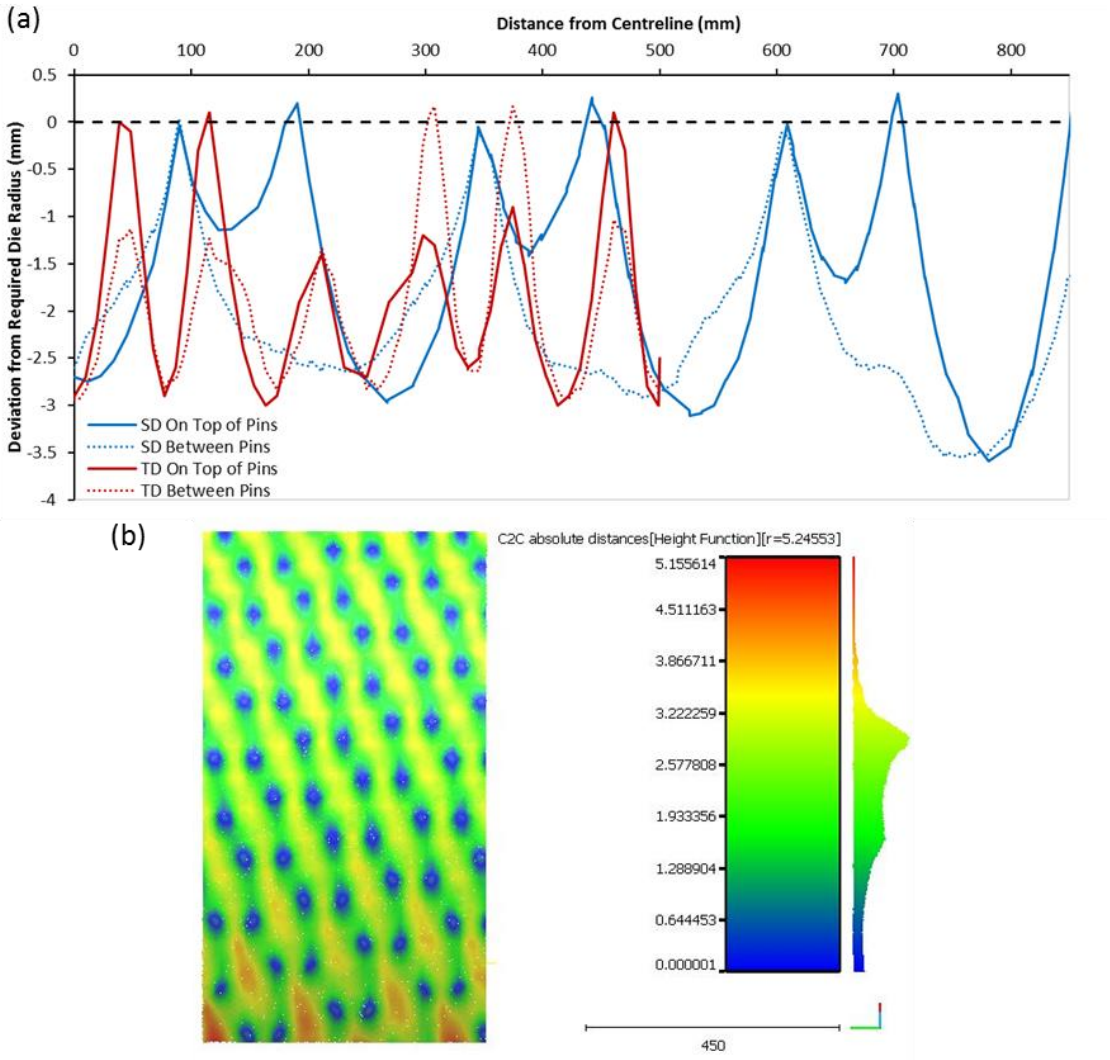

Figure H-13: TCP6 section line (a) & surface defect (b) analyses results

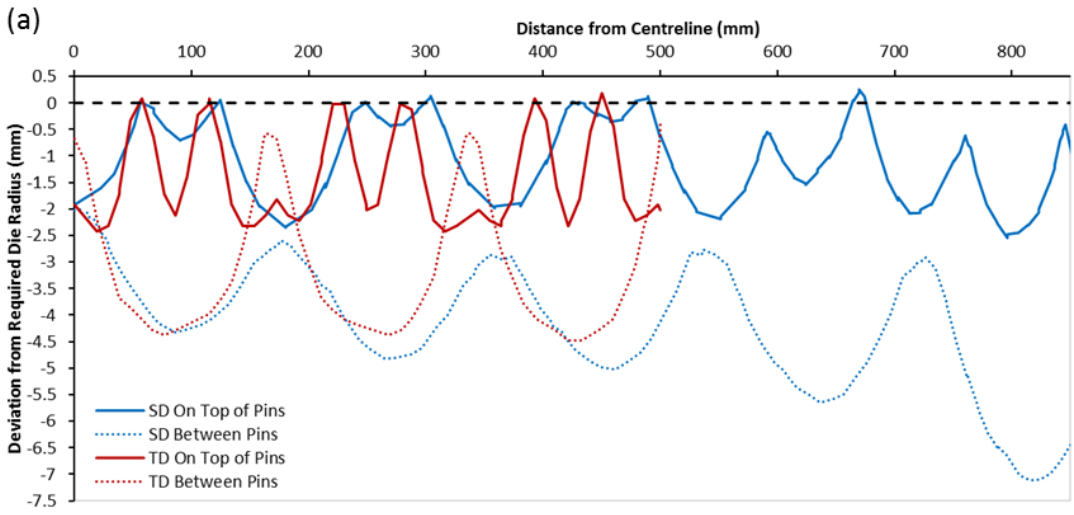

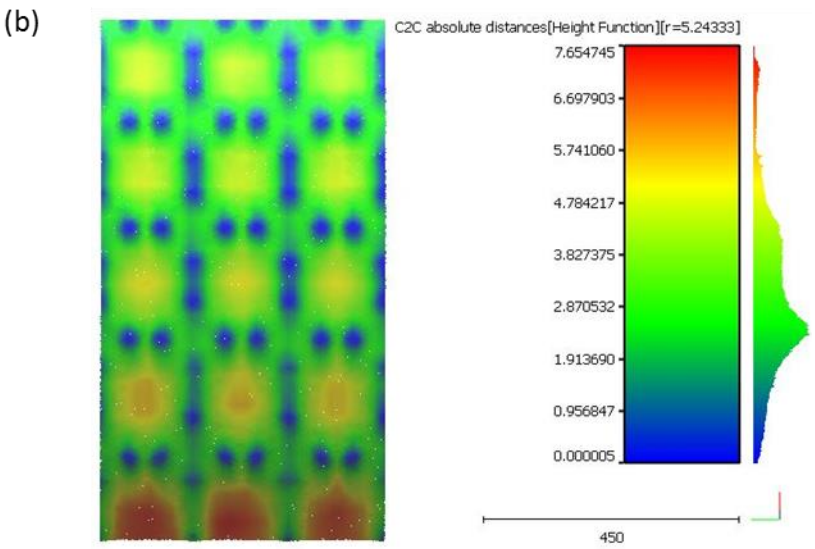

Figure H-14: RTCP1 section line (a) & surface defect (b) analyses results

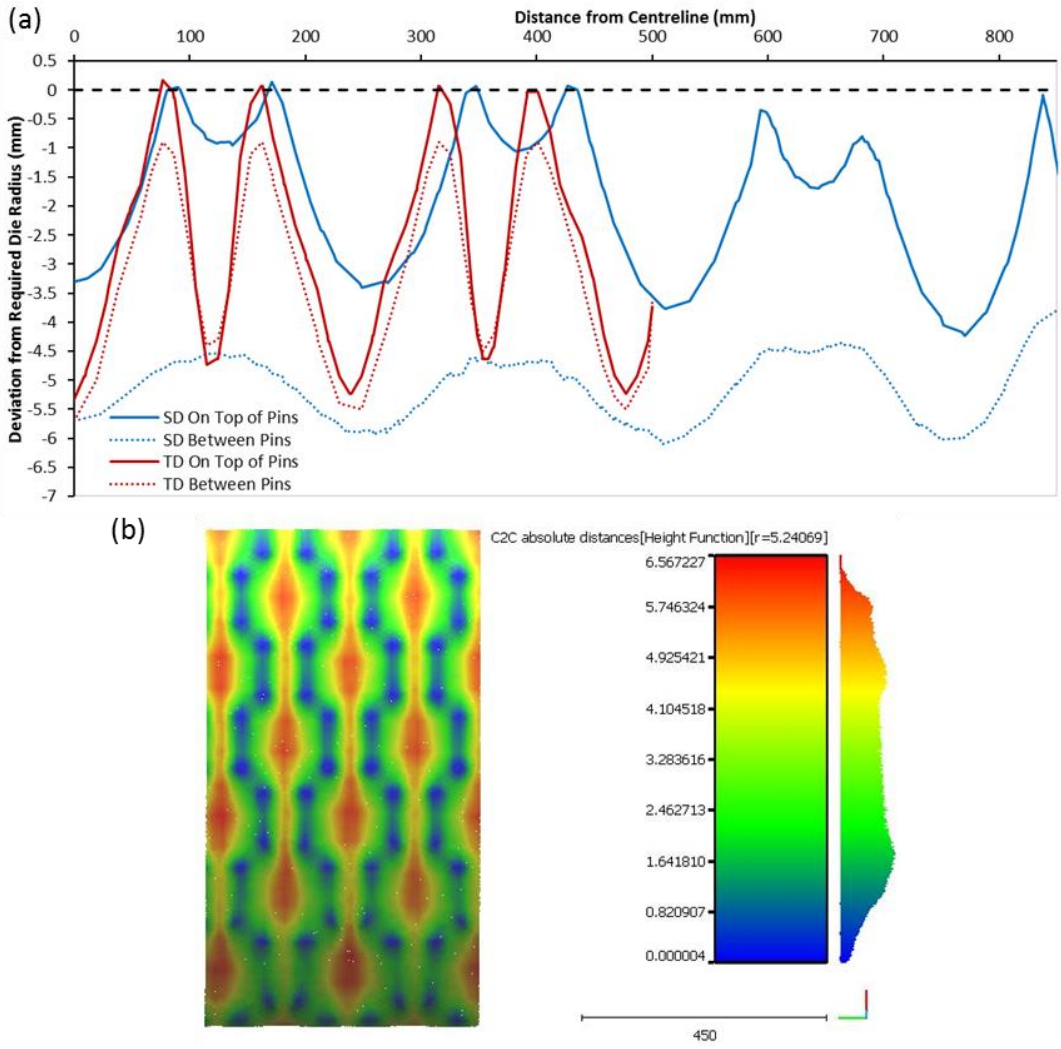

Figure H-15: RTCP1 section line (a) & surface defect (b) analyses results

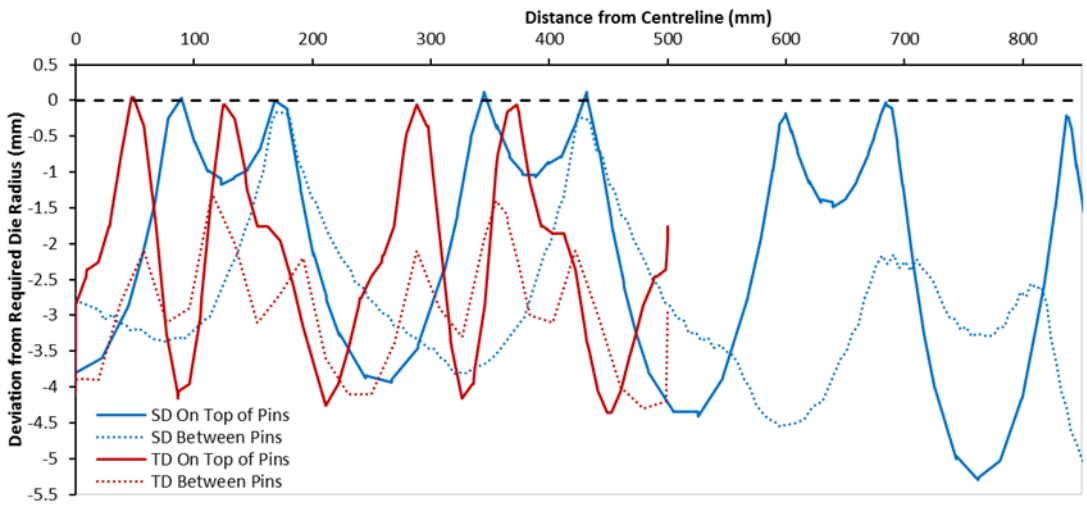

Figure H-16: RTCP3 section line analysis results

Appendix I. Additional Phase 2 Results

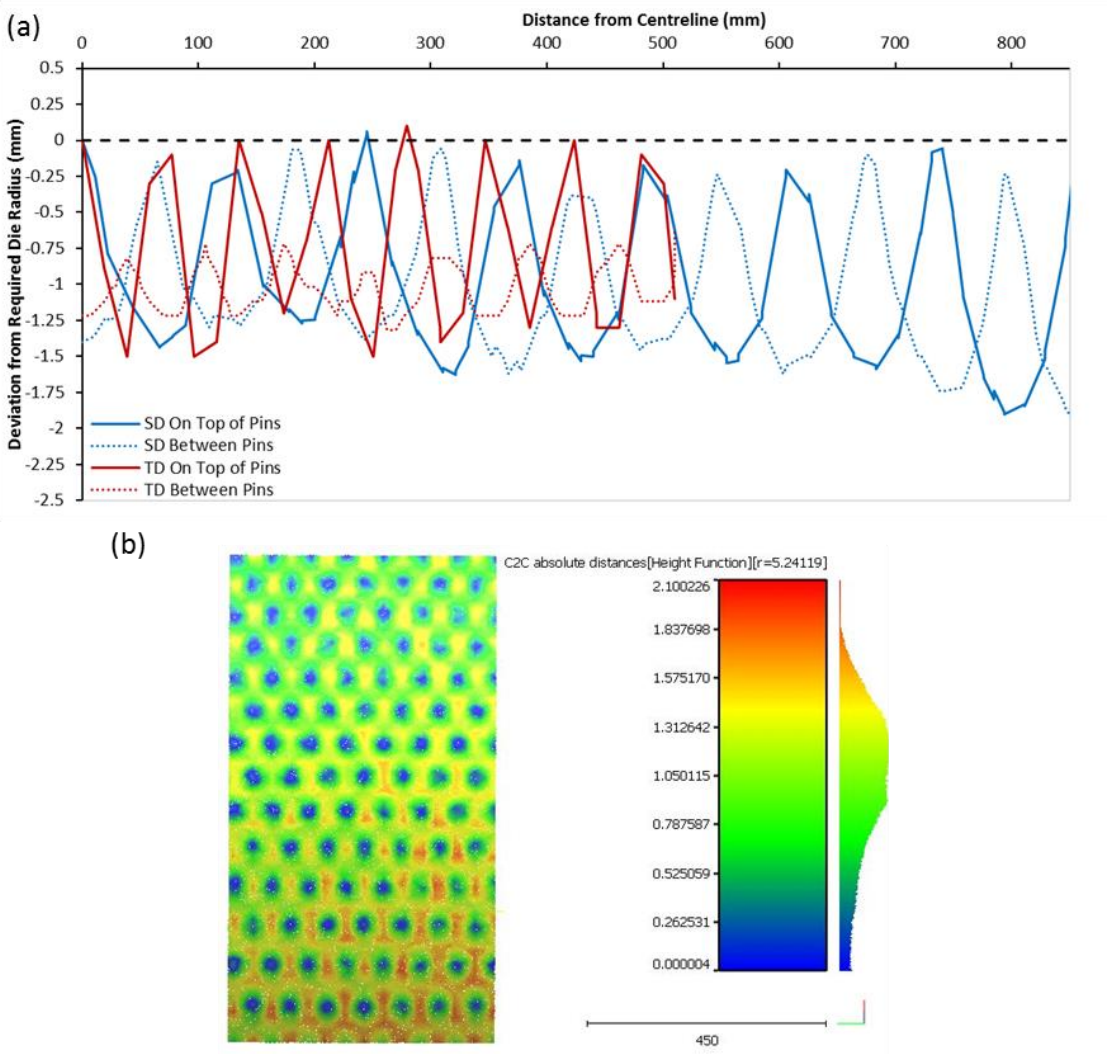

Figure I-1: The HCP1 Round r200 section line (a) & surface defect (b) analyses results

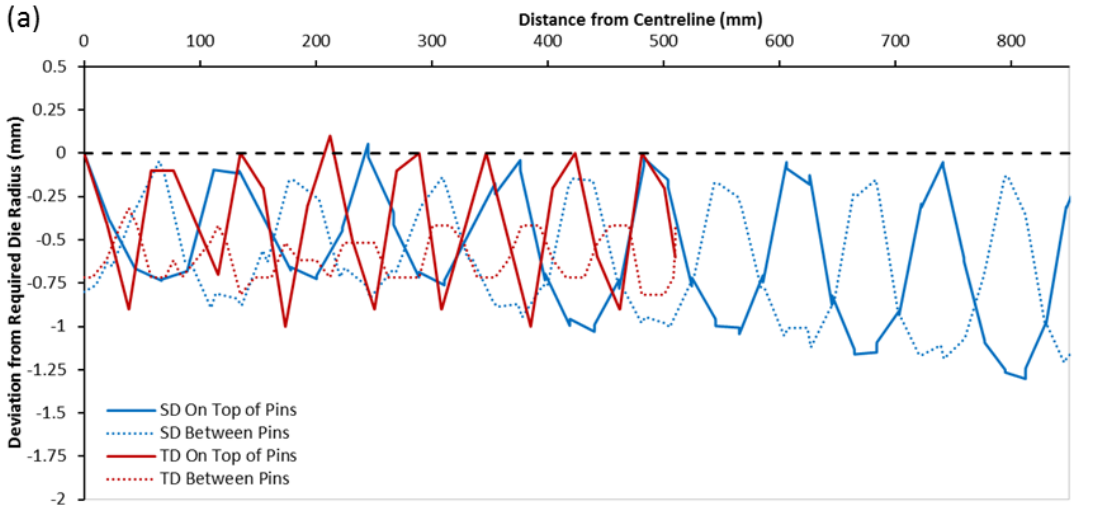

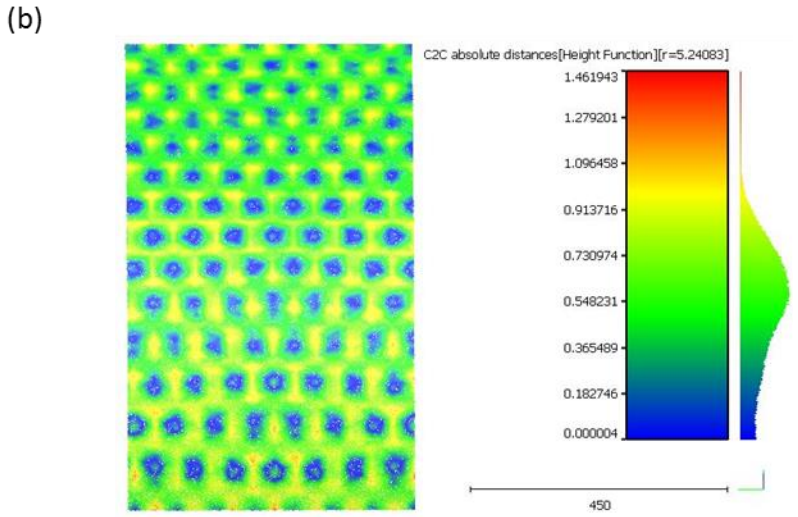

Figure I-2: The HCP1 Round r400 section line (a) & surface defect (b) analyses results

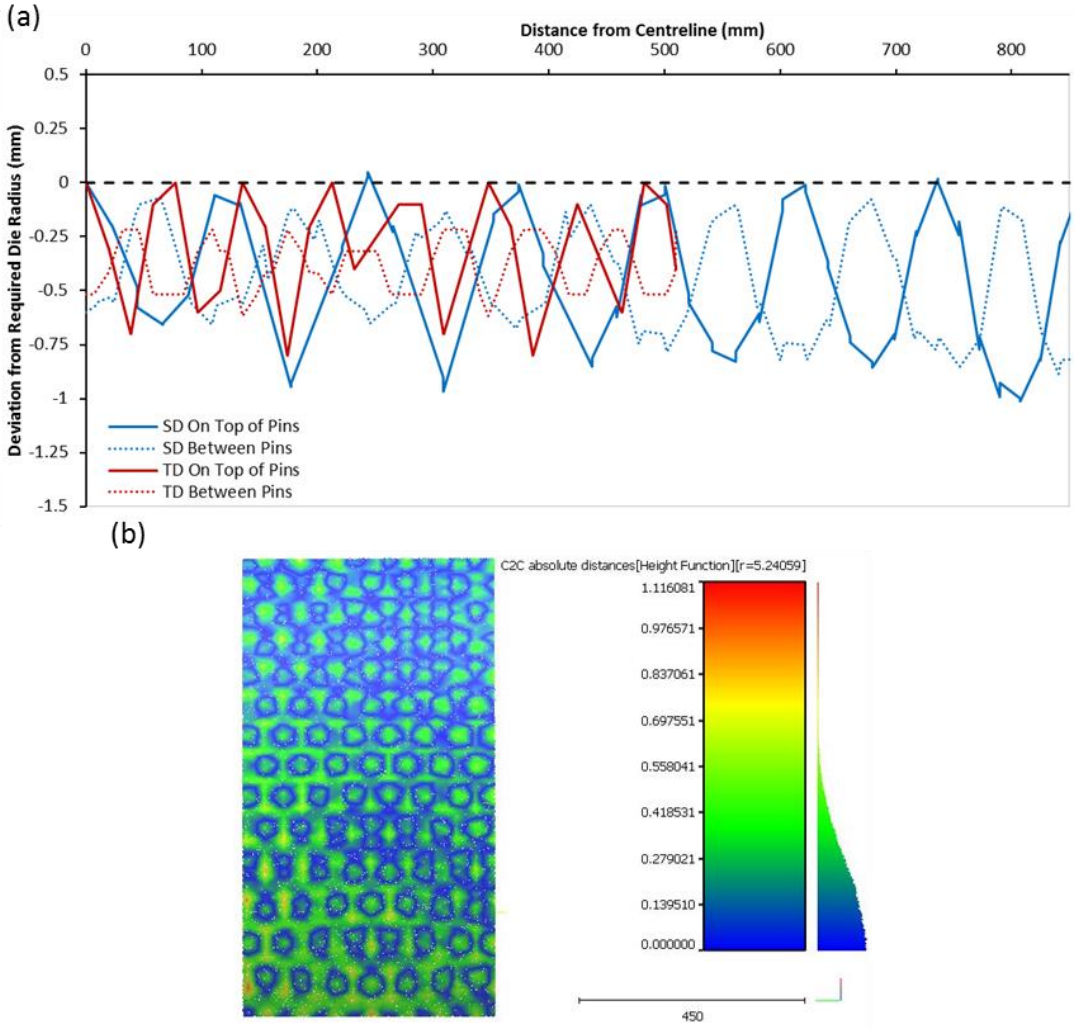

Figure I-3: The HCP1 Round r600 section line (a) & surface defect (b) analyses results

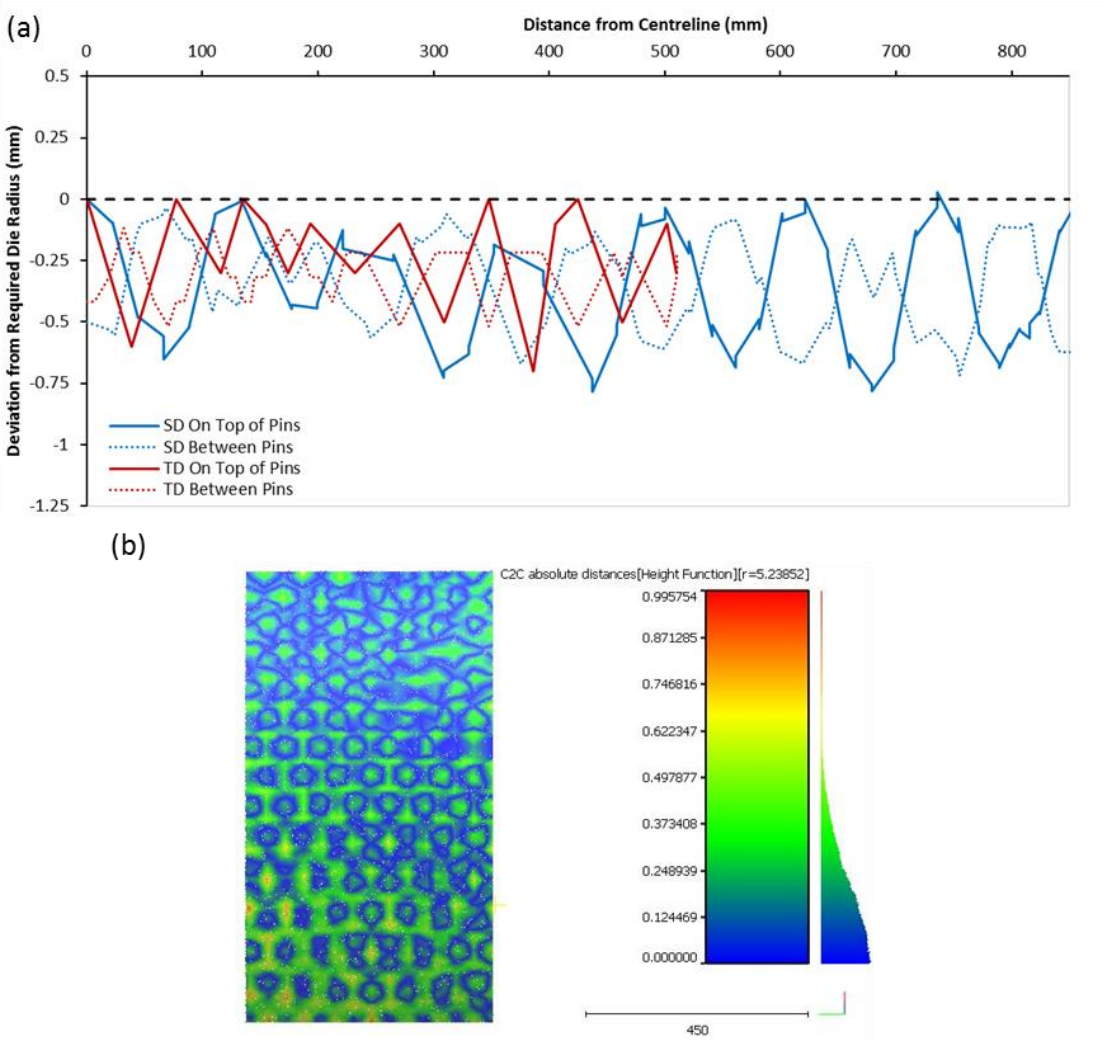

Figure I-4: The HCP1 Round r800 section line (a) & surface defect (b) analyses results

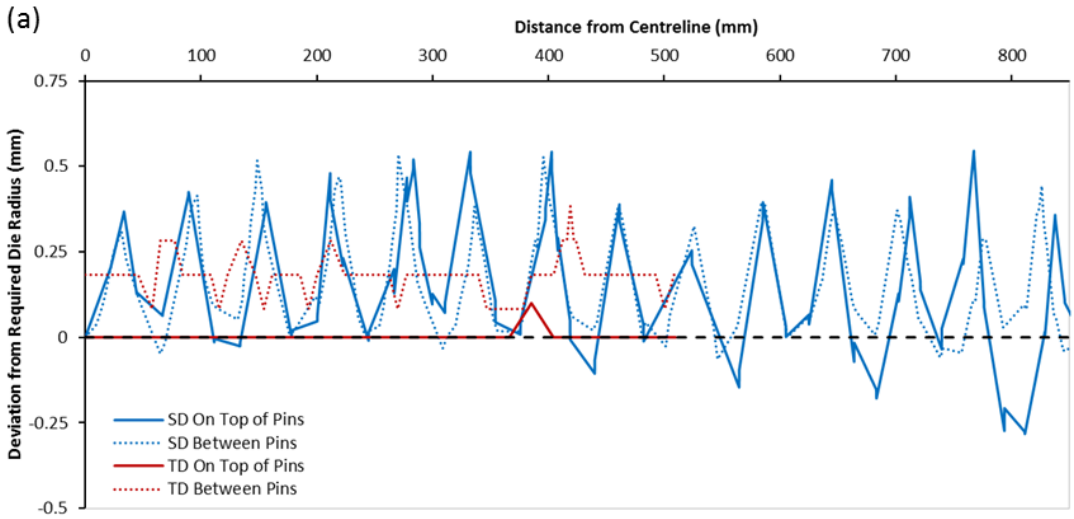

(b)

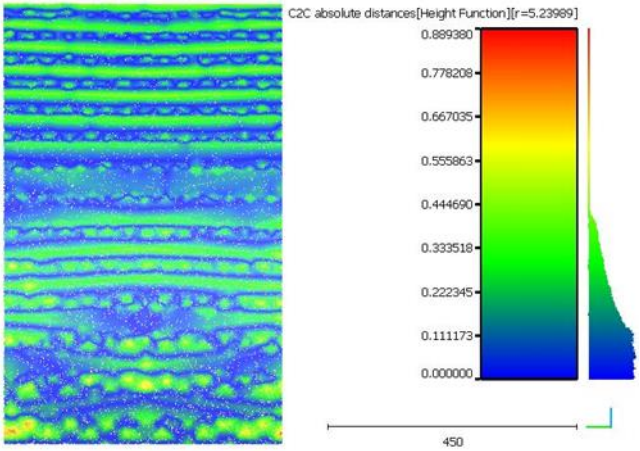

Figure I-5: The HCP1 Shaped Flat section line (a) & surface defect (b) analyses results

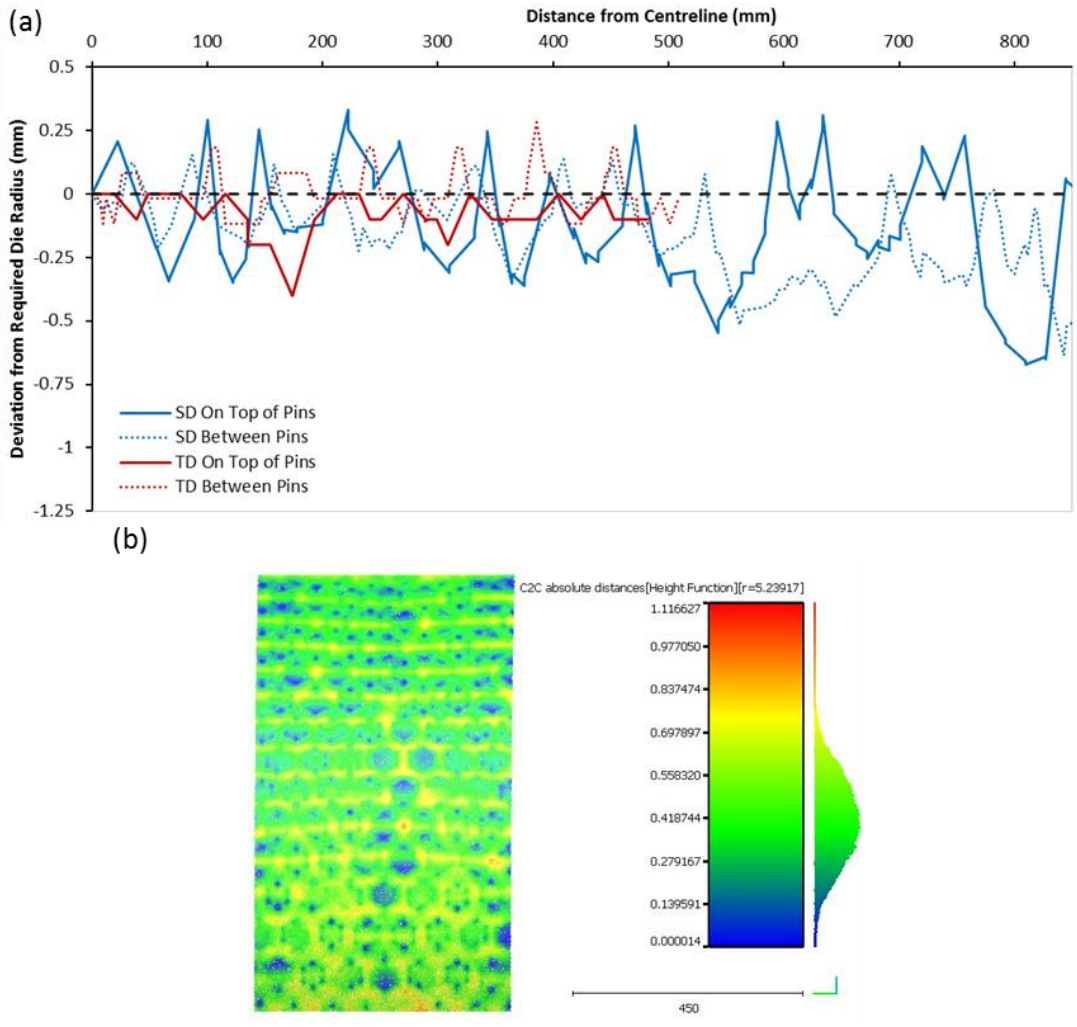

Figure I-6: The HCP1 Shaped Flat MP section line (a) & surface defect (b) analyses results

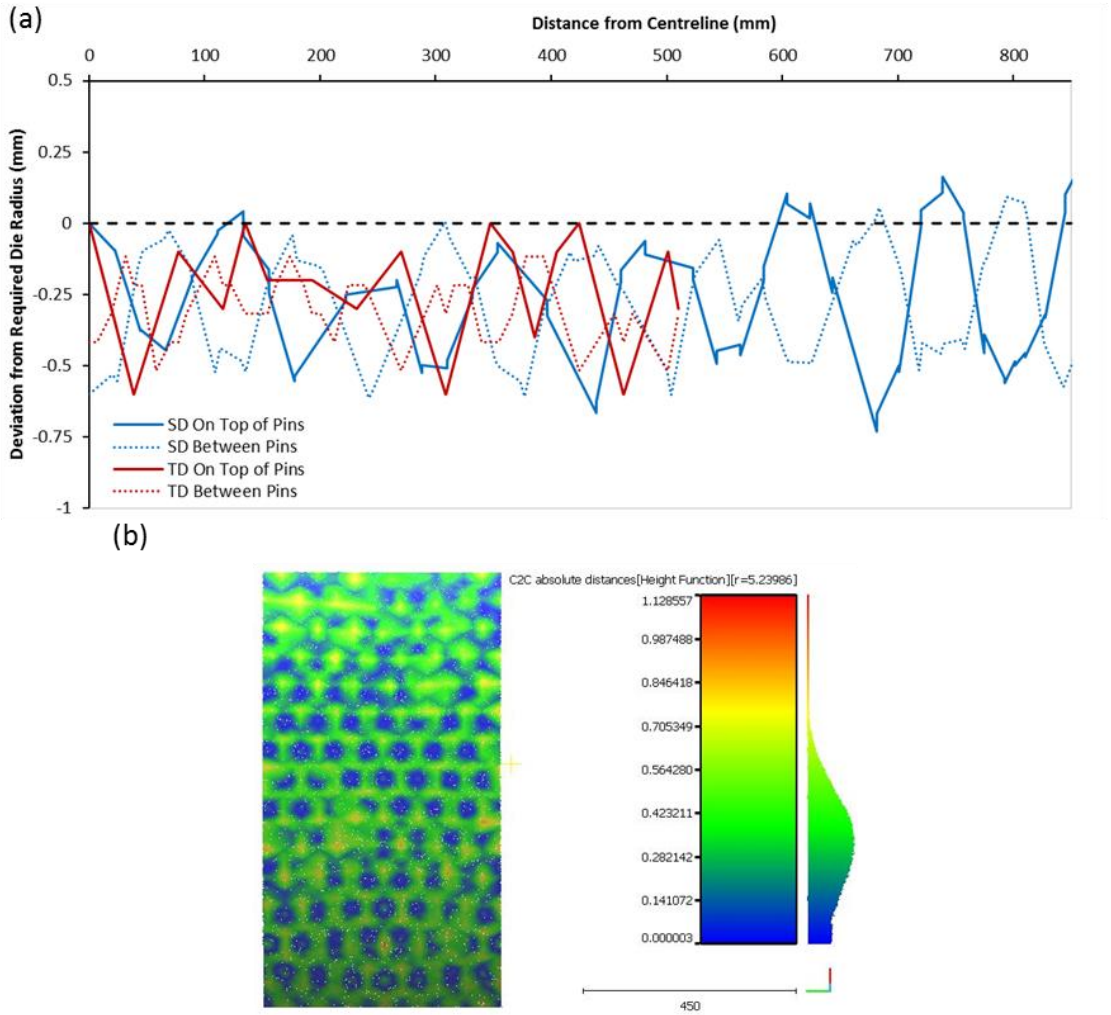

Figure I-7: The HCP1 Shaped r800 section line (a) & surface defect (b) analyses results

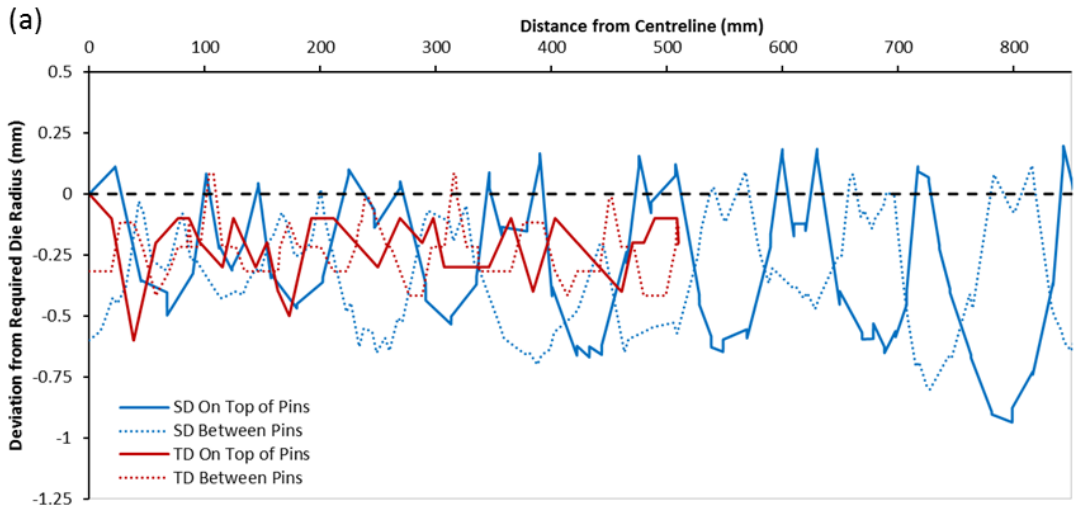

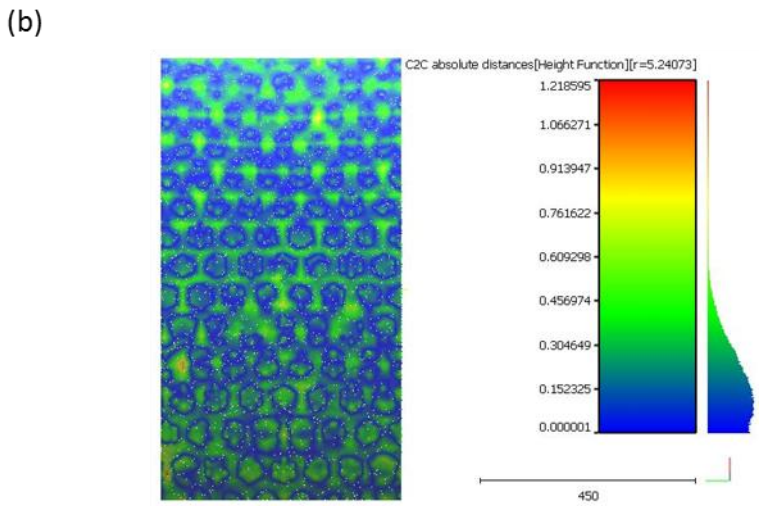

Figure I-8: The HCP1 Shaped r800 MP section line (a) & surface defect (b) analyses results

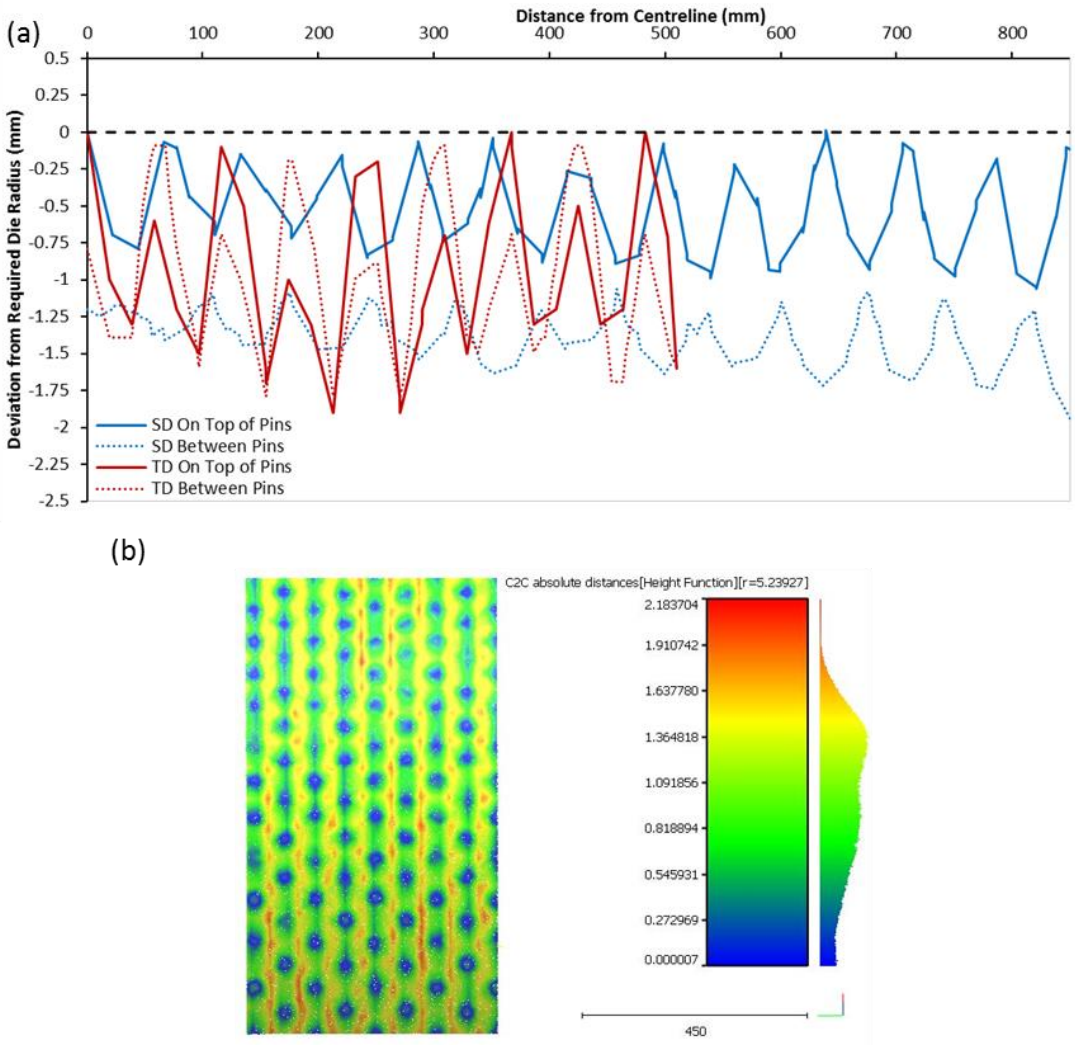

Figure I-9: The HCP2 Round r200 section line (a) & surface defect (b) analyses results

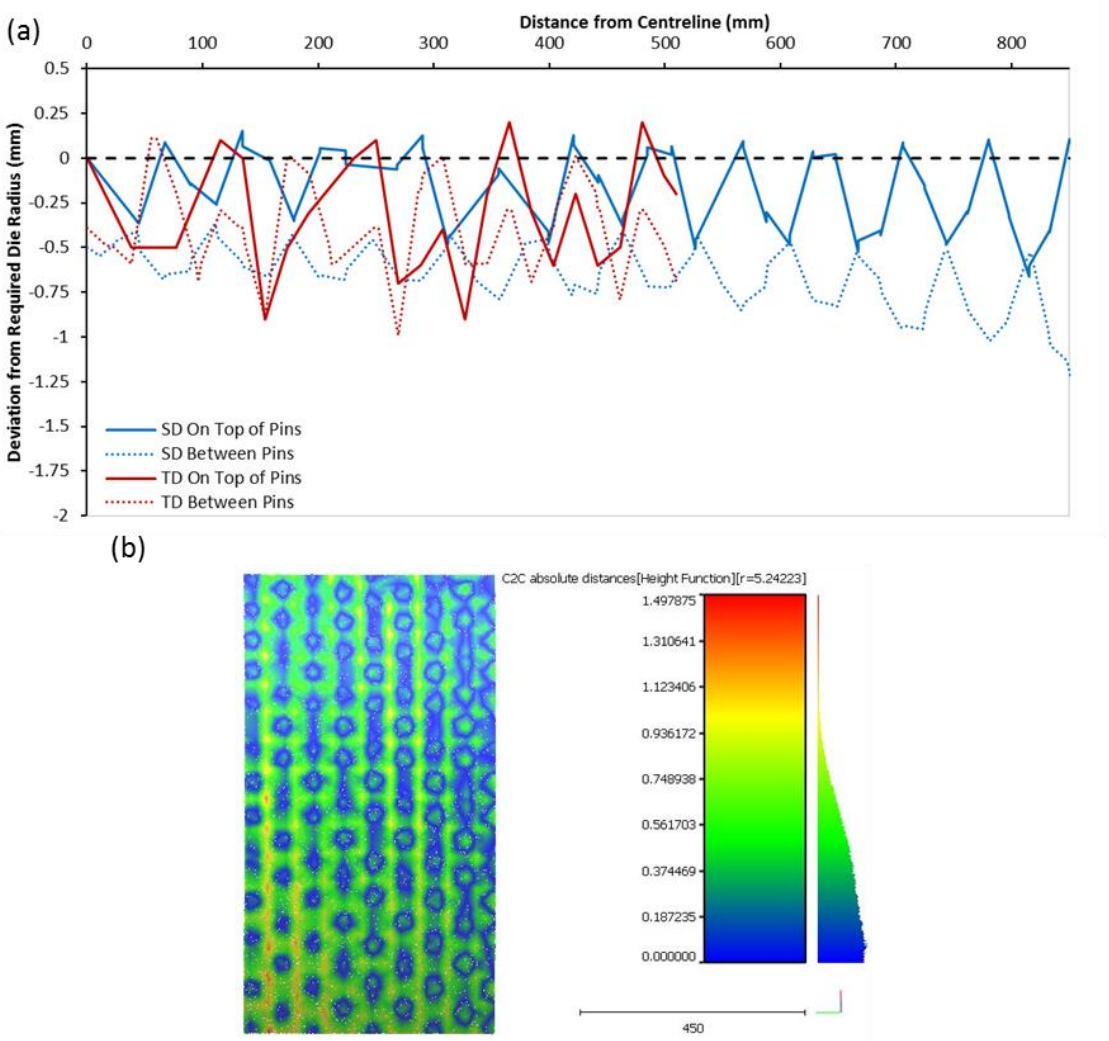

Figure I-10: The HCP2 Round r400 section line (a) & surface defect (b) analyses results

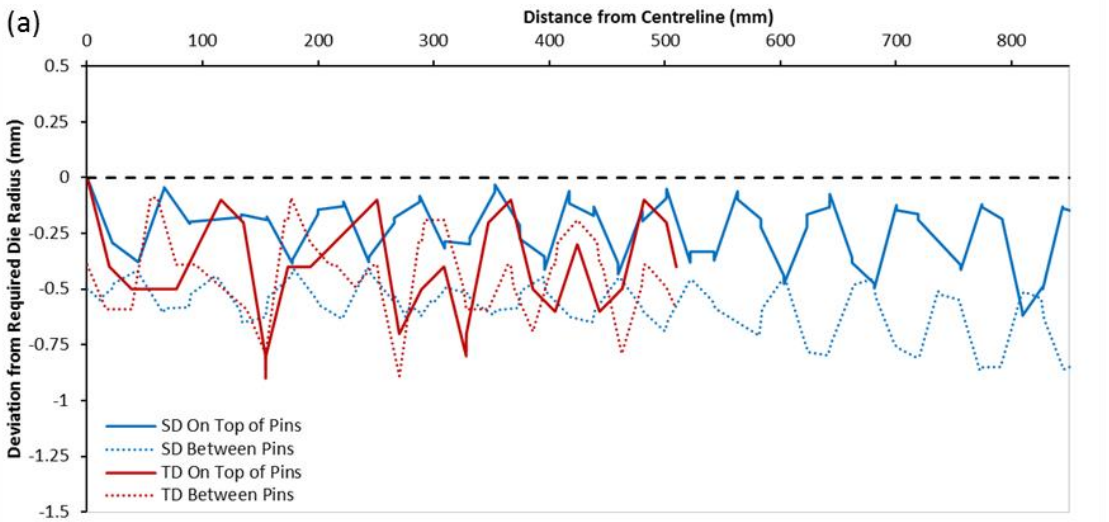

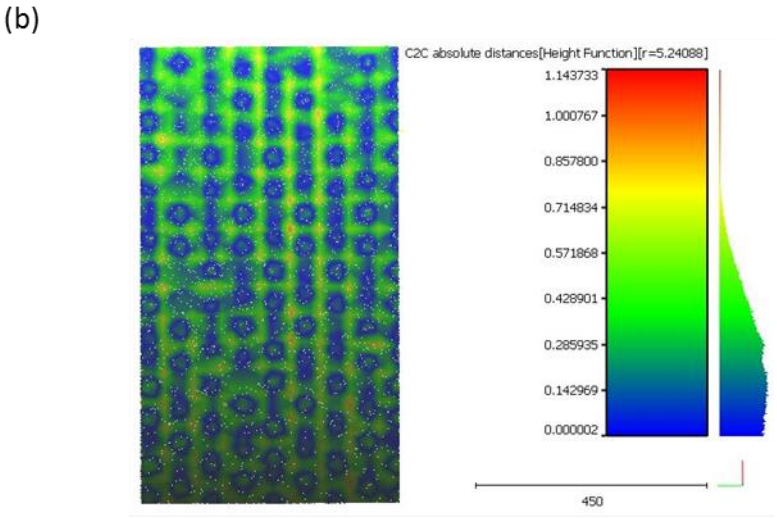

Figure I-11: The HCP2 Round r600 section line (a) & surface defect (b) analyses results

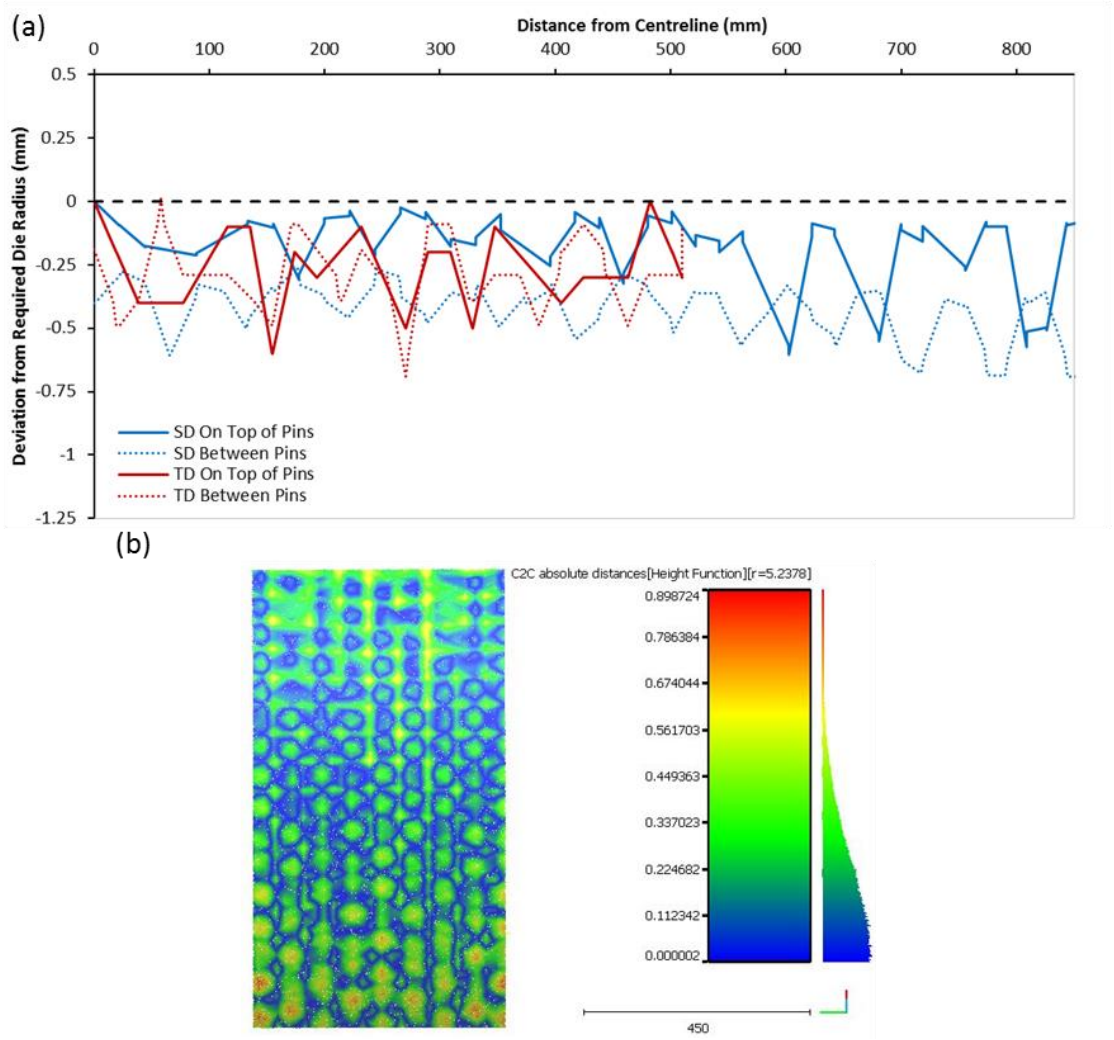

Figure I-12: The HCP2 Round r800 section line (a) & surface defect (b) analyses results

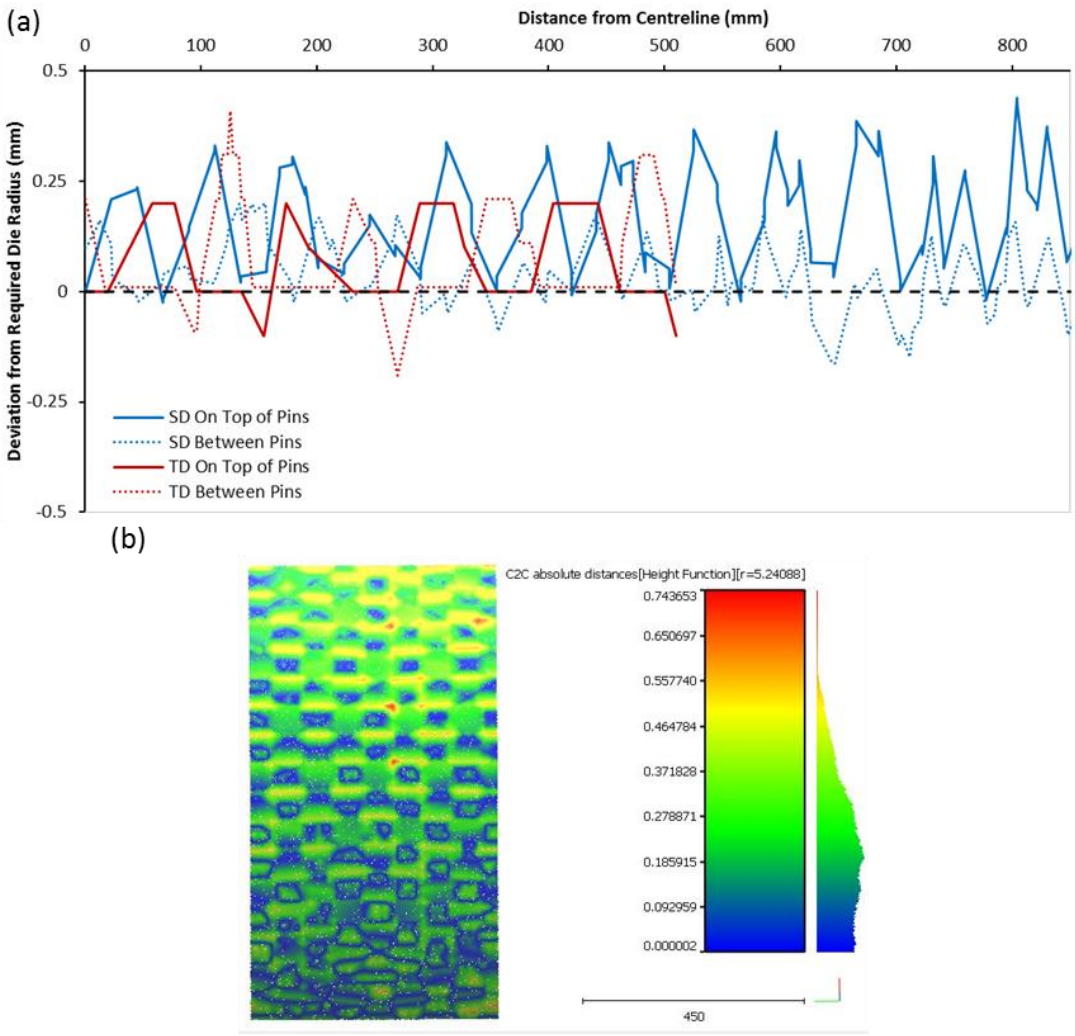

Figure I-13: The HCP2 Shaped Flat section line (a) & surface defect (b) analyses results

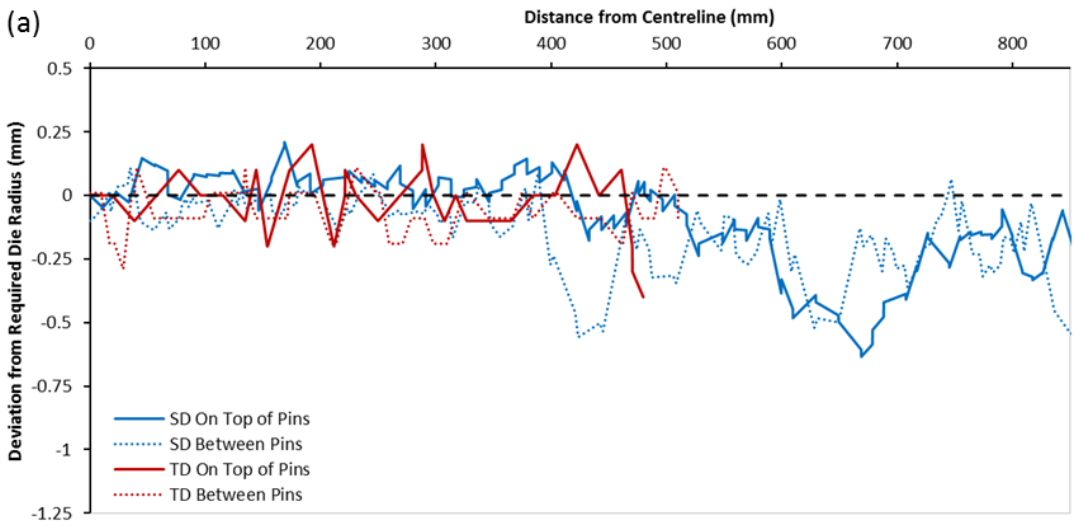

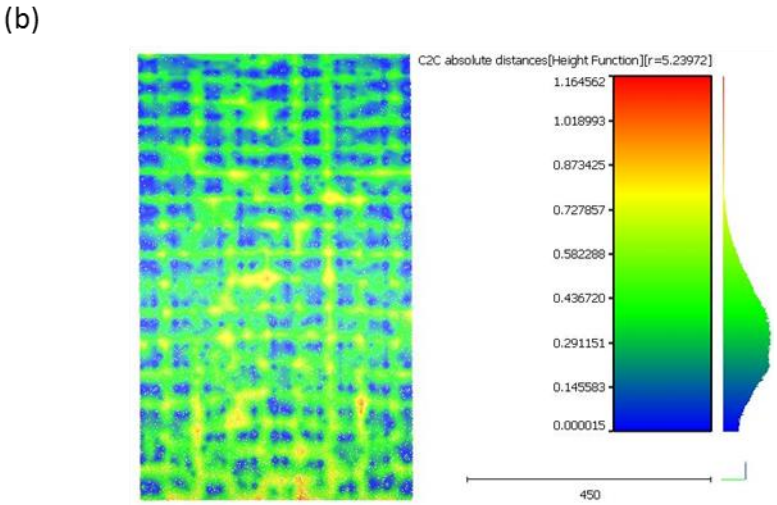

Figure I-14: The HCP1 Shaped Flat MP section line (a) & surface defect (b) analyses results

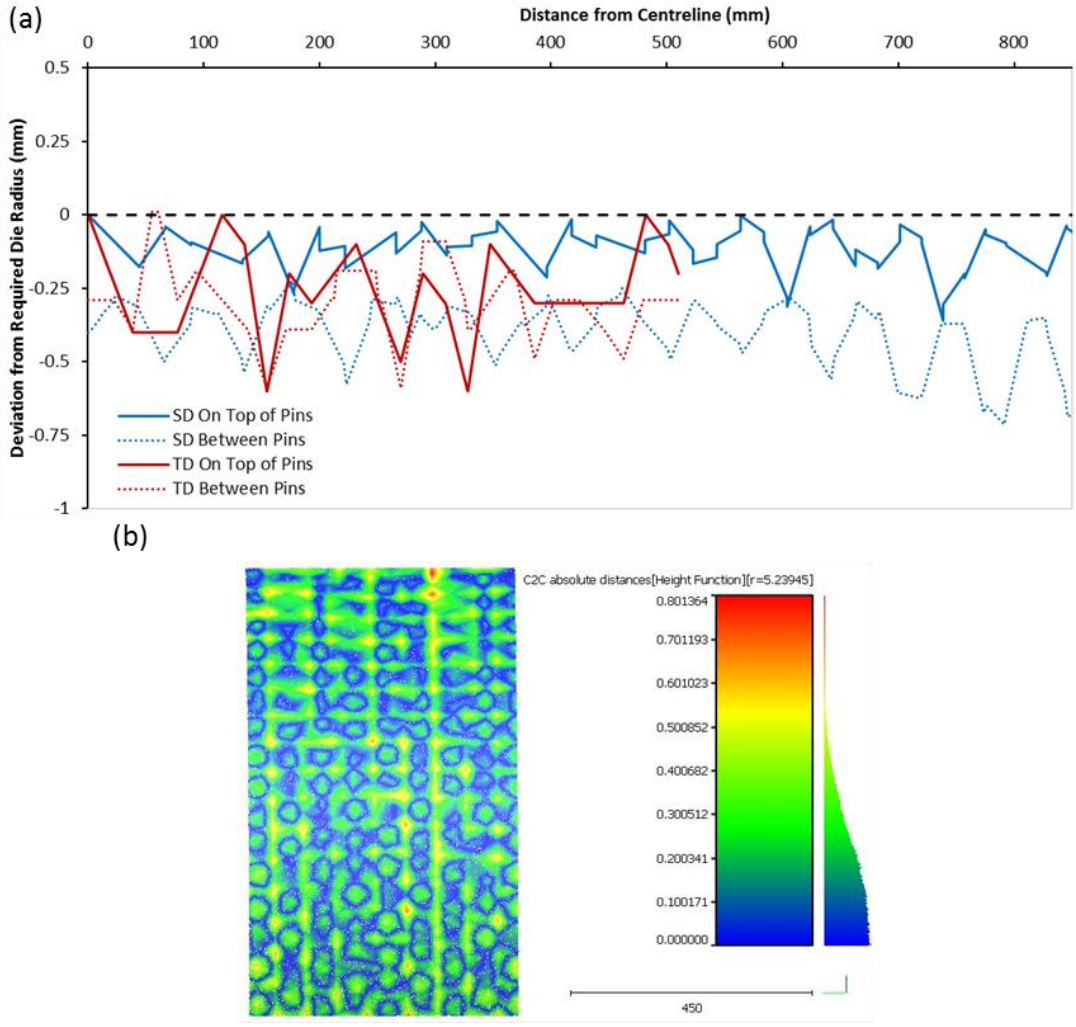

Figure I-15: The HCP2 Shaped r800 section line (a) & surface defect (b) analyses results

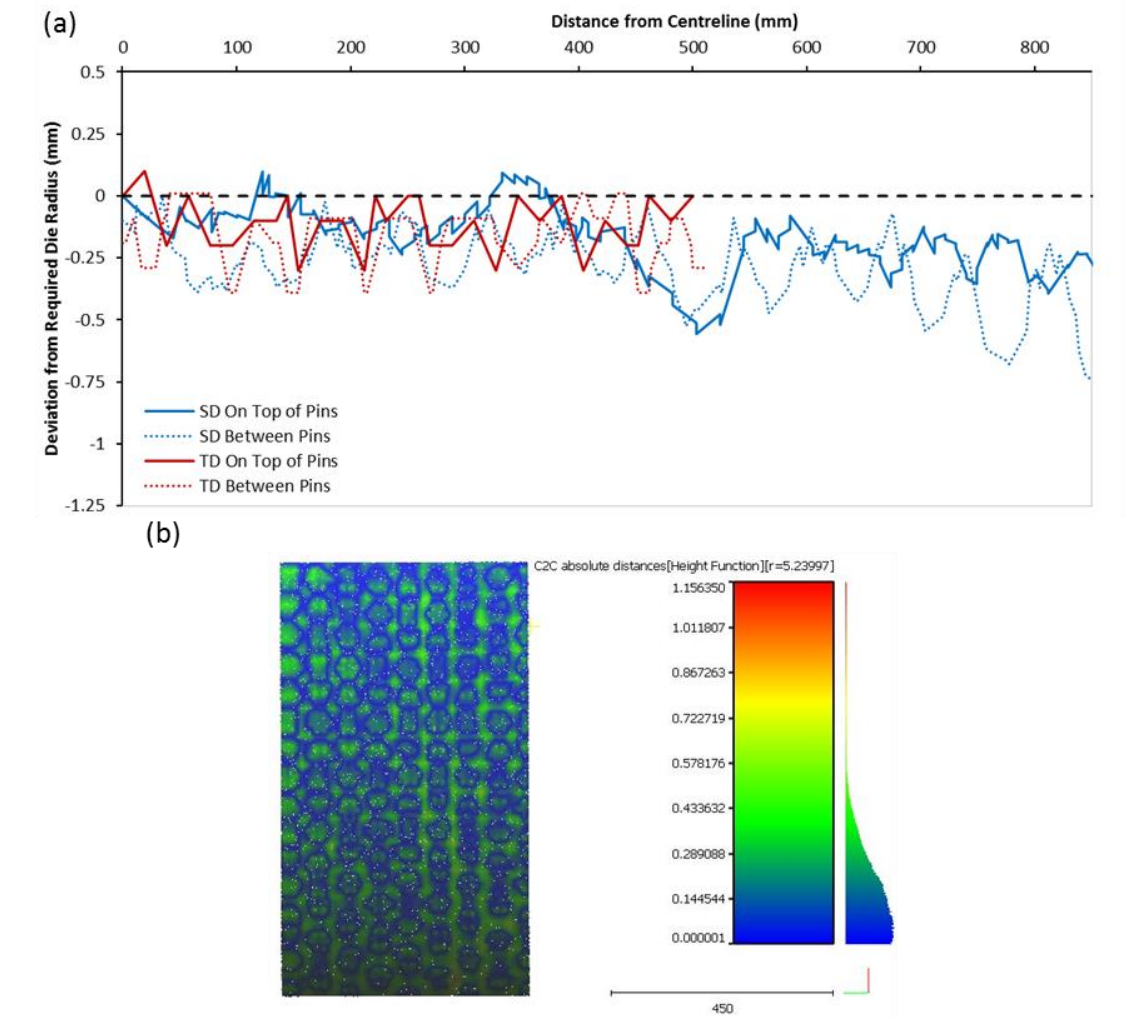

Figure I-16: The HCP2 Shaped r800 MP section line (a) & surface defect (b) analyses results

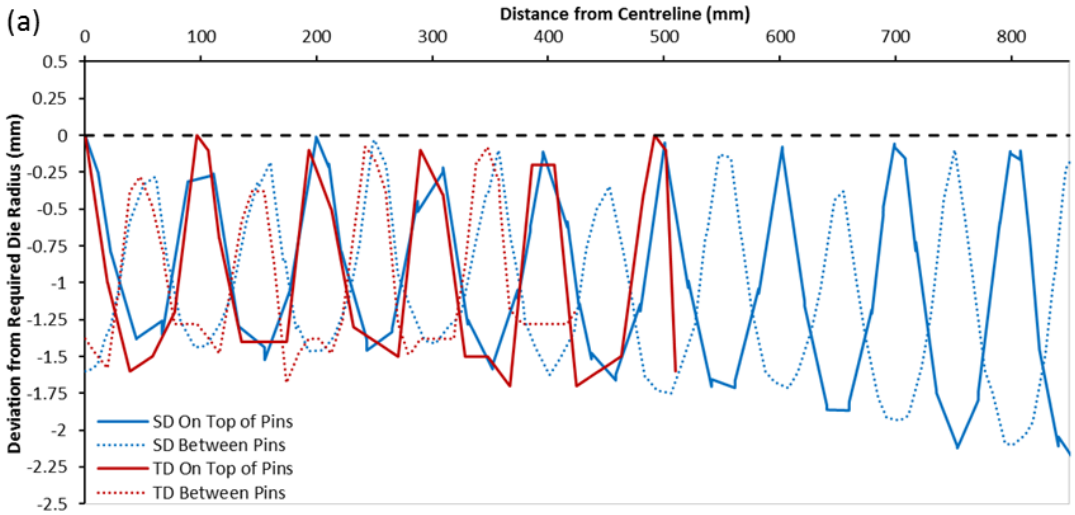

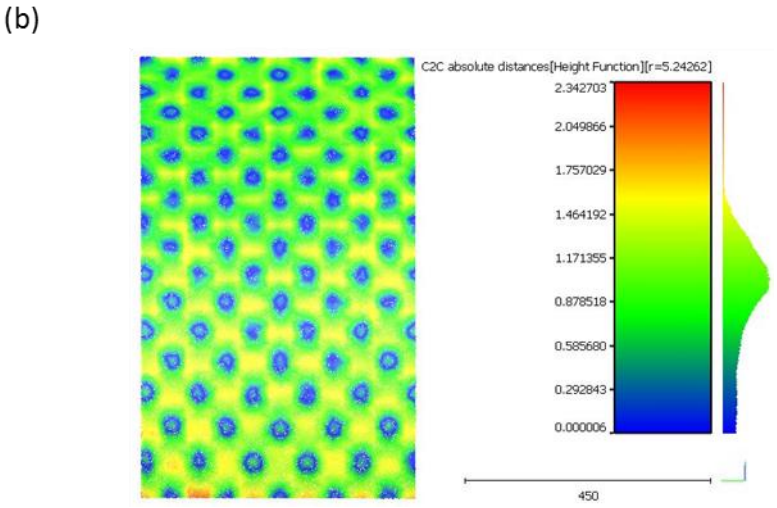

Figure I-17: The RCP3 Round r200 section line (a) & surface defect (b) analyses results

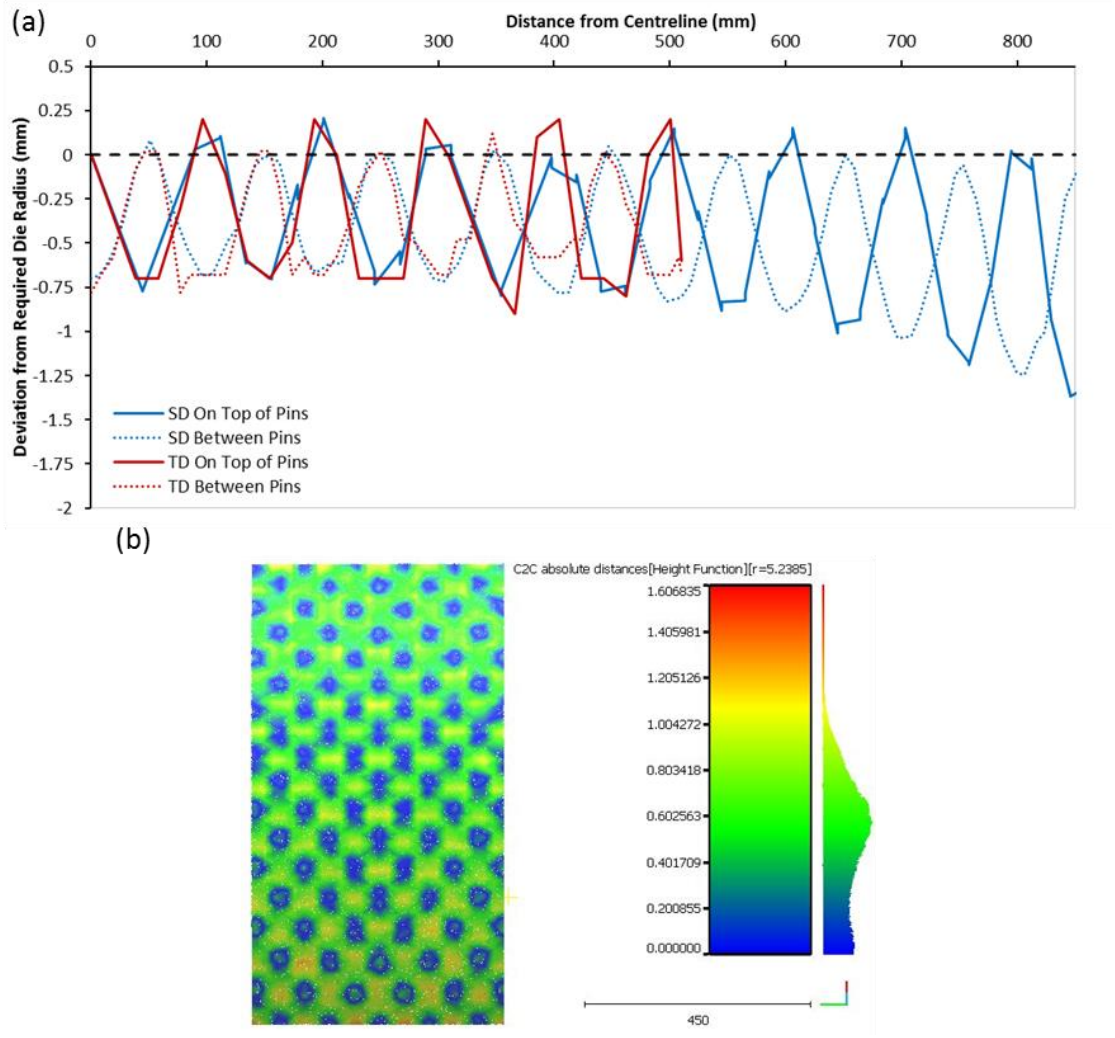

Figure I-18: The RCP3 Round r400 section line (a) & surface defect (b) analyses results

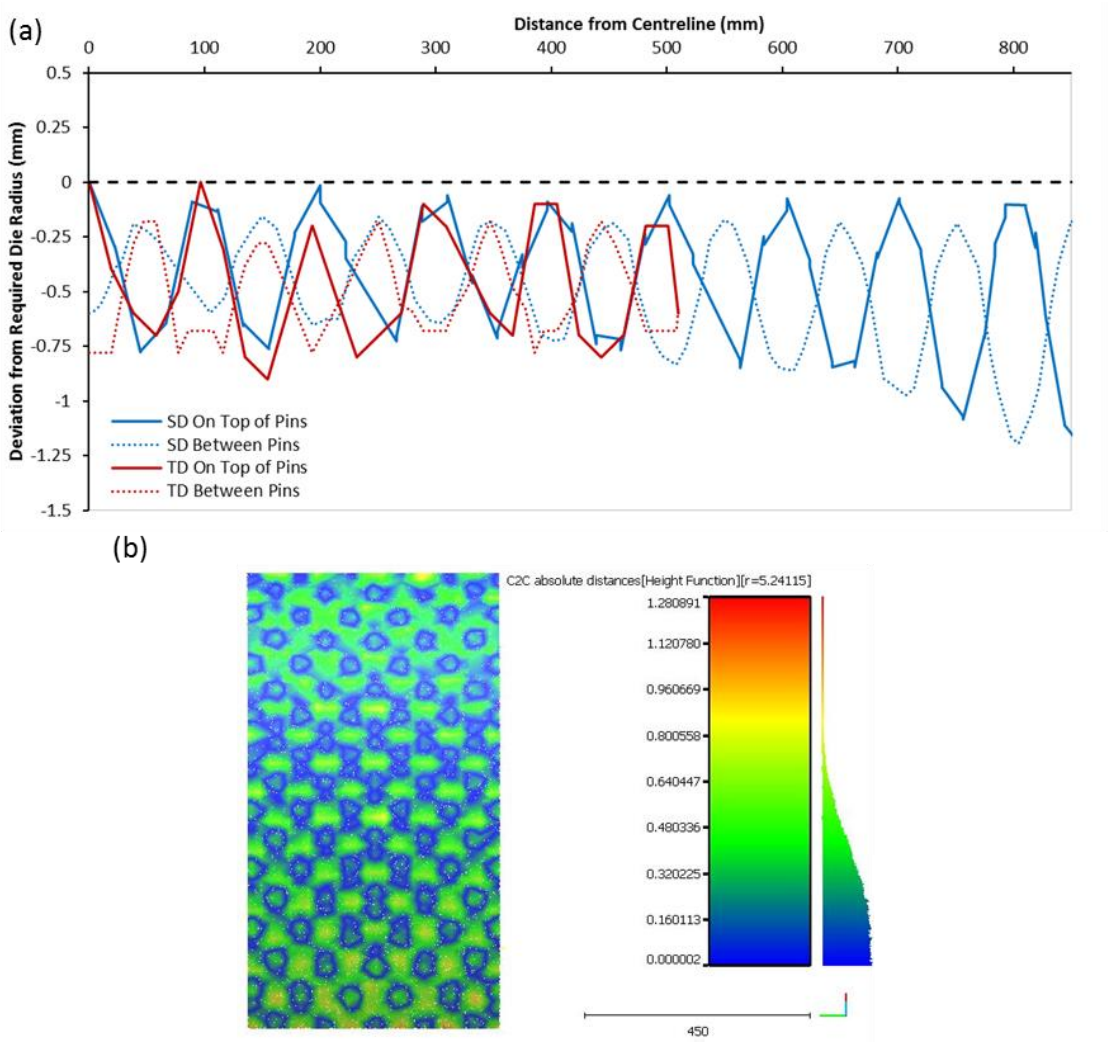

Figure I-19: The RCP3 Round r600 section line (a) & surface defect (b) analyses results

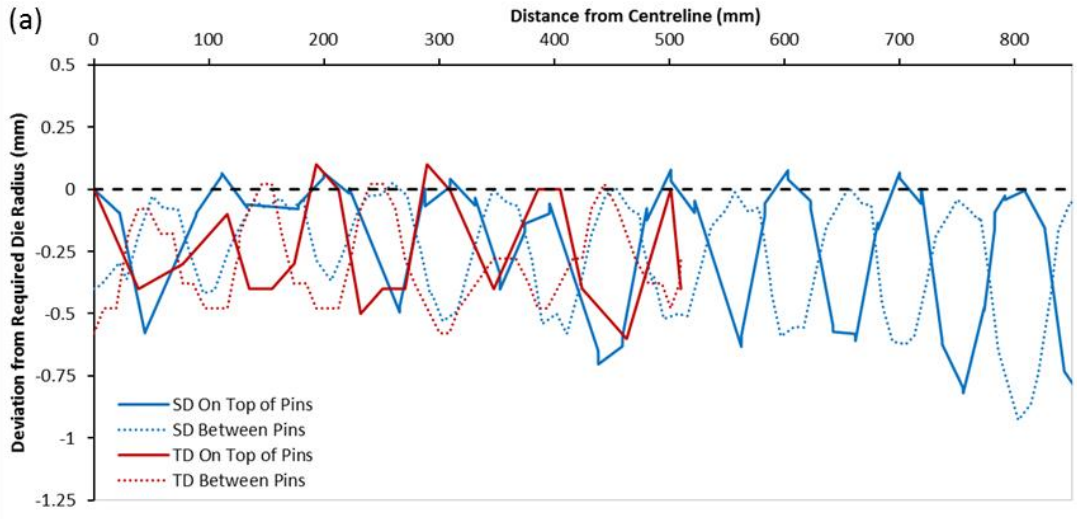

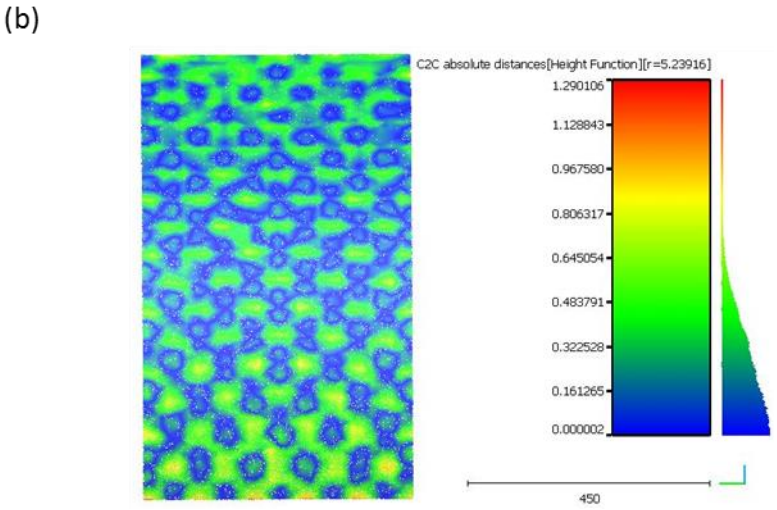

Figure I-20: The RCP3 Round r800 section line (a) & surface defect (b) analyses results

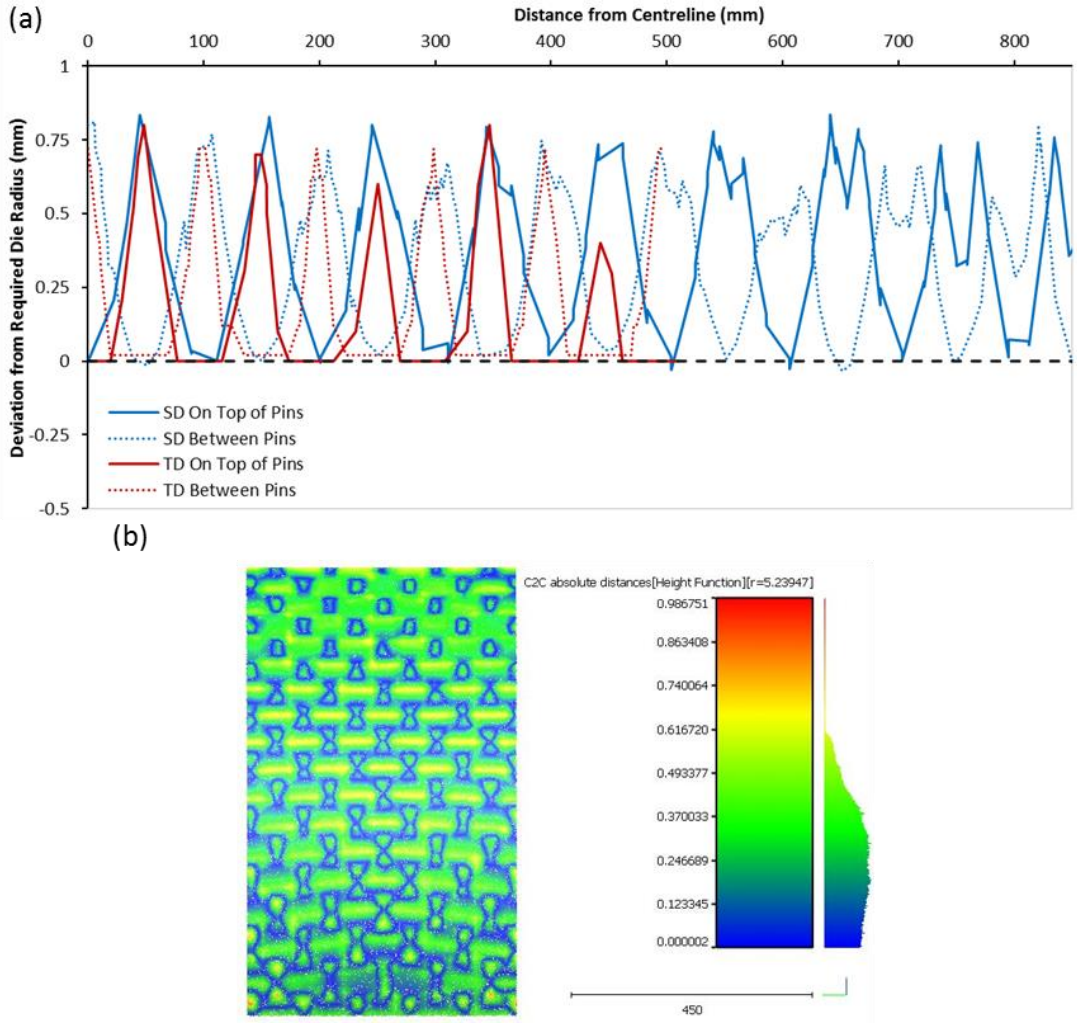

Figure I-21: The RCP3 Shaped Flat section line (a) & surface defect (b) analyses results

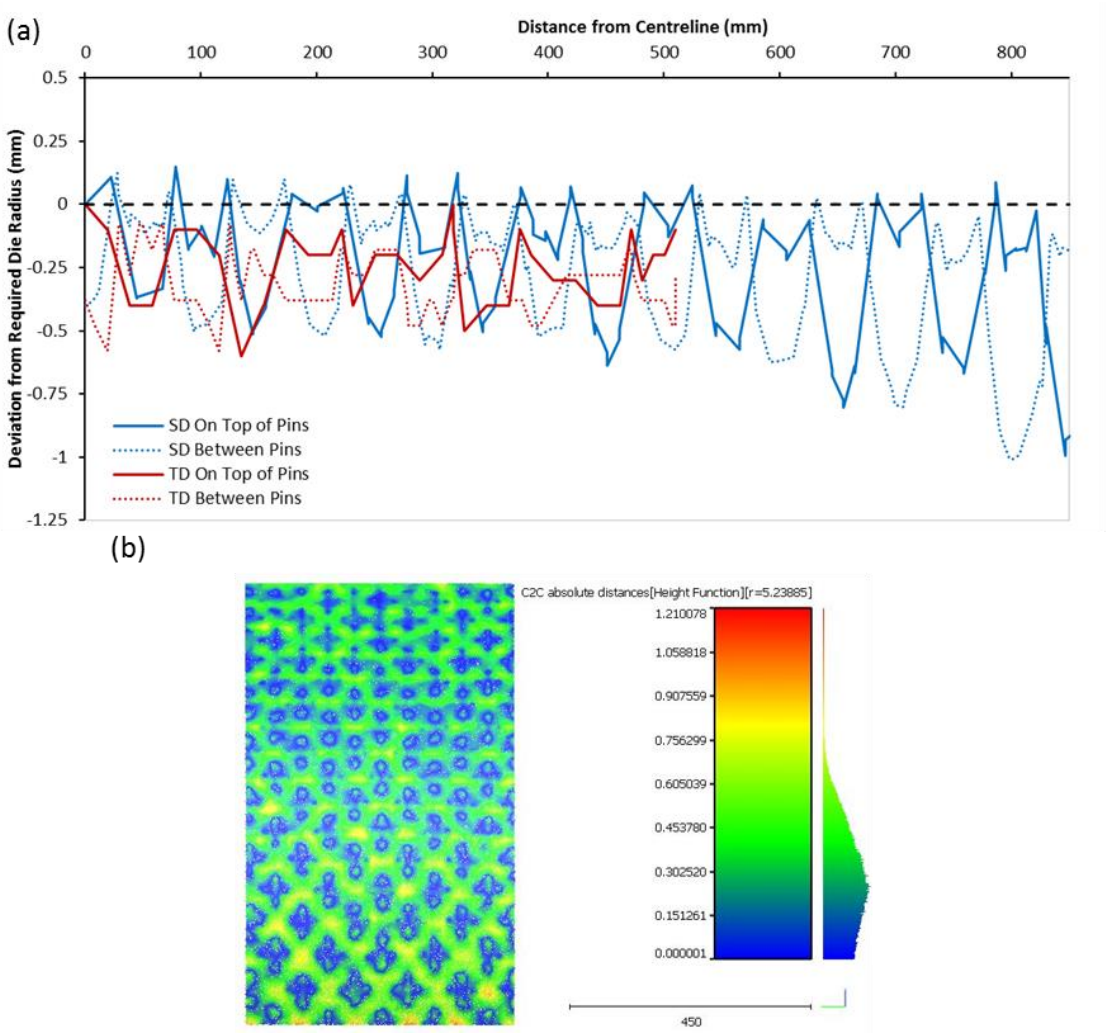

Figure I-22: The RCP3 Shaped Flat MP section line (a) & surface defect (b) analyses results

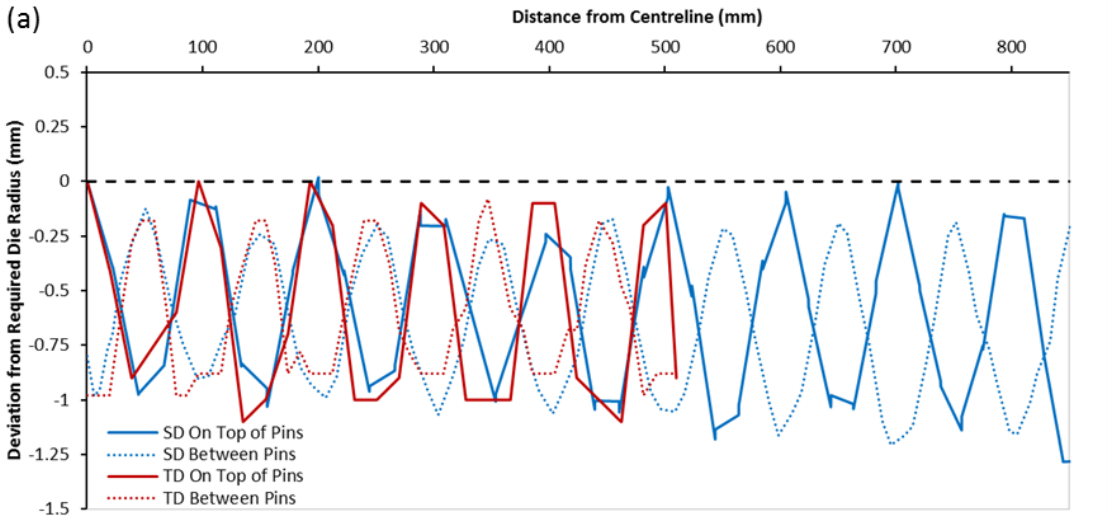

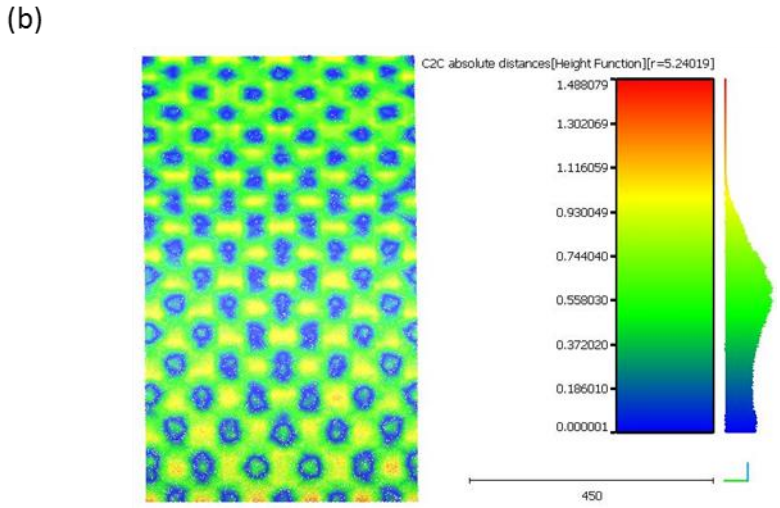

Figure I-23: The RCP3 Shaped r800 section line (a) & surface defect (b) analyses results

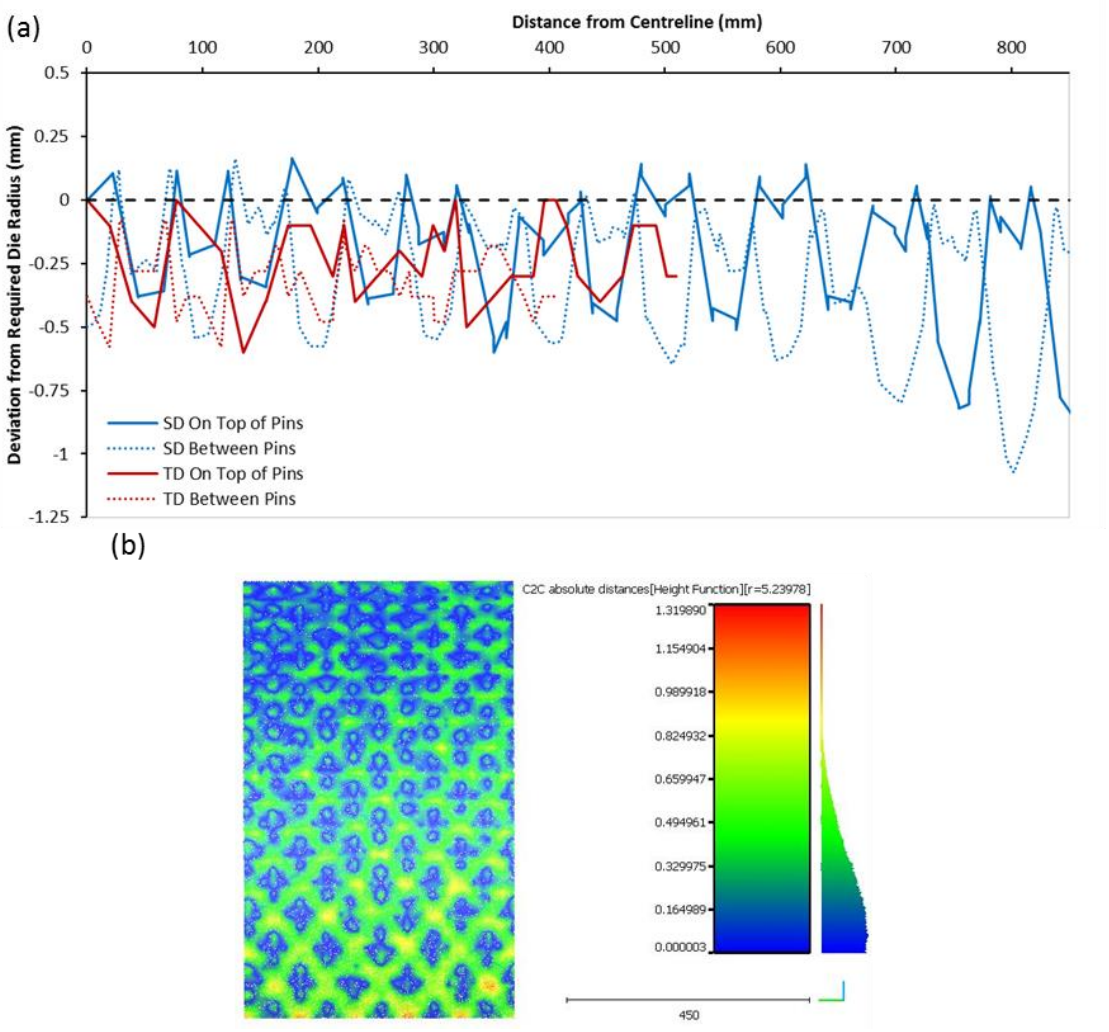

Figure I-24: The RCP3 Shaped r800 MP section line (a) & surface defect (b) analyses results

Appendix J. Chapter 4 Analyses Comparisons

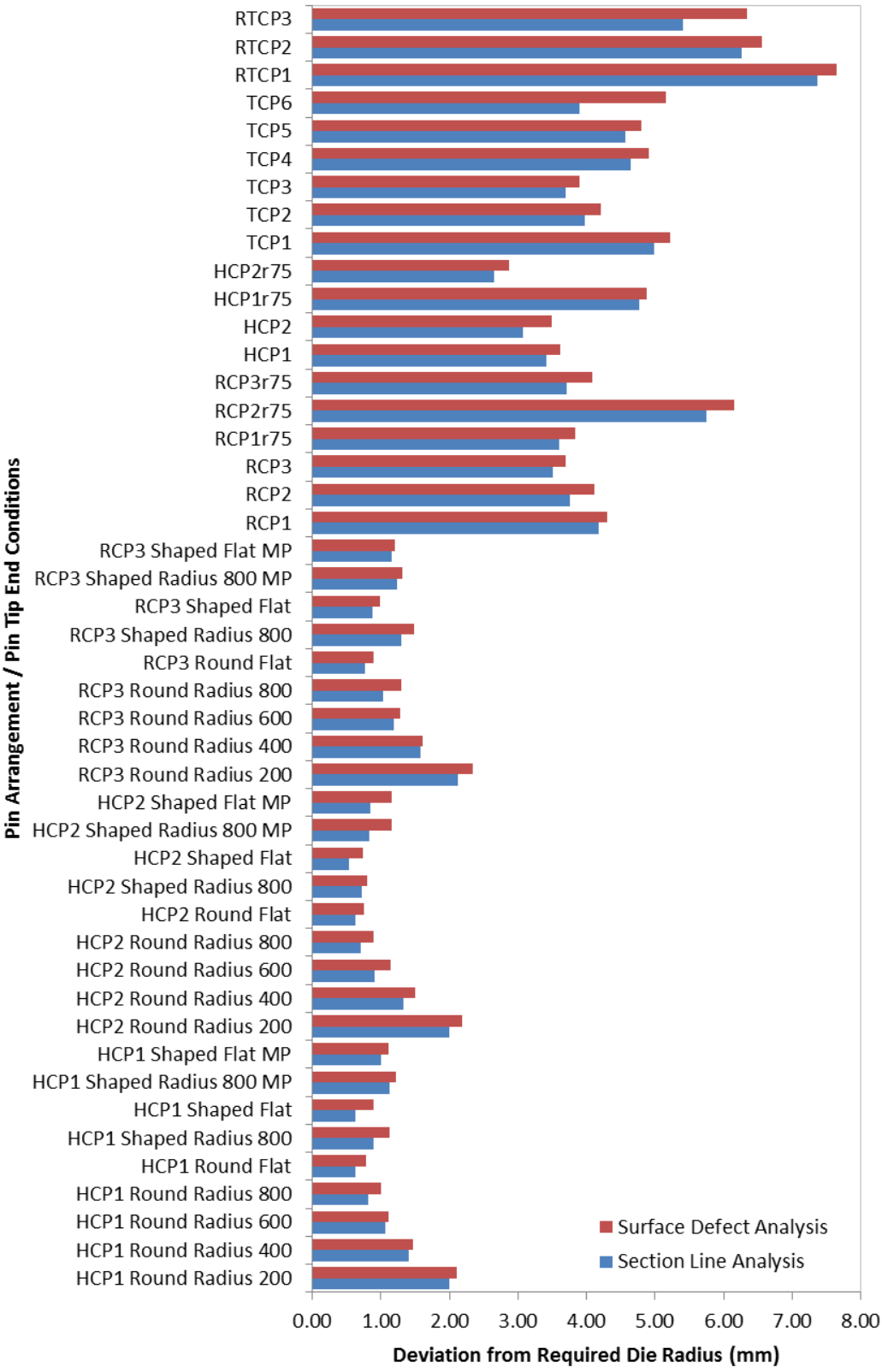

Figure J-1: A comparison of the results from the surface defect & section line analyses presented in Chapter 4

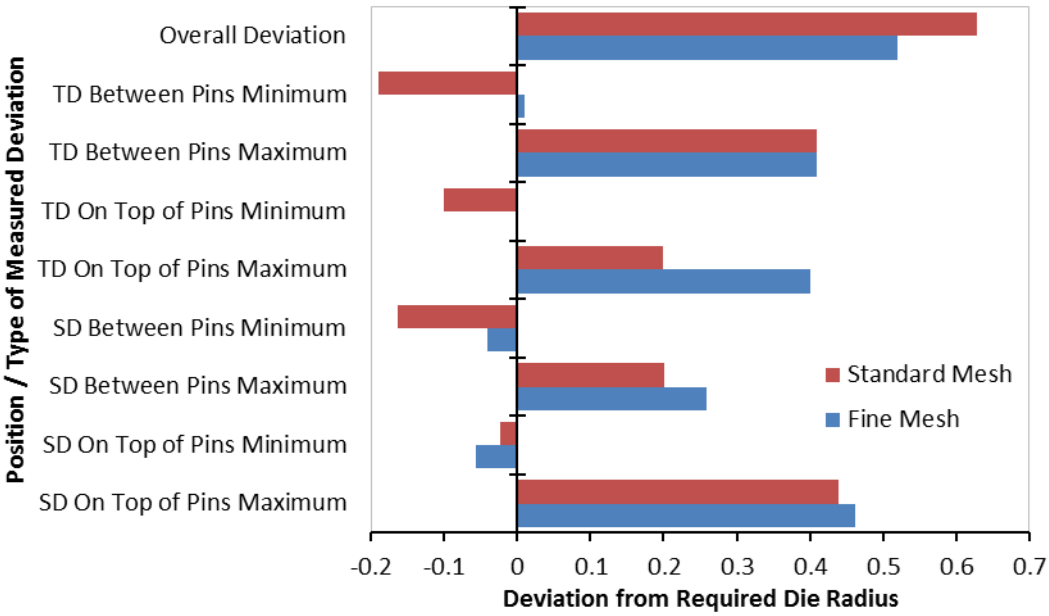

Figure J-2: Chapter 4 HCP2 with round flat pivoted pin tips standard mesh & fine mesh simulations section line analyses results comparison

Appendix K. The 3 Axes Pin Actuation Drive Unit

Since the lab scale machine will eventually be fitted with 32 mm diameter pins, to stretch smaller parts in double curvature, the proposed design of the pin actuation unit has been developed for these smaller diameter pins. The cylindrical pin design allows for pin height adjustment from above. This enables the pins to be located on a solid base, minimising component dimensional accuracy problems associated with machine deflection due to loading. The sequential set up procedure used here, where the heights of six pins can be adjusted simultaneously from above the machine, would offer a cost saving over the set up procedures discussed in Chapter 2, where pins are actuated from below, while still yielding a comparable set up time.

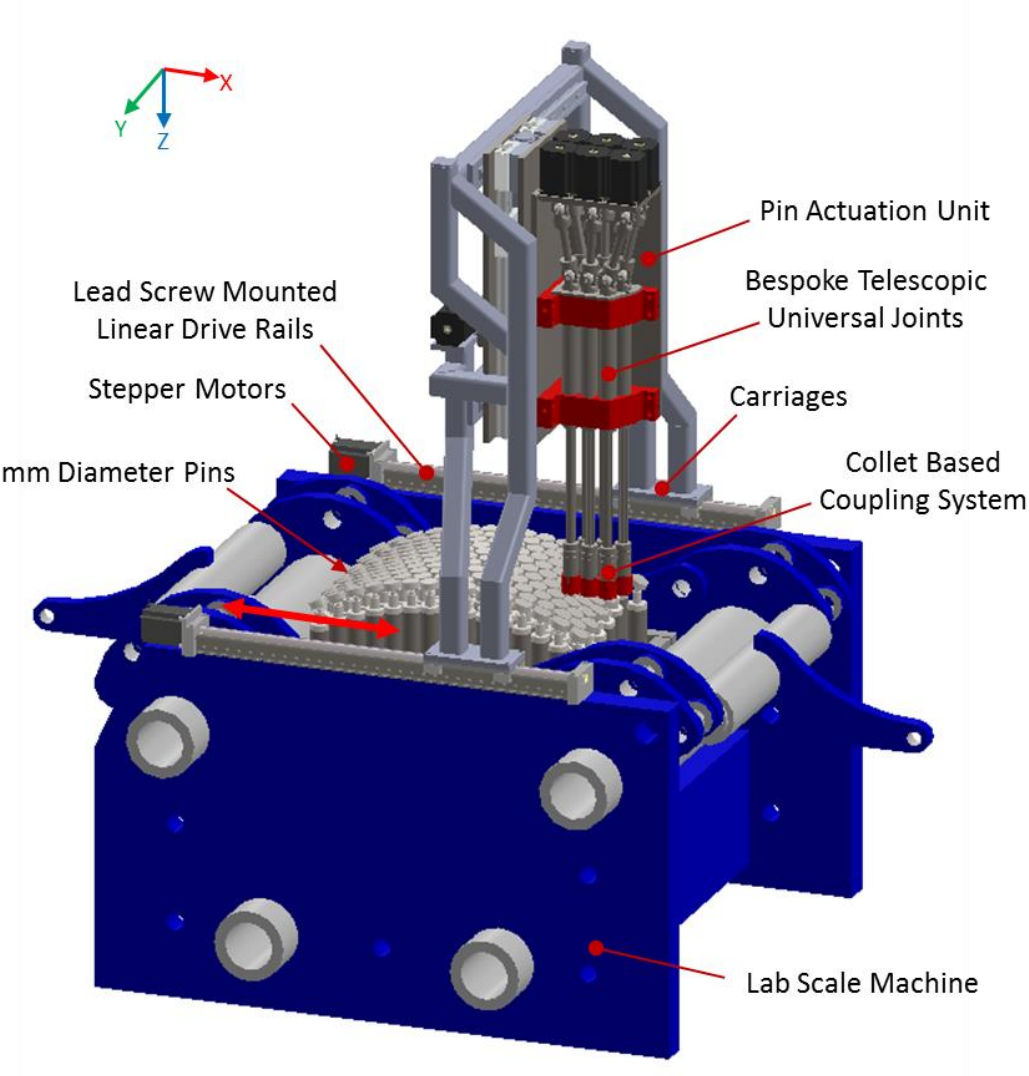

Figure K-1: A proposed design for actuation of 32 mm diameter pins from above showing motion along the X axis

The pin actuation unit, shown in Figure K-1 is carried on a frame, designed in steel box section (40 mm by 40 mm with 4 mm thick walls) welded to two carriages containing lead screw nuts. Positioning of the unit along the X axis is controlled through stepper motors rotating lead screws mounted on two linear drive rails. The backplate of the pin actuation unit is located on sliders which move along linear slide rails attached to the cross members of the frame. Positioning of the unit along the Y axis is controlled through a single stepper motor rotating a lead screw passing through a flanged nut on the lead screw bracket affixed to the backplate [see Figure K-2 (a)].

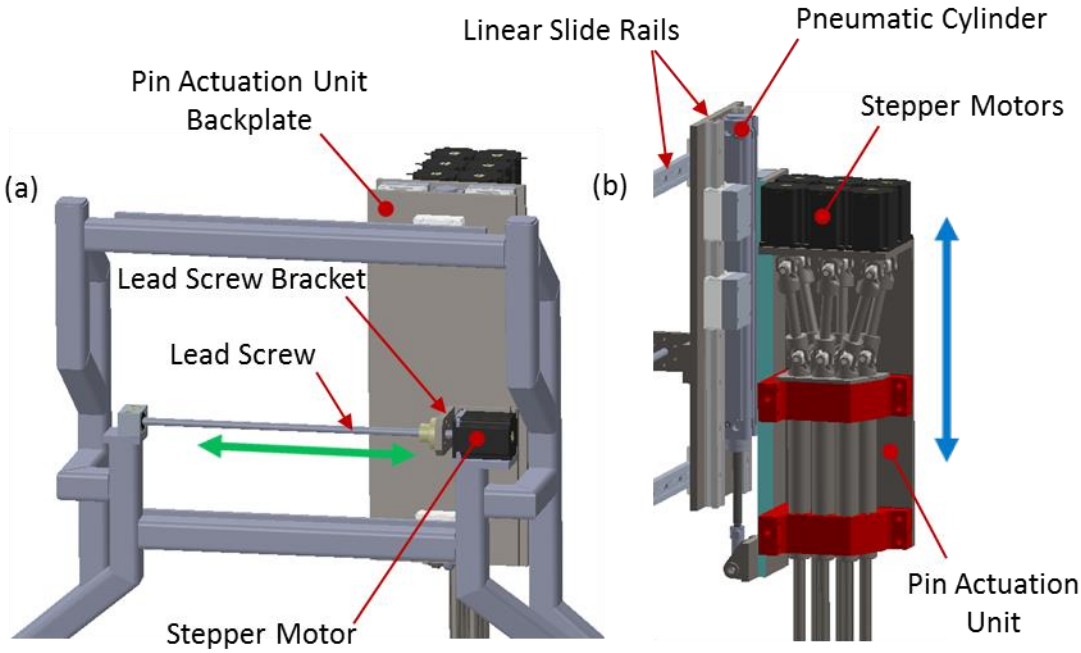

Figure K-2: Motion of the pin actuation unit along the Y axis (a) and along the Z axis (b)

The pin tips are removed from the pins before their heights are adjusted. When the pin actuation unit is positioned above a set of pins it is lowered down onto them through the extension of a pneumatic cylinder, affixed to the backplate, while being guided along two slide rails [see Figure K-2 (b)].

The coupling system used here [see Figure K-3 (b) & (c)] is based on a collet normally used in mill tool holding. Each of the six collets, in the pin actuation unit, fit over a length of reduced diameter at the top of the 32 mm

diameter pins. When the actuation unit is lowered onto the pins, springs located in the cylinders of the six bespoke telescopic universal joints [see Figure K-3 (a)] ensure that a force is applied onto each collet based coupler affixed to the bottom of the telescopic rams. When this force is applied at the mating conical surfaces of the plastic collet and steel ram end piece, the inner diameter of the collet is reduced to grip the pins. Six stepper motors mounted at the top of the pin actuation unit are used to rotate the bespoke telescopic joints in plastic plain bearings and adjust the heights of the six pins along their threaded lower sections.

When the pin actuation unit is raised again, the springs located in the coupling system apply a force onto each collet to release its grip on their corresponding pins. Note that the two pieces of the captive collet are shown apart in Figure K-3 (c) for clarity. The collet and sleeve are actually manufactured in the captive position shown in Figure K-3 (b).

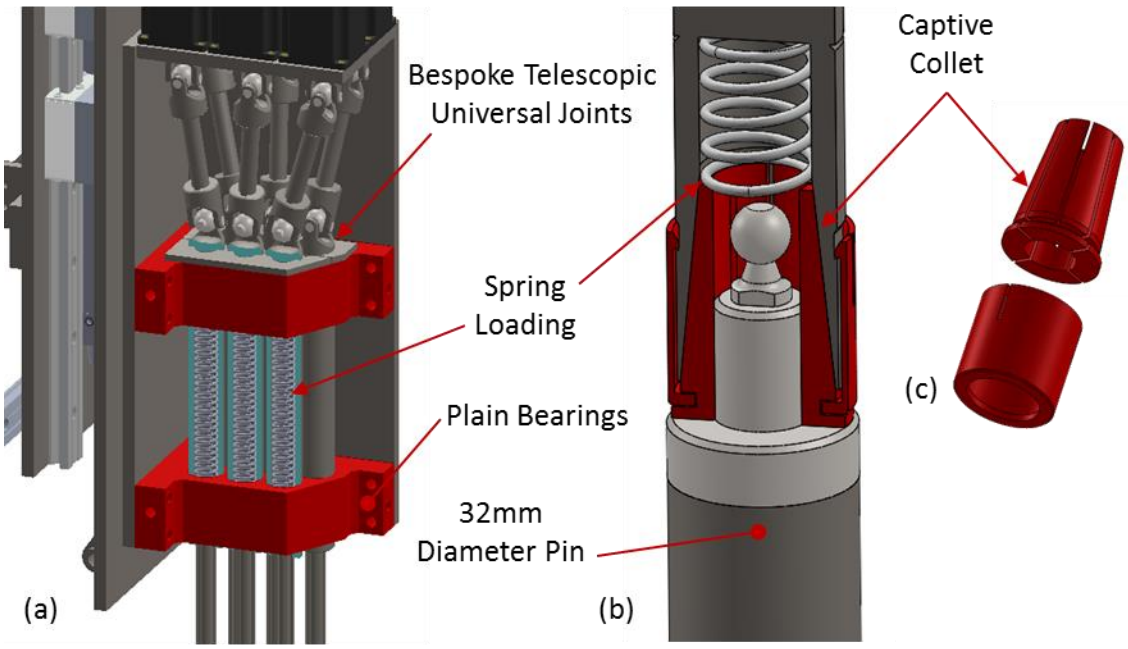

Figure K-3: Spring loading of the telescopic universal joint units (a) and coupling system (b) with an exploded view of the captive collet (c)

The pin actuation unit shown here is set to adjust the heights of pins in the HCP2 pin layout. The unit can also be rotated through 90 degrees about the Z axis to adjust the heights of pins in the HCP1 pin layout.

Appendix L. Additional Contour Maps Relating to Simulations over a Single Layer of Interpolation

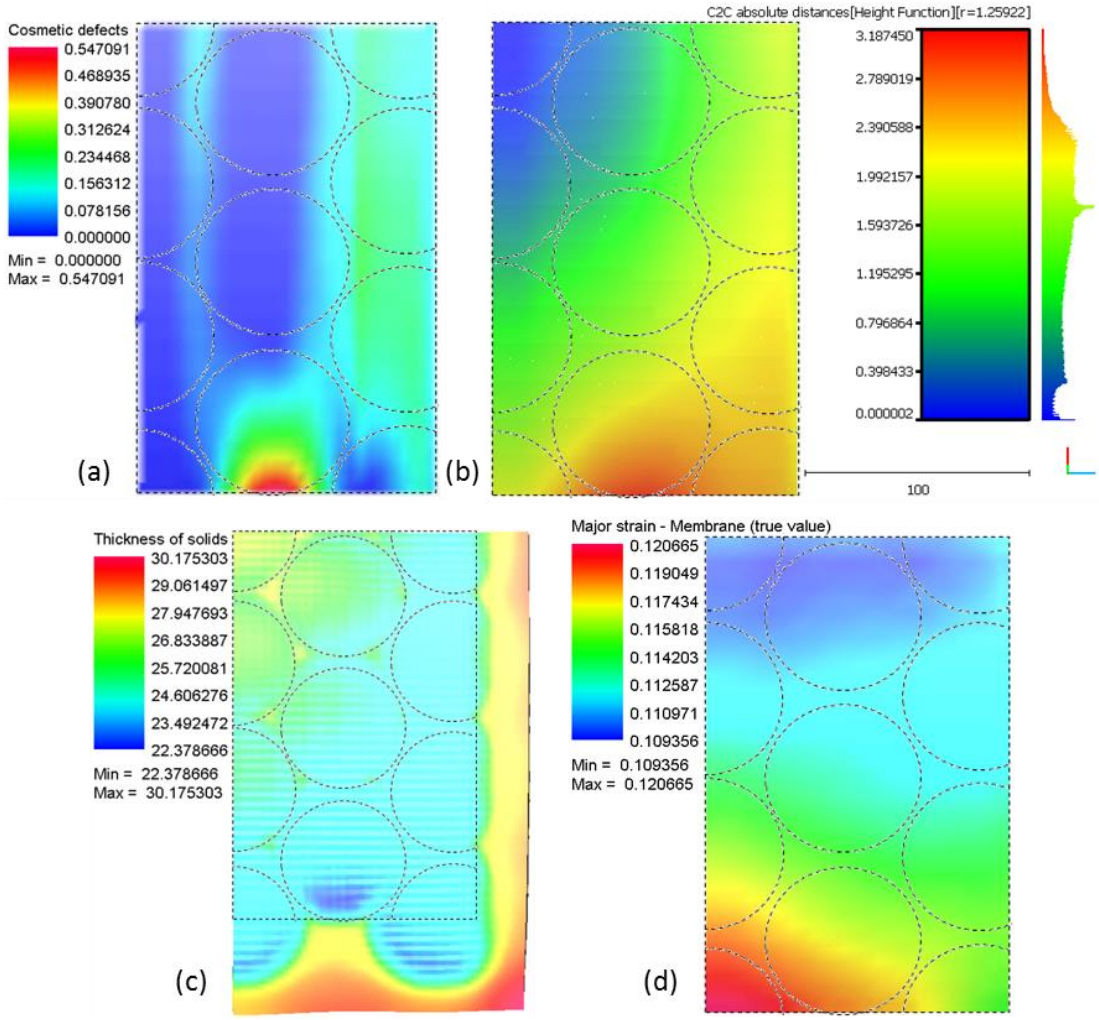

Figure L-1: Cosmetic defect (a) C2C absolute distance (b) Thickness of solids (c) & Major strain (d) contour maps for the 30 Red simulation

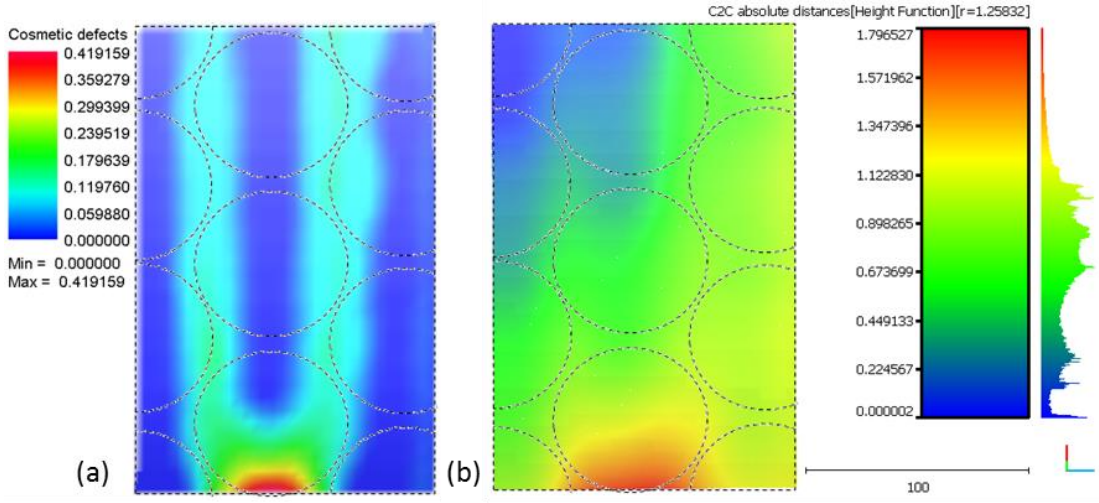

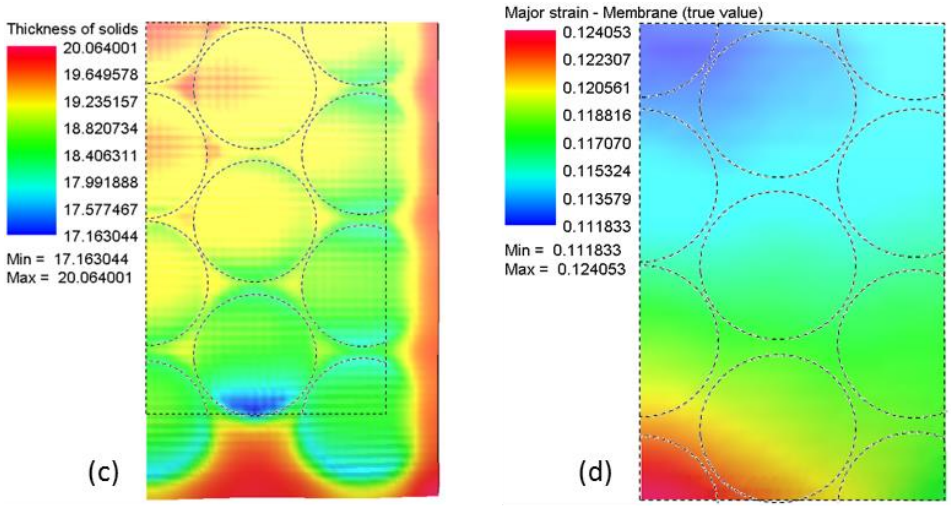

Figure L-2: Cosmetic defect (a) C2C absolute distance (b) Thickness of solids (c) & Major strain (d) contour maps for the 20 Purple simulation

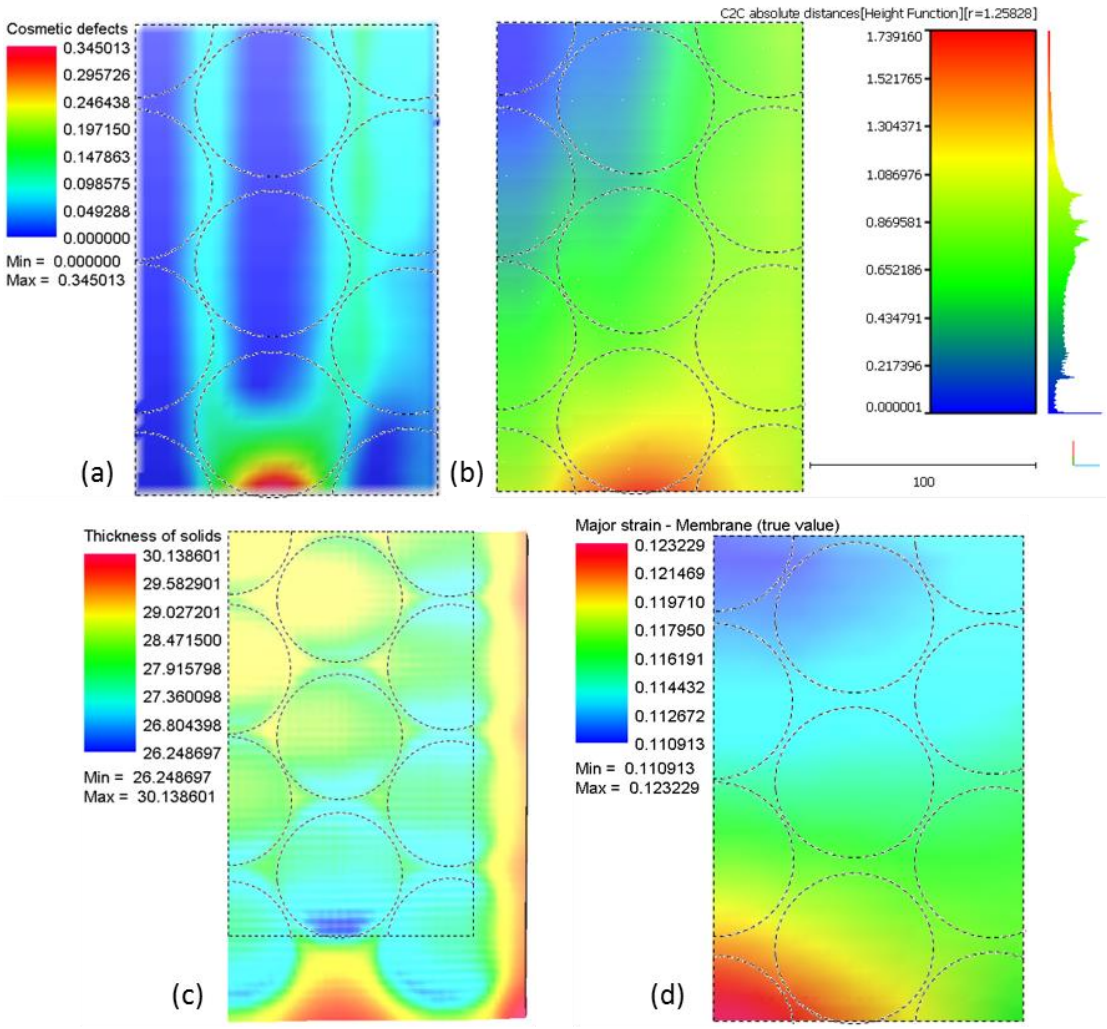

Figure L-3: Cosmetic defect (a) C2C absolute distance (b) Thickness of solids (c) & Major strain (d) contour maps for the 30 Purple simulation

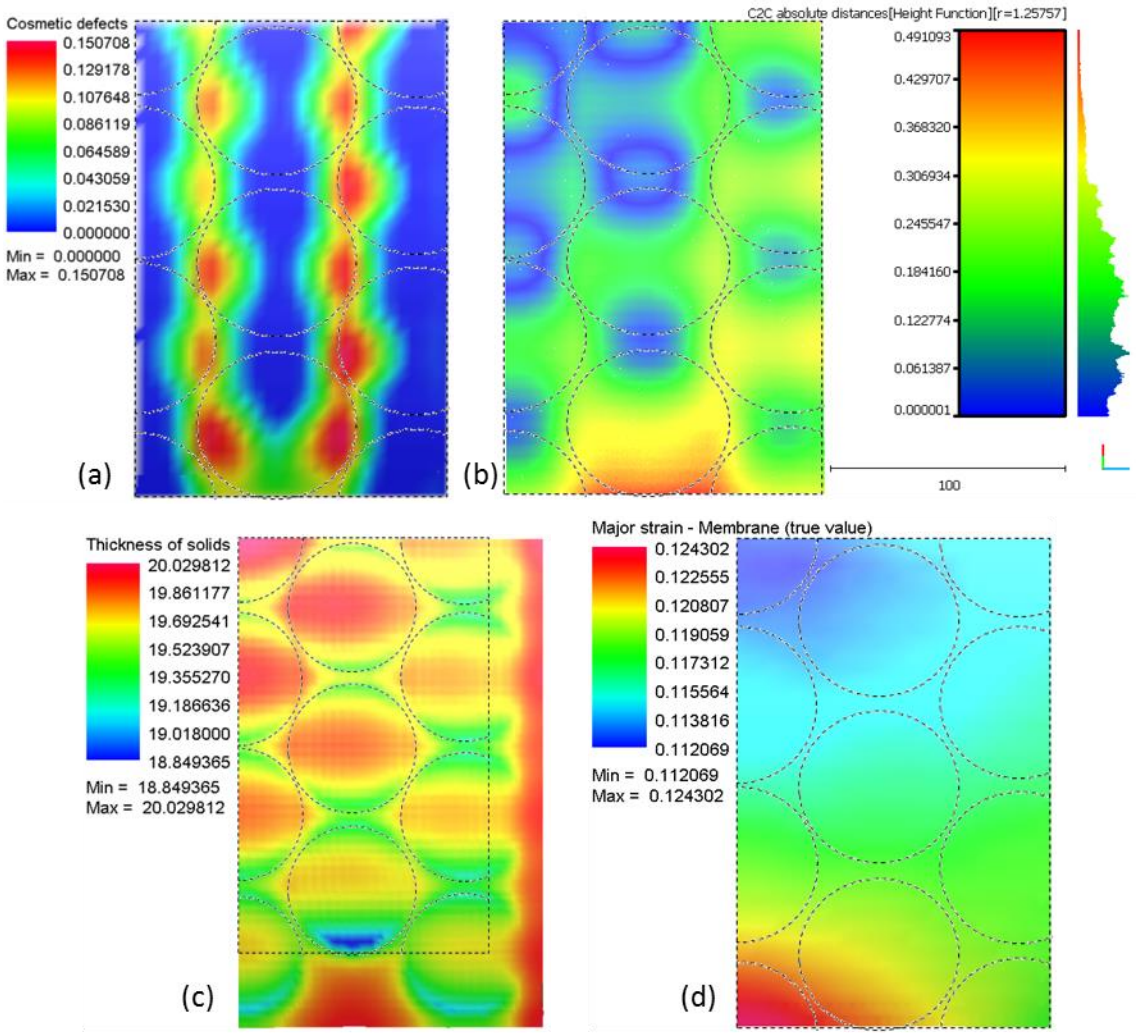

Figure L-4: Cosmetic defect (a) C2C absolute distance (b) Thickness of solids (c) & Major strain (d) contour maps for the 20 Green simulation

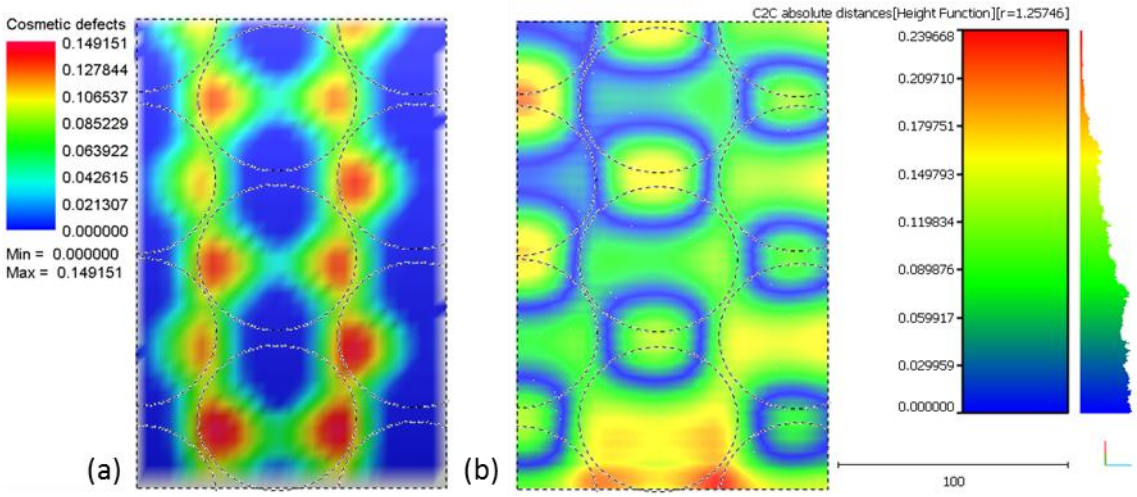

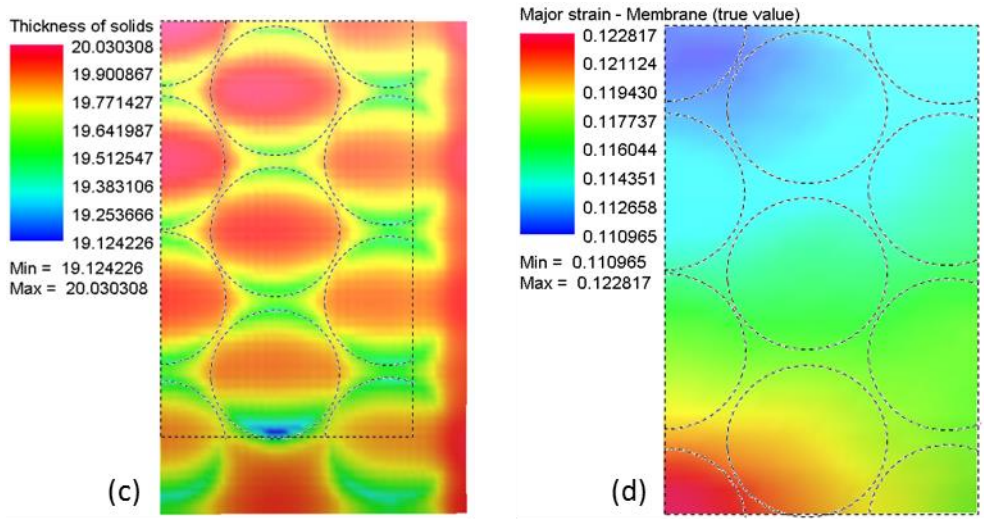

Figure L-5: Cosmetic defect (a) C2C absolute distance (b) Thickness of solids (c) & Major strain (d) contour maps for the 20 Orange simulation

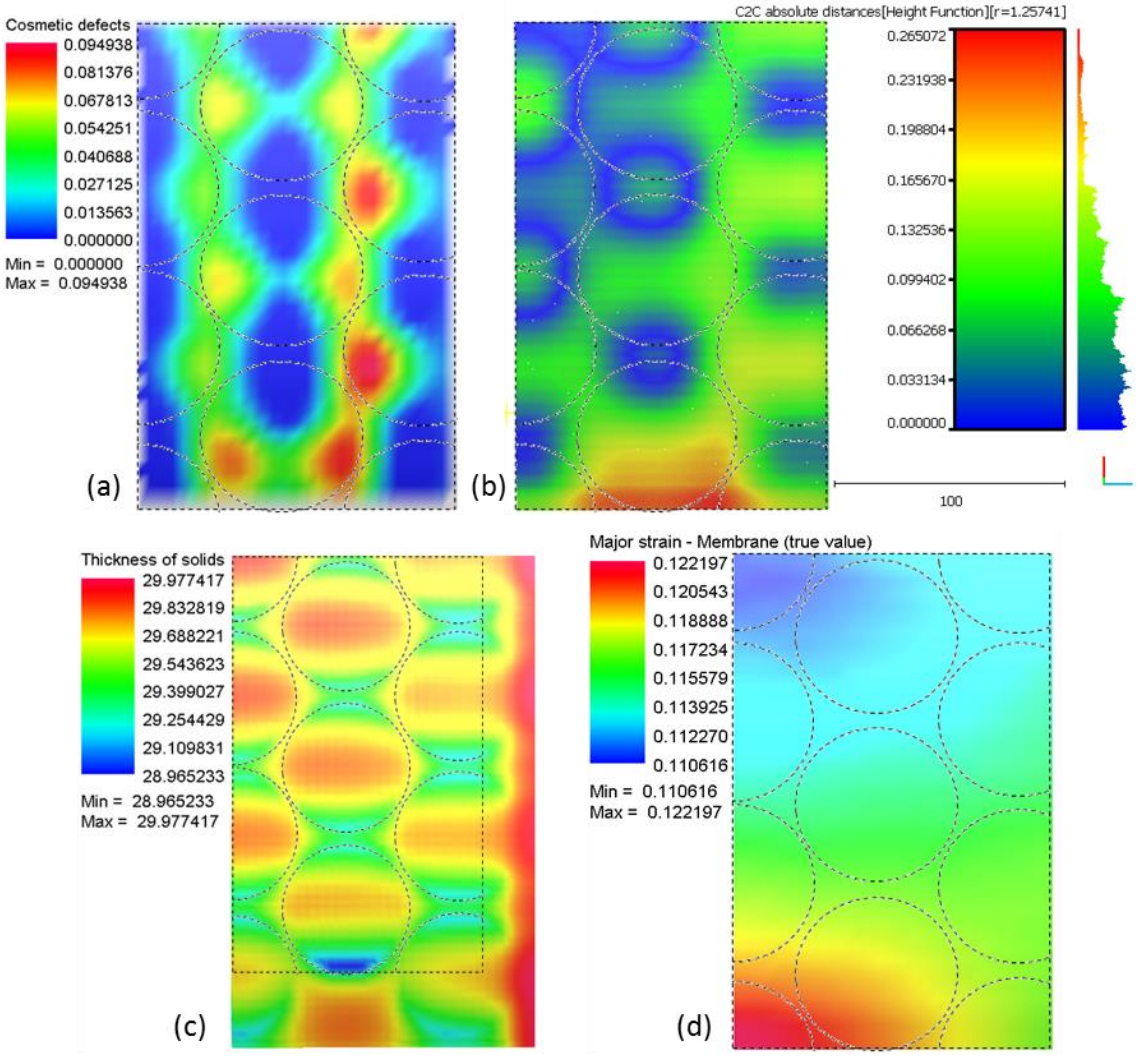

Figure L-6: Cosmetic defect (a) C2C absolute distance (b) Thickness of solids (c) & Major strain (d) contour maps for the 30 Orange simulation

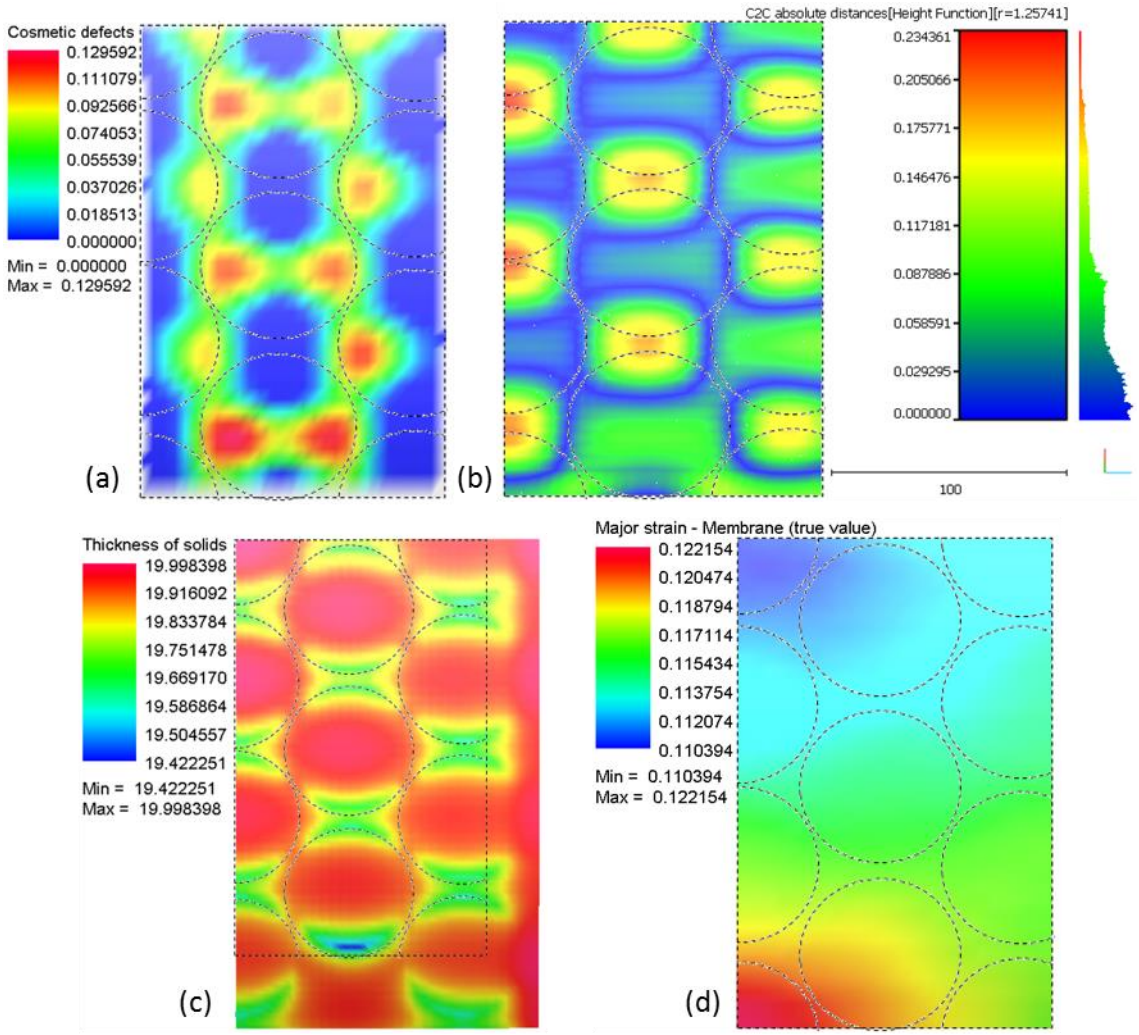

Figure L-7: Cosmetic defect (a) C2C absolute distance (b) Thickness of solids (c) & Major strain (d) contour maps for the 20 Blue simulation

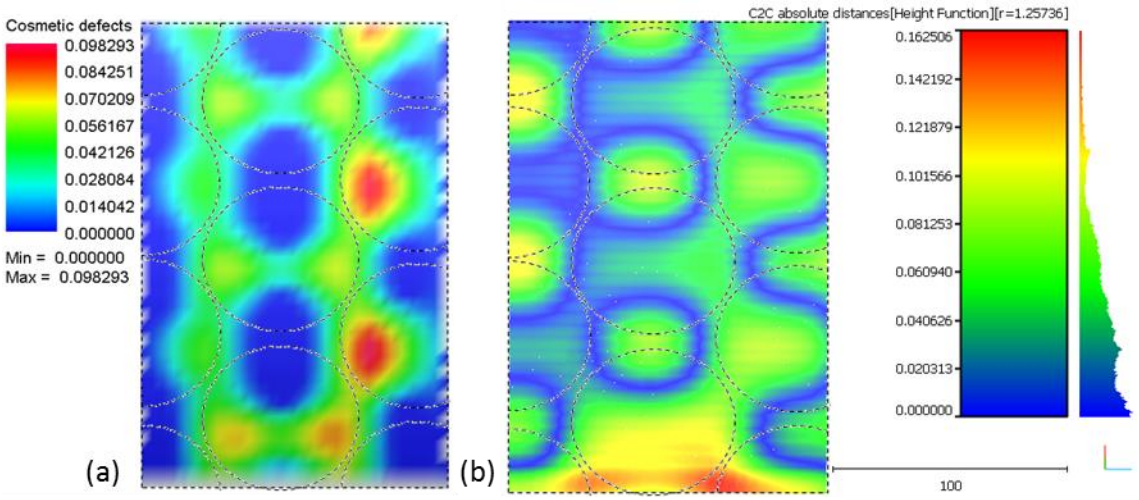

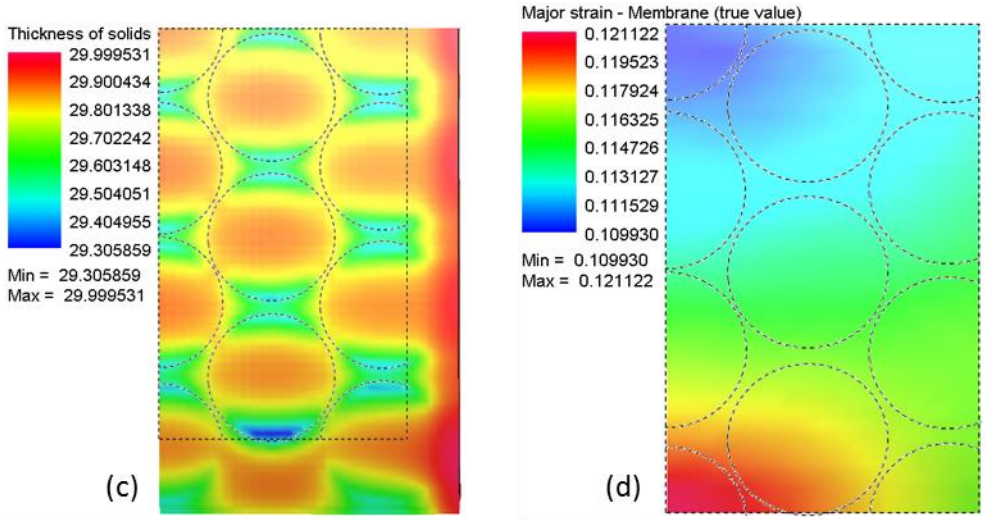

Figure L-8: Cosmetic defect (a) C2C absolute distance (b) Thickness of solids (c) & Major strain (d) contour maps for the 30 Blue simulation

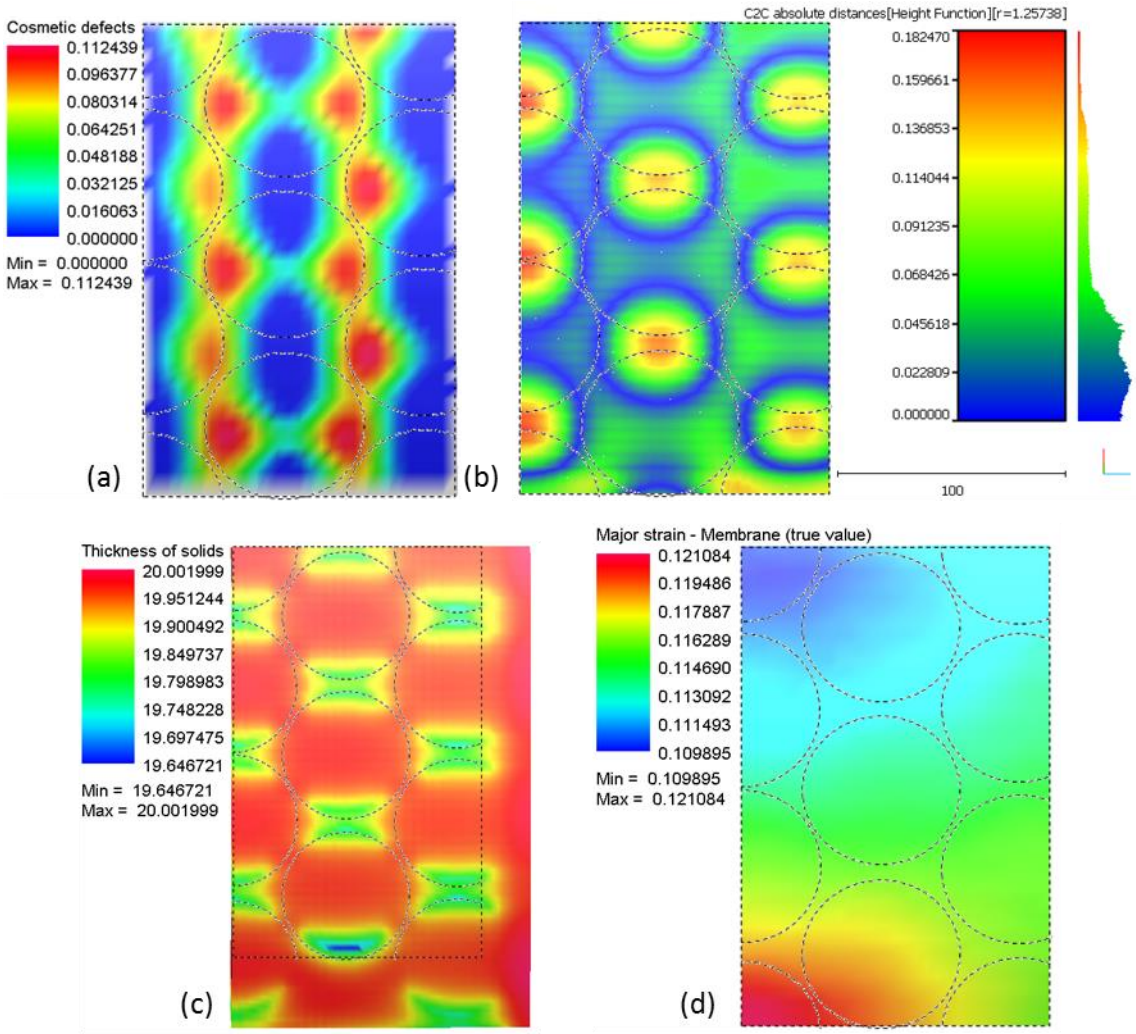

Figure L-9: Cosmetic defect (a) C2C absolute distance (b) Thickness of solids (c) & Major strain (d) contour maps for the 20 Brown simulation

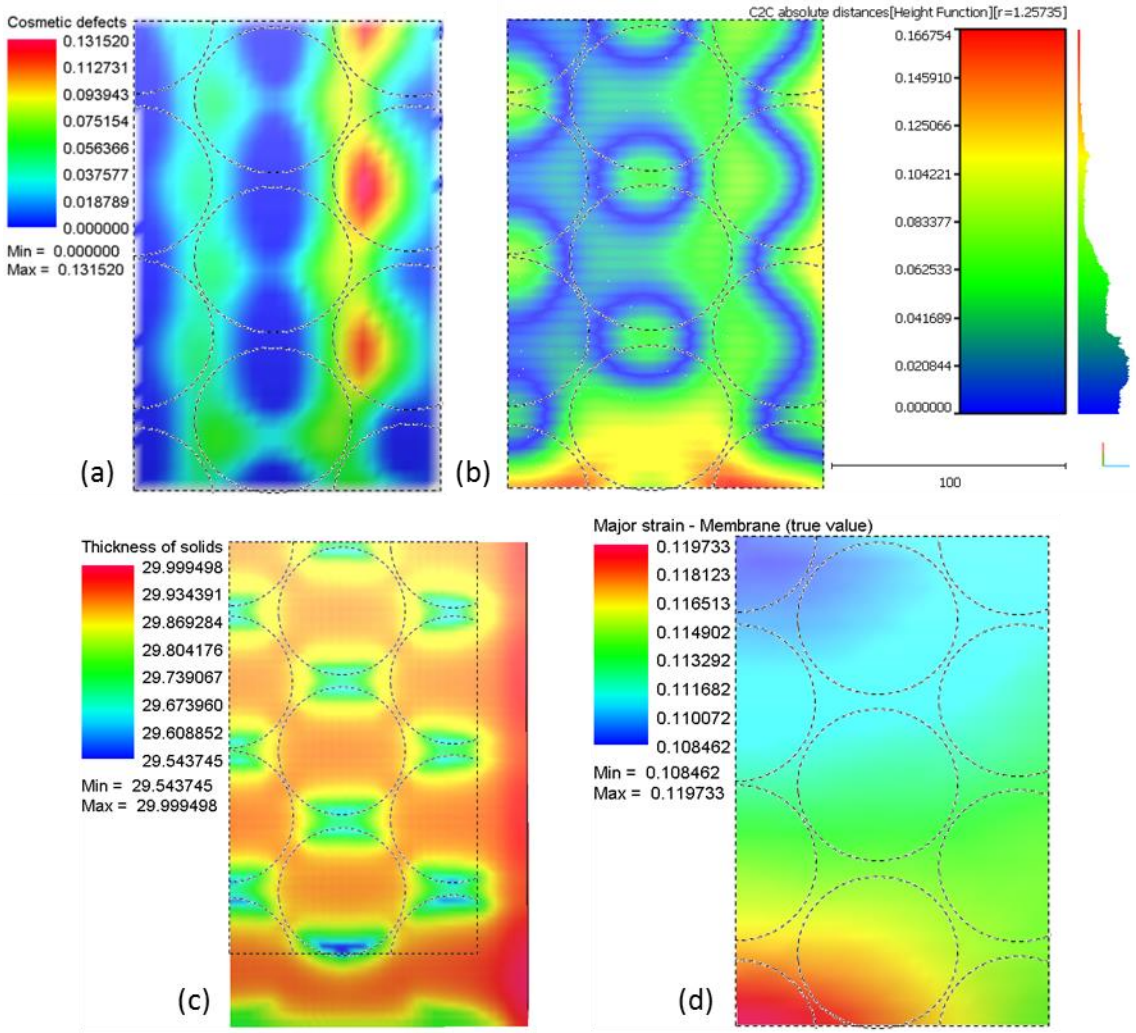

Figure L-10: Cosmetic defect (a) C2C absolute distance (b) Thickness of solids (c) & Major strain (d) contour maps for the 30 Brown simulation

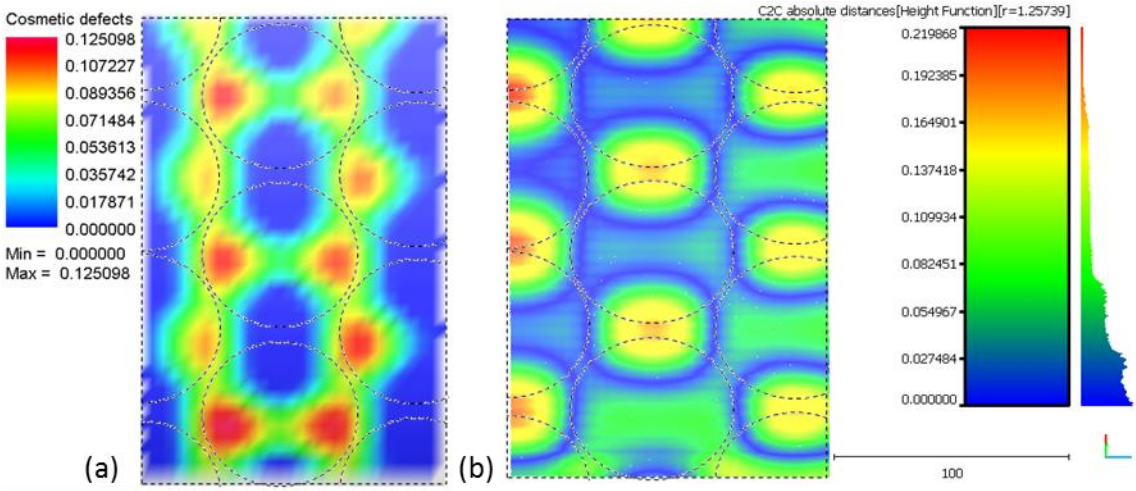

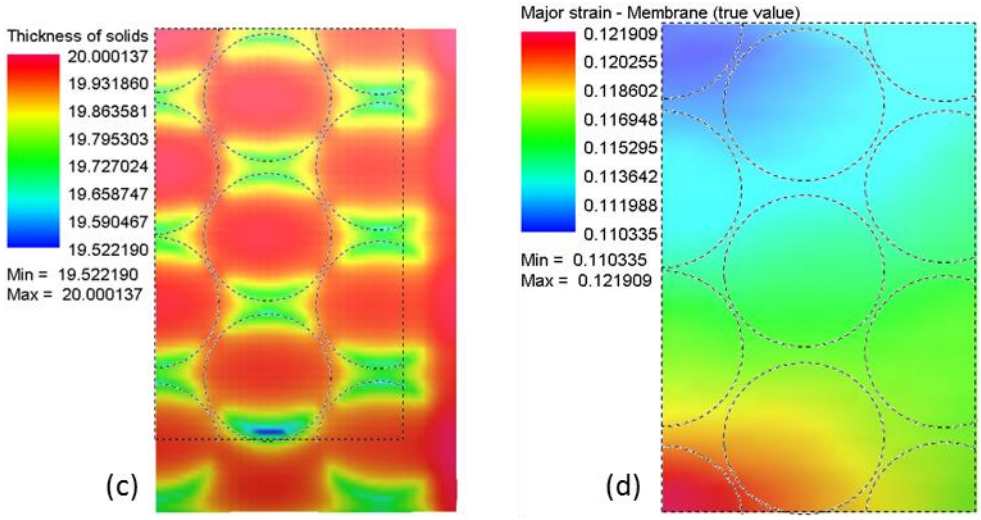

Figure L-11: Cosmetic defect (a) C2C absolute distance (b) Thickness of solids (c) & Major strain (d) contour maps for the 20 Violet simulation

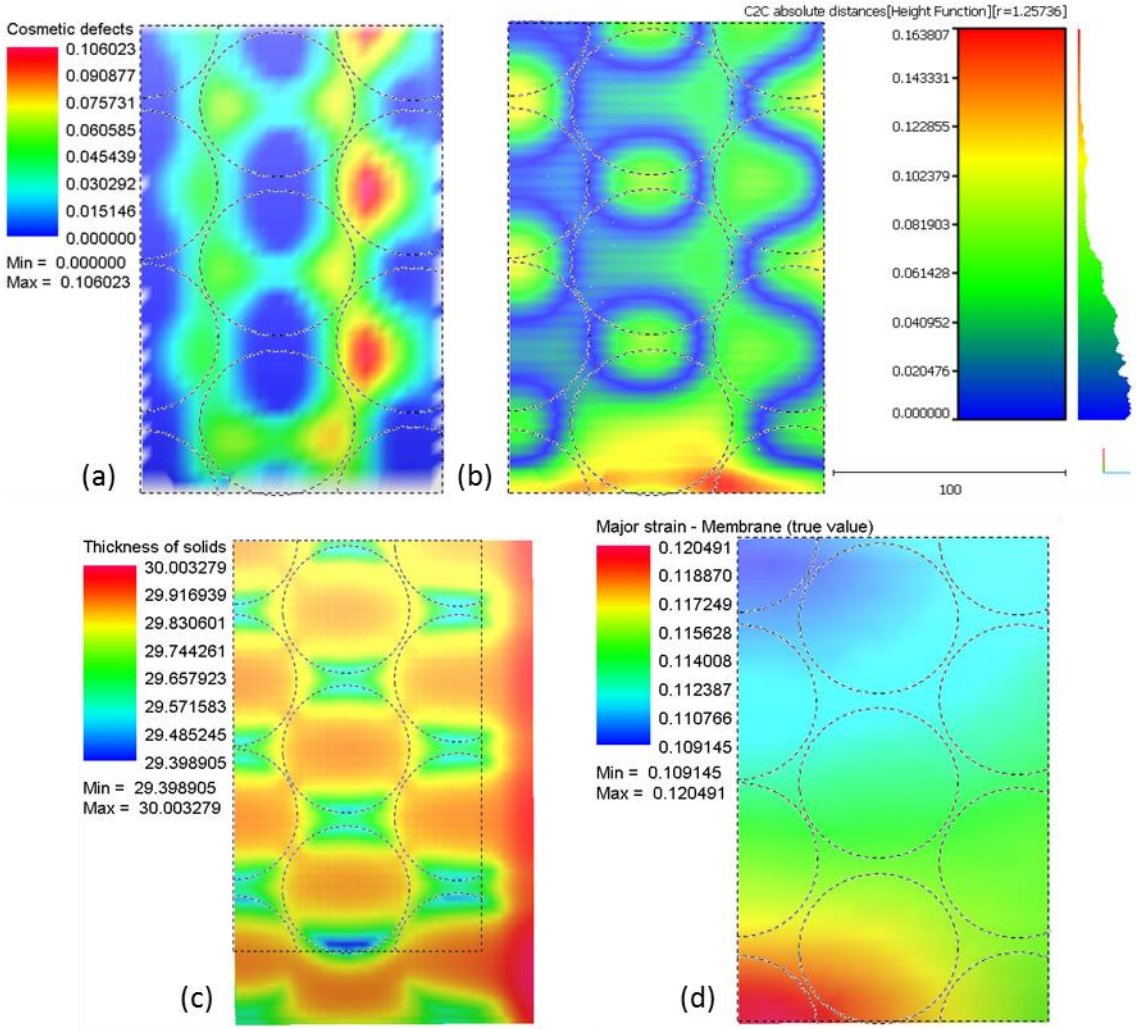

Figure L-12: Cosmetic defect (a) C2C absolute distance (b) Thickness of solids (c) & Major strain (d) contour maps for the 30 Violet simulation

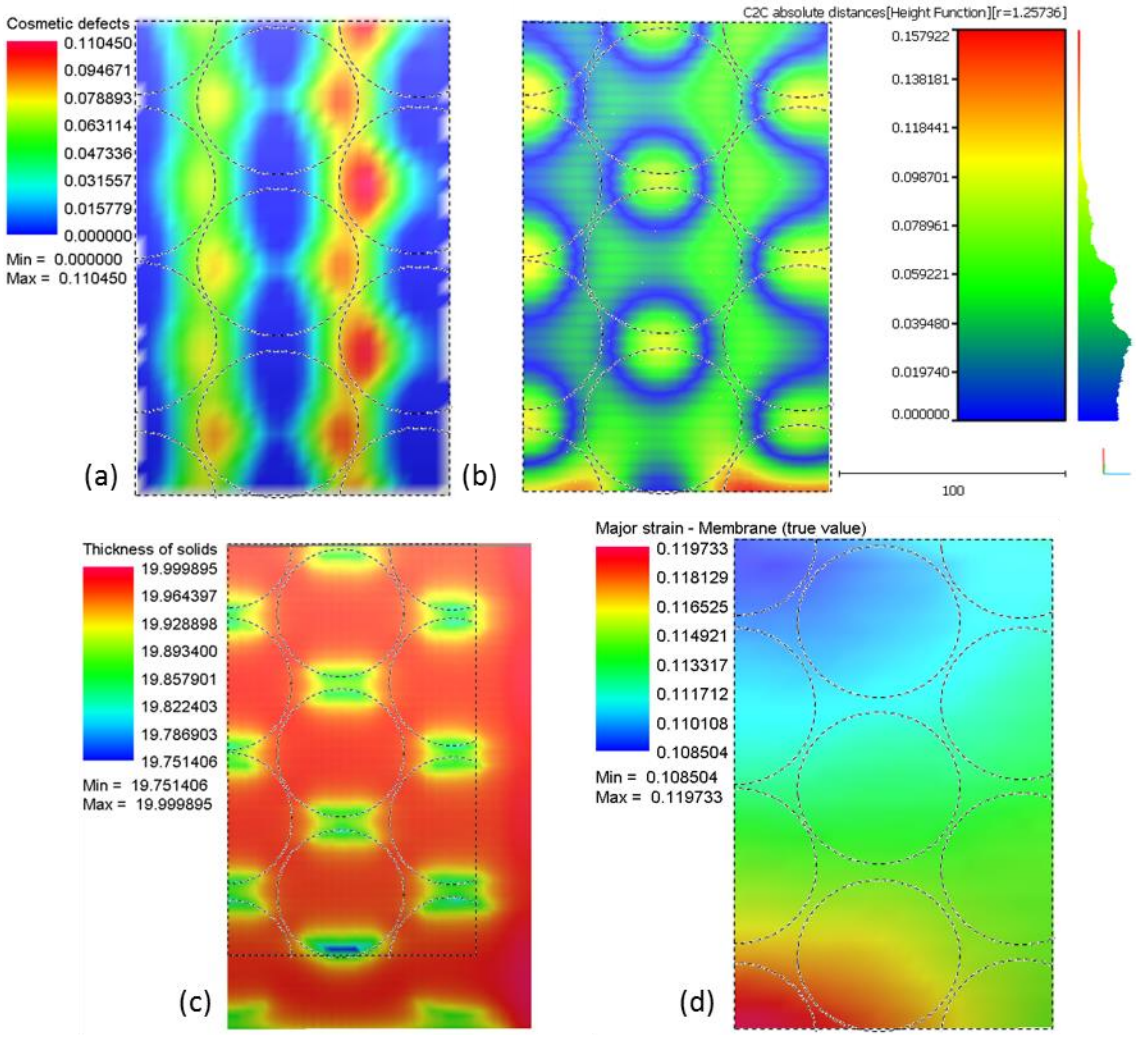

Figure L-13: Cosmetic defect (a) C2C absolute distance (b) Thickness of solids (c) & Major strain (d) contour maps for the 20 Grey simulation

Appendix M. Contour Maps Relating to Simulations with Corrected Pin Heights

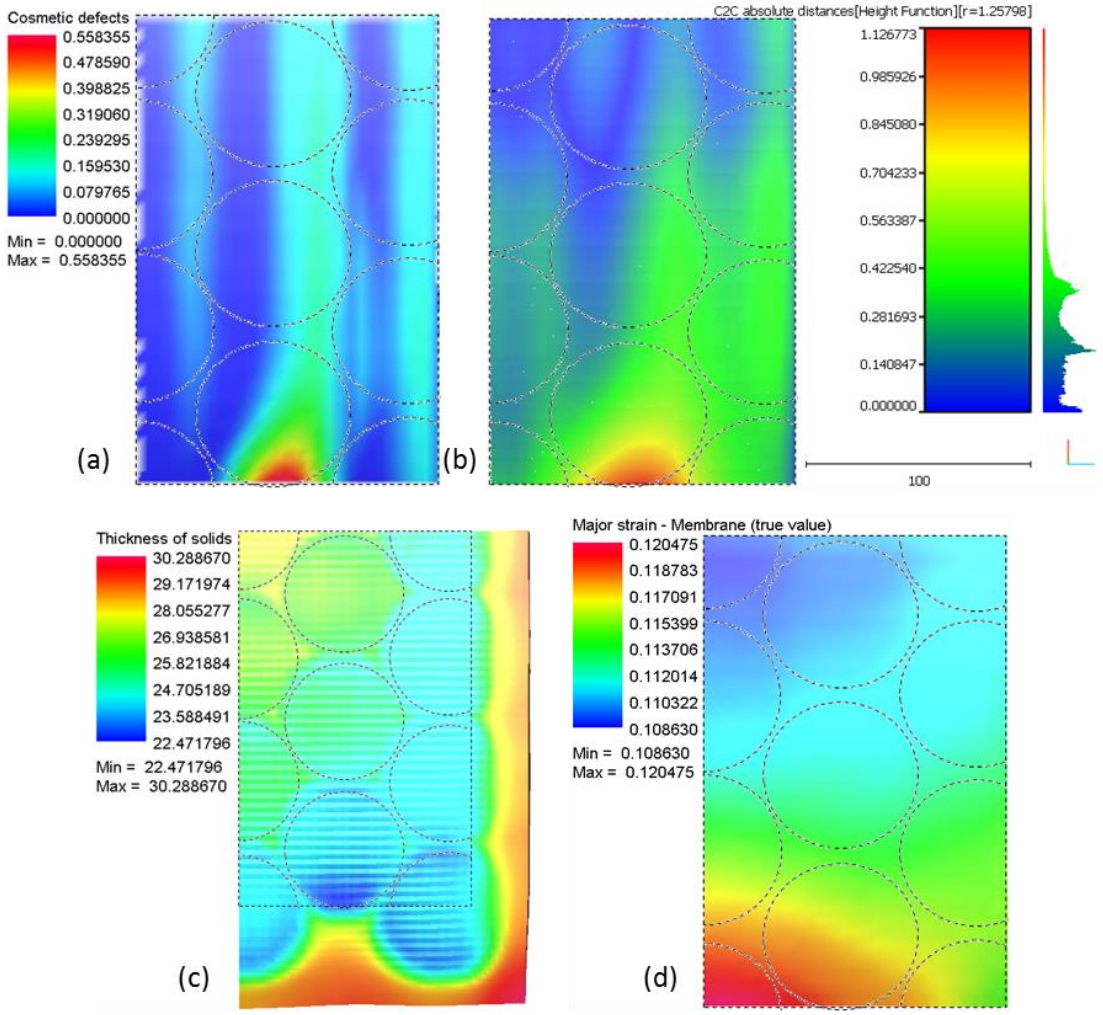

Figure M-1: Cosmetic defect (a) C2C absolute distance (b) Thickness of solids (c) & Major strain (d) contour maps for the Corrected 30 Red simulation

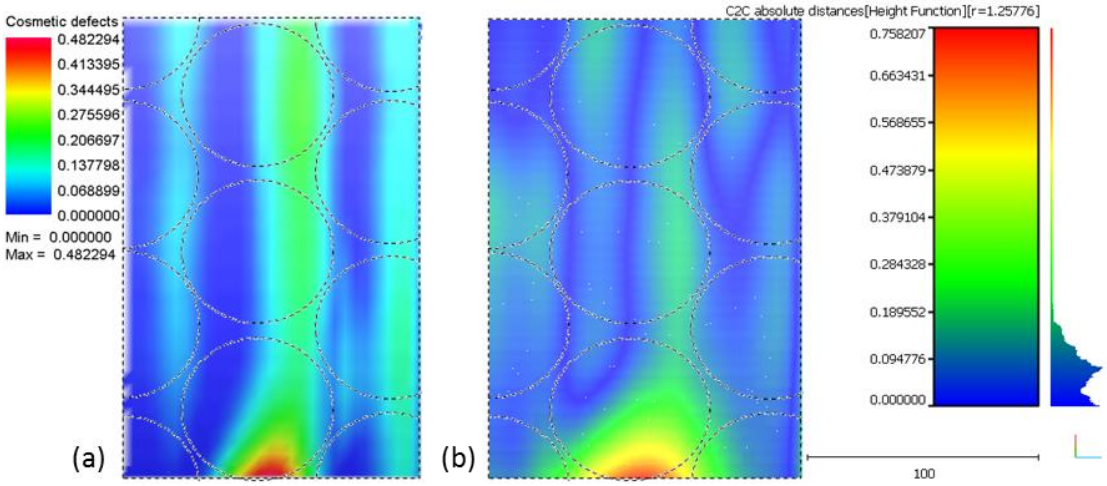

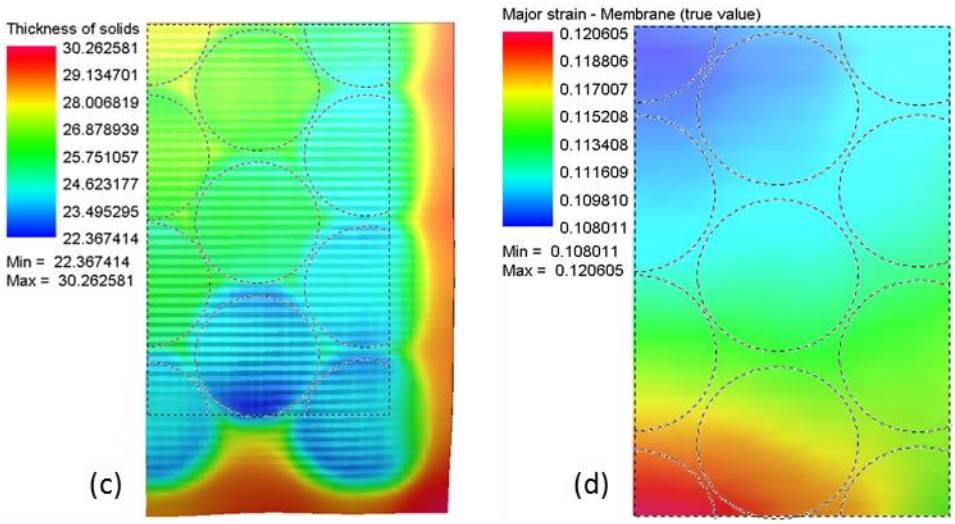

Figure M-2: Cosmetic defect (a) C2C absolute distance (b) Thickness of solids (c) & Major strain (d) contour maps for the Corrected 2 30 Red simulation

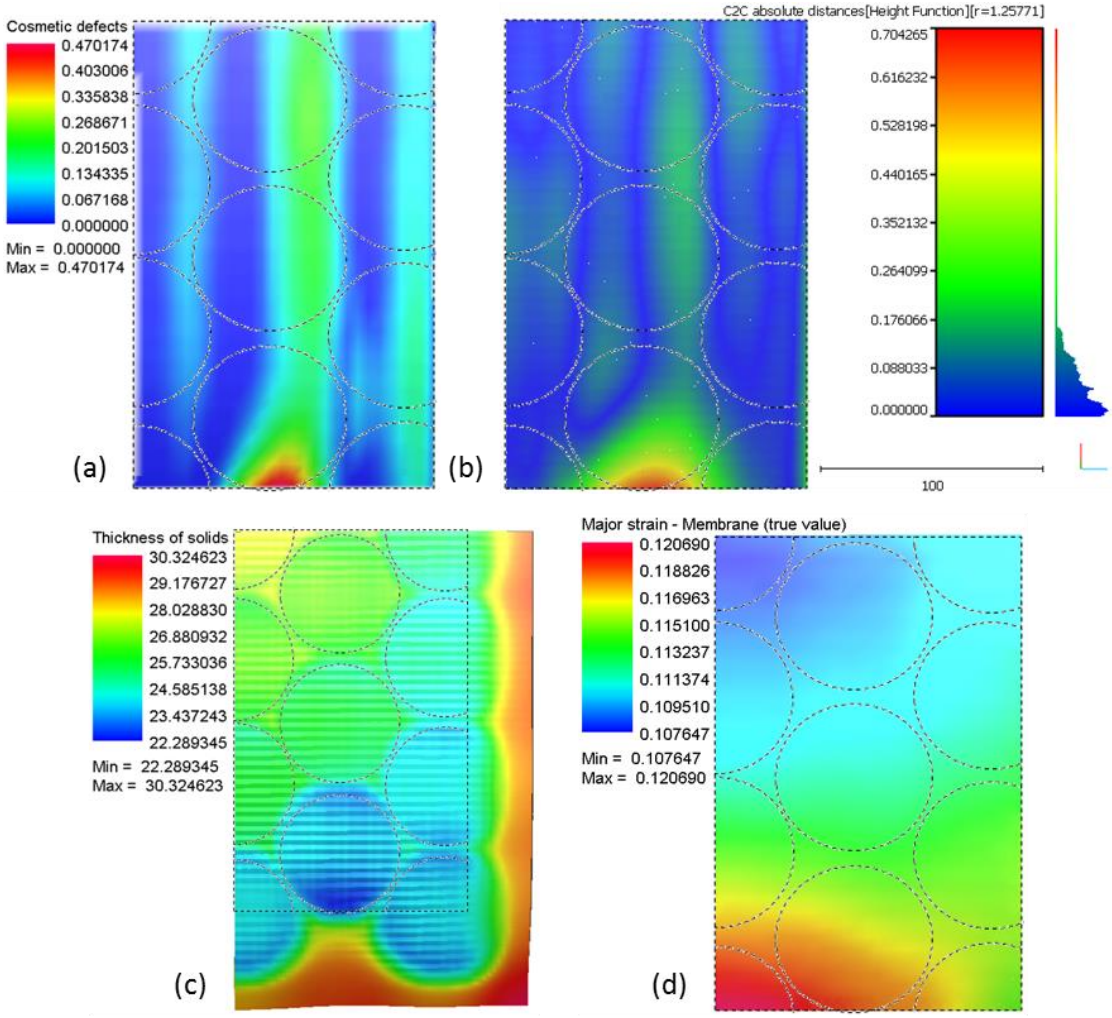

Figure M-3: Cosmetic defect (a) C2C absolute distance (b) Thickness of solids (c) & Major strain (d) contour maps for the Corrected 3 30 Red simulation

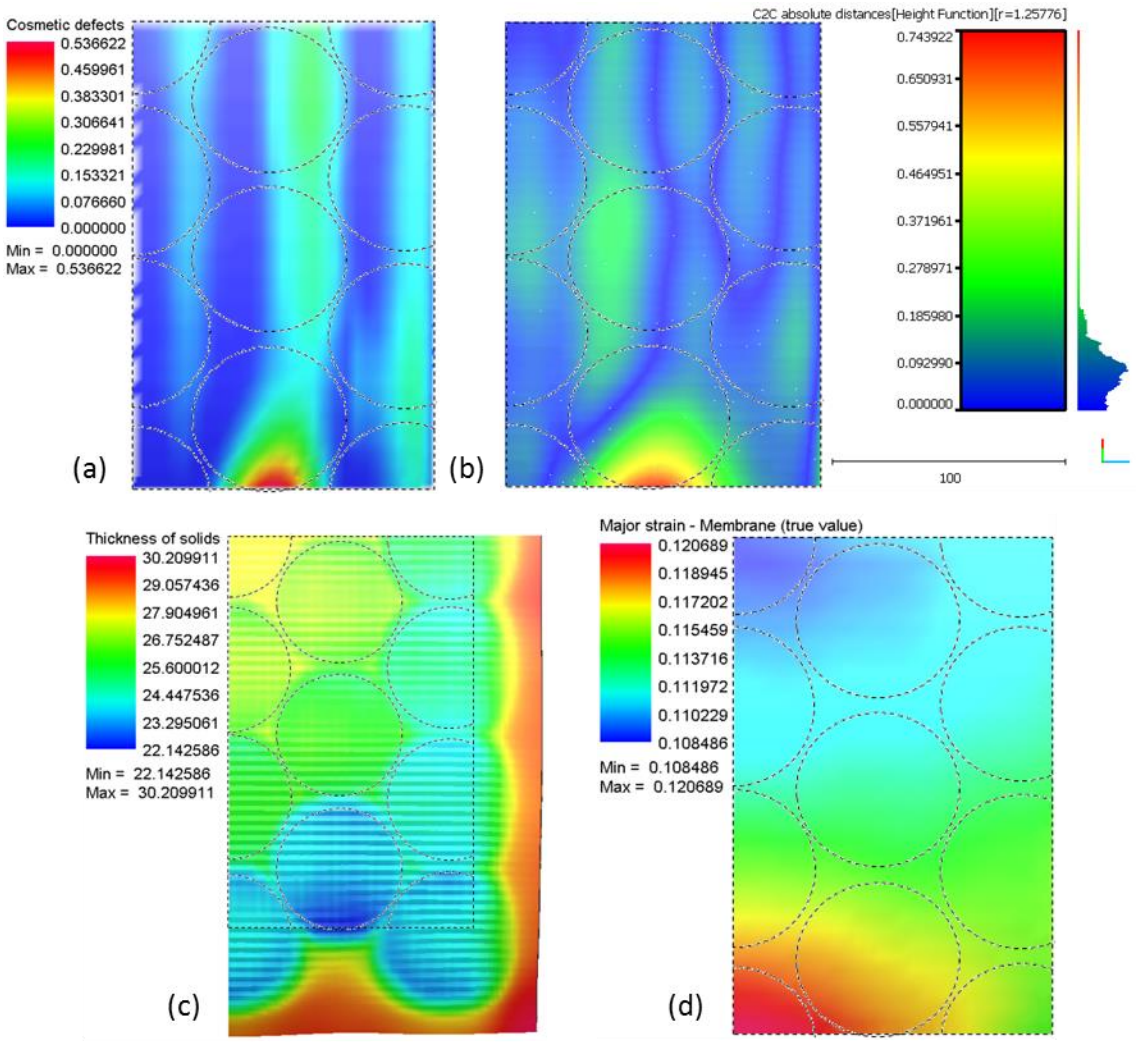

Figure M-4: Cosmetic defect (a) C2C absolute distance (b) Thickness of solids (c) & Major strain (d) contour maps for the Estimated 30 Red simulation

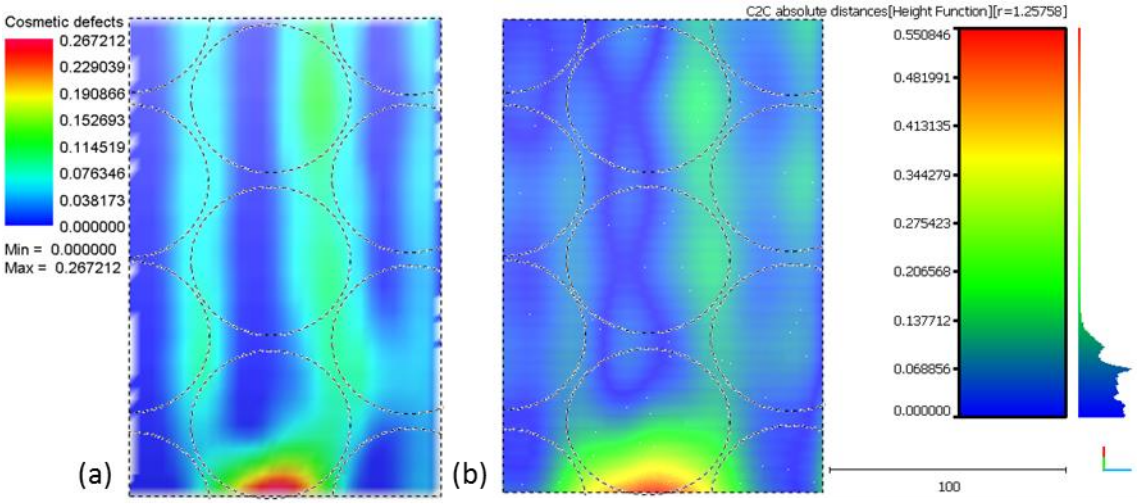

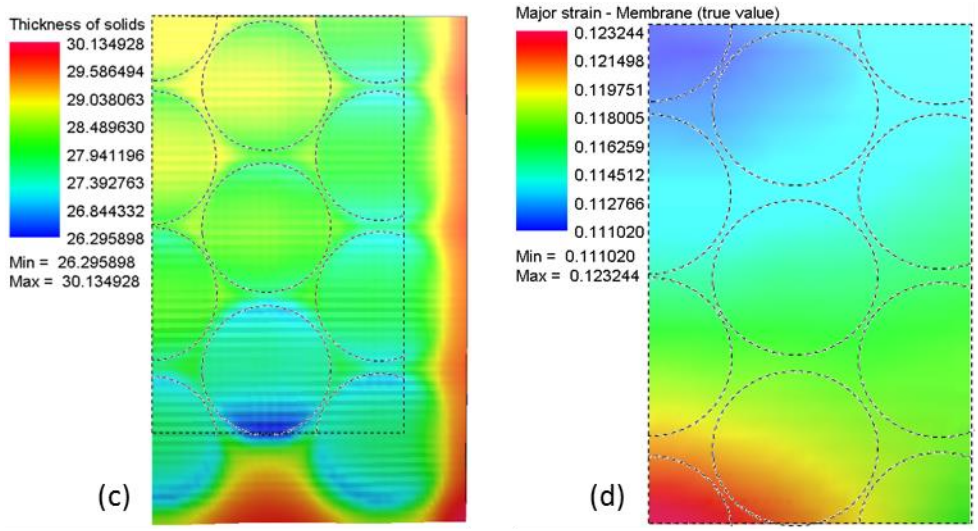

Figure M-5: Cosmetic defect (a) C2C absolute distance (b) Thickness of solids (c) & Major strain (d) contour maps for the Corrected 30 Purple simulation

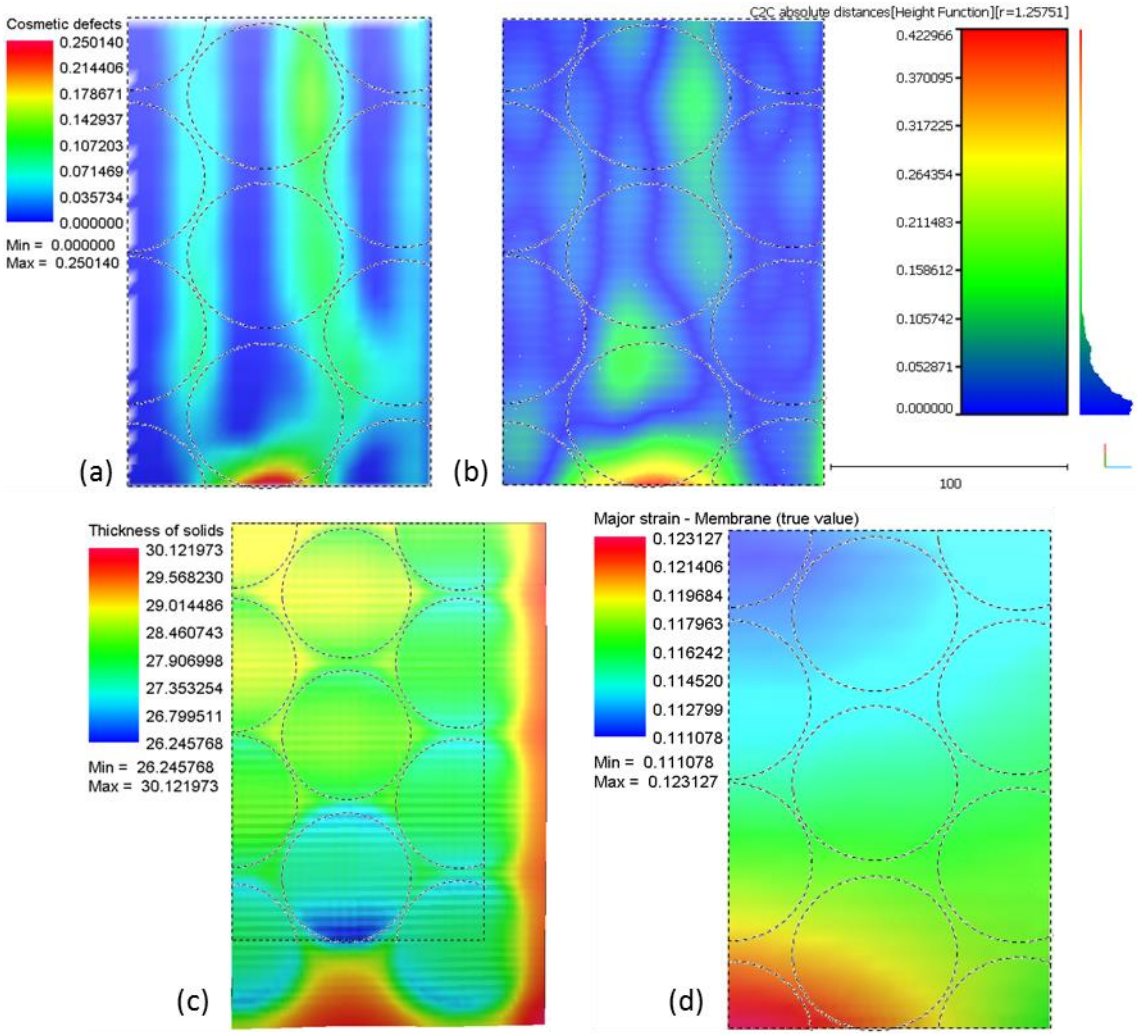

Figure M-6: Cosmetic defect (a) C2C absolute distance (b) Thickness of solids (c) & Major strain (d) contour maps for the Corrected 2 30 Purple simulation

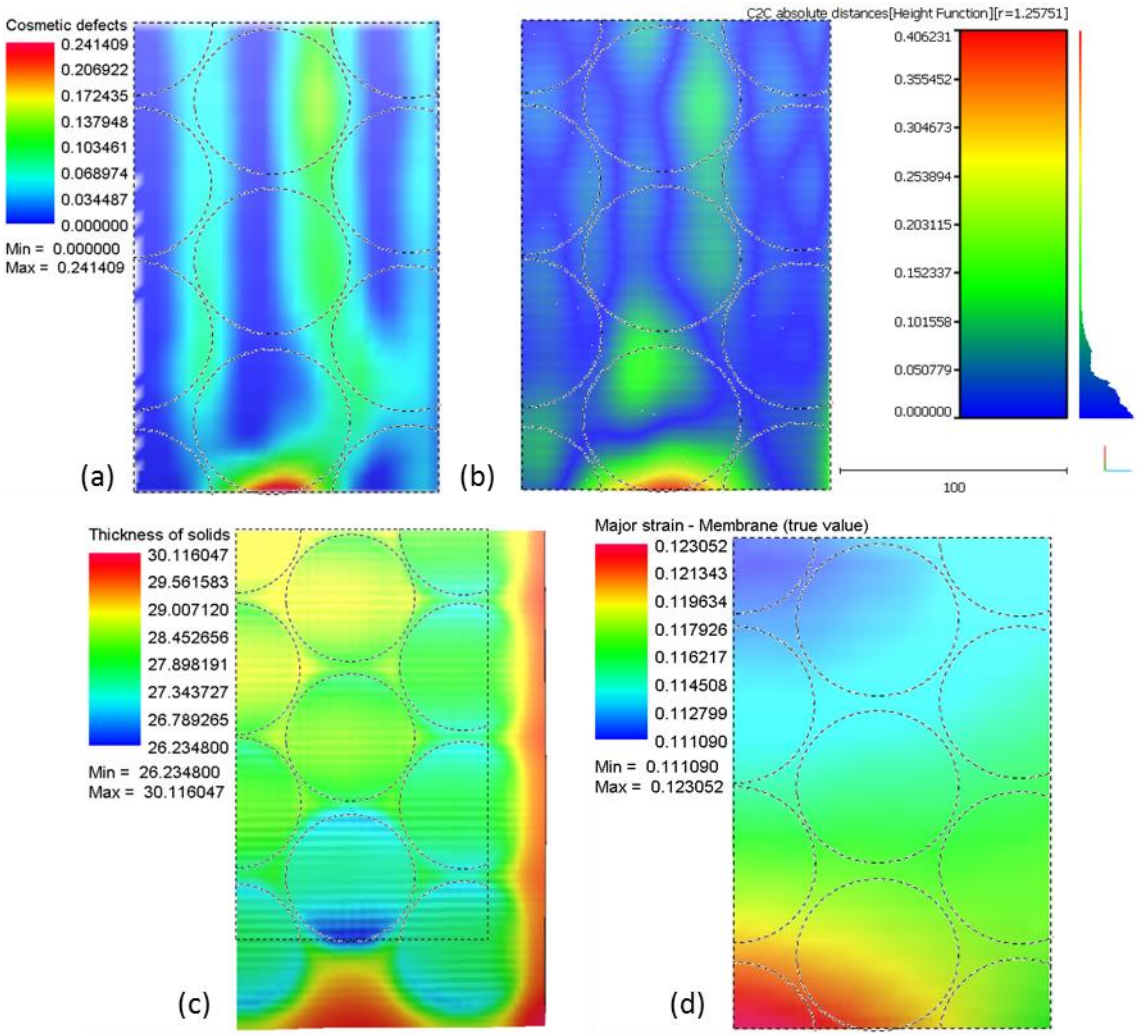

Figure M-7: Cosmetic defect (a) C2C absolute distance (b) Thickness of solids (c) & Major strain (d) contour maps for the Corrected 3 30 Purple simulation

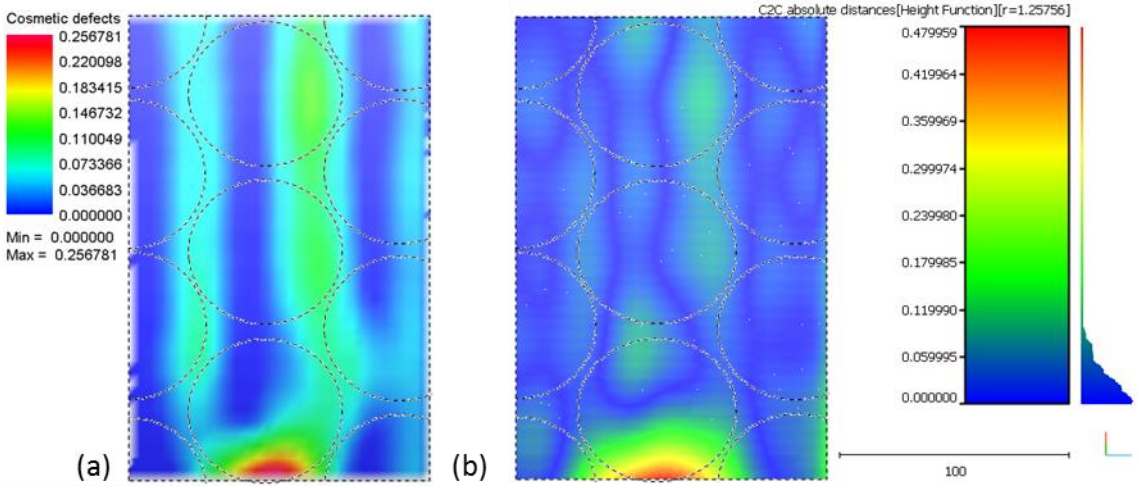

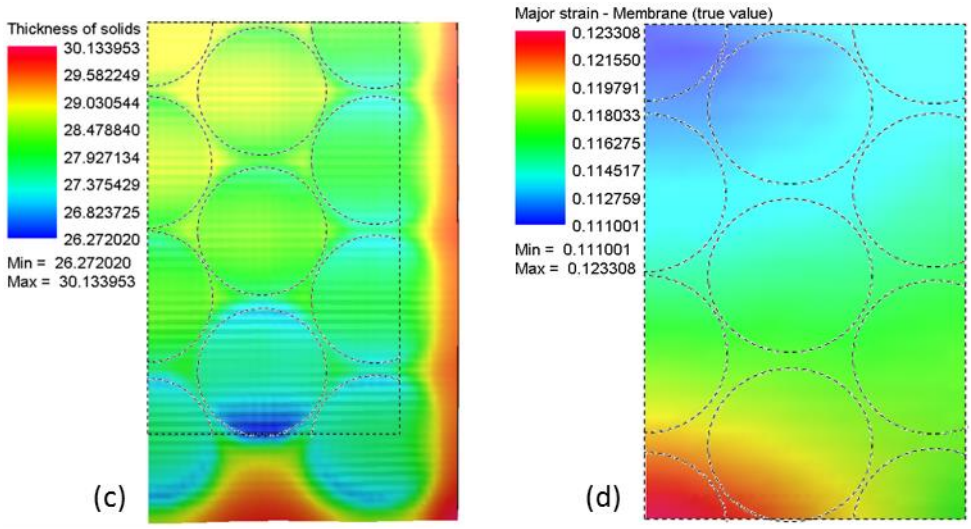

Figure M-8: Cosmetic defect (a) C2C absolute distance (b) Thickness of solids (c) & Major strain (d) contour maps for the Estimated 30 Purple simulation

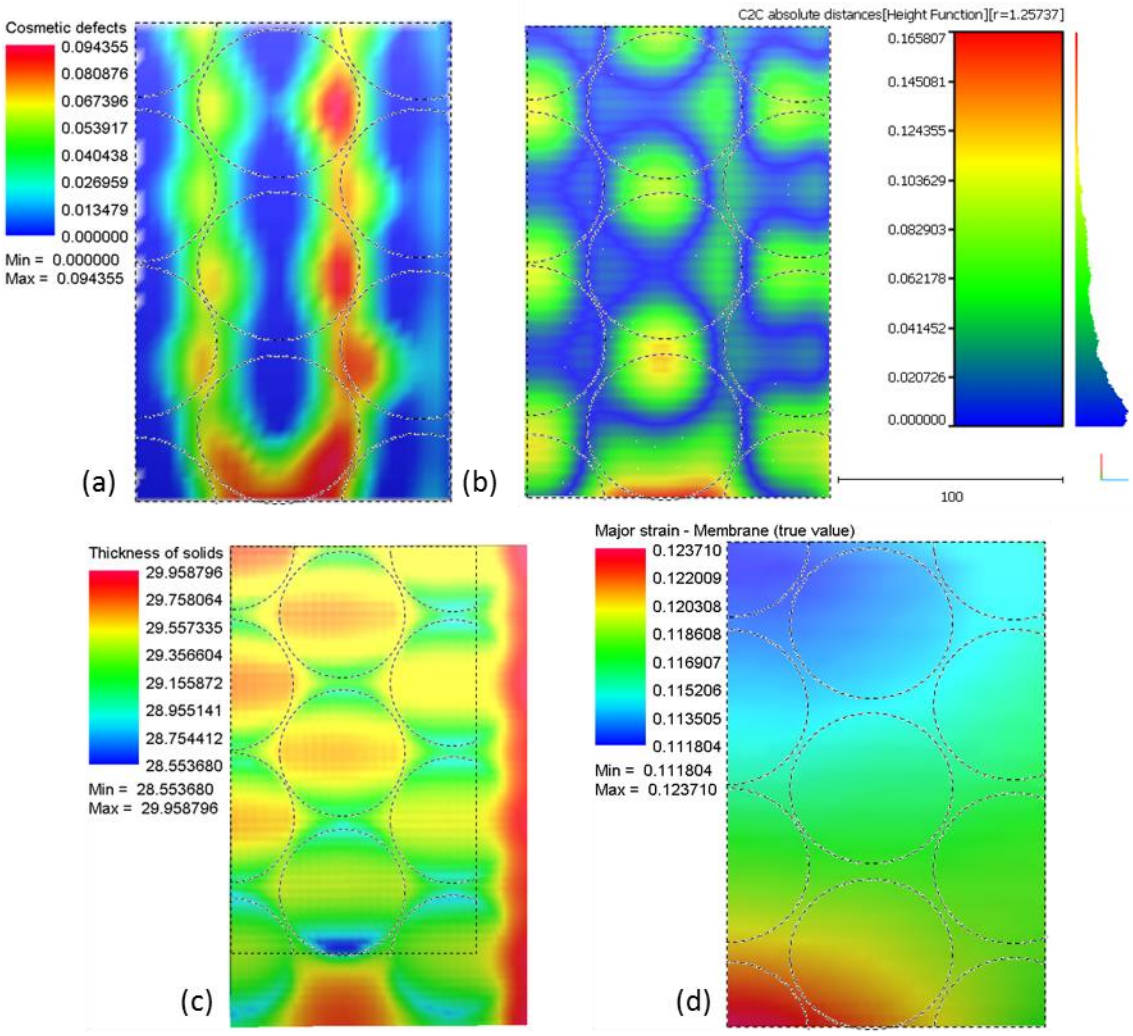

Figure M-9: Cosmetic defect (a) C2C absolute distance (b) Thickness of solids (c) & Major strain (d) contour maps for the Corrected 30 Green simulation

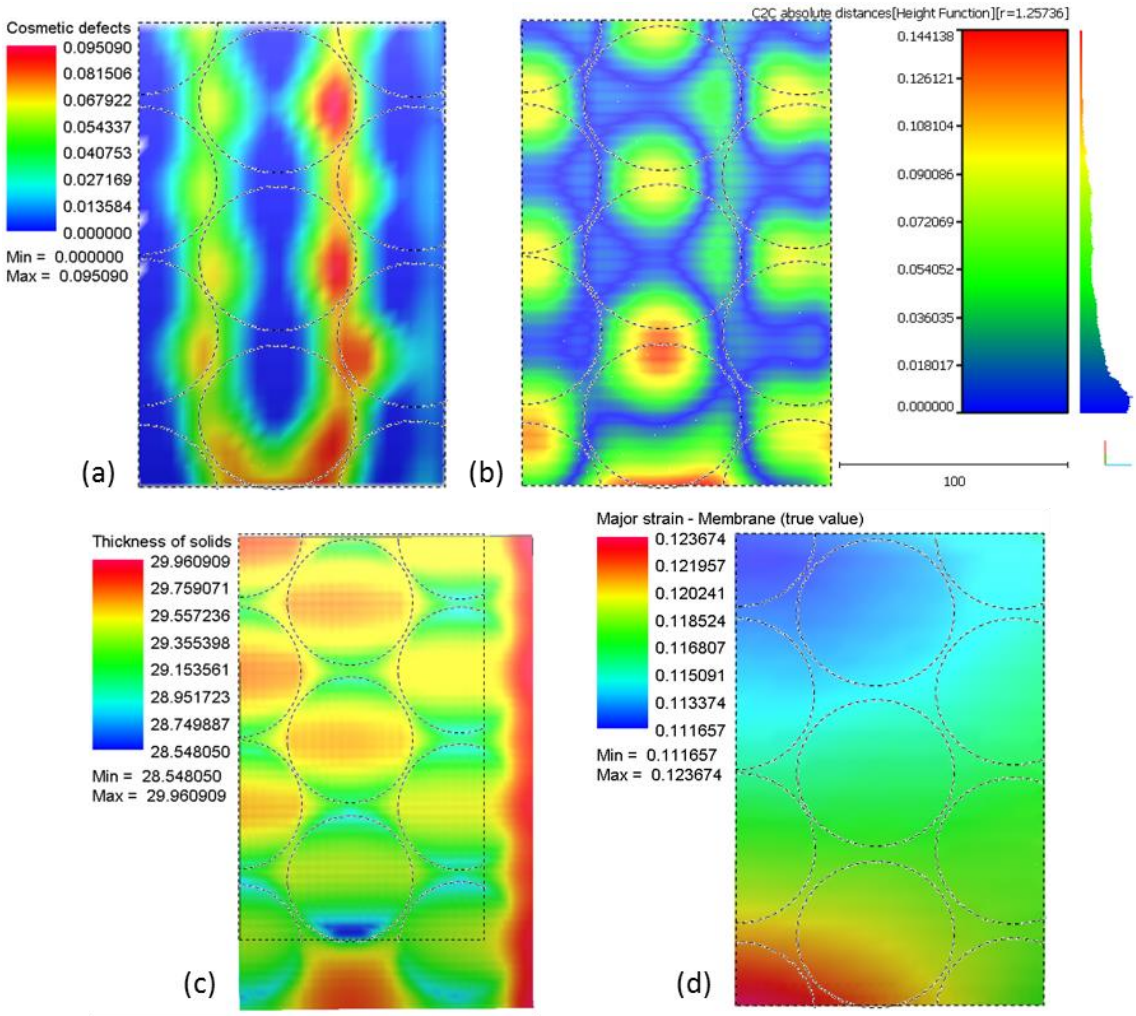

Figure M-10: Cosmetic defect (a) C2C absolute distance (b) Thickness of solids (c) & Major strain (d) contour maps for the Corrected 2 30 Green simulation

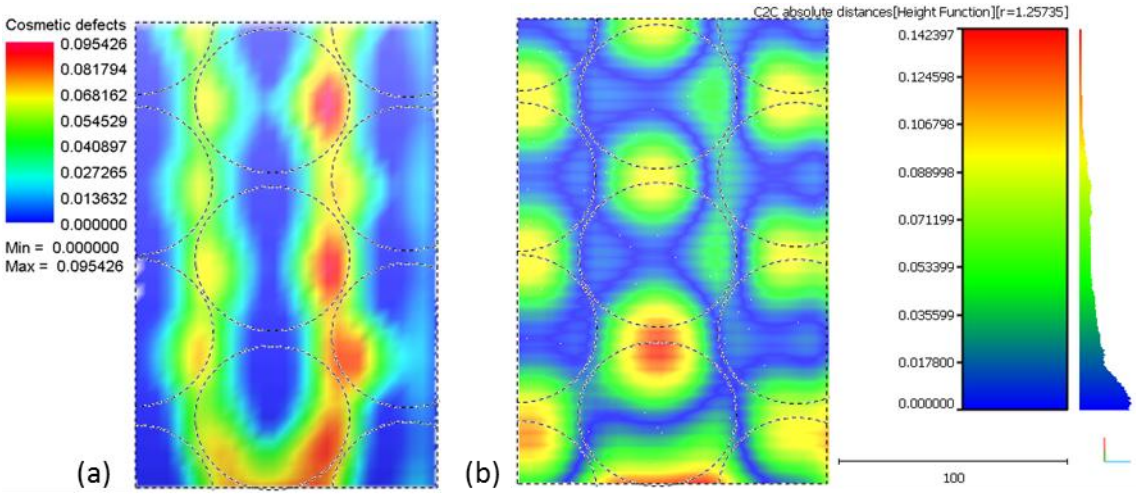

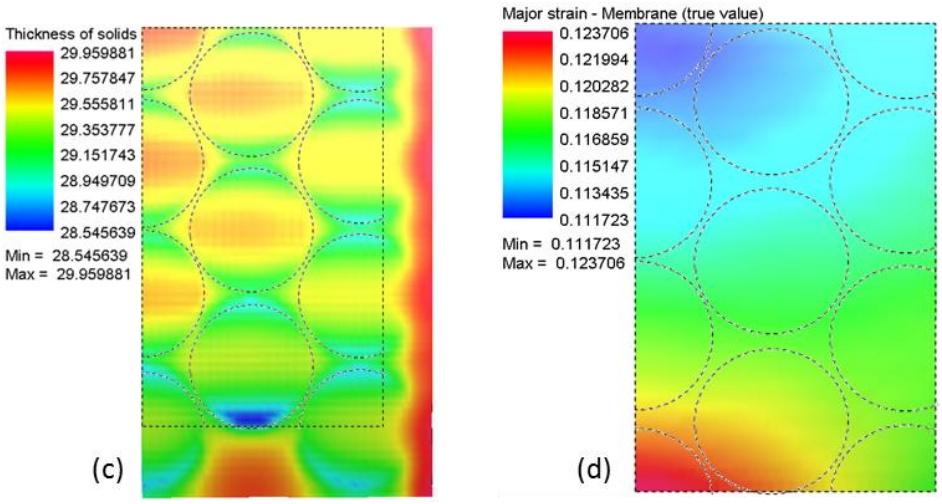

Figure M-11: Cosmetic defect (a) C2C absolute distance (b) Thickness of solids (c) & Major strain (d) contour maps for the Corrected 3 30 Green simulation

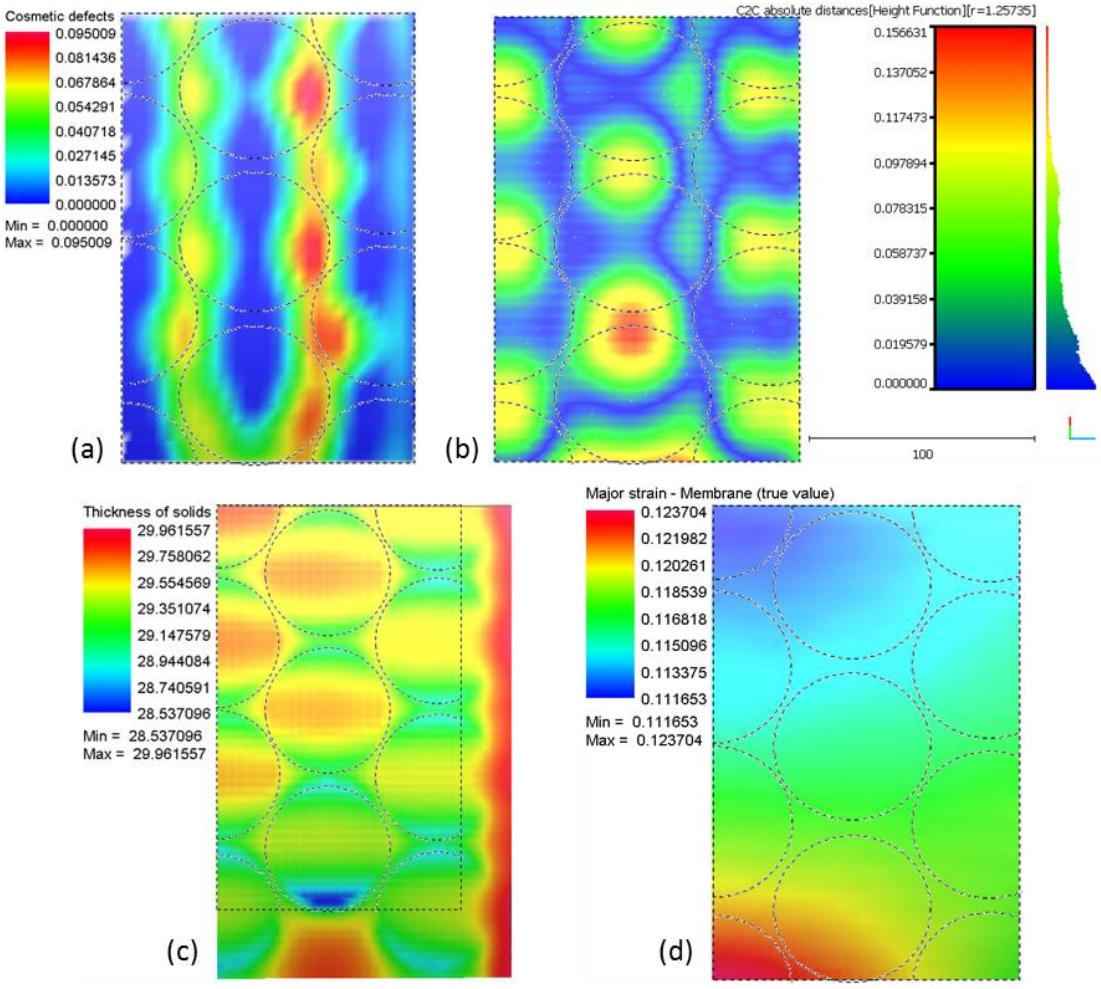

Figure M-12: Cosmetic defect (a) C2C absolute distance (b) Thickness of solids (c) & Major strain (d) contour maps for the Estimated 30 Green simulation

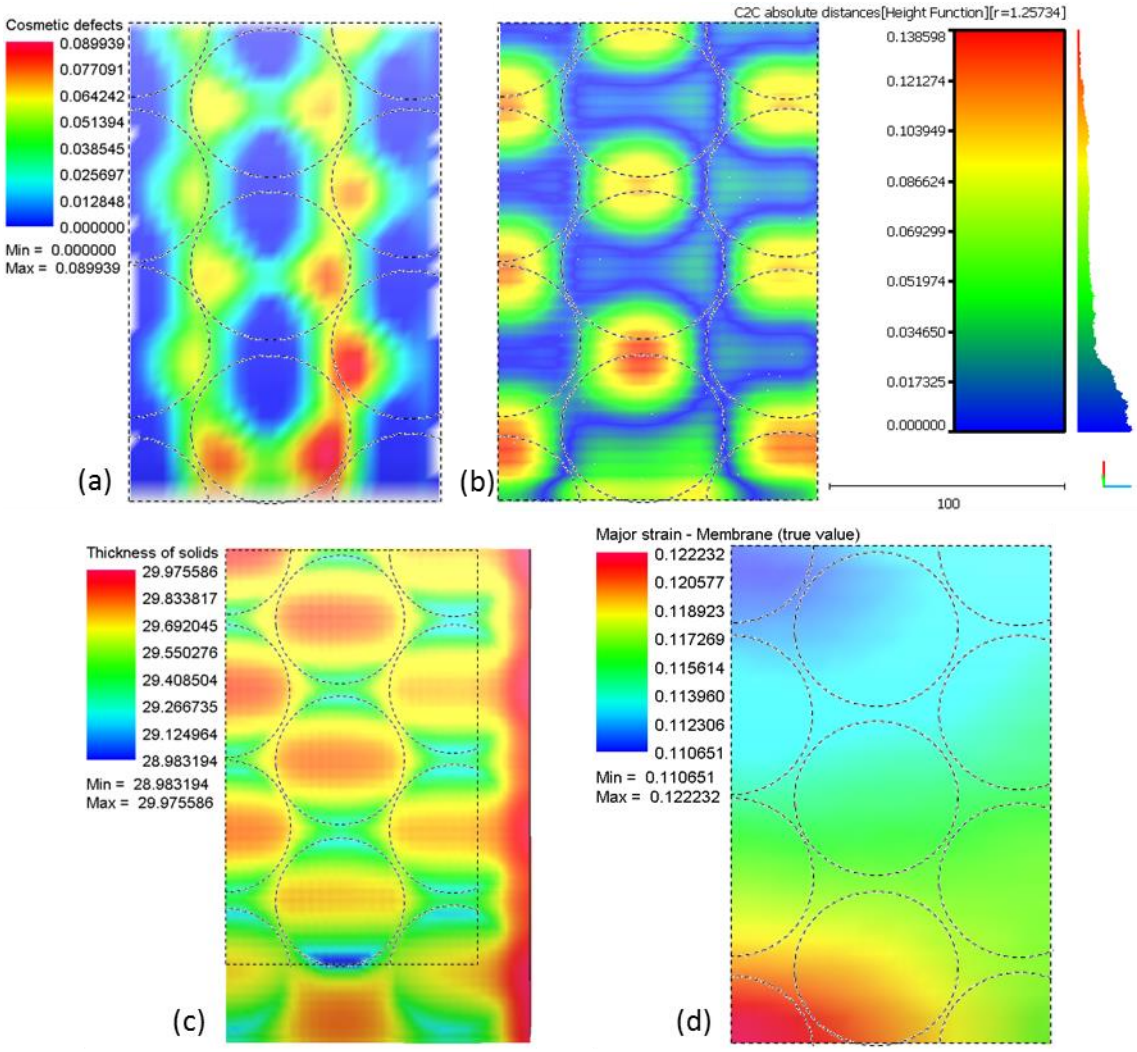

Figure M-13: Cosmetic defect (a) C2C absolute distance (b) Thickness of solids (c) & Major strain (d) contour maps for the Corrected 30 Orange simulation

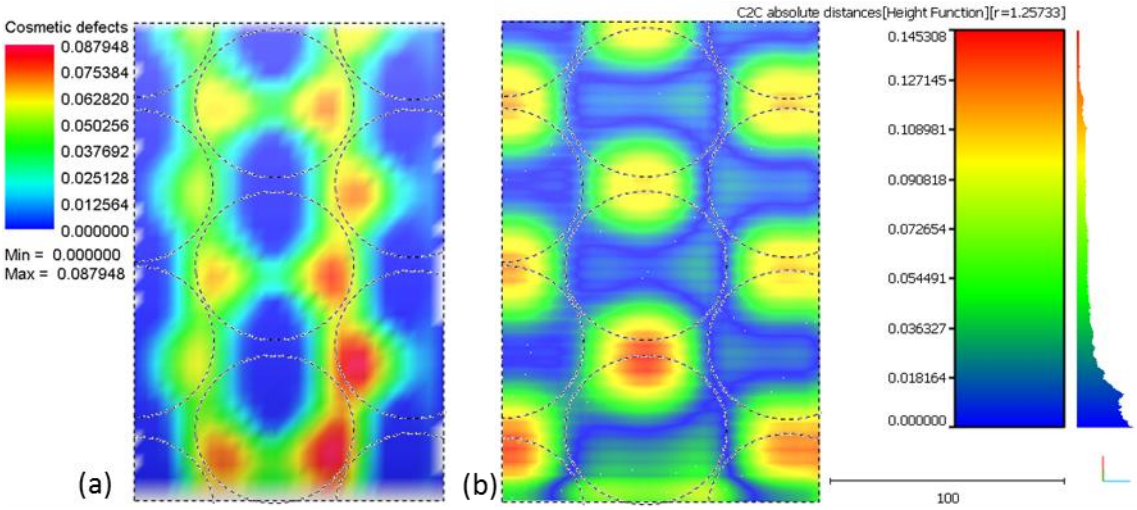

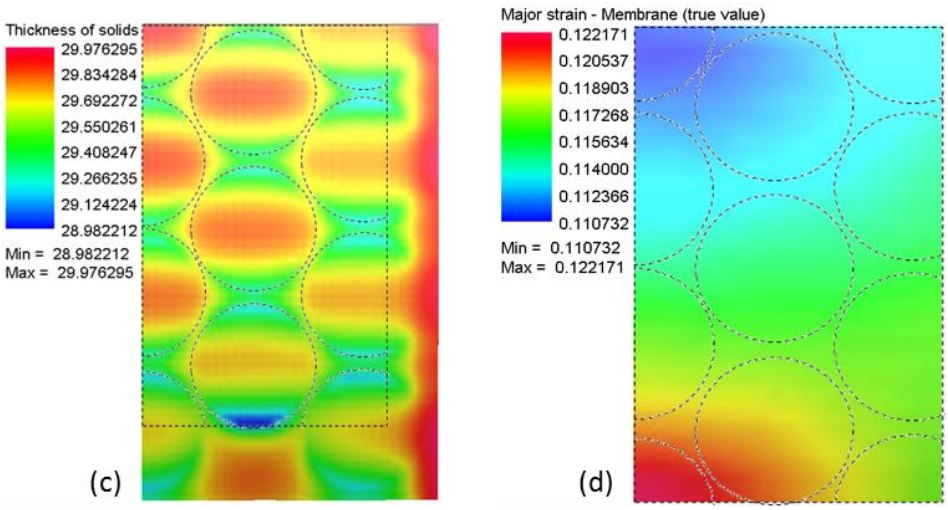

Figure M-14: Cosmetic defect (a) C2C absolute distance (b) Thickness of solids (c) & Major strain (d) contour maps for the Corrected 2 30 Orange simulation

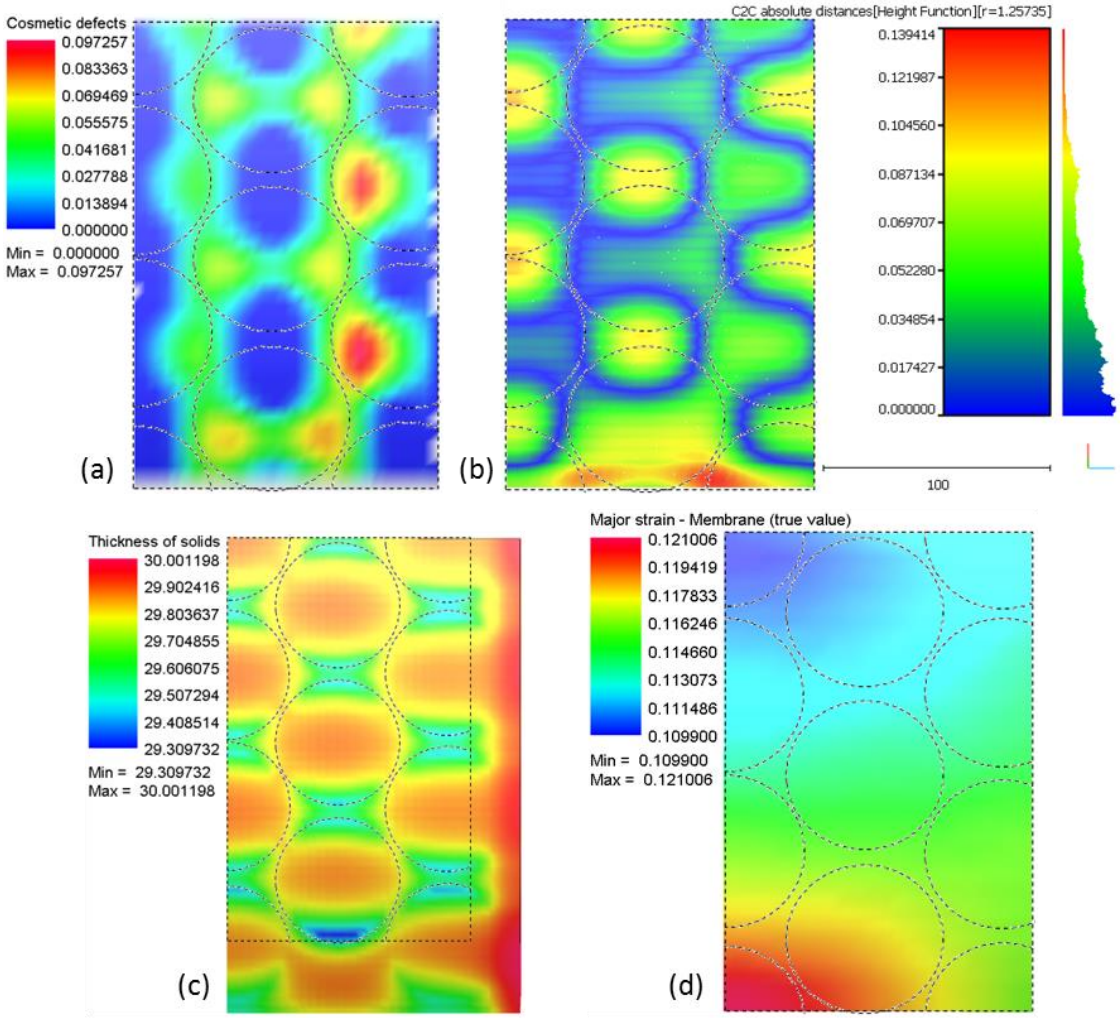

Figure M-15: Cosmetic defect (a) C2C absolute distance (b) Thickness of solids (c) & Major strain (d) contour maps for the Corrected 30 Blue simulation

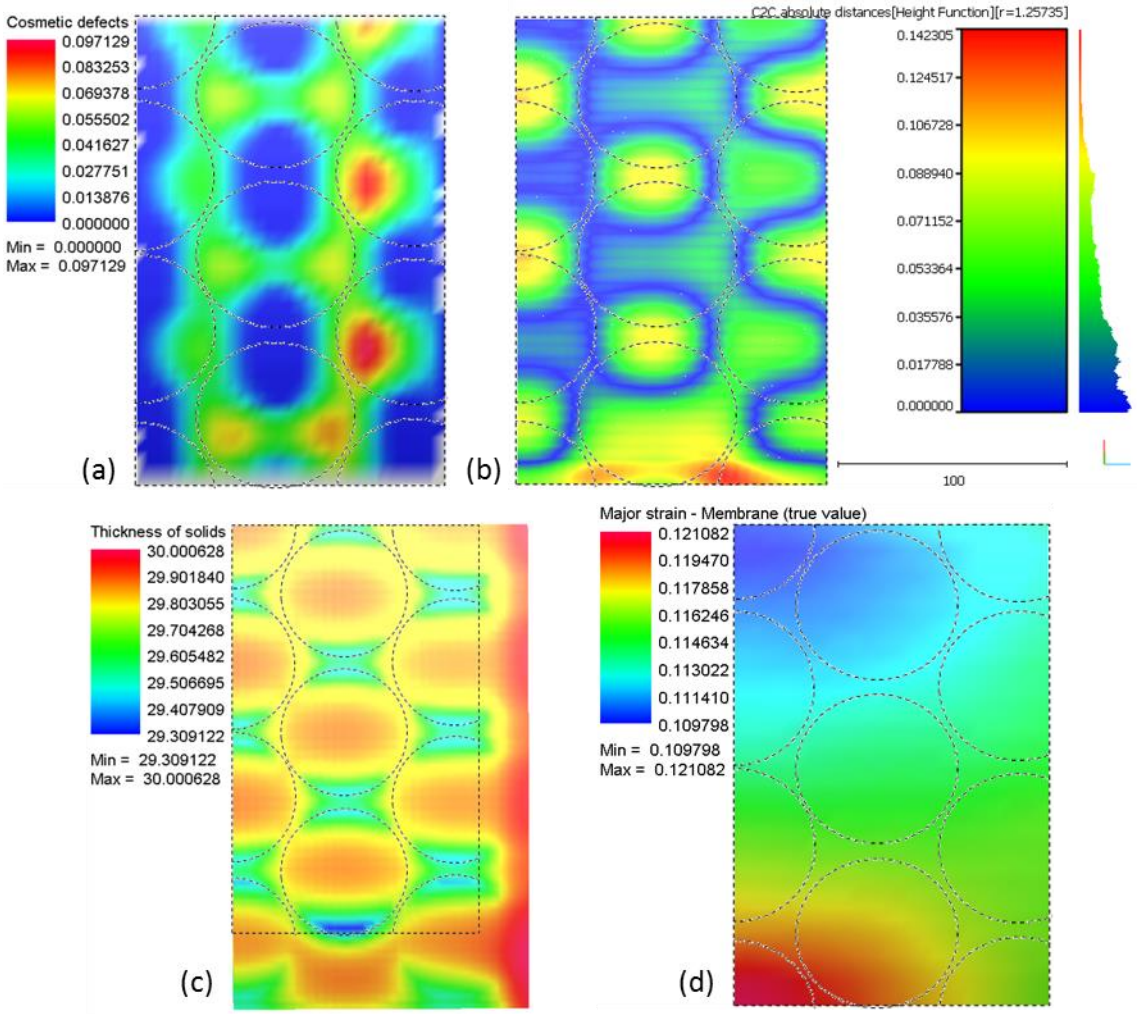

Figure M-16: Cosmetic defect (a) C2C absolute distance (b) Thickness of solids (c) & Major strain (d) contour maps for the Corrected 2 30 Blue simulation

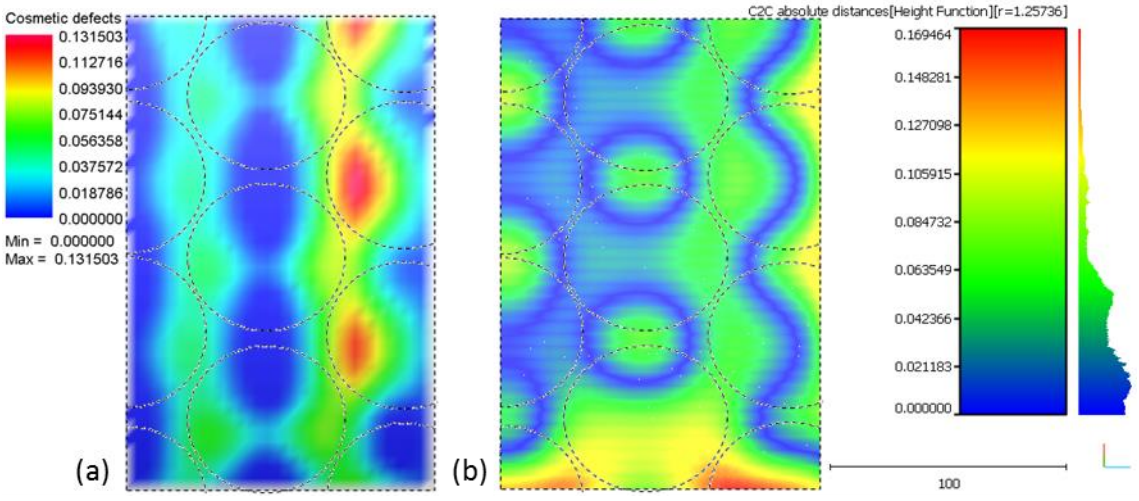

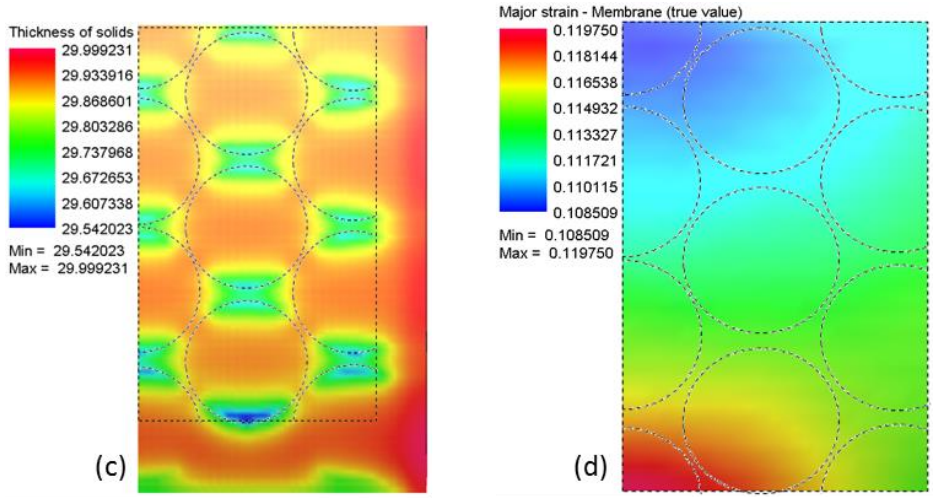

Figure M-17: Cosmetic defect (a) C2C absolute distance (b) Thickness of solids (c) & Major strain (d) contour maps for the Corrected 30 Brown simulation

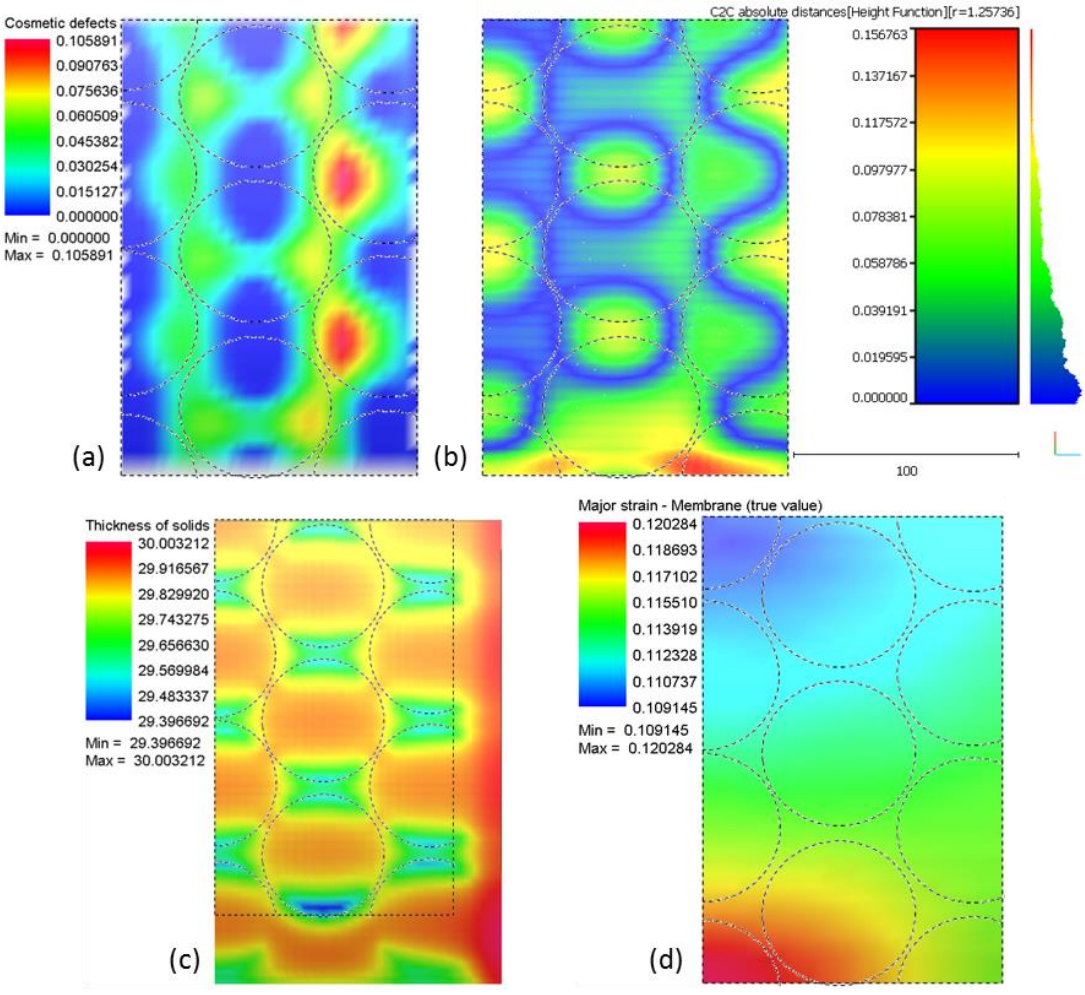

Figure M-18: Cosmetic defect (a) C2C absolute distance (b) Thickness of solids (c) & Major strain (d) contour maps for the Corrected 30 Violet simulation

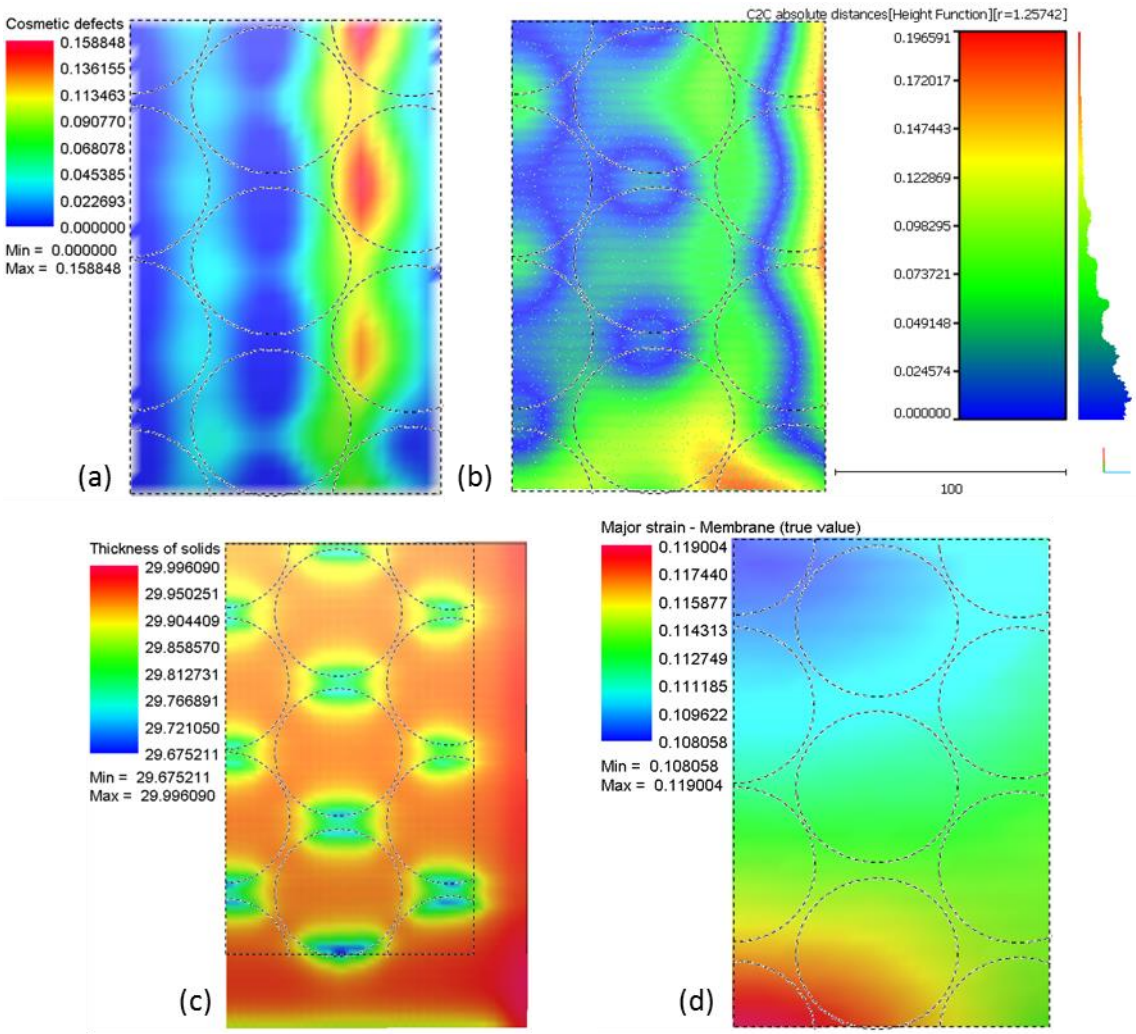

Figure M-19: Cosmetic defect (a) C2C absolute distance (b) Thickness of solids (c) & Major strain (d) contour maps for the Corrected 30 Grey simulation

Appendix N. Additional Contour Maps Relating to Simulations over Multiple Layers of Interpolation

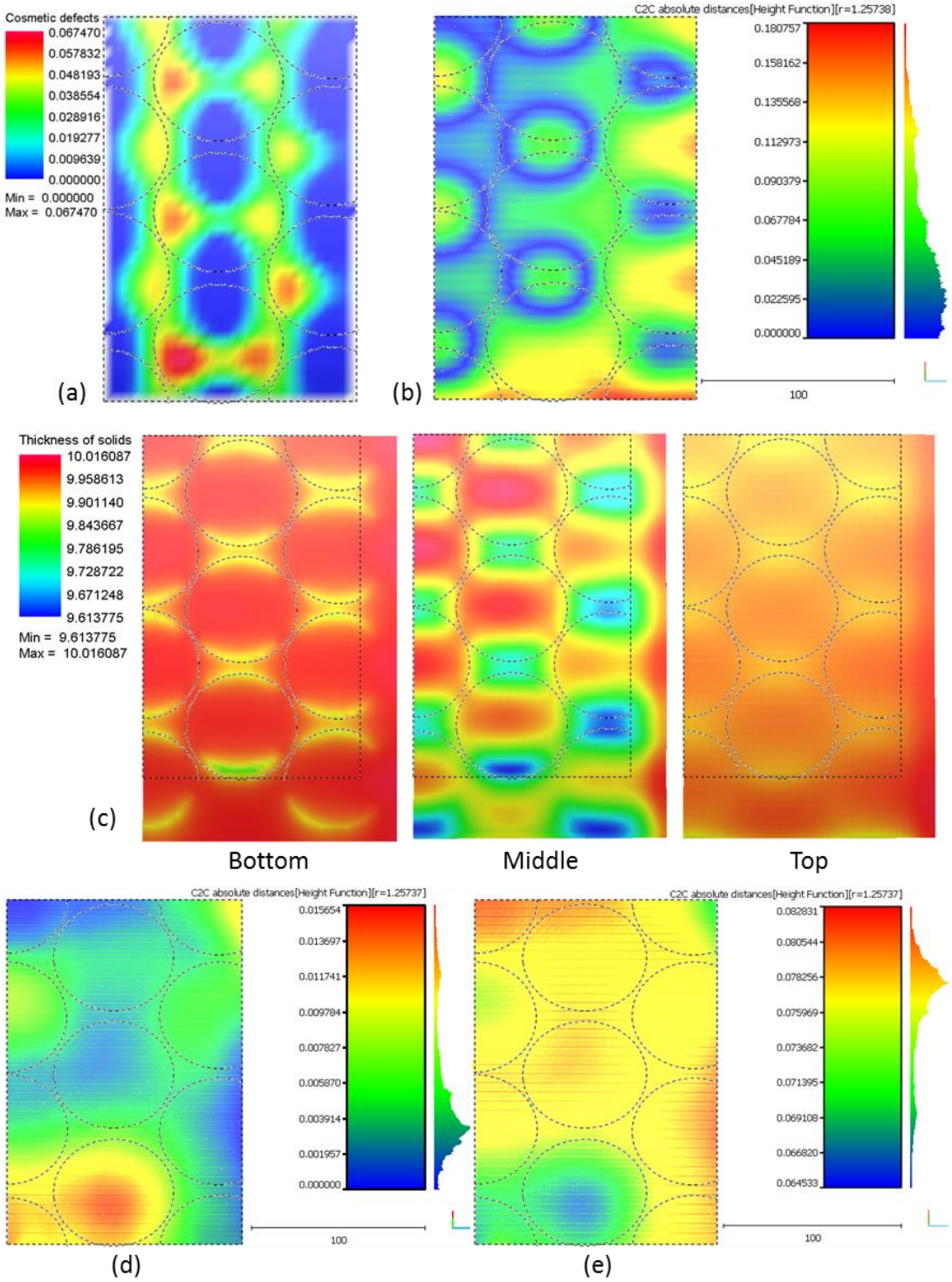

Figure N-1: Cosmetic defect (a) C2C absolute distance (b) & Thickness of solids (c) contour maps for the 30 Brown-Green-Brown* simulation with C2C comparisons with the trimmed part from the 30 Brown-Green-Brown simulation at the reference (d) & simulation (e) positions

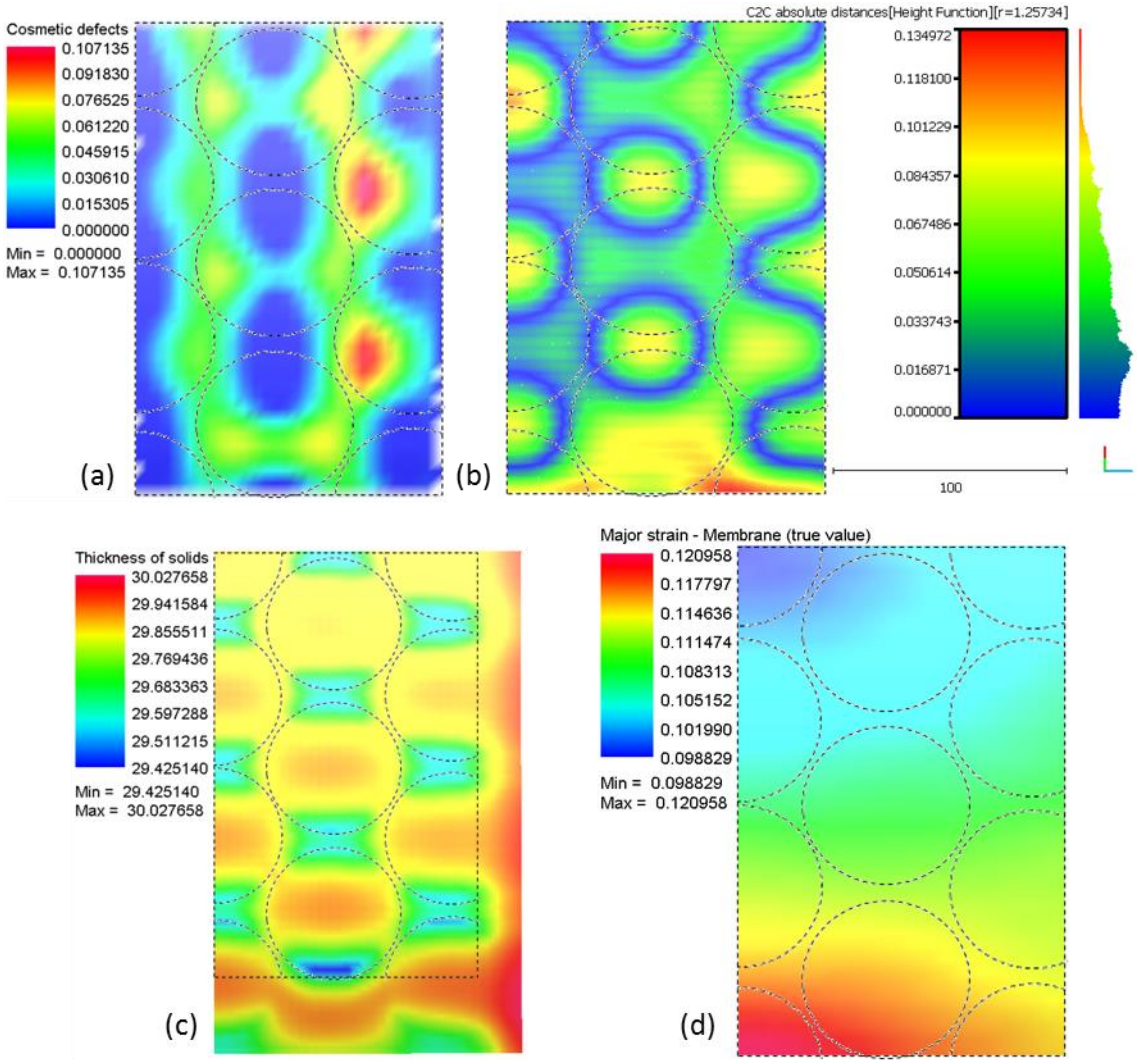

Figure N-2: Cosmetic defect (a) C2C absolute distance (b) Thickness of solids (c) and Major strain (d) contour maps for the 30 Brown-Green-Brown Glued simulation

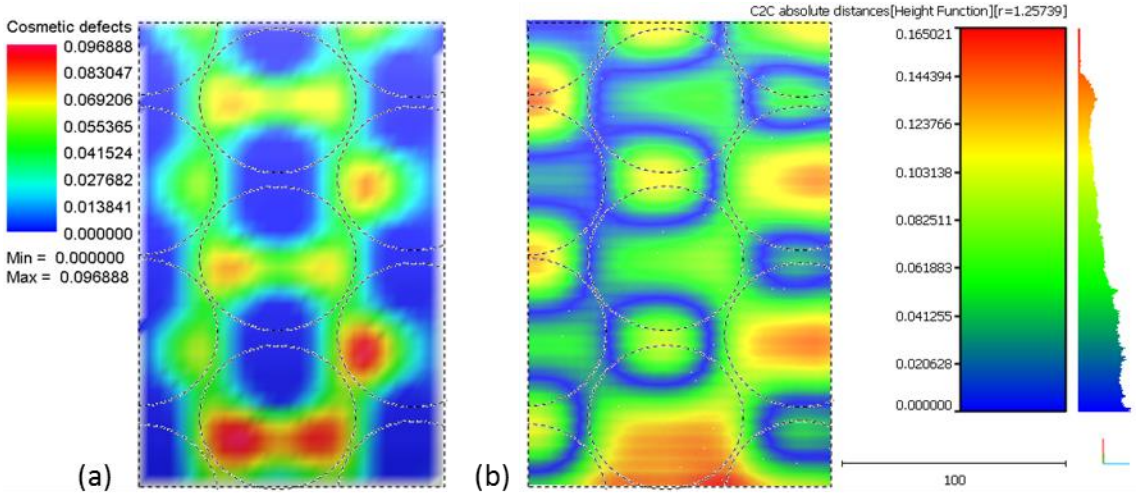

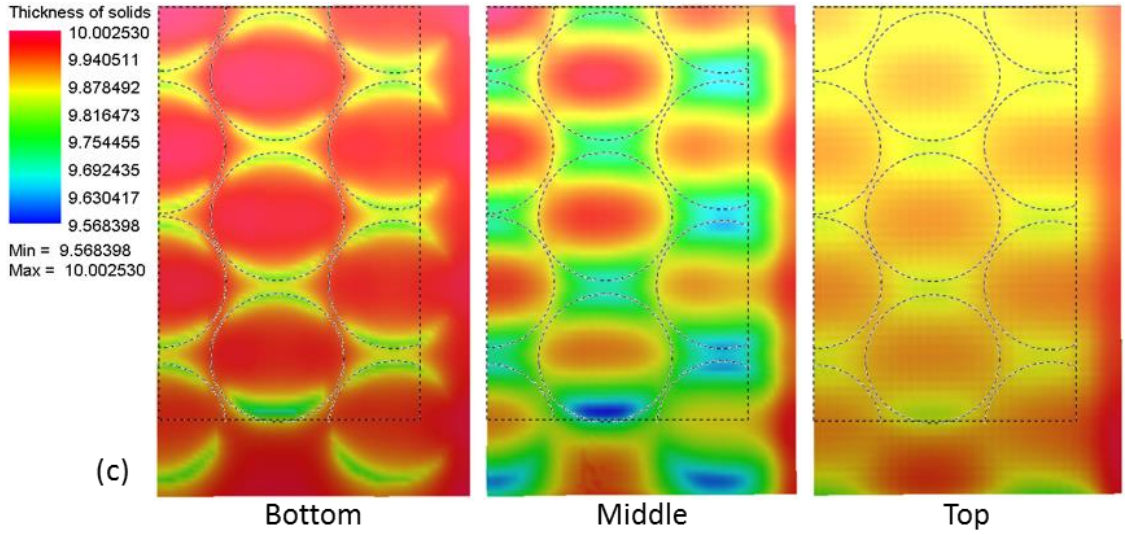

Figure N-3: Cosmetic defect (a) C2C absolute distance (b) and Thickness of solids (c) contour maps for the 30 Blue-Green-Blue simulation

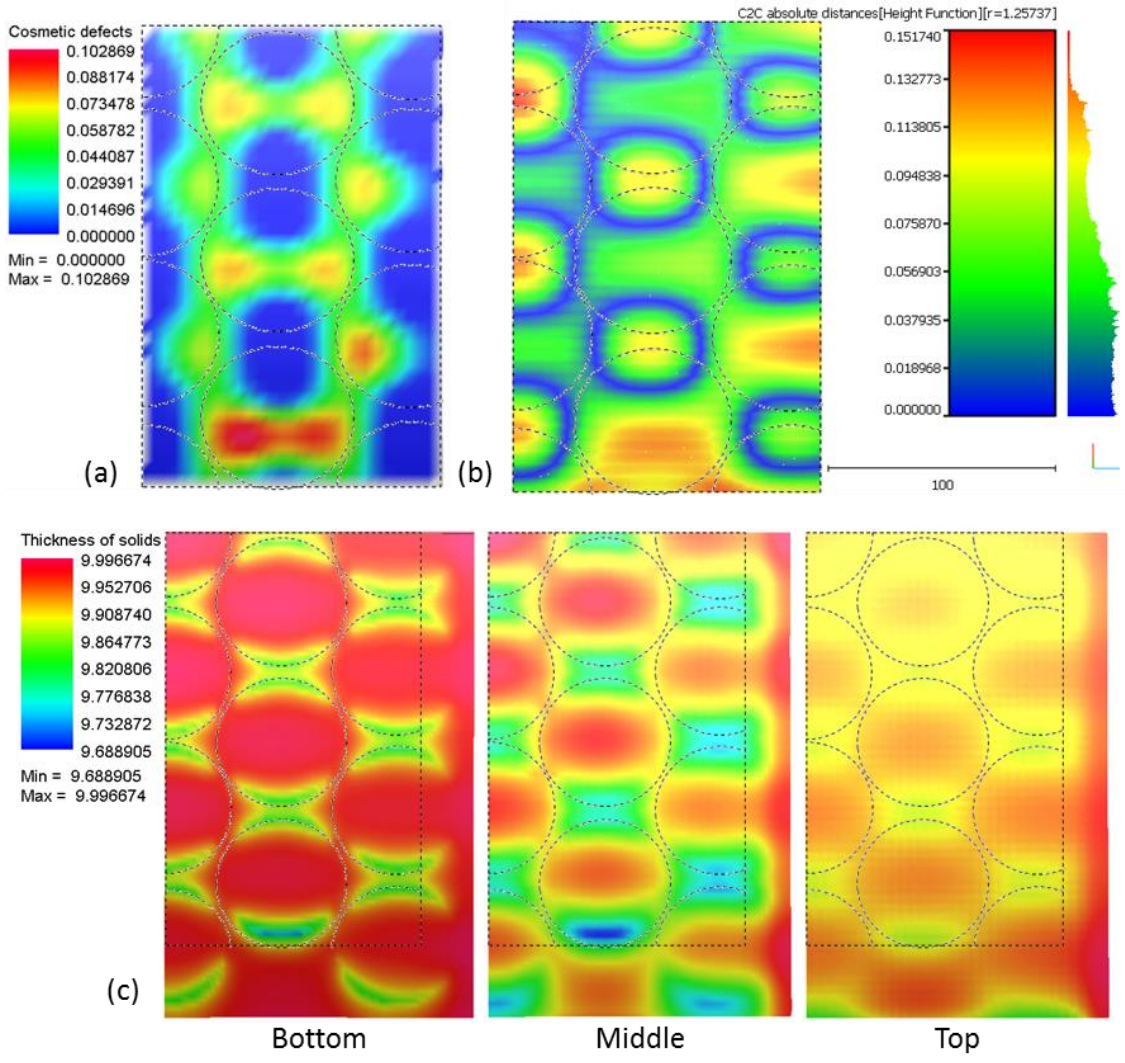

Figure N-4: Cosmetic defect (a) C2C absolute distance (b) and Thickness of solids (c) contour maps for the 30 Violet-Orange-Violet simulation

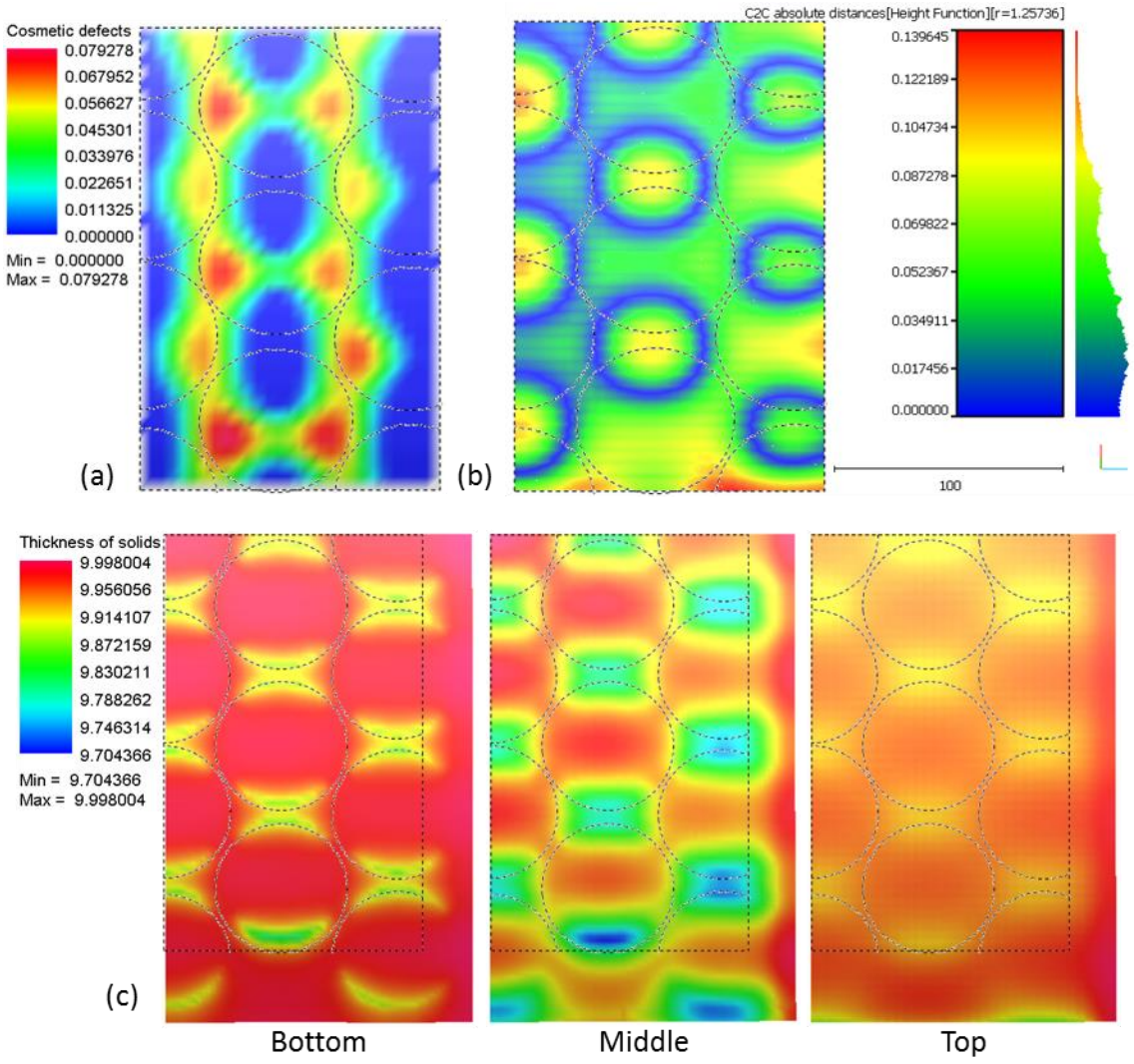

Figure N-5: Cosmetic defect (a) C2C absolute distance (b) and Thickness of solids (c) contour maps for the 30 Brown-Orange-Brown simulation

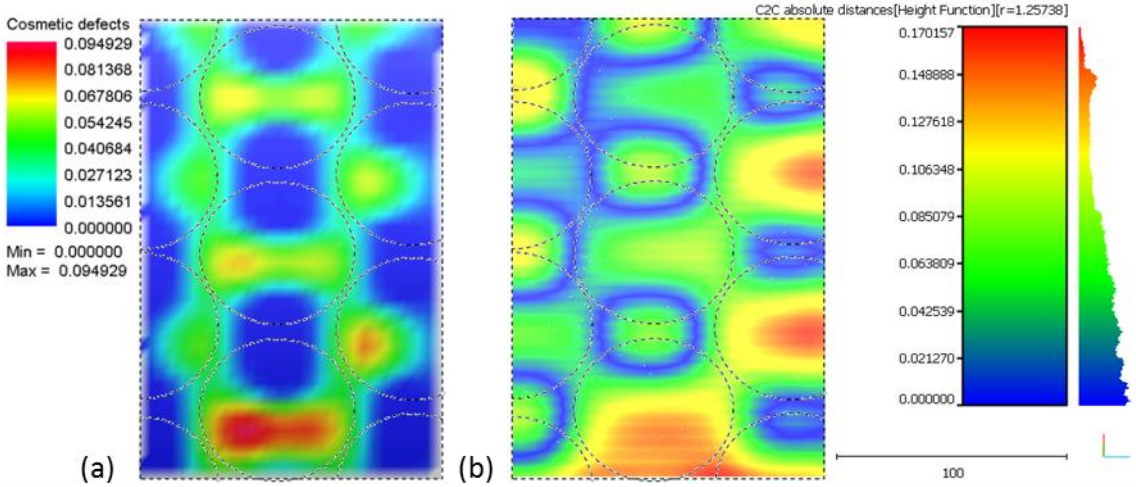

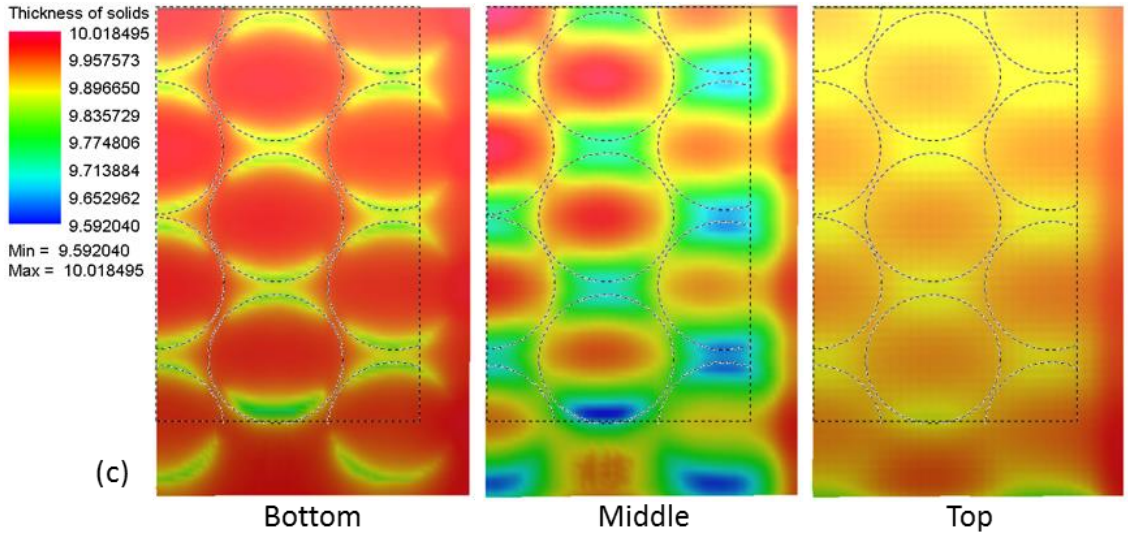

Figure N-6: Cosmetic defect (a) C2C absolute distance (b) and Thickness of solids (c) contour maps for the 30 Violet-Green-Violet simulation

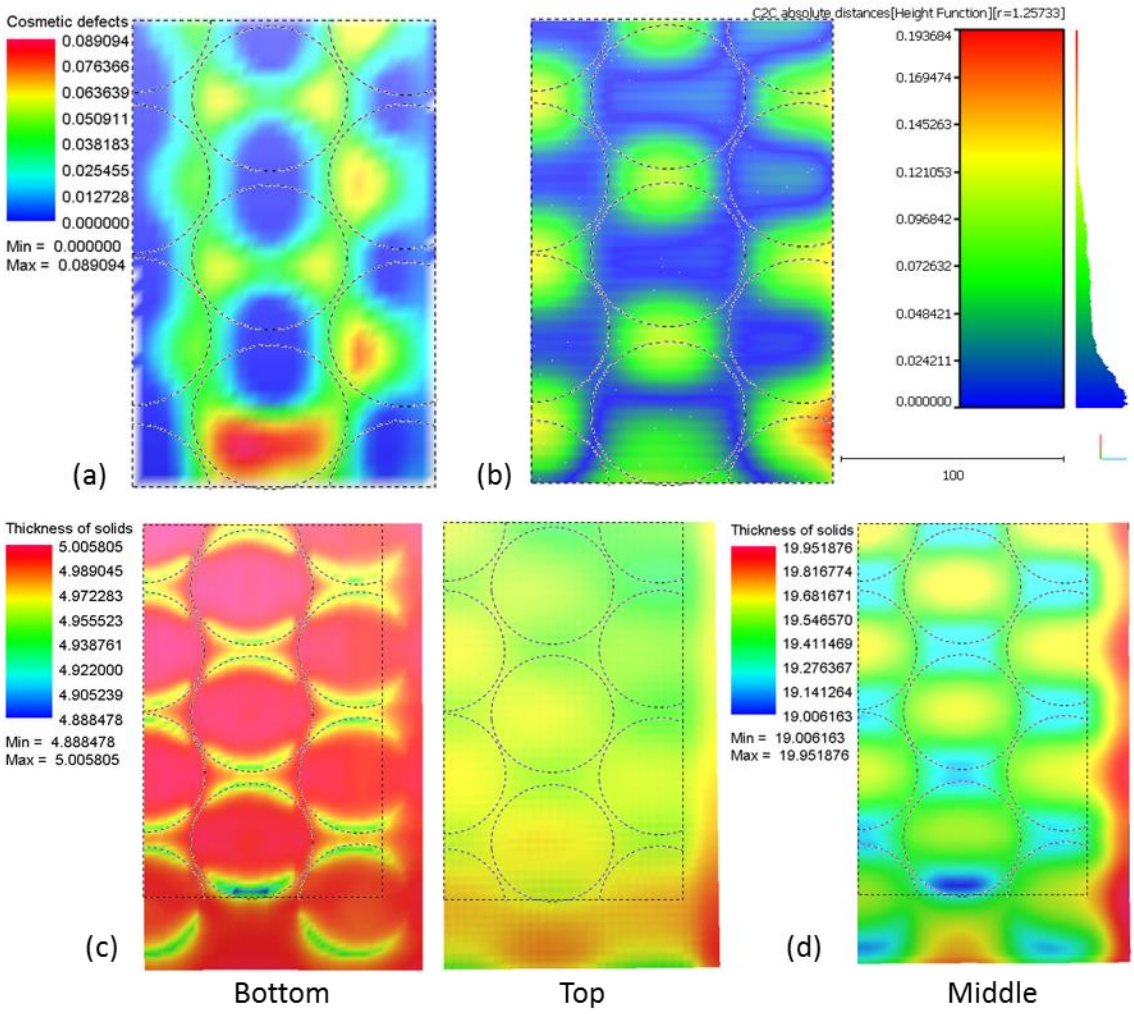

Figure N-7: Cosmetic defect (a) C2C absolute distance (b) Thickness of solids-5 mm (c) and Thickness of solids-20 mm (d) contour maps for the 30 Brown(5)-Green(20)-Brown(5)* simulation

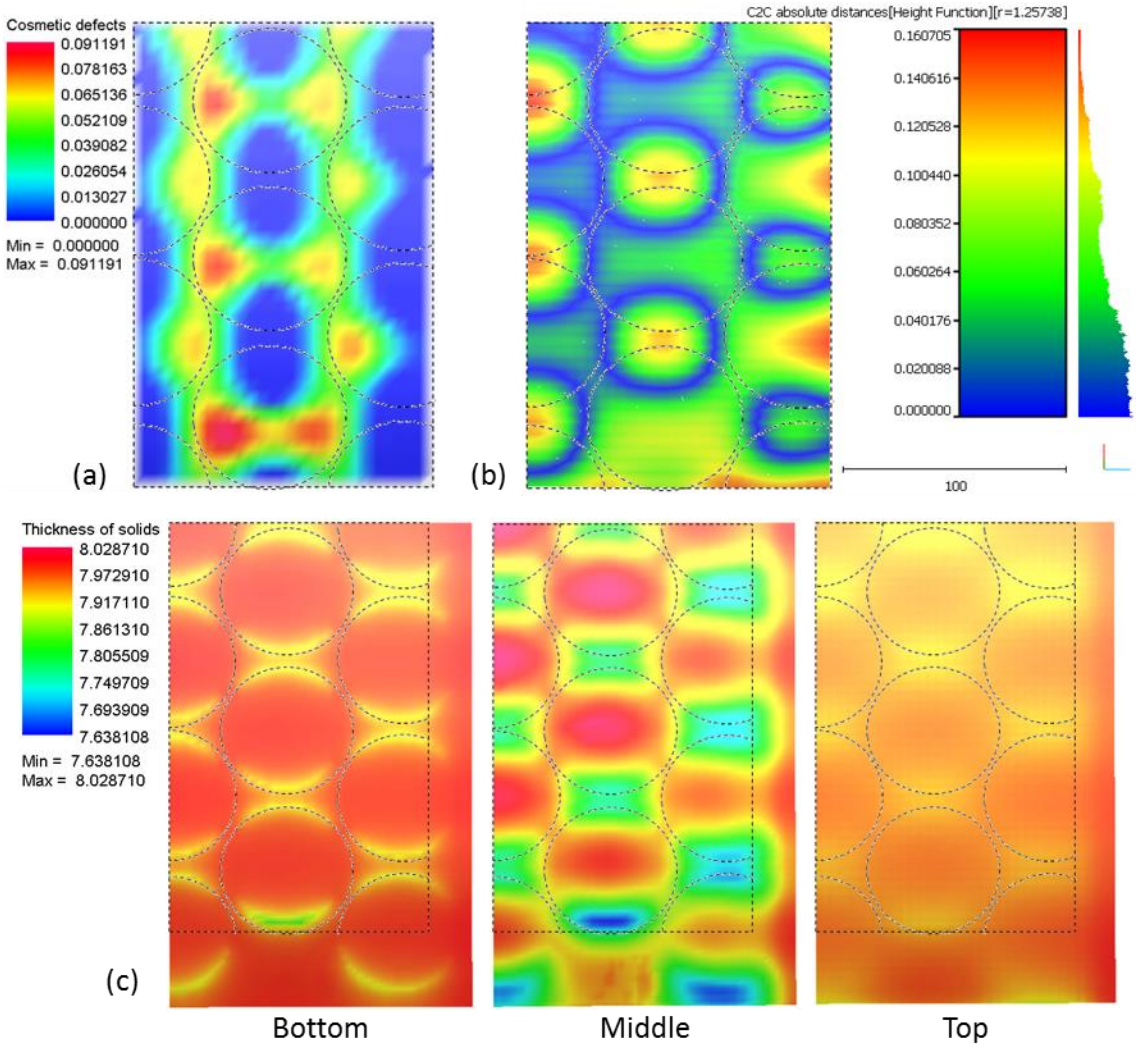

Figure N-8: Cosmetic defect (a) C2C absolute distance (b) and Thickness of solids (c) contour maps for the 24 Brown-Green-Brown simulation

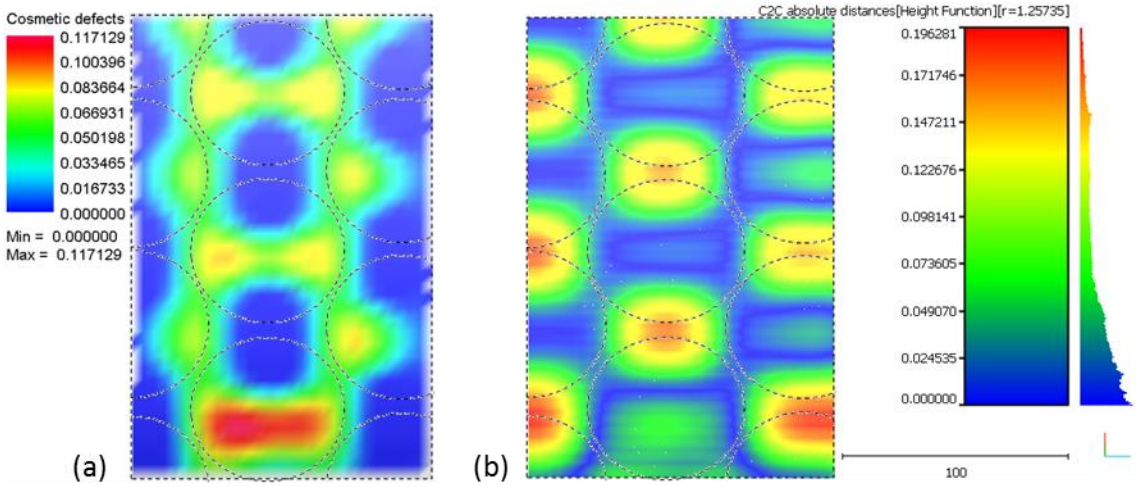

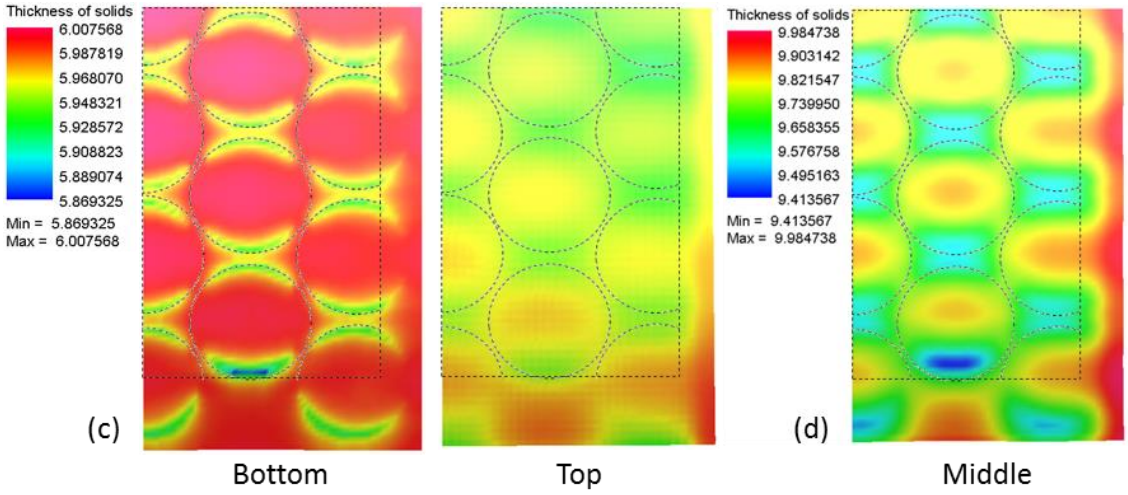

Figure N-9: Cosmetic defect (a) C2C absolute distance (b) Thickness of solids-6 mm (c) and Thickness of solids-10 mm (d) contour maps for the 22 Brown(6)-Green(10)-Brown(6)* simulation

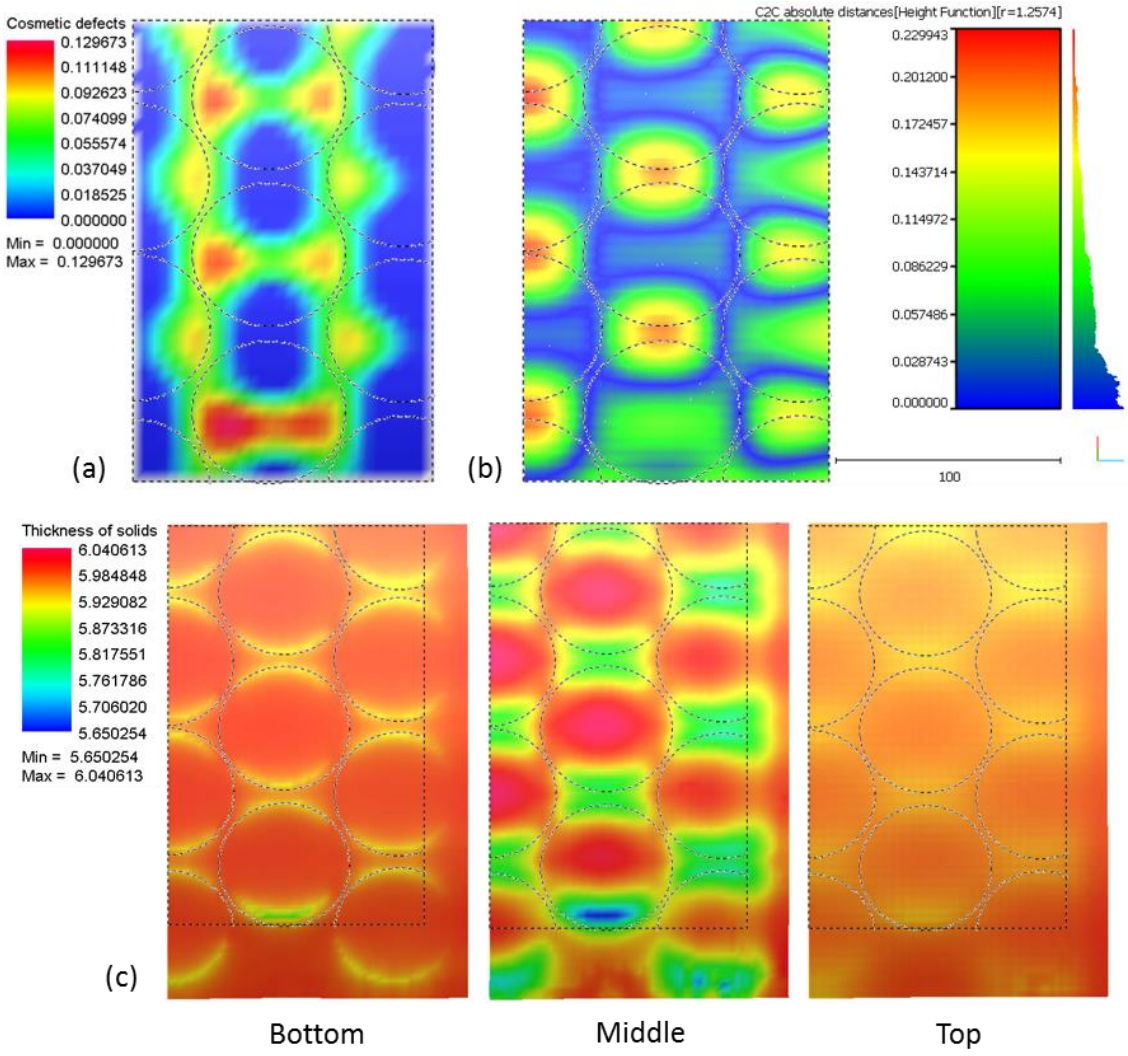

Figure N-10: Cosmetic defect (a) C2C absolute distance (b) and Thickness of solids (c) contour maps for the 18 Brown-Green-Brown simulation

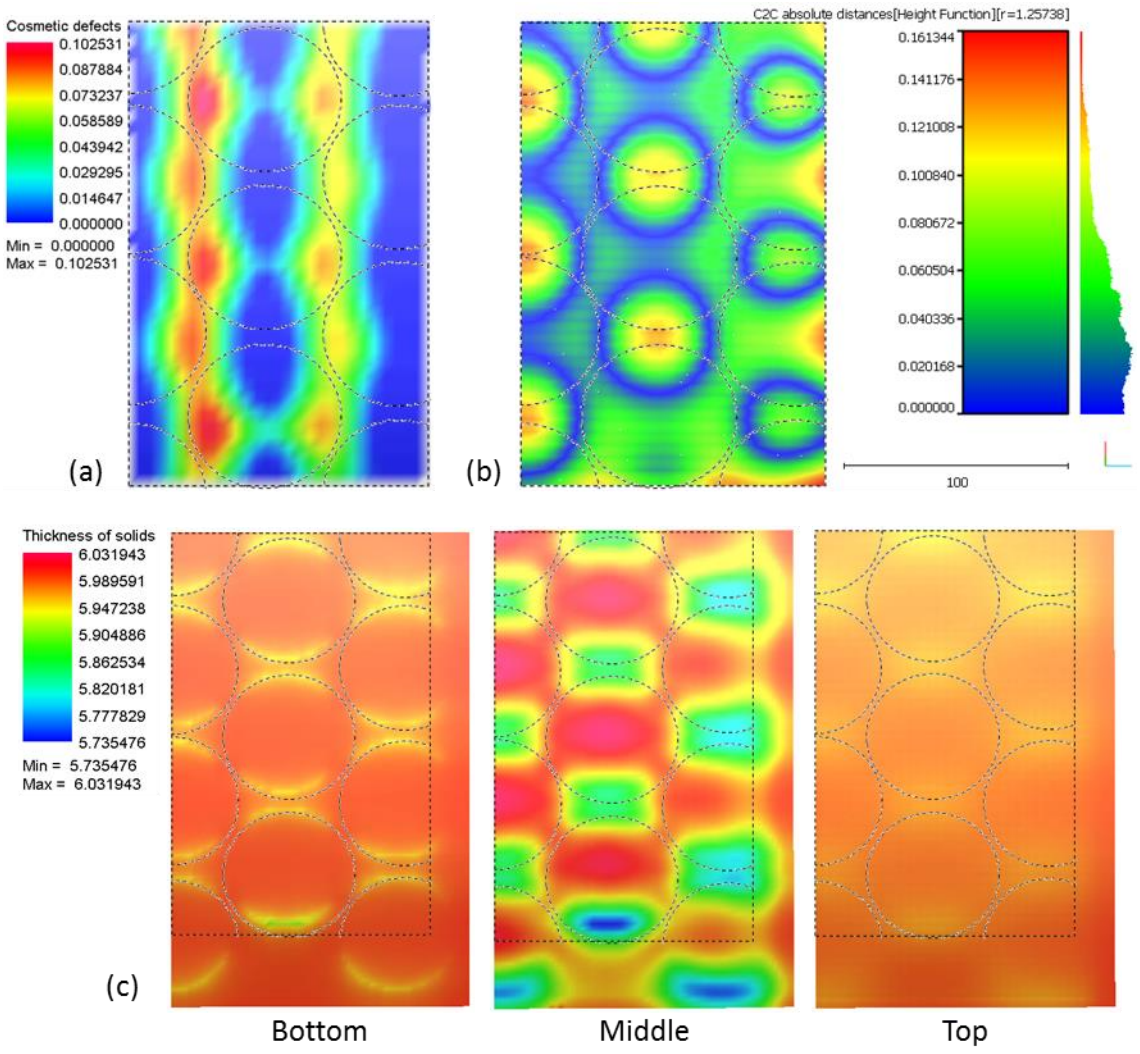

Figure N-11: Cosmetic defect (a) C2C absolute distance (b) and Thickness of solids (c) contour maps for the 18 Grey-Green-Grey* simulation

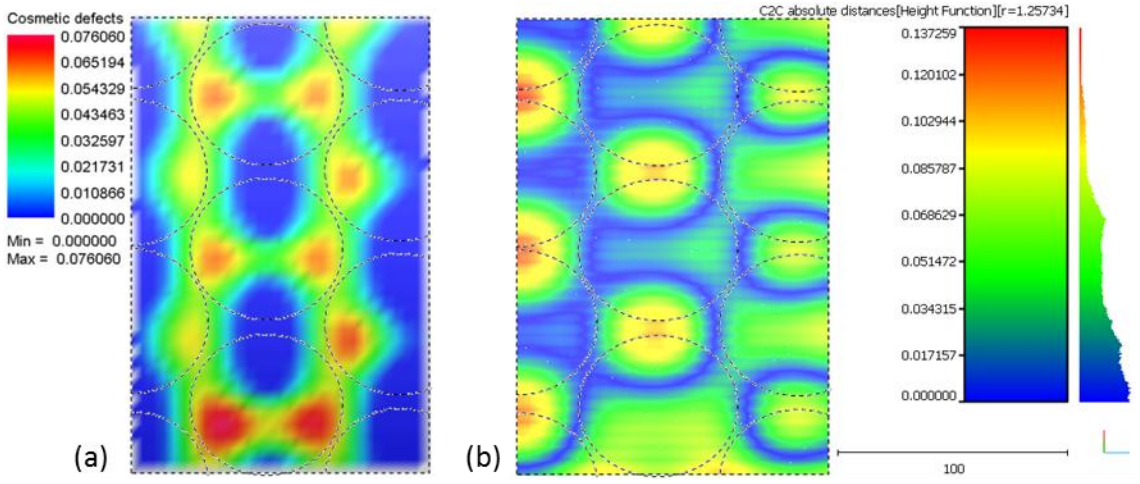

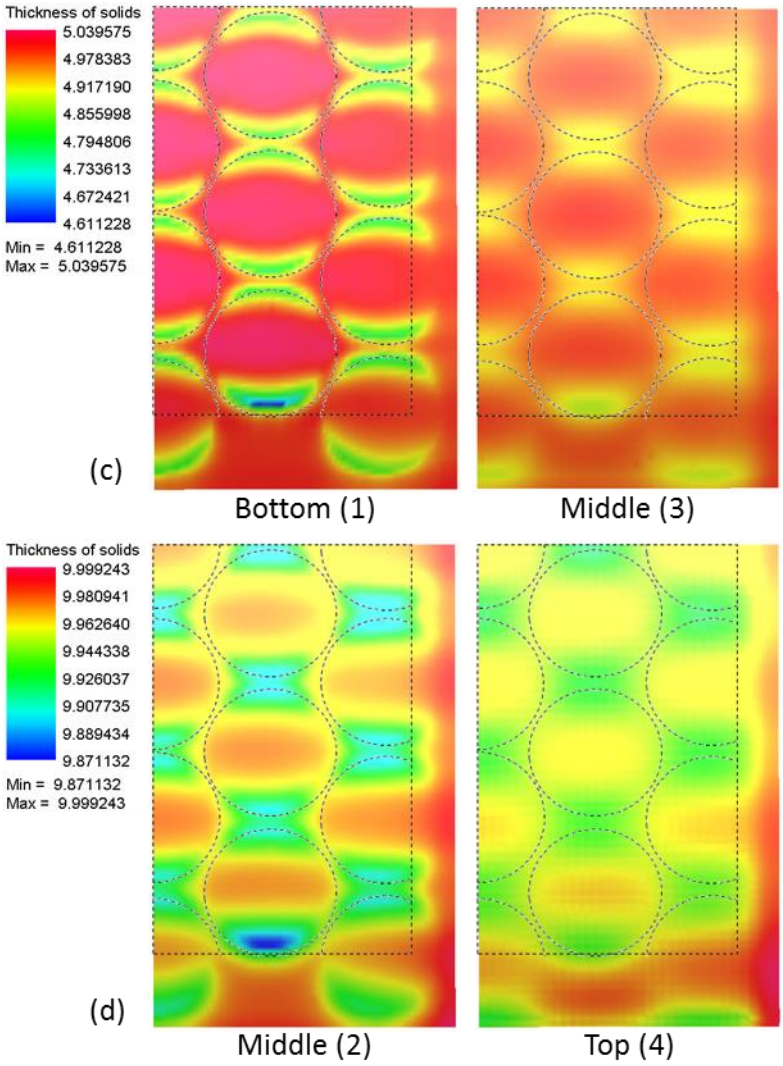

Figure N-12: Cosmetic defect (a) C2C absolute distance (b) Thickness of solids-5 mm (c) and Thickness of solids-10 mm (d) contour maps for the 30 Orange-Brown-Orange-Brown simulation

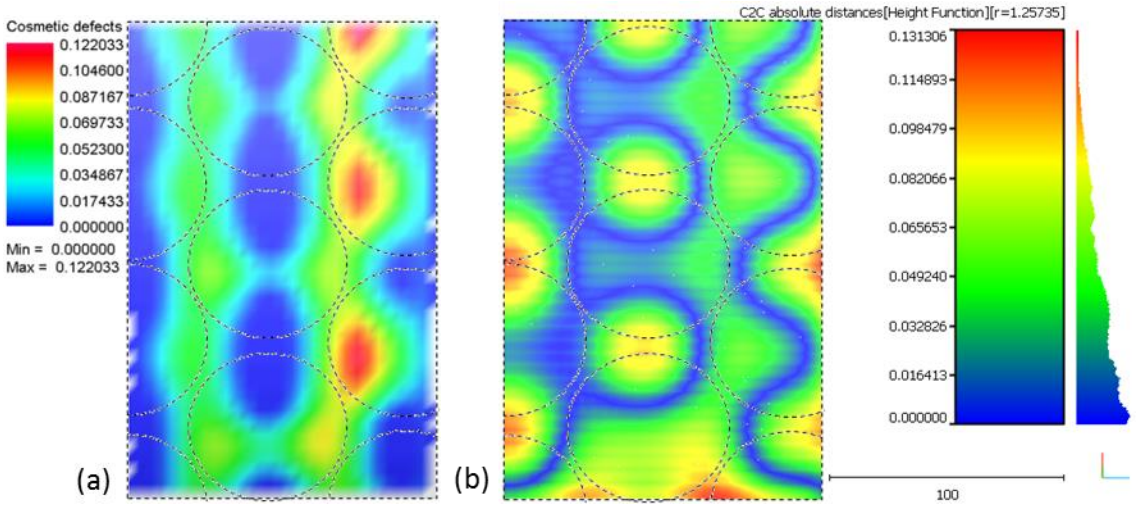

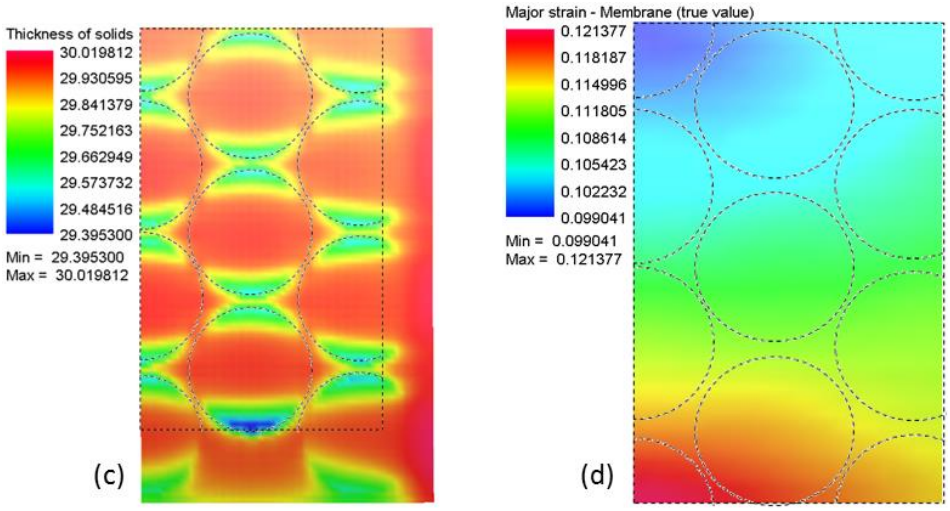

Figure N-13: Cosmetic defect (a) C2C absolute distance (b) Thickness of solids (c) and Major strain (d) contour maps for the 30 Green-Brown-Green-Brown Glued simulation

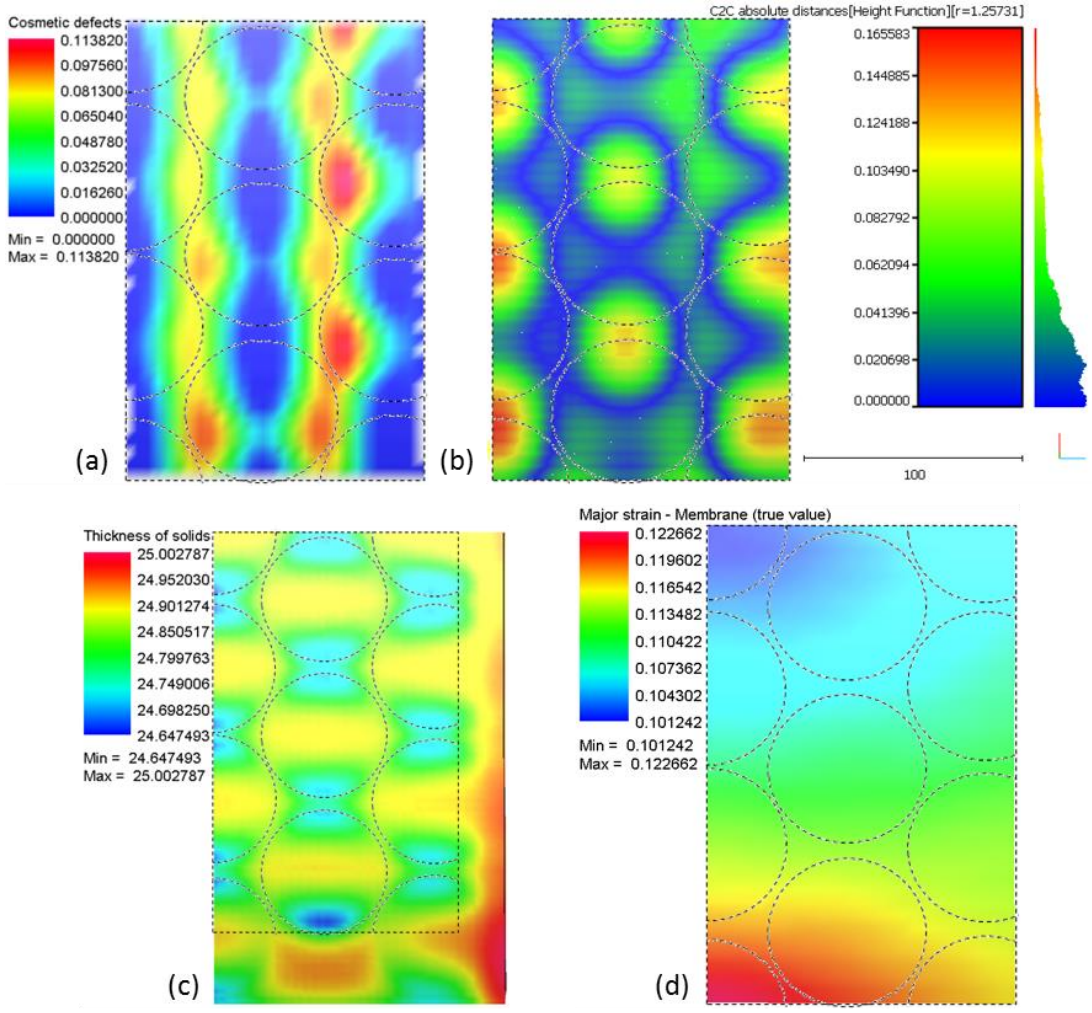

Figure N-14: Cosmetic defect (a) C2C absolute distance (b) Thickness of solids (c) and Major strain (d) contour maps for the 30 Green-Brown-Green-Brown Glued Discs* simulation

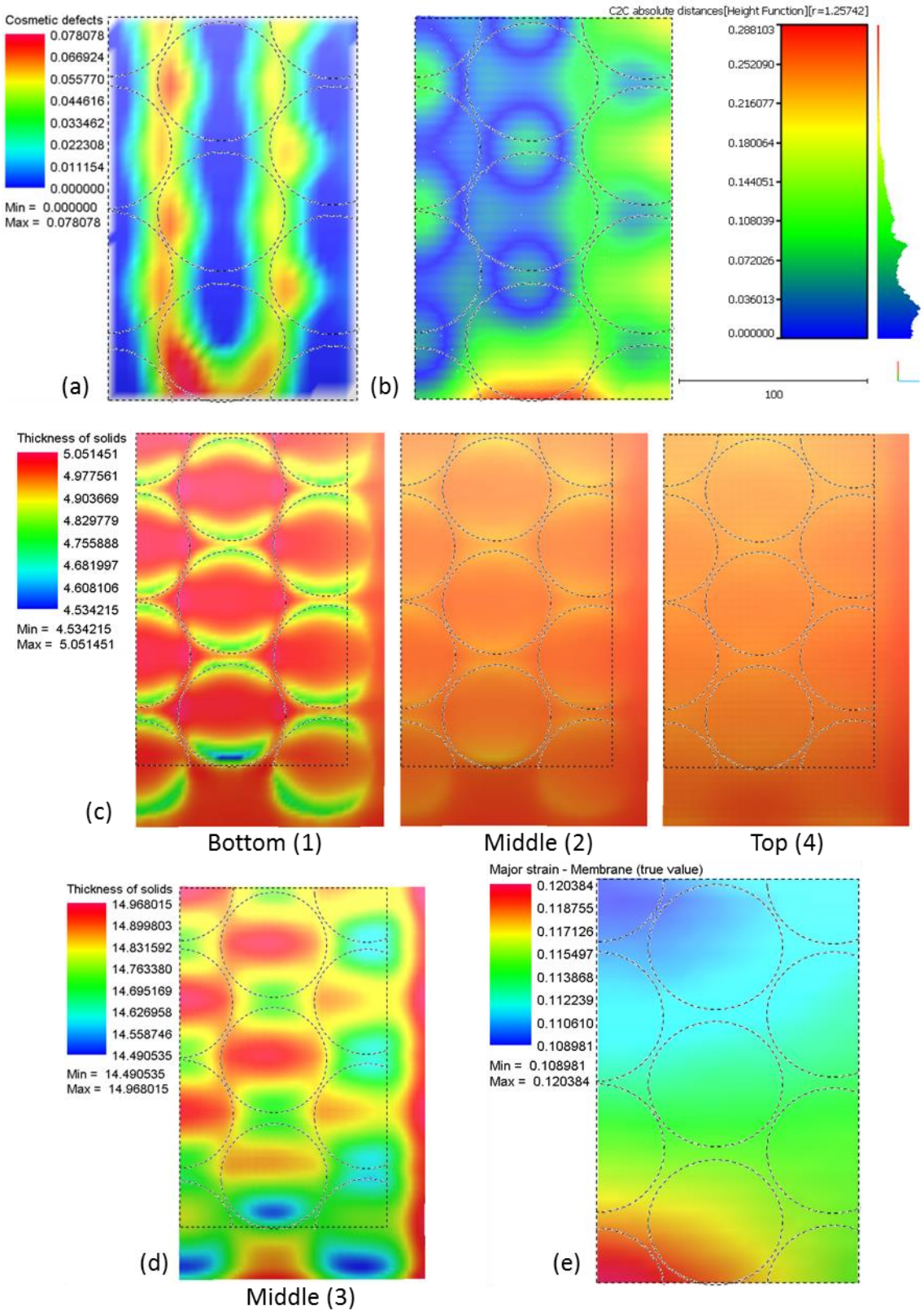

Figure N-15: Cosmetic defect (a) C2C absolute distance (b) Thickness of solids-5 mm (c) Thickness of solids-15 mm (d) and Major strain (e) contour maps for the 30 Green(5)-Brown(5)-Green(15)-Brown(5)* simulation

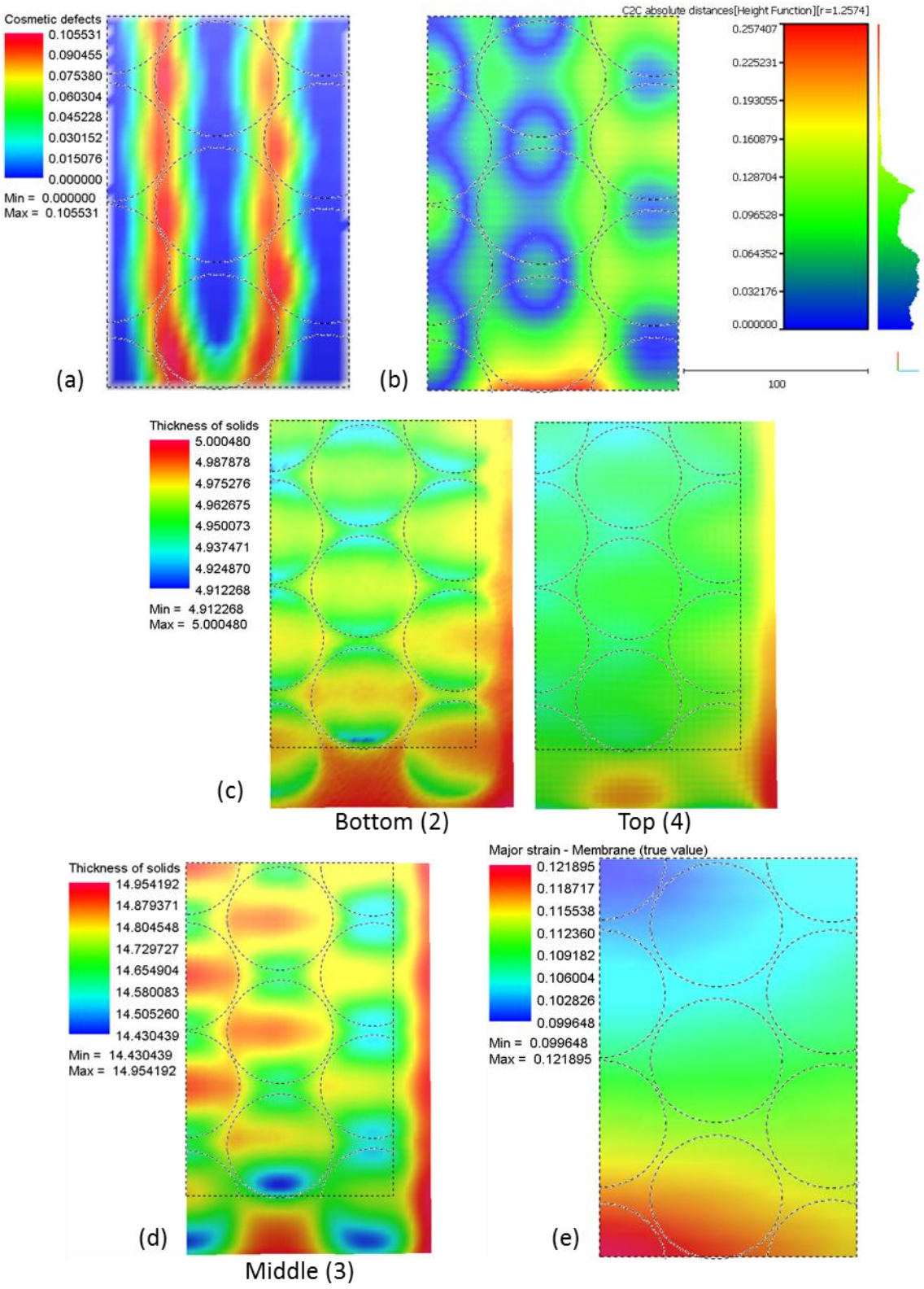

Figure N-16: Cosmetic defect (a) C2C absolute distance (b) Thickness of solids-5 mm (c) Thickness of solids-15 mm (d) and Major strain (e) contour maps for the 30 Green(5)-Brown(5)-Green(15)-Brown(5) Discs* simulation

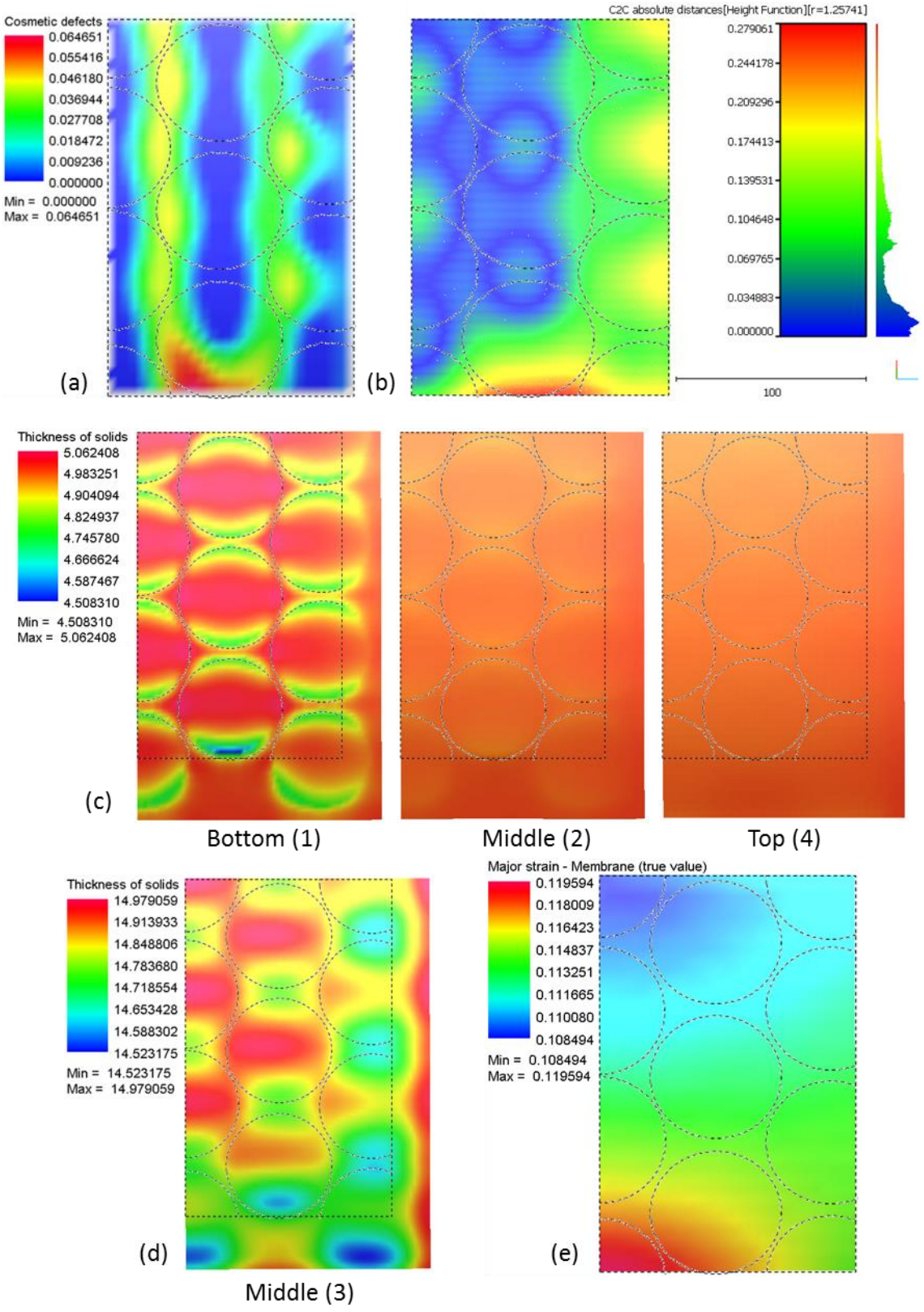

Figure N-17: Cosmetic defect (a) C2C absolute distance (b) Thickness of solids-5 mm (c) Thickness of solids-15 mm (d) and Major strain (e) contour maps for the 30 Green(5)-Grey(5)-Green(15)-Grey(5)* simulation

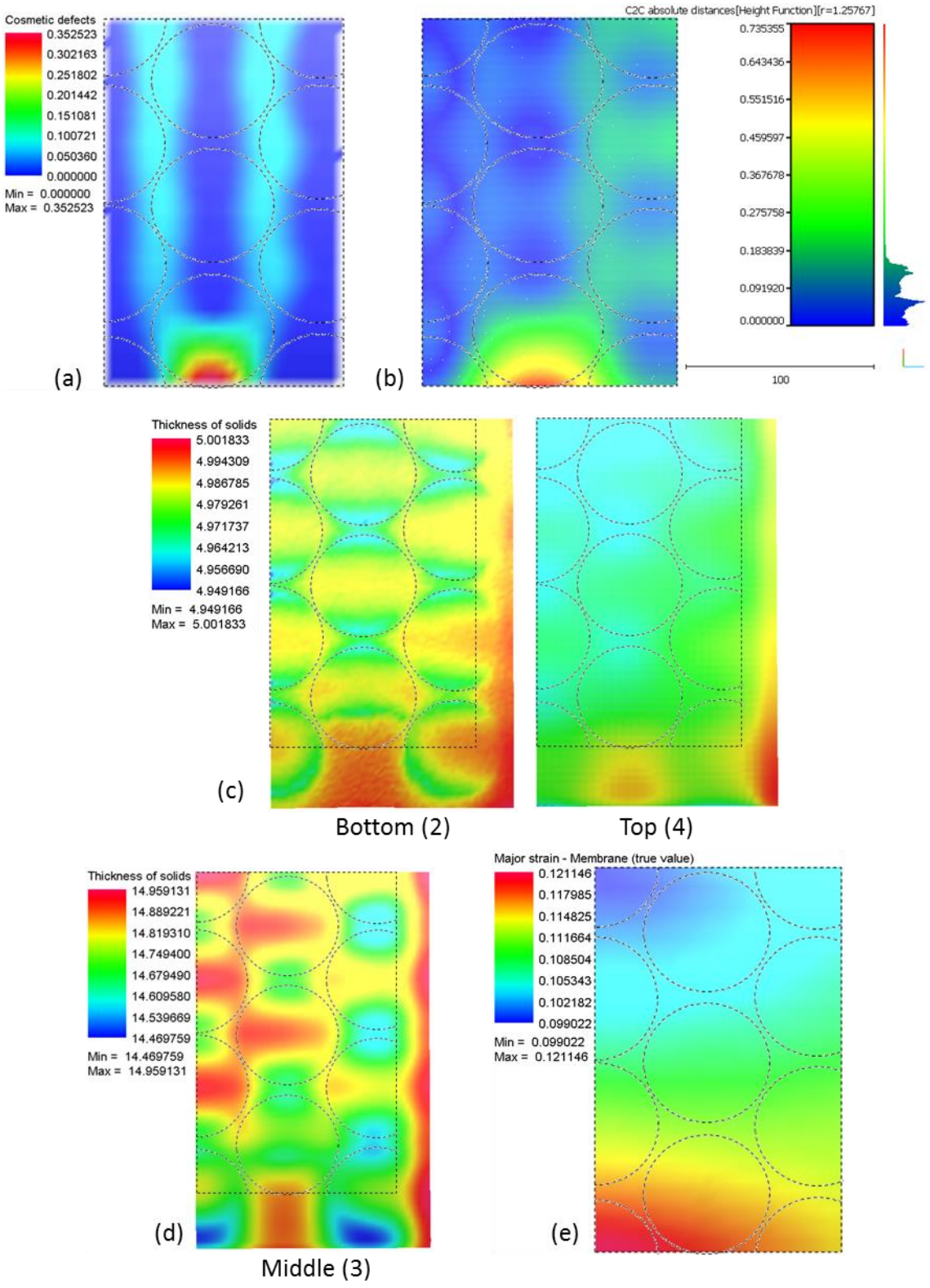

Figure N-18: Cosmetic defect (a) C2C absolute distance (b) Thickness of solids-5 mm (c) Thickness of solids-15 mm (d) and Major strain (e) contour maps for the 30 Green(5)-Grey(5)-Green(15)-Grey(5) Discs* simulation

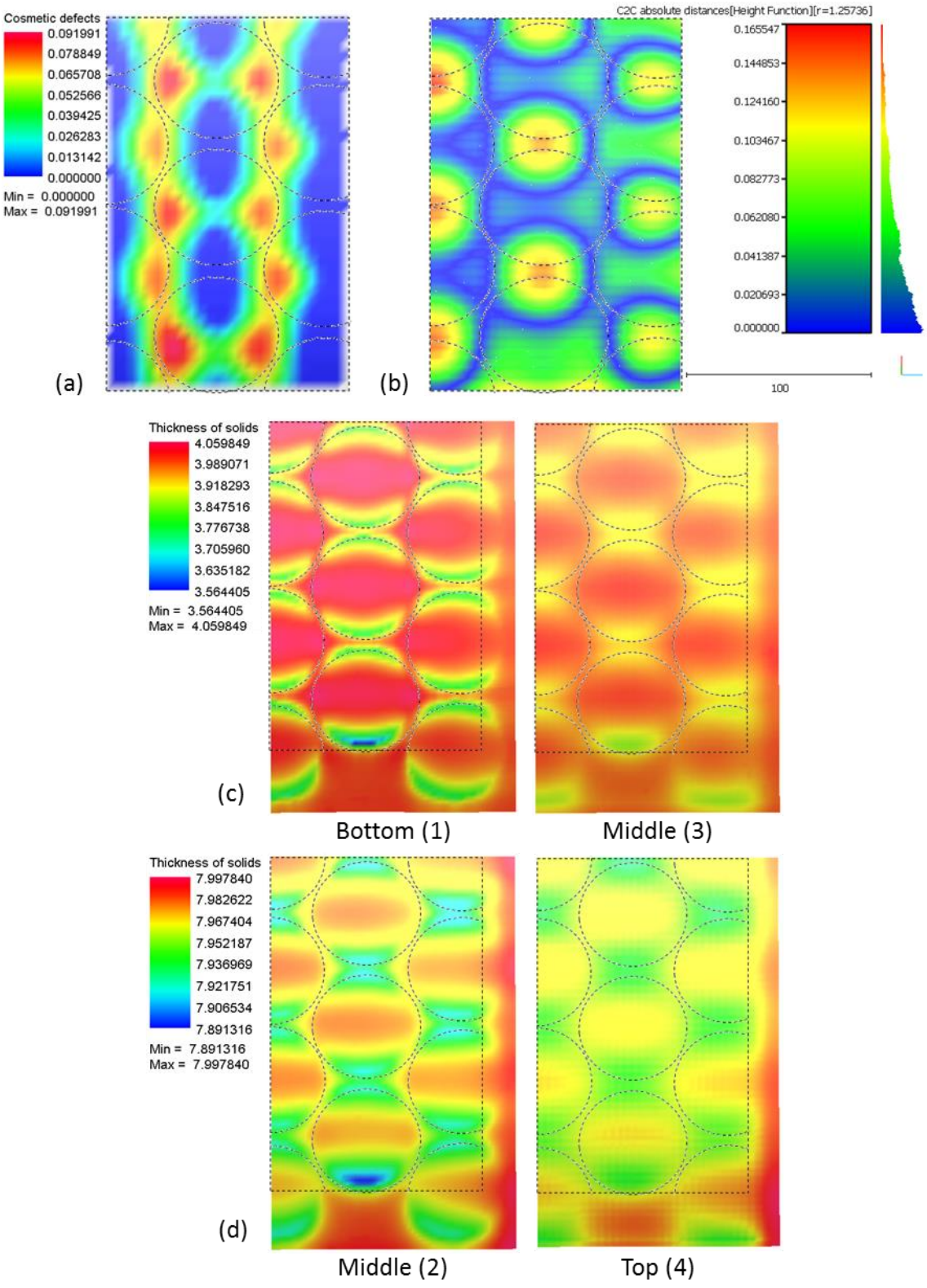

Figure N-19: Cosmetic defect (a) C2C absolute distance (b) Thickness of solids-4 mm (c) and Thickness of solids-8 mm (d) contour maps for the 24 Green-Brown-Green-Brown simulation

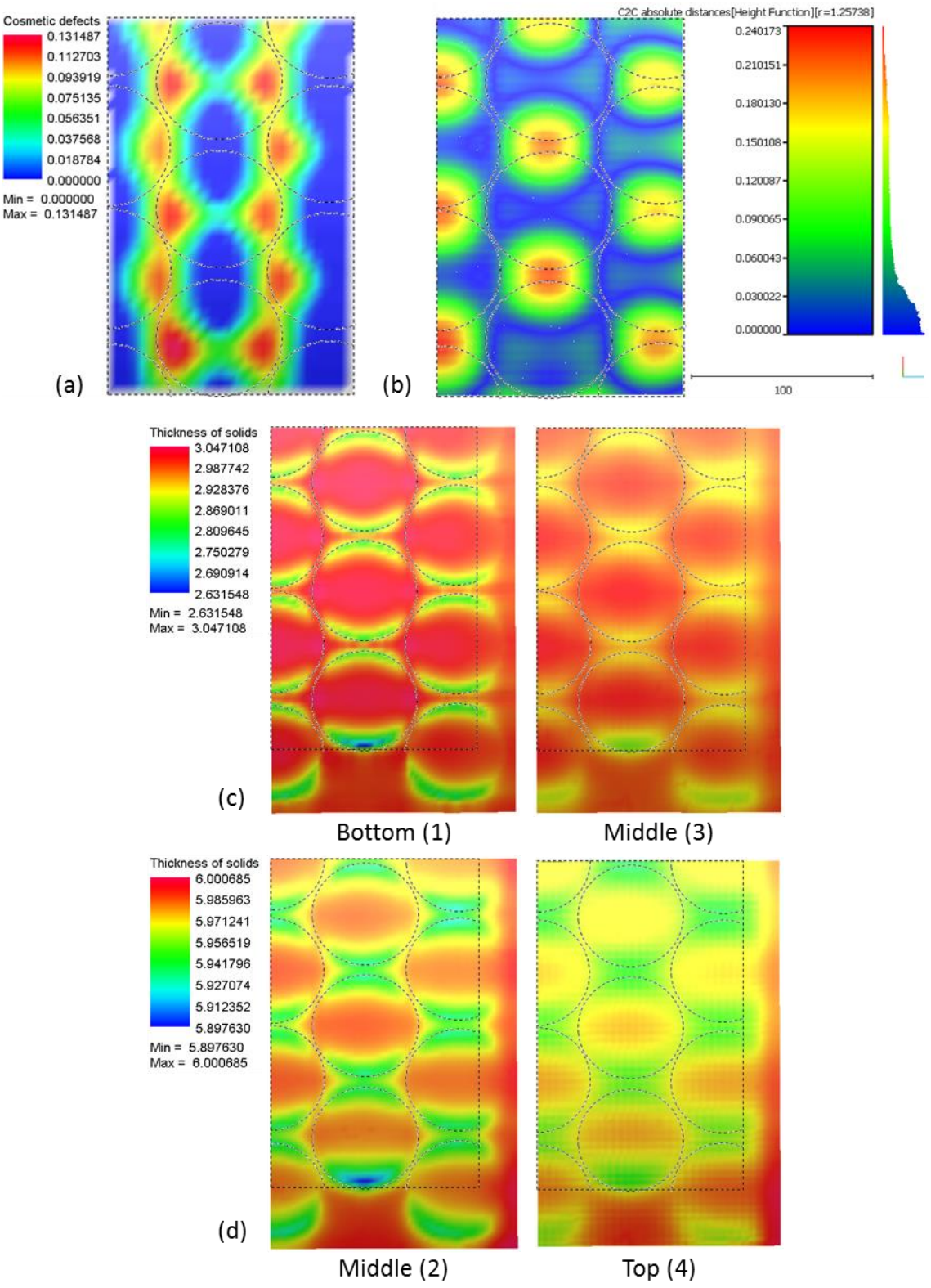

Figure N-20: Cosmetic defect (a) C2C absolute distance (b) Thickness of solids-3 mm (c) and Thickness of solids-6 mm (d) contour maps for the 18 Green-Brown-Green-Brown simulation

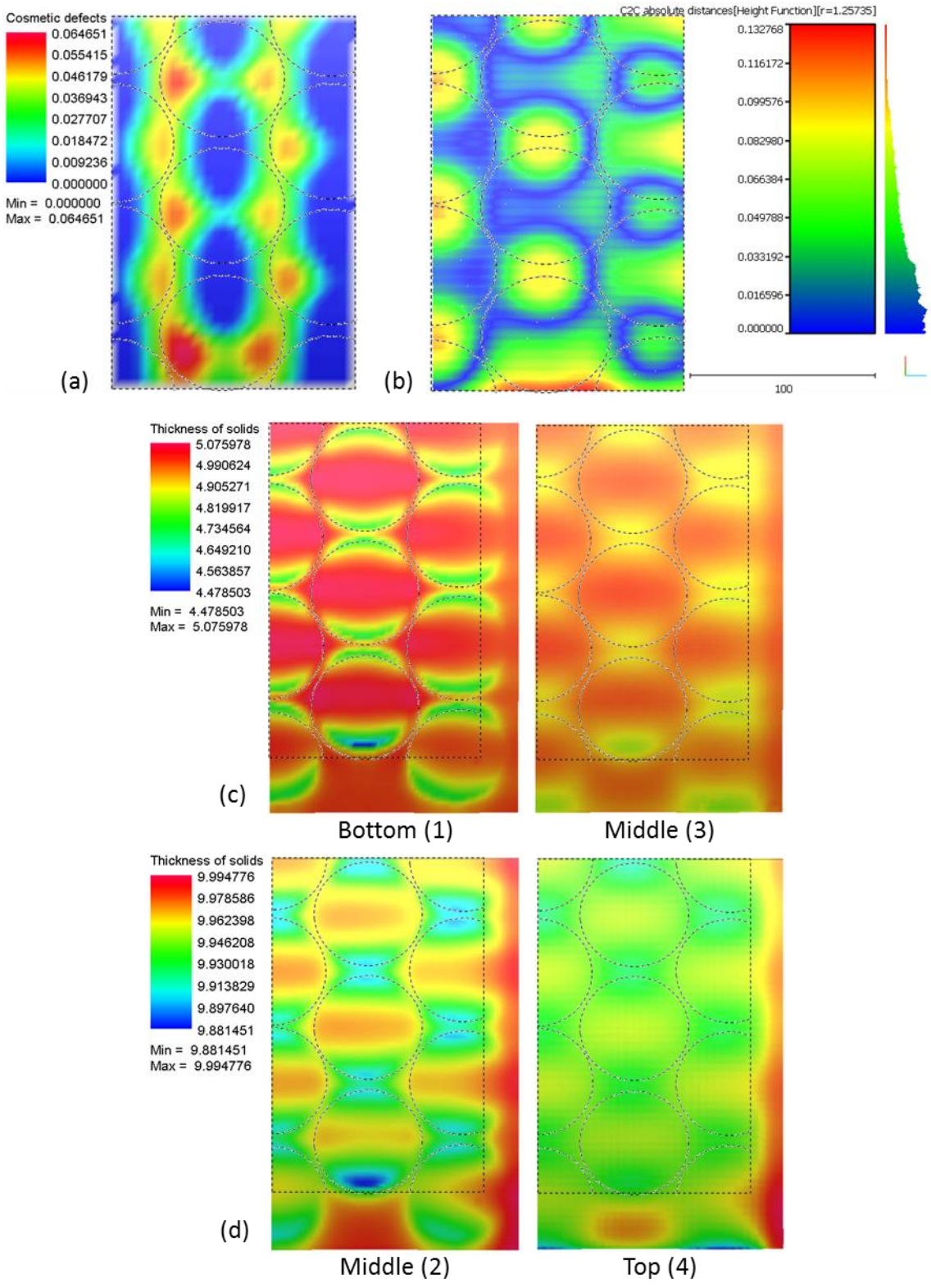

Figure N-21: Cosmetic defect (a) C2C absolute distance (b) Thickness of solids-5 mm (c) and Thickness of solids-10 mm (d) contour maps for the 30 Green-Brown-Green-Brown simulation

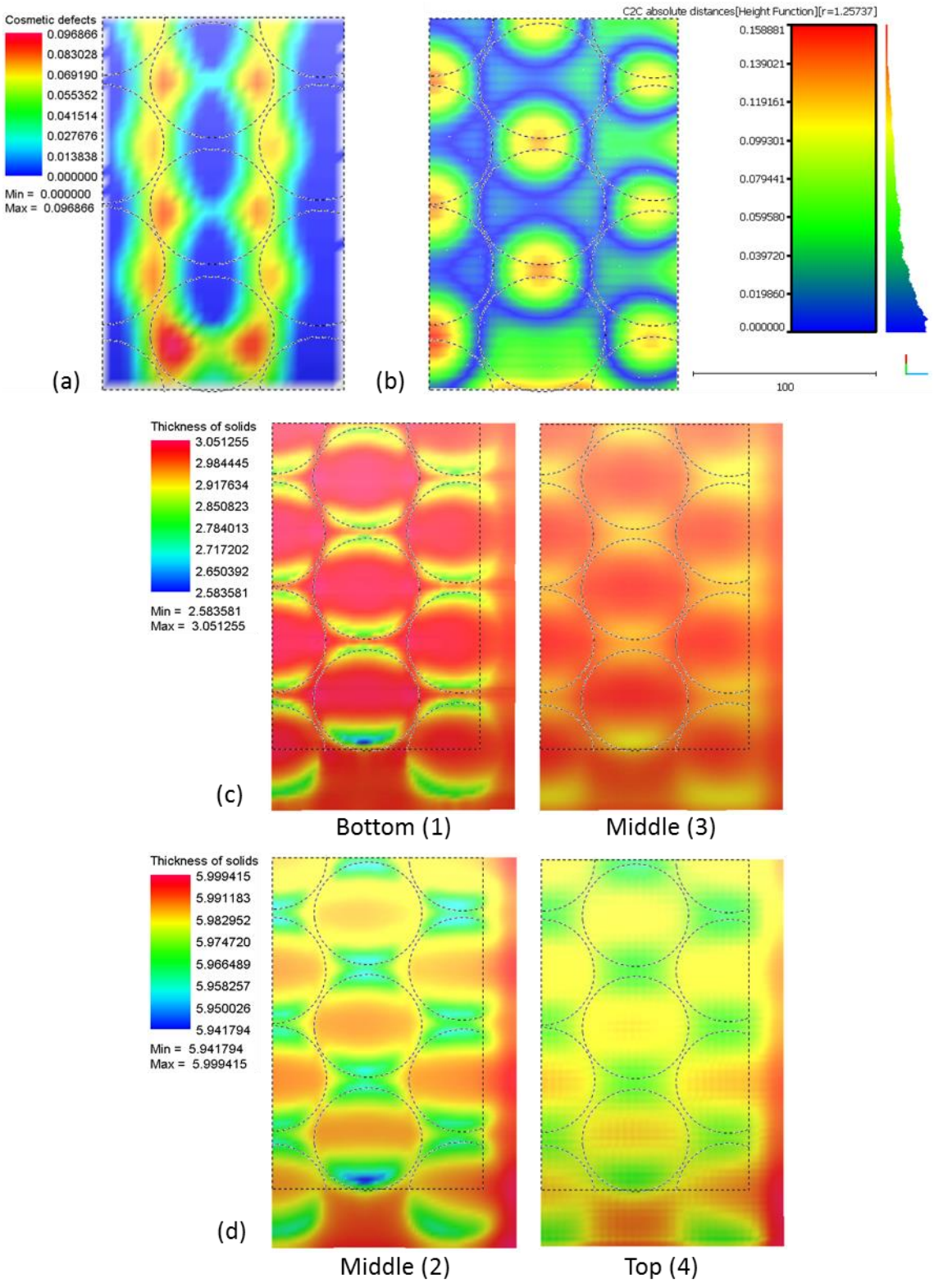

Figure N-22: Cosmetic defect (a) C2C absolute distance (b) Thickness of solids-3 mm (c) and Thickness of solids-6 mm (d) contour maps for the 18 Green-Grey-Green-Grey simulation

Appendix O. Contour Maps Relating to Simulation Validation

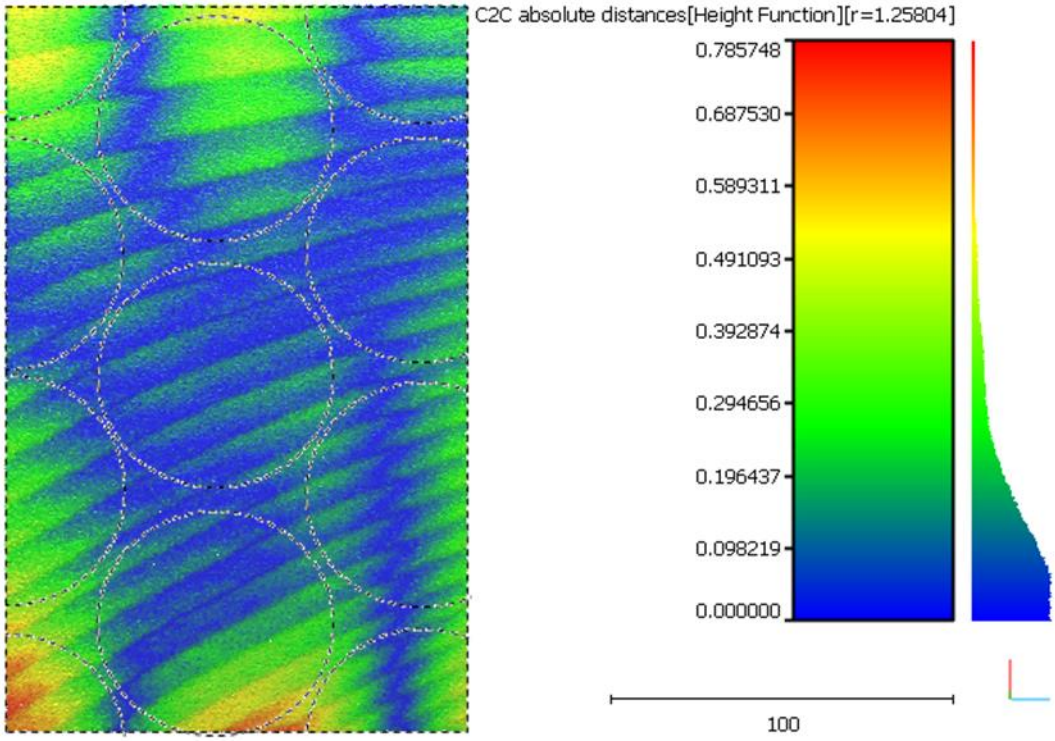

Figure O-1: A contour map showing deviation of the trimmed surface from a scan of the 30 GBGB practical test to that from the corresponding simulation

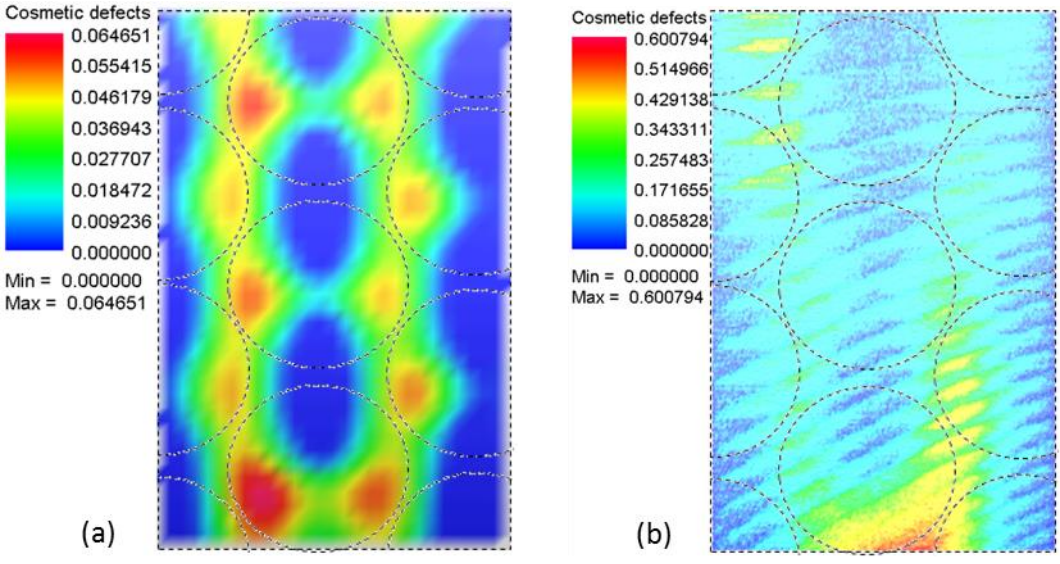

Figure O-2: Contour maps showing a comparison of the stoning defects detected in the 30 GBGB practical test (b) and the corresponding simulation (a)

Appendix P. Additional Contour Maps Relating to Simulations of an Industrial Scale Process

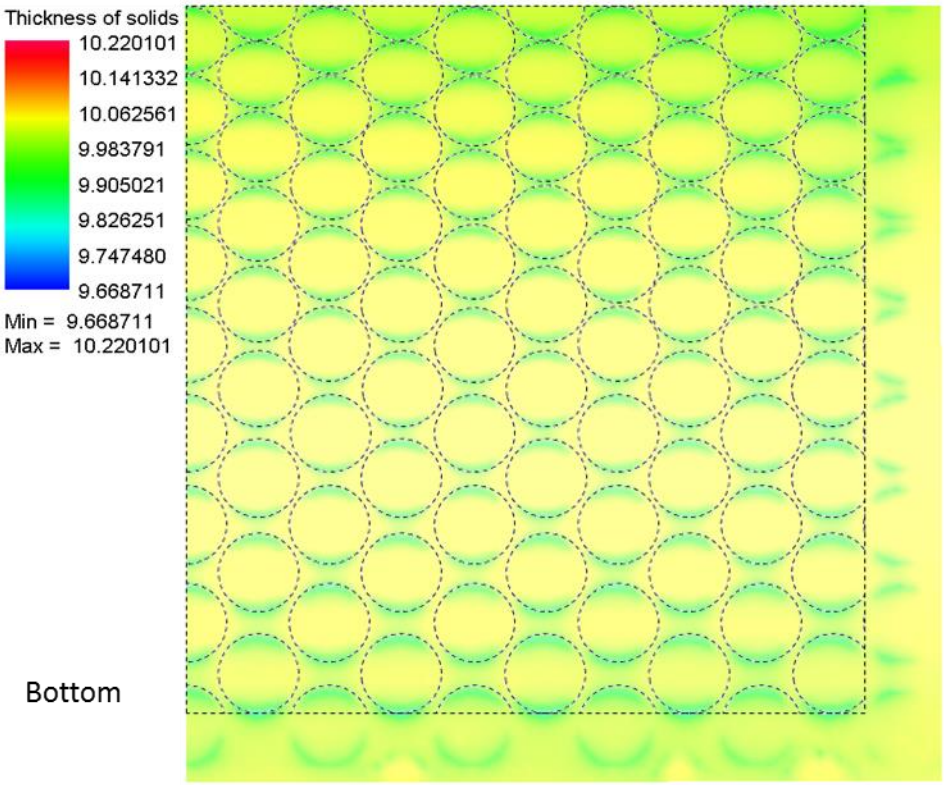

Bottom

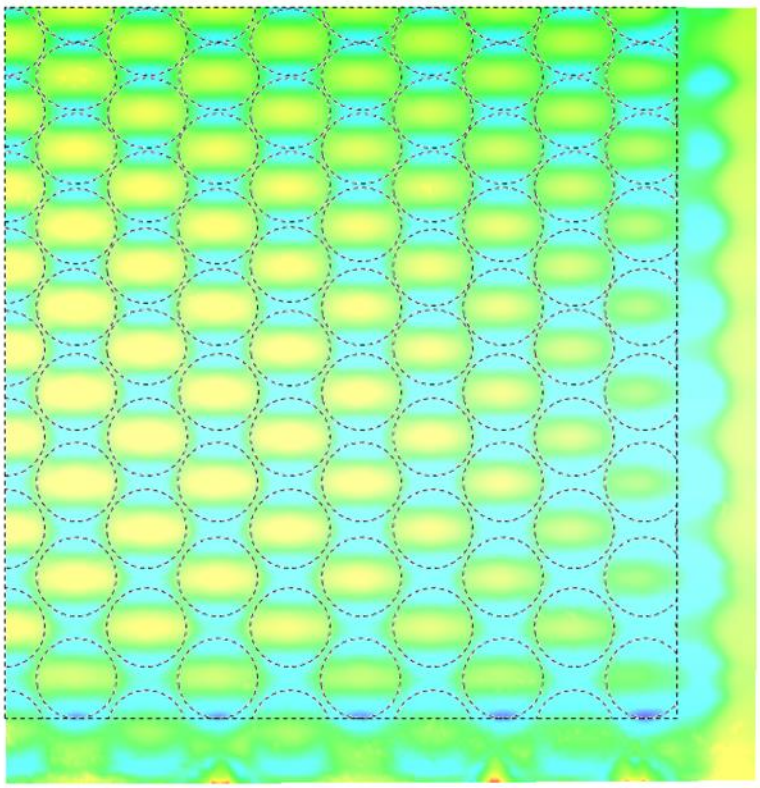

Middle

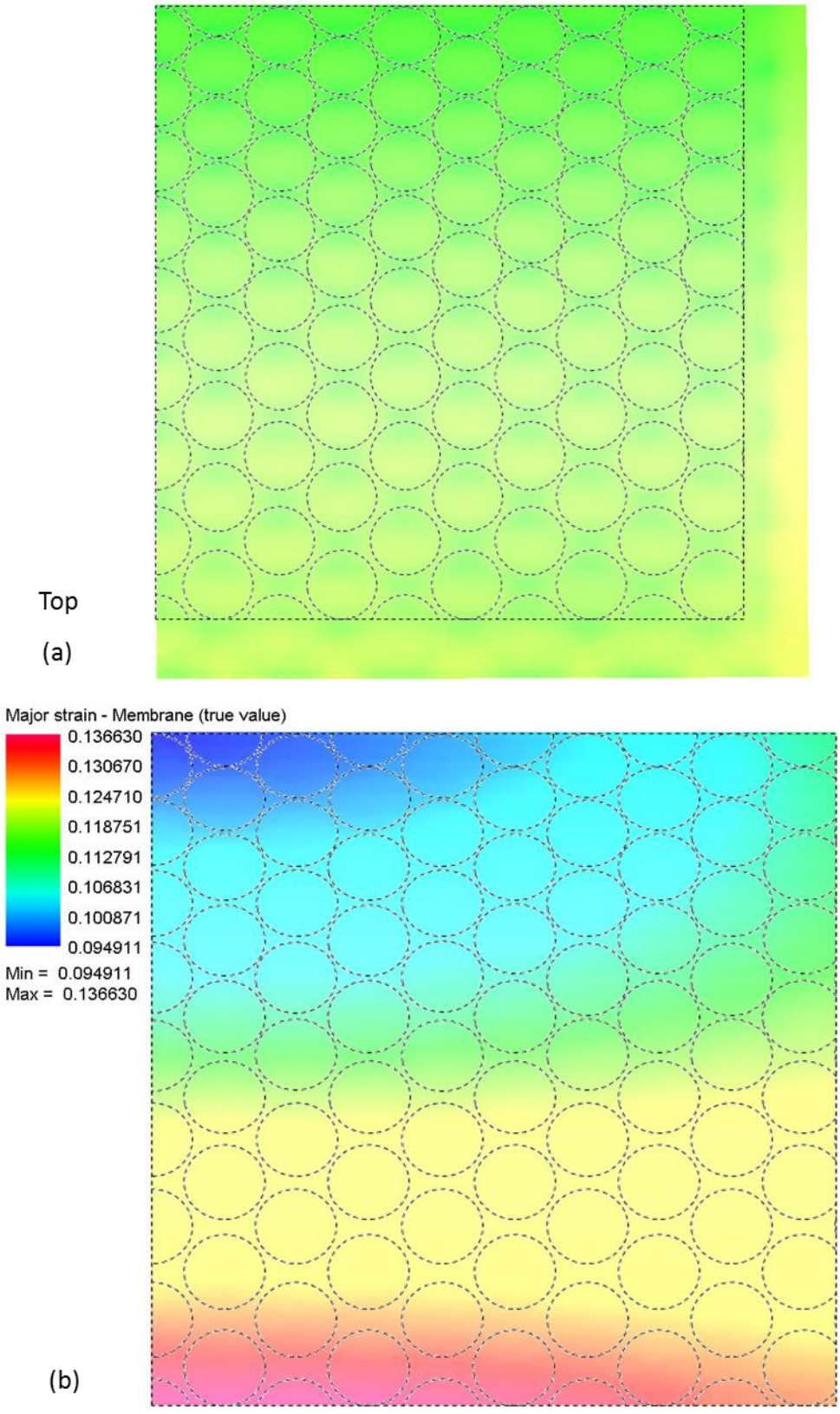

Figure P-1: The Thickness of solids (a) and Major strain (b) contour maps for the 1.2m 30 Brown-Green-Brown simulation

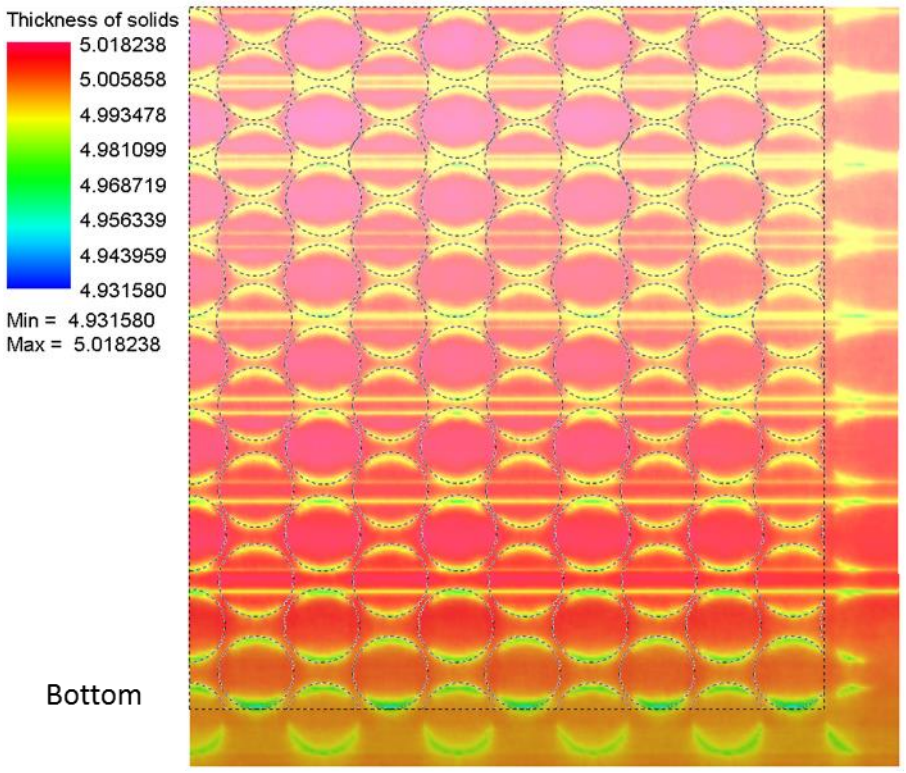
Thickness of solids
5.018238
5.005858
4.993478
4.981099
4.968719
4.956339
4.943959
4.931580
Min = 4.931580
Max = 5.018238
Bottom

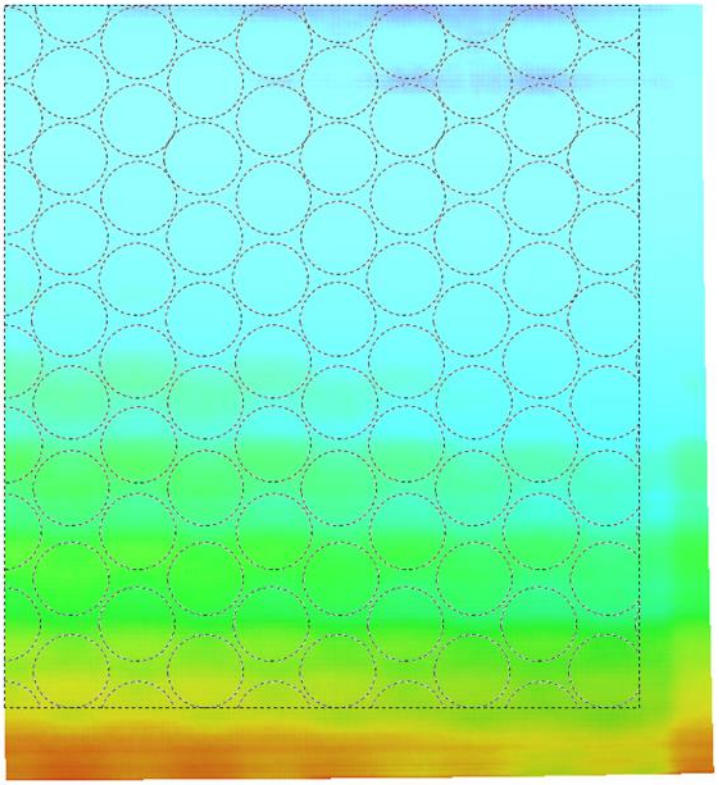
Top

(a)

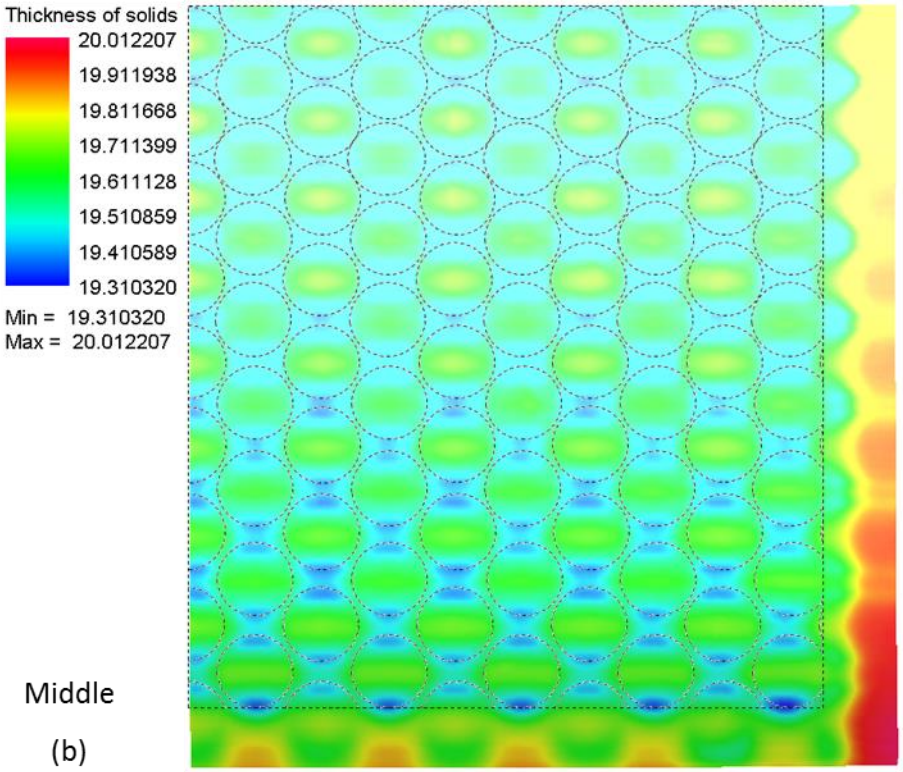

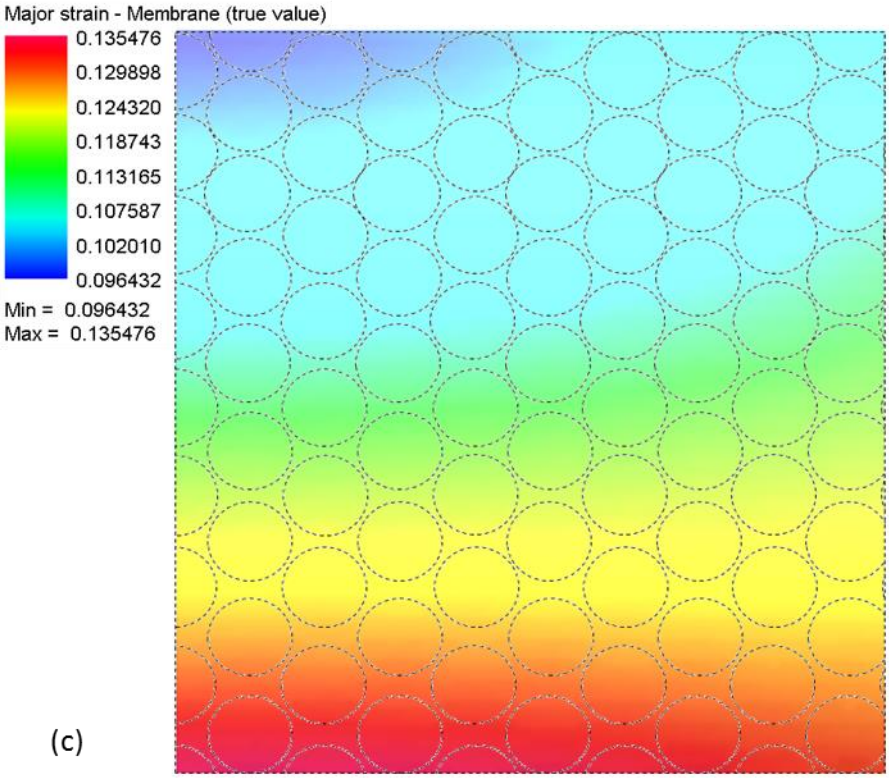

Figure P-2: The Thickness of solids-5 mm (a) Thickness of solids-20 mm (b) and Major strain (c) contour maps for the 1.2m 30 Grey(5)-Green(20)-Grey(5)* simulation

Appendix Q. Possible Solutions to Issues Identified with AMFOR's Preferred Machine Layout

The guide shown in Figure Q-1 is located on the transverse walls of the industrial scale machine. Non-tangential contact is now present in the region between the drum and guide (at the centre of the die). The guide helps to ensure that the blank is in tangential contact with the die and hence the forces on the die are more uniform. This will lead to relatively consistent compression of the interpolator across the width of the die.

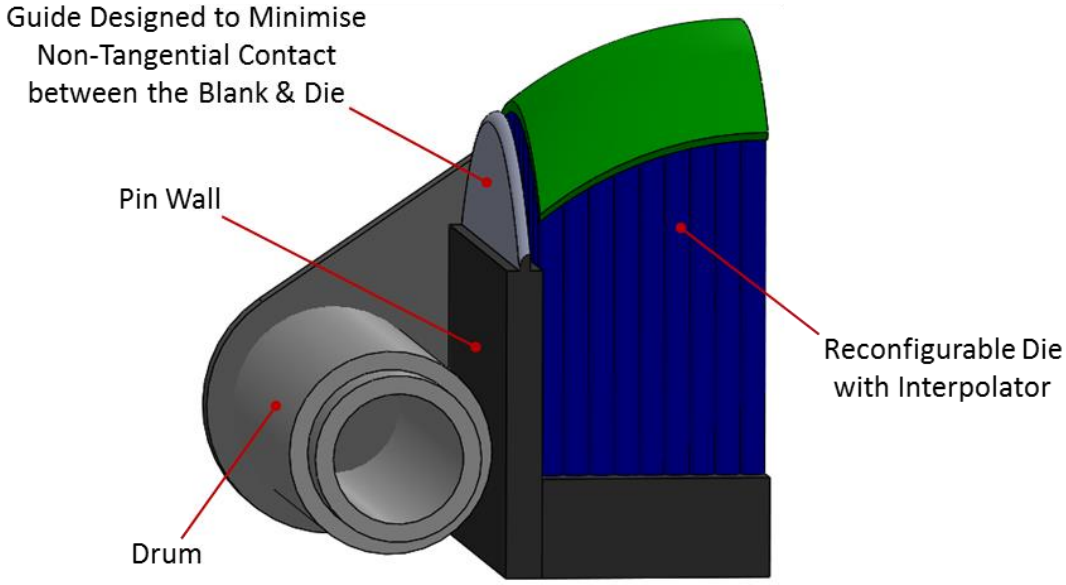

Figure Q-1: Guide fitted to the industrial scale machine to minimise non-tangential contact between the blank and die

A number of sectional drum and grip mechanisms, such as the one shown in Figure Q-2, could be positioned on the industrial scale machine with their slide plates located on runners fixed to its transverse walls. The sectional drum and grip mechanisms would be allowed to rotate about thrust bearings between the pivot brackets and slide plates. This would allow the clamping line to be of similar profile to that present at the die edges and allow the blank to be stretched with more uniform strain across its width. The mechanism shown here employs a motor driven worm gear to rotate the drum, and stretch the blank. It should be noted that the motor shown is selected to fit the component with no calculations concerning the torque

required to stretch a given material carried out at his time. A draft angle has been added to the eccentric cam grip to allow for gripping a part with anticlastic curvature, but the overall height of the mechanism limits the possible degree of curvature in the clamping line.

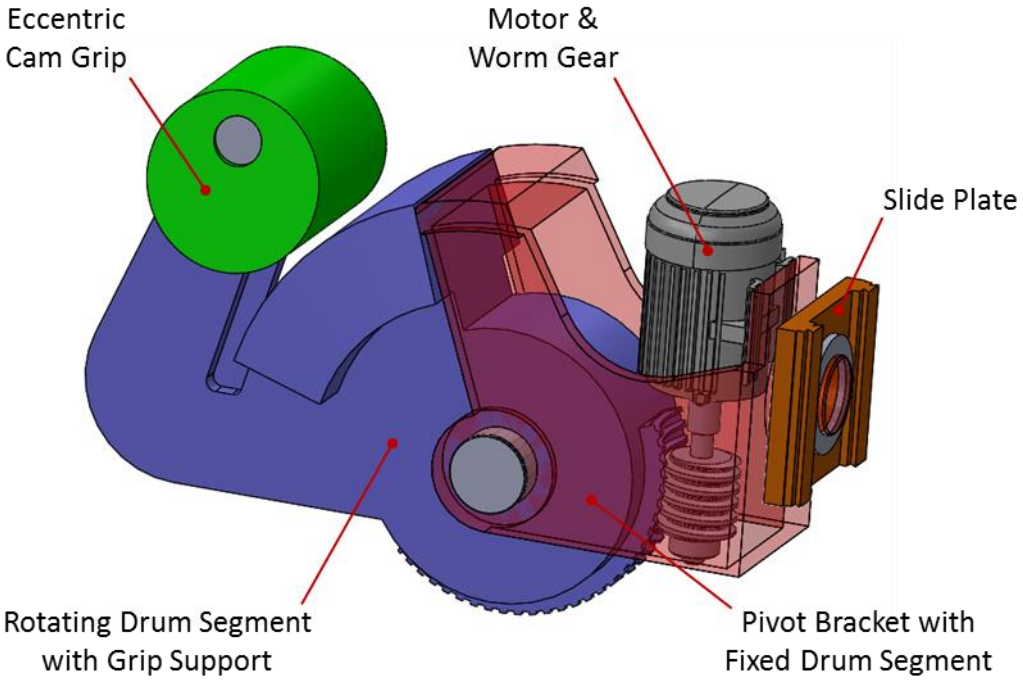

Figure Q-2: A possible design of a sectional drum and grip mechanism

The pin design shown in Figure Q-3 employs a hexagonal sleeve to solve the problem of the element of chaos present when circular pins are stacked against each other. The hexagonal sleeve is located on the pin body via a number of radial bearings. This would still allow for the more cost effective technique of adjusting the heights of pins from above via the hexagonal coupling shown here (or the collet based coupling system outlined in Appendix K. Figure K-3). Five bearings and housings are shown here, but the number, and location, of bearings and housings should be decided upon after further study of the forces transmitted through the die and the load bearing capability of the hexagonal sleeve used.

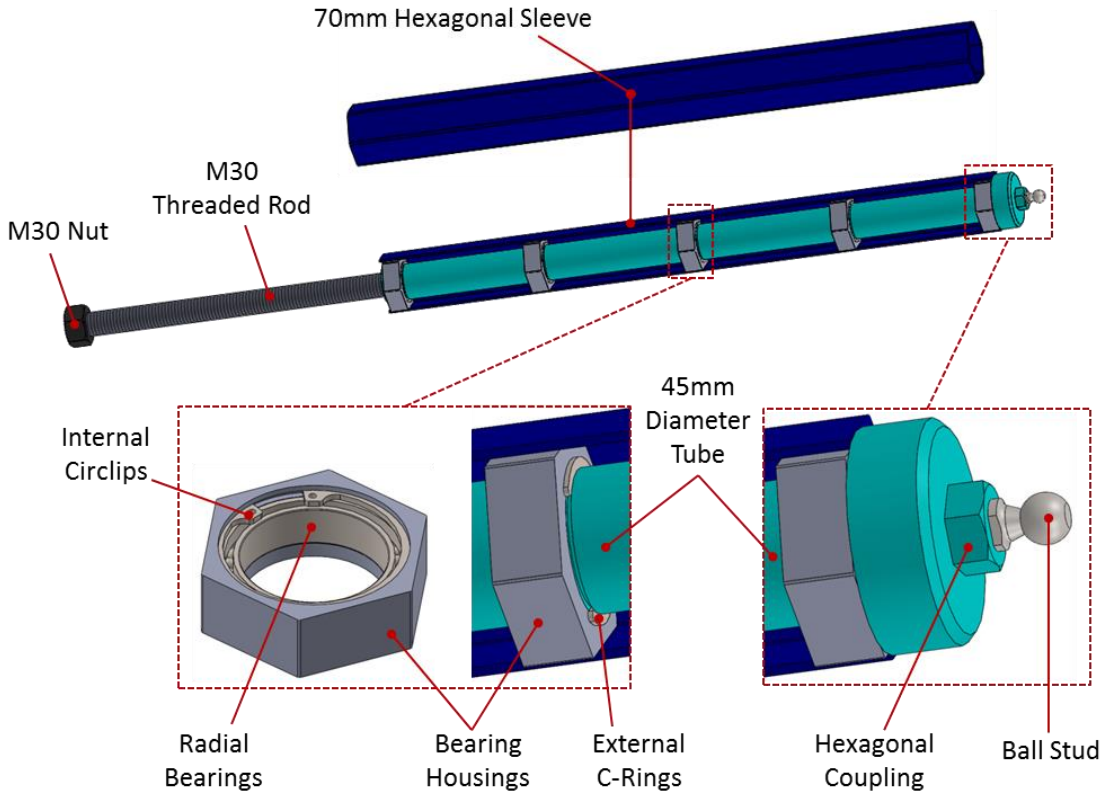

Figure Q-3: A pin design incorporating a hexagonal sleeve

The partial drum shown in Figure Q-4 would allow the drum to be moved closer to the die, and hence, reduce the material wastage on an industrial scale machine employing AMFOR's preferred machine layout.

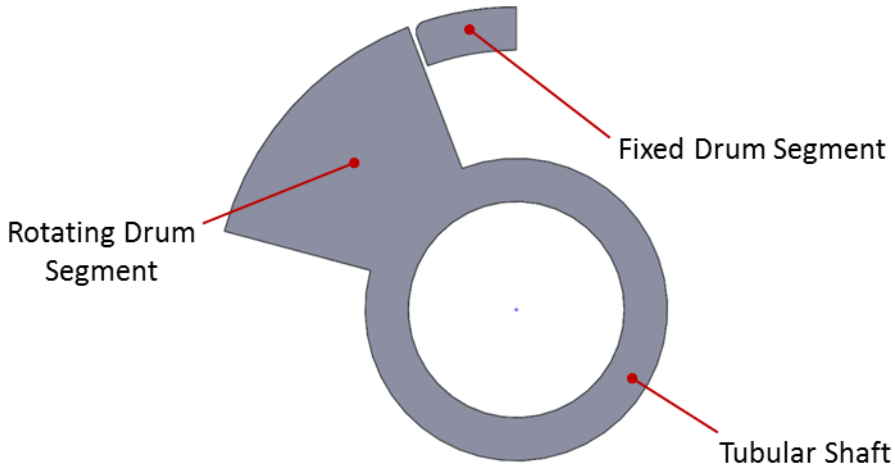

Figure Q-4: A cross-sectional view of a possible partial drum design

References

ASM International, 1988. *ASM Handbook Volume 14 Forming and Forging*. 9th ed. Columbus: ASM International.

Bae, C. et al., 2012. Multi Point Stretch Forming Applied to Curved Hull Plate of Aluminium Ship. *Transactions of the Society of CAD/CAM Engineers,* 17(3), pp. 188-197.

Banabic, D. et al., 2008. *Influence of Constitutive Equations on the Accuracy of Prediction in Sheet Metal Forming Simulation*. Interlaken, Numisheet.

Banabic, D. & Sester, M., 2012. Influence of Material Models on the Accuracy of the Sheet Forming Simulation. *Materials and Manufacturing Processes,* 27(3), pp. 304-308.

Berteau, J., 1994. *Variable Shape Mould*. U.S., Patent No. 5330343A.

Boas, R., 1997. *Sequential Set-up Mechanism Design for a Reconfigurable Sheet Metal Forming Die*. Massachusetts: MIT.

Brown, R., 2006. *Physical Testing of Rubber*. 4th ed. New York: Springer Science & Media, Inc..

Cai, Z., Wang, S., Xu, X. & Li, M., 2009. Numerical simulation for the multi-point stretch forming process of sheet metal. *journal of materials processing technology,* Volume 209, pp. 396-407.

Eigen, G., 1992. *Smoothing Methods for Descrete Die Forming*. Massachusetts: MIT.

ESI Group, 2013. *PAM-STAMP 2G 2012.2 Users Guide*. Paris: ESI.

Feng, W. W. & Hallquist, J. O., 2012. *On Mooney-Rivlin Constants for Elastomers*. Detroit, DYNAlook.

Finckenstein, E. & Kleiner, M., 1991. Flexible Numerically Controlled Tool System for Hydro-Mechanical Deep Drawing. *CIRP Ann,* 40(1), pp. 311-314.

Forsyth, R., 2007. *Active Reconfigurable Stretch Forming.* WO, Patent No. 2007085041A1.

Girardeau-Montaut, D., 2015. *CloudCompare 3D point cloud and mesh processing software.* [Online]
Available at: http://www.danielgm.net/cc/doc/qCC/CloudCompare_v2.6.1_-_User_manual.pdf
[Accessed 10 August 2015].

Haas, E. & Kesselman, M., 1996. *Adjustable Form Die.* WO, Patent No. 9617697A1.

Haas, E., Schwarz, R. & Papazian, J., 2000. *Modularised Reconfigurable Heated Forming Tool.* U.S., Patent No. 6089061A.

Haas, E., Schwarz, R. & Papazian, J., 2002. Design and Test of a Reconfigurable Forming Die. *Journal of Manufacturing Processes,* 4(1), pp. 77-85.

Hardt, D. E., Webb, R. D. & Suh, N., 1982. Sheet Metal Die Forming Using Closed Loop Shape Control. *CIRP Annals, Manufacturing Technology,* 31(1), pp. 165-169.

Hepburn, C., 1992. *Polyurethane Elastomers.* 2nd ed. London: Elsevier Science Publishers Ltd..

Hicks, A., 1961. *Three Dimensional Die.* U.S., Patent No. 2968838A.

Hill, R., 1950. *The Mathematical Theory of Plasticity.* 1st ed. Oxford: Oxford University Press.

Hoffman, P., 1992. *Conformable Tool.* U.S., Patent No. 5168635A.

Hoppel, C. P. R., Bogetti, T. A. & Gillespie, J. W., 1995. Effects of Hydrostatic Pressure on the Mechanical Behaviour of Composite Materials. *Journal of Thermoplastic Composite Materials,* 8(4), pp. 375-409.

Humphrey, D., 1971. *Mould Forming Device.* U.S., Patent No. 3596869A.

Im, Y., Walczyk, D. & Schwarz, R. P. J., 2000. A Comparison of Pin Actuation Schemes for Large-Scale Discrete Dies. *Journal of Manufacturing Processes,* 2(4), pp. 247-257.

Kutt, L. M. et al., 1999. Non Linear Finite Element Analysis of Springback. *Communications in Numerical Methods in Engineering,* Volume 15, pp. 33-42.

Lange, K., 1985. *Handbook of Metal Forming.* 1st ed. Dearborn: Society of Manufacturing Engineers.

Leacock, A., 2006. A mathematical description of orthotropy in sheet metals.. *Journal of the Mechanics and Physics of Solids,* 54(2), pp. 425-444.

Lee, G. & Kim, S., 2012. Case Study of Mass Customisation of Double Curved Metal Facade Panels using a New Hybrid Sheet Metal Processing Technique. *Journal of Construction Engineering and Management,* Volume 138, pp. 1322-1330.

Li, M. et al., 2011. *Study of a Flexible Stretch Forming Machine.* Aachen, Wiley.

Li, M., Liu, Y., Su, S. & Li, G., 1997. Multipoint Forming: A Flexible Manufacturing Method for a 3D Surface Sheet. *Journal of Materials Processing Technology,* Volume 87, pp. 277-280.

Liu, C. et al., 2010. *Digitally Adjustable Tooling Technology for Manufacturing of Aircraft Panels.* Changsha, IEEE.

Liu, C., Li, M. & Fu, W., 2008. Principles and Apparatus of Multi-Point Forming for Sheet Metal. *International Journal of Advanced Manufacturing Technology,* Volume 35, pp. 1227-1233.

Marciniak, Z., Duncan, J. & Hu, S., 2002. *Mechanics of Sheet Metal Forming.* 2 ed. London: Butterworth-Heinemann.

Martin, G. M., Roth, F. L. & Stiehler, R. D., 1957. Behaviour of "Pure Gum" Rubber Vulcanizates in Tension. *Rubber Chemistry and Technology,* 30(3), pp. 876-888.

Munro, C. & Walczyk, D., 2007. Reconfigurable Pin-Type Tooling: A Survey of Prior Art and Reduction to Practice. *Journal of Manufacturing Science and Engineering,* Volume 129, pp. 551-565.

Nakajima, N., 1969. A Newly Developed Technique to Fabricate Complicated Dies and Electrodes With Wires. *Bulletin of JSME,* 12(54), p. 1546–1554..

Oniga, E., Savu, A. & Negrila, A., 2016. The Evaluation of CloudCompare Software in the Process of TLS Point Clouds Registration. *RevCAD Journal of Geodesy and Cadastre,* Volume 12, pp. 117-124.

Papazian, J. et al., 2001. *Pin Tip Assembly in Tooling Apparatus for Forming Honeycomb Cores.* U.S., Patent No. 6209380B1.

Papazian, J. M., 2002. Tools of Change. *Mechanical Engineering CIMA,* Issue Feb.

Paunoiu, V., Cekan, P., Gavan, E. & Nicoara, D., 2008. Numerical Simulation in Multlpoint Forming. *International Journal of Material Forming,* 1(1), pp. 181-184.

Paunoiu, V., Epureanu, A., Nicoara, D. & Ciocan, O., 2006. A Review of Sheet Metal Forming Methods using Reconfigurable Dies. *The Annals of "Dunarea de Jos" University of Galati,* Volume V, pp. 45-50.

Paunoiu, V. et al., 2006. Design of a Experimental Reconfifurable Die for Sheet Metal Forming. *Annals of "Dos de Jos" University of Galati,* Volume V, pp. 60-65.

Paunoiu, V., Oancea, N. & Nicoara, D., 2004. *Simulation of Plate's Deformation Using Discrete Dies.* Columbus, AIP.

Paunoiu, V., Teodor, V. & Epureanu, A., 2009. *Springback Compensation in Reconfigurable Multipoint Forming.* Genoa, WSEAS.

Paunoiu, V., Teodor, V., Gavan, E. & Nicoara, D., 2009. Algorithm for the Geometric Configuration of the Reconfigurable Multipoint Forming Dies. *Annals of "Dunarea de Jos" University of Galati,* Volume V, pp. 95-100.

Paunoiu, V. et al., 2011. Study of the Tool Geometry in Reconfigurable Multipoint Forming. *Annals of "Dunarea de Jos" University of Galati,* Volume V, pp. 139-144.

Pinson, G., 1980. *Apparatus for Forming Sheet Metal.* U.S., Patent No. 4212188A.

Puanoiu, V. & Teodor, V., 2009. Geometric Reconfiguration of the Multipoint Forming Dies using Reverse Engineering. *Annals of "Dunarea de Jos" University of Galati,* Volume V, pp. 415-418.

Qi, H. & Boyce, M., 2005. Stress–Strain Behavior of Thermoplastic Polyurethanes. *Mechanics of Materials,* 37(8), pp. 817-839.

Rao, P. & Dhande, S., 2002. A Flexible Surface Tooling for Sheet Forming Processes: Conceptul Studies and Numerical Simulation. *Journal of Materials Processing Technology,* Volume 124, pp. 133-143.

Rivai, W. et al., 2014. Numerical Simulation of Multipoint Forming with Circular Die Pins in Hexagonal Packing. *Applied Mechanics and Materials,* Volume 493, pp. 589-593.

Schroeder, T. & Stevenson, R., 1998. *Device for Generating a Fixture.* U.S., Patent No. 5738345A.

Schuler GmbH, 1998. *Metal Forming Handbook.* 1st ed. Berlin: Springer.

Seo, Y., Kang, B. & K, j., 2012. Study on Relationship between Design Parameters and Formability in Flexible Stretch Forming Process. *International Journal of Precision Engineering and Manufacturing,* 13(10), pp. 1797-1804.

Socrate, S. & Boyce, M. C., 2001. A Finite Element Based Die Design Algorithm for Sheet Metal Forming on Reconfigurable Tools. *Journal of Engineering Materials and Technology,* Volume 123, pp. 489-495.

Sullivan, E. et al., 2000. *Individual Motor Pin Module.* U.S., Patent No. 6012314A.

The Manufacturing Technology Centre, 1999. *AUTOMAN*. [Online]
Available at: http://www.the-mtc.org/our-projects/automan#top
[Accessed 5 December 2016].

van West, A., 2017. *3ders.org*. [Online]
Available at: http://www.3ders.org/articles/20151209-best-3d-scanners-2015.html
[Accessed 10 February 2017].

Walczyk, D. & Hardt, D., 1998. Design and Analysis of Reconfigurable Discrete Dies for Sheet Metal Forming. *Journal of Manufacturing Systems,* 17(8), pp. 214-224.

Walczyk, D., Lakshmikanthan, J. & Kirk, D., 1998. Development of a Reconfigurable Tool for Forming Aircraft Body Panels. *Journal of Manufacturing Systems,* 17(4), pp. 287-296.

Wang, S., Cai, Z. & Li, M., 2010. Numerical Investigation of the Influence of Punch Element in Multi-Point Stretch Forming Process. *International Journal of Advanced Manufacturing Technology,* Volume 49, pp. 475-483.

Whitacre, F., 1971. *Incremental Die Construction having a Hole Piercing Capability*. U.S., Patent No. 3559450A.

Wolak, J., Bodoia, J. & and Sherrer, R., 1973. A Preliminary Study of an Infinitely Variable Surface Generator and its Application to Die Forming. *Manuf. Eng. Trans.,* Volume 2, pp. 155-160.

Wood, L. A., 1977. Uniaxial Extension and Compression in Stress-Strain Relations of Rubber. *Journal of Research of the National Bureau of Standards,* 82(1), pp. 57-63.